Institute for Risk and Disaster Reduction
University College London

# Deformation-Induced Electric Currents in Marble Under Simulated Crustal Conditions: Non-Extensivity, Superstatistical Dynamics and Implications for Earthquake Hazard

Alexis Cartwright-Taylor


Submitted in accordance with the requirements
for the degree of Doctor of Philosophy at University College London

March 2015

# Declaration

I, Alexis Cartwright-Taylor, confirm that the work presented in this thesis is my own. Where information has been derived from other sources, I confirm that this has been indicated in the thesis.

Signature: _____ Date: _____

# Abstract

This thesis investigates electric current signals generated spontaneously in specimens of Carrara marble during deformation under crustal conditions. It extends previous work where similar currents were observed during uniaxial deformation of marble. Since marble is a non-piezoelectric material, one of the main questions is how these currents are related to the mechanical processes of deformation. Another question is whether it is possible to extract from these electric currents information about the deformation dynamics. This is particularly important in light of recent claims that geoelectric anomalies observed in the field are related to crustal deformation and can inform us about changes in the organisation of the fault network in a focal region prior to an earthquake.

Using an approach that combines rock deformation experiments and statistical modelling, I examine how these electric currents evolve with deformation at the laboratory scale and make several original discoveries regarding their behaviour. To establish how the current signals varied with experimental condition and deformation mechanism across the brittle-ductile transition, I conducted constant strain rate triaxial compression experiments recording differential electric current flow through the rock samples at various confining pressures, strain rates and pore fluid conditions. I acquired mechanical data, ultrasonic velocities and acoustic emissions simultaneously, along with electric current, to constrain the relationship between electric current and deformation. For the statistical modelling, I used a novel entropy-based model, derived from non-extensive statistical mechanics (Tsallis, 1988), which has the advantage of including a term to account for interactions in the system. Interactions are effectively modelled by the non-extensive $q$-parameter.

Small (nanoAmpere) electric currents *are* generated and sustained during deformation under all the conditions tested. Spontaneous electric current flow in the dry samples is seen only in the region of permanent deformation and is due to the presence of localised electric dipoles. This current flow is correlated to the damage induced by microcracking, with a contribution from other intermittent ductile mechanisms. Current and charge densities are consistent with proposed models of crack separation charging and migrating charged edge dislocations. The onset of current flow occurs only after a 10% reduction in P-wave velocity, implying that some degree of crack damage and/or crack connectivity is required before current will flow through the samples. Electric current evolution exhibits three separate time-scales of behaviour, the absolute and fluctuating components of which can be related to the evolution of stress, deformation mechanism, damage and localisation of deformation leading up to sample failure. In the brittle regime, electric current exhibits a precursory change as the stress drop accelerates towards failure, which is particularly distinct at dynamic strain rates.

Current and charge production depend strongly on the experimental conditions. Power-law relationships are seen with confining pressure and strain rate, with the first corresponding to increased microcrack suppression and the second to time-dependent differences in

deformation mechanism across the brittle-ductile transition. In the presence of an ionic pore fluid, electrokinetic effects dominate over solid-state mechanisms but development of the crack network and charge contribution from solid-state deformation processes drive the variation in electrokinetic parameters.

Current flow in the dry samples is approximately proportional to stress within 90% of peak stress. In the fluid-saturated samples, proportionality holds from 40% peak stress, with a significant increase in the rate of current production from 90% peak stress, and is associated with fluid flow during dilatancy. This proportionality, together with the power-law relationship between current and strain rate is reminiscent of power-law creep, where deformation rate varies as a power-law function of stress, and suggests that the electric signals could be used as a proxy for stress.

High frequency fluctuations in the electric current signal can be described by 'fat-tailed' $q$-Gaussian statistics, consistent with an origin in non-extensive statistical mechanics. These distributions can be explained as arising from superstatistical dynamics (Beck, 2001; Beck and Cohen, 2003), i.e., the superposition of local mechanical relaxations in the presence of a slowly varying driving force. The macroscopic distribution parameters provide an excellent prediction of the experimentally observed mean energy dissipation rate of the system (as modelled by the superstatistical $\beta$-parameter), particularly at slow strain rates. Furthermore, characteristic $q$-values are obtained for different deformation regimes across the brittle-ductile transition, and the evolution of $q$ during deformation reveals a two-stage precursory anomaly prior to sample failure, consistent with the stress intensity evolution as modelled from fracture mechanics. These findings indicate that the dynamics of rock deformation are reflected in the statistical properties of the recorded electric current.

My findings support the notion that electric currents in the crust *can* be generated purely from deformation processes themselves. Scaling up the laboratory results to large stressed rock volumes at shallow crustal pressures and constant crustal strain rates, deformation induced transient telluric current systems may be as large as $10^6$ A, even accounting for $> 99\%$ dissipation, which corresponds to a huge accumulated net charge of $10^{22}$ C. This implies that a significant amount of charge from deforming tectonic regions contributes to the Earth's telluric currents and electric field, although due to conduction away from the stressed rock volume, it is unlikely that accumulated charge of this quantity would ever be measured in the field.

Electric current evolution and its precursory characteristics can be related to models for electric earthquake precursors and fault-zone damage organisation, developed from field observations, providing experimental support for them. However, given the oscillatory nature of the current evolution observed during cataclastic flow processes in the laboratory, there is a high probability of false alarms. Furthermore, the potential for electric anomalies to be useful as earthquake precursors remains contentious due to the difficulties of separating deformation-induced signals from other telluric noise and the wider issue of establishing a statistically significant link with earthquakes.

# Acknowledgements

I would like to thank the many people who have supported and assisted me during the course of this thesis. Very little of the work presented here could have been undertaken if it were not for the many colleagues, friends and family members who have helped and advised me in countless ways.

Firstly, I extend my appreciation to my supervisors Peter Sammonds and Filippos Vallianatos for their guidance and encouragement. Without their invaluable intellectual, pastoral and financial support, this thesis would never have come to fruition.

I also acknowledge UCL Impact, the UCL Institute for Risk and Disaster Reduction and the Technological Educational Institute (TEI) of Crete in Chania for my studentship. Additional funding came from the UCL Roberts Fund, the UCL Graduate School, the Reid Trust and ERASMUS, which allowed me to attend several conferences and training courses and enabled me to spend three months working at the TEI in Chania.

Experimental studies are, by their nature, difficult and frustrating. I owe huge thanks to Nic Brantut, Neil Hughes, Steve Boon and John Bowles for their advice and assistance in the laboratory. Their expertise, willingness to help and seemingly endless patience ensured the success of my experimental program and helped to maintain my sanity. I also thank Jim Davy for his company during many hours of sample preparation, and Rosie, Jen, Celine, Leisa and Danuta for their administrative and IT support.

To all my fellow PhD students, and particularly Nikki, Mike, Marie and Alexandra (ma posse, innit), thank you for being there and sharing with me this interminable trudge through science. Your friendship, hilarious banter, supportive hugs and the many agreeable hours spent with you chatting and drinking (tea and beer) have made it all worthwhile. I would also like to thank the two Georges for our extensive, non-extensive discussions and my friends at the TEI in Greece, Despina and Eleonora, for welcoming me so warmly into their lives and showing such kindness during my stay.

Finally, I would like to express my gratitude to my friends outside UCL and to my family for their unwavering love and support through everything. Mum and Dad, thank you especially for taking me in when I came back from Crete with a dog, and for taking the time to look after us both while I was writing up. Your excellent catering and accommodation facilities, dog walking services and proof-reading skills meant that the only thing I had to worry about was this thesis, which I dedicate to you.

# Table of Contents

# List of Figures

# List of Tables

# Chapter 1

# Introduction

## 1.1 Introduction

Earthquakes have long been associated with electromagnetic disturbances in the atmosphere such as earthquake lights and ionospheric turbulence (e.g., Davies and Baker, 1965; Derr, 1973; Molchanov and Hayakawa, 1998b; Heki, 2011; Cahyadi and Heki, 2013) and transient electrical effects in the lithosphere; anomalies in the naturally-occurring electrical (telluric) currents that flow throughout the earth's crust (e.g., Gokhberg et al., 1982; Varotsos et al., 1993; Uyeda et al., 2002; Enomoto et al., 2006; Fan et al., 2010). These phenomena have been observed in the field and are sometimes found to precede large earthquakes. Over the years they have been considered as promising candidates for earthquake precursors, forming the basis of attempts at earthquake prediction such as the VAN earthquake prediction technique (Varotsos et al., 1982). However, the VAN prediction claims have proved highly controversial for several reasons (summarised by Mulargia and Gasperini, 1996a); not least because of the different ways in which the texts of the VAN predictions (given in Dologlou, 1993) can be interpreted. They also raised a great deal of debate regarding their statistical significance (Wyss and Allman, 1996; Kagan, 1996; Honkura and Tanaka, 1996; Aceves et al., 1996), their greater likelihood of following periods of enhanced seismicity rather than preceding them (Mulargia and Gasperini, 1992; 1996b) and their non-uniqueness; i.e., that any of several earthquakes in the same focal region could be arbitrarily correlated with a particular prediction (Stavrakakis and Drakopoulos, 1996). See the special edition of Geophysical Research Letters (1996): Volume 23, Issue 11 for the full debate. Contributors to this debate also highlighted the difficulties associated with statistically evaluating an earthquake prediction method (Stark and Davis, 1996; Utada, 1996) and made recommendations for earthquake prediction standards (Jackson, 1996; Rhoades and Evison, 1996; Burton, 1996; Riedel, 1996; Tselentis and Melis, 1996; Kagan and Jackson, 1996). Since then, the mainstream scientific community has moved away from this earthquake prediction discussion to testing actual forecasts against null hypotheses of random or random and clustered models on a public web site (Collaboratory

for the Study of Earthquake Predictability [CSEP] http://www.cseptesting.org/), thereby avoiding the problems associated with earthquake prediction, not least in deciding what to publish (*pers. comm.* Main, 2015).

In addition to the problems associated with making predictions from observations of atmospheric and lithospheric electric signals, the underlying causes and relationship to fracture of these anomalies are still largely unknown. The technical difficulties involved in monitoring and processing anomalous electromagnetic signals detected in the field (Gokhberg et al., 1995), together with their transient nature (Bernard, 2001), the long distances over which they travel, the lack of a both statistically significant link with earthquakes and an experimentally proven generation mechanism and the many other possible sources that may contribute to such anomalies, such as the sensitivity of the measurement position and both artificial and atmospheric noise contamination (Mulargia and Gasperini, 1996a; Michael, 1997), mean that the answers to such questions have, historically, remained elusive (Yoshida et al., 1997; 1998). It was only very recently that Orihara et al. (2012) demonstrated rigorously that the correlation between the appearance rate of 19 telluric current anomalies observed on Kozu-shima Island, Japan (1997-2000) and the occurrence rate of 23 nearby earthquakes was far beyond chance. Their potential as precursory signals therefore remains controversial, with the two main problems concerning the generation mechanism for the electric field and propagation mode of the electromagnetic (EM) waves. Understanding pre-earthquake electrical signals is important not only to develop a deeper understanding of the physical mechanisms behind the earthquake preparation process but also to make sense of other pre-earthquake phenomena, including effects on humans and animals (Tributsch, 1983). Such psychological and physiological effects (e.g., Shitov, 2010; Anagnostopoulos et al., 2013) may in fact be directly related to low frequency radiation emitted from the earth in the days preceding an earthquake (Freund, 2011a; Anagnostopoulos et al., 2013).

The perceived failure of attempts to predict earthquakes and the controversy surrounding electric earthquake signals and earthquake prediction in general (e.g., Geller, 1997; Geller et al., 1997; Main, 1997), following the idea that earthquakes are non-linear, chaotic phenomena (Bak and Tang, 1989) and therefore unpredictable (Kagan, 1997), led to a strong shift in the focus of electric earthquake signals research from field observations to the laboratory. The rock physics approach to understanding geophysical processes stems from the idea that it is the microscopic deformation of rock, as a material, that governs the macroscale behaviour of the crust (Sammonds, 1999). Through experiments and modelling, rock physicists seek to further understand microscale rock deformation and apply this understanding to the crustal scale. In the laboratory, conditions in the shallow crust can be simulated and rock deformation carefully controlled. Under such precise conditions, small-scale experiments can reproduce large-scale geodynamic processes. In particular, they can exhibit the processes of compaction, dilatancy and fracture which are thought to be characteristic of crustal deformation during the earthquake cycle (Mogi, 1985). Such experiments are essential to investigate and isolate the different processes that

occur during rock deformation and fracture, providing information that can help explain field observations and constrain theoretical models. Experimental methods are based on monitoring, using geophysical techniques, the deformation in a sample under load. During deformation, energy is released in the form of elastic and electromagnetic waves and electric charges. Elastic and electromagnetic waves are detected as acoustic emissions (AE) and electromagnetic emissions (EME) recorded at the sample surface. Electric charges, due to the electrical polarisation of newly created crack surfaces, can be detected as electric potential difference or electric current flow measured between two electrodes at the sample surface. Changes in stress, strain, elastic wave velocities and pore fluid volume are also recorded. These monitoring techniques are sensitive to latent damage in rock samples prior to macroscopic failure (e.g., Scholz, 1968a; Lockner et al., 1991; Sammonds et al., 1992; Yoshida et al., 1998; Clint, 1999; Yoshida, 2001; Schubnel et al., 2003; Gueguen and Schubnel, 2003; Stavrakas et al., 2003; 2004; Eccles et al., 2005; Vallianatos et al., 2012c) and multi-parameter studies are important to test and constrain proposed models for precursory phenomena (Bernard, 2001).

Over the last three decades, numerous experimental studies to understand the generation and propagation mechanisms behind electrical fracture phenomena have been undertaken. These studies have since established that electromagnetic emissions and electrical signals due directly to the fracturing process do indeed accompany rock deformation on the laboratory scale and often precede fracture (e.g., Brady and Rowell, 1986; Yamada et al., 1989; Yoshida et al., 1998; Clint, 1999; Yoshida, 2001; Stavrakas et al., 2003; Freund, 2002; Eccles et al., 2005). Progress in understanding the mechanisms behind these phenomena and relating them to field observations is ongoing (e.g., Freund, 2011a; Pulinets and Ouzounov, 2011). The earliest loading experiments, on quartz-bearing rocks under atmospheric conditions, demonstrated that electromagnetic emissions due to stress-induced piezoelectric fields do indeed accompany fracture (e.g., Nitsan, 1977; Warwick et al., 1982; Ogawa et al., 1985; Brady and Rowell, 1986). Subsequent studies, under simulated crustal conditions, highlighted the dominance of electrokinetic (streaming) potentials induced by fluid flow during dilatancy (see Section 3.5.2) and the piezoelectric effect as mechanisms for electric potential and electric current variations prior to and during shear fracture (Jouniaux and Pozzi, 1995a;b; 1997; Yoshida et al., 1997; 1998; Clint, 1999; Yoshida, 2001; Eccles et al., 2005).

More recently, electric current signals and electromagnetic emissions recorded during deformation of dry, quartz-free rocks (Rabinovitch et al., 2000; 2001; Freund, 2002; Freund et al., 2006; Frid et al., 2003; Stavrakas et al., 2003; Anastasiadis et al., 2004; Triantis et al., 2006; Tsutsumi and Shirai, 2008) suggested the existence of a universal electrification mechanism, beyond those of the piezoelectric and electrokinetic effects. The basis of such a mechanism involves the creation, migration and cooperation under stress of electrically charged defects within ionic solids, leading to the presence of localised electric dipoles. Electric dipoles are generated in the following basic ways: (i) ionic charge separation, which occurs when bonds are broken during fracture, (ii) stress-induced charge

imbalance in an initially uncharged rock, due to anions and cations having different formation energies (iii) the migration of electrons and positive holes via empty valance bands on broken bonds, and (iv) the emission of charged particles into the void space of the developing crack network, leading to ionisation of the void space and the generation of localised dipoles as the void space geometry changes. The formation of such a dipole, for example at a single crack, leads to strongly directive electric and magnetic fields around it (Figure 1.1 (a)). Along a fault plane, the overall dipole is the vector sum of all the individual dipoles, for example at each asperity, leading to strongly directive electric and magnetic fields around the whole plane (Figure 1.1 (b)). The situation is further complicated by the presence of dipoles generated by several mechanisms, their relative orientation and interaction.

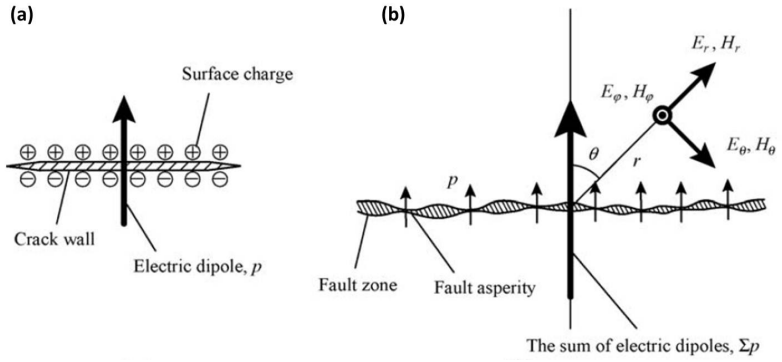


Figure 1.1: Schematic diagram showing electric dipoles ($p$) and electric ($E$) and magnetic ($H$) fields. (a) At a single crack; an electric dipole is formed by surface charges on a pair of separate crack walls leading to strongly directive electric and magnetic fields around the crack. (b) At a stick-slip plane on the laboratory scale or a fault plane on the geophysical scale; a large electric dipole is the vector sum of small ones at each asperity and forms strongly directive electric and magnetic fields around the plane during stick-slip or faulting. After Takeuchi and Nagahama (2006).

Several individual mechanisms have been proposed (Varotsos et al., 2011b) for the generation of dipoles and current flow (see Section 3.5.1), including (i) stress-activated highly mobile charge carriers in the form of positive holes (Freund, 2010) leading to a stress-induced electromotive force (Takeuchi and Nagao, 2013), (ii) charge separation on fractured surfaces (Ogawa et al., 1985; Yamada et al., 1989; Enomoto and Hashimoto, 1990) causing electron and ion emission from fresh crack surfaces (Brady and Rowell, 1986) and the oscillation of ions on these surfaces (Frid et al., 2003), (iii) changes in stress-induced polarisation (Varotsos et al., 1999; Makhmudov and Kuksenko, 2005; Ma and Cross, 2005; Zubko et al., 2007), (iv) motion of charged edge dislocations (Slifkin, 1993; Mavromatou and Hadjicontis, 1994; Vallianatos et al., 2004) and the transfer of point defects (Freund et al., 1994), and (v) electric dipoles generated perpendicular to stick-slip surfaces due to the formation of charges in disordered surface layers between separated asperities along the stick-slip plane (Takeuchi and Nagahama, 2004; 2006). It is apparent that any of these mechanisms may be operative during rock deformation and so a deeper understanding of the generated signals is essential.

Fracture in the Earth's crust is driven by slow forcing from the underlying mantle and

takes the form of localised earthquake faulting on a large scale. This rock deformation under conditions of stress is the fundamental governing factor behind the understanding of a wide range of geophysical quandaries from the driving forces of plate tectonics to earthquake prediction. Under an applied stress rocks deform elastically, plastically, by fracturing, brittle (cataclastic) flow and frictional sliding (stick-slip) along a fault (e.g., Scholz, 1968a; Scholz et al., 1972; Fredrich et al., 1989; Sammonds et al., 1989; Glover et al., 1996; Sammonds and Ohnaka, 1998; Tuffen et al., 2008). The magnitude and direction of the applied stress, the rate and duration of loading, ambient pressure and temperature, the presence of fluids and previous deformation history all control the overall mechanical response of the crust (e.g., Sammonds et al., 1992; Main et al., 1994). The acceleration from stable, quasi-static crack growth to unstable, dynamic failure is extremely rapid, non-linear, and difficult to predict for individual events. However, complex non-linear systems 'self-organise' spontaneously to produce order and pattern in population dynamics (Sornette and Sornette, 1989; Bak and Tang, 1989; Bak, 1990; 1996; Ito and Matsuzaki, 1990; Main, 1991; Bak et al., 2002), for example the fractal (self-similar) geometry of crack and earthquake populations (e.g., Main et al., 1990; Shcherbakov and Turcotte, 2003). Studying these complex fracture populations requires a different approach from the mechanics of a single earthquake. Statistical physics, by means of probability theory, allows the macroscopic properties of large populations (i.e., the large-scale laws of a physical system) to be calculated from specified microscopic elements of the system and their interactions. It addresses the micro to macro scaling problem by deriving theoretical models from the known mechanics of processes such as friction, damage, rupture and fluid-rock interactions at the microscopic scale. These models of microscopic dynamics, although often simplistic, can effectively reproduce the macroscopic statistical behaviour of fracture populations. Statistical physics has proved to be a very useful tool for analysing seismicity patterns and scaling up laboratory results (see Main et al., 1993; Main, 1996; Rundle et al., 2003; Sornette and Werner, 2009). Arguably, its application to the problems of earthquake geophysics is therefore not only appropriate but necessary to understand crustal dynamics. Indeed, the complementary nature of a rock physics approach combined with a statistical physics approach, whereby rock physics experiments provide parameters to underpin statistical physics models, is apparent.

With observational evidence suggesting that the crust is continuously on the brink of failure (Main, 1991; Lee et al., 2002; Rundle et al., 2003), modern theories of earthquakes hold that they are critical phenomena. This implies a system maintained permanently far from equilibrium 'on the edge of chaos', with an inherent random element and self-organising 'avalanche' dynamics strongly sensitive to small stress perturbations (Main, 1997). Experiments and field observations have shown that brittle and plastic rock deformation exhibits such complex, non-equilibrium and intermittent behaviour that is characteristic of self-organised critical systems with long-range *interactions* and is expressed as scale-invariant, multi-fractal distributions (e.g., Bak and Tang, 1989; Main et al., 1994; Weiss and Marsan, 2003; Richeton et al., 2005; Sammonds, 2005; Pollitz et al., 2012). Clas-

sical (Boltzmann-Gibbs) statistical mechanics was defined only for *equilibrium* systems containing independent, *non-interacting* particles. Thus, the question is raised regarding its validity for the study of correlated dynamic systems exhibiting the behaviour just described. However, Tsallis (1988) introduced a generalisation of the Boltzmann-Gibbs formula particularly suited to the study of such systems, which has become a very useful tool for describing their complexity (Telesca, 2011). In order to further understand the many geophysical processes that exhibit this kind of dynamics, and to approach the question of scaling, this concept, known as 'non-extensive statistical physics' (Tsallis, 1988; 2009a), has recently been applied in the earth sciences. It offers a consistent theoretical framework in which to analyse rock fracture populations, seismicity patterns and other fracture-related phenomena and has been applied with some success to describe fault population distributions in Greece (Vallianatos et al., 2011a) and on Mars (Vallianatos and Sammonds, 2011; Vallianatos, 2013a), the distribution of tectonic plate areas (Vallianatos and Sammonds, 2010), global seismicity prior to mega-earthquakes (Vallianatos and Sammonds, 2013), regional seismicity patterns around the world (e.g., Abe and Suzuki, 2003; 2005; Telesca, 2010a;b; Telesca and Chen, 2010; Telesca, 2010c; 2011; Valverde-Esparza et al., 2012; Vallianatos et al., 2012b; 2013b; Michas et al., 2013; Papadakis et al., 2013), laboratory acoustic (Vallianatos et al., 2012a), electromagnetic (Vallianatos et al., 2012c) and pressure-stimulated current (Stergiopoulos et al., 2013) emissions and the relaxation of pressure-stimulated (Vallianatos and Triantis, 2012; 2013) and depolarization currents (Vallianatos et al., 2011b). The distribution functions of real earthquakes have been well-described by seismicity models based on Tsallis statistics (e.g., Sotolongo-Costa and Posadas, 2004; Silva et al., 2006; Vilar et al., 2007; Sotolongo-Costa, 2012) and other models of self-organised systems (e.g., Olami et al., 1992) have also been found to yield Tsallis statistics similar to real earthquakes (Caruso et al., 2007; Zhang et al., 2011). Models regarding the role of electromagnetic emissions in the earthquake preparation process have also been developed (e.g., Papadimitriou et al., 2008; Contoyiannis and Eftaxias, 2008; Eftaxias, 2010; Potirakis et al., 2011; 2013a;b; Minadakis et al., 2012). These applications have demonstrated the suitability and usefulness of the Tsallis approach as a tool for understanding rock deformation and pre-failure anomalies, allowing inferences to be made regarding the earthquake triggering mechanism, differences in seismic environment, the organisation of the fracturing system in time and space, the development of instability as a major failure approaches and the potential for fracture-related electric phenomena to provide significant information about the state of the system.

## 1.2 Purpose and Scope of Investigation

Freund (1999; 2003b) and Freund et al. (2006) noted that a central issue in the study of pre-seismic electric field anomalies is a lack of understanding of the physical processes that lead to the emission of electric and electromagnetic (EM) signals from the ground. A fundamental concern is that pre-earthquake electric phenomena require the generation

of electric currents in the ground, with some particularly large anomalies requiring very strong currents. A necessary avenue of investigation, therefore, is the study of electric current as a fracture phenomenon. To date, three groups have directly investigated electric current generated during laboratory rock deformation. Early work by Yoshida (2001) measured electric current directly during deformation of saturated granites, sandstone (quartz-rich) and gabbro (quartz-free) under simulated crustal conditions. He inferred that the current generated was caused by an electrokinetic effect due to the water flow associated with accelerating dilatancy prior to fracture. Yoshida's (2001) work on the electrokinetic effect was carried out on quartz-free basalt samples for which no precursory electric potential (EP) signals were detected in a dry situation (Yoshida et al., 1998; Eccles et al., 2005). In contrast, similar experiments under dry, atmospheric conditions investigating electric current generated within deforming marble samples (e.g., Stavrakas et al., 2003; Anastasiadis et al., 2004; Triantis et al., 2006; Kyriazopoulos et al., 2011a; Stergiopoulos et al., 2013) have shown that electric currents can in fact accompany the process of crack formation and growth even in dry, quartz-free rocks. The group detected electric current variations beyond the material's elastic limit immediately prior to macroscopic sample failure, coining the phrase 'pressure-stimulated currents' (PSC) to describe their observations; small ($10^{-12}$ - $10^{-9}$ A), transient, polarising electric currents from a solid undergoing a gradual change in pressure. They invoked the migration of charged edge dislocations to explain their observations. Finally, Freund's group (e.g., Freund, 2002; Freund et al., 2006) conducted an investigation of currents flowing from stressed to unstressed regions of rock by loading one end of a large block, mainly on granite but also on quartz-free gabbro (Takeuchi and Nagao, 2013). They argue that their positive-hole mechanism, which involves the rock behaving like a semiconductor when stressed, provides a unifying theory that can answer both the generation and propagation problems (Freund, 2010; 2011a; Takeuchi and Nagao, 2013).

No previous work has extended to crustal conditions the investigation of electric current generation in a deforming quartz-free rock that *does* exhibit precursory electric signals under dry, atmospheric conditions. It is this gap in the literature that my thesis addresses; I show how these electric current signals behave during deformation under crustal conditions. To accomplish this, I conducted a comprehensive series of novel laboratory experiments, using a triaxial deformation ensemble to measure electric current generated within Carrara marble under a variety of simulated lithospheric conditions. I chose Carrara marble for the following reasons: (a) it is non-piezoelectric, (b) it is pure, isotropic, mono-minerallic, compact and crystalline with very low porosity; i.e., good for isolating the effects of crack damage, (c) it undergoes the brittle-ductile transition at room temperature, (d) its behaviour at crustal conditions, micro-mechanisms of deformation and slip systems are well-known, and (e) marble was the material used in the previous uniaxial experiments investigating electric current during deformation of quartz-free rocks referred to above. Additional parameters, including stress, strain, pore fluid volume, ultrasonic wave velocities and acoustic emissions, I acquired simultaneously to help constrain the

relationship between electric current and stress-induced damage within the rock.

In particular, I addressed the following questions: (i) How do the electric current signals evolve with damage during the deformation cycle? (ii) How do the environmental conditions (strain rate, effective pressure and pore fluid salinity) affect the form of the signals? (iii) How do the signals change with deformation mechanism across the brittle-ductile transition? The results presented in this thesis will show that electric current signals in the dry samples arise mainly from the damage caused by microcracking, with a contribution from other intermittent ductile mechanisms, and that a certain amount of crack damage and/or crack connectivity is required before current will flow. The signals exhibit precursory characteristics as the stress drop accelerates towards failure and changes in both the absolute and fluctuating components the signal correspond to changes in the evolution of stress, accumulation of damage and localisation of deformation leading up to sample failure, as well as to changes in deformation mechanism. The influence of microcrack suppression with increasing effective pressure is clearly seen in the rate of electric current flow, as well as the quantity of current generated and charge accumulated. Changes in these variables with strain rate correspond to time-dependent differences in deformation mechanism across the brittle-ductile transition. In the presence of deionised water, electrokinetic effects dominate only in the elastic region of deformation, after which solid-state mechanisms dominate. Whereas, in the presence of an ionic pore fluid electrokinetic effects dominate over solid-state mechanisms. These differences show that the development of the crack network and charges from solid-state deformation processes contribute to the variation in electrokinetic parameters during deformation of fluid-saturated samples. In addition, I will show that electric current flow may be used as a proxy for stress, given the observed proportionality between current flow and differential stress under all the conditions tested. These findings contribute new data and fresh insight to the understanding of spontaneous electric current flow in stressed rocks.

Furthermore, by analysing the data with a Tsallis statistical physics approach, I addressed the following additional questions: (iv) Does the Tsallis approach describe the system effectively? (v) What are the parameters? (vi) How do they change with environmental condition and deformation mechanism? (vii) What can they tell us about the dynamics of the described systems, both in the laboratory and in the field? This thesis will demonstrate that the high frequency fluctuations of electric current exhibit 'fat-tailed' distributions are effectively described by $q$-Gaussian statistics, consistent with an origin in non-extensive statistical mechanics. That is, that the electric current fluctuations result from processes occurring on the fractal structures that develop within the rock matrix during deformation. Characteristic $q$-values are obtained for different deformation regimes and environmental conditions across the brittle-ductile transition, and the evolution of $q$ during deformation reveals a two-stage precursory anomaly prior to sample failure, consistent with the stress intensity evolution as modelled from fracture mechanics. Moreover, these distributions can be explained as arising from superstatistical dynamics (Beck, 2001; Beck and Cohen, 2003), i.e., the superposition of local mechanical relaxations in the presence of a slowly

varying driving force. The macroscopic $q$-Gaussian distribution parameters provide an excellent prediction of the experimentally observed mean energy dissipation rate of the system (as modelled by the superstatistical $\beta$-parameter), particularly at slow strain rates. My findings show that the dynamics of rock deformation, at least at the laboratory scale, *are* reflected in the statistical properties of the recorded electric current, lending weight to the suitability of the Tsallis approach itself for investigating fracture phenomena. They shed further light on the dynamics of fracture-induced electrical signals throughout the deformation cycle, with positive implications for earthquake hazard mitigation.

Through answering these questions, my thesis contributes new knowledge and information towards addressing the suggestion of Main (1997) that "in the absence of reliable prediction methods, we should concentrate on hazard mitigation based on a better understanding of earthquake source mechanisms [and] their statistical properties".

## 1.3 Thesis Outline

This thesis is divided into 11 chapters which detail previous work and present theories, the acquisition of experimental data, the main results and their interpretation, conclusions drawn and potential avenues for further research. Chapter 2 reviews our knowledge of the physics of earthquakes and crustal deformation and discusses the application of statistical mechanics to these processes. It also provides a rationale for, and review of, the application of the relatively new field of non-extensive statistical mechanics to the study of fracture-related phenomena. Field observations of electric phenomena in the Earth's crust and atmosphere, and laboratory studies related to understanding the mechanisms behind these observations are outlined in Chapter 3. This chapter also discusses the non-extensive approach to scaling of electric phenomena as well as the main theories for their generation, both solid-state (excluding the piezoelectric effect, which is beyond the scope of this study) and electrokinetic. Chapter 4 reviews the principles of experimental rock physics; theories and experimental techniques used during this study.

Particulars of the experimental program and the techniques used to collect, calibrate and process the large quantities of accurate experimental data, are described in Chapter 5. Modifications made to the existing apparatus are also detailed in this chapter, together with development of the electric current acquisition system that I designed specifically for this project. Chapter 6 presents the experimental material and the techniques used for its characterisation, together with the associated results. This includes developing a procedure for introducing fracture damage into the low porosity samples in order to conduct accurate experiments with pore fluid.

The main experimental results obtained from this study are given in Chapters 7 through 10. These comprise: (i) a description of the mechanical behaviour and deformation style of the experimental material, (ii) observations of electric current and ultrasonic velocity during

rock deformation at conditions across the brittle-ductile transition, (iii) the influence of confining pressure, deformation rate, pore fluid and pore fluid salinity on these data, (iv) correlation of the electric current data with damage, and (v) a summary of the results presented in each chapter, together with deductions that were made regarding the influence of deformation on the electric current signals.

Chapter 11 presents results from the non-extensive approach to modelling the dynamics of electric current fluctuations, accompanied by a discussion regarding the relationship between the non-extensive properties of these fluctuations and the processes of deformation occurring in the rock specimens. Finally, in Chapter 12, I review the work that was done and draw the main conclusions, discussing the implications and applications of this research in the field of earthquake hazard, before suggesting possible directions for future research.

# Chapter 2

# Earthquakes, Crustal Deformation and Statistical Mechanics

## 2.1 Introduction

Earthquakes have great scientific and socio-economic significance (Rundle et al., 2003). Their devastating effects, from the seismic waves of the main shock to the subsequent landslides and tsunamis they generate, have killed many thousands of people and caused property and infrastructure losses costing billions of dollars. For example, the five most deadly earthquakes of the last decade combined caused the deaths of more than 700,000 people (USGS, 2012), while total overall losses from the five most expensive exceeded $400 billion (III, 2014). The potential for extensive damage and loss of life in large urban centres along active plate boundaries and on diffuse networks of active faults within continental interiors around the globe is so great (England and Jackson, 2011; McCloskey, 2011) that reliable earthquake forecasting continues to be a much sought-after goal. As a result, a great many programs searching for reliable precursory phenomena have been undertaken. Potential precursory phenomena include changes in seismicity, changes in seismic velocity, tilt and strain precursors, electromagnetic signals, telluric anomalies, hydrological phenomena, and chemical emissions (Turcotte, 1991; Scholz, 2002). A few successes have been reported, but no reliable forecast has yet been made. Earthquake prediction is thus an enduring question in geophysics and much work has gone into investigating the statistical behaviour and physical mechanisms of precursory phenomena.

Our understanding of the physics of earthquakes began with the advent of plate tectonic theory in the 1960s. This paradigm shift (Kuhn, 1962; Wilson, 1968) provided the first unified explanation of major geologic phenomena, particularly earthquakes and volcanic activity, in terms of plate formation, evolution and interaction (Dewey and Bird, 1970). The relative motion of these plates against each other causes interactions between plate boundaries, inducing stresses within the plates leading to the occurrence of dynamic pro-

cesses such as folding, mountain-building, basin subsidence, earthquakes and volcanism. In fact, because earthquakes occur primarily at plate boundaries, the global distribution of earthquake occurrence and focal mechanism provided some of the strongest evidence for the geometry of plate boundaries and their respective motions (Isacks et al., 1968; Stein and Klosko, 2002). Three types of plate boundary exist: (1) divergent, where new oceanic lithosphere is formed during spreading at mid-ocean ridges, (2) convergent, where collision causes the destruction of oceanic lithosphere as one plate is subducted beneath another, and (3) sliding, where lithosphere is conserved and plate motion occurs along transform faults parallel to the boundary (Stein and Klosko, 2002; Uyeda, 2002). These margins can be illustrated in terms of the style of earthquake faulting that occurs, since the direction of relative motion between plates is reflected in earthquake slip vectors (i.e., the motion on the fault plane). Broader and more detailed explanations regarding plate tectonics, faulting, seismology and other aspects of earthquake geophysics are given by Kearey and Vine (1990), Lay and Wallace (1995), Shearer (1999), Scholz (2002), Stein and Wysession (2003), Lee et al. (2002; 2003) and Fowler (2005), among others.

The existence of such intense deformation at plate boundaries, as well as of intraplate earthquakes and deformation, implies (a) that, rather than being rigid, 'plates move without deformation until they meet strong stress' (Uyeda, 2002) and (b) that stresses strong enough to cause failure along planes of weakness exist throughout the crust, not only at plate boundaries. Earthquakes can therefore be considered as a relaxation mechanism of the Earth's moving crust, which becomes loaded with inhomogeneous stresses (Sotolongo-Costa et al., 2000). Once an earthquake occurs, the whole landscape of crustal stresses redistributes itself, and a new event will occur when the accumulated local stress intensity again surpasses the threshold somewhere else. Natural faults in the Earth's crust are zones of localised shear that are weaker than the surrounding intact rock (Lockner and Beeler, 2002). Slip occurs along these pre-existing faults, either slowly and continuously as aseismic creep or rapidly as earthquakes with long inter-event times during which little or no slip occurs. The physics of individual earthquakes are generally explained by stick-slip behaviour and elastic rebound; rupture initiates when the shear stress on the fault exceeds its local strength and propagates if the shear stress remains sufficient to overcome friction (Ohnaka, 2013; Scholz, 2002). This motion relieves elastic strains in the surrounding rock, generating seismic waves and heat. Earthquake faulting has thus been thought of mainly as a frictional phenomenon, with brittle fracture playing a secondary role in the lengthening of faults and frictional wear (Scholz, 1998). However, crustal faults have complex, fractal geometries that include irregular, interlocked surfaces, offset segments, bends and junctions. The natural tendency for these irregular fault surfaces to move apart during sliding is suppressed at depth as compressive stresses increase due to the overburden. Instead, fault slip at depth must involve continual fracture of asperities or interlocked regions and grinding and crushing of grains. Ohnaka (2003) recently developed a unifying constitutive law for earthquake rupture that governs both frictional slip failure and shear fracture of intact rock. Breaking of asperities may control the position and timing of earthquake

nucleation (Lockner and Beeler, 2002). Therefore, studying brittle fracture or simply the 'failure' of intact rock is as important as studying the frictional properties of pre-existing faults.

## 2.2 Conditions in the Earth's crust

### 2.2.1 Stress and pressure

Tectonic stresses, commonly superimposing the overburden pressure of overlying rock and pressure due to trapped pore fluids, are responsible for the stress state in the upper crust and therefore its deformation. The key tectonic stresses acting at plate boundaries are: (1) ridge push; a compressive stress acting normal to the ridge axis, (2) slab pull; a tensile stress acting normal to the trench axis and (3) trench suction, a tensile stress that pulls the overriding plate towards the trench. Deformation occurs when these tectonic stresses exceed the lithospheric stress present in a unit volume of crust. The magnitudes of these tectonic stresses are estimated to be 20-30 MPa, 0-50 MPa and 20 MPa respectively, known from *in-situ* stress measurements compiled from all over the world by the World Stress Map Project (WSMP) (e.g., Zoback and Zoback, 1989). Measurements were inferred from borehole breakouts, hydraulic fracturing, volcanic alignment, earthquake focal mechanisms and transform fault azimuths (see Vita-Finzi, 2003). These stress maps indicate the presence of relatively small differential stresses in the shallow crust, around an order of magnitude smaller than dry compressive strengths (Ambrasey, 1970; Paterson and Wong, 2005). Also, the maximum horizontal stress in several plates is sub-parallel to the direction of absolute plate motion, suggesting that the plate driving forces also dominate stress distribution in the plate interior (Zoback and Zoback, 1989; Zoback and Magee, 1991). Further evidence suggests that the upper lithosphere is always close to failure stress (Ruff, 2002). This includes stress data from intraplate boreholes (e.g., Brudy et al., 1997) and intraplate seismicity induced by small stress perturbations from other earthquakes, pore fluids or reservoir impoundment (Zoback and Zoback, 2002). Stress magnitudes derived from Coulomb failure theory are consistent with *in-situ* magnitudes (Townend and Zoback, 2000).

Lithostatic pressure, $P_l$ is the vertical component of stress acting on a buried rock mass and is the product of the rock density, $\rho$, the acceleration due to gravity, $g$ and the depth, $z$ ($P_l = \rho g z$). With an average crustal density of 2500 kgm$^{-3}$, the average geobaric gradient calculated from this equation is 25 MPa/km but this varies locally with tectonic setting due to temperature and pressure effects on rock density (Fowler, 2005). As depth increases, the overburden pressure serves to compact and deform crustal rocks. This increases their density and rigidity, an effect particularly noticeable in the uppermost 5 km as existing pores, fractures and joints gradually close and before thermal expansion tends to counteract these effects with further depth. Since water and aqueous solutions

are ubiquitous in the upper crust, $P_l$ is often superimposed by a pore fluid pressure ($P_p$), acting normal to the surface of grains, which reduces the effect of the confining $P_l$ on the rock. The presence of highly pressurised crustal fluids reduces the lithostatic stresses sufficiently for thrust faulting to occur at great depths (Hubbert and Rubey, 1959) and can explain the relatively small stresses seen in the crustal stress maps. Stress rotation within the fault damage zone allows high pore fluid pressure to develop without causing hydrofracture and enables slip on unfavourably-oriented 'weak' faults (Faulkner et al., 2006). These fluids, often also at high temperatures, can cause mineral reactions, phase transitions and microstructural changes that strongly affect the elastic properties of rocks (Lebedev et al., 1996). The amount of fluid present depends on tectonic setting and depth, with larges volumes present in the shallow crust and volume decreasing with depth (Nur and Walder, 1990). According to Brace and Kohlstedt (1980), compelling evidence exists for pore and/or fracture connection to 5 km depth, while there are good arguments for interconnection to a depth of 8 km and the possibility for appreciable transmissivity down to about 20 km. Fluids down to around 11 km depth were sampled in the Kola super-deep drill hole (Clarke et al., 1986), which also found an increase in the salinity of these fluids with depth. It is often assumed that $P_p$ increases linearly with depth, in a relationship analogous to the overburden pressure. Calculated in this way, the pore pressure gradient is 10 MPa/km (c. 40 % of $P_l$). This is known as the hydrostatic gradient (i.e., equal to the pressure of a column of water of height equal to the lithostatic column of rock) and it holds down to a depth of $\sim$ 8 km (Brudy et al., 1997). However, much higher 'suprahydrostatic' $P_p$ gradients, which significantly reduce the stresses required for brittle failure (Streit and Cox, 2001), are known to occur in regions of tectonic activity. These are controlled either dynamically by the sealing of faults, stratigraphically by impermeable rock layering (Nur and Walder, 1990) or simply by tectonic compression (Price and Cosgrove, 1990).

### 2.2.2 Deformation rate

Rates of tectonic deformation (strain rates) in the crust can vary widely. Data compiled for a variety of tectonic regimes indicate rates ranging from $10^{-12}$ to $10^{-17}$ $s^{-1}$ (Carter and Tsenn, 1987) with rock type and environmental conditions exerting a strong influence on the rate (Donath and Fruth, 1971). Typical values are of the order of $10^{-14}$ $s^{-1}$ (Whitten, 1956; Wood, 1973). However, such slow strain rates are unfeasible in a laboratory setting where rates down to $10^{-8}$ $s^{-1}$ are the slowest achievable. Laboratory strain rates can be extrapolated to crustal rates by means of theoretical models (e.g., Rutter, 1995; Covey-Crump, 1998). Typical strain rates used in conventional constant strain rate experiments are $10^{-4}$ to $10^{-6}$ $s^{-1}$; the same were employed for this study.

Recently Ojala et al. (2004) showed the acceleration in the rate of laboratory acoustic emissions that precedes sample failure occurs later and is much steeper at slower strain rates. Their data suggests that rock failure becomes increasingly unpredictable as the strain rate decreases. Since crustal strain rates are considerably smaller than laboratory

rates, this strain rate dependence may explain why earthquake precursors are not as easily recognisable in the field as in the laboratory.

### 2.2.3 Temperature

Temperature shows an overall increase with crustal depth. The geothermal gradient varies from as little as 10°C/km in deep sedimentary trenches to >100°C/km in active volcanic areas, with an average of 30-50°C/km for crustal rock (Fowler, 2005).

### 2.2.4 Electrical conductivity

The electrical conductivity of rock has been measured using electromagnetic field techniques and shown to depend on a variety of factors, including porosity, crack network connectivity, mineral composition, pore fluid salinity, effective stress and fluid flow (e.g., Brace et al., 1965; Brace and Orange, 1966; Brace and Martin, 1968; Brace et al., 1968). A lower limit of $10^{-6}$ $Sm^{-1}$ for crustal conductivity values by Brace (1971), inferred from laboratory experiments under drained conditions (constant $P_p$) is a somewhat conservative estimate compared with field observations of conductivities between $10^{-5}$ and $10^{-2}$ $Sm^{-1}$ (Keller et al., 1966; Anderson and Keller, 1966), a finding that suggests additional mechanisms present in the crust compared with that of simple crack closure under increasing lithostatic pressure. Crustal conductivity can be split into three regions (Shankland and Ander, 1983): (1) a high conductivity surface layer associated with groundwater and saturated sediments, (2) a low-conductivity layer (LCL) corresponding to the crystalline basement and (3) a deeper high-conductivity layer (HCL) (Figure 2.1).

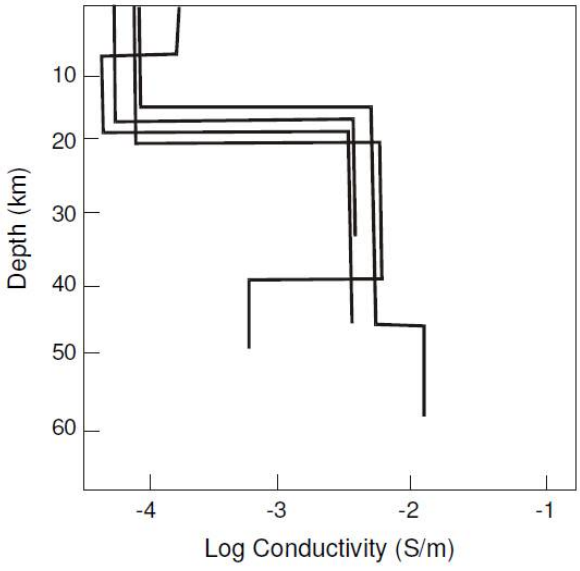


Figure 2.1: Variation of electrical conductivity with depth in the continental crust, showing the LCL and HCL regions (Shankland and Ander, 1983)

Tectonically active regions show systematically higher LCL conductivities than do intraplate areas (Schwarz, 1990) and the difference between these two regions may be attributed to the abundance of a highly conducting material such as free aqueous fluid, since even the most resistive crust is much more conductive than dry laboratory specimens. An increase in the solubility of ionic materials with temperature (i.e., depth) increases the fluid conductivity, diminishing the fluid volume required to maintain a given conductivity. Therefore, conductivities corresponding to the crystalline basement suggest the presence of crustal rocks with brine-saturated porosity of 0.01-0.1 %; more so in tectonic regions than within plates, where crustal dynamics encourage fluid flow and crack connectivity (Shankland and Ander, 1983). The transition from LCL to HCL in the continental middle crust (10-20 km) is marked by low velocity layers in deep seismic soundings, characterised by an increase in electrical conductivity and attributed to separation between brittle and weak parts of the crust (Pavlenkova, 2004). Data from the Kola super-deep borehole indicates that an increase in porosity, pore fluid flow and pore fluid salinity at these depths is responsible for these observations. At a depth of 7-12 km the hole reaches a zone of weakened rocks (cataclasites) and higher fluid flow (Pavlenkova, 1991) where deformation is accommodated by a multitude of extremely fine, fluid-saturated shear cracks. High electrical conductivities in the lower crust, both in stable and tectonically active regions, have been explained in terms of super-critical fluids in interconnected pores and microcracks (Vanyan and Shilovski, 1989). However, plausible arguments exist for the presence, not only of free fluids, but also of carbon (graphite) layers, other conducting minerals (e.g., sulphides) or rock melt to explain the conductive structures seen in the lower crust (Schwarz, 1990). For example, Glover and Vine (1992) suggest that high conductivity structures may be explained by carbon-enhanced conduction pathways created during compaction. Such arguments have been supported by experiments on rock recovered from KTB boreholes (Duba et al., 1994; Shankland et al., 1997), with results implying that crustal conduction is likely to be due to the combined presence of conducting carbon and brine fluids. Similar KTB studies (Haak et al., 1997) have shown strong horizontal anisotropy which can be explained by zones of cataclastic deformation enriched in graphite. However, since the graphite would form equally on both sides of the fault, it does not explain the difference in signals recorded across the faults (Shankland and Ander, 1983). More recently, Glover and Adam (2008) reported laboratory results showing that progressive shearing of a fracture in carbon-bearing rock can result in a weaker, more electrically conductive fracture. This led them to postulate that the presence of either carbon or fluids could be responsible for the anisotropy of high conductivity zones, since both reduce the effective shear stress on faults at depth but fluids progressively reduce the electrical conductivity in the direction of shear while carbon progressively increases it. Thus, carbon-bearing rocks may cause the conductive zone where the direction of highest conductivity is both in the plane of the shear zone and in the same direction as the shear direction, while brine-saturated rocks may cause the conductive zone where the direction of highest conductivity is perpendicular to the predominant shear direction.

## 2.3 Statistical Physics Approaches to Crustal Deformation

Rocks behave elastically (to a first approximation) at low temperature and pressure and at high strain rates, showing linearity between stress and strain. Directly solving the laws of elasticity leads to periodic cycles in earthquake occurrence (Turcotte et al., 2000). In reality, however, earthquake occurrence is not periodic; one of the fundamental observations of earthquake physics is the tendency for seismic activity to cluster in space and time (Rundle et al., 2000). The behaviour of the crust is therefore extremely complex and by no means time-predictable (Main, 1996). Complex phenomena often exhibit scale-invariant geometries and power-law scaling statistics, many examples of which can be found in the earth sciences (see Turcotte, 1992 for a review). Earthquakes obey a variety of empirical scaling relations, including the following well-established empirical laws of statistical seismicity (Main, 1996; Rundle et al., 2003; Sornette and Werner, 2009, and references therein): (1) the Gutenberg-Richter power-law (Gutenberg and Richter, 1944; 1954) for the distribution of earthquake magnitudes, (2) the Omori-Utsu law (Omori, 1894; Utsu, 1961) for decay in the rate of aftershocks following a mainshock (inversely proportional to time with a power index), (3) the inverse Omori law for foreshocks, (4) aftershocks trigger their own aftershocks and aftershocks do not exhibit properties distinguishable from mainshocks, (5) power-law tail in the distribution of distances between mainshocks and aftershocks, (6) power-law scaling of earthquake hypocentre spacings in both space and time, (7) the fertility law (earthquakes of magnitude $M$ trigger around $10^{aM}$ aftershocks with $a \leq b \sim 1$), (8) Bath's law (difference in magnitude between a mainshock and its largest aftershock are approximately constant, independent of the mainshock magnitude) and (9) the scale-invariance over several orders of magnitude of the fault populations upon which earthquakes are concentrated and their power-law (fractal) length distributions. These classic examples demonstrate the complex and scale-invariant nature of earthquake phenomena and are the reason for interest in applying the techniques of statistical physics and complex systems to crustal deformation (Abe and Suzuki, 2003). Any general statistical physics model for faulting and earthquakes must explain these empirical facts (Main, 1996).

### 2.3.1 Earthquake scaling and fractal fault populations

Fragmentation in shear zones (Sammis et al., 1986) indicates that, in order to accommodate plate motion, tectonic processes have caused the lithosphere to fragment into a power-law distribution of block sizes over a wide range of scales. This has important implications for the frequency-size distributions of faults and earthquakes. Flaws are present in the Earth on all scales, from microcracks to plate-rupturing faults (Main et al., 1990). Some are distributed on one characteristic length scale (e.g., joints, 'characteristic' earthquakes) but most exhibit scale invariance over a specified range of sizes. This means that the geometrical characteristics of, for example, fault lengths or other geological fabrics,

are independent of the measuring scale. Such scale-invariant objects are said to exhibit self-similarity; an infinite nesting of features on all scales where each portion can be considered a reduced-scale image of the whole (Mandelbrot, 1967; 1982). The static geometry of such objects can be described by a fractal (fractional) dimension and the distribution of features with such geometry can only be described by a power law (Mandelbrot, 1982). In geology and geophysics, this takes the form:

$$N(l) = Cl^{-D} \tag{2.1}$$

where $N$ is the number of features (e.g., faults or fractures) within a discrete length interval $l - \frac{\delta l}{2} \leq l < l + \frac{\delta l}{2}$, $C$ is a constant and the power law exponent $D$ is the fractal dimension of the system (Turcotte, 1992; Main, 1996). In the case of earthquakes, this relation scales with rupture area as well as fault length: $N = CA^{-\gamma}$, where $N$ is the number of earthquakes per unit time with rupture area greater than $A$ occurring in a specific region and $C$ and $\gamma$ are constants with fractal dimension $D = 2\gamma$ (Turcotte et al., 2000).

The most famous of the seismic scaling relations described above is the Gutenberg-Richter frequency-magnitude relation (Gutenberg and Richter, 1944; 1954):

$$logN = a - bm \tag{2.2}$$

where $N$ is the number of earthquakes in the magnitude range $m - \frac{\delta m}{2} \leq m < m + \frac{\delta m}{2}$ and $a$ and $b$ are empirical constants (Richter, 1958). The scaling factor, $b$, is known as the seismic $b$-value. This relation is the direct result of a relatively constant earthquake stress drop over a power-law distribution of fault lengths (Main et al., 1990; Turcotte et al., 2000), i.e., a power-law distribution of seismic event magnitudes implies a power-law distribution of fracture sizes. The $b$-value is related to the fractal dimension, $D$, as follows: $D = \frac{3b}{c}$. For intermediate earthquakes, $c = \frac{2}{3}$ (Kanamori and Anderson, 1975) and therefore, $b = \frac{D}{2} = \gamma$. These results have allowed the development of theoretical models relating $b$-value, stress intensity factor (a measure of the stresses at crack tips), stress and crack length (Main et al., 1989; 1990; Meredith et al., 1990). The $b$-value varies generally between 0.5 and 1.5 ($1 \leq D < 3$) with a typical 'background' value of $b$ close to 1 ($D \approx 2$), characteristic of more diffuse fault systems, whereas fault systems where motion is concentrated along a dominant fault have $b$ closer to 0.5 ($D \approx 1$). According to the fracture mechanics model of Main et al. (1990), this is because critical coalescence of microcracks (earthquake foreshocks) occurs when $b = 0.5$ ($D = 1$), while random processes such as background seismicity are associated with $b = 1$ ($D = 2$). Positive feedback in the stress concentration on the dominant flaw such as during shear localisation and strain softening occurs when $b < 1$ ($D < 2$), whereas highly diffuse fracture systems and negative feedback in stress concentration, such as during the early stages of crack nucleation and dilatancy, occur at low stress intensities and are associated with $b > 1$ ($D > 2$). Agreement between the models, earthquake statistics and experimental results was proved when $b$-

values were derived from acoustic emissions measured in the laboratory (Sammonds et al., 1992).

The self-similar, fractal nature of fracture and faulting, illustrated in Figure 2.2, is widely documented from both field and laboratory observations (e.g., Main et al., 1990; Sornette et al., 1990a; Scholz, 2002; Sornette, 2006). Fault populations display power-law size distributions over a wide range of scales (Scholz et al., 1993; Schlische et al., 1996), although exponential distributions have also been observed (Cowie et al., 1993). Experimental evidence supports both types of distribution and suggests that different strain regimes may be responsible (Spyropoulos et al., 1999), although neither a power-law nor exponential function can describe the full range of data from different tectonic environments (Schultz et al., 2010). It has also been suggested that the total offset on a fault is related to its length in a fractal manner, although this may be more typical of the static fault dimensions and not of active fault growth (Cartwright et al., 1996; Moreland and Roberts, 1999). Furthermore, the roughness of fault and fracture surfaces also exhibits self-affine (anisotropic scale-invariance) or self-similar (isotropic scale-invariance) scaling (e.g., Brown and Scholz, 1985; Power and Tullis, 1991; Schmittbuhl et al., 1995; Scholz, 2002). However, microscopic analysis of faults confirm a complex interplay of cracks acting with different mechanisms and at different scales (Vermilye and Scholz, 1998), more complex than simple fractal behaviour. Spatial variability, clustering and intermittency in earthquake and fault populations in diverse tectonic regions is quantitatively consistent with multifractal scaling (Geilikman et al., 1990; Hirata and Imoto, 1991), where the range of scales depends on the feature's location within the set (Sornette, 2006). Additionally, multifractal clustering of faults and earthquake locations is consistent with two observations: (1) the observed concentration of seismic moment or energy release on large dominant faults and (2) the presence of some seismicity everywhere, including areas remote from plate boundaries (Main, 1996).

Studies of different fault maps (Ouillon and Sornette, 1996) have shown that due to structural heterogeneity induced by particular tectonic environments, structures with different fractal geometries occur separately within distinct and limited ranges. Similarly, although the power-law fault growth model of Cowie and Scholz (1992a) can provide an estimate of how the seismogenic potential of a fault varies over time, fault growth within different lithologies and tectonic environments requires different exponents with no single power-law distribution fitting all situations, possibly due to structures such as joints and fault segment boundaries acting as effective barriers to rupture at different length scales (Cowie and Scholz, 1992b; Hatton et al., 1994). Fracture and faulting can therefore be better modelled as a hierarchical process, controlled mainly by geometry and pre-existing heterogeneity (Sornette, 2006). Earthquakes occur on this complex hierarchy of faults in response to tectonic stresses (Turcotte et al., 2000), exhibiting scale-invariance in the sense that the stress drop associated with dynamic slip is relatively constant and relatively small (3MPa compared with tectonic and lithostatic stresses of the order of 10-100MPa) over a wide range of scales. Figure 2.3 shows the power-law relationship between earthquake stress

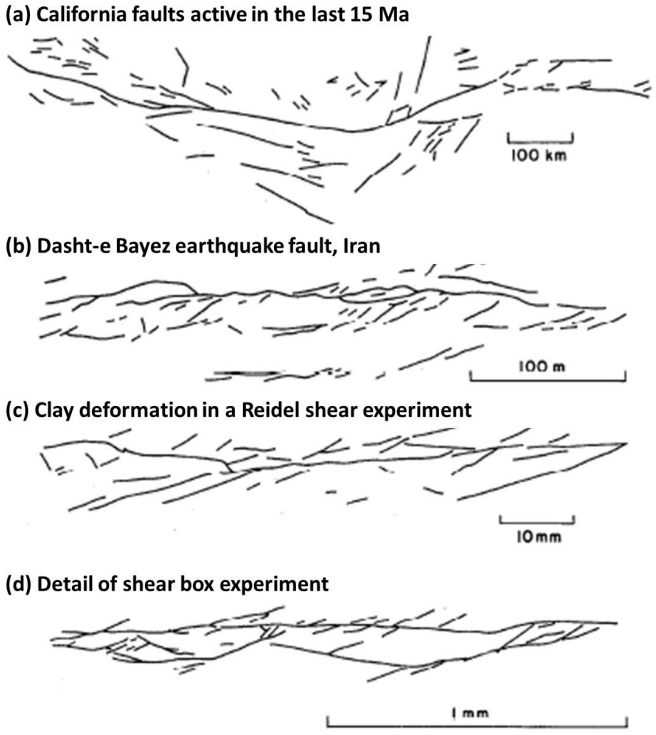


Figure 2.2: Traces of fault populations on a range of scales, from crustal faults (a) and (b) to laboratory experiments (c) and (d) (after Main et al., 1990). The patterns are scale invariant: without scale bars it would be difficult to distinguish between them.

drop and source dimension (Abercrombie, 1995). Additionally, seismicity can be induced by stress perturbations smaller than the stress drop in individual events, i.e., earthquakes can be triggered (Brune, 1979), both by previous earthquakes at relatively great distances (e.g., Hill and other authors, 1993; Stein et al., 1994; Gomberg and Davis, 1996; Stark and Davis, 1996; Pollitz et al., 2012) or by local changes in pore fluid pressure through anthropogenic activity (Segall, 1989).

The ubiquity of the Gutenberg-Richter relation globally, regionally and even down to the laboratory scale, implies universal multifractal behaviour of earthquakes and fault systems, which in turn demonstrates complexity and chaotic behaviour in the deformation and fracture of the Earth's crust (Turcotte et al., 2000). Although absolute prediction of the time and place of a slip event (or earthquake) is not possible for a chaotic system, probabilistic forecasts are still possible (Rundle et al., 2003). Elastically-governed slider-block models illustrate this transition very well; one block displays periodic, stick-slip behaviour, while a pair of slider blocks exhibit deterministic chaos (Huang and Turcotte, 1990). When large arrays of blocks are considered, power-law distributions for slip event sizes are obtained, and behaviour characteristic of self-organising critical systems is displayed (e.g., Burridge and Knopoff, 1967; Otsuka, 1972; Carlson and Langer, 1989; Huang et al., 1992; Olami et al., 1992; Barriere and Turcotte, 1994). Some degree of predictability is now recognised in these types of systems (Jordan, 2006; Helmstetter et al., 2006). Reviews of a wide variety of slider-block models can be found in Turcotte (1992), Carlson et al.

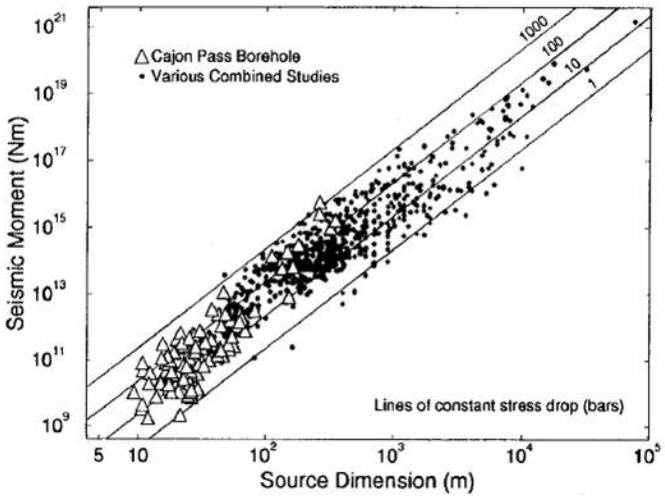


Figure 2.3: Scaling of seismic moment as a function of source size (after Abercrombie, 1995). The straight lines are predicted scaling laws at different stress drops (in bars) from a simple dislocation model of the seismic source.

(1994) and Rundle and Klein (1995). Studies using these kinds of models have established that although complexity in the stress field and in the spatio-temporal patterns of earthquakes can occur solely due to nonlinear dynamics (Shaw, 1993; 1994; 1995; Ben-Zion and Rice, 1997), crustal heterogeneity is a dominant factor in the multi-scale complex nature of earthquakes and faulting (Ouillon and Sornette, 1996; Scholz, 1991; 2002). The behaviour of such models illustrates that the simple extrapolation of the properties of a few elementary particles cannot necessarily fully describe the behaviour of large and complex aggregates of these particles. Instead, at each level of complexity entirely new properties appear (Anderson, 1972; Sornette, 2006). Such systems can reproduce the scaling and power-law distributions associated with ensembles of many cracks and earthquakes.

### 2.3.2 Self-organised criticality and critical point phenomena

Self-organised criticality (Bak et al., 1987; Tang and Bak, 1988; Bak and Tang, 1989; Bak, 1990) offers an overarching concept for the scale-invariant behaviour observed in nature. Broadly, a self-organised critical (SOC) system is one externally driven to a stable but critical state which, when perturbed from that state, will spontaneously evolve back to the balanced state. Such systems are characterised by an extremely large susceptibility to external factors and strong correlation between different parts of the system (Sornette, 2006). Input into the system is continuous, but release occurs in a discrete set of events characterised by self-similar size distributions and fractal geometries; behaviour relatively insensitive to the details of the dynamics. These dynamic events manifest as statistical fluctuations or 'avalanches'. Avalanches correspond to rare and sudden transitions occurring over very short time intervals compared to the external driving force. These events provide an insight into the driving forces behind an otherwise balanced system. However, their power-law size distributions and spatio-temporal correlations mean that very large

events occur relatively frequently, exerting a significant impact on society in the form of large natural or anthropogenic catastrophes.

An important sub-class of SOC phenomena consists of out-of-equilibrium systems, driven with constant rate and made of many interactive components, which have the following fundamental properties (Sornette, 2006): (1) highly nonlinear behaviour, i.e., a threshold response, (2) a very slow driving rate, (3) a globally stationary state, characterised by stationary statistical properties and (4) power-law distributions of event sizes and fractal geometries (including long-range correlations). One system that obeys these four conditions very well is the Earth's crust (Bak and Tang, 1989; Grasso and Sornette, 1998; Sornette and Sornette, 1989; Sornette et al., 1990b; Sornette, 1991; Sornette and Virieux, 1992). The slow driving rate (cm/yr), due to the tectonic forces at plate boundaries (Section 2.2), is separated by around nine orders of magnitude from the slip velocity of earthquakes (m/s). This large separation of timescales, combined with the threshold response of dynamic rupture or a frictional stick-slip instability, make crustal deformation one of the best natural examples of SOC (see reviews in Sornette, 1991; Main, 1996). Existence of an instability threshold allows the system to accumulate and store the slowly increasing stress until the critical level is reached and an earthquake is triggered. This dynamic response is decoupled from the driving force by the timescale separation and reflects the critical organisation of the crust. Additionally, scale invariance and long-range interactions are reflected in the power-law behaviour and fractal properties of the crust. Faults and earthquakes exist and interact across scales spanning at least ten orders of magnitude (from tens of microns to thousands of km); a critically stressed crust can produce earthquakes of all sizes (Main, 1996; Madariaga and Olsen, 2002). This led several groups to suggest that self-organised criticality is a natural explanation for the Gutenberg-Richter law (Sornette and Sornette, 1989; Bak and Tang, 1989; Ito and Matsuzaki, 1990; Correig et al., 1997). Moreover, a cellular-automata model for distributed seismicity, derived with a fractal distribution of box sizes, was shown to generate foreshocks, aftershocks and satisfy Gutenberg-Richter statistics (Barriere and Turcotte, 1991; 1994). Different portions of the crust become correlated at long distances by the action of earthquakes, which 'transport' the stress field fluctuations back and forth many times between these different parts to finally organise the system. Long-term, fractal organisation of faulting within the crust, together with its associated stationary statistical properties, is evidence that the crust is not in a transient phase, but in a marginally stable, stationary state.

The notion of SOC provides a scientific rationale for the *a priori* assumption of stationarity used as a first step in the prediction of the future level of seismic hazard (Main, 1996). A constant energy flux is crucial to the development of a self-organising system (Sornette and Sornette, 1989). Essential features of SOC models for earthquakes include a constant strain rate boundary condition, tectonic stress as the critical parameter ($\sigma_c$), dynamic fluctuations consisting of small stress drops ($\Delta\sigma_c << \sigma_c$) and power-law distributions in source length, seismic moment or energy (Main, 1996). Solutions of such models with elasticity incorporated have shown that the spatial correlation of stress (and strain) fluc-

tuations around the average stress (and strain) is long-range and decays as a power law (Sornette, 2006). This prediction, that the stress field exhibits long-range spatial correlations as well as amplitude fluctuations, illustrates the spontaneous organisation of the fault structure on which the earthquake activity is clustered. As well as reflecting the organising principle leading to SOC, stress fluctuations are an active and essential component of it. SOC in the Earth is therefore also consistent with the observation of induced seismicity since such stress perturbations, even relatively small ones, can trigger earthquakes (Main, 1996; Grasso and Sornette, 1998). This observation, that a substantial fraction of the crust is close to rupture instability, combined with the localisation of seismicity on faults means that although presently quiescent, a significant fraction of the crust is susceptible to rupture. Thus, Scholz (1991) argues that the lithosphere is everywhere in a state of SOC and on the brink of failure; whenever the crust is loaded, earthquakes are induced whether the area is tectonically active or not (Rundle et al., 2003). However, Sornette (2006) argues that not all of the crust is in a state of marginal stability; because of the existence of this finite fraction of susceptible crust, there is a complementary finite fraction of the crust that is relatively stable and resistant to perturbations. Consequently the crust is, on average, far from rupture and it is the strong, clustered stress fluctuations characteristic of SOC that bring the susceptible fraction of the crust close to rupture. Confirmation that global seismicity is in a near-critical state, with large fluctuations in mean energy occurring for small changes in entropy, was supplied by Main and Al-Kindy (2002). They concluded that this proximity to the critical point implies a finite but perhaps low degree of statistical predictability in the population dynamics.

The applicability of self-organised criticality to some systems has, however, been questioned (Sykes et al., 1999). For example, extrapolation of the Gutenberg-Richter trend predicts occurrence probabilities for the largest earthquakes that are larger than the observed probabilities and Hatton et al. (1994) argue against the range of applicability of the total offset to fault length relationship. Such systems are sensitive to external conditions and are more accurately described as 'sub-critical' with intermittent criticality (Main, 1996; Main and Al-Kindy, 2002). The process of rupture in terms of fault formation, nucleation and propagation can be explained in terms of critical point phenomena. For example, Lei and Satoh (2007) inferred indicators of critical point behavior prior to rock failure from pre-failure damage in the form of acoustic emissions. An analogue model by Cowie et al. (1993) showed the progression from fault nucleation to a sub-critical growth of earthquakes during fault growth simply from the statistical physics of elastic-brittle interactions in heterogeneous granular materials. In the laboratory, crack coalescence and interaction to form a macroscopic fault is associated with a decreasing $b$-value (Sammonds et al., 1992) and the effects are influenced by stress intensity and by the presence of fluids (Meredith et al., 1990). Fault nucleation, therefore, cannot be classed as a process of self-organised criticality because the changing $b$-value implies a sub-critical process (first-order phase transition). Interestingly, however, the $b$-value does become roughly constant during frictional sliding (Sammonds and Ohnaka, 1998) indicating proximity to the critical point

(second-order phase transition) and large fluctuations (Rundle et al., 2003). Nevertheless, the question of crustal deformation has potentially far more complex problems requiring solution than either SOC or the theory of critical phenomena promises to deliver (Sornette and Werner, 2009) and the recent introduction of a statistical mechanics for complex systems which operate far from equilibrium (Tsallis, 1988) may offer further insight.

## 2.4 Non-Extensive Statistical Mechanics

### 2.4.1 Introduction

Statistical mechanics attempts to relate the macroscopic, measurable properties of a dynamic system to an underlying quantitative picture of its microscopic mechanics (Ford, 2011). The basic assumption is that the detailed behaviour of the elementary particles is irrelevant; it is their average behaviour and therefore their statistical properties that are important. The concept arose from thermodynamics, where thermodynamic systems containing of the order of $10^{23}$ molecules can be sufficiently characterised by a handful of macroscopic properties (energy, pressure, temperature, etc.) and the behaviour of individual molecules does not affect the overall equation of state. The state of such systems is generally described by the probability distribution function of a physical observable, the mean of which is the overall macroscopic property. Gaussian (normal) distributions are often seen in systems where the dynamics are dominated by a large number of small random events, such as the erratic motion of a small particle in water (Brownian motion). However, in some systems, the dynamics are dominated by rare and large fluctuations which result in long, power-law tailed distributions, known as Lévy distributions, which are associated with a divergence of the first and/or second moment of these distributions (Lutz, 2003; 2004; Douglas et al., 2006). Seismicity is an example of this kind of non-equilibrium dynamics, as shown by Sotolongo-Costa et al. (2000) who established that the seismicity of Southern Spain (1985-1994) could be described both spatially and temporally by a Lévy flight with anomalous diffusion.

The basis of statistical mechanics is the concept of entropy, $S$, which is a measure of the disorder of a system. While energy deals with the *possibilities* of a system, entropy deals with the *probabilities* of those possibilities (Tsallis, 2009a). Entropy is, *by definition*, an extensive property; i.e., it is proportional to the number of elements, $N$, in the system ($S(N) \propto N, N \to \infty$) and the laws of thermodynamics require that it remains so (Tsallis, 2013; Cartwright, 2014). The classical definition, introduced by Ludwig Boltzmann (1872; 1877) over a century ago, is $S = k_B \ln W$, where $k_B$ is the Boltzmann constant and W is the total number of possible configurations (microstates) in the system. Under this definition, the probability of each microstate occurring is equal. If the system has lots of different microstates, $i$, each with their own probability, $p_i$ of occurring, the equation generalises to $S_{BG} = -k_B \sum_{i=1}^{W} p_i \ln p_i$, as shown by Gibbs (1902).

However, there are cases where the Boltzmann-Gibbs formula does not keep entropy extensive. Such systems include out-of-equilibrium, strongly correlated and multifractal systems. According to Sornette (2006), Boltzmann-Gibbs statistics are not expected to hold for strongly correlated, self-organising systems with avalanche-like dynamics (e.g., SOC models) because the avalanches themselves are vehicles for the correlations and spontaneous self-organisation. Due to the effective long-range coupling induced by large avalanches, the Boltzmann-Gibbs entropy ($S_{BG}$) of the system no longer scales with the number of elements in it (i.e., it is no longer extensive) and consequently, the system's energy cannot be partitioned without changing its organisation. This implies serious limitations to the application of $S_{BG}$ in Earth systems. For example, Englmant et al. (1987) maximised $S_{BG}$ to study fragmentation phenomena but could not obtain the scaling present in the size distribution of fragments and the resulting size distribution function does not agree with the all experimental results. Tsallis (2009a) provides a detailed review of historic literature expounding the limitations of $S_{BG}$. Accordingly, based on the arguments given above regarding the complex, critical nature of deformation in the Earth's crust, it is apparent that a statistical mechanics approach based on the classical Boltzmann-Gibbs entropy is not necessarily the most appropriate for studying fracture phenomena. A broader approach is needed.

### 2.4.2 Tsallis entropy

Rock deformation in the Earth's crust, both brittle and plastic, involves complex non-equilibrium phenomena such as multi-fractal distributions, self-organised criticality, long-range interactions and intermittency (e.g., Pollitz et al., 2012; Sammonds, 2005; Richeton et al., 2005; Weiss and Marsan, 2003; Main et al., 1994; Bak and Tang, 1989). In cases where there are strong correlations between the elements of a system, i.e., the probability of a certain microstate occurring depends strongly on the occurrence of another microstate, the Tsallis (1988) entropy, $S_q$, which is a generalisation of the Boltzmann-Gibbs entropy, may be more appropriate than the classical Boltzmann-Gibbs entropy. The form of this generalisation was inspired by the fractal properties of complex dynamic systems and is defined as:

$$S_q = k_B \frac{1 - \sum_{i=1}^{W} p_i^q}{q - 1}, q \in \Re \tag{2.3}$$

where $q$ is a system-dependent parameter, W is the number of possible microstates and $k_B$ is the Boltzmann constant. The value of $q$ is either more or less than one in such systems - effectively to bias the probabilities of certain microstates occurring (Tsallis, 2009a; Cartwright, 2014) - but, in the limit where $q$ approaches 1, the Tsallis entropy reduces to the Boltzmann-Gibbs entropy. Power laws naturally emerge when $S_q$ is maximised. This theory of non-extensive statistical mechanics (NESM) (Tsallis, 1988), pioneered by the Tsallis group (see Tsallis, 2009a, for a full review), therefore offers a consistent theoretical approach for analysing rock fracture populations and other fracture phenomena which exhibit power-law behaviour. My thesis is concerned with investigating the applicability

of the Tsallis approach to fracture-induced electric current emissions.

$S_q$, defined as in Equation 2.3, maintains thermodynamic extensivity for a wide range of complex systems but, when $q \neq 1$, violates the additivity principle of independent systems. This states that for any two probabilistically independent systems, $A$ and $B$, the total entropy of the system equals the sum of the entropies of its parts: $S(A+B) = S(A)+S(B)$ (Penrose, 1970). However, in terms of $S_q$ (Tsallis, 1988; 2009a):

$$S_q(A+B) = S_q(A) + S_q(B) + \frac{(1-q)}{k_B} S_q(A) S_q(B) \tag{2.4}$$

which means that when $q = 1$, the third term in Equation 2.4 disappears and the individual elements of the system, $A$ and $B$, are therefore independent of each other ($S_q \equiv S_{BG}$). When $q \neq 1$, the total entropy does *not* equal the sum of the parts; the third term in Equation 2.4 is no longer zero, $A$ and $B$ are therefore not independent of each other and the $q$-parameter effectively describes the interaction between the two systems, i.e., it is a measure of the strength of their correlations. The further $q$ is from one, the more influence the third term has on the total entropy and the greater the coupling between events. In terms of earthquakes and fracture, this $q$-index may be physical; a measure of the dynamic stability of the crack network. As the stability of one crack becomes increasingly dependent on the stability of the other cracks, the total stability of the system decreases. Therefore, $q$-values far from one mean that the fault planes are far from equilibrium and more earthquakes can be expected (Sotolongo-Costa and Posadas, 2002).

For the particular case of equal probabilities $S_q = k_B \ln_q W$, where the $q$-logarithm function $\ln_q$ is defined as:

$$\ln_q x \equiv \frac{x^{1-q} - 1}{1-q} \tag{2.5}$$

where $x > 0$ and $\ln_1 x = \ln x$ and which, given the appropriate $q$-value that describes the distribution of $x$, is linear with $x$ (Abe and Suzuki, 2005; Tsallis, 2009a). It's inverse, the $q$-exponential probability distribution $e_q^x$, which can be derived from the maximum entropy principle (see Tsallis, 1988; Abe and Suzuki, 2005; Tsallis, 2009a;b), is given by:

$$\mathrm{e}_q^x \equiv [1 + (1-q)x]_+^{1/1-q} \tag{2.6}$$

where $\mathrm{e}_1^x = \mathrm{e}^x$ and $[z]_+ \equiv max\{z, 0\}$.

More generally, maximising $S_q$ under appropriate constraints using the Lagrange multipliers method (see Umarov et al., 2008; Tsallis, 2009a;b) yields a $q$-Gaussian probability distribution:

$$p_q(x) = \frac{1}{Z_q(B)} (1 + B(q-1)x^2)^{-1/q-1} \tag{2.7}$$

for $1 \leq q < 3$, where $B$ is a scaling parameter and $Z_q(B)$ is the partition function ($\frac{1}{Z_q(B)} = p_q(x)_{max}$). This converges to a Gaussian (normal) distribution as $q \to 1$, while the Cauchy distribution is recovered when $q = 2$ (Umarov et al., 2008).

The conditions under which this is done are as follows:

$$\int p(x)dx = 1 \tag{2.8}$$

$$\int P^{(q)}(x)U(x)dx = U_q \tag{2.9}$$

where $P^{(q)}(x) = \dfrac{p(x)^q}{\int p(x)^q dx}$ is the escort probability (Tsallis, 2009a), $U(x)$ is the function under study which describes the system's behaviour and $U_q$ is known as the $q$-average (Tsallis, 2001).

In the case of a parabolic function $U(x) = x^2$, $U_q$ becomes a generalised variance $\sigma_q^2$ (Beck and Cohen, 2003), which corresponds to the intensity of the dynamic variable $x$. Applying the Lagrange multiplier method and the variational principle to the Tsallis generalised entropy function, $S_q[p] = k\dfrac{1}{q-1}(1-\int p(u)^q du)$, $q > 1$ under the constraints of Equations 2.8 and 2.9 (see Tsallis, 2009a, Section 3.5) yields a generalised normal distribution:

$$p(x) = \frac{1}{Z_q(B)}\left\{1 + B(q-1)U(x)\right\}^{-1/q-1} \tag{2.10}$$

where $Z_q$ is a generalised partition function. Particularly, in the case of $U(x) = x^2$, this generalised normal distribution becomes the $q$-Gaussian distribution (Equation 2.7), where $Z_q(B) = (B(q-1))^{-1/2}\dfrac{\Gamma(1/2)\Gamma(1/(q-1)-1/2)}{\Gamma(1/(q-1))}$ and $\Gamma(v)$ is a gamma function defined as $\Gamma(x) = \int_0^\infty e^{-t}t^{v-1}dt$.

Figure 2.4 shows the various forms of the $q$-Gaussian (a) and $q$-exponential (b) distributions for different values of $q$. It can be seen from these figures that the $q$-index has most influence over the shape of the tails of the distribution and is therefore essential for describing the probabilities of extreme events. Both these distributions are characterised by power-law tails that emerge naturally from maximising the Tsallis entropy (Tsallis, 1999).

It should be noted here that is also possible to derive fat-tailed distributions from conventional statistical mechanics by explicitly introducing the broad-band fractal nature of the structures involved through a geometric degeneracy term (e.g., Main and Burton, 1984). The conventional entropy can be used to derive the Helmholtz Free energy, and from that the associated thermodynamic parameters. Both approaches are consistent with a near-critical system with system-spanning correlations, where sub-domains of the system are not independent.

There are many physical and mathematical mechanisms that generate power-law distributions and self-similar behaviour and an active field of research is understanding how the microscopic laws select a particular mechanism (see Sornette, 2006, for a detailed review). The advantage of using the Tsallis approach is that because of its basis in thermodynamics, it does not rely on empirical statistical fits (Tsallis, 2013; Cartwright, 2014); the $q$-parameter can be calculated directly from first principles (Caruso and Tsallis, 2008).

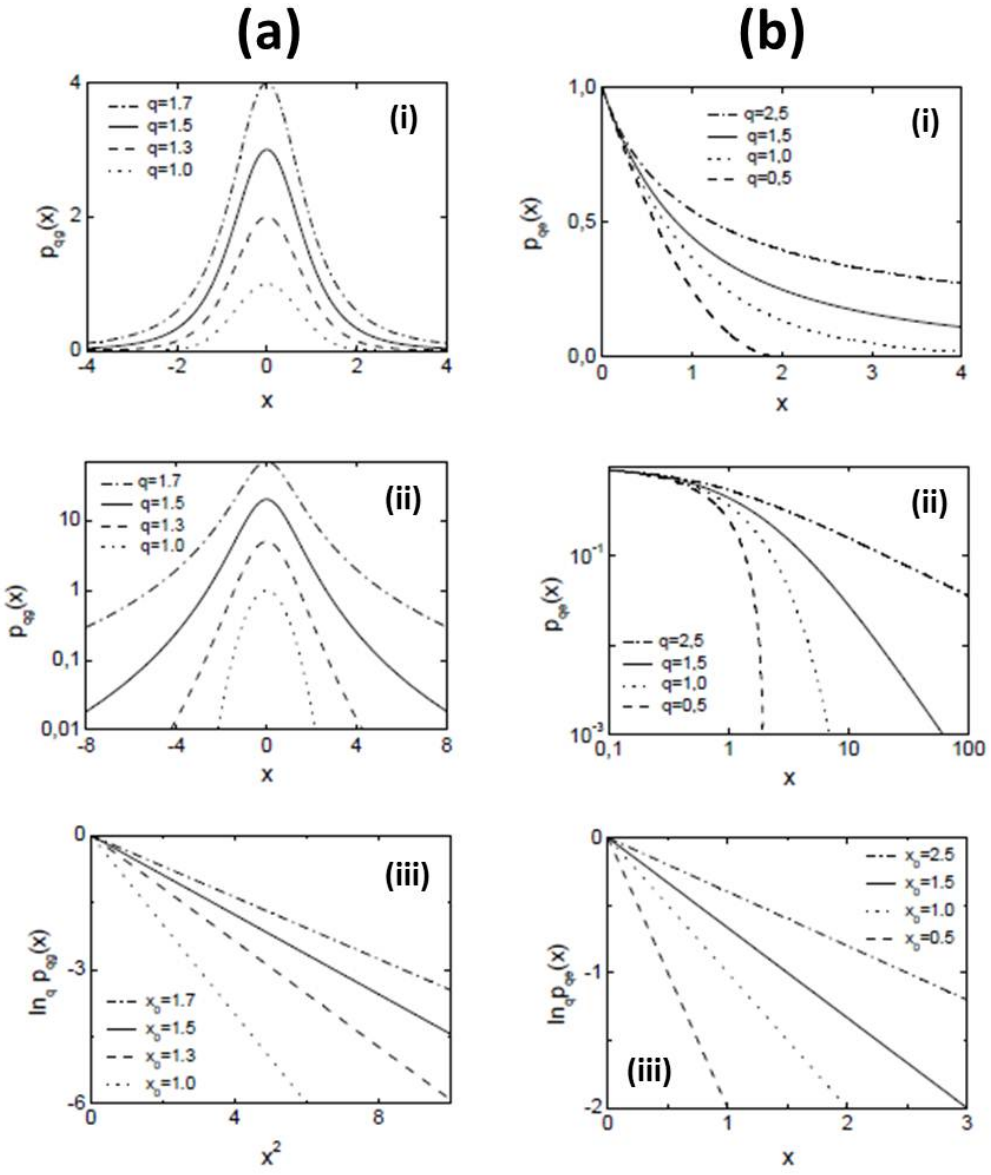


Figure 2.4: Tsallis distributions (a) $q$-Gaussian (b) $q$-exponential for typical values of $q$. Plots of $p_q(x)$ versus $x$ with $1/Z_q(B) = 1/B = 1$ are given in (i), while (ii) show the same curves but on a linear-log scale (a) and on a log-log scale (b). Some curves in (a) have been vertically shifted for better visualisation. Plots of $\ln_q p_q(x)$ for $1/Z_q(B) = 1$ and typical values of $1/B$ are given in (iii) versus $x^2$ (a) and versus $x$ (b). After Picoli Jr. et al. (2009).

For example, Lutz (2003) demonstrated theoretically that Tsallis statistics appear naturally in the anomalous region of atomic transport in optical lattices (intermediate regime between diffusive motion in deep optical potentials and ballistic motion in shallow potentials) and derived an analytical expression for $q$ in terms of the microscopic parameters of the quantum-optical system. Solutions to the momentum equation for describing atomic motion in the optical potential are exactly given by Tsallis distributions, the shapes of which (and therefore the $q$-value) are solely dependent on the potential depth, $U_0$. Empirical evidence that Tsallis statistics correctly give the microscopic energy distribution for a known system was later provided by Douglas et al. (2006), who demonstrated experimentally that the momentum distribution of cold atoms in dissipative optical lattices is a Tsallis distribution whose $q$-parameter can be varied by changing the depth of the optical lattice. The momentum distribution changes from a Gaussian distribution ($q = 1$) at deep potentials to a $q$-Gaussian (power-law tail, $q \neq 1$) at shallow optical potentials.

However, because deformation in the Earth's crust is so complex, establishing associated theoretical $q$-values from first principles is difficult. For observational data, empirical fitting of the distribution is necessary for its determination. This is no different from how distribution parameters for other accepted theories are employed in practice, although some detractors argue that the introduction of an additional parameter (i.e., the $q$-index) would naturally return a better empirical fit to the data (Cartwright, 2014). However, use of the Tsallis approach is justified by the fact that it is (1) defined *a priori*, (2) specific to the behaviour or geometry of the system (e.g., power-law, fractal) and (3) maintains extensivity. Thus, the use of additional parameters does not simply over-parameterise the problem; it is in fact necessary, as dictated by the dynamics of the system in question (Tsallis, 2013).

The introduction of $S_q$ expands the range over which statistical mechanics can be applied beyond simple, random systems with smooth geometries to more complex, strongly correlated systems with fractal or multifractal geometries that operate far from equilibrium (Tsallis, 2013). Over the past 25 years, Tsallis statistics have been shown to describe many such systems in fields across physics, chemistry, biology, earth sciences, medicine, informatics, economics and more, resulting in some significant scientific advances. For instance, black holes can now be defined in terms of their volume rather than their area (Tsallis and Leonardo, 2013), the survival rate of cells with increasing chemotherapy dose is more precisely predicted (Sotolongo-Grau et al., 2010; 2013) and improved image analysis techniques have more accurately segmented tissues in MRI scans and mammograms (Diniz et al., 2010; Mohanalin et al., 2010). Additionally, the Tsallis approach offers a better description of the energy distribution in SOC models (Sornette, 2006). Since systems at criticality also exhibit fractal geometries, connections exist between $q$ and the critical phenomenon (Tsallis, 2009a). Thus, the Tsallis approach has also been applied to the problem of crustal deformation and used to describe patterns of seismicity.

### 2.4.3 Application of Tsallis entropy to the Earth's deforming crust

Abe and Suzuki (2003; 2004; 2005) were the first to use the Tsallis approach in the Earth sciences. Their research, studying spatial and temporal patterns of seismicity, highlighted the scale-free, correlated nature of both the times (Abe and Suzuki, 2005) and distances (Abe and Suzuki, 2003) between successive earthquakes in California and Japan. They showed that these regions' power-law statistics can be represented by the $q$-exponential distribution, which exhibits a long power-law tail, with $q_t > 1$ for inter-event times and $q_d < 1$ for inter-event distances with $q_t + q_d \sim 2$, known as spatio-temporal *duality*. Similar results have since been verified numerically using the 2D Burridge-Knoppoff slider-block model (Hasumi, 2007; 2009) and reported empirically for global seismicity (Vallianatos and Sammonds, 2013), for seismicity in Iran (Darooneh and Dadashinia, 2008), for regional seismicity (Michas et al., 2013) and aftershock sequences (Vallianatos et al., 2012b) in the Corinth Rift and for laboratory acoustic emissions (Vallianatos et al., 2012a). They also established that aftershock sequences exhibit an aging phenomenon (Abe and Suzuki, 2004), i.e., that the smaller the time between successive aftershocks, the faster the decay in correlation between aftershock events (Abe et al., 2005b). Tsallis statistics have since been widely applied to global and regional patterns of seismicity, fault populations and laboratory-scale fracture phenomena.

#### 2.4.3.1 Spatio-temporal patterns of seismicity

Further studies have confirmed that the $q$-exponential distribution provides an excellent description of earthquake spatial and temporal distributions (see Table 2.1 for $q$-values). For instance, inter-event times and distances for several regions along the Hellenic Subduction Zone (HSZ) (Papadakis et al., 2013). Here, $q$-values for inter-event times ($q_t$) remain fairly constant across the different zones, with the highest temporal clustering to the south of Crete, possibly reflecting the fact that time evolution of seismicity is a long term process in the Hellenic arc. On the other hand, $q$-values for inter-event distances ($q_d$) vary more widely suggesting a variation in spatial clustering between the seismic zones. In Iran, Darooneh and Dadashinia (2008) found that $q_t$ and $q_d$ remained approximately constant with occurrence period and regional extent but moved further away from an uncorrelated state, increasing and decreasing respectively by $\sim 0.3$ with an increasing threshold magnitude. This indicates greater correlation in the timing between larger events and that a large-magnitude earthquake is more likely to trigger another quake in adjacent faults. Spatio-temporal $q$-values of the aftershock sequence of the Aigion earthquake, Corinth Rift (Vallianatos et al., 2012b) are similar to those found elsewhere, as are $q_t$ values for the recent seismic unrest at Santorini volcano (Vallianatos et al., 2013b). The clustering effect of aftershocks on the inter-event time distribution for historical Greek seismicity (Antonopoulos et al., 2014) indicates a stronger time correlation between main earthquakes with their aftershocks than without. Finally, although cumulative inter-event times for recent seismicity in the Corinth Rift (Michas et al., 2013) are well-described by a

$q$-exponential, their probability density, which exhibits two power-law regions for shorter and longer inter-event times, can best be described by a $q$-generalised gamma distribution that accounts for correlation, non-stationarity and memory effects at all-time scales.

Table 2.1: Spatio-temporal $q$-values for seismicity in various regions worldwide

| **Region** | **Seismicity data analysed** | $q_t$ | $q_d$ | **Reference** |
|---|---|---|---|---|
| Global | 1981-2011 | 1.5 | 0.29 | Vallianatos and Sammonds 2013 |
| California | 1984-2001 | | 0.773 | Abe and Suzuki 2003 |
| California | 1984-2002 | 1.13 | | Abe and Suzuki 2005 |
| Japan | 1993-1998 | | 0.747 | Abe and Suzuki 2003 |
| Japan | 1993-1998 | 1.05 | | Abe and Suzuki 2005 |
| Iran | 1996-2005 | $1.32 \pm 0.246$ | $0.733 \pm 0.115$ | Darooneh and Dadashinia 2008 |
| Greece | 1976-2009 with aftershocks | 1.24 | | Antonopoulos et al. 2014 |
| Greece | 1976-2009 without aftershocks | 1.14 | | Antonopoulos et al. 2014 |
| HSZ* | 1976-2009 | $1.1 \pm 0.06$ | $0.485 \pm 0.185$ | Papadakis et al. 2013 |
| Corinth Rift | 2001-2008 | 1.25 | | Michas et al. 2013 |
| Corinth Rift | Aigon aftershocks | 1.58 | 0.53 | Vallianatos et al. 2012b |
| Santorini | 2011-2012 | 1.52 | | Vallianatos et al. 2013b |

*Hellenic Subduction Zone

#### 2.4.3.2 Earthquake magnitude distributions

Modelling of frequency-magnitude distributions is mainly based on a non-extensive modification of the Gutenberg-Richter law first derived by Sotolongo-Costa and Posadas (2004) in their fragment-asperity interaction model for earthquakes (Section 2.4.4.1). Cumulative magnitude distributions for seismicity in several regions have been well-predicted by this model and the associated $q$-values for earthquake magnitudes ($q_m$) can be found in Table 2.2. $q_m$ values for California, the Iberian Peninsula and Andalucía (Sotolongo-Costa and Posadas, 2004) were found to be similar to those in Italy (Telesca, 2010c) and Taiwan (Telesca and Chen, 2010) as well as those along individual faults in the USA, Turkey and Brazil (Silva et al., 2006; Vilar et al., 2007), with $q_m$ in the range $1.6 - 1.7$. Seismicity in the Javakheti Highlands, Georgia (Matcharashvili et al., 2011) exhibited a comparatively high $q_m$ over the whole period of observation. However, in consecutive, overlapping 10-year windows (with 1-year shift) $q_m$ values fell within the range reported worldwide. Conversely, $q_m \sim 1.4$ for seismicity in Greece (Michas et al., 2013; Papadakis et al., 2013; Antonopoulos et al., 2014), possibly due to the volcanic nature of the environment. Volcano-seismicity in the Mediterranean exhibits smaller values than purely tectonic environments, with $q_m$ in the range $1.4 - 1.6$. The difference between $q_m$ values for volcano-seismicity at Vesuvius compared with those for tectonic seismicity across the whole Italian territory may provide a potential way to distinguish between tectonic and volcanic seismicity (Telesca, 2010c). It is attributed to either: (a) a different mechanism of earthquake generation; fracture of intact rock at Vesuvius rather than the fault slip typical of tectonic earthquakes or (b) the different intensity of the seismic activity; a lower $q$-value at Vesuvius may represent seismic quiescence and a physical state closer to equilibrium in comparison to the Italian seismicity.

In Taiwan (Telesca and Chen, 2010) and Greece (Antonopoulos et al., 2014), $q_m$ remained

approximately the same after the aftershocks were removed, indicating that the fragment-asperity approach is robust for clustered as well as de-clustered seismicity. Antonopoulos et al. (2014) also computed a $q$-dependent hazard function for the probability that at least one earthquake of magnitude larger than $M$ will occur in the next time interval $\Delta T$, if the last earthquake occurred $T$ days ago. Variations in $q_m$ across regions along the Hellenic Subduction Zone (HSZ) (Papadakis et al., 2013) are strongly related to the energy release rate in each zone, with more active zones yielding higher $q$-values. In Italy, spatial variation in $q_m$ from 1.4 to 1.7 (Telesca, 2010a) suggests that earthquake triggering is governed by different mechanisms in different areas; stick-slip where $q_m$ is lower and fragment-asperity interaction where $q_m$ is higher. Areas with lower $q_m$ are distinguished by relatively large events, characteristic of the large energy release involved in the collision and breakup of irregular surfaces of faults during stick-slip. The variation in $q_m$ across four Mexican subduction regions (Valverde-Esparza et al., 2012), although small, appeared to relate to the inclination angle of the subducting slab; relatively higher $q$-values were associated with a steeper dip angle. For California earthquakes that occurred only in 2010 (Telesca, 2011), $q_m$ is relatively small and decreases with increasing threshold magnitude, which the authors attribute to the necessity of smaller events in an earthquake system to redistribute the stress and initiate a state where correlation and interactions can take place also among higher events. Smaller events may behave as links among the higher events, where the correlations are transferred, thus producing an enhancement of the $q$-value. At Santorini volcano (Vallianatos et al., 2013b), the magnitude distribution departs from the power-law frequency-magnitude distribution at higher magnitudes, exhibiting a bimodal character. However, this complexity is well-modelled by the fragment-asperity model. The bimodal character is also seen in the global magnitude distribution (Vallianatos and Sammonds, 2013), where $q_m$ for intermediate events falls within the range reported worldwide.

Table 2.2: Earthquake magnitude $q$-values for seismicity in various regions worldwide

| **Region** | **Seismicity data analysed** | $q_m$ | **Reference** |
|---|---|---|---|
| Global | 1981-2011 | 1.6 | Vallianatos and Sammonds 2013 |
| Italy | 2005-2009 | 1.67 | Telesca 2010c |
| Taiwan | 1990-2007 with aftershocks | 1.68 | Telesca and Chen 2010 |
| Taiwan | 1990-2007 without aftershocks | 1.69 | Telesca and Chen 2010 |
| Greece | 1976-2009 with aftershocks | 1.44 | Antonopoulos et al. 2014 |
| Greece | 1976-2009 without aftershocks | 1.46 | Antonopoulos et al. 2014 |
| Mexico | 1988-2010 four subduction zones | $1.67 \pm 0.03$ | Valverde-Esparza et al. 2012 |
| California | 2010 | $1.51 \pm 0.04$ | Telesca 2011 |
| California | NEIC - no dates given | 1.65 | Sotolongo-Costa and Posadas 2004 |
| Iberian Peninsula | IGN - no dates given | 1.64 | Sotolongo-Costa and Posadas 2004 |
| Andalucía | IAG - no dates given | 1.60 | Sotolongo-Costa and Posadas 2004 |
| Javakheti Highlands | 1960-2008 | 1.81 | Matcharashvili et al. 2011 |
| HSZ* | 1976-2009 | $1.43 \pm 0.09$ | Papadakis et al. 2013 |
| Corinth Rift | 2001-2009 ($\leq$ 35 km depth) | 1.37 | Michas et al. 2013 |
| Samambaia fault | BSRBG - no dates given | 1.60 | Silva et al. 2006 |
| New Madrid fault | NEIC - no dates given | 1.63 | Silva et al. 2006 |
| Anatolian fault | NEIC - no dates given | 1.71 | Silva et al. 2006 |
| San Andreas fault | 2004-2006 | 1.68 | Vilar et al. 2007 |
| Vesuvius | 1972-2007 ($M \geq 1.9$) | 1.48 | Telesca 2010c |
| Etna | 1832-2005 ($M \geq 2.2$) | 1.57 | Telesca 2010c |
| Santorini | 2011-2012 | 1.39 | Vallianatos et al. 2013b |

*Hellenic Subduction Zone

The generally excellent agreement between cumulative earthquake magnitude distributions

and the non-extensive fragment-asperity magnitude distribution (Equations 2.12, 2.13 and 2.14) indicates that the fragment-asperity model provides a good description of seismicity in a variety of regional tectonic and volcanic environments. Values of $q_m$ in the range $1.6 - 1.7$ seem to be consistent for global and regional seismicity across *tectonic* environments, indicating a certain universality in the non-extensive characterisation of seismic energy distributions (Vilar et al., 2007; Telesca, 2011).

#### 2.4.3.3 Earthquake preparation

Tsallis statistics have also helped to characterise the earthquake preparation stage, in terms of both seismicity and pre-seismic electromagnetic emissions (PEME). Non-extensive properties of PEME and their role in earthquake preparation are discussed in Chapter 3. Seismic magnitudes surrounding the $M_L = 5.8$ 2009 L'Aquila earthquake (Telesca, 2010b) show an increase in $q_m$ from 1.48 to 1.74 in the days before the main shock, indicating an increase in the degree of out-of-equilibrium state immediately prior to the main event. This observation is supported by seismicity data surrounding the $M = 7.2$ 1995 Kobe earthquake (Papadakis et al., 2014). Here, a significant and sudden jump in the $q_m$ value from 1.48 to 1.49 was observed on 9th April 1994, several months prior to the main shock. This indicates the start of a transition phase towards the main shock. Whereas $q_m$ had been consistently in the range 1.47-1.48 during the two years preceding this jump, immediately after the jump it increased gradually over the following nine months from 1.49 to a peak of 1.5 at the event occurrence time. In the case of the Kobe earthquake, the jump in $q$ is attributed to six $M = 4.1$ events occurring within five days of each other, while for L'Aquila, it is attributed to one event of $M = 4.1$ occurring six days prior to the main shock. Conversely, a significant relative increase in $q_m$ for 10-year Georgian sub-catalogues (Matcharashvili et al., 2011) that included the strongest earthquakes was attributed by the authors to a more correlated behaviour within the system of 'fault fragments' when a strong earthquake strikes or immediately afterwards, during aftershock activity. Smaller $q_m$ values found during seismically quiet times were attributed to decreased correlations during the earthquake generation stage, under an essentially decreased tectonic stress. Their study does not focus in detail on the earthquake preparation stage but their association of an increase in $q_m$ with increased seismic activity does support the interpretations of Papadakis et al. (2014) and Telesca (2010b) to some extent.

Taking a slightly different non-extensive approach than the fragment-asperity model, Vallianatos and Sammonds (2013) established that global seismicity can be well-described by a $q$-exponential distribution where the presence of two entropic indices ($q$ and $r$, equivalent to two different $q$-values) describes a crossover between different types of behaviour. The solution defines three regions: (1) very small events, (2) moderate events and (3) very large events, where the transition between each region occurs at crossover values $M_{c1}$ (depends on $q$ only) and $M_{c2}$ (depends on $q$ and $r$). Global seismic moment distributions modelled in this way yield a $q$-parameter for moderate events of 1.6 which remains fairly constant

even during preparation for the Honshu and Sumatra mega-earthquakes, indicating an independence from the influence of mega-events. On the other hand, the $r$-parameter for large events describes the preparatory process approaching mega-events as it rises from 1, consistent with an exponential roll-off in the years up to 1994, to 1.42 in the 10 years leading up to the Sumatra event. Immediately after Sumatra it rises further, to 1.5, and then even slightly further, to 1.52, until the Honshu event. This change in $r$ was attributed to an increase in the rate of strong earthquakes and the increasing importance of long-range interactions and global organization of seismicity before mega events.

The jump in $q_m$ prior to large earthquakes, seen both regionally and globally, illustrates the increasing rate of intermediate-sized events prior to the main shock. In most cases, this accelerating moment release is consistent with critical point behaviour (Jaume, 2000) where a growing correlation length in the Earth's crust allows progressively larger earthquakes to occur. Lithospheric instability prior to large earthquakes is therefore consistent with the symptoms of instability in a complex dynamic system before a catastrophe (Vallianatos and Sammonds, 2013).

#### 2.4.3.4 Return distribution of 'avalanche' sizes

Another important quantity used to further understand the physics of earthquakes is the return distribution (Celikoglu and Tirnakli, 2012). A return is defined as the difference between the sizes of successive avalanches. $q$-Gaussian distributions (normal with a power-law-tail) have been found to arise in the return distributions of earthquake sizes, i.e., differences in the energy released by successive earthquakes. For example, at Santorini volcano during the 2011-2012 unrest (Vallianatos et al., 2013b), the $q$-Gaussian distributed returns yielded $q_r = 2.24$, implying that complex correlations and non-linear dynamics control the evolution of volcano-seismicity. This value is in agreement with that generated from the Ehrenfest dog-flea SOC model (Bakar and Tirnakli, 2009). Globally and in northern California (Caruso et al., 2007) return distributions yielded $q_r = 1.75$, consistent with their respective $q_m$ values. Caruso et al. (2007) also found that the return distributions for avalanche sizes generated using the Olami-Feder-Christensen SOC model yielded $q$-Gaussian distributions, with $q_r = 2$. Their findings (a) give further support to the hypothesis that seismicity can be explained within a self-organized criticality scenario when long-range interactions are considered and (b) indicate that, although a certain degree of statistical predictability is possible due to the existence of temporal and spatial correlations among earthquakes, it is not possible to predict the magnitude of seismic events.

#### 2.4.3.5 Fault lengths and tectonic plate areas

A study of fault lengths in the Hellenic Arc (Vallianatos et al., 2011a) has shown that they follow a $q$-exponential distribution with $q_l = 1.16$, which is low compared with reported $q_m$ values. The authors attribute this to the analysis being based on an entire fault system, including faults that are not currently or recently active and therefore not interacting with the active faults. These observations are supported by similar studies of fault populations on Mars (Vallianatos and Sammonds, 2011; Vallianatos, 2013a). The fault length set for the whole planet yields $q_l = 1.22$ and contains two different $q$-exponential subsystems; with normal faults, where $q_l = 1.28$, exhibiting a greater degree of correlation than thrust faults, where $q_l = 1.11$. Fault lengths in the Valles Marineris extensional province yielded $q_l = 1.15$ for independent, non-interacting faults and $q_l = 1.75$ for coupled faults. Furthermore, a study of the Earth's tectonic plate areas (Vallianatos and Sammonds, 2010) has shown that for the 40 intermediate-sized plates that follow a power-law distribution (all apart from the five smallest and seven largest), $q_a = 1.75$, suggesting a high degree of coupling between these plates.

#### 2.4.3.6 Laboratory-scale fracture phenomena

The non-extensive approach has also been applied to a variety of laboratory-scale fracture phenomena, both acoustic and electric. The application of Tsallis statistics to electric phenomena is discussed in Chapter 3. Similarities in $q$-values between laboratory AE and seismicity were highlighted by the application of a $q$-exponential model to the magnitude, inter-event time and inter-event distances of acoustic emissions (AE) during triaxial compression of Etna basalt (Vallianatos et al., 2012a), which yielded $q_m = 1.82$, $q_t = 1.34$ and $q_d = 0.65$. Yamasaki and Nanjo (2009) analysed the temporal change of the spatial patterns of acoustic-emission events, distinguishing the nucleation phase from other phases such as the pre-nucleation and propagation phases. They found that the fracturing process is associated with a phase transition from the sub-critical to critical state with small-scale correlations increasing gradually from pre-nucleation to failure. Large-scale correlations, on the other hand, decrease sharply immediately after nucleation, increase gradually during the propagation phase and decrease sharply again at failure.

#### 2.4.3.7 Other applications in the Earth sciences

The Tsallis approach has also been applied to many other problems in earth sciences, including the development of risk assessment functions for a range of natural hazards (Vallianatos, 2009). The common feature between all the hazards (earthquakes, rockfalls, forest fires and landslides) was a power-law size distribution and a relationship between the power-law size distribution exponent $b$ and the non-extensive $q$-parameter was obtained: $b = \dfrac{2-q}{q-1}$. Other studies include polarity reversals of the geomagnetic field (Vallianatos,

2011), watershed distribution in tectonic areas (Vallianatos and Kouli, 2013), rockfalls (Vallianatos, 2013b), landslides (Chen et al., 2011) and temperature distributions and radon emission at Stromboli volcano (Gervino et al., 2004).

It should be noted here that the majority of studies referred to above do not quote their $q$-values with errors. The few studies that do provide error values (see Tables 2.1 and 2.2) indicate errors of up to 0.1 for $q_m$ and up to 0.2 for $q_t$ and $q_d$. This should be taken into account when considering the robustness and/or uniqueness of the inferences made.

### 2.4.4 Non-extensive dynamic models

#### 2.4.4.1 Fragment-asperity interaction model

A non-extensive model for earthquake generation was first introduced by Sotolongo-Costa and Posadas (2004) and later refined by Silva et al. (2006), Darooneh and Mehri (2010) and Telesca (2011; 2012). This general model for earthquake dynamics, derived from first principles, consists of two rough profiles interacting via irregular fragments which fill the gap between them (Figure 2.5). These fragments are produced by local breakage on the surfaces that occur during fault slip, equivalent to the generation of fault gouge, and the model demonstrates the influence of fragment size distributions on the earthquake energy distribution. In the model, the fragments play an important role in the earthquake triggering process; as stress between the two fault surfaces increases, rough fragments act both as roller bearings which accelerate the slip process and as hindering entities which concentrate the growing stress until their fracture and subsequent liberation triggers an earthquake. This process of violent fragmentation, especially when high energies are involved, leads to long-range interactions between all parts of the object being fragmented (Sotolongo-Costa and Posadas, 2004; Telesca, 2012). The sum of the entropies of the parts that constitute the fragmenting object after the division is larger than the entropy of the whole object (Sotolongo-Costa et al., 2000). Therefore, the Tsallis approach is appropriate for analysing the complex mechanism of relative fault surface displacement. Sotolongo-Costa and Posadas (2004) deduced the following energy distribution function for which the Gutenberg-Richter law is a special case:

$$\log(N(>m)) = \log N + \left(\frac{2-q}{1-q}\right) \log\left[1 + a(q-1)(2-q)^{(1-q)/(q-2)} 10^{2m}\right] \qquad (2.11)$$

They first maximised the entropy for fragment surface area, $A_f$ to obtain a fragment size distribution function and then related the released relative energy, $\epsilon$, with the linear dimension, $r$, of the fragments ($\epsilon \sim r$, as $A_f$ scales with $r^2$) in order to obtain the energy density function. Finally, the cumulative magnitude distribution was obtained from the relationship between earthquake magnitude, $m$, and $\epsilon$: $m \propto \log(\epsilon)$. $a$ is the proportionality constant between $\epsilon$ and $r$.

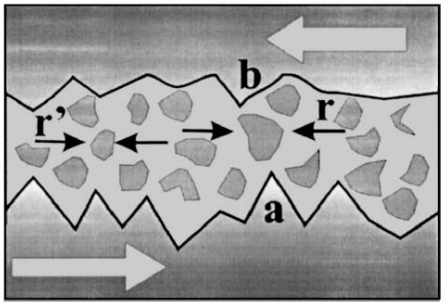


Figure 2.5: Illustration of the relative motion of two irregular fault surfaces with fragmented material filling the space between them (reproduced from Sotolongo-Costa and Posadas, 2004).

Silva et al. (2006) improved on this function in two ways: (i) by defining the $q$-expectation (mean) values in terms of the escort probability as proposed by Abe and Suzuki (2005) (ii) by assuming that $\epsilon \sim r^3$, in agreement with the standard theory of seismic moment (Lay and Wallace, 1995), and specifying $m = \frac{1}{3}\ln(\epsilon)$. They obtained the following cumulative magnitude distribution:

$$\log\left(\frac{N(>m)}{N}\right) = \left(\frac{2-q}{1-q}\right)\log\left[1-\left(\frac{1-q}{2-q}\right)\frac{10^{2m}}{a^{2/3}}\right] \tag{2.12}$$

where the $a$-parameter is a physical quantity characterising the energy density. The behaviour of $a$ almost mirrors that of $q$; increasing during seismically quiet periods and decreasing in periods where strong earthquakes occur (Matcharashvili et al., 2011). This suggests that, under the influence of a rapidly released stress, the contribution of large size fragments to the fragment-asperity interaction is prevalent ($a$ is lower), as opposed to relatively quiet periods when accumulated stress energy is released gently through the relative movement of smaller fragments ($a$ is higher).

Telesca (2011) used the relation $m = \frac{2}{3}\log(\epsilon)$ to obtain a slightly different cumulative magnitude distribution;

$$\log\left(\frac{(N>m)}{N}\right) = \left(\frac{2-q}{1-q}\right)\log\left[1-\left(\frac{1-q}{2-q}\right)\frac{10^{m}}{a^{2/3}}\right] \tag{2.13}$$

and later (2012) took a maximum likelihood approach to estimating the non-extensive parameters when he also introduced a further minor modification with the incorporation of the threshold magnitude, $m_c$, for catalogue completeness:

$$\log\left(\frac{(N>m)}{N}\right) = \left(\frac{2-q}{1-q}\right)\log\left[\frac{1-\left(\frac{1-q}{2-q}\right)\frac{10^{m}}{a^{2/3}}}{1-\left(\frac{1-q}{2-q}\right)\frac{10^{m_c}}{a^{2/3}}}\right] \tag{2.14}$$

These fragment-asperity-derived magnitude-frequency distributions are more realistic than the Gutenberg-Richter relation, which displays power-law scaling only for intermediate-sized earthquakes. They exhibit both the power-law tail and the kneel-down at small

magnitudes, together with an excellent fit to seismicity patterns of several regions (Section 2.4.3). Using this model, Telesca (2012) found that the maximum likelihood $q$-value ($q_c$) was related to the maximum likelihood Gutenberg-Richter $b$-value (Aki, 1965) as follows: $b = \frac{2 - q_c}{q_c - 1}$ , equivalent to the relationship derived by Vallianatos (2009). However, this relationship is affected by the scaling constraints between $\epsilon$ and $r$ and between $\epsilon$ and $m$ used in the different models above. For instance, based on the Silva et al. (2006) model, Sarlis et al. (2010a) also related the $b$-value analytically to the Tsallis $q$-index, yielding $b = 2\left(\frac{2 - q}{q - 1}\right)$. A slightly different modification for the fragment-asperity model was introduced by Darooneh and Mehri (2010), who, inspired by the fractal nature of the fragments, adopted the scaling $\epsilon \sim \exp(A_f^{1/a})$ and used the same constraints as Silva et al. (2006). They argue that their $q$-stretched exponential cumulative frequency-magnitude distribution provides a better empirical fit than the distributions of Sotolongo-Costa and Posadas (2004) and Silva et al. (2006), supported by analysis of data from Iran and California. However, further testing of the different versions is required to confirm this.

#### 2.4.4.2 Superstatistics

Superstatistics is a powerful tool for understanding the dynamics of a large variety of complex systems, including those that display Tsallis-type behaviour. The concept was first introduced by Beck (2001) and Beck and Cohen (2003) and can be applied to explain the qualitative variation in a distribution at multiple hierarchical scales (Beck, 2001; Wilk and Wlodarczyk, 2000). It describes the superposition of equilibrium dynamics; local or short-timescale fluctuations that combine to produce a higher-order overall distribution, and is physically relevant for driven non-equilibrium systems where the environmental conditions fluctuate on a large scale (Beck et al., 2005b; Sornette, 2006; Hanel et al., 2011). That is, when the slowly fluctuating variable (e.g., changing temperature of the environment) changes so slowly that the rapidly fluctuating variable (e.g., velocity of a Brownian particle within the environment) has time to relax to a Gaussian distribution between the changes of the environment (Van der Straeten and Beck, 2009). In mathematical terms, consider that the intermittent, non-linear dynamics of a representative state variable, $u(t)$, at short timescales is described by the probability density function $p(u|\beta)$, where $\beta$ is a parameter. If $\beta$ itself varies such that the external forcing fluctuates at longer timescales, $u(t)$ is driven to a new local equilibrium. When the timescale of variation in $\beta$ is much larger than the one of $u(t)$, the probability distribution function of $u(t)$ can be obtained as a superposition of temporary equilibria (Beck, 2001).

Often the relevant measured time series consists of short timescale Gaussian processes whose variance evolves on a longer timescale. A complex system such as this is mathematically described as the multi-scale superposition of several statistics. One corresponds to local equilibrium processes on a mesoscopic level, which can be modelled by a linear Langevin equation and lead locally to Gaussian behaviour. The other corresponds to a slowly varying parameter of the whole system. Essential for this approach is the fact that

there is sufficient timescale separation, i.e., the local relaxation time of the system must be much shorter than the typical timescale on which the slowly varying parameter, $\beta$, changes (Yalcin and Beck, 2013). It has been shown that Tsallis statistics are obtained when $\beta$ follows a gamma distribution (Beck, 2001). Below, the model is formalised for the purposes of this study. Primarily, the one-variable Beck model is introduced, showing the appearance of a $q$-Gaussian distribution caused by the fluctuating $\beta$ parameter.

Consider the following Langevin equation for one variable:

$$\dot{u} = -\gamma u + \sigma L(t) \tag{2.15}$$

where $L(t)$ is Gaussian white noise with $\langle L(t)\rangle = 0$ and $\langle L(t_1)L(t_2)\rangle = 2\delta(t_1 - t_2)$, $\gamma$ is a friction constant and $\sigma$ modulates the amplitude of $L(t)$. Beck (2001; 2013) and Beck and Cohen (2003) considered the case that $\sigma$ fluctuates in time so that $\beta = \frac{\gamma}{\sigma^2}$ of the system obeys a stochastic differential equation:

$$\dot{\beta} = a_1(\beta, t) + a_2(\beta, t)W(t) \tag{2.16}$$

where W(t) is Gaussian white noise with $\langle W(t)\rangle = 0$ and $\langle W(t_1)W(t_2)\rangle = 2\delta(t_1 - t_2)$, which is statistically independent from the fluctuations of $u$. Rather than specifying the forms of $a_1$ and $a_2$, the following properties about the fluctuation of $\beta$ are assumed: (1) the timescale of the $\beta$ fluctuation is longer than that of $u$, such that the system can temporarily reach local equilibrium before $\beta$ varies significantly and (2) $\beta$ has a stationary distribution function. Upon these assumptions, the distribution function of $u$ in equilibrium can be approximately evaluated. In local equilibrium where $\beta$ can be taken as constant, $u$ is distributed as:

$$p(u|\beta) = \sqrt{\frac{\beta}{2\pi}} \exp\left(-\frac{\beta}{2}u^2\right) \tag{2.17}$$

i.e., a normal distribution: $f(x, \mu, \sigma) = \frac{1}{\sigma\sqrt{2\pi}} \exp(\frac{-(x-\mu)^2}{2\sigma^2})$, with mean $\mu$ and standard deviation $\sigma$. At equilibrium (when $u$ is normally distributed), $\beta$ reduces to a generalised variance, $\beta = \frac{1}{\sigma^2}$.

If $u$ is observed over a longer timescale in which $\beta$ fluctuates, the distribution of $u$ unconditioned to $\beta$ is given by:

$$p(u) = \int p(u|\beta)f(\beta)d\beta \tag{2.18}$$

Assuming the stationary distribution function of $\beta$ to be a $\Gamma$-distribution;

$$f(\beta) = \frac{1}{\Gamma(a)} \left(\frac{a}{\beta_0}\right)^{\alpha} \beta^{\alpha-1} \exp\left(-\frac{a\beta}{\beta_0}\right), \beta_0 > 1 \tag{2.19}$$

the average of $\beta$, $\langle\beta\rangle$, is given by $\beta_0$ and the variance of $\beta$ is given by $\langle\beta^2\rangle - \langle\beta^2\rangle^2 = \frac{\beta_0^2}{\alpha}$.

In this case, Equation 2.18 is calculated as:

$$p(u) = \frac{\Gamma(\alpha + \frac{1}{2})}{\Gamma(\alpha)\Gamma(\frac{1}{2})} \left(\frac{\beta_0}{\alpha}\right)^{\frac{1}{2}} \left(1 + \frac{\beta_0}{2\alpha}u^2\right)^{-a-\frac{1}{2}} \tag{2.20}$$

which is the form of the $q$-Gaussian distribution derived from Equation 2.10 where $U(x) = u^2$ and $p(u) \propto (1 + B(q-1)u^2)^{-1/q-1}$. Moreover, the parameters $q$ and $B$ are related to the average value, $\beta_0$ by:

$$\beta_0 = \int f(\beta)\beta d\beta = (3-q)B \tag{2.21}$$

Beck-Cohen superstatistics have also shown that there is a simple link between the $q$-exponential function (with $q \geq 1$) and the gamma distribution with $n$ degrees of freedom: $q = \frac{n+2}{n} \geq 1$ (Tsallis, 2009a). Another typical distribution that arises for $f(\beta)$ is the lognormal distribution. This occurs when, instead of being the sum of the contributing random processes, $\beta$ is the product of these processes. That is, an N-particle non-extensive system with non-linear fluctuating friction forces reduces to the product of one-particle non-extensive systems.

There are several interesting applications of superstatistics to earth physics. For example, it has shown that low degrees of freedom describe the temporal evolution of the Aigion earthquake aftershock seismicity (Vallianatos et al., 2012b) as well as the nucleation and propagation of fracture in terms of acoustic emissions (Vallianatos et al., 2012a). For both these systems, the observed long-term $q$-exponential distribution of inter-event times is a superposition of exponential distributions where the parameter $\beta$ fluctuates. The presence of superstatistics is also used to explain the $q$-exponential distribution of pressure-stimulated current relaxation during abrupt uniaxial load-unload cycles in amphibolite and marble samples (Vallianatos and Triantis, 2013). Wider applications include wind velocity fluctuations, hydro-climatic fluctuations, surface temperature distributions, cosmic rays, solar flares, mathematical finance, quantum systems at low temperatures, train delay statistics and cancer survival statistics. Further details can be found in Beck (2008), Beck (2013), Yalcin and Beck (2013) and references therein. One of the most successful applications of superstatistics has been in the study of turbulence, both hydrodynamic and atmospheric (e.g., Beck et al., 2005b;a; Beck, 2007). Turbulence of fluids and seismicity / brittle fracture have many features in common (Kagan, 2006); hierarchically organised and self-similar structures that extend over several orders of magnitude and scale-invariant statistics. Also, the structures that control deformation patterns in both are comparable in size to the maximum size of the region over which they act. This similarity led Kagan (1992) to describe seismicity as the 'turbulence of solids'. It is fitting, therefore, to apply the superstatistics concept to the problem of crustal deformation, on which it may shed further light.

## 2.5 Conclusion

In conclusion, analysing different complexity levels in the fracturing process is essential to understanding crustal dynamics. Fracture phenomena, as with most of the Earth's processes, usually have non-equilibrium stationary states whose dynamics can, in some cases, be more accurately addressed through non-extensive Tsallis statistics (Tsallis, 1988; 2009a) and the concept of superstatistics (Beck, 2001; Beck and Cohen, 2003) than with classical Boltzmann-Gibbs statistics, which assume an equilibrium system comprising independent, non-interacting particles. These techniques have been applied to fracture processes at different spatial and temporal scales. Additionally, the broad applicability of the Tsallis entropy to systems with fractal geometries means that it has the potential to be useful for multi-hazard assessments and analysing multiple monitoring datasets, providing a consistent parameter with which to measure the stability of the overall system and thus give an indication of the potential hazard. It is therefore appropriate to study the electric current generated during deformation of non-piezoelectric rocks using these methods, as I have done for my thesis.

# Chapter 3

# Electrical Phenomena in the Earth's Crust

## 3.1 Introduction

Earthquake precursors comprise a wide variety of physical phenomena that have been reported to precede some earthquakes (Scholz et al., 1973; Rikitake, 1987; Cicerone et al., 2009). These phenomena include: (a) seismic foreshocks, including high-frequency energy emissions and very low frequency seismic motions not detected by conventional seismographs; (b) anomalies in the Earth's magnetic and electric fields, including in the ELF, ULF, VLF and RF fields, visible earthquake lights, variations in electrical resistivity and d.c. telluric current anomalies; (c) anomalous gas release from the crust, mainly radon but also other gases; (d) ground dilatancy and surface deformation, including ground elevation changes over tens of kilometres and variations in sound wave velocity; (e) groundwater level changes; and (f) surface temperature changes.

In addition, more enigmatic changes have been reported, such as strange animal behaviour and possible human premonition (Rikitake, 1976; Tributsch, 1983; Bolt, 2003). These include psychological and physiological effects that may, in fact, be directly related to electric field changes and low frequency electromagnetic (EM) radiation emitted from the earth in the days preceding an earthquake (Freund, 2011a; Anagnostopoulos et al., 2013). This is because our neural network radiates and receives signals continuously in the ELF band, particularly at frequencies <100 Hz; i.e., the frequency range associated with seismic zone EM radiation (Athanasiou et al., 2011). Moreover, the pineal gland has been shown to be very sensitive to variations in EM fields (Braud and Dennis, 1989; Wilson et al., 1990; Lerchl et al., 1991; Kay, 1994), inducing chemical changes that affect stress responses, with marked effects on emotion, behaviour, cognition, mental activity and psychological condition (Close, 2012), which may even lead to hallucinations (Strassman, 1990). For example, Ikeya et al. (1996) found that a characteristic electric field strength of 1000 $\mathrm{Vm}^{-1}$

induced panic in their experimental animals. Human health certainly seems to be affected by an impending earthquake. Shitov (2010) found that incidence rates of physical diseases; such as gastritis, hypertension, musculoskeletal conditions and blood disease, showed a gradual rise in the years leading up to the 2003 $M7.5$ Chuya earthquake in Russia, a sharp spike in the year of the earthquake and a gradual decay in the year following. While Anagnostopoulos et al. (2013) reported a similar connection between hospital admissions of patients with psychiatric disorders and seismic activity in Crete. Other studies have shown a potential connection between pre-seismic changes in groundwater chemistry and animal health (Grant et al., 2011; Inan et al., 2012; Freund and Stolc, 2013).

The concept of earthquake forecasting relies on the belief that these physically measurable phenomena exhibit specific signatures which are related to an imminent earthquake in some way (Sornette et al., 1990a), with the ultimate goal being intermediate-term forecasting of the time, location and size of a major earthquake. According to Russian theorists, the 'standard' signature of an earthquake precursor (Figure 3.1) is a reduction in any particular phenomenon some time prior to the earthquake, followed by a recovery when the earthquake is imminent (Sammonds, 2008). The duration time $T$ of the precursor scales logarithmically with the earthquake magnitude $M$ according to $\log T = aM - b$ (Tsubokawa, 1969; 1973; Scholz et al., 1973; Whitcomb et al., 1973; Rikitake, 1975). Models of anelastic deformation in the earthquake preparation zone help to explain the duration of earthquake precursors because the dilatant volume is proportional to the earthquake magnitude (Sammonds, 2008). For example, Rikitake (1987) invoked the the dilatancy-diffusion model of Scholz et al. (1973) to explain the two classes of intermediate-term earthquake precursors observed in Japan; the first due to dilatancy and the second related to fluid diffusion. However, Mogi (1985) noted that the relationship between precursors and earthquakes was in need of clarification. This is still the case 30 years later. Jordan et al. (2011) states that the two hypotheses on which earthquake prediction strategy is predicated; (i) that large earthquakes result from deformation sequences that yield precursory changes in the regional stress and strain fields and (ii) that information regarding an impending earthquake can be extracted from these changes, have yet to be empirically validated. Moreover, the positive absence of precursors recorded prior to the heavily monitored 2004 Parkfield earthquake (Bakun et al., 2005) and the almost total absence of dilatant strain acceleration prior to the 2009 L'Aquila earthquake (Amoruso and Crescentini, 2010) provide counter-evidence for an earthquake preparation zone or limit it to a very small volume ($< 100$ km$^3$). Nevertheless, significant progress has been made, both in terms of monitoring precursory activity (e.g., Hickman et al., 2004; Roeloffs and Langbein, 1994; Bakun and Lindh, 1985) and in understanding the mechanisms of earthquake nucleation and rupture and their connection with potential precursors (e.g., Main and Meredith, 1989).

At first, the concept of self-organised criticality (SOC) and the notion that earthquakes are critical point phenomena (see Chapter 2) gave rise to the idea that earthquakes were unpredictable and that the anomalies observed prior to earthquakes were not real pre-

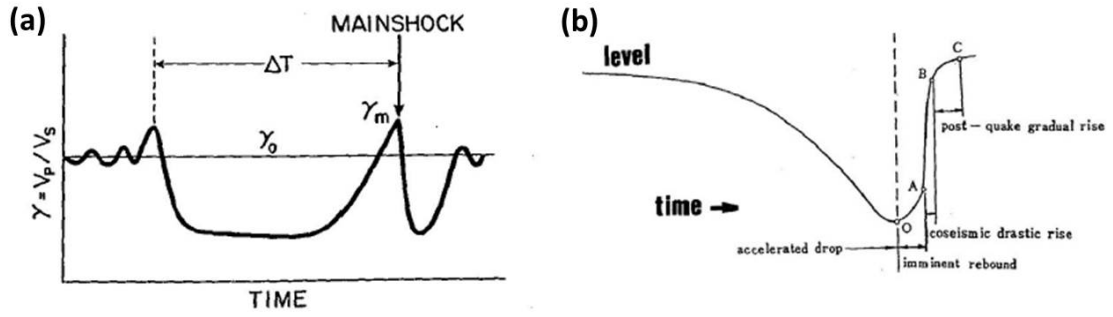


Figure 3.1: Earthquake precursors: (a) 'standard' signature, where the precursor, $\gamma$, begins to drop before the earthquake and recovers when it is imminent (in this case, $\gamma$ is the ratio between compressional and shear wave velocities) and (b) groundwater change prior to 1976 $M$7.8 Tangshan earthquake in China - note the precursory recovery immediately before the large coseismic rise. Taken from Sammonds (2008).

cursors (e.g., Kagan, 1997; Geller et al., 1997). In a self-organised critical system (SOC) there is little difference between small and large avalanches. This implies that 'large earthquakes are small earthquakes that did not stop' (Sornette and Werner, 2009), i.e., that any small earthquake may cascade into a larger event, and that prediction is therefore unreliable (Leary, 1997; Geller, 1997; Geller et al., 1997). This conflicted entirely with observations that precursory signals characterise the earthquake preparation zone (e.g., Scholz et al., 1973; Rikitake, 1987) and its implications regarding earthquake prediction research provoked a long debate in the journal Nature (Main, 1999, and contributors). However, as Didier Sornette pointed out at the end of the debate, specific precursory patterns in space and time are the hallmarks of criticality, and the lack of predictability in standard SOC models is due to the absence of geometry. Clear proof of the possible coexistence between critical-like precursors of large earthquakes and long-term SOC of the crust was provided by Huang et al. (1998) who showed that significant precursory activity is characteristic of the avalanche dynamics of large events within hierarchical geometric structures. Since earthquake precursors result from non-linear processes developing on the same fractal structures as earthquakes (the fault network and rock matrix), their characteristic parameters are likely to obey some power-law distribution. This idea led Bernard (2001) to propose a generalised SOC framework for the crust, where the interacting instabilities leading to power-law distributions are not only earthquakes and faults, but also other transient phenomena, such as fault creep and episodic fluid flow, that show precursory activity. His model implies significant coupling and cross-triggering between all types of instability on these structures. Subsequently, researchers have recognised some degree of predictability in earthquake systems (Jordan, 2006; Helmstetter et al., 2006); a recognition based on the long-range spatial and temporal correlations that characterise SOC models of earthquakes and fault networks (Miltenberger et al., 1993; Sornette et al., 1994; 1995). Thus, long-range organisational structures, such as accelerating moment release (see Jaume, 2000), may precede large earthquakes. This idea underlies the pattern recognition method of Gelfand et al. (1976), which was later developed extensively by Keilis-Borok and Soloviev (2003).

However, after decades of research, the goal of reliable, intermediate-term earthquake forecasting remains elusive and contentious (Holliday et al., 2005). The recent trial of seven public officials, from the Italian National Department for Civil Protection (DCP), in L'Aquila, Central Italy, drew global attention to the issue after an amateur seismologist, whose hobby was monitoring atmospheric radon emissions in an attempt to predict earthquakes, noted increased radon emissions in the week preceding the 2009 $M6.3$ L'Aquila event and reported an imminent 'catastrophic' earthquake to the local mayor (Alexander, 2010). The relatively complacent response from the DPC in the days leading up to the devastating main shock led to these seven men being prosecuted "for having given out falsely reassuring information to members of the public" and issuing "incomplete, imprecise and contradictory information on the nature, causes, dangers and future development of seismic activity in the area in question" (Alexander, 2014a). They were subsequently convicted on the charge of manslaughter and sentenced to six years in prison. All but one of these L'Aquila scientists have since been acquitted, with the exception detained for mistakes in communicating the risk. Full details of the highly controversial case are described by Alexander (2014a;b) and Gabrielli and Di Bucci (2014). Immediately following the L'Aquila disaster, the DCP requested that the International Commission of Earthquake Forecasting for Civil Protection (ICEF) to assess the scientific knowledge of earthquake predictability and provide guidelines for the implementation of operational earthquake forecasting. The subsequent report (Jordan et al., 2011) assesses the lessons learned from the disaster in terms of developing an operational forecasting policy to deal with future event clusters and provides a set of recommendations on the utilisation of such a policy.

The acquisition of multiparameter data is essential for establishing the possible causes of any precursory signal and developing quantitative models to describe the mechanisms. For example, the reported absence of a strain signal from strain meters 30 km from the 1988 Loma Prieta earthquake source allowed Johnston (1990) to specify constraints on the process that generated the precursory electromagnetic anomaly reported by Fraser-Smith et al. (1990). Strain meters and tilt meters 20 km away from the 1995 Aigon earthquake source allowed Pinettes et al. (1998) to reject the hypothesis that the seismic-electric signals (SES) reported by Varotsos et al. (1996) were precursory. The causes of other reported precursors, such as the geochemical anomalies (Tsunogai and Wakita, 1995; Igarashi et al., 1995), low-lying fog and unusual clouds (Tsukuda, 1997) observed before the 1995 Kobe earthquake or the clustered foreshocks preceding the 1995 Kozani-Grevena earthquake (Bernard et al., 1997) and the 1992 Landers earthquake (Dodge et al., 1995), remain unknown due to a lack of additional data. These examples emphasise the importance of multiparameter experiments in the field, such as the Parkfield, CA experiment (Roeloffs and Langbein, 1994; Bakun and Lindh, 1985), and in the laboratory.

Controversy surrounding the reliability of earthquake precursors stems from the fact that the related publications often do not provide enough information to assess the significance of the temporal correlation between the precursory signal and the subsequent earthquake (Geller, 1997; Michael, 1997; Bernard, 2001). This means that the anomalous signal may

be purely coincidental or could be explained by anthropogenic or other random noise, as with the explanation of Pham et al. (1999) regarding the origin of SES reported by the VAN group (Varotsos et al., 1996). Although this explanation was later contested by Rokityanski and Varotsos (2006) using a more recent data set from the same area. Recently, Cicerone et al. (2009) conducted a comprehensive review of the published literature and compiled a database of earthquake precursors in their various forms. Since selection could not be based on temporal correlation, it was instead based on two other important criteria: (1) the anomalies were observed in credible, controlled, calibrated experiments and (2) accepted physical models exist to explain their occurrence. The ubiquity of non-seismic precursory anomalies is highlighted in the numerous studies that were included in their database; 43 reporting electric and magnetic field variations, 64 reporting gas emissions, 35 reporting groundwater level changes, 8 reporting surface temperature changes and 21 reporting surface deformation. Extensive work on foreshock activity has also been carried out (e.g., Jones and Molnar, 1976; Reasenberg, 1999), which reveals that most foreshocks take place within ∼30 days of the main shock, i.e., within the same time-frame as the most frequently reported non-seismic precursors (Cicerone et al., 2009), highlighting the possibility that their generation mechanisms are physically linked.

This investigation is concerned with electric phenomena related to crustal deformation and the electric currents required to generate them. For this reason, the subsequent sections will focus only on these topics. First, field observations of electric phenomena are summarised, followed by laboratory observations of electric signals during rock deformation and fracture. Findings and implications of studies that use a Tsallis entropy approach to the analysis of electric phenomena are then examined. Finally, potential generation mechanisms most relevant to this study are described.

## 3.2 Field Observations of Electric Phenomena

Electric phenomena related to earthquakes have been observed in the field for centuries (Milne, 1890) and comprise a wide variety of anomalies. These include:

- Earthquake lights
- Atmospheric and ground electromagnetic anomalies
- Ionospheric disturbances and oscillations

Interest in earthquake prediction in the 1970s and 1980s led to the development of some field monitoring stations, notably in Japan, China, Russia, Greece and California. However, lack of coverage of these stations, the long distances from the assumed sources at which they were detecting anomalies and various types of noise contamination, meant that the results were generally ignored by the scientific community at large (Gokhberg

et al., 1995). It was the studies of Smith and Johnston (1976), Gokhberg et al. (1982) and Warwick et al. (1982) that brought the study of electric signals as precursory phenomena to the scientific fore. Smith and Johnston (1976) reported variations in the geomagnetic field 11 km from an earthquake on the San Andreas fault which could not be explained by ionospheric disturbances or telluric currents from other sources. The latter two studies, respectively, reported anomalous radio emissions several hours prior to three Japanese earthquakes ($1980 - 1981$) and six days before the great Chilean earthquake of 1960. All three groups suggested that a piezoelectric mechanism, due to deformation of quartz crystals in the rock formation, was responsible for the anomalies. The field observations of Warwick et al. (1982) were later reproduced with a non-piezoelectric model involving the formation and oscillation of double electric layers (Section 3.5.2.1) and incorporating pressure variations and fluid saturation (Khatiashvili and Perel'man, 1989).

Since then, a great deal of literature has been published on the subject of electric phenomena related to earthquakes, including observed anomalies, instrumentation, experiment design and potential mechanisms. Several books have been written on the subject, including those of Gokhberg et al. (1995), Hayakawa (1999), Hayakawa and Fujinawa (1994), Hayakawa and Molchanov (2002) and Varotsos et al. (2011b). Reviews can be found in Park et al. (1993), Johnston (1997), Tzanis and Vallianatos (2001), Uyeda et al. (2009b) and Hayakawa and Hobara (2010). Other work can be found in special editions of journals, such as those in Physics and Chemistry of the Earth (Volume 34, 2009; Volume 31, 2006) and Tectonophysics (Volume 431, 2007). The controversial nature of non-seismic earthquake phenomena, and how efforts to find acceptable physical explanations have been frustrated in the past, have also been discussed (Gokhberg et al., 1995; Johnston, 1997; Sornette, 1999; Wyss and Booth, 1997). The rest of this section focuses on some key observations.

### 3.2.1 Earthquake lights

Earthquake lights (Figure 3.2) are luminous phenomena in the atmosphere that have long been reported to precede and accompany earthquakes (see reviews by Derr, 1973; 1986; Tributsch, 1983). Notable sightings include: (a) those photographed in Japan during an episode of the Matsushiro earthquake swarm (Yasui, 1968; Corliss, 2001), (b) those observed during the Saguenay earthquake sequence in Canada (Ouellet, 1990; St-Laurent, 2000), (c) those reported to accompany the 1995 $M7.1$ Kobe earthquake in Japan (Tsukuda, 1997; Enomoto and Zheng, 1998; Kamogawa et al., 2005) and (d) those observed in the months preceding and following the 2009 $M6.3$ L'Aquila earthquake in Italy, the locations of which indicate a correlation between electrical discharge and asperities (Fidani, 2010). St-Laurent et al. (2006) suggested that earthquake lights may arise due to the stress-activation of positive hole charge carriers (Section 3.5.1.3) and the accumulation of high charge carrier concentrations at asperities in the crust where stress rates increase very rapidly as an earthquake approaches. Their model proposed that when this accu-

mulation of charge carriers reaches a critical concentration, positive holes form solid state plasma that propagates rapidly through the rock volume as an expanding charge cloud. At the air-rock interface, the charge cloud discharges (analogous to a corona discharge) accompanied by light emission and high frequency electromagnetic radiation. Very recently, Theriault et al. (2014) compiled all reliable reports of earthquake lights they could find since 1600 A.D., focusing on the best-documented earthquakes in the Americas (27) and Europe (38). Of these 65 earthquakes, 85% occurred along an active or ancient rift zone, while 97% occurred where the rupturing fault was almost vertical (i.e., a rift, a graben or a strike-slip fault). This steep geometry may facilitate rapid flow of stress-induced electric charges to the Earth's surface, whereupon their interaction with the atmosphere creates a luminous glow. It should be noted, however, that an assessment of false alarms (i.e., lights occurring without earthquakes) and misses (earthquakes occurring without lights) has not been undertaken.

Figure 3.2: Sketch of a luminous phenomena as reported by J.A. Dallaire (St-Laurent et al., 2006).

### 3.2.2 Electromagnetic anomalies

Anomalous electromagnetic (EM) signals have also been detected before, during and after earthquakes. These signals span the electromagnetic spectrum, from infrared (IR) signatures (Pulinets et al., 2006; Ouzounov et al., 2007) and radio frequency signals in the kHz to MHz range (Gokhberg et al., 1982; Warwick et al., 1982; Fujinawa and Takahashi, 1990; Vallianatos and Nomikos, 1998; Eftaxias et al., 2001; Kapiris et al., 2004; Contoyiannis et al., 2005; Papadimitriou et al., 2008), through to ultra-low frequency (ULF) magnetic field energy bursts (Fraser-Smith et al., 1990; 1991; Molchanov et al., 2003; 2004; Bleier et al., 2009; Bortnik et al., 2010) and slow moving, direct current (d.c.) telluric current anomalies (Varotsos and Alexopoulos, 1984a;b; Burton, 1985; Varotsos et al., 1993; 1996; Zhao and Qian, 1994; Enomoto et al., 2006; Zhao and Qian, 2009) and magnetic field changes (Yen et al., 2004). Due to the large amounts of data required to be collected before infrequent earthquakes and the lack of sufficient instrumentation to cover large areas, these phenomena are difficult to monitor in both space and time (Bleier et al., 2009). Therefore, determining whether or not they correlate to specific earthquake preparation processes poses a significant challenge.

Measurements of these signals can be classified into three types (Takahashi et al., 2007):

(1) passive ground-based observations, (2) ground-based observations with the use of transmitter signals and (3) satellite observations. Passive ground-based observations are generally made with arrays of electrode dipoles buried in the ground or in boreholes and proton-precession or fluxgate magnetometers (e.g., Fraser-Smith et al., 1990; Molchanov et al., 1992; Varotsos et al., 1993; Kopytenko et al., 1993; Lighthill, 1996; Hayakawa et al., 1996a; 2000; Uyeda et al., 2002; Hattori et al., 2002; Hattori, 2004; Hattori et al., 2004), while observations with transmitter signals are made with arrays of radio antennae, electric dipole antennae and magnetic loop antennae (e.g., Gokhberg et al., 1982; Gufeld et al., 1994; Hayakawa et al., 1996b; Molchanov and Hayakawa, 1998b; Biagi et al., 2011). Dense arrays of observations are required, since electric and magnetic field anomalies have a strong directional variation. The importance of using a network of sensors when searching for pre-seismic electromagnetic signals is underscored by the propagation model of (Bortnik et al., 2010), who found that deep nulls in the detected signal power develop in the non-cardinal directions relative to the orientation of the source current. Thus, a station well within the detectable range but located in those regions are unlikely to observe a signal. Further difficulties in determining whether these signals are related to earthquakes come from the problems of ground attenuation and the ability to separate them from noise (e.g., Pham et al., 1999; Drakopoulos and Stavrakakis, 1996; Nagao et al., 1996), including background variations in the Earth's magnetic and electric fields, electrochemical disturbances (e.g., the influence of rainwater on the sensors) and anthropogenic noise.

Signals in the ULF band ($<$ 3 kHz) are of particular interest due to their ability to penetrate the crust. They are the highest frequency signals able to reach the Earth's surface with little attenuation if generated at typical shallow earthquake nucleation depths ($\sim$10 km) (Karakelian et al., 2002) and can therefore be related to earthquake source depths (Takahashi et al., 2007; Harada et al., 2004). Reported ULF variations (on the order of $10^{-7} - 10^{-5}$ s) are very fast compared with the time-scale variations of external fields such as the geomagnetic field, the geoelectric potential or electrokinetic potential which are of the order of the macroscopic stress changes ($10^{5} - 10^{8}$ s). This observation led Molchanov and Hayakawa (1995; 1998a) to suggest electrification due to the opening of microcracks, which occurs on a similar time-scale ($10^{-7} - 10^{-4}$ s), as a possible mechanism for these ULF emissions. However, the nanoTesla ULF magnetic anomalies preceding the Loma Prieta earthquake (Mueller and Johnston, 1990; Fraser-Smith et al., 1990; 1991; Bernardi et al., 1991; Molchanov et al., 1992) were attributed to electrokinetic effects (Fenoglio et al., 1995) and the formation of a highly conductive region along the fault resulting from a precursory re-organisation in the geometry of the fluid-filled porosity in the fault zone ('dilatant-conductive' effect) (Merzer and Klemperer, 1997).

Recent observations of signals in the kHz to MHz frequency range preceding several earthquakes in Greece (Eftaxias et al., 2001; Kapiris et al., 2004; Contoyiannis et al., 2005; Papadimitriou et al., 2008) and the 2009 L'Aquila earthquake in Italy (Contoyiannis et al., 2010) have shown that anti-persistent MHz anomalies precede persistent kHz ones. This indicates a two-stage earthquake preparation process that evolves to a critical point

(Kapiris et al., 2003), if, as the authors suggest, these EM emissions are produced by the opening of cracks prior to the rupture itself. Laboratory studies (see Section 3.3.1) have shown that opening cracks produce EM emissions in the kHz to MHz range. Thus, the EM emissions themselves can be considered as precursors of general fracture and damage evolution during mechanical loading of materials can be monitored in real time using fracture-induced electromagnetic (EM) fields (Bahat et al., 2005). Simultaneous acoustic and electromagnetic emissions observed under field conditions in caves and attributed to pressure variations inducing frictional sliding and charge separation between adjacent rock blocks (Bella et al., 1994; 1995) support this idea. Based on a focal area consisting of (a) a backbone of strong and large entities distributed along the activated fault and (b) a strongly heterogeneous medium that surrounds the family of strong entities and prevents free slip, the two-stage earthquake preparation model (Kapiris et al., 2004; Contoyiannis et al., 2005) suggests the following: (1) the MHz anomalies are due to the fracture of the highly heterogeneous system that surrounds the fault, with their anti-persistency indicating the presence of a negative feedback mechanism that arrests the cracking rate and induces stability, and (2) the kHz anomalies reflect the fracture of entities sustaining the system, with their persistency implying a positive feedback mechanism that accelerates the cracking rate towards rupture. Therefore, it may be possible for EM emissions to indicate the transition from sub-critical crack propagation to dynamic coalescence as discussed by Main et al. (1990).

D.C. geoelectric (telluric) and geomagnetic ground signals linked with earthquakes, including volcano-tectonic seismicity, have been recorded in Japan (Uyeda et al., 2000; 2002; Enomoto et al., 2006; Takahashi et al., 2007; Nagamoto et al., 2008), China (Fan et al., 2010; Zhao and Qian, 1994; Zhao et al., 2002; Zhao and Qian, 2009; Li et al., 2007; Liu et al., 2011), Greece (Varotsos and Alexopoulos, 1984a;b; Varotsos et al., 1993; 1996), California (Fraser-Smith et al., 1990; Bleier et al., 2009) and the Soviet Union (Gokhberg et al., 1995; 1982; Kopytenko et al., 1993; Molchanov et al., 1992). These signals are low frequency ($\leq$ 1 Hz) electric field variations, known as seismic electric signals (SES), that sometimes precede earthquakes with a lead time from several hours to several weeks (Eftaxias, 2010; Varotsos et al., 2011b). They are detected as transient anomalies in the Earth's telluric currents, which are electric currents that flow in the crust. In the field, the measured quantity is the change in potential difference between electrodes a few hundred metres apart. These changes, of the order of milliVolts over areas of 1km$^2$, have been claimed as precisely correlated with earthquakes (Varotsos and Alexopoulos, 1984a;b; Varotsos et al., 1993; 1996). Specifically, the lead time for a single SES is usually around 11 days or less, while case studies for SES activity in the 1980s-90s (Varotsos, 2005) gave rise to an empirical rule: at least three weeks elapses between initiation of SES activity and the occurrence of a strong ($> M_w = 5$) earthquake. The strongest earthquake usually occurs during the fourth week, otherwise smaller events ($M_w \sim 5$) occur during this week and the strongest earthquake occurs after an additional two to three weeks. Later case studies indicated a longer lead time on some occasions. Another systematic observation of

these SES is that the logarithm of their amplitude scales with the magnitude of the eventual earthquake, with a form similar to the Gutenberg-Richter law for seismicity (Varotsos and Alexopoulos, 1984a; 1986; Varotsos and Lazaridou, 1991). This implies that both the source of the SES and the future focal region have a fractal geometry (Varotsos et al., 2011b), an interpretation supported by the observation that geoelectric time series can show fingerprints of self-organised systems (Cuomo et al., 1998). Further findings include the consistency of polarity from a given dipole orientation for a particular seismic area and a consistent ratio between SES amplitude in the NS and EW directions over a range of magnitudes for a given seismic area.

These systematic features led Varotsos and Alexopoulos (1984a;b) to develop a prediction method, known as VAN (after Varotsos-Alexopoulos-Nomikos). Although Varotsos et al. (1996) claimed to have successfully predicted Greek earthquakes from geoelectrical measurements using this method, tests showed lack of statistical significance (Wyss and Allman, 1996; Kagan, 1996) and noise contamination (Gruszow et al., 1996), while the scanty details given in the prediction texts (Dologlou, 1993) and their non-uniqueness (Stavrakakis and Drakopoulos, 1996) allow for different interpretations (Mulargia and Gasperini, 1996a), making it difficult to falsify the predictions. In addition, Burton (1985) questioned the validity of the predictions and their usefulness to a civil protection agency, stressing that such predictions require substantial verification given the large number of earthquakes that occur in the monitored region. He emphasised the importance of community preparedness and civil protection measures to damage mitigation, whether or not the impending earthquake was predicted, and highlighted the potential for funds to be diverted from these more practical aspects in the wake of the VAN prediction claims. Furthermore, Mulargia and Gasperini (1992) showed, using the VAN group's own published work, that the success of their predictions could confidently be ascribed to chance and that the forecasts worked much better in reverse time, i.e. they were more likely to follow periods of enhanced seismicity than precede them, indicating that the observed electrical anomalies (SES) may be a response to events that have occurred, rather than precursors of the impending ones.

However, recent analysis of all available SES data from Greece over the last two decades established that for 'non-thrust' earthquakes, a power law emerges between the SES lead time and the stress drop of the subsequent earthquake (Dologlou, 2008). The associated critical exponent is close to those that govern fracture processes and that found between the logarithm of SES amplitude and earthquake magnitude. In addition, Varotsos et al. (2007) have reported precursory electric pulses that occur minutes to seconds before the main rupture that may be considered co-seismic as the main rupture initiates, although there is no specific mention of a clear co-seismic electrical anomaly in studies by the VAN group. Even more recently, Telesca et al. (2014) found a clear correlation between deformation intensity along the Taiwan orogeny and the Fisher-Shannon information properties of geoelectric signals recorded at three stations in Taiwan. This influence of long-term deformation processes on low-frequency geoelectric signals could not be explained by short

time-scale piezoelectric and electrokinetic effects, implying that strain buildup and geoelectric signal generation in areas of intense deformation like Taiwan may be connected by other physical processes, such as the deformation mechanisms themselves.

### 3.2.3 Ionospheric disturbances and oscillations

Other studies have focused on ionospheric disturbances and oscillations, such as those accompanying the 1995 Kobe earthquake, which began a few days before and decayed over a few days after the quake (Molchanov and Hayakawa, 1998b). Plasma density variations and total electron content (TEC) disturbances are the physical quantities measured, using both ground-based ionosounder data (e.g., Pulinets, 1998a; Liu et al., 2000; 2002; 2004; 2011; Molchanov et al., 2003; 2004; Trigunait et al., 2004; Cahyadi and Heki, 2013) and topside sounding by satellites (e.g., Pulinets, 1998b; Parrot et al., 2006b; Sarkar et al., 2007; Akhoondzadeh et al., 2010). A great many papers have been published on seismo-electromagnetic disturbances of the neutral and ionized upper atmosphere and their possible generation mechanisms (e.g., Hayakawa, 1999; Hayakawa and Molchanov, 2002; Pulinets and Boyarchuk, 2004; Pulinets, 2004; Hayakawa et al., 2004; Hayakawa and Hobara, 2010; Pulinets and Ouzounov, 2011; Klimenko et al., 2011; Zolotov et al., 2012, and references therein).

### 3.2.4 Satellite observations

Satellite observations of anomalous electric and magnetic field variations associated with earthquakes have come from instruments on the following Earth-observing satellites: (a) Interkosmos-19 (Larkina et al., 1983; 1989; Parrot, 1994), (b) GEOS-2 (Parrot and Lefeuvre, 1985; Matthews and Lebreton, 1985), (c) COSMOS-1809 (Serebryakova et al., 1992), (d) AUREOL-3 (Serebryakova et al., 1992; Parrot, 1994), (e) DE-2 (Henderson et al., 1993), (e) Interkosmos-24 (Shalimov and Gokhberg, 1998; Molchanov et al., 1993) and (f) ISIS 2 (Rodger et al., 1996). For example, Larkina et al. (1983) reported VLF ($0.1 - 16$ kHz) electromagnetic anomalies associated with eight earthquakes ($M = 5.0 - 6.1$) worldwide between 1979 and 1980. June 2004 saw the launch of DEMETER, a micro-satellite with a two-year mission dedicated to investigating electromagnetic effects related to seismic activity and anthropogenic EM-wave influences on the ionosphere (Parrot, 2002). The first results from this mission (e.g., Parrot et al., 2006a) were published in a special issue of Planetary and Space Science (Volume 54, Issue 5). Notable results published since then include systematic perturbations in electron and ion densities in the ionosphere close to the eventual epicentres of several earthquakes (Sarkar et al., 2007; Akhoondzadeh et al., 2010) and enhanced ULF radiation in the weeks preceding the 2010 $M_w 7$ Haiti earthquake (Athanasiou et al., 2011).

### 3.2.5 Statistical correlation of electric phenomena with earthquakes

The correlation of electric phenomena with earthquakes, together with their potential as precursors useful for intermediate-term earthquake forecasting, remains controversial. For example, even the most frequently cited reports of precursory electromagnetic activity before the Loma Prieta earthquake (Fraser-Smith et al., 1990; Bernardi et al., 1991) have been recently called into question (Campbell, 2009; Thomas et al., 2009). However, these authors provide conflicting alternatives for the anomalies; Campbell (2009) attributed them to a coincidental disturbance in the natural solar-terrestrial geomagnetic field, while Thomas et al. (2009) concluded that they were an artifact due to a malfunction in the sensor system. Moreover, Hayakawa et al. (2011) suggest that their arguments are not strong enough to preclude the presence of precursory seismogenic ULF emissions. Although causal relations between coseismic magnetic field changes and earthquake stress drops (Figure 3.3) were established more than a decade ago (Mueller and Johnston, 1998; 1990; Johnston et al., 1994; Johnston and Mueller, 1987), the existence of precursory electromagnetic signals had not yet been clearly demonstrated in the early years of the 21st century, in spite of relatively high quality monitoring over the previous 25 years (Johnston, 2002). For example, Parrot et al. (2006a) reported seven studies that took a statistical approach with satellite data (Larkina et al., 1983; Parrot and Lefeuvre, 1985; Matthews and Lebreton, 1985; Henderson et al., 1993; Molchanov et al., 1993; Parrot, 1994; Rodger et al., 1996), four had found a statistical correlation between electromagnetic emission and seismic activity and three had not. Two of the four studies reporting a correlation used data from ∼300 earthquakes (Parrot and Lefeuvre, 1985; Parrot, 1994), whereas the remaining studies considered less than 70 earthquakes in their analysis. However, neither study indicated whether the anomalous signals occurred prior to, coincident with, or subsequent to the earthquakes that were analyzed.

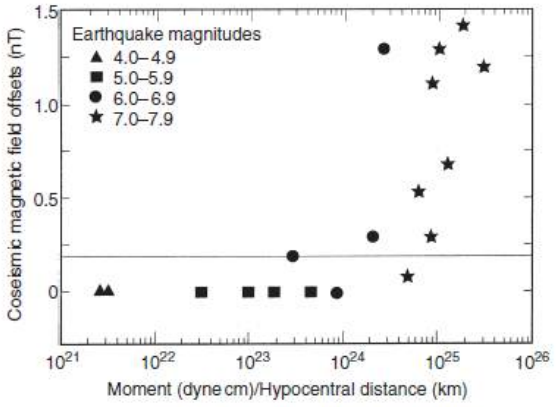


Figure 3.3: Coseismic magnetic field offsets as a function of seismic moment scaled by hypocentral distance (from Mueller and Johnston, 1998). Of the 18 events analysed, it is apparent that maximum coseismic offsets are around 1.5 nT and that coseismic magnetic effects are observed above the measurement resolution (horizontal line) only for large earthquakes ($M \geq 6$).

Very recently, Orihara et al. (2012) demonstrated rigorously that the statistical correlation between the appearance rate of 19 telluric current anomalies observed on Kozu-shima Is-

land (1997-2000) and the occurrence rate of 23 nearby earthquakes was far beyond chance. Additionally, the statistical analysis of Akhoondzadeh et al. (2010) showed good agreement between the DEMETER ionospheric electron density data and ground-based GPS Total Electron Content data, with the anomalous deviations having a different sign from earthquake to earthquake and their amplitude depending on the eventual event magnitude. Furthermore, striking similarities were noted in magnetic pulsations, air conductivity changes, and IR signals in a study relating laboratory-scale ($cm^3$ rock samples) and field-scale ($m^3$ boulder) deformation experiments to data from the 2007 $M5.4$ Alum Rock earthquake (Bleier et al., 2010).

### 3.2.6 Crustal currents required for observable electric signals

If they are truly related to the earthquake preparation process, the observed electric phenomena require electric currents to flow through the crust. The long distances and great altitudes over which these phenomena have been detected combined with their often high strength (particularly those of the low frequency anomalies), suggest that the ground currents causing them must be quite strong (Freund et al., 2004; 2006). This raises questions about the mechanisms that can generate powerful electrical currents in the crust and the minimum electrical current necessary to produce an observable electromagnetic signal on the ground. Using a relatively simple model of an underground current source co-located with the earthquake hypocentre, Bortnik et al. (2010) estimated the magnitude of the seismo-telluric current required to produce observable electromagnetic ground signals at a given distance from the epicenter and for an assumed ground conductivity. The model is based on fault geometry from the 2007 Alum Rock earthquake and shows that for an observed 30 nT pulse at 1 Hz, seismo-telluric currents of $\sim 10 - 100$ kA are expected. When typical values of ground conductivity are assumed, the minimum current required to produce an observable signal at 30 km range was found to be $\sim$1 kA; a relatively low value according to the authors. Even when large values of ground conductivity are assumed, electromagnetic signals >1 pT are readily detectable within 30 km of the epicenter.

## 3.3 Laboratory Studies of Electric Phenomena

The variability in observations of electric phenomena in the crust, the lack of consensus regarding their origin and the search for plausible mechanisms to explain their occurrence, combined with the the controversy surrounding VAN and the lack of a systematic approach to field monitoring, revealed the need for a more systematic, laboratory-based approach to the investigation of electrical signals emitted during rock deformation. Work to establish the mechanisms by which rocks emit radio wave energy when crushed was started as early as the 1950s in Russia (Karasev et al., 1953; Martyshev, 1965; Parkhomenko and Martyshev, 1975, and references therein), Japan (Mizutani et al., 1976; Ishido and Mizutani,

1981; Ogawa et al., 1985) and the USA (Nitsan, 1977; Warwick et al., 1982). These studies demonstrated that ordinary crustal rocks produced electricity when shocked or fractured and discussed these observations mainly in terms of the piezoelectric effect of quartz and electrokinetic effects. The experimental work of Brady and Rowell (1986) and Cress et al. (1987) provided a further significant step by demonstrating that luminous phenomena were produced during the fracture of both piezoelectric and non-piezoelectric rocks, in air and underwater. This indicates that any instrumentally recorded earthquake is capable of producing luminous phenomena and provides an explanation for sightings of earthquake lights at sea (Derr, 1986). By means of spectroscopic analysis, they also discriminated between several proposed mechanisms for these phenomena; (a) frictional heating of rock fragments, (b) electrostatic discharge due to piezoelectric effects or charge separation on fractured surfaces, (c) plasmas produced by rapid and intense heating of the rock and (d) excitation of the ambient atmosphere by electron or ion bombardment. Their evidence confirmed that a piezoelectric discharge was not the source of visible light, neither was frictional heating of rock fragments nor heat-induced plasmas in the rock; they found that the most likely source of visible light was that of atmospheric bombardment by exo-electrons emitted from fresh fracture surfaces. This work, using a 'soft' testing machine (where violent failure of the sample occurs at the rock's peak strength), therefore provides strong evidence that the luminous phenomena were indeed produced by micro-fracturing events. It supports the work of Goncharov et al. (1980), who observed a significant increase in both AE and EM pulse activity after the peak stress during uniaxial compression using a 'stiff' testing machine.

Since then, the generation of electromagnetic emissions and transient electric potential or electric current signals during the loading of rock samples, both prior to and during rupture, has been demonstrated in a number of laboratory experiments involving both dry and fluid-saturated rock specimens (e.g., Enomoto and Hashimoto, 1990; Enomoto et al., 1994; Fiffolt et al., 1993; Hadjicontis and Mavromatou, 1994; 1996; Yoshida et al., 1997; 1998; Yoshida, 2001; Yoshida and Ogawa, 2004; Mori et al., 1998; Clint, 1999; Frid et al., 1999; 2003; Rabinovitch et al., 1999; 2001; Freund and Borucki, 1999; Freund, 2000; Iida et al., 2000; Takeuchi and Nagahama, 2001; Stavrakas et al., 2003; Anastasiadis et al., 2004; Eccles et al., 2005). Several different electrification mechanisms are thought to be responsible for these observations, with piezoelectric and electrokinetic effects being the most commonly investigated. Piezo-electricity has been shown to electrify quartz-bearing rocks (Nitsan, 1977; Warwick et al., 1982; Enomoto et al., 1994; Yoshida et al., 1994; 1997; 1998; Sasaoka et al., 1998; Eccles et al., 2005) and, although the possibility exists of a self-cancellation effect unless a large proportion of quartz crystals are aligned (Tuck et al., 1977), these studies have demonstrated the association of macroscopic piezoelectric signals, both precursory and coseismic, with microfracturing. Electrokinetic effects due to fluid flow have also been demonstrated (Mizutani et al., 1976; Ishido and Mizutani, 1981; Morgan et al., 1989; Jouniaux and Pozzi, 1995a;b; 1997; Yoshida et al., 1998; Yoshida, 2001; Eccles et al., 2005). In experiments focusing on the effects of pore water movement

(Yoshida, 2001), convection currents flowed prior to the main fracture with a current density of $\sim$1 mAm$^{-2}$ and showed good correlation with both dilatancy rate and water flow rate. They were therefore attributed to an electrokinetic effect due to water flow associated with accelerating dilatancy before the main fracture. These and other observations (Chen et al., 1994; Yoshida et al., 1998; Gensane et al., 1999; Eccles et al., 2005), combined with theoretical fault-zone models (Scholz et al., 1973; Fenoglio et al., 1995; Patella et al., 1997) show that, in the immediate vicinity of the fault zone, precursory and coseismic signals may be caused by fluid flow driven into the dilatant region by the accelerating dilatancy (microcracking). In their studies of electrical potential changes prior to shear fracture in dry and saturated sandstone and basalt samples, Yoshida et al. (1998), Clint (1999) and Eccles et al. (2005) concluded that piezoelectric and electrokinetic effects are the *dominant* mechanisms for precursory electric signals since neither study observed any precursory electric potential signals in dry, non-piezoelectric basalt samples.

However, neither the piezoelectric effect nor the electrokinetic effect can explain why dry, quartz-free rocks also generate electric phenomena during deformation (Cress et al., 1987; Enomoto et al., 1994; Fiffolt et al., 1993; Hadjicontis and Mavromatou, 1994; 1996; Freund and Borucki, 1999; Freund, 2000; Rabinovitch et al., 2001; Frid et al., 2003; Stavrakas et al., 2003; Anastasiadis et al., 2004; Tsutsumi and Shirai, 2008; Nardi and Caputo, 2009; Baddari et al., 2011), or that the stress sensitivity coefficient, which determines the dependence of the transient electric field on the applied stress rate, is comparable in both quartz-bearing and quartz-free rocks (Vallianatos and Tzanis, 1998; 1999). Moreover, electrokinetic effects are normally short-lived and very weak on a macroscopic scale and therefore may be undetectable at long distances from the source (Vallianatos et al., 2004). This may be because of rapid attenuation of currents with distance (Bernard, 1992) or due to limitations on the size of the electrokinetic coupling coefficient contrasts and pressure differences necessary to drive strong currents (Vallianatos et al., 2004). The experiments of Morgan et al. (1989) and Jouniaux and Pozzi (1995a) indicate that naturally-occurring contrasts are relatively small and conductive pore fluids may inhibit the coefficient and its increase with permeability, while Tzanis et al. (2000) suggest that small earthquake stress drops ($\sim$3 MPa on average) mean that stress heterogeneities near an active fault would be unlikely to generate current-driving pressure differentials sufficient to observe effects far from source. Although Jouniaux and Pozzi (1995b) propose that vertical fluid flow variations may be responsible for self-potential anomalies away from the earthquake epicentre due to an earthquake-related underground water level change, these combined observations indicate that solid-state mechanisms, related to the deformation process itself, must also contribute to electric phenomena in the crust.

### 3.3.1 Microfracturing electrification

Microfracturing electrification, i.e. spontaneous charge production associated with the opening and propagation of microcracks and the resulting appearance of transient electric

and electromagnetic emissions, has been discussed in connection with laboratory experiments by several authors. For instance, Warwick et al. (1982), Ogawa et al. (1985) and Enomoto and Hashimoto (1990) reported charge densities of $10^{-3} - 10^{-2}$ $Cm^{-2}$ associated with opening microcracks, while Enomoto and Hashimoto (1990; 1992) reported typical charge amounts of $10^{-13} - 10^{-10}$ C and a net charge production rate of $\sim$0.6 $Cm^{-3}s^{-1}$ associated with indentation fracture. Scaling this up to a massive failure over several metres at ground level, Enomoto and Hashimoto (1990) suggested that the potential charge generated may be comparable to that produced by one bolt of lightning ($\sim$1 C). Electric, electromagnetic (EM) and charged particle emission have also been observed to occur concurrently with acoustic emissions (AE) during rock deformation (Yamada et al., 1989; Fiffolt et al., 1993; Chen et al., 1994; Enomoto et al., 1994; Hadjicontis and Mavromatou, 1994; 1996; Yoshida et al., 1994; 1997; Frid et al., 2000; 2003; Rabinovitch et al., 2001; Yoshida and Ogawa, 2004; Nardi and Caputo, 2009).

The uniaxial and triaxial deformation experiments of Frid et al. (1999; 2000; 2003) and Rabinovitch et al. (1998; 1999; 2001) recorded EM radiation in the 1 kHz to 10 MHz frequency range from several different materials. They established several important features: (a) both the rate of EM emissions and their amplitudes increase in the region of permanent deformation prior to failure (i.e. in the presence of microcracking) and (b) the shape of the EM pulse changes immediately prior to collapse (from 97% of the failure strength), with higher frequency emissions giving way to lower frequency events and the time interval between the start of the pulse and the peak amplitude increasing. Rabinovitch et al. (2001) established a Gutenberg-Richter type relation for laboratory fracture-induced electromagnetic radiation, where the slope of the EM pulse amplitude - Benioff strain release curve exhibits a power-law intermediate stage, the slope of which decreases in the seconds prior to collapse. The group has since used these observations to monitor and forecast rock failure and rock bursts in coal mines (Frid and Vozoff, 2005) as well as to develop a model for EM pulse emission based on oscillating electric dipoles due to the breaking of bonds at the tip of a moving fracture (Frid et al., 2003; Bahat et al., 2005; Rabinovitch et al., 2007). Baddari et al. (2011) noted that EM emissions intensified immediately before strong acoustic events and that the amplitude and duration of EM emissions were greater than those of AE during the nucleation of isolated microcracks, with this relationship reversing during crack coalescence.

Recently, combined acoustic and EM emissions have been used to improve Kaiser effect estimates for *in-situ* stress measurements (Mori et al., 2006; Mori and Obata, 2008) based on the notion that EM and electric potential anomalies are due to electrification between fresh crack surfaces and that the true stress history of the rock can be established by distinguishing AE due to fresh cracks (with accompanying EM emissions) from frictional AE (no accompanying EM emissions) (Mori et al., 1998; Iida et al., 2000; Sikula et al., 2002). In contrast, electric signals have been seen to accompany AE and stress drops associated with individual stick-slip events in granite (Takeuchi and Nagahama, 2001) and in quartz-free basalt and peridotite (Tsutsumi and Shirai, 2008). However, these

occur only during the *initiation* of slip, not the remainder, suggesting that two processes are essential for detectable electric signals: rapid slip along the fault *and* separation across the fault. Takeuchi and Nagahama (2001; 2002a;b) observed voltage changes induced by stick-slip events along a pre-cut shear surface in granite cores. These changes occurred milliseconds before the slip motion and were proportional to the subsequent stress drop, causing the authors to infer that local charge distributions or emission of charged particles due to fracturing may occur due to the failure of asperities along the fault plane just before slip. Further experiments (Takeuchi et al., 2004; Takeuchi and Nagahama, 2006) established that fracturing or frictional slipping can indeed lead to the release of strongly directive charges which form electric dipoles oriented perpendicular to the stick-slip plane. In addition, Tsutsumi and Shirai (2008) found that electric potential (EP) amplitudes in their quartz-free rocks exhibited anisotropy due to electric polarization normal to the fault surface, with the electrode pair oriented parallel to the strike of the fault yielding higher EP amplitudes than the pair oriented normal to the fault. These amplitudes also increased with both normal stress and stress drop, implying that the mechanism involved acts to increase the signal intensity with increasing stress. After observing EP signals within areas of high strain, Yoshida et al. (1997) established the possibility of a casual relationship between crack growth and EP and that mapping EP may yield spatial information about crack evolution. Furthermore, Shinbrot et al. (2012) have shown experimentally that voltage signals are produced by the opening and closing of crack-like defects in organic powders and that slip events in these cohesive powders can also produce electrical signals, with signals sometimes appearing several seconds in advance of the slip events. Recently, they demonstrated that these effects also occurred when polymeric disks and glass particles were used (Shinbrot et al., 2014).

### 3.3.2 Battery effect of stress application to rocks

An alternative view of electrification in rocks was demonstrated by Freund and Borucki (1999), Freund (2000; 2002; 2007a;b; 2010; 2011b), Freund et al. (2004; 2006) and Takeuchi et al. (2006). Bursts of charge were generated during low to medium velocity impact of a variety of igneous rocks, including quartz-free rocks (Freund and Borucki, 1999; Freund, 2000; 2002). Initially activated in a small volume near the impact point, these charge clouds then spread through the rock volume, causing the rock to become momentarily conductive and electrically polarised (with electric potentials exceeding +400 mV) and emit both visible light and electromagnetic radiation. These charge clouds were similar to those released during indentation fracture of rocks (Enomoto and Hashimoto, 1992), which propagated through the rock media to produce a detectable transient electric signal at a distance from the fracture point of nearly 20 times the fracture size. Enomoto and Hashimoto (1992) suggested that water molecules and some polar minerals may play an important role in the observed signal propagation. However, Freund (2000) suggested an alternative mechanism involving the propagation of stress-activated positive hole charge carriers (Section 3.5.1.3). Further experiments showed that uniaxial loading of the central

part of dry tiles of several types of rocks (granite, anorthosite, gabbro, limestone, and marble) and glass (Freund et al., 2004; Takeuchi et al., 2006) and one end of large, long rock blocks (Freund et al., 2006; Freund, 2007a;b), generated two currents. One is a positive current that flows from the stressed part of the rock volume through the surrounding unstressed rock volume to an electrode at the edges of the tiles or the unstressed end of the blocks. The other is a negative current that flows directly from the stressed rock volume into the loading pistons, in the case of the centrally loaded tiles, or into a copper electrode attached directly to the stressed end of the rock block. In addition, a positive potential was observed on the surface of the unstressed part of both the tiles and the blocks. Currents generated in the tiles were of the order of $10^{-4} - 10^{-5}$ $Am^{-2}$ for silicate rocks (both quartz-rich and quartz-free) and $10^{-6} - 10^{-7}$ $Am^{-2}$ for carbonate rocks. In the large rock blocks loaded at one end, the two electrodes were connected to each other via an outer electric circuit as well as via the rock volume and the positive current flowed through at least 1 m of unstressed rock to meet the negative current arriving through the outer electric circuit. The two outflow currents are coupled via their respective electric fields and fluctuate, forming part of a battery current. In the ground, closure of the current loop is more difficult to achieve (Freund, 2011a) but may occur when the positive potential generated in the surrounding unstressed rock volume reaches and exceeds the Schottky barrier, causing electrons to flow in from the ground (Freund et al., 2004). Other scenarios, such as encountering a rock-water or rock-air interface or conduction deep in the hot and ductile mid-crust have also been proposed (Freund, 2011a). These results imply that transient, fluctuating currents of considerable magnitude could build up in the Earth's crust prior to major earthquakes (Freund et al., 2006).

### 3.3.3 Pressure-stimulated currents

The idea that fracturing produces electric currents in rocks was further demonstrated by Stavrakas et al. (2003; 2004), Anastasiadis et al. (2004) and Vallianatos et al. (2004). These authors measured electric currents during uniaxial deformation of dry marble samples at atmospheric pressure, coining the phrase 'pressure-stimulated currents' (PSC) to describe the small ($10^{-12}$ - $10^{-9}$ A), transient, polarising electric currents emitted from a solid undergoing a gradual change in pressure. Their observations, which they attributed to the movement of charged edge dislocations (MCD; Section 3.5.1.2) under stress (Vallianatos and Tzanis, 1998; 1999), included:

1. Peaks of PSC above background that coincided with abrupt increases and decreases in stress (Stavrakas et al., 2003; Anastasiadis et al., 2004). In the elastic region, the maximum amplitude of the PSC peaks were directly proportional to the stress rate of the corresponding abrupt stress variation (Stavrakas et al., 2003; Anastasiadis et al., 2004; Vallianatos et al., 2004), with the relationship deviating from linearity in the region of permanent deformation due to the changing Young's Modulus (Anastasiadis et al., 2004). Also, the PSC polarity coincided with the sign of the abrupt stress

variation (Stavrakas et al., 2003).

2. A PSC signal (Figure 3.4 (a)) above background during loading at a constant stress rate, which was only observed beyond the elastic region ($\sigma > 60\%$ of the failure stress). It increased between 60 and 75% of the failure stress in proportion to $1/y$, where $y$ is the normalised Young's Modulus ($E_{eff}/E$), for each loading cycle (Stavrakas et al., 2004) and reached a positive peak at 80% (Stavrakas et al., 2003) before reducing steeply as the sample approached failure, reversing polarity in the process (Stavrakas et al., 2003; 2004). The correlation of PSC with $1/y$ deviated from linearity above 90% of the failure stress (Stavrakas et al., 2004) and the absolute value of the negative peak was systematically observed to be three times that of the positive peak (Stavrakas et al., 2003), although similar experiments by Vallianatos et al. (2004) showed the negative peak to be six times that of the positive peak. The variation in PSC signal was attributed to MCD due to a decreasing Young's Modulus beyond the material yield point (Stavrakas et al., 2003; 2004).

3. Evidence of strain hardening (Figure 3.4 (b)); a smaller positive current peak (Stavrakas et al., 2003) and a decrease in both overall PSC and overall $1/y$ (Stavrakas et al., 2004) was observed with each subsequent cycle. This 'memory effect' under sequential loading cycles may be the reason for weak or absent electric earthquake precursors during an aftershock sequence (Stavrakas et al., 2004).

4. The form of the PSC signal was associated with the sample fracture mode; a single PSC peak if failure occurs along a shear fracture and a sequence of PSC emissions if failure is irregular axial splitting. This indicates that each fracture plane activates an electrical process (Anastasiadis et al., 2004).

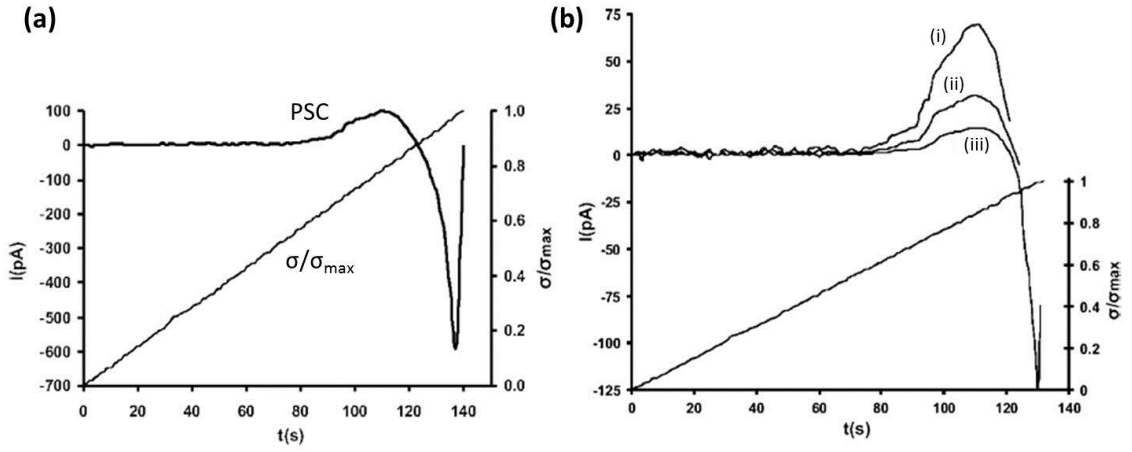


Figure 3.4: PSC signals and normalised stress with respect to time during uniaxial compression (a) to failure and (b) during three sequential loading cycles; the final cycle (iii) took the sample to failure. From Vallianatos et al. (2004).

Comparable results were obtained in similar uniaxial experiments on samples of cement (Kyriazopoulos et al., 2011a;b; Stergiopoulos et al., 2013), where PSC were generated beyond the material yield point and increased rapidly towards failure, and amphibolite

specimens (Triantis et al., 2007), in which the work-hardening history of the sample was expressed in the PSC signals. Further experiments on marble (Triantis et al., 2006; Anastasiadis et al., 2007a;b; Triantis et al., 2008) verified that:

1. PSC originated from the change in Young's Modulus rather than the change in stress rate, with the total charge released during deformation reaching consistent values regardless of the stress rate (Triantis et al., 2006).

2. PSC peaks produced during abrupt stress steps in the region of permanent deformation, when normalised by the stress rate of the stress step, are directly related to the damage parameter, $D = 1 - y$, that quantifies the deviation from linear elasticity and the concentration of microcracks (Triantis et al., 2006).

3. A linear relationship exists between $D$ and the PSC signal up to 80% of the failure stress during deformation at both a constant stress rate and a constant deformation rate (Anastasiadis et al., 2007a).

4. The PSC reaches a maximum value just before failure at ∼98% of the failure stress during constant deformation rate experiments, above which it decreases rapidly (Anastasiadis et al., 2007a).

5. Strain hardening effects can be seen where PSC peak amplitudes decrease exponentially during sequential load-unload procedures, while the stress value at the PSC onset increases logarithmically as the number of loading cycles increases (Anastasiadis et al., 2007b).

6. Under a constant stress rate, electric charge increases linearly with strain from the yield point (∼70%) to ∼98% of the failure stress (Triantis et al., 2008), with a proportionality constant of 0.16 $\mu$C. This constant is independent of stress rate and apparently characteristic for marble. Non-linearity between released charge and accumulated strain indicates imminent failure.

All of these observations are consistent with the predictions of the MCD model, indicating that the movement of charged edge dislocations occurring in samples under stress may be responsible for the measured PSC. In addition, Vallianatos and Triantis (2008) demonstrated that (a) PSC from marble and cement samples subject to uniaxial compression obey a frequency-size law similar to the Gutenberg-Richter law, with $b \sim 1$, (b) PSC waiting times show self-similarity in their probability density function, which is well-approximated by a gamma function, indicating a broad distribution of waiting times and (c) the cumulative PSC energy release as failure approaches can be described by a power-law time-to-failure expression based on irreversible thermodynamics. They suggest that these similarities with AE and seismicity statistics imply a connection with fracture phenomena at much larger scales and that a basic general mechanism lies behind all these phenomena.

One of the aims of this thesis is to investigate in detail the characteristics of these currents under simulated crustal conditions and establish how they might vary with pressure and deformation rate across the brittle-ductile transition.

## 3.4 Tsallis Approach to Scaling of Electric Phenomena

Two major problems hinder the compilation of viable, self-consistent theories for the generation and propagation of electric phenomena in the crust (Vallianatos et al., 2004): (1) how laboratory results may scale up to the enormous, heterogeneous rock volumes involved in the preparation of large earthquakes and (2) the relative contribution, efficiency and interaction of the different electrification mechanisms. Deformation- and fracture-related electromagnetic (EM) phenomena at both laboratory and field scales have been shown to exhibit universal, power-law scaling properties similar to those of laboratory-scale acoustic emissions and large-scale seismicity (e.g., Rabinovitch et al., 2001; Vallianatos and Tzanis, 2003; Vallianatos and Triantis, 2008; Varotsos, 2005; Dologlou, 2008; Papadimitriou et al., 2008; Contoyiannis et al., 2010; Frid et al., 2011; Vallianatos et al., 2012c; Potirakis et al., 2013b); for instance, yielding comparable Gutenberg-Richter $b$-values and Benioff strain release parameters. These similarities may be viewed as the outcome of irreversible dynamics in a scale-invariant, complex, disordered system, with long-range interactions and 'memory' (Vallianatos et al., 2011a;b). For example, EM emissions observed during the last stage of the rupture process radiate, by whatever mechanism, from the population of self-similar crack-clusters. Since this system is significantly more complex than a single opening crack, the properties of the EM emissions are governed by the characteristics of these self-similar structures rather than by the characteristics of individual cracks (Potirakis et al., 2013a). Therefore, a statistical physics approach is appropriate to the study of these EM phenomena. In particular, the Tsallis entropy approach (Section 2.4.2), already applied successfully to the study of seismicity and acoustic emissions (Section 2.4.3), is also relevant to the study of fracture-related electric phenomena and may be useful in addressing the question of scaling.

### 3.4.1 Laboratory-scale electric fracture phenomena

Non-extensivity has been shown to be a feature of EM radiation emitted during uniaxial compression of several different rock types (Vallianatos et al., 2012c), of the relaxation of depolarization currents in stressed calcite samples (Vallianatos et al., 2011b) and of the relaxation of PSC in abruptly stressed amphibolite and marble specimens (Vallianatos and Triantis, 2012; 2013). EM emissions from samples subject to uniaxial stress (Nardi and Caputo, 2009) exhibit power-law scaling in their energy release and inter-event time distributions (Vallianatos et al., 2012c). These distributions can be described by Tsallis $q$-exponential distributions, with respective $q$-values $q_e = 1.67$ and $q_t \approx 1.7$, indicating long-

range correlations between EM emissions. These $q$-values are close to those for seismicity and acoustic emissions (Section 2.4.3), supporting the idea that the fracture network dynamics are far from equilibrium and highly correlated. Additionally, by applying a spring-block model (Hasumi, 2007), Vallianatos et al. (2012c) established that the inter-event time distribution is controlled by the frictional properties of the material.

Relaxation times of PSC in stressed rocks (Vallianatos and Triantis, 2012) follow $q$-exponential distributions with a stress-dependent $q$-value, $q_{\tau_r}$, which increases from 1 to 1.5 as the high applied stress under which relaxation occurs increases from within the elastic limit to a value close to the fracture limit. PSC relaxation is attributed to a rapid decrease in microcrack production once the stress is held constant. A super-statistical model shows that $q_{\tau_r}$ may increase with applied stress due to an increasing number of PSC relaxation sub-domains formed by an increasingly complex fracture network (Vallianatos and Triantis, 2012). This indicates that PSC relaxation is a process of moving charged elements driven by the complex network of fracture clusters (created during loading) and their interactions, and that the variation in $q_{\tau_r}$ may reflect the development of the network. For instance, during the initial relaxation cycles to a stress beyond the elastic limit, cracks begin to nucleate and grow solely by propagation of their tips, creating a multifractal network from an initially random distribution. Thus, the size-distribution of cracks (and consequently the PSC relaxation time) follows a $q$-exponential with $q_{\tau_r}$ increasing away from 1. As the density of cracks increases, the degree of crack interaction peaks as stress field interactions begin to shield unfavourably positioned cracks and inhibit the nucleation of new ones, leading to a peak in the $q$-value. Conversely, over the course of five loading cycles to a high applied stress of 85% of the fracture stress (Vallianatos and Triantis, 2013), $q_{\tau_r}$ decreases (from 1.5 to 1.2). This implies a decreasing contribution from the nucleation of new microcracks and an increasing contribution from the growth and coalescence of existing ones, which occurs as population self-organises with subsequent cycles and serves to reduce the contribution of crack interaction to the relaxation process. Thus, $q \to 1$ as the $q$-exponential size distribution approaches an exponential due to crack coalescence, eventually leading to a regime where the largest cracks have an almost random size distribution.

### 3.4.2 Earthquake preparation and the role of EM emissions

Pre-seismic electromagnetic emissions activated along a single fault are well-described by the non-extensive fragment-asperity model (Section 2.4.4.1) for earthquake dynamics (Papadimitriou et al., 2008; Kalimeri et al., 2008; Contoyiannis et al., 2010; Eftaxias, 2010; Minadakis et al., 2012; Potirakis et al., 2012). Based on the identification of a precursory EM signal where initial MHz emissions are followed by strong impulsive kHz emissions prior to failure on both laboratory and geophysical scales (Eftaxias et al., 2001; 2002; Frid et al., 2003; Contoyiannis et al., 2005), non-extensive analysis of the kHz emissions associated with the $M5.9$ 1999 Athens earthquake exhibited $q_m = 1.8$ for the first two

phases, increasing to 1.84 for the final phase (Papadimitriou et al., 2008). The similarity of these values to those ($q_m = 1.82$) for the kHz emissions associated with the $M$6.3 2009 L'Aquila earthquake (Eftaxias, 2010) and those seen for seismicity and laboratory acoustic emissions supports the possibility that (a) the EM pulses are related to fracture and slip along the fault and (b) the activation of a single fault can be considered as a footprint of the self-affine nature of fracture and faulting; i.e., it is both a reduced image of regional seismicity and a magnified image of laboratory microfracture. In terms of the fragment-asperity model, these authors infer that a sequence of precursory EM pulses occurs when the fragments between fault surfaces fracture and suggest that, by detecting the pattern of alterations in the EM emissions and discriminating between 'injury levels' of the focal area, the Tsallis entropy provides evidence for changes in state approaching the point of global instability. The increase in $q$-value also indicates a significant increase in organisation and the appearance of persistency at the tail of the recorded EM emissions.

Comparable non-extensive analysis of kHz EM emissions associated with both the Athens earthquake and the $M$6.5 1995 Kozani-Grevena earthquake, led Kalimeri et al. (2008) to propose a quantitative strategy for monitoring the potential focal area of an impending earthquake based on a Tsallis-like time-dependent entropy. Temporal evolution of the Tsallis entropy from the kHz EM emissions associated with the Athens and the $M$6 2008 Methoni earthquakes (Potirakis et al., 2012) implies the emergence of two separate kHz precursory epochs from the kHz EM background: (i) an initial epoch characterised by anomalies sparsely distributed in time with a higher degree of organisation than the background and (ii) a final epoch characterised by a further significant increase in the degree of organisation. The authors infer that, since anomalous behaviour coincides with the appearance of higher levels of organisation, the Tsallis entropy reliably distinguishes candidate EM precursors from background noise. Minadakis et al. (2012) argue that these two epochs can be explained in terms of the fragment-asperity model where the first reflects breakage of the fragments filling the gap between the two rough fault surfaces while the second is concerned with the fracture of the large, strong 'teeth' that comprise the rough fault surfaces themselves, i.e., the entities sustaining the system.

An important recent development in the study of electric phenomena and seismicity, which complements the Tsallis approach and has been shown to be a useful representation of complex and critical phenomena (Abe et al., 2005a; Varotsos et al., 2011a), is the concept of natural time (Varotsos et al., 2011b). In a time series comprised of $N$ events, the natural time, $\chi_k = k/N$, serves as the index for the occurrence of the $k$th event, which implies an internal system 'clock' whereby time proceeds when an event takes place (Uyeda et al., 2009b). Natural time analysis investigates the evolution of the pair of variables $\chi_k$ and $Q_k$, where $Q_k$ is the energy of the $k$th event. Figure 3.5 shows how a time series of events in conventional time is represented in natural time. Full details of the methodology are given by (Varotsos et al., 2011b). The approach has been used to identify features in geoelectric time series that may indicate the approach to an 'electrical' critical point, assumed to shortly precede a 'mechanical' critical point (e.g., Varotsos et al., 2005; 2006;

Sarlis et al., 2008; 2010a;b; 2013; Uyeda et al., 2009a; Potirakis et al., 2013a; Varotsos et al., 2013; Vallianatos et al., 2013a; 2014). Within this concept, MHz EM emissions, seismic electric signals (SES), foreshock seismic activity, volcanic-swarm seismic activity and laboratory acoustic emissions all exhibit critical characteristics which the authors argue support the hypothesis that the electric phenomena investigated are seismogenic and precursory. Indeed, Varotsos et al. (2011b) claim that if the seismicity from the onset of SES detection onwards is analysed in natural time, critical behaviour is observed a few days before the impending main shock.

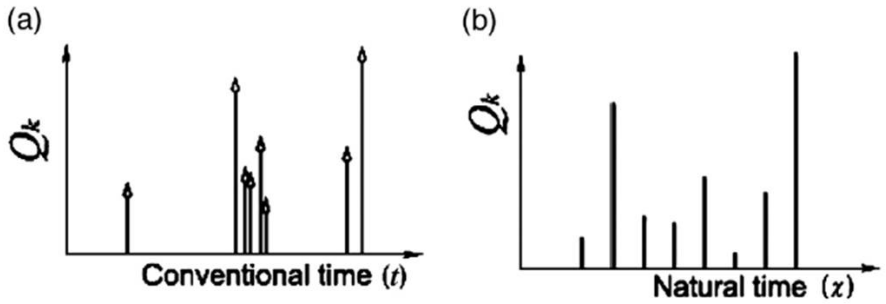


Figure 3.5: Time series (a) in conventional time $t$, and (b) in natural time $\chi$. From Uyeda et al. (2009b).

## 3.5 Theoretical Models for Electrical Phenomena

Models proposed to explain the generation of earthquake-related electric phenomena can be divided into four different classes (Varotsos et al., 2011b): (i) solid state generation mechanisms, (ii) electrokinetic processes, (iii) earthquake rupture as a critical point and (iv) other processes, such as magma flow. This section will briefly discuss relevant solid state mechanisms and electrokinetic theory. Of the solid-state mechanisms, the piezoelectric effect is an important one but is not discussed here as this thesis is concerned with electric signal generation in non-piezoelectric rocks.

### 3.5.1 Solid state generation mechanisms

As evident from the discussion in Section 3.3, pressure-stimulated currents, electric potential variations and electromagnetic signals have been detected during deformation of dry, quartz-free rocks. Their existence supports the idea of a universal, deformation-induced electrification mechanism in the crust beyond those of the piezoelectric and electrokinetic effects and they are widely attributed to deformation processes preceding macroscopic failure (Hayakawa and Molchanov, 2002). These processes, both brittle and plastic, include migration of point defects and dislocations as well as frictional slip and microcrack nucleation, propagation and coalescence. Several mechanisms related to these processes have been considered.

Fluctuations in the stresses acting on a solid affect both the formation and migration

energies of defects within that solid (Varotsos et al., 1998). Migration of defects within a crystal lattice is the mechanism behind crystal plastic deformation (Poirier, 1985) and is a function of stress because the resistance to passing an obstacle decreases with increasing shear stress (Hunt et al., 2009). Crystal imperfections consist of point, line, planar or volume defects (Figure 3.6). They disturb the local arrangement of atoms from a perfect crystal lattice and therefore can significantly modify the properties of the grains (Hull and Bacon, 2001). The activation energy required to create or migrate a defect is a function of its excess volume (Varotsos et al., 2011b). Defects within ionic solids often carry an electric charge. Their migration or cooperation are therefore the basis for the majority of solid state electrification models.

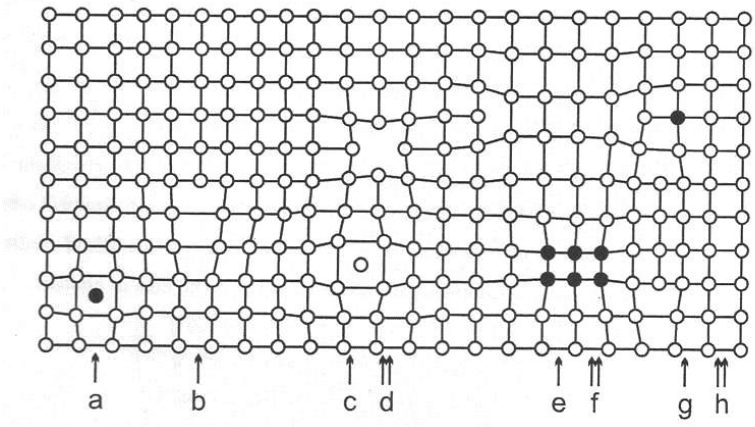


Figure 3.6: Types of crystal defects: (a) interstitial impurity atom, (b) edge dislocation, (c) self interstitial atom, (d) vacancy, (e) precipitate of impurity atoms, (f) vacancy type dislocation loop, (g) interstitial type dislocation loop and (h) substitutional impurity atom. After Helmut and Kolbesen (1976).

*Point defects* exist as one of three types: vacancies, interstitial and substitutional defects. Vacancies are holes or vacant sites in the crystal lattice (Figure 3.6 (d)) which may form a dislocation loop if they join up (Figure 3.6 (f)). Interstitial defects insert extra atoms between crystal lattice sites and are either intrinsic or extrinsic; an intrinsic defect displaces an atom from the crystal structure onto an interstitial site (Figure 3.6 (c)), while an extrinsic defect inserts an alien atom onto the interstitial site (Figure 3.6 (a)). If the interstitial defects group together, they form interstitial dislocation loops in the crystal structure (Figure 3.6 (g)). Substitutional defects are another type of extrinsic defect; they replace an atom from one of the lattice sites with an alien one (Figure 3.6 (e) and (h)). Point defects are associated with electrical polarisation effects since, in ionic materials, they carry an effective electric charge. As such, they must come in pairs or higher combinations that balance the overall charge. The charge can be balanced in one of two ways: by having a vacancy on both a cation and an anion site (a Schottky defect - after Schottky, 1935), or by having an interstitial ion of the same type as the vacancy was made from (a Frenkel defect - after Frenkel, 1926). Point defects migrate either by changing places with neighbouring ions on occupied lattice sites or by hopping to a neighbouring interstitial site or vacancy.

*Dislocations* are linear defects in the crystal structure where lattice planes are offset relative to each other (Figure 3.6 (b), (f) and (g)). There are two main types of dislocation: (a) edge dislocations, where an extra partial plane of atoms is present in the crystal structure and (b) screw dislocations, where the lattice plane spirals around the screw axis. Screw dislocations are uncharged so would not contribute to an electrification mechanism. Thus, the electrification model discussed in Section 3.5.1.2 concerns only edge dislocations. In an ionic crystal, an edge dislocation line may be oriented such that it carries an electric charge or, if the line itself is uncharged, the jogs within it are charged. Jogs are the points where the edge of the extra half plane of atoms steps abruptly from one slip plane to an adjacent parallel one. Charged jogs attract charged point defects. Thus, an uncharged dislocation line can carry a cloud of charged point defects.

Point defects and dislocations can be considered to be *charge-trapping centres* since they can capture and release charged particles, such as electrons, which can then diffuse through the material via the defect traps (Davies, 1964).

#### 3.5.1.1 Pressure-stimulated currents (PSC) model

The PSC model (Varotsos and Alexopoulos, 1986) motivated SES research in Greece (Varotsos and Alexopoulos, 1984a;b; Varotsos et al., 1998; 2011b). The presence of impurity ions of a different valence to the lattice ions (e.g., $Ca^{2+}$ in a $Na^{+}Cl^{-}$ crystal) introduces an equivalent number of cation vacancies to maintain charge neutrality. These vacancies are bound; each is negatively charged and attracted to its associated impurity cation. It therefore lies in the vicinity of the cation (at one of its neighbouring sites), forming an electric dipole ($Ca^{2+}$-cation vacancy). This dipole can change orientation in space by the vacancy jumping from one neighbouring site to another but the bound cation vacancy motion requires an activation energy $g$ in order to overcome a potential barrier. The time needed for such a dipole to change orientation is related to the relaxation time, $\tau_r$:

$$\tau_r = \frac{1}{\lambda\nu}\exp(\frac{g}{kT}) \tag{3.1}$$

where $\lambda$ is the number of jump paths available with an attempt frequency $\nu$, $k$ is the Boltzmann constant and $T$ is the temperature.

A solid containing electric dipoles due to defects can, under isothermal conditions, emit an electric current solely as a result of a variation in pressure (Varotsos and Alexopoulos, 1986; Varotsos et al., 1998; 2011b). Under pressure, the solid absorbs energy which allows the dipoles to re-orientate themselves more quickly, decreasing the relaxation time. Therefore, as the pressure increases, the dipoles have more chance of aligning cooperatively and emitting a current. The current density, $j$ is given by:

$$j\frac{d\tau_r}{dt} + \tau_r\frac{dj}{dt} = -j \tag{3.2}$$

Since maximum current density $j_m$ occurs when $\frac{dj}{dt}|_{j=j_m} = 0$, the condition for full co-operative rotation of dipoles and the appearance of a maximum absolute emitted current is:

$$\frac{d\tau_r}{dt}|_{j=j_m} = -1 \tag{3.3}$$

Combining this condition with Equation 3.1 for any (not necessarily constant) stress rate, $\dot{\sigma}$, leads to:

$$\frac{\dot{\sigma}\nu}{kT} = -\frac{1}{\tau_{r\sigma_m}} \tag{3.4}$$

where $\tau_{r\sigma_m}$ is the relaxation time at the stress at which $j_m$ is seen.

Thus, in an initially unpolarised solid and under the action of an applied stress, an electric current is emitted that maximises when the gradual variation in stress causes the relaxation time to decrease with a rate obeying $\dot{\sigma}\nu\tau_r = -kT$. During the earthquake preparation stage the stress, $\sigma$, gradually varies. Current is emitted when the stress reaches a critical value $\sigma_{cr}$, at which the relaxation time is sufficiently small to allow the electric dipoles to align quickly enough to emit a transient electric signal. $\sigma_{cr}$ does not have to coincide with the fracture stress. An avalanche of alignment (second-order dynamic phase transition) takes place as cooperative reorientation of the dipoles occurs due to the migration of defects in the crystal lattice. Since a continued increase in stress will eventually result in material failure, the emission of this current can be considered a precursor to the failure of the solid. The lead time, $\Delta t$, between the emission of electric current at $\sigma_{cr}$ and the impending failure at $\sigma_f$ is a function of stress rate $\dot{\sigma}$, given by $\Delta t = (\sigma_f - \sigma_{cr})/\dot{\sigma}$. In terms of the earthquake preparation area, the stress field within the rock volume varies gradually but $\sigma_{cr}$ is not reached simultaneously by different sub-volumes, so a series of transient current emissions is expected as each volume reaches $\sigma_{cr}$. Dramatically larger current emissions than those from simple dipole re-orientation may result due to other, more complicated, polarisation processes. These processes may also be explained by the PSC model, provided they can be described by a single relaxation time.

In a situation where deformation is inhomogeneous, such as in an earthquake preparation zone, the dipoles align in the direction of the stress gradient (Fischbach and Nowick, 1958). Polarisation occurs, with the direction of current flow governed solely by the applied stress gradient, because the effect of the stress gradient is similar to that of an electric field, a phenomenon known as deformation-induced charge flow (Fischbach and Nowick, 1958; Varotsos et al., 2001; 2011b). The pressure-stimulated current model is unique among other models in that the gradual increase of stress itself would generate spontaneous electric signals without requiring any sudden change of stress such as micro-fracturing (Uyeda et al., 2009b). It also explains why some electric phenomena exhibit critical dynamics.

#### 3.5.1.2 Movement of charged edge dislocations

The motion of charged edge dislocations (MCD) under stress, has been described in both the elastic domain (e.g., Slifkin, 1993; Hadjicontis and Mavromatou, 1994; 1996) and during crack nucleation and propagation beyond the material yield point (e.g., Ernst et al., 1993; Vallianatos and Tzanis, 1998; 1999; Tzanis and Vallianatos, 2002). Under the action of a shear stress, a dislocation line will glide as a unit from one position to an adjacent one. When several dislocations move in this way it results in slip, which can be thought of as the movement of one layer of atoms over another on 'slip planes'. This kind of slip can occur even at relatively low applied stresses since the introduction of mechanical energy serves to overcome the glide plane resistance potential. Whitworth (1975) provides a thorough background on charged edge dislocations. Concentration of stress and crack opening takes place when, after some critical stress threshold, edge dislocations multiply, migrate and pile up against an obstacle. In thermal equilibrium, dislocation lines are surrounded by a Debye-Hueckel charge cloud and are electrically neutral. However, during dynamic processes dislocations move and neutrality can no longer be maintained.

Let $\Lambda^+$ be the density of edge dislocations of the type required to accommodate uniaxial compression (or tension) and $\Lambda^-$ be the density of dislocations of the opposite type. The motion of charged dislocations produces a transverse polarization $P$:

$$P = (\Lambda^+ - \Lambda^-)\ q_l\ \frac{\delta x}{\sqrt{2}} = \delta\Lambda\ q_l\ \frac{\delta x}{\sqrt{2}} \tag{3.5}$$

where $q_l$ is the charge per unit length on the dislocation ($\sim 10^{-11}$ $\mathrm{Cm}^{-1}$). Ignoring screw dislocations (uncharged), the plastic contribution to strain, $\varepsilon$, when dislocations of Burger's vector $\mathbf{b}$ move through a distance $\delta x$ is:

$$\varepsilon = (\Lambda^+ - \Lambda^-)\ \mathbf{b}\ \frac{\delta x}{2} \tag{3.6}$$

The rate of change of polarisation is, by definition, the electric current density, $J$, which is proportional to the strain rate $d\varepsilon/dt$:

$$J = \frac{\sqrt{2}}{\beta}\ \frac{q_l}{\mathbf{b}}\ \frac{d\varepsilon}{dt} \tag{3.7}$$

where $\beta = \dfrac{\Lambda^+ + \Lambda^-}{\Lambda^+ - \Lambda^-}$; a constant usually between 1 and 1.5. When multiplied by the electrode area, $A$, this gives rise to a current:

$$I = \frac{\sqrt{2}}{\beta}\ \frac{q_l}{\mathbf{b}}\ A\ \frac{d\varepsilon}{dt} \tag{3.8}$$

or

$$I = \frac{\sqrt{2}}{\beta}\ \frac{q_l}{\mathbf{b}}\ \frac{A}{E_{eff}}\ \frac{d\sigma}{dt} = \gamma\ \frac{d\sigma}{dt} \tag{3.9}$$

where $E = d\sigma/d\varepsilon$ is the effective Young's Modulus and $\gamma$ stands for a proportionality

factor dependent on the Young's Modulus of the material. Thus, the PSC amplitude is expected to be proportional to the strain rate and decrease with increasing strain when the stress rate is constant.

A moving dislocation can emit or absorb vacancies at a jog, thereby changing the electrical charge of the jog and moving it along the dislocation by one inter-atomic spacing. Since cation and anion vacancies are not formed with equal probability, a dislocation will not have equal numbers of negative and positive jogs. Formation energy for an anion vacancy is larger than that for a cation vacancy and dislocations carry a net charge because the jogs must establish equilibrium with each species of point defect, which results in more jogs of one sign than the other (Varotsos et al., 2011b). A moving edge dislocation will therefore achieve a net positive charge as cation vacancies will be preferentially lost from the jogs. As these positively charged dislocations move from regions of stress concentration, they leave behind a net excess of negatively charged cation vacancies.

To establish whether the motion of charged edge dislocations during massive crack formation and propagation could be the source of an electric earthquake precursor, Vallianatos et al. (2004) used the MCD mechanism to describe the observable macroscopic ULF field generated by a superposition of multiple simultaneous tiny sources (individual cracks). The resulting model gave a good approximation of the asymmetric bell-shaped anomalies in the ULF time series preceding two Greek earthquakes. Other models have combined dipole polarisation and the motion of charged dislocations under the influence of evolving stresses along a fault plane (Teisseyre, 1992; 1996; 1997; 2001; Teisseyre and Nagahama, 1998; Nagahama and Teisseyre, 1998) or suggested that large-scale motion of lattice defects could be the result of a phase transition (e.g., from hydrous to anhydrous form of a mineral) under compression (Lazarus, 1996).

#### 3.5.1.3 Positive hole charge carriers and p-type semi-conduction

This mechanism involves the activation of positive-hole type dormant charge carriers in stressed igneous and high-grade metamorphic rocks (Freund et al., 1994; Freund and Borucki, 1999; Freund, 2000; 2002; Freund et al., 2004; 2006; Freund, 2010; 2011a). Experimentally, positive charge flow has been shown to be activated by the application of inhomogeneous stresses and the passage of acoustic waves (Section 3.3.2). The mechanism is based on the fact that oxygen anions can exist in two oxidation states: 2- and 1-. According to the model, positive holes are electronic holes in the oxygen $O^{2-}$ sub-lattice where an $O^{-}$ occupies a site crystallographically assigned to $O^{2-}$, thereby carrying an excess positive charge. Under normal conditions, these positive holes exist in a dormant form; as positive hole pairs (PHP), which are chemically equivalent to peroxy bonds, $O^{-}$ – $O^{-}$, but with about half the inter-atomic distance (Freund, 2002; 2003a). In silicate minerals they are believed to link $SiO_4$ tetrahedra: $O_3Si/^{OO}\backslash SiO_3$, residing in the 2p-dominated valence bands, which are in electronic contact. When they migrate, they travel

at the upper edge of the valence band, meaning that (a) they are not stopped by grain boundaries and (b) they should be able to jump them with relatively little scattering or attenuation (Freund, 2002; 2003a). Thus, they should be able to travel across macroscopic distances.

It is generally agreed that PHP are introduced into oxides and silicates via dissolution of small quantities of water during crystallisation or recrystallisation in $H_2O$-laden environments (Freund et al., 2004). The dissolved $H_2O$ converts to hydroxyls, $O_3Si$-OH, by means of the following reaction: $O_3Si/^{O}\backslash SiO_3 + H_2O \Rightarrow O_3Si/^{OH}_{HO}\backslash SiO_3$. A peroxy bond is formed when the two hydroxyl $O^{2-}$ anions each transfer an electron to their respective protons, $H^+$, thereby changing from the -2 to the -1 oxidation state and forming an $H_2$ molecule: $O_3Si/^{OH}_{HO}\backslash SiO_3 \Rightarrow O_3Si/^{OO}\backslash SiO_3$. It can be assumed that PHP are present in most crustal rocks due to the presence of molecular $H_2$ (Freund et al., 2002). However, it is uncertain whether they can also be activated in carbonate minerals, since free $CO_4$ is unstable and the tetrahedral form is not its lowest energy structure (Cabria et al., 2012). Although, given that two phases (one crystalline and one amorphous) of $CO_4$ can be obtained under very high pressures (Cabria et al., 2012), it may be possible for a small quantity of hydroxyls to become structurally incorporated during recrystallisation in a very high pressure environment, such as found in active tectonic regions. This is consistent with observations that currents detected in limestone and marble were one to two orders of magnitude smaller than those detected in granite (Takeuchi et al., 2006).

Most crustal rocks are good insulators. Any increase in their electrical conductivity, locally or with depth along the geotherm, is usually attributed to (a) pore water, (b) intergranular carbon films or (c) incipient partial melting (Section 2.2.4). However, positive hole activation can turn rocks into pure p-type semiconductors, affecting not only the electrical conductivity of rocks but also other geophysical and geochemical properties (Freund, 2001). Peroxy bonds can be broken by propagating cracks and migrating point defects and dislocations, or being transiently strained by passing seismic waves (Freund et al., 2004). Once active, the flow of positive holes propagates transient currents through the rocks, leading to increased electrical conductivity, electromagnetic emission, positive surface potentials, corona discharges, positive ion emission and mid-infrared radiation (Freund, 2003b), such as are reported to precede earthquakes.

#### 3.5.1.4 Surface charging

Several models for the generation of electric signals are based on the emission, diffusion and recombination of surface charges on crack walls or fault surfaces. However, charge production and current generation during crack opening is a short-lived effect, comparable to the duration of crack opening itself (Molchanov and Hayakawa, 1995; 1998b; Vallianatos et al., 2004; Tzanis and Vallianatos, 2002), or whatever other process separates the charges, since the potential difference and, therefore, the current appears only while the charges are

separating. Therefore, if any long-lasting signal of this type is to be observed, it will have to be generated by the superposition of signals from all the simultaneously propagating cracks and will evolve in time just like crack propagation (Vallianatos et al., 2004). Since shear deformation increases the number of dislocations and point defects in the material undergoing deformation, all of the mechanisms described below also involve the migration of dislocations or point defects under stress, and the presence of locally formed electric dipoles.

Common to these surface charging mechanisms is the formation of an electric double layer (Section 3.5.2.1), which can be modelled as a system of capacitors or electric dipoles (Khatiashvili and Perel'man, 1989). Although a key part of the electrokinetic theory (Section 3.5.2), electric double layers (EDLs) are not only produced by fluid flow; they also occur when rough surface layers interact (Takeuchi and Nagahama, 2004). Thus, EDLs are widespread in rocks and make an essential contribution to electric signals generated during deformation. In fact, Khatiashvili and Perel'man (1989) found that the formation and oscillation of EDLs induced by tectonic processes was likely to be the main contribution to EM radiation, with variations in external pressure or changes of water content, for example, leading directly to EM emissions. Their early theoretical work on the mechanisms for EM radiation in non-piezoelectric media showed that EM radiation can be generated during the formation of charged dislocations, fracturing of ionic crystals, emergence of small charged or magnetised particles in dielectric media, formation of EDLs on media interfaces and by high-frequency oscillations of any of these formations.

**Contact (including frictional) or separation electrification** occurs when two types of rocks (or mineral grains) with different work functions come into contact (Ogawa et al., 1985; Enomoto and Hashimoto, 1990). Electrons move across the potential barrier at the contact surface between two types of rocks (or mineral grains) from the rock of lower work function to the rock of higher work function. This generates a contact potential ($V_c$) of $\sim$1 V between the surfaces, leading to the formation of an electric double layer (EDL) across the contact plane. The charge densities on both surfaces, $\varsigma_1$ and $\varsigma_2$ respectively, are given by $\varsigma_1 = -\varsigma_2 = C_i V_c$, where $C_i$ is the electrostatic capacitance per unit area of the contact plane. Conversely, the process of charge movement reverses when a heterogeneous rock sample breaks or cracks. Electrons move back from the rock or mineral grain of lower potential to that of higher potential via a tunnel effect until the separation distance $d$ becomes $d_l \cong 10$ Å (Harper, 1951). As $d$ increases, $C_i$ decreases and $V_c$ increases until $d = d_l$ and the charge movement stops. At $d = d_l$, the charge density, $\varsigma = \frac{\epsilon_m}{d_l} V_c$, where $\epsilon_m$ is permittivity of the medium. Ogawa et al. (1985) estimated this charge density due to separation charging to be $\sim 10^{-2}$ Cm$^{-2}$.

**Microfracturing electrification** models (O'Keefe and Thiel, 1995; Molchanov and Hayakawa, 1995; 1998a) consider the discharge characteristics of 'capacitors', the plates

of which are the two separating surfaces of a crack. Charge separation occurs due to the breaking of ionic bonds, after which further separation of the crack surfaces decreases the capacitance. Conservation of charge means that the potential difference across the crack increases. Charge relaxation during the opening of a fracture is the source of each micro-current, which depends on the time taken to open the crack and the conductivity of the rock medium. For dry rock conditions, with resistivity $\rho_d$ of the order $10^6 - 10^4$ $\Omega$m and permittivity $\epsilon_d$, any charge and electromagnetic fluctuations with source dimension $l \approx 10^{-4} - 10^{-1}$ m (typical cracks) will disappear after a time $t_e \approx \epsilon_d \rho_d \approx 10^{-5} - 10^{-7}$ s (if no external sources are applied). This is comparable to the duration of crack opening ($10^{-4} - 10^{-7}$ s). Rapid generation of microcracks in the focal area leads to wide-band EM noise, which dissipates outside the source region, with ULF emissions reaching the ground surface. Molchanov and Hayakawa (1995; 1998a) assume a normal distribution of microcracks, together with intermittent opening and healing and a progression in crack size due to stress corrosion. Other models (e.g., Stoll and Wilkinson, 2010) simulate crack propagation in terms of discrete dislocations moving at the crack tip. In such a case, electrification from moving edge dislocations at the crack tip (the MCD mechanism; see Section 3.5.1.2) would contribute to electrification from the capacitance effect.

**Electron acceleration and bombardment** due to the release of charged particles from fractured surfaces ionises the void space within the crack and any fluid or gas within that space (Brady and Rowell, 1986; Cress et al., 1987; Enomoto and Hashimoto, 1990). The high charge densities produced by charge separation on fractured surfaces, for example during cleavage cracking of a single crystal, generate strong electric fields. These strong fields cause the emission and acceleration of high-energy electrons capable of ionising nearby atoms and molecules by inelastic collisions. An electric double layer (EDL) results from the presence of ionised trapped or flowing gases or fluids within a gas- or fluid-saturated rock mass (Enomoto, 1996; Scudiero et al., 1998; Enomoto, 2012).

**Charges released from charge-trapping centres** on the surface of sheared asperities (Takeuchi and Nagahama, 2004) were inferred from laboratory stick-slip tests (Takeuchi and Nagahama, 2001; 2002a;b). Fracture and frictional sliding generates disordered layers on the interface surfaces, leading to the release of positive and negative charges from charge-trapping centres in these layers. These charges form an electric double layer (EDL) at the interface between disordered surface layers, equivalent to a contact electrification. When this EDL is separated due to further shearing, a positive and a negative surface charge are formed. Based on their findings of a proportional relationship between electric signal intensity and contact area along the stick-slip plane, Takeuchi and Nagahama (2004) argue that this mechanism applies to sheared fault asperities since the shearing generates disordered surface layers and new point defects. In a simple fault model (Figure 3.7), they assume electric dipoles on sheared asperities and incorporate fractal distributions for fault asperity numbers and areas.

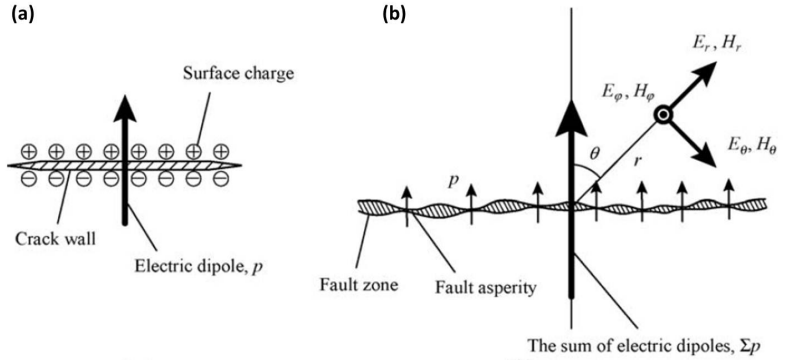


Figure 3.7: Schematic diagram showing electric dipoles ($p$) and electric ($E$) and magnetic ($H$) fields. (a) At a single crack; an electric dipole is formed by surface charges on a pair of separate crack walls leading to strongly directive electric and magnetic fields around the crack. (b) At a stick-slip plane on the laboratory scale or a fault plane on the geophysical scale; a large electric dipole is the vector sum of small ones at each asperity and forms strongly directive electric and magnetic fields around the plane during stick-slip or faulting. After Takeuchi and Nagahama (2006).

**Oscillation of electric dipoles** formed along a fracture plane (Rabinovitch et al., 2007) may be an additional source for EM radiation in fault zones. During the breaking of bonds by the propagating fracture, atoms are moved away from their original steady state positions and oscillate around their new positions on either side of a newly created crack. These atoms are connected to other atoms and movement of all these atoms leads to surface vibrational waves, where positive charges move in opposite phase to negative ones while decaying exponentially into the material (similar to Rayleigh waves). The resulting oscillating electric dipoles form freely propagating EM radiation fields at the oscillation frequency (Takeuchi and Nagahama, 2006).

### 3.5.2 Electrokinetic theory

Electrokinetic effects (Overbeek, 1952; Mizutani et al., 1976; Ishido and Mizutani, 1981; Jouniaux and Pozzi, 1995a;b; 1997; Johnston, 1997) are applicable to electric phenomena observed in saturated rocks. They are the electrical currents (and magnetic fields) generated by fluid flow through the crust due to a charged interface at the solid-liquid boundaries. This interface is known as the electric double layer (EDL) and is related to the electrokinetic properties of the two-phase system (Overbeek, 1952). In a two-phase solid-liquid system, there are four main electrokinetic effects involving charge flow (Shaw et al., 1992): (i) electro-osmosis; the movement of liquid past the solid phase due to an applied electric potential gradient, (ii) streaming potential; the electric potential gradient produced in the presence of a pressure gradient due to tangential movement of the two phases past each other, (iii) electrophoresis; movement of colloidal particles in an applied electric field and (iv) sedimentation potential; electric field generation due to the movement of charged particles. Effects requiring the application of an electric field are not discussed as this study is concerned only with naturally occurring electric signals in geological systems.

#### 3.5.2.1 Electric double layer and zeta potential

When the solid and liquid phases come into contact, charge separation occurs at the interface between them. This causes an electric potential to develop across the interface. As discussed above (Section 3.5.1.4), an EDL may also occur at the interface of two solid phases and between a solid phase and gas phase. Several mechanisms are assumed to cause the charge separation, including ionisation of surface groups, adsorption of species and dipole orientation. Overbeek (1952) describes this interface, the EDL, as an excess charge of one polarity at the solid phase compensated with an oppositely charged distribution of counter ions at the fluid phase. The concentration of ions in the EDL is statistically a Boltzmann distribution, decreasing exponentially into the electrically neutral fluid bulk. Currently accepted physical models for the EDL were introduced in the 1910s and further developed by Stern (1924). As shown in Figure 3.8, the solid-liquid boundary comprises an inner adsorbed layer and a diffuse outer layer (Ishido and Mizutani, 1981; Morgan et al., 1989; Clint, 1999). The rigid inner mono-layer is made up of adsorbed molecular ions in the plane of the solid surface, formed due to electrostatic attraction from ions in the liquid phase. These ions fully populate the solid surface. Further out, the diffuse layer ($S_1$) consists of the counter-ionic charge density in the immediate fluid phase. An electric potential ($\Psi_0$) is set up on the surface which decreases to a lower value, the zeta potential ($\zeta$) at the slipping plane ($S_2$). The thickness of the diffuse layer in a brine solution decreases with increasing concentration (Clint, 1999). In compact, homogeneous rock, such as marble, the calcite grains are separated by intergranular cracks. Since an electrical double layer exists at the interface between the marble grains and the saturating pore fluid, an interaction between the EDL's of opposite grains can be expected. $\Psi_0$ at each grain surface decreases as a function of the distance between grains to a minimum potential ($\zeta$) halfway between them. Since the ion concentration decreases exponentially into the fluid bulk, so does the electric potential.

#### 3.5.2.2 Streaming current and streaming potential

When a fluid pressure gradient is introduced into a saturated rock sample, the outer diffuse layer moves in the fluid flow direction. This generates a convective electric current which accumulates charge at one end of the sample and produces an electric field, causing the production of a secondary, conductive electric current opposing the primary flow. In a steady state situation with the streaming current taking all paths through the rock, the two currents will be equal and opposite. Streaming potential is the potential difference that develops between the two ends of the sample.

In a porous medium, electric current density, $\mathbf{i}$, and the fluid volume flux, $\mathbf{j}$, are both related to the pore pressure, $P_p$, and electric potential, $V$, (de Groot et al., 1962; Pride, 1994) as follows:

$$\mathbf{i} = -\frac{\kappa_f}{F_1}\,\nabla V + \frac{\epsilon_f \zeta}{\eta F_2}\,\nabla P_p \tag{3.10}$$

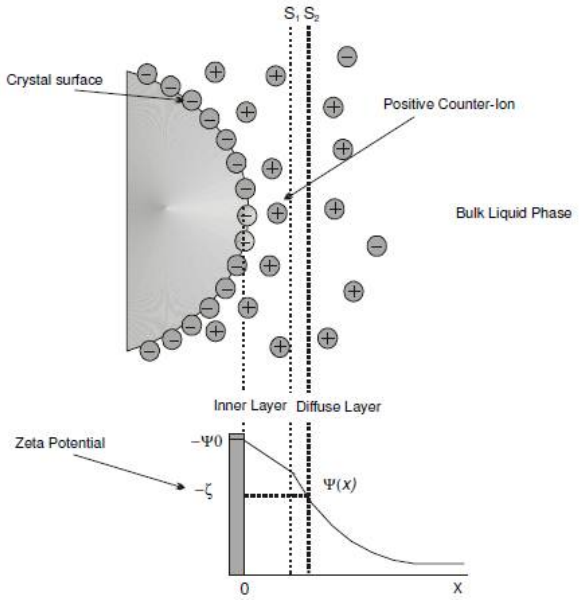


Figure 3.8: Formation of the electric double layer (EDL) and the variation of zeta potential with distance from the crystal structure. After Clint (1999).

$$\mathbf{j} = \frac{\epsilon_f \zeta}{\eta F_2} \nabla V - \frac{k}{\eta} \nabla P_p \tag{3.11}$$

where $\kappa_f$ and $\epsilon_f$ are the electrical conductivity and the relative permittivity of the fluid, $\zeta$ is the zeta potential, $\eta$ is the fluid viscosity and $k$ is the permeability. $F_1$ is the formation factor, defined as the ratio of $\kappa_f$ to the bulk conductivity of the fluid-filled rock ($\kappa_b$), and $F_2$ is the formation factor when surface conduction is absent. These equations indicate that the electric currents and streaming potentials are sensitive to heterogeneity in porous media (Sill, 1983).

According to the capillary model of Ishido and Mizutani (1981), $F_1$ and $F_2$ are functions of the porosity $\varphi$, tortuosity $T$ ($T = l'/l$ where $l'$ is the real length of the fluid flow path and $l$ is the apparent path length), hydraulic radius $r$ and surface conductivity $\kappa_s$ of the flow path:

$$\frac{1}{F_1} = \frac{\varphi}{T^2}(1 + \frac{2\kappa_s}{r\kappa_f}) \tag{3.12}$$

$$F_2 = \frac{T^2}{\varphi} \tag{3.13}$$

and the permeability, $k$, is represented as:

$$k = \frac{\varphi}{T^2} \frac{r^2}{b} \tag{3.14}$$

where $b$ is a constant (8 for capillaries with circular cross-section or 3 for slot-shaped cross-section).

The streaming current coefficient, $C_c$, is the ratio $-\mathbf{i}/\nabla P_p$ in the presence of a constant electric potential (i.e., $\nabla V = 0$) (Sill, 1983; Yoshida, 2001), and is also a function of the

connectivity of the fluid path network:

$$C_c = \frac{\epsilon_f \zeta}{\eta F_2} = \frac{\varphi}{T^2}\frac{\epsilon_f \zeta}{\eta} \tag{3.15}$$

Both $k$ and $C_c$ have the same dependency on $\varphi$ and $T$, but their dependence on $r$ differs. Since $\varphi = rS$, where $S$ is the specific internal area of the sample ($m^{-1}$), $k$ depends on $r^3$ while $C_c$ depends only on $r$. This factor of $r^2$ difference is due to the fact that the volume flow rate of a viscous fluid through a tube is proportional to the square of the cross-sectional area, whereas the amount of transported electric charge is proportional only to the cross-sectional area (Yoshida, 2001). This is because the number of charged particles distributed along the boundary are proportional to the capillary circumferential length and consequently the hydraulic radius, and the flow velocity around the boundary is also proportional to the hydraulic radius. Experimental observations have shown that, because both are functions of the connectivity of the flow path network, the streaming current coefficient seems to be proportional to square root of the permeability and that both parameters decrease with increasing effective confining pressure (Yoshida, 2001).

With no leaking current and no external current sources, the induced convection current due to $\nabla P_p$ would be balanced by the compensating conduction current (obeying Ohm's law) due to $\nabla V$, and:

$$\Delta V = \frac{F_1}{F_2}\frac{\epsilon_f \zeta}{\eta \kappa_f}\Delta P_p \tag{3.16}$$

This equation is known as the Helmoltz-Smoluchowski equation, which predicts that the streaming potential under an applied pressure gradient is dependent on the zeta potential of the rock-fluid system. It is applicable only to a situation where the flow is laminar and the pore fluid volume conductance is large in caparison to the surface conductance (Clint, 1999). The streaming potential coefficient, $C_p$, is the ratio $\Delta V/\Delta P_p$:

$$C_p = \frac{\Delta V}{\Delta P_p} = \frac{F_1}{F_2}\frac{\epsilon_f \zeta}{\eta \kappa_f} = \frac{C_c F_1}{\kappa_f} = \frac{C_c}{\kappa_b} \tag{3.17}$$

## 3.6 Conclusion

Detectable electric signals sometimes precede and accompany earthquakes in the field and experimental studies have established the existence of generation mechanisms related to seismic processes. It is clear from these studies that some electric phenomena in the crust (a) can be directly attributed to the process of deformation itself (e.g., those generated during deformation of dry, non-piezoelectric rocks), (b) exhibit statistical features similar to those seen in seismicity and (c) reveal complex dynamics and criticality, which can be investigated using the concepts of non-extensive statistical physics. These phenomena require currents to be generated in, and flow in, the crust.

Since non-piezoelectric, carbonate rocks are commonly found in tectonically active ar-

eas, it is important to study electric current signals generated in non-piezoelectric rocks under crustal conditions. Studies investigating electric current generation in dry, non-piezoelectric rocks have so far been restricted to atmospheric conditions. Crustal conditions can be simulated in the laboratory using a high-pressure triaxial apparatus. It is thus the aim of this thesis to extend the study of electric current in non-piezoelectric, carbonate rocks to seismogenic crustal conditions, with the use of such an ensemble.

In addition, given that a range of solid-state processes may be responsible for such signals; processes which depend considerably on the preferred mode of deformation, it is also important to establish how different deformation mechanisms in the brittle upper crust and across the brittle-ductile transition may affect the generation of these currents. Both brittle and plastic deformation (i.e., microfracture, cataclastic flow, twinning and dislocation glide) of rocks under stress are complex processes that exhibit critical, 'avalanche-like' dynamics (Sammonds, 2005) in response to the localised concentration of stress intensity. Electric current signals generated by these processes should exhibit similar dynamics, the study of which may be appropriately addressed with a non-extensive approach.

# Chapter 4

# Principles of Experimental Rock Physics

## 4.1 Introduction

Variations in the crustal stress field are both the driver and consequence of geological processes such as plate tectonics, regional deformation and the mechanics of earthquakes and faulting. As the continuum equivalent of force, stress variations are involved in any mechanical process in the solid or fluid Earth (Ruff, 2002) and it is these variations that are responsible for deformation and the style of faulting in tectonic regions. Deformation occurs if the tectonic stresses exceed the existing lithostatic stress in a unit volume of rock. Accordingly, the direction and magnitude of these stresses in rock bodies are central to our understanding of crustal processes. *In-situ* stresses can be determined both directly and indirectly (Section 2.2). However, direct methods often involve drilling and pumping fluids into the crust, which is both very expensive and actually alters the stress-strain history of the rock.

An appropriate alternative to field measurements is to use experimental rock physics techniques to measure stress, strain and monitor the physical properties of a rock during deformation. Details about microscopic processes are revealed from the evolution of these properties, which include acoustic emissions, elastic wave velocities, electrical properties, permeability and pore fluid volume and chemistry. Laboratory rock deformation experiments attempt to reproduce the crustal stress field by simulating *in-situ* conditions in a repeatable and controlled environment. Such experiments are not capable of accommodating the geological length scale or duplicating the geological time scale and are therefore not scaled simulations of lithospheric processes (Zhu, 2007). They do, however, provide us with the means to:

- Control environmental and boundary conditions

- Measure the physical properties of rocks and seek constitutive relations between them
- Understand deformation mechanisms and isolate individual deformation processes that operate simultaneously in the field

As a result, experimental studies of rock mechanics have greatly enhanced our understanding of earthquakes and related crustal processes (Lockner and Beeler, 2002). It is from such experiments that some of the fundamental fracture mechanisms are being clarified. For example, the acoustic emission (laboratory analogue to earthquakes) results of Lockner et al. (1991; 1992) clearly show pre-nucleation activity, fault nucleation and fault propagation. Additionally, while these small-scale experiments are not exact simulations of tectonic rupture, they can reproduce various features of the earthquake cycle (Mogi, 1985) and are therefore indispensable in the study of earthquakes and fracture phenomena. The microfracturing that occurs during deformation can reproduce many statistical features of seismicity, including the Gutenberg-Richter frequency-magnitude distribution (Scholz, 1968b), aftershock decay sequences (Scholz, 1968c), recurrence intervals (Davidsen et al., 2007) and Tsallis parameters (Vallianatos et al., 2012a).

Fractures are ubiquitous in the upper lithosphere, from major fault zones to continental shields and present at all scales from microcracks to macroscopic fractures within rocks (Main et al., 1990; Schubnel et al., 2006a). Indeed, earthquakes themselves are 'simply' brittle fractures propagating dynamically through the crust along lines of weakness. The evolution of crack distributions and crack networks within a rock mass submitted to crustal conditions may play a major role in the earthquake preparation process (Gueguen and Schubnel, 2003). Understanding the evolution of the cracking process and how it relates to the distribution of stress, to fluid flow, to chemical reactions and to telluric (crustal) currents is a major goal in the field of earthquake geophysics. Laboratory experiments are essential to progress this understanding. However, the effects of scale must always be borne in mind when extrapolating laboratory results to field observations as the jointed structure of a large rock mass at a coarser scale than most laboratory specimens has an important influence on its mechanical behaviour. Often the properties of the joints govern its strength almost entirely and the blocks between the joints behave as rigid elements (Paterson and Wong, 2005). This leads to a distinction between the behaviour of the 'rock material' and the behaviour of the 'rock mass' (Jaeger and Cook, 1979). Laboratory experiments usually provide information about the rock material properties with additional steps required to determine the rock mass properties, although the effects of scale are less significant when the processes involved are pervasive down to the microscale, such as with microcracking or crystal plasticity.

This chapter describes the observations and theory necessary to understand the processes taking place during rock deformation experiments and how stress and strain describe the deformation of a material.

## 4.2 Stress

A body being acted upon by an external force is said to be in a state of stress (Nye, 1985). As discussed in Section 4.1, variations in stress are responsible for deformation in the Earth's tectonic regions, as well as in laboratory deformation experiments. Stresses can be categorised into two different types of forces acting upon a continuous medium: (i) body forces due to gravitational acceleration and (ii) surface forces acting over a particular surface area. Since stress is a generalisation of the concept of pressure (Gilman, 2003), it is defined as the ratio of the applied surface force, $F$, to the surface area over which it acts, $A$. The stress vector at any point on the surface is the limiting value of this ratio, $\frac{\partial F}{\partial A}$, as $\partial A$ tends to zero.

In a sample subject to pressure but in static equilibrium, a unit cube of material will have forces acting on each face. These forces can be resolved into three mutually orthogonal stress dipoles, one normal to the surface and two parallel to it. The stress tensor, $\sigma_{ij}$ $(i, j = 1, 2, 3)$, is a second-order tensor which accounts for the orientation and strength of these stresses and can vary with time for a given material element or location (Fung, 1965; Aki and Richards, 1980; Ruff, 2002). In 3-D space, nine stress components in the three principal directions, $x_1$, $x_2$ and $x_3$, (Figure 4.1 (a)) are required to completely describe the stress at any point:

$$\sigma_{ij} = \begin{pmatrix} \sigma_{11} & \sigma_{12} & \sigma_{13} \\ \sigma_{21} & \sigma_{22} & \sigma_{23} \\ \sigma_{31} & \sigma_{32} & \sigma_{33} \end{pmatrix} \tag{4.1}$$

where each component represents the stress acting on the face normal to $x_i$ in the direction of $x_j$, i.e., $\sigma_{12}$ is the force acting perpendicular to $x_1$ in the direction of $x_2$. If all possible stresses are plotted an ellipsoid is obtained (Figure 4.1 (b)), known as Lam*é*'s stress ellipsoid (Jaeger et al., 2007). Within the tensor, *normal* stresses are the $\sigma_{ii}$ components, while *shear* stresses are the $\sigma_{ij}$ $(i \neq j)$ components (Figure 4.1 (a)). Static equilibrium requires that $\sigma_{ij} = \sigma_{ji}$, so the stress tensor is symmetric about the diagonal. If this is not the case, the body is subject to a torque and therefore no longer in static equilibrium.

The three stress dipoles acting on each face are commonly referred to as the principal stresses (Ruff, 2002) and it is useful to separate the stress state induced by them into an isotropic part and a deviatoric part (see Ranalli, 1995). Normal stresses correspond to the isotropic part and shear stresses correspond to the deviatoric part. The overall hydrostatic (isotropic) pressure, $P$, is defined as the mean value of the three on-diagonal terms of the stress tensor (the normal stresses) (Poirier, 1985; Jaeger et al., 2007):

$$P = \frac{1}{3}\sum_{i=1}^{3}\sigma_{ii} = \frac{1}{3}(\sigma_{11} + \sigma_{22} + \sigma_{33}) = \frac{1}{3}\sigma_{ii} \tag{4.2}$$

and the sum of these on-diagonal terms is independent of the co-ordinate system. The term on the far right-hand side is the customary Einstein tensor notation, which omits

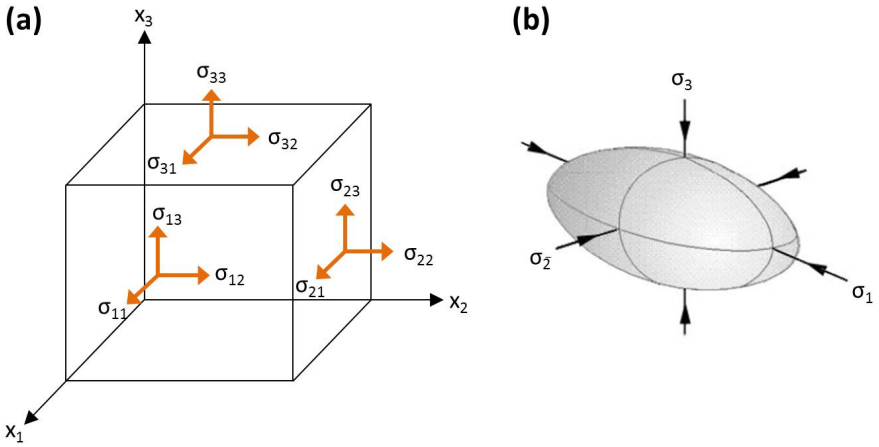


Figure 4.1: Schematic diagrams showing (a) components of the stress tensor, $\sigma_{ij}$, and (b) Lamé's stress ellipsoid produced by plotting all possible stresses through a point. Each orange vector in (a) represents one component of the stress tensor, e.g., $\sigma_{12}$ is the force acting on the face perpendicular to $x_1$ in the direction of $x_2$, while in (b) $\sigma_{ii}$ is represented as $\sigma_i$. N.B. Compressive stress is positive.

the summation symbol and assumes implicitly the summation over repeated subscripts.

The deviatoric stress is the part of the stress state that differs from the isotropic state. The deviatoric stress in a particular direction is the deviation in that direction from the mean stress on the sample. The full stress tensor can therefore be split into its hydrostatic and deviatoric parts as follows (Poirier, 1985; Jaeger et al., 2007):

$$\begin{pmatrix} \sigma_{11} & \sigma_{12} & \sigma_{13} \\ \sigma_{21} & \sigma_{22} & \sigma_{23} \\ \sigma_{31} & \sigma_{32} & \sigma_{33} \end{pmatrix} = \begin{pmatrix} P & 0 & 0 \\ 0 & P & 0 \\ 0 & 0 & P \end{pmatrix} + \begin{pmatrix} \sigma_{11} - P & \sigma_{12} & \sigma_{13} \\ \sigma_{21} & \sigma_{22} - P & \sigma_{23} \\ \sigma_{31} & \sigma_{32} & \sigma_{33} - P \end{pmatrix} \tag{4.3}$$

The off-diagonal components of the deviatoric stress are equal to the corresponding (shear) components of the total stress. The deviatoric stress is zero only when the stress state is completely isotropic (i.e., when the normal stresses are equal from all directions). Under a non-isotropic stress state, some (or all) of the deviatoric components depart from zero. The deviatoric stress drives yield and flow and is particularly important in permanent deformation (Frost and Ashby, 1982).

Since the axes, $x_1$, $x_2$ and $x_3$ are arbitrary, it is convenient for problems of tectonics to define a principal coordinate system that reflects the conditions of the stress field. By convention, the greatest stress is defined with direction parallel to $x_1$ and, therefore, with magnitude $\sigma_{11}$, while the least stress is defined with direction parallel to $x_3$ and, therefore, with magnitude $\sigma_{33}$. Under these conditions, the shear (off-diagonal) stresses vanish (Nye, 1985) and only the three principal stresses acting *along* the principal axes are required to fully describe the stress field. The principal stresses are usually denoted $\sigma_1$, $\sigma_2$ and $\sigma_3$ ($\sigma_1 \geq \sigma_2 \geq \sigma_3$). The stress state can therefore be specified either by the full matrix of

stress components (Equation 4.1) or by the principal stresses:

$$\begin{pmatrix} \sigma_1 & 0 & 0 \\ 0 & \sigma_2 & 0 \\ 0 & 0 & \sigma_3 \end{pmatrix} \tag{4.4}$$

and their respective orientations; $x_1$, $x_2$ and $x_3$. This concept is important because the Earth's surface, being in contact with a fluid (either air or water), cannot support shear traction. It is therefore a principal stress plane, with one principal stress normal to the Earth's surface and the other two acting in an approximately horizontal plane. Evidence from stress indicators at depth, such as earthquake focal mechanisms, suggests that this stress coordinate system is valid not just at the Earth's surface but also to the depth of the brittle-ductile transition in the upper crust (e.g., Zoback and Zoback, 1989; Zoback, 1992; Brudy et al., 1997; Zoback and Zoback, 2002).

It should be noted here that *compressive* stress is defined as *positive* throughout this thesis, in line with convention in the Earth Sciences and because *in-situ* stresses at depth in the Earth's crust are always compressive (Zoback and Zoback, 2002).

The above definition of principal axes is also important experimentally because, when the shear stresses are zero, the only non-isotropic stress in the system is the differential stress, $\sigma$:

$$\sigma = \sigma_{max} - \sigma_{min} = \sigma_1 - \sigma_3 \tag{4.5}$$

In the laboratory, a simulated crustal stress state is achieved through simple axial compression superimposed on a hydrostatic pressure. The stress state within the specimen therefore consists of two equal principal stresses normal to the compression axis ($\sigma_2 = \sigma_3$) with the third, larger stress ($\sigma_1$) parallel to it, as shown in Figure 4.2. This is known as conventional triaxial compression. For the specific case of uniaxial compression, $\sigma_2 = \sigma_3 = 0$. The compressive stress, $\sigma_1$, causes failure on a plane lying at angle $\theta$ to $\sigma_1$ and the normal ($\sigma_n$) and shear ($\tau$) stresses acting *on the failure surface* are given by:

$$\sigma_n = \frac{(\sigma_1 + \sigma_3)}{2} + \frac{(\sigma_1 - \sigma_3)}{2}\cos(2\theta) \tag{4.6}$$

and

$$\tau = \frac{(\sigma_1 - \sigma_3)}{2}\sin(2\theta) \tag{4.7}$$

where $\frac{(\sigma_1 + \sigma_3)}{2}$ is the mean stress within the sample, $\frac{(\sigma_1 - \sigma_3)}{2}$ is the deviatoric stress (i.e., the non-hydrostatic component), $(\sigma_1 - \sigma_3)$ is the differential stress and $\theta$ is the angle between the normal to the inclined plane and the direction of principal axial stress ($\sigma_1$).

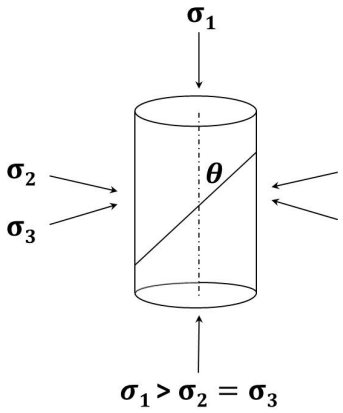


Figure 4.2: System of stresses in a conventional triaxial compression experiment

## 4.3 Strain

Strain of a body is simply any change in size or shape that it has undergone due to the action of an external force (Twiss and Moores, 1992). Forces applied to a body can translate its position, rotate it and induce stresses within it that result in strain (Gilman, 2003). Any solid body subject to a stress can experience strain. The displacement tensor describes a body's deformation by connecting the position ($x_j$) of a body segment with its displacement ($u_i$) (Gilman, 2003; Jaeger et al., 2007) where each component is:

$$D_{ij} = \frac{\partial u_i}{\partial x_j} \tag{4.8}$$

This displacement tensor can be split into two components; a rotation tensor ($\omega_{ij}$) and a strain tensor ($\varepsilon_{ij}$). The rotation tensor is the anti-symmetric part of the displacement tensor ($\omega_{ij} = \frac{1}{2}(D_{ij} - D_{ji})$) while the strain tensor is the symmetric part:

$$\varepsilon_{ij} = \frac{1}{2}(D_{ij} + D_{ji}) = \frac{1}{2}\left(\frac{\partial u_i}{\partial x_j} + \frac{\partial u_j}{\partial x_i}\right) \tag{4.9}$$

As with the stress tensor, this symmetry implies that the body experiencing the strain is in static equilibrium and all possible strains in three dimensions can be represented by an ellipsoid.

Strain is caused by the relative displacement of individual points within a solid body, leading to changes in length, volume and angle between body segments. Similar to stress, there are two main types of strain; normal strain and shear strain. Normal strain relates to the material stretching or compressing and can be linear or volumetric, while shear strain relates to the angular distortion of the material; i.e., when the body changes shape without changing volume (Jaeger et al., 2007). The three dimensional strain tensor describes the entire volume and shape change possible in the body and can be split into a matrix representing the shape change at constant volume (shear strains) and a diagonal matrix

representing the volume change (normal strains).

Shear strain, $\varepsilon_{shear}$ is calculated using the change in angle, $\psi$, of the body segment shape caused by the strain:

$$\varepsilon_{shear} = 0.5 \tan(\psi) \tag{4.10}$$

Linear strain is a contraction of the deformation tensor into one dimension and defined as the ratio of the change in length of a body segment, $\delta l$ to its original length $l_0$. If $l$ is the final length, the strain, $\varepsilon$, experienced by that segment during the period of observation is as follows:

$$\varepsilon = \frac{\delta l}{l_0} = \frac{l_0 - l}{l_0} \approx D_{11} = \frac{\partial u_1}{\partial x_1} \tag{4.11}$$

This is the most commonly used definition of strain. In this thesis, *positive* strain is defined as *shortening* along the relevant dimension.

Volumetric strain, $\varepsilon_v$, is defined as the ratio of the change in volume of a body segment, $\Delta V$ to its original volume $V_0$ and is calculated in the same way as linear strain. It is approximately equal to the sum of the on-diagonal terms of the strain tensor:

$$\varepsilon_v = \frac{\Delta V}{V_0} \approx \sum_k \varepsilon_{kk} = \frac{\partial u_1}{\partial x_1} + \frac{\partial u_2}{\partial x_2} + \frac{\partial u_3}{\partial x_3} \tag{4.12}$$

where the mean normal strain, $\varepsilon_m$, is one-third of the volumetric strain ($\varepsilon_m = \frac{1}{3}(\varepsilon_v)$). The volumetric strain is therefore analogous to the definition of hydrostatic pressure from the stress tensor (Equation 4.3) and independent of the principal axes. The principal strain axes ($x_1$, $y_1$ and $z_1$) are those oriented such that the shear strains are zero, along which the principal strains ($\varepsilon_1$, $\varepsilon_2$ and $\varepsilon_3$) obey the condition $\varepsilon_1 \geq \varepsilon_2 \geq \varepsilon_3$. However, the question of whether the principal stress axes coincide with the principal strain axes depends on the stress-strain relationship of the rock (Jaeger et al., 2007).

## 4.4 Relationship between Stress and Strain

The relationship between stress and strain is the basis of theoretical rock mechanics and is essential for interpreting rock physical properties from rock physics measurements. Under an applied stress, the strain within a deforming specimen can be either *elastic*, which is recoverable, or *permanent*, which is not. Figure 4.3 shows schematically the typical stress-strain response seen during a compressional rock deformation experiment. The stress-strain cycle is important because the total work done by the external loading agency on the sample during deformation, per unit volume of rock, is equal to the area under the stress strain curve (Jaeger et al., 2007).

Until a specimen is subject to stress, it cannot have any elastic strain. Once a stress is applied, the strain is initially elastic and can be described by Hooke's law, which states

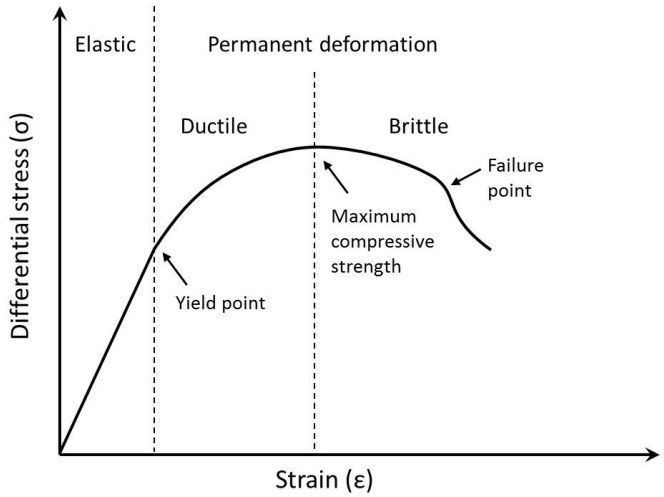


Figure 4.3: Relationship between stress and strain during compression of a solid.

that the differential stress (Equation 4.5) is directly proportional to strain:

$$\sigma = E\varepsilon \tag{4.13}$$

where $E$ is the Young's Modulus (after Young, 1807). Since triaxial deformation is simply confined uniaxial compression, $E$ can, for the purposes of this study, be defined as the ratio of the axial stress to the axial strain (Mavko et al., 2009):

$$E = \frac{\sigma_1}{\varepsilon_1} \tag{4.14}$$

Beyond the limit of proportionality, this ratio is referred to as the *effective* Young's Modulus, $E_{eff}$ (Turcotte et al., 2003) throughout this thesis. The limit of this proportional relationship is the elastic limit or yield point of the material. Before this point, the sample will return to its original size and shape if the stress is removed.

Above the elastic limit, deformation occurs by means of permanent changes to the rock structure and the stress-strain relationship is no longer linear; the ability of the rock to support a load decreases and so less stress is required to achieve a particular increase in strain. This permanent deformation is characterised by a decreasing $E_{eff}$ and by an overall increase in the volume of the rock, a phenomenon known as *dilatancy*. It continues until the stress is removed or the sample breaks. If the applied load is removed after the yield point, the strain will reduce elastically until the differential stress reaches zero. The sample will not return to its original shape and size due to the damage it has sustained and the residual strain at zero stress is referred to as *permanent* or *inelastic* strain (Ohnaka, 2013). In experiments of rock deformation, two types of permanent deformation can be distinguished; *ductile* and *brittle*, with ductile deformation occurring first. The transition from elastic to ductile occurs at the yield point and the differential stress at this point is known as the *yield stress*. During ductile deformation, the gradient of the stress-strain curve ($E_{eff}$) remains positive and the rock continues to support an increasing load. Ductile

deformation is the capacity for substantial change in shape without macroscopic failure (Paterson and Wong, 2005; Jaeger et al., 2007) and increasing permanent strain with a positive $E_{eff}$ is often referred to as *strain hardening*. Brittle deformation is seen once the rock loses its ability to resist the applied load; $E_{eff}$ becomes negative and the rock deteriorates physically until failure occurs. This increase in permanent strain with a negative $E_{eff}$ can also be described as *strain softening*. The transition from ductile to brittle behaviour occurs at the maximum differential stress ($E_{eff} = 0$) and rock failure is regarded as a continuous process occurring throughout the region of brittle deformation (Jaeger et al., 2007). The range of stresses and strains over which a rock exhibits either of these two types of behaviour is governed by the rock's mineralogy and microstructure, together with environmental conditions such as confining pressure, deformation rate and temperature (Jaeger et al., 2007).

## 4.5 Deformation Mechanisms under Triaxial Compression

### 4.5.1 Development and propagation of cracks

Early experimental work established that, beyond the yield point, the decrease in $E_{eff}$ and corresponding dilatancy, which represents an increase in porosity, can be attributed to the formation and extension of open microcracks oriented parallel to the direction of the maximum principal stress (Brace and Orange, 1966; Scholz, 1968d; Stanchits et al., 2006; Jaeger et al., 2007). It has also been shown that dilatancy (i.e., microfracturing) begins at stresses between about 55% and 65% of the compressive strength (Brace and Orange, 1966; Scholz, 1968d; Hallbauer et al., 1973), occurs throughout the entire volume of the rock (Cook, 1970) and becomes increasingly heterogeneous as failure is approached, indicating the development of a shear zone (Spetzler and Martin, 1974; Hadley, 1975). With increasing stress, more microcracks nucleate and they begin to grow, interact and coalesce. The cracking accelerates steadily until a rapid increase occurs just prior to failure, marking the formation of a fault. Macroscopic brittle failure occurs when there are sufficient microfractures to form a discrete fault zone that ruptures the sample. The inelastic stress-strain behaviour of brittle rocks can be completely accounted for by the strains contributed by this cracking activity Scholz (1968d). These microfractures are the sources of the macroscopic cracks that appear when the applied stress exceeds 85% of the maximum stress that the rock can sustain and are the most dominant factor of all heterogeneities that govern the failure nucleation process in rock samples (Lei et al., 2000b).

Under triaxial compression, two principal modes of fracturing can be distinguished (Griggs and Handin, 1960; Paterson and Wong, 2005): (1) *extension* fracturing, where separation occurs normal to the failure surface which, in turn, is generally oriented normal to the minimum principal stress axis and (2) *shear* fracturing where the relative displacement is

parallel to the fracture surface, with the surface itself being <45° to the axis of maximum principal stress. The appearance of extension fractures in the absence of macroscopic tensile stress suggests that extension fractures most likely originate in response to local tensile stresses around flaws or cracks on a microscopic scale (Scholz et al., 1986; Paterson and Wong, 2005).

Fracture occurs when the energy available for crack initiation or growth is equal to or greater than the resistance to crack initiation or growth (Ohnaka, 2013). This energy-based approach for fracture criterion was first proposed by Griffith (1921; 1924) who explained crack initiation in a bi-axial stress field as the result of pre-existing cracks and flaws. Brace (1964) suggests that grain boundaries act as or contain microcracks while joints and faults can be regarded as macrocracks. In tension, failure takes place when the maximum tensile stress in the most favourably orientated crack reaches a critical value. However, a rock under compression is eight times stronger (according to Griffith) than one in tension and failure in compression is not the result of crack growth from a single flaw. The necessary conditions for crack initiation in compression are (1) that the process causes the total energy in the system to decrease or remain constant and (2) that the stress concentration at the crack tip exceeds that required to split atomic bonds (Orowan, 1949). A subsequent modification to include the effects of crack closure in compression improved this description of fracture initiation (McClintock and Walsh, 1962). However, Scholz (1968d) showed that the inhomogeneity inherent in rock will produce fluctuations in the stress field sufficient to arrest cracks shortly after they have been initiated, while Brace and Bombolakis (1963) and Hoek and Bieniawski (1965) showed that cracks in compression do not propagate in an unstable manner indefinitely, but become stable and stop after propagating some fraction of their original length. Thus, the modified Griffith criteria for brittle fracture are initiation criteria only and cannot describe crack growth, interaction and coalescence. These issues are addressed with damage mechanics approaches, which follow the fundamentals of Griffith theory in that they consider isolated cracks in an otherwise homogeneous medium that initiate at the most favourable positions. Cracks then develop at a high angle to the initial crack, creating 'wing cracks' (e.g., Costin, 1985; Horii and Nemat-Nasser, 1985; Ashby and Hallam, 1986; Sammis and Ashby, 1988; Ashby and Sammis, 1990) which grow when a stress intensity factor $K$ at the crack tip becomes greater than the fracture toughness $K_c$ of the surrounding medium. In fact, the fracture mechanics model of Main et al. (1990) showed that, in terms of rock fracture, stress is not usually as significant as stress intensity and the geometric signature of the length distribution of microcracks is well-correlated with the stress intensity. Wing cracks develop at the tips of sliding intergranular cracks and tend to align with the maximum principal stress (Ashby and Hallam, 1986; Schulson et al., 1999). In these micro-dynamical models, crack interaction and faulting is understood to be the effect of widely distributed cracking which amplifies the stress intensity factor ($K$) and allows crack growth under lower differential stresses. These theories can therefore explain the strain softening region beyond peak stress.

Under compressional loading, cracks nucleate and grow from defects within the rock body where stress is most concentrated (Ashby and Sammis, 1990). This can be at the edges of pore spaces, inclusions and existing microcracks. At first, a kind of negative feedback means that successive crack nucleation sites avoid each other as each crack relieves the local stress concentration surrounding it (Main et al., 1993). Thus, crack growth in compression is initially evenly distributed throughout the sample, macroscopically stable and quasi-static. Each increment of crack advance requires an increase in stress, i.e., an additional increment of load, until, at a critical crack density, the cracks begin to interact (Ashby and Sammis, 1990). At this stage, neighbouring cracks can nucleate a larger-scale crack through positive reinforcement of the stress field at the crack tip (Main et al., 1993). This stable crack linkage generates localised avalanches of cracks as the positive and negative reinforcement mechanisms vie for dominance. A multi-crack state is formed by repeated, frustrated microcrack events as the energy balance and local stress field tips from favouring rupture for a small increment and/or local coalescence to favouring arrest when the local stress concentration is relieved. As conditions become more dynamic and critical, the positive feedback between incremental crack growth and further growth takes over, leading to a runaway dynamic instability and, ultimately, sample failure (e.g., Sammonds, 1999; Main et al., 1993; Ashby and Sammis, 1990).

Both the distribution and coalescence of these microcracks exert a controlling influence on the macroscopic deformation style and stress-strain behaviour of a stressed rock (Main et al., 1990), since they correspond to different physical processes occurring within it. These processes vary according to conditions of pressure, temperature and deformation rate.

### 4.5.2 Influence of strain rate and temperature

Rocks become stronger and more brittle with an increase in strain rate (Kato et al., 1992). At high strain rates and low temperatures rocks are brittle-elastic. They deform elastically at stresses up to about half their failure strength, whereupon cracks nucleate and propagate until they interact and weaken the rock, eventually coalescing to form a large fracture or failure surface (Figure 4.4 (a) and (b)), at which point the rock fails. At slow strain rates and high temperatures, rocks are ductile-plastic; the stress-strain curve does not have a distinct maximum to indicate the onset of failure. 'Failed' rock specimens have a characteristic barrel-like shape (Figure 4.4 (e)).

Laboratory studies have shown that rock strength and the amount of permanent strain it can sustain prior to failure both depend on the deformation rate. Room temperature, triaxial experiments on limestone and various igneous rocks found that compressive strength increased by about 10% with each $10^3$ increase in strain rate for strain rates $\leq 10^{-1}\mathrm{s}^{-1}$ (e.g., Brace and Martin, 1968; Masuda et al., 1987; Masuda, 2001); values similar to uniaxial experiments carried out on marble and granite by Mogi (1959; 1962c). The amount of

permanent strain prior to failure increases with decreasing strain rate (e.g., Heard, 1963; Mogi, 2007) as the rock sample has more time to accommodate each incremental increase in stress through some mechanism of unrecoverable deformation, brittle or plastic. Strain rate has a greater influence on ductile deformation at higher temperatures than it does on brittle deformation at low temperatures (see Rutter, 1972b). The influence of strain rate and temperature on the dynamic deformation mechanism can be visualised by means of principal stress failure maps (e.g., Rocchi et al., 2003).

### 4.5.3 Influence of effective confining pressure

Effective confining pressure ($P_{eff}$) exerts significant influence over the deformation of rock (Paterson, 1958; Murrell, 1965; Byerlee, 1967; Rummel and Fairhurst, 1970; Wawersik and Brace, 1971; Ohnaka, 1973; Baud et al., 2000). An elevated $P_{eff}$ suppresses microfracturing by increasing the energy barrier that must be overcome in order for crack surfaces to separate and cracks to propagate (Francois and Wilshaw, 1968). Therefore, increasing $P_{eff}$ usually increases the compressive strength of the material (i.e., it supports a higher differential stress prior to the onset of dynamic failure). It also increases the amount of strain accommodated before failure. As a rock mass begins to fail, the ability of one region of rock to support an additional load decreases. This can be compensated for by some of the load being transferred to adjacent regions of rock (Jaeger et al., 2007), as occurs on large fault segments in the field. Due to the increased strength of the rock, compensation becomes more likely as $P_{eff}$ increases and results in further deformation before failure.

Under very shallow crustal conditions ($\leq$0.5km), $P_{eff}$ supporting the rock is negligible, due either to the surrounding rock providing little or no confining pressure and/or the pore pressure being high. Compression under these conditions tends to cause elastic deformation followed by abrupt failure in the form of longitudinal (axial) splitting (Figure 4.4(a)). Such fracture surfaces are somewhat irregular with a combination of shear and extension fractures. At moderate depths (2-10km), $P_{eff}$ increases due to higher confining pressures and relatively low pore fluid pressures. The surrounding rock therefore supports the deforming part, suppressing axial failure and encouraging the coalescence of fractures along a single shear fault (Figure 4.4 (b)) (brittle-elastic behaviour). Shear fracturing is the dominant brittle failure mode at all but the very lowest confining pressures, with the angle of shear failure rarely departing from 20-30° to the axis of maximum principal stress (Ismail and Murrell, 1976; Lockner, 1993; Reches and Lockner, 1994; Healy et al., 2006). At $P_{eff}$ conditions approaching the brittle-ductile transition, the discrete shear failure plane becomes a broader zone of intense deformation and fine-scale fracturing (Jaeger et al., 2007). In this case, separation may not occur readily at the failure zone after the test. These macroscopic bands of intense deformation broaden with increasing $P_{eff}$ and may sometimes occur along a pair of conjugate shear planes (Figure 4.4 (c)). As $P_{eff}$ increases further, above the brittle-ductile transition into the semi-brittle regime, deformation is accommodated by cataclastic flow, manifest in networks of small, conjugate, mainly inter-

granular shear fractures distributed throughout the sample and visible on the specimen surface at large strains (Figure 4.4 (d)) (Jaeger et al., 2007). In fact, observations of fault gouge particle size distributions (Sammis et al., 1986) may be explained by microcrack suppression under confinement and the accommodation of strain in macroscopic shear zones by scale-independent cataclasis. Eventually, at the elevated $P_{eff}$ associated with great depth, deformation is accommodated by plastic deformation of individual mineral grains (ductile-plastic behaviour). A rock specimen deformed under such conditions would end up barrel-shaped with no evidence of fracturing (Figure 4.4 (e)).

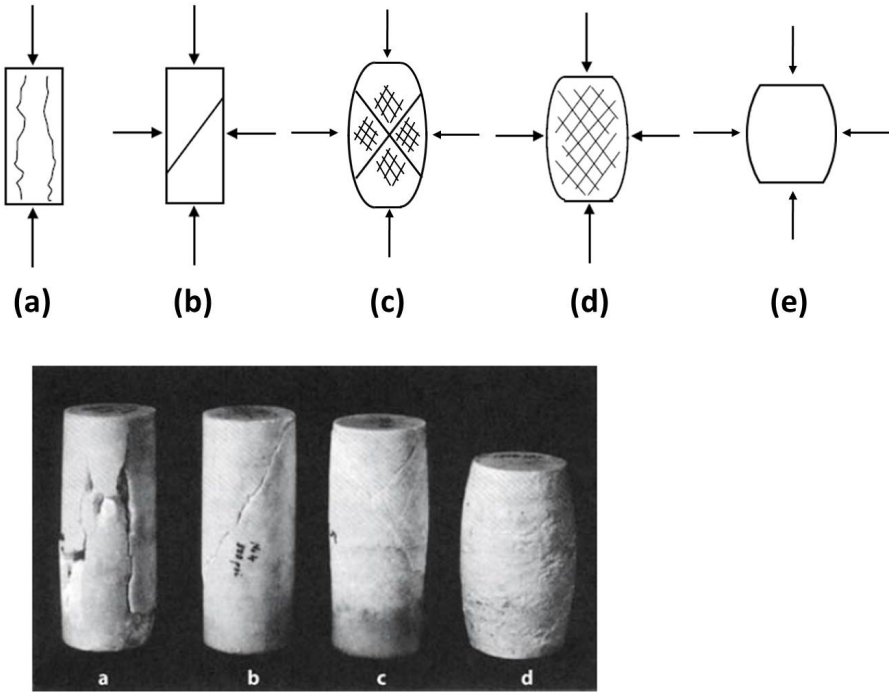


Figure 4.4: Deformation styles observed during triaxial compression: (a) axial splitting (at very low confining pressures), (b) single shear fracture, (c) conjugate shears, (d) ductile behaviour (multiple shears; cataclastic flow) and (e) ductile-plastic behaviour. Schematic modified from Jaeger et al. (2007). Photograph shows equivalent styles in Wombeyan marble at (a) atmospheric pressure, (b) 3.5 MPa, (c) 35 MPa and (d) 100 MPa (Paterson and Wong, 2005; Paterson, 1958).

The influence of confining pressure on deformation is clearly demonstrated in the stress-strain curves of marble (von Karman, 1911; Paterson, 1958). It is clear from these curves (Figure 4.5) that increasing $P_{eff}$ results in an increased yield stress, overall strength, strain at which peak stress occurs and degree and extent of strain hardening. The degree and extent of strain softening decreases. Furthermore, Paterson (1958) found that the angle of the shear failure zone increased from about 25° to 33° as $P_{eff}$ increased from zero to 30 MPa and the mode of failure changed at different values of $P_{eff}$. The transition from ductile to brittle behaviour (i.e., peak stress) occurs at strains up to 5% for $P_{eff}$ <50 MPa, with brittle behaviour clearly seen at $P_{eff}$ <20 MPa.

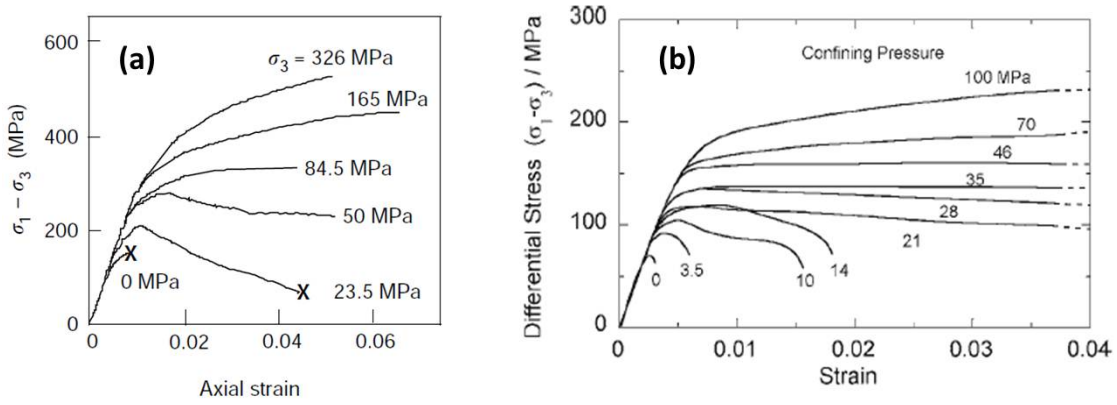


Figure 4.5: Stress-strain curves for (a) Carrara marble (von Karman, 1911) and (b) Wombeyan marble (Paterson, 1958) at various confining pressures. Reproduced from Paterson and Wong (2005); Jaeger et al. (2007).

### 4.5.4 The brittle-ductile transition

Mechanisms of brittle deformation involve the nucleation, propagation and coalescence of cracks into a shear fault along which the rock fails. Ductile deformation mechanisms can be (a) entirely brittle, involving distributed microfracturing and friction acting on the microcrack surfaces and fragment particle interfaces that develop in the rock during loading (cataclasis), (b) entirely plastic, involving twinning, dislocation creep, diffusion creep and viscous flow, or (c) a combination of the these. The distinction between brittle failure and ductile deformation is macroscopic; depending on whether or not the rock can undergo substantial permanent strain without large-scale fracture. However, ductile rocks still behave elastically to transient perturbations of stress; transmitting seismic waves, for example, or brittle failure under a sharp stress transient such as loading after a nearby earthquake (Ruff, 2002). The brittle-ductile transition is defined as the region over which deformation changes from purely brittle mechanisms to ductile mechanisms and is characterised by a change in the shape of stress-strain curve (Figure 4.5). Micro-mechanics of the brittle-ductile transition in marble were studied by Fredrich et al. (1989). Values of 3-5% strain to failure usually define the position of the ductile to brittle transition (Heard, 1960; Evans et al., 1990). The brittle-ductile transition in continental crust occurs at a depth of $\sim$ 15 km (Ruff, 2002). As discussed above, transition is favoured by increasing pressure and temperature and decreasing strain rate. Varying the environmental conditions in this way increases the amount of inelastic strain accommodated by ductile mechanisms before the brittle failure process (strain softening) starts.

Ductile deformation occurs because rocks are inherently heterogeneous, containing a variety of mechanical flaws and sources of stress concentration such as microcracks, pores and grain boundaries, not to mention various types of mineral grains (Ohnaka, 2013). The dominance of one ductile mechanism over the other depends on the environmental conditions and the rock's mineralogy and microstructure. At shallow crustal levels, where lithostatic pressures and temperatures are low, ductile deformation is generally cataclastic

(i.e., brittle) since the rocks are consolidated, with grains locked in place by irregularity of shape, cohesive grain boundaries and cement. During cataclasis, individual grains behave as rigid particles that break and slide relative to one another to accommodate changes in shape. The two main mechanisms involved are microfracturing and the relative displacement of the fracture surfaces against each other, equivalent to frictional sliding along lots of small faults (Scholz, 1968d). This causes fragmentation as the rough fracture surfaces interact. Cataclastic processes generally occur in the upper part of the crust in areas of moderate to high strain, particularly in fault zones and form rocks called cataclasites, recognisable from cycles of cementation and re-fracturing evident within them. At deeper crustal levels, where temperatures and pressures are high, plastic deformation, in the form of dislocation creep and diffusion creep, occurs within the individual mineral grains due to the presence of various defects in their crystal lattices, such as point defects, dislocations and twin boundaries. A further mechanism for ductile deformation is dissolution creep, which occurs under stress in the presence of water. One of the ways stress concentrates within a rock sample is by the pile-up of lattice dislocations. Dislocations move through the sample in response to an increase in stress and then accumulate at some structural boundary, such as a grain boundary. As the dislocations pile-up, stress is no longer relieved by their motion and it concentrates in the area of the pile-up, causing bonds to break and initiating a crack (Wong, 1990). This process is thought to be the atomic-scale mechanism for crack tip propagation as well as crack initiation since in order to propagate, a crack tip must initiate failure by breaking bonds (Cottrell, 1958; Cleri et al., 1997).

## 4.6 Measuring Dilatancy in the Laboratory

A number of techniques are used to estimate cracking within a rock, variations in which have been considered as possible precursors to macroscopic fracture. The three techniques relevant to this study are:

- Acoustic emissions measurements
- Elastic wave velocity measurements
- Pore fluid volume measurements (during saturated experiments)

### 4.6.1 Acoustic emissions

Acoustic emissions (AE) are transient elastic waves generated by the rapid release of energy within a material and are, therefore, the laboratory analogue to earthquakes (large seismic events). They are emitted in response to increasing stress during processes of deformation such as from propagating crack tips, twin formation and dislocation pile-up, as well from frictional motions along rough surfaces, such as stick-slip (Sammonds and

Ohnaka, 1998), fragment roll (Sotolongo-Costa and Posadas, 2004) and frictional sliding along a fault (Scholz, 1968d; Varotsos et al., 2002). Each wave packet is considered to be an individual AE event. Micro-seismicity produced by such defects on the grain scale are typically recorded within the 100-2000 kHz range and early studies by Mogi (1962c; 1968) and Scholz (1968d) showed that AE events and dilatancy increase simultaneously during deformation. This demonstrated that AE events occur due to microfracturing within the rock (Mogi, 2007) and can therefore be considered a reliable proxy for crack growth.

Numerous studies have shown that AE output increases exponentially in rock with increasing stress, with a maximum number of events immediately prior to macroscopic failure (Scholz, 1968d; Ohnaka and Mogi, 1982; Sammonds et al., 1992; Cox and Meredith, 1993; Lockner, 1993; Stanchits et al., 2006; Fortin et al., 2006), although Byerlee (1993) noted that $< 1\%$ of microcracks generate detectable AE. AE frequency and source characteristics have been used to characterise the microfracturing process both in uniaxial compression (Ohnaka and Mogi, 1982) and during triaxial deformation (Scholz, 1968a;b;c; Sammonds et al., 1992; Lockner, 1993; Vallianatos et al., 2012a). These studies confirmed the results of Brace et al. (1966), revealing, in the close correlation between AE and stress-strain behaviour, that the onset of dilatancy does indeed occur at one-third to two-thirds of the fracture stress. Additionally, Ohnaka and Mogi (1982) noted five stages of AE activity correspondent with the five regions of deformation defined by Brace (1964). Other studies, which monitored AE during cyclic stressing of rock samples, have demonstrated the existence of a 'stress memory' effect in rocks (see reviews by Li and Nordlund, 1993; Holcomb, 1993; Lockner, 1993; Lavrov, 2003), allowing an estimate of the stress history of a rock sample from laboratory experiments. Typically, new microcrack damage is generated only once the previous maximum stress has been exceeded; a phenomenon now known as the Kaiser effect after Kaiser (1953) first reported it in metals.

3-D source location techniques have been used to develop spatial maps of AE hypocentres during deformation (e.g., Mogi, 1968; Scholz, 1968a; Lockner et al., 1991; 1992; Lockner and Byerlee, 1992; Lockner, 1993; Zang et al., 1996; Clint, 1999; Lei et al., 2000a; Jouniaux et al., 2001; Lei et al., 2004), highlighting the anisotropic and inhomogeneous nature of microcrack development (Figure 4.6). These studies have shown the evolution of fracture from microcrack nucleation, propagation and coalescence through to fault generation, localisation and dynamic propagation to failure. Fracture distribution is initially fairly homogeneous throughout the sample until failure is approached, whereupon localisation of microcracks around weak spots is observed, with some clusters forming the eventual fault plane while the propagation of other clusters is arrested. More recently, AE locations during deformation have been determined from continuous recordings of ultrasonic waveforms during deformation (e.g., Benson et al., 2007).

Analysis of AE source mechanisms (Stanchits et al., 2006) identified different source types at different stages of deformation. AE sources consistent with pore collapse were associated with initial compaction of the sample, followed by an increase in the relative contribution

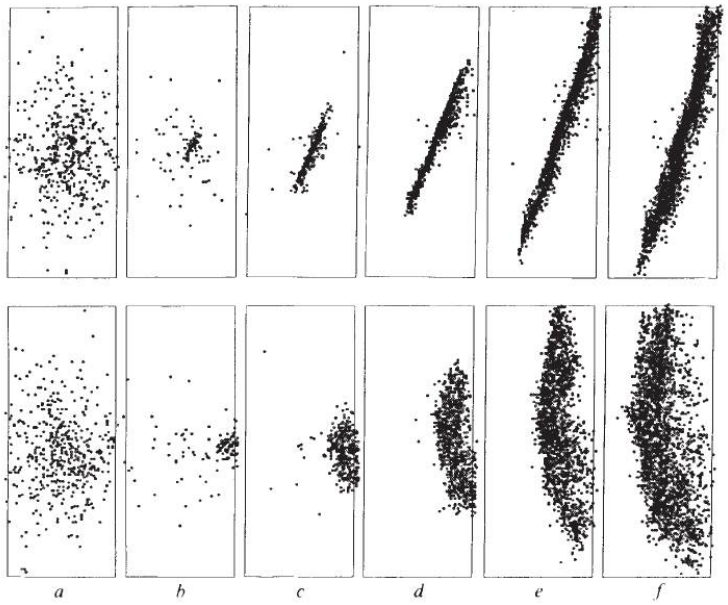


Figure 4.6: Sequential plots of AE locations where upper plots show events viewed along strike of the eventual fault plane and lower plots show the same events when the fault plane is viewed face on (from Lockner et al., 1991). Distributed microcracks are seen in *a*. The fault nucleates in *b* and propagates across the sample in *c-f*. A distinct fracture front develops in *d-f* as the fault grows.

of tensile-type sources during the ductile region and early stages of brittle deformation. This transition from tensile to shear strain has since been observed using seismic moment tensor analysis (Graham et al., 2010). Approach to failure is characterised by a decrease in the number of tensile-type events with a concomitant increase of double-couple, shear-type events, indicating that shear fractures connect previously formed tensile cracks. This result provided experimental evidence for theoretical models of crack development, such as wing-crack models (Costin, 1985; Horii and Nemat-Nasser, 1985; Ashby and Hallam, 1986; Sammis and Ashby, 1988; Ashby and Sammis, 1990).

Frequency-magnitude plots for AE have revealed statistical relationships similar to those for seismicity, including frequency-magnitude distributions, with $b$-values (Mogi, 1962c;b; Scholz, 1968b) and Tsallis $q$-parameters (Vallianatos et al., 2012a) in the laboratory similar to those seen in the field, foreshock sequences (Mogi, 1962c;b), aftershock decay sequences (Scholz, 1968c) and recurrence intervals (Davidsen et al., 2007). Mogi's modelling work (1962a; 1963a; 1963b), in which he treated microfracturing as a stochastic process, led him to qualitatively relate the $b$-value to the degree of heterogeneity of the model material. The notion that regional variations of seismic $b$-value may reflect variations of the state of stress in the crust came from the findings of Scholz (1968b); that the state of stress rather than the heterogeneity of the material plays the most important role in determining the value of $b$. These two opposing views were aligned in the work of Main et al. (1989) who showed that in fact the localised stress intensity, which relates stress to heterogeneity, is what governs the $b$-value. As shown in Figure 4.7 (a), AE $b$-values exhibit a decrease during stress-induced dilatancy corresponding to an increasing number of large amplitude events as failure is approached, with a minimum denoting macroscopic failure (Scholz,

1968b; Sammonds et al., 1992). This behaviour has been observed in the seismicity preceding several historical earthquakes (Scholz et al., 1973) and therefore linked to the state of crustal stress prior to these events. Where dynamic failure is preceded by a precursory strain energy release (strain softening), fracture mechanics models for increasing damage predict two minimum $b$-values separated by a temporary maximum, which correspond to intermediate and short term seismic precursors separated by seismic quiescence (Main et al., 1989; 1992; Meredith et al., 1990). These minima were seen in saturated rock deformation experiments and associated with falling pore fluid pressure during dilatancy and the corresponding stress relaxation (Sammonds et al., 1992) (Figure 4.7 (b)). Zang et al. (1996) observed differences in AE activity due to the presence of pore fluid, with a lower onset and number of AE in wet specimens compared with dry specimens and $b$-values from wet experiments exhibiting a drop and then recovery before failure. Furthermore, Scholz (1968b;d) observed that the activity and frequency-magnitude relation of AE accompanying frictional sliding on a macroscopic fracture plane was quite different from that observed during the deformation of brittle rocks but similar to that observed during cataclastic deformation of marble. He found that marble, which deforms cataclastically at relatively low confining pressures, exhibits an AE frequency-magnitude relation similar in form to that found for brittle deformation but characterised by very high $b$-values over the entire range of stress. The similarity of these $b$-values to those found during frictional sliding along a fault, as well as in the lower stress regions of deforming brittle rocks, indicates that cataclastic deformation is mainly due to stable intergranular sliding.

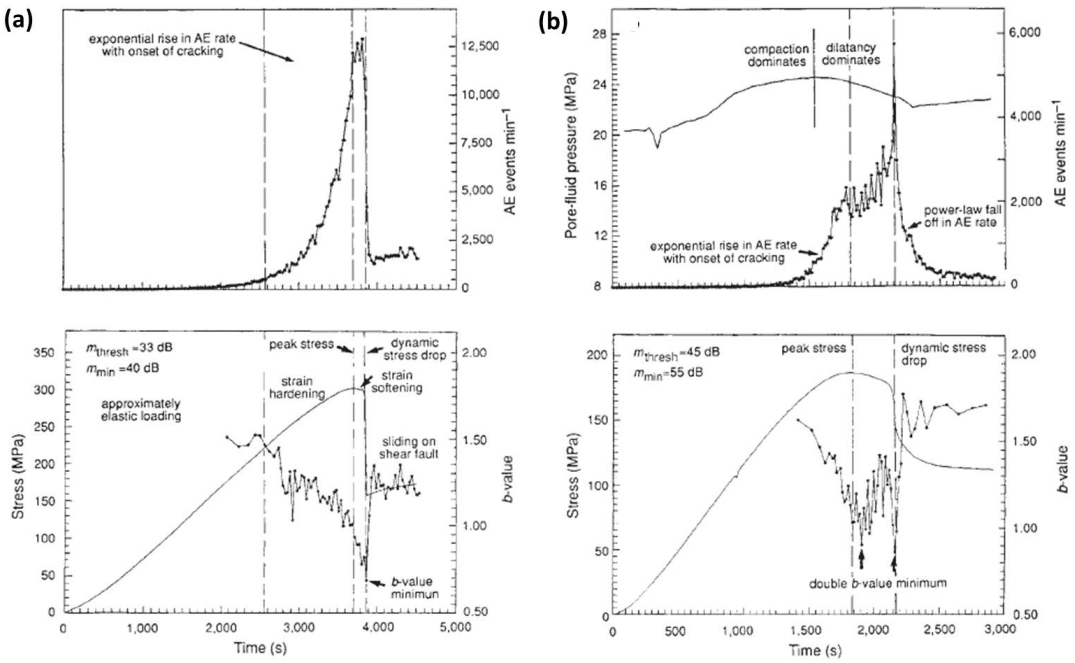


Figure 4.7: Evolution of AE event rate, stress and $b$-value during deformation of Darley Dale sandstone at $10^{-5}$ $s^{-1}$ and 50 MPa for (a) an air-dried specimen and (b) a saturated sample at constant pore fluid volume. After Sammonds et al. (1992)

### 4.6.2 Elastic wave velocities

In order to extract information regarding the physical state of a rock from seismic and seismological data, it is important to understand and quantify variations in the velocity of elastic waves as they pass through the rock (Gueguen and Schubnel, 2003). In the study of earthquake precursors, elastic wave velocity variations have been used to quantify precursory damage accumulation (Chun et al., 2004; Volti and Crampin, 2003; Gao and Crampin, 2004). A rock's physical properties are affected significantly by the volume, distribution and shape of the pore space (Walsh, 1965; O'Connell and Budiansky, 1974; Paterson and Wong, 2005). Due to the large velocity contrast between dry air and mineral crystals (Mavko et al., 2009; Nur, 1971; Nur and Simmons, 1969) and the resulting attenuation effect of space within a solid, elastic wave velocities are substantially reduced by the presence of thin cracks. This dependence of elastic wave propagation on a rock's microstructure means that velocity measurements can be used to calculate the dynamic elastic moduli and velocity anisotropy and give an insight into other physical properties of the rock. Seismic wave velocities are extremely important for determining the dynamic elastic constants of a cracked solid. When applied to the crack face, the stress field of an elastic wave produces an additional strain which would not exist in the absence of the crack; crack edges are deformed only a small amount and very transiently by the passing waves, causing them to behave elastically. Fracturing a rock creates a secondary porosity where fractures are aligned with the local stress field, making the transport properties of the rock anisotropic (Nur, 1971; Nur and Simmons, 1969). Aligned fractures exert a strong anisotropy on rocks. The effect of these structures on the elastic wave velocities and permeability is often much greater than other variables such as mineral alignment and grain shape fabric (Mavko et al., 2009; Nur, 1971; Birch, 1960).

Additionally, velocity variation during deformation can help to track the evolution of microfracture damage within the deforming rock sample. Elastic wave velocities (Birch, 1960; 1961; Walsh, 1965; Anderson et al., 1974; O'Connell and Budiansky, 1974; Hadley, 1976; Soga et al., 1978; Sayers and Kachanov, 1995; Gueguen and Schubnel, 2003; Reuschle, 2003; Fortin et al., 2005; Takemura and Oda, 2005) have been found to significantly decrease with increasing dilatancy. In general, experimental studies show that wave velocities increase with increasing confining pressure and decrease with increasing deviatoric stresses; both observations have been related to the pressure-induced closure and stress-induced opening of narrow cracks (e.g., Gueguen and Palciauskas, 1994; Paterson and Wong, 2005). In a stressed rock volume, tensile cracks open preferentially normal to the maximum compressive stress direction, resulting in anisotropy of the elastic wave velocities. The speed of waves propagating in the direction normal to the planes of preferred crack orientation is more significantly decreased than the speed of waves traveling parallel to the crack planes (Nur, 1971; Schubnel et al., 2003). Assuming a transversely isotropic distribution of cracks, the observed elastic wave speeds may be used to estimate the respective anisotropic elastic constants and crack damage (Mavko et al., 2009; Soga et al., 1978; Ayling et al., 1995;

Schubnel et al., 2003).

The effect of triaxial deformation on compressional ($V_P$) and shear ($V_S$) wave velocities can be investigated through velocity measurements across the sample (see Section 6.4 for details of measurement techniques). Wave velocities are usually measured axially along the sample during a triaxial deformation experiment (e.g., Sammonds et al., 1989; Yoshida, 2001; Ayling et al., 1995; Read et al., 1995; Schubnel et al., 2006a) and the typical effect on both wave types along this axis is shown in Figure 4.8. Initially, an increase is seen during linear elastic deformation due to the closure of pores and existing cracks oriented normal or sub-normal to the loading direction as the sample compacts. Since P-waves are longitudinal and therefore more sensitive to voids aligned normal to the axial stress than transverse $V_S$ waves, which are more sensitive to voids aligned parallel to the axial stress, $V_P$ increases more than $V_S$ during initial void closure. As closure becomes progressively more difficult, the velocities each reach a plateau before decreasing again as the material yields and new cracks begin to open in the dilatancy stage. Once the material yields, the decrease in $V_S$ is greater than in $V_P$, suggesting that dilatancy occurs by growth of tensile cracks along the axis of maximum compressional stress. Once failure has occurred, both velocities stabilise as frictional slip occurs along the failure surface. Velocity measurements are therefore a useful way to establish the development of crack anisotropy during rock deformation. Additionally, Schubnel et al. (2006a) used velocity measurements to invert for crack density and aspect ratio in several different rock types, establishing that both parameters decrease as a function of confining pressure.

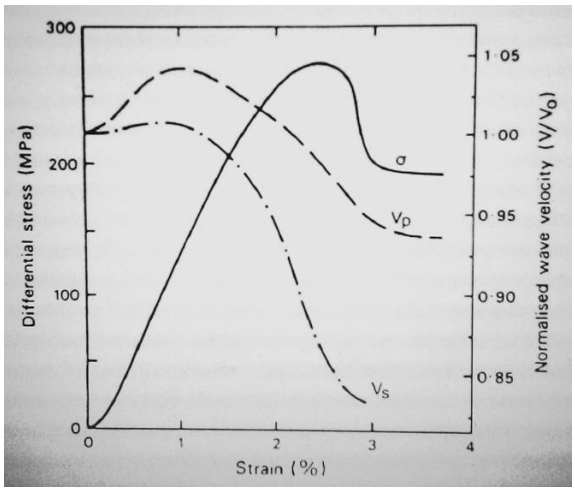


Figure 4.8: Variations in compressional ($V_P$) and shear ($V_S$) wave velocities in a dry sample of Darley Dale sandstone deformed at $10^{-5}$ $s^{-1}$ and 50 MPa. Reproduced from Sammonds et al. (1989).

A broad distinction can be made between porous and compact rocks (Paterson and Wong, 2005). Porous rocks are those with a substantial amount of intergranular pore space of more or less equal dimensions; mainly sedimentary rocks with high initial porosity (>5%). The role of the pore space in limiting the cohesion between grains or during compaction strongly influences their properties. In contrast, compact rocks are those of very small initial porosity (<3%); mainly crystalline igneous and high-grade metamorphic

rocks whose properties depend largely on the crack-like nature of their pore space. This study is concerned with the deformation behaviour of marble; a compact, crystalline, metamorphic carbonate. Velocity measurements are, therefore, a good way of establishing the evolution of crack damage during deformation, since the void space of marble is almost entirely due to microcracks rather than pores between rounded grains. Indeed, velocity variations during cataclastic deformation and stress relaxation of low-porosity, calcite-rich rocks (Schubnel et al., 2005) highlighted both (a) the competition between dilatant (crack opening and frictional sliding) and compactive (pore closure) micro-mechanisms and (b) the lack of systematic correlation between elastic properties (mainly sensitive to crack density) and volumetric strain (more sensitive to porosity) and their dependence on the strain rate, stress conditions and pore pressure.

### 4.6.3 Pore fluid volume measurements

Volumetric strain within a rock volume can be measured directly from pore fluid volume variations under a constant pore fluid pressure by means of a pore volumometer (see Chapter 5). It has been shown that pore volume increases with increasing dilatancy (Sammonds et al., 1992; Benson et al., 2007).

## 4.7 Crack Density Models

Micro-structural information such as the crack density and mean aspect ratio of propagating cracks can be inferred from AE event rates and velocity changes (e.g., Ayling et al., 1995; Read et al., 1995) and used to predict the mechanical behaviour (Cox and Meredith, 1993) resulting from a stress distribution modified by the presence of damage. This is examined through the variation of overall elastic properties and compared with theoretical models for the elasticity of cracked solids. For example, Cox and Meredith (1993) and Sammonds et al. (1994) calculated stress-strain characteristics from laboratory AE data based on the models of Walsh (1965) and Bruner (1976) and compared them with the observed mechanical behaviour. Walsh's simple model for the effect of 'dilute, non-interacting cracks' on the elasticity of the solid performed as adequately as Bruner's until the strain softening stage of the test where Bruner's improved treatment accounting for crack interactions proved superior. His approach was based on the self-consistent effective medium model of O'Connell and Budiansky (1974) and Budiansky and O'Connell (1976). These models have since been superceded by the non-interaction approximation of Kachanov (1994), which is rigorous with known assumptions and can be solved explicitly. The crack density model used in Chapter 6 is that presented in Sayers and Kachanov (1995) for an isotropic matrix containing a random distribution of crack centres and orientations. In this case, Kachanov (1994) showed that the effective Young's Modulus, $E_{eff}$

and shear modulus $\mu_{eff}$ of a rock can be written as:

$$\frac{E_0}{E_{eff}} = 1 + \left(1 + \frac{3}{5}\left[\left(1 - \frac{\nu_0}{2}\right)\frac{\delta}{1+\delta} - 1\right]\right)h\rho \tag{4.15}$$

and

$$\frac{\mu_0}{\mu_{eff}} = 1 + \left(1 + \frac{2}{5}\left[\left(1 - \frac{\nu_0}{2}\right)\frac{\delta}{1+\delta} - 1\right]\right)\frac{h\rho}{1+\nu_0} \tag{4.16}$$

where the Young's Modulus, $E_0$, shear modulus, $\mu_0$ and Poisson's ratio, $\nu_0$, are those of the crack-free matrix and the scalar $h = \dfrac{16(1-\nu_0^2)}{9(1-\nu_0/2)}$ is the appropriate one for a non-interactive penny-shaped crack geometry (Kachanov, 1994; Sayers and Kachanov, 1995). The parameter $\delta$ is a non-dimensional number referred to as the saturation parameter and is defined by $\delta = (1-\nu_0/2)h\dfrac{E_0\xi}{K_f}$. This coefficient essentially compares the fluid bulk modulus, $K_f$, to the crack bulk modulus, $E_0\xi$, assuming that all changes in the crack volume are due to aperture variations.

## 4.8 Deformation of Fluid Saturated Rocks

### 4.8.1 The law of effective stress

Pressurised pore fluids within a rock body act to reduce its overall strength, both in porous rocks (Zang et al., 1996; Masuda, 2001; Baud et al., 2000) and in compact, crystalline rocks (Lajtai et al., 1987; Dennis and Atkinson, 1982). Weakening due to pore fluid is also seen during cataclastic flow (Bernabe and Brace, 1990; Read et al., 1995; Zhu and Wong, 1997). This weakening is due to reduction in the normal stress acting on the rock, equivalent to a reduction in confining pressure. This can be explained in terms of Terzaghi's principle (Terzaghi, 1943):

$$\sigma_n{}' = \sigma_n - \alpha P_p \tag{4.17}$$

where $\sigma_n$ is the total normal macroscopic stress, $\alpha$ is the effective stress coefficient and $P_p$ is the pore fluid pressure. Terzaghi's principle states that $\alpha = 1$, which is consistent with many experimental studies (e.g., Murrell, 1965). However, values of $\alpha \neq 1$ have also been reported (e.g., Bernabe, 1986). This is due to dilatancy hardening, which occurs when the pore pressure inside a sample drops. It causes the effective pressure to increase, meaning that greater differential stress is required for deformation than when pore pressure can be maintained constant. It can be expected to affect frictional sliding or cataclastic flow whenever permeability is low relative to the strain rate and dilation accompanies deformation. In order for the mechanical behaviour of dry and saturated samples to be comparable, dilatancy hardening must not occur. The strain rate above which dilatancy hardening occurs is known as the critical strain rate (Brace and Martin, 1968). For most rocks, the law of effective stress only holds when the strain rate is less than this critical value, which depends on the permeability of the rock, viscosity of the pore fluid and sample

geometry (Brace and Martin, 1968). The lower the permeability of the rock, the slower the critical strain rate. For example, Rutter (1972a) found that Terzaghi's principle held for the deformation of Solenhofen limestone at $P_c = 60$ MPa, provided the strain rate did not exceed $10^{-6}$ $s^{-1}$ while Brace and Martin (1968) established that critical strain rates for Westerly granite and San Marcos gabbro were $3x10^{-7}s^{-1}$ and $5x10^{-8}s^{-1}$ respectively.

### 4.8.2 Permeability

The flow of fluid through a rock is determined by the connectivity of the pore space. Permeability is the resistance to the flow of fluid through a porous medium. The presence of microcracks makes it much easier for fluid to flow through any rock body because they constitute a macroscopic fluid flow network; they make the rock permeable. This effect has been observed experimentally in various rock types (e.g., Fischer and Paterson, 1992; Peach and Spiers, 1996) and discussed in terms of percolation theory (Dienes, 1982; Madden, 1983; Rivier et al., 1985). The total porosity, microcrack distribution and the pore space connectivity and geometry of the pore space all affect the permeability of a rock (Mavko et al., 2009; Gueguen and Palciauskas, 1994). If the porosity of a rock is lower than a critical value, known as the percolation threshold (Gueguen and Schubnel, 2003), then there is no percolator pathway across the sample and no flow is expected to occur (Meredith et al., 2012). Just above the percolation threshold, permeability is extremely sensitive to very small changes in microcrack density. For example, Meredith et al. (2012) found that for an isotropic tight rock with very small permeability and porosity, a modest change in total porosity (from 1% to 5% or so) due to thermally-induced microcracks resulted in an extremely non-linear permeability increase of seven or more orders of magnitude. Therefore, permeability also increases with dilatancy (Zoback and Byerlee, 1975; Brace, 1978; Homand-Etienne and Troalen, 1984; Fischer and Paterson, 1992; Zhang et al., 1994; Zhu and Wong, 1997; Mitchell and Faulkner, 2008). Additionally, cyclic loading experiments have shown that permeability increases far more dramatically just prior to failure (an order of magnitude increase beyond about 80% of peak stress) than during the initial stages of deformation (increase of only 2-3 times the initial permeability) (Mitchell and Faulkner, 2008) and that the static elastic moduli also change during deformation (Heap and Faulkner, 2008). Permeability development is also sensitive to effective pressure and strain. For example, Zhang et al. (1994) found that, at effective pressures less than 50 MPa, the permeability of Carrara marble increases by one to two orders of magnitude with an initial 2-5% strain and an accompanying increase of 0.005-0.01 in apparent connected porosity. Permeability increased only slightly with further shortening up to 18% and an increase in apparent connected porosity up to 0.08. By contrast, at effective pressures of 150 to 200 MPa, the permeability did not increase substantially until specimens were shortened by about 8%.

### 4.8.3 Stress corrosion

The presence of chemically active fluids can cause 'stress corrosion' (Atkinson, 1984) at crack tips, which means that cracks can grow sub-critically at values of stress intensity, $K$, well below the fracture toughness, $K_c$. Sub-critical crack growth causes more distributed damage around a propagating crack compared to dynamic fracture (Atkinson, 1982). Rostom et al. (2012) found that the salinity of the pore fluid affects sub-critical crack propagation. They established the presence of a threshold in pore fluid composition that separates two regimes of crack propagation: (1) weakening conditions at low salinity, where crack propagation is favored, and (2) strengthening conditions for higher concentrations of NaCl, where crack propagation slows down. They interpret this behaviour to be the result of electrostatic surface forces that modify the repulsion forces between the two surfaces of the crack.

## 4.9 Evolution of Physical Properties during Deformation

Rock deformation during a typical triaxial compression cycle involves the nucleation and coalescence of cracks on a microscopic scale that may, in the brittle and semi-brittle regimes, eventually localise into one or more macroscopic faults. Since microfractures significantly effect the physical properties of a rock (Simmons and Brace, 1965; Walsh, 1965; Schubnel et al., 2006a) and make it much more mechanically compliant, these microscopic processes can be described from bulk rock physics measurements. A typical deformation cycle, as represented by the stress-strain curve for experimental rock samples, can be divided into five specific regions first proposed by Brace (1964). The variation in some of these physical properties in each of these regions can be seen in Figure 4.9 (a). A similar cycle was later presented by Scholz et al. (1973) in his dilatancy-diffusion hypothesis to explain observed precursory effects during the earthquake preparation process in terms of fracture and fluid flow (Figure 4.9 (b)).

**Region I - crack closure ('settling down'):** Initially, deformation becomes more difficult with increasing stress resulting in a concave upward trend in the stress-strain curve. This compaction of the sample is most likely due to the preferential closure of cracks and pores oriented at high angles to the loading axis which reduces the void space and causes the pore volume and permeability to decrease while both $V_P$ and $V_S$ increase. Very little, if any, AE activity occurs during this stage and deformation is reversible although some slight hysteresis may be observed.

**Region II - linear elasticity (Hooke's law):** In this region, the stress is directly related to strain so the stress-strain curve remains very nearly linear (quasi-linear) and deformation is elastic. Although behaviour can be hysteretic, loading and unloading in this region will not produce irreversible changes in the properties or structure of the rock. Pore volume and permeability continue to decrease in this region and velocities increase,

indicating that crack and pore closure is still prevalent. The electrical resistivity of the sample also tends to increase as cracks and pores close, although effects vary with rock type.

**Region III - dilatancy:** During the third stage, irreversible changes occur in the rock that lead to unrecoverable strain once the load is removed (Jaeger et al., 2007). At a stress of about two thirds of the peak stress (Hallbauer et al., 1973; Anastasiadis et al., 2004; Jaeger et al., 2007), the stress-strain curve begins to curve downwards towards a zero gradient. This marks the onset of microcrack formation within the sample and is known as strain hardening; deformation is *ductile*, permanent and becomes easier with increasing stress until the sample can no longer support any further increase in stress (peak strength of the material). New microfractures are evenly distributed throughout the sample, although some orientation-induced anisotropy develops as they preferentially grow parallel to the direction of maximum principal stress. From 50-75% of peak stress, the AE rate begins to increase exponentially and the *b*-value decreases slowly from the initial steady value of ∼1.5 to ∼1 (Figure 4.7 (a)). As cracks open the sample dilates, causing the pore volume and permeability to increase as new pathways are created for fluid flow. Parallel to the loading axis, $V_S$ decreases faster than $V_P$, indicating that the new microcracks form preferentially orientated parallel with or slightly oblique to the loading axis. Electrical resistivity decreases markedly during dilatancy (Glover et al., 1996; Yoshida et al., 1998; Eccles et al., 2005) and is one of the properties most strongly affected as new crack space is created.

**Region IV - coalescence of microcracks; formation of macroscopic fracture:** The process of failure is considered to be continuous throughout this region (beyond peak stress), in which the rock physically deteriorates. Once peak stress is reached, the rock's ability to support a load decreases and the slope of the stress-strain curve becomes negative. This is known as strain softening and deformation in this region is considered to be *brittle* (Jaeger et al., 2007). With continued deformation, maximum damage accumulates in the rock sample causing velocities in all directions to continue to decrease (with $V_S$ decreasing faster than $V_P$) and the AE rate to reach a steady peak before dropping significantly once major failure occurs, in line with the associated stress drop. AE output increases exponentially and the *b*-value decreases rapidly to $\sim 0.5$ immediately prior to the major stress drop, indicating accelerated crack growth and coalescence associated with the formation of a macroscopic failure plane. Crack coalescence rapidly increases the pore volume and provides additional fluid and electrical pathways so permeability and electrical conductivity also increase significantly in this region.

**Region V - frictional sliding along failure surfaces:** The stress-strain curve flattens off once macroscopic failure occurs as stress becomes independent of strain and stable sliding occurs along the failure plane(s). Physical properties such as elastic wave velocities, pore volume, permeability and electrical conductivity settle to a constant level, while the AE rate is reduced to a lower level associated with sliding and the *b*-value recovers to an

intermediate value of 1-1.5. This is likely due to the steady roll and fracture of fragments on the failure surfaces as they slide against each other, with an approximately constant coefficient of friction.

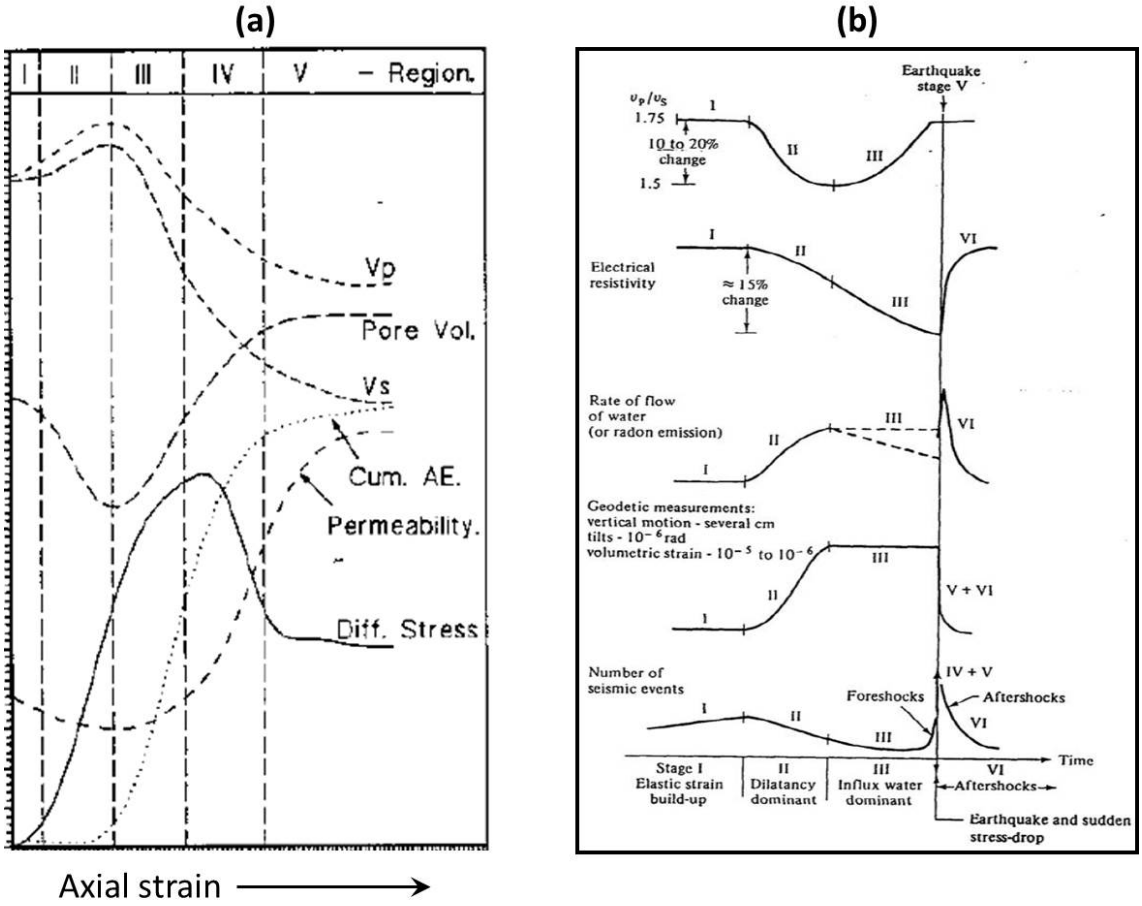


Figure 4.9: Variation of rock physical properties (a) during a typical triaxial compression experiment, modified from Clint (1999), and (b) during the earthquake cycle for the dilatancy-diffusion model, after Scholz et al. (1973). Region I in (a) is not represented in the stages of (b), so regions II and III in the experimental rock deformation cycle equate to stages I and II in the earthquake cycle, while region IV represents both stages III and IV.

# Chapter 5

# Experimental Approach

## 5.1 Introduction

In order to investigate electric current emissions generated during deformation under shallow crustal conditions, this thesis consists of both an experimental stage and a theoretical stage. This chapter will focus on the experimental approach.

The primary objectives of the experimental stage were to establish the following:

- The specific environmental conditions under which electric current emissions occur (crustal pressures, deformation rates and pore fluid presence and composition) and the influence of these conditions on the detected electric current.
- The influence of deformation mechanism on the detected electric current and how electric current emissions relate to damage evolution and fracture during deformation.

To this end, the experimental program comprised a series of room temperature, constant strain rate triaxial compression experiments on specimens of Carrara marble.

During a triaxial deformation experiment, pressure conditions and deformation rates can be controlled and varied as required. Experiments under these conditions allow us to simulate deformation under lithospheric conditions by providing the natural principal stresses (a combination of shear and normal stresses) encountered in the shallow crust. These stresses vary over time and alter the geometry of the rock matrix, causing electrical changes, fluid interactions, elastic wave emissions and chemical reactions. Measuring these properties provides indirect information about the behaviour of the rock and the microscopic processes involved, providing evidence to support and constrain theoretical models. Inferences can then be made about how these processes produce macroscopic deformation and how signals measured in the field could be interpreted. The advantage of laboratory experiments is that it is possible to measure independently the dynamic variables causing and produced by deformation, enabling discrimination between individual mechanisms.

Constant strain rate experiments were conducted in order to obtain the full stress-strain curve beyond peak strength. Constant stress rate uniaxial compression experiments on marble (Stavrakas et al., 2003) had previously demonstrated that an electric current was emitted during the ductile phase of deformation immediately prior to macroscopic failure. In these experiments, failure occurred at peak stress (i.e., the uniaxial compressive strength of the rock). During a triaxial compression experiment in which stress is the controlled variable, violent failure of the rock specimen also occurs near the point of maximum stress. If the full stress-strain curve beyond the point of peak strength is to be obtained, it is necessary to control the strain in the rock specimen rather than the stress, setting it to increase monotonically (Jaeger et al., 2007). This region beyond the point of peak strength is important since it is the region of permanent deformation during which the rock's ability to support a load decreases (the brittle region or 'failure preparation zone'). Microcracks formed during the ductile stage of initial yield extend and coalesce, eventually leading to macroscopic sample failure. This approach to failure is extremely important in the study of earthquake precursors. In their experiments, Stavrakas et al. (2003; 2004) and Anastasiadis et al. (2004) established that electric current emissions were associated with a changing effective Young's Modulus from the onset of permanent deformation to failure. Thus, to investigate the current generated under triaxial conditions through all stages of deformation from the ductile initial yield through peak strength into the brittle 'failure preparation' region and ultimately to failure, it was therefore necessary to use a constant strain rate during this study rather than controlling the stress rate.

Overall, 58 experiments were conducted on specimens of Carrara marble; 46 under dry conditions to investigate the effect of confining pressure and strain rate on electric current emissions, and 12 under saturated conditions to investigate the effect of pore fluid on electric current emissions (see Tables 5.1 and 5.2 for full details of environmental conditions). Damage to the rock during deformation was tracked by simultaneously monitoring ultrasonic wave velocity changes, acoustic emissions and mechanical loading information as well as recording the electric current.

Experimental conditions were as follows:

- Experiments to investigate the effect of confining pressure ($P_c$) were conducted at a strain rate of $10^{-6}$ $s^{-1}$ and $P_c$ ranging from 10 MPa to 100 MPa.
- Experiments to investigate the effect of strain rate were conducted at 30 MPa $P_c$ and strain rates between $10^{-4}$ and $10^{-6}$ $s^{-1}$.
- Experiments to establish the influence of the presence and composition of pore fluid were conducted on pre-fractured samples under drained conditions at 30 MPa effective pressure ($P_{eff}$) and $10^{-6}$ $s^{-1}$ strain rate. Pre-fractured samples were cracked by means of thermal treatment followed by mechanical loading of the dry specimens (one sample was only cracked mechanically). A relatively low $P_{eff}$ was used to minimise the effect of dissolution; calcite is practically insoluble in water at room temperature and pressure

(0.0014 g per 100 g $H_2O$ - from Crystran Ltd) but the solubility increases at elevated pressures (Hellmann et al., 2002). $P_c$ of 50 MPa and pore fluid pressure ($P_p$) of 20 MPa were used, yielding a $P_c : P_p$ ratio, $\lambda$, of 0.4; similar to that found in the shallow crust. Samples were saturated with two different types of pore fluid. One was de-ionised water to ensure minimal effect of ions. The other was an ionic brine solution made up from Instant Ocean synthetic sea salt, the composition of which can be found in Table 10.1.

- Cyclic loading experiments were conducted on both dry and saturated samples at 30 MPa $P_{eff}$ and 2x10$^{-6}$ s$^{-1}$ strain rate.
- Additional experiments where the strain rate was changed in stages during the experiment itself were conducted at 10, 20 and 30 MPa.

Of the 46 dry experiments conducted, only 25 yielded useful electrical results. 20 of these are presented in this thesis (see Table 5.1). Of the remaining five, two were conducted as cyclic loading experiments and three were conducted with a varying strain rate. Time restrictions precluded full data analysis so the results from these five experiments are not presented in this thesis. Of the 12 saturated experiments, six were conducted at a strain rate of 1x10$^{-6}$ s$^{-1}$ and only two of these yielded useful electrical results. These two (see Table 5.2) are presented in this thesis. The other six were conducted at 2x10$^{-6}$ s$^{-1}$ to determine the effects of cyclic loading. Again, time restrictions precluded full data analysis so the results from these six experiments are not presented in this thesis.

The experimental procedure and configuration of the triaxial apparatus were based on those of Yoshida (2001), the only author to have previously measured electric current under triaxial conditions, and those of Yoshida et al. (1998), Clint (1999) and Eccles et al. (2005) who had investigated electric potential changes and acoustic emissions during triaxial deformation. However, I designed the electric current data acquisition system specifically for this study. Electrode configurations used here differed necessarily from the studies mentioned above in order to accommodate differential current measurements into the existing sample assembly. Experiments were conducted using the triaxial ensemble in the Rock and Ice Physics Laboratory (RIPL) at UCL (Sammonds, 1999), to which some design modifications were made to ensure the quality of the electrical data.

This chapter presents details of the experimental data acquisition during this study. A description of the apparatus incorporating the design modifications introduced for electric current measurements is given first, followed by the instrumentation, data logging procedures and data reduction methods. After this, there is a description of the equipment calibrations and sample preparation procedure. Finally, the full experimental procedure and sources of experimental error are presented.

Table 5.1: Environmental conditions and acquisition information for experiments carried out under *DRY* conditions

| **Sample** | **Confining pressure (MPa)** | **Strain rate ($s^{-1}$)** | **Cyclic loading** | **No. of acoustic emissions channels** | **No. of electrical channels** | **Velocity survey intervals (mins)** |
|---|---|---|---|---|---|---|
| CM01 | 30 | $1x10^{-4}$ | No | 10 | 4 | Every 25kN |
| CM02 | 30 | $1x10^{-4}$ | No | 10 | 4 | 2 |
| CM03 | 30 | $1x10^{-4}$ | No | 10 | 4 | 2 |
| CM06 | 30 | $1x10^{-5}$ | No | 10 | 4 | 2 |
| CM07 | 30 | $1x10^{-6}$ | No | 10 | 4 | 2 |
| CM04 | 30 | $1x10^{-4}$ | No | 10 | 4 | 2 |
| CM05 | 30 | $1x10^{-6}$ | No | 10 | 1 | 5 |
| CM08 | 10 | $1x10^{-6}$ | No | 10 | 1 | 5 |
| CM09 | 30 | $1x10^{-6}$ | No | 10 | 1 | 60 |
| CM10 | 30 | $1x10^{-6}$ | No | 10 | 2 | 60 |
| CM11 | 30 | $1x10^{-6}$ | No | 10 | 3 | 60 |
| CM12 | 30 | $1x10^{-6}$ | No | 10 | 4 | 60 |
| CM13 | 30 | $1x10^{-5}$ | No | 10 | 1 | 10 |
| CM14 | 30 | $1x10^{-5}$ | No | 10 | 1 | 10 |
| CM15 | 30 | $1x10^{-4}$ | No | 10 | 1 | 8 |
| CM16 | 30 | $1x10^{-6}$ | No | 10 | 1 | 60 |
| CM17 | 30 | $1x10^{-6}$ | No | 10 | 1 | 60 |
| CM18 | 30 | $1x10^{-4}$ | No | 10 | 1 | 3 |
| CM19 | 30 | $1x10^{-5}$ | No | 10 | 1 | 10 |
| CM20 | 30 | $1x10^{-5}$ | No | 10 | 1 | 10 |
| CM21 | 20 | $1x10^{-6}$ | No | 10 | 1 | 60 |
| CM22 | 30 | $5x10^{-6}$ | No | 10 | 1 | 30 |
| CM23 | 30 | $5x10^{-5}$ | No | 10 | 1 | 5 |
| CM24 | 30 | $1x10^{-5}$ | No | 10 | 1 | 10 |
| CM25 | 30 | $5x10^{-6}$ | No | None | 1 | No surveys |
| CM26 | 30 | $5x10^{-5}$ | No | None | 1 | No surveys |
| CM27 | 30 | varied | No | 10 | 2 | No surveys |
| CM28 | 10 | varied | No | 10 | 2 | 5 |
| CM29 | 20 | varied | No | 10 | 2 | 5 |
| CM30 | 30 | varied | No | 10 | 2 | 5 |
| CM32 | 75 | $1x10^{-5}$ | No | 10 | 1 | 5 |
| CM34 | 100 | $1x10^{-5}$ | No | 10 | 2 | 5 |
| CM35 | 100 | $1x10^{-6}$ | No | 10 | 2 | 5 |
| CM49 | 30 | $1x10^{-5}$ | Yes | 10 | 2 | 5 |
| CM53 | 30 | $2x10^{-6}$ | Yes | 10 | 2 | 5 |
| CM54 | 100 | $1x10^{-6}$ | No | None | 2 | No surveys |
| CM57 | 100 | $1x10^{-6}$ | No | 10 | 2 | 30 |
| CM58 | 60 | $1x10^{-6}$ | No | 10 | 2 | 30 |
| CM59 | 100 | $1x10^{-5}$ | No | 10 | 2 | 5 |
| CM60 | 20 | $1x10^{-6}$ | No | 10 | 2 | 10 |
| CM63 | 60 | $1x10^{-6}$ | No | 10 | 3 | 10 |
| CM64 | 60 | $1x10^{-6}$ | No | 10 | 3 | 10 |
| CM65 | 20 | $1x10^{-6}$ | No | 10 | 3 | 10 |
| CM66 | 10 | $1x10^{-6}$ | No | 10 | 3 | 10 |
| CM67 | 100 | $1x10^{-6}$ | No | 10 | 3 | 10 |
| CM68 | 30 | $1x10^{-6}$ | No | 10 | 3 | 10 |

N.B. Highlighted rows are the experiments presented in this thesis

Table 5.2: Environmental conditions and acquisition information for experiments carried out under *SATURATED* conditions

| **Sample** | **Thermally cracked** | **Strain reached during dry mechanical cracking (%)** | **Pore fluid** | **Pore pressure (MPa)** | **Confining pressure (MPa)** | **Strain rate ($s^{-1}$)** | **Cyclic loading** | **No. of acoustic emissions channels** | **No. of electrical channels** | **Velocity survey intervals (mins)** |
|---|---|---|---|---|---|---|---|---|---|---|
| CM50 | No | 1 | Water | 20 | 50 | $2x10^{-6}$ | No | 10 | 2 | 5 |
| CM51 | No | 1.5 | Water | 20 | 50 | $1x10^{-6}$ | No | 10 | 2 | 5 |
| CM52 | No | 1.5 | Water | 20 | 50 | $2x10^{-6}$ | Yes | 10 | 2 | 5 |
| CM61 | No | 1.5 | IO brine | 20 | 50 | $1x10^{-6}$ | No | 10 | 2 | 5 |
| CM42 | Yes | 1.5 | IO brine | 20 | 50 | $1x10^{-6}$ | No | 10 | 2 | 5 |
| CM43 | Yes | 1.5 | IO brine | 20 | 50 | $2x10^{-6}$ | Yes | 10 | 2 | 5 |
| CM44 | Yes | 2 | IO brine | 20 | 50 | $1x10^{-6}$ | No | 10 | 2 | 10 |
| CM45 | Yes | 2 | IO brine | 20 | 50 | $2x10^{-6}$ | Yes | 10 | 3 | 10 |
| CM62 | No | 2 | IO brine | 20 | 50 | $2x10^{-6}$ | Yes | 10 | 3 | 10 |
| CM46 | Yes | 2 | Water | 20 | 50 | $1x10^{-6}$ | No | 10 | 3 | 10 |
| CM47 | Yes | 2 | Water | 20 | 50 | $2x10^{-6}$ | Yes | 10 | 3 | 10 |
| CM48 | Yes | 2 | Water | 20 | 50 | $1x10^{-6}$ | No | 10 | 3 | 10 |

N.B. Highlighted rows are the experiments presented in this thesis

## 5.2 Triaxial Deformation Apparatus

### 5.2.1 Introduction

Triaxial deformation is the most widely used procedure to simulate the natural stress state within the crust. Testing machines in use today still contain all the major components present in the pioneering apparatus of von Karman (1911), together with improved capabilities such as the application of pore fluid pressure and ability to achieve high pressures and temperatures. Paterson and Wong (2005) provide an excellent review of the development of triaxial testing machines.

Experiments in this study were performed using a stiff, fully compensated, servo-controlled triaxial ensemble, designed by Prof. P. Sammonds (Sammonds, 1999) and located in the Rock and Ice Physics Laboratory (RIPL) at University College London (Figure 5.1). It is a 'conventional' triaxial cell; capable of deforming the sample uniaxially under hydrostatic stress conditions, i.e., in the presence of a confining pressure. As a result, two of the three principal stresses are always equal during experimentation (Figure 5.2 (c)).

### 5.2.2 Pressure vessel

The pressure vessel (Figure 5.2 (a)) is 1060 mm long and has 130 mm internal and 400 mm external diameters. It is made from 3.5% nickel chrome alloy steel (fully heat-treated to Rockwell C hardness of c.37) and weighs approximately 750 g. In its present setup, electrically isolated from the sample assembly, it is capable of achieving a maximum axial force of 1500 kN and confining pressures up to 200 MPa (equivalent to the hydrostatic pressure at approximately 7 km depth), ideal for studying processes operating within the Earth's brittle crust, such as earthquakes.

The vessel contains a vertically positioned, stepped, balanced ram arrangement located inside a servo-controlled loading frame (Figure 5.3). The pressure balancing, i.e., pressure applied to the bottom surface is matched by an equal pressure on the upper surface, ensures that the ends of the sample were loaded to the same pressure as the applied confining pressure prior to any additional loading by the actuator piston. The vessel is connected to the actuator piston and load cell via a yoke (Figure 5.2 (b)) and under test conditions is shielded by a plastic guard for safety. The rock sample assembly, described in Section 5.2.4, separates top and bottom rams (Figure 5.3) and loading occurs through the top piston and top ram. An o-ring and mitre ring system seals the closures and pistons, effective due to their excellent elastic properties.

Figure 5.1: Triaxial deformation ensemble and instrumentation at UCL

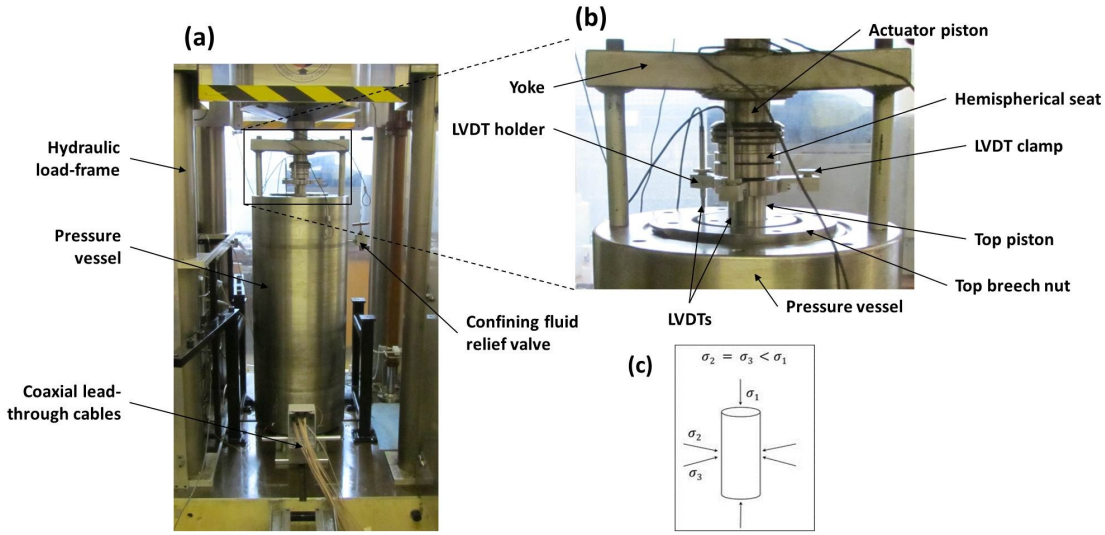


Figure 5.2: The pressure vessel at UCL Rock and Ice Physics Laboratory: (a) Photograph of the pressure vessel within its hydraulic load-frame (b) Close-up photograph of components at top of pressure vessel (c) System of principal stresses within a conventional triaxial compression experiment; $\sigma_3$ is the confining pressure and $\sigma_1$ is the loading pressure and $\sigma_3 = \sigma_2 < \sigma_1$

### 5.2.3 Actuator piston

The hydraulic actuator piston applies the axial load during an experiment. It is powered by a hydraulic ringmain and can operate in both directions, allowing control of both loading and unloading. It and the connected load cell are mounted onto a moving machine crosshead (Figure 5.1), independent from the actuator, controlled using a hydraulic clamping/unclamping system. The maximum compressive load that the actuator piston can achieve is 1.5 MN (c.150 tonnes) applied over a 40 mm diameter sample, equal to a pressure of 1193 MPa; more than sufficent for the experiments in this study, where the maximum applied stress was less than 200 MPa. Closed-loop control of the actuator is maintained by the servo-controller which uses either the load transducers, a large internal linear variable displacement transducer (LVDT) (accurate to 0.1 V) or more sensitive external LVDTs (accurate to 0.01 V) to provide the feedback signal. The actuator can be set to advance at a constant rate to apply a constant axial strain rate on the sample. This is done by means of a ramp generator, which uses feedback signals from the two externally mounted LVDTs (Figure 5.2 (a) and (b)). Using feedback signals from the load transducers in the load cell, it can also be set to maintain a constant loading rate, resulting in a constant axial stress rate being applied to the sample. A third mode is also available whereby a constant applied load is exerted on the sample (conventional creep or relaxation experiments). The feedback control loop helps to ensure a stiff loading system which unloads at a faster rate than the sample. This prevents the premature catastrophic failure of the rock that is likely to occur in a system which is not stiff (Rist et al., 1991). The internal LVDT is mounted inside the crosshead and was used to move the ram more quickly and less accurately than the externally mounted LVDTs, such as during experi-

mental setup and dismantling stages. The externally mounted LVDTs were used during the experiment itelf when more accurate displacement measurements were required. A hemispherical seat between the actuator piston and the top piston ensures even loading of the sample during an experiment.

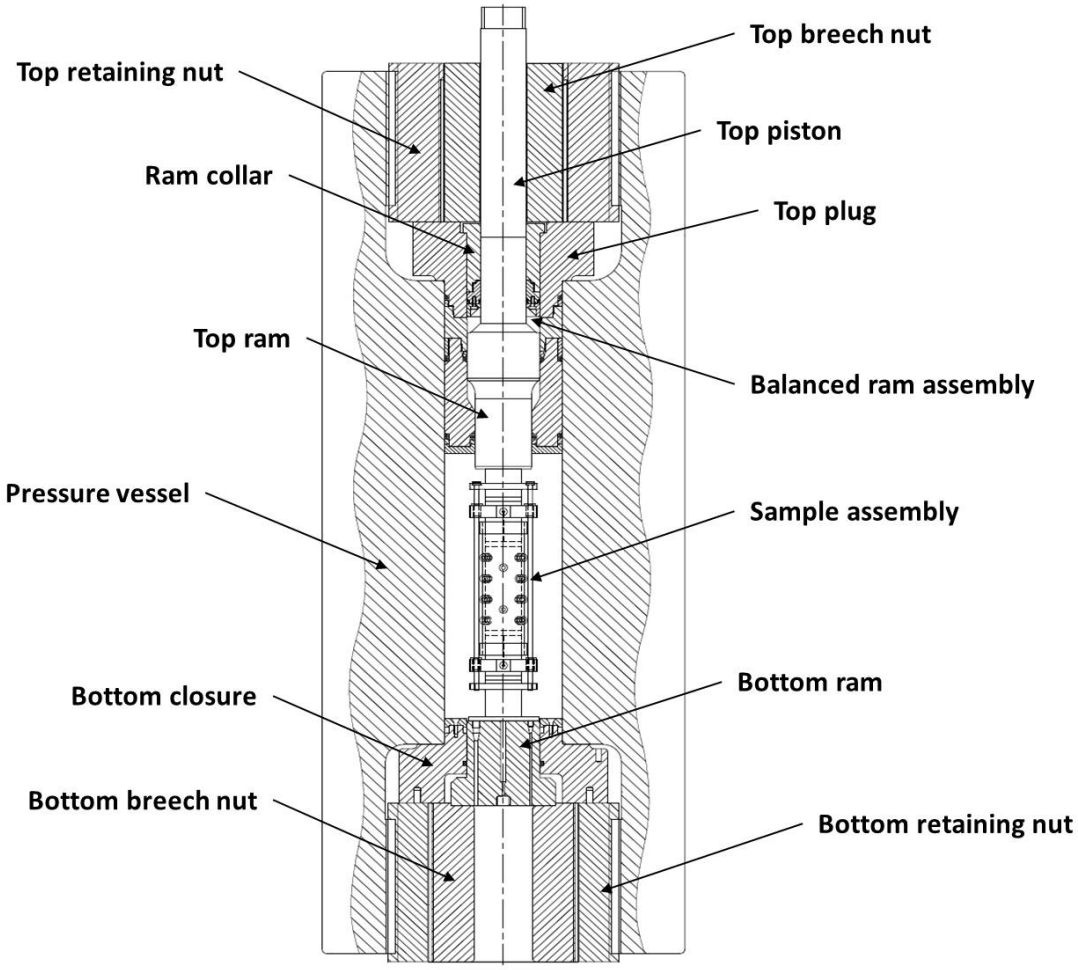


Figure 5.3: 2D cross-section of the triaxial ensemble at UCL (courtesy of N. Hughes)

### 5.2.4 Rock sample assembly

The sample assembly was placed atop the base plate assembly (Figures 5.4 and 5.5) and sealed within the pressure vessel during testing. The rock sample must be completely electrically isolated from its surroundings as well as isolated from the confining medium. Additionally, pore fluid must be able to penetrate the rock homogeneously. This section details the electrical isolation, pore fluid and jacketing systems as well as the sensor arrangement and lead-through system which relayed the data from the sensors inside the pressure vessel to the instrumentation.

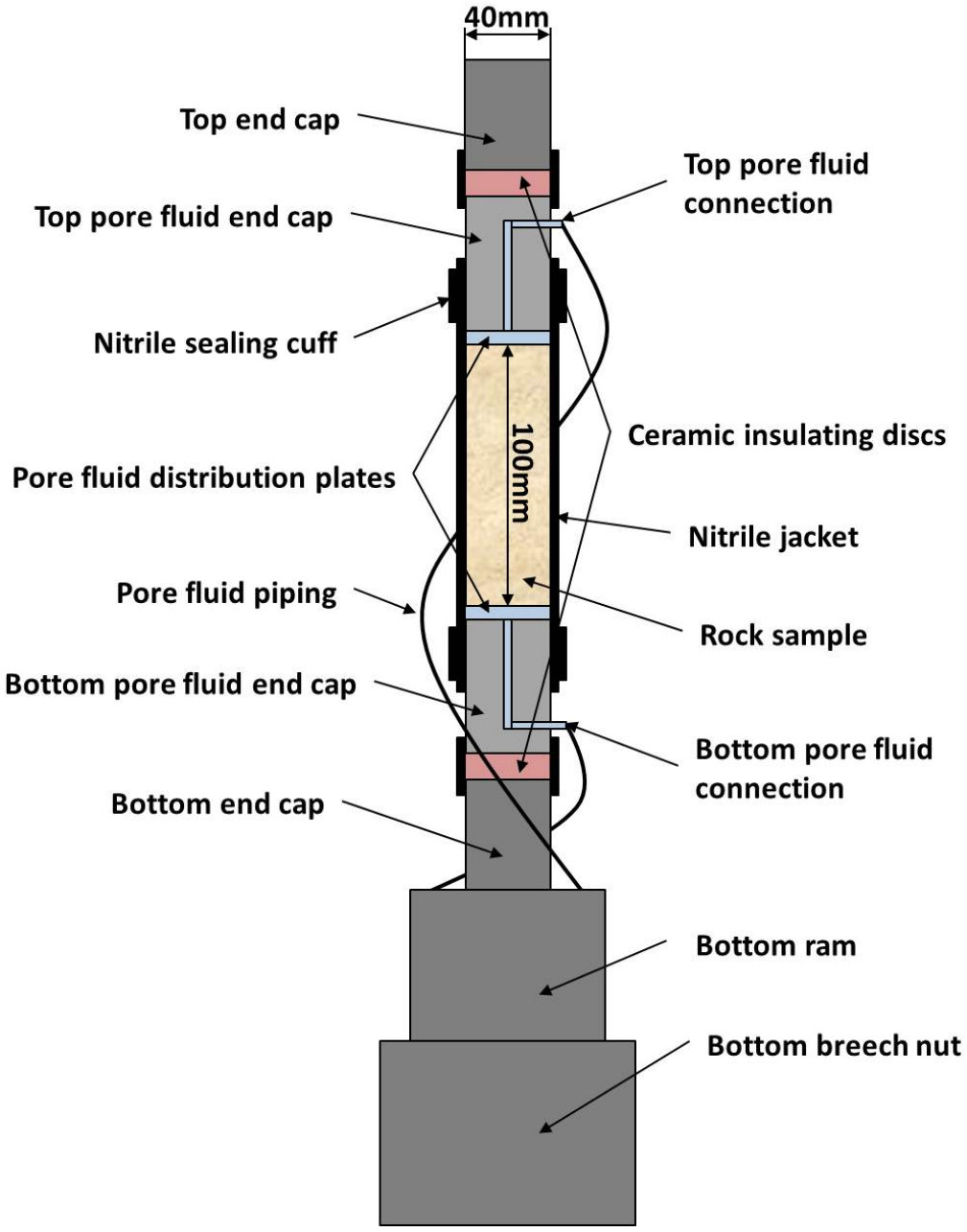


Figure 5.4: 2D schematic cross-section of the sample assembly showing all the main components (modified from Clint (1999))

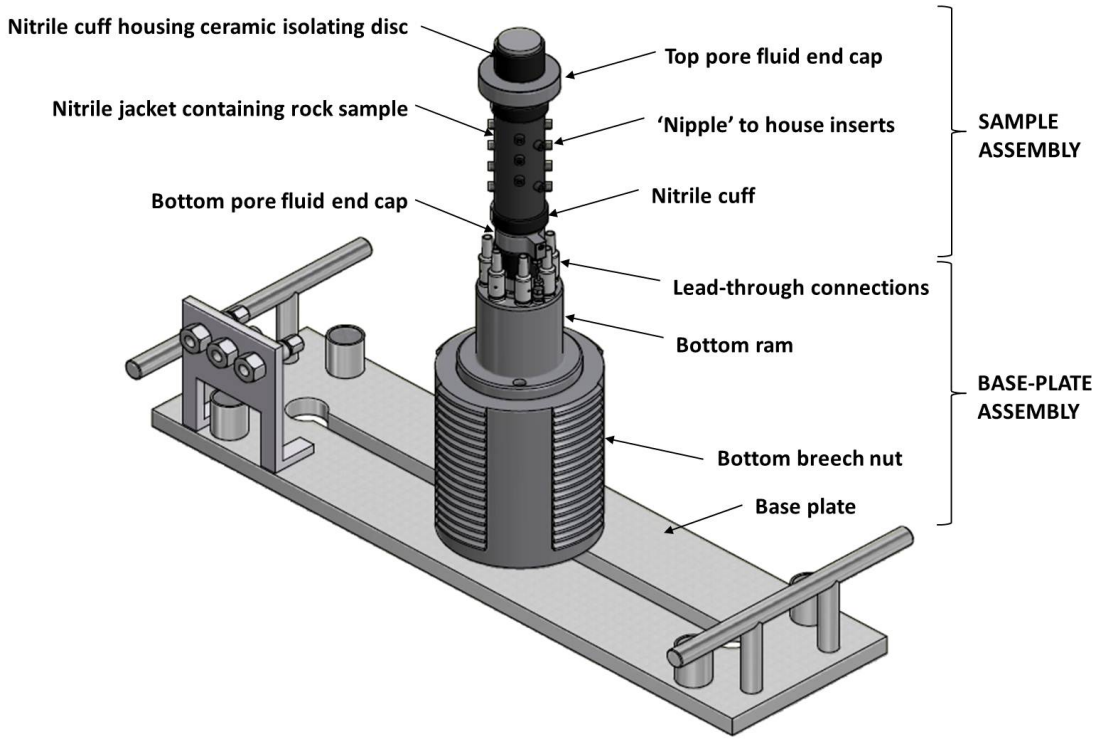


Figure 5.5: 3D diagram of the sample assembly and base plate assembly (courtesy of N. Hughes)

#### 5.2.4.1 Jacketing system and sensor inserts

A jacketing system, modified slightly for this study from the original design by Peter Sammonds and Lazlo Lombas (Lazlo Lombas Consultancy), was used to isolate the pore fluid pressure and sample from the confining silicone oil. This served to prevent the oil from entering the cracks and pores in the rock, allowing pore fluid conditions to be controlled independently. The jackets are made from 3 mm thick fluoroelastomer nitrile with an internal diameter of 40 mm to fit snugly around the sample and are rated for pressures up to 400 MPa and temperatures up to 100°C. Rock samples were placed inside the jacket and sealed onto the pore fluid end caps with two nitrile cuffs stretched over each end of the jacketed sample (Figure 5.5). Application of confining pressure serves to improve the seal by pressing the jacket firmly against the rock surface.

Sensors comprised 5 mm diameter aluminium and brass inserts which were housed in the 18 nitrile 'nipples' extruding from the jacket (Figure 5.6). The nipples contained internal o-rings in their circumference, effectively sealing the inserts inside them and holding them in direct contact with the sample. The inserts were concave at one end to ensure that the whole surface of the insert was in contact with the convex sample surface. Application of confining pressure ensured excellent contact of the inserts with the sample surface throughout testing. Sensor configurations varied slightly during the study, full details of which are discussed in Chapters 7 through 10, which present the experimental results.

Brass inserts (Figure 5.7 (b) and (c)) were used as electrodes for the electric current measurements, with current flow between two electrodes being the quantity measured.

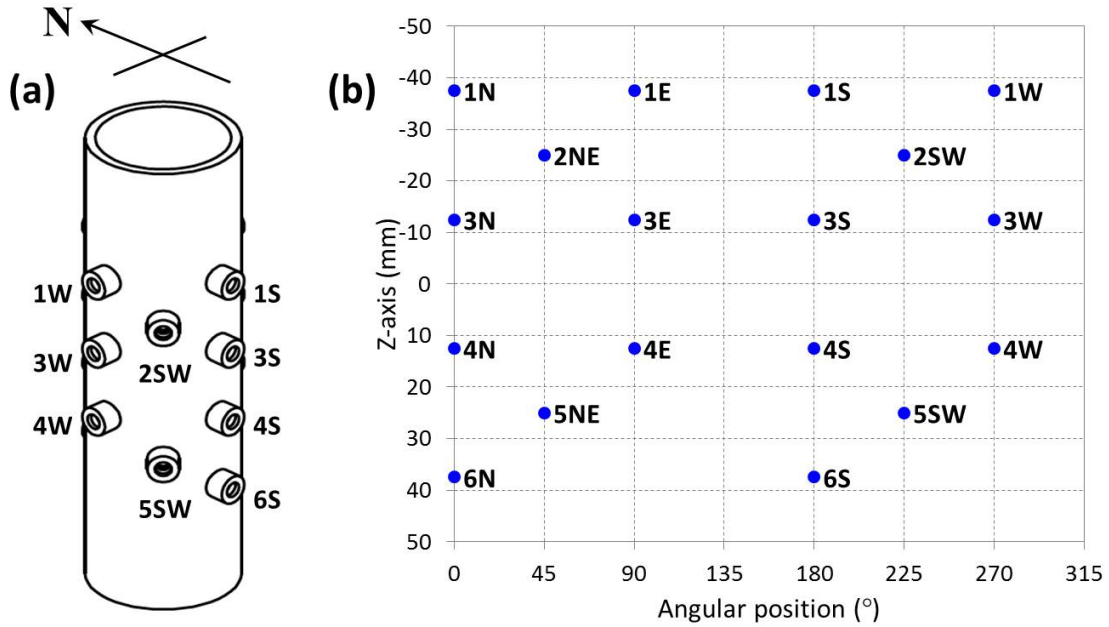


Figure 5.6: Sensor arrangement around the sample jacket: (a) 3D diagram of the jacket showing the positions of inserts with their labels (b) Angular position of each of the sensor inserts on the sample jacket

The signal wire inside a coaxial cable was soldered into the pin on one brass insert and the earth wire was soldered into the pin on another, making an electrode pair (Figure 5.7 (a) and (c)). The wires at the other end of the cable were separated and soldered into separate pin connectors to connect into the two lead-through connections for one particular channel. Any exposed wires were covered with heat shrink, black for negative (earth wire) and red for positive (signal wire).

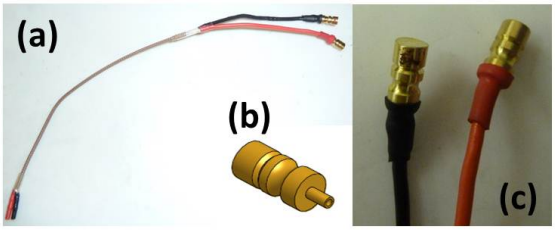


Figure 5.7: Electrodes: (a) Photograph of electrode pair with lead-through connector pins (b) 3D diagram of brass insert showing grooves which sealed into the nipple o-rings (c) Close-up photograph of electrode pair

The aluminium inserts were used to make piezoelectric transducers for detecting acoustic emissions and measuring ultrasonic wave velocity through the sample (Figure 5.8). Piezoelectric crystals (PZT-5A lead zirconate titanate manufactured by Boston Piezo-Optics, Inc), which convert mechanical wave energy into an electric signal, were attached to the flat end of the aluminium inserts which were then screwed into a specially designed stainless steel housing. This housing contains a hole arrangement through which the signal wire of a coaxial cable was soldered onto an electrode consisting of a small disk of adhesive copper tape attached to one side of a plastic insulating disk sitting inside the housing. Care was taken to ensure no contact of the solder or disk with the housing itself. Once the

insert was screwed into the housing, the signal wire was compressed between the copper tape and the piezoelectric crystal ensuring good electrical contact. The transducer was then grounded to the housing by soldering the earth wire of the coaxial cable to a pin screwed into the side of the housing. As with the electrodes, the wires at the other end of the cable were separated and soldered into separate pin connectors to connect into the two lead-through connections for one particular channel. Both compressional (P-wave) and transverse (S-wave) PZT crystals were glued directly onto the inserts to ensure good mechanical contact with the sample. Care was taken with the square 3 mm x 3 mm S-wave crystals to orientate the direction of motion either vertically or horizontally with respect to the concavity of the insert so that the sensor detected either horizontally or vertically polarised S-waves. Once screwed into the housing, the top of the housing was marked with the direction of crystal orientation so that the sensor could be correctly aligned prior to each experiment. The 3 mm diameter P-wave crystals were attached such that the positive direction was towards the top of the housing and the negative direction towards the insert. Exposed wires were covered with heat shrink, black for ground and red for signal. S-wave transducers were distinguished using small pieces of yellow and black heat shrink; yellow on top of black for horizontally aligned sensors and black on top of yellow for vertically aligned sensors.

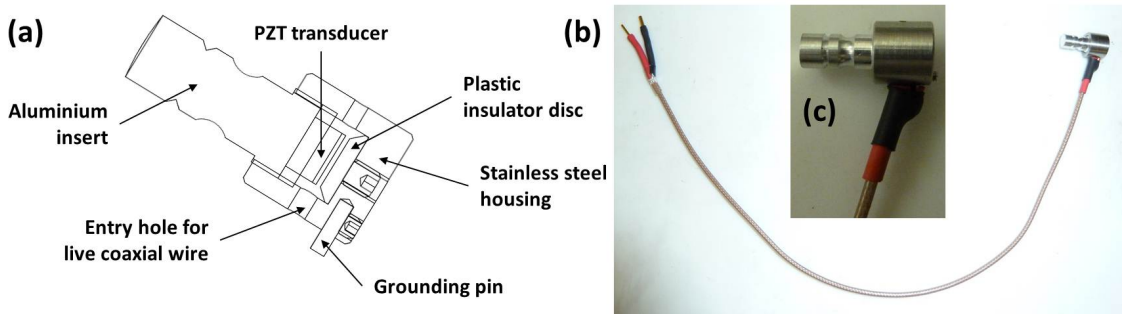


Figure 5.8: Piezoelectric transducers: (a) 2D cross-section of piezoelectric transducer showing aluminium insert, housing and arrangement within the housing (b) Photograph of piezoelectric transducer (c) Close-up photograph of piezoelectric transducer

#### 5.2.4.2 Lead-through system

Data collected inside the vessel was relayed to the instruments outside the vessel by a special lead-through system, designed to ensure isolation of the sample assembly from the auxiliary instruments and the rest of the vessel. The lead-throughs consisted of a ceramic plug (Figure 5.9 (a)) housing eight brass pins (Figure 5.9 (b)), seven with male connectors at one end and one with a female connector. The pins were sealed using a standard o-ring and PTFE backing ring arrangement and were positioned in the plug such that the connector end came out at the top end of the plug when plugged into the bottom ram (Figure 5.10). The top end of the plug and connectors reside inside the pressure vessel during an experiment. The coaxial pin connectors on the sensors were plugged into these

male and female connectors prior to lowering the pressure vessel over the sample assembly, allowing the acoustic and electrical data to be relayed to the pins from the sensors. Four coaxial cables were numbered and soldered to the pins at the bottom of the ceramic plug in such a way that it was certain which pins related to which cable. The pins were arranged such that six of the male connectors and the female connector were positioned around the edge of the plug while the remaining male connector sat in the centre. The first cable was soldered to the central male pin (earth/negative) and the female pin (signal/positive). The subsequent cables were then soldered to the remaining male pins so that, looking at the top of the plug, each cable was connected first signal and then earth consecutively in a clockwise direction (Figure 5.9 (c)). All soldered connections were covered in insulating polyolefin heat shrink. The cables were then fed through the bottom breech nut and were connected into either the picoammeter or the AE recording system (see Section 5.3), depending on the type of relayed information, via BNC connections. Since 18 channels were available in the jacket, five lead-through plugs were installed in the bottom ram, sealed with the o-ring and PTFE backing system and each with four coaxial lead-through cables which were soldered as per the system just described and numbered consecutively up to 20, clockwise within each ceramic plug and clockwise around the bottom ram. When setting up an experiment, care was always taken to record which sensors were connected to which lead-through pins before lowering the vessel onto the sample assembly.

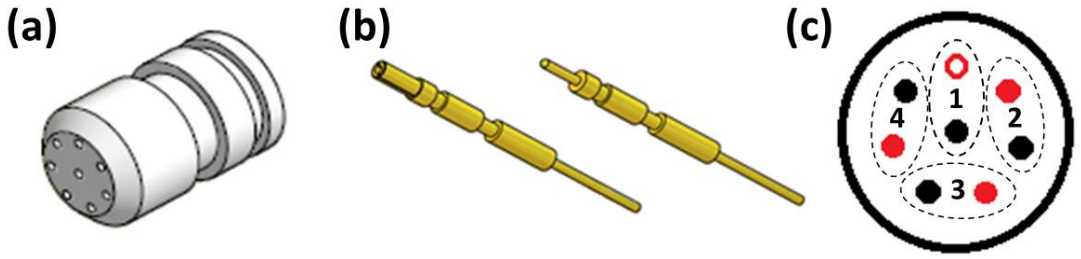


Figure 5.9: 3D diagram of (a) ceramic plug with holes for eight (b) brass connector pins soldered to four coaxial cables as per (c); filled circles - male connectors, open circle - female connector, red - signal/positive connection, black - earth/negative connection

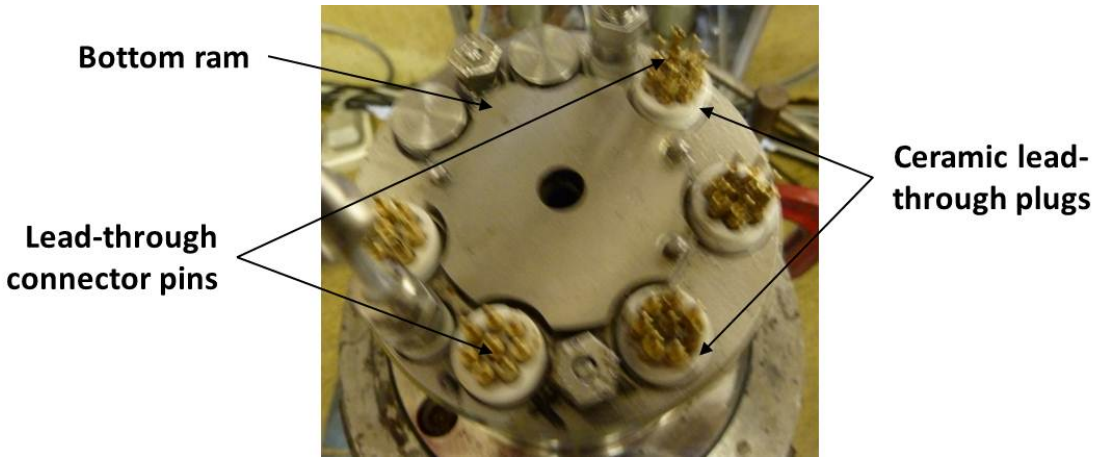


Figure 5.10: Plan view photograph of the lead-through plug arrangement in the bottom ram

#### 5.2.4.3 Pore fluid

Pore fluid was introduced to the sample through connections in the top and bottom pore fluid end caps of the sample assembly (Figure 5.4). The pipes carrying the pore fluid seal into these termination fittings by means of a 20° cone-shaped end which clamps around the pipe when the fitting is screwed tight. Within the jacket, pore fluid distribution plates were placed at both ends of the sample to allow pore fluid to spread evenly across the sample ends before permeating into the sample. In order to ensure complete saturation, the pressurised fluid permeates through the sample from the bottom to the top. During saturated deformation experiments, drained conditions were used so that fluid could flow in or out of either end of the sample to maintain the set pore pressure. For experiments measuring permeability and streaming current, the pore fluid connection at the top of the sample was opened, allowing fluid to flow up the sample in the direction of the pressure gradient. The pore fluid piping exits the vessel through a ceramic plug sealed into the bottom ram with the standard o-ring and PTFE backing ring system (Figure 5.11).

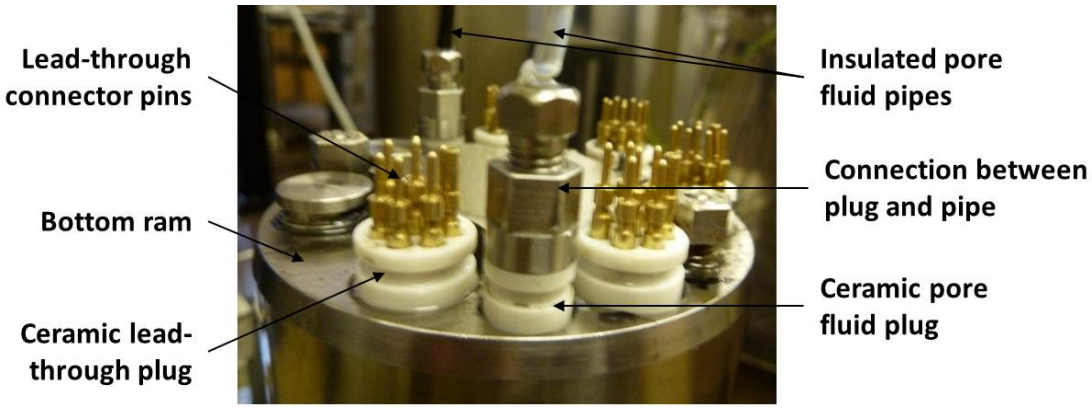


Figure 5.11: Side view photograph of the bottom ram pore fluid plug arrangement

#### 5.2.4.4 Electrical isolation

Electrical isolation of the sample is essential to eliminate noise in the electric current measurements. Inside the pressure vessel, an insulating confining medium was used and the whole sample assembly was isolated from the rest of the vessel by means of:

- Two ceramic insulating discs placed above and below the top and bottom pore fluid end caps (see Figure 5.4).
- Insulating polyolefin heat shrink around the sensor wires, lead-through connections and whole length of pore fluid piping.
- Seven ceramic plugs in the bottom ram, five encasing the lead-through connections and two encasing the pore-fluid piping (Figures 5.10 and 5.11).

- Ceramic insulating disks either side of both connections between the pore fluid piping and the pipework to the pore fluid intensifier.

The pressure vessel itself acted as a Faraday cage to shield the sample assembly from any external electrical noise and all auxiliary instruments were grounded. Because the electric currents being measured were so small (pA to nA), decent signals were difficult to obtain as laboratory electrical noise continued to affect the readings even after grounding the system. This meant that only around half of the experiments yielded useable signals.

### 5.2.5 Pressure application systems

#### 5.2.5.1 Intensifiers / pore fluid volumometers

Both the confining pressure and the pore pressure were regulated using a system of highly sensitive intensifiers / pore fluid volumometers, which also monitored the change in pore volume during experimentation (Figure 5.12). The intensifiers used in the UCL Rock and Ice Physics Laboratory incorporate high-response servo-valves and feedback loop control techniques to obtain the high accuracy and resolution required during testing; maintaining pressure stability whilst achieving the required control response. The ratio of the larger low pressure piston area to the smaller high pressure piston area enables accurate control of the pressure in the high pressure cyclinder. Each intensifier of known volume was fitted with a pressure transducer connected to a digital controller. Temperature-induced pressure fluctuations were minimised by controlling the temperature in the laboratory with an air conditioning unit. The change in fluid volume within the intensifier was monitored by an integrated LVDT which measured the displacement of the piston. Once connected into the pore fluid pipe network, this volume change equated to the precise pore volume change within the fully saturated sample, allowing pore volume variations during deformation to be quantified.

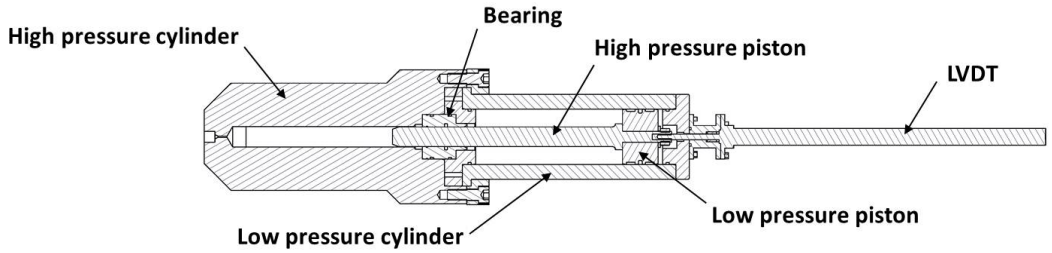


Figure 5.12: 2D cross-section of a typical intensifier/pore volumometer used in the UCL Rock and Ice Physics Laboratory (courtesy of N. Hughes)

#### 5.2.5.2 Confining pressure

A confining medium exerts a hydrostatic force on the rock sample during deformation, maintaining pressure in the two principal stress directions, $\sigma_2$ and $\sigma_3$ (Figure 5.2 (c)). Silicone oil with viscosity of 100 cS was used as the confining medium, chosen for the following reasons: (a) it has a low coefficient of volume expansion (Table 5.3), (b) the flash point is above 150°C and (c) silicone oil is an electrical insulator, important to ensure isolation of the sample assembly. It was purchased from Dow Corning Ltd and some of its physical properties are given in Table 5.3. Pressure was achieved using a two-stage hydraulic pump manufactured by Stanstead Fluid Power. This pump is theoretically capable of attaining a maximum pressure of 400 MPa. However, the pump was unable to kick into the second stage for the entirety of this study and so could only apply a pressure up to 30 MPa. For all experiments requiring a confining pressure above 30 MPa, the pressure was initially applied using the pump and then topped up using the intensifier hand pump to manually pump oil from the reservoir, through the intensifier and into the vessel.

Table 5.3: Physical properties of 100 cS silicone oil at room temperature and pressure

| **Property** | **100 cS silicone oil** |
|---|---|
| Specific gravity at 25°C | 0.960 |
| Coefficient of thermal expansion per °C | 0.00095 |
| Surface tension at 25°C ($Nm^{-1}$) | 20.9 |
| Flash point (°C) | >150 |

As the oil entered the vessel, displaced air was expelled through a relief valve situated at the top of the vessel. Once silicone oil began to flow out of the relief valve in a steady stream, the vessel was free of air and confining oil filled the volume along the loading ram anulus above an intermediate region of the upper piston. At this point, the relief valve was closed and pressurisation of the oil inside the vessel could begin. This procedure ensures an equal hydrostatic stress is applied to all regions of the sample prior to the application of deviatoric stress, the basis of the balanced ram arrangement. Once the desired confining pressure was reached, the vessel was isolated and the confining pressure allowed to regain thermal equilibrium. Confining pressure was monitored by a pressure transducer and was maintained constant during experimentation using a 22 $cm^3$ high-precision, servo-controlled intensifier. The jacketing system (Section 5.2.4) ensured that the rock sample was completely isolated from the confining fluid.

#### 5.2.5.3 Pore pressure

As discussed in Sections 2.2 and 4.8, most crustal rocks are saturated with fluid which exerts a hydrostatic pressure within the void space. This pore pressure acts normal to the surface of the grains, reducing the effect of the external stresses acting on the rock. Pore pressure was monitored by a pressure transducer situated in the pore fluid pipe

network close to the sample. During experimentation, it was maintained constant by a 60 $cm^3$ servo-controlled intensifier connected to the sample assembly via a network of high-pressure piping (Figure 5.13). All piping has an internal diameter of $^1/_{16}$" and is capable of maintaining a maximum pressure of 400 MPa. Full saturation of specimens was checked by ensuring that the pore fluid pressure remained constant for at least one hour after equilibration. Connection of the pore fluid plumbing system to both ends of the sample helped to ensure that pore pressure equilibrium was maintained even in samples with low permeability (Paterson and Wong, 2005). In order to ensure electrical isolation of the sample assembly, the pore fluid piping was encased in insulating polyolefin heat shrink and passed through a ceramic plug in the bottom ram. It then fed through the bottom breech nut to a connection on the base plate outside the vessel which connected with the piping from the pore fluid intensifier (Figure 5.14). At this connection, the pore fluid passed through ceramic insulating blocks, which ensured that the fluid in the sample remained isolated from the fluid in the intensifier.

All saturated experiments were conducted under a confining pressure ($P_c$) of 50 MPa and a pore pressure ($P_p$) of 20 MPa. First, the $P_c$ was taken to 30 MPa and then the sample saturated with a $P_p$ of 20 MPa (see Section 5.5.5) before the $P_c$ was taken up to 50 MPa. The whole set-up was then left overnight to allow time for the pressures within the vessel to fully equilibrate and to ensure complete rock saturation. This pressure application protocol ensured two things:

1. That the sample was never subjected to an effective confining pressure ($P_{eff}$) greater than the target $P_{eff}$ required for that particular experiment.
2. The $P_p$ never exceeded the $P_c$ since this situation would lead to a pore fluid overpressure and cause silicone oil to enter the jacket, rendering the experiment useless.

#### 5.2.5.4 Pore fluid separators

In order to establish the effect of ions on the generation of electric current, the experimental program involved using an ionic salt solution as one type of pore fluid (the other was de-ionised water). Since this type of fluid is corrosive, causing rust and damage to the internal seals and materials of the intensifiers, two fluid separators were installed; one connected to the sample fluid inlet and the other to the sample fluid outlet. Figure 5.15 shows the main components. The design is basically that of a pressure vessel (50 $cm^3$ internal volume) with a moving inner plug (shuttle) sealed using a central piston GLYD seal with wear rings on the outer ends. This sealing system can support up to 100 MPa of pore fluid pressure on either side of the shuttle. Fluid flows into and out of either end of the separators through two outer flanges screwed into position and sealed with mitre rings.

The separators were plumbed into the fluid piping system between the pore fluid intensifier and the sample (Figure 5.16). One end of each separator was connected to the intensifier

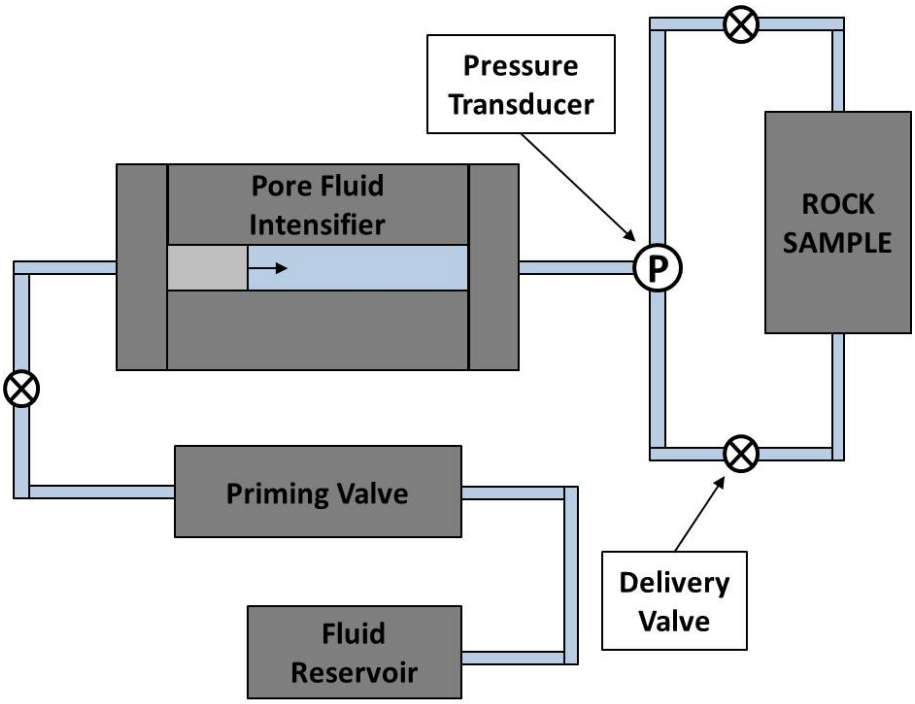


Figure 5.13: Schematic diagram of the pore fluid pipe network (modified from Clint (1999))

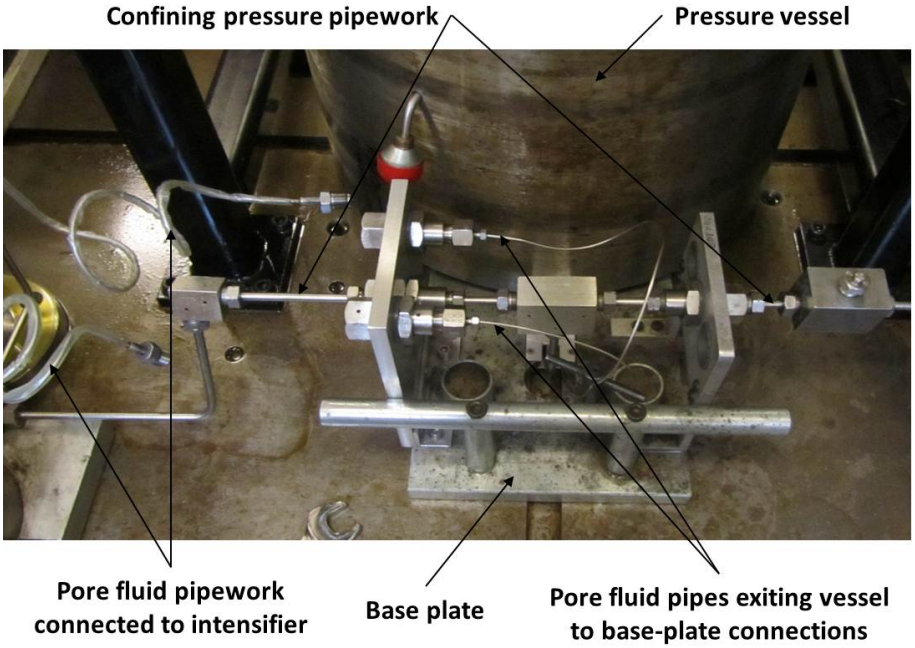


Figure 5.14: Photograph of pore fluid and confining pressure connections outside the pressure vessel

outlet and de-ionised water passed into it, displacing the shuttle to the other end and expelling all the air in that end. The salt solution was then introduced to that end using a manual pump, pushing the shuttle back towards the intensifier end and expelling any air in that side through a bleed valve. When the shuttle reached the intensifier end, it was certain that the separator was full of brine and that any air had been expelled. Once set-up in this way, the pore fluid piping from the outlet at the brine end of the separator could be connected to the fluid piping around the rock sample at the exit from the base plate assembly (Figure 5.14). Pressure could then be applied using the pore fluid intensifier. It was applied by the introduction of pressurised water from the intensifier into the separator, pushing the shuttle and compressing the brine on the other side to the required pressure. Pressure transducers on each separator monitored the pressure in the fluid pipes close to the sample.

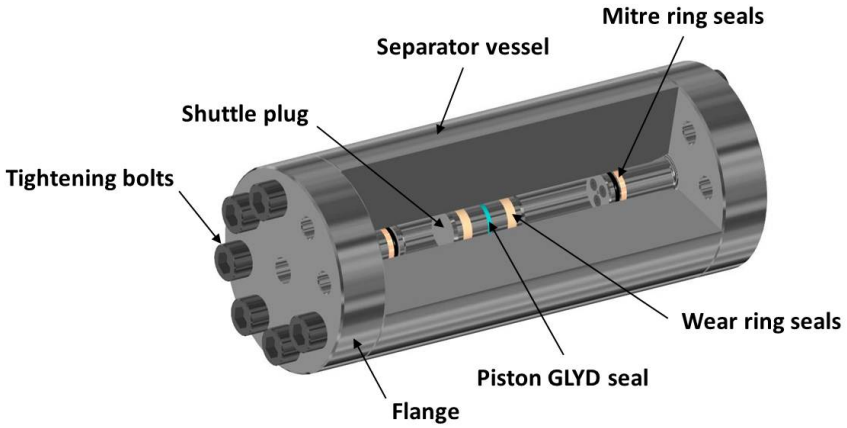


Figure 5.15: 3D cut-away section showing the main separator components (courtesy of N. Hughes)

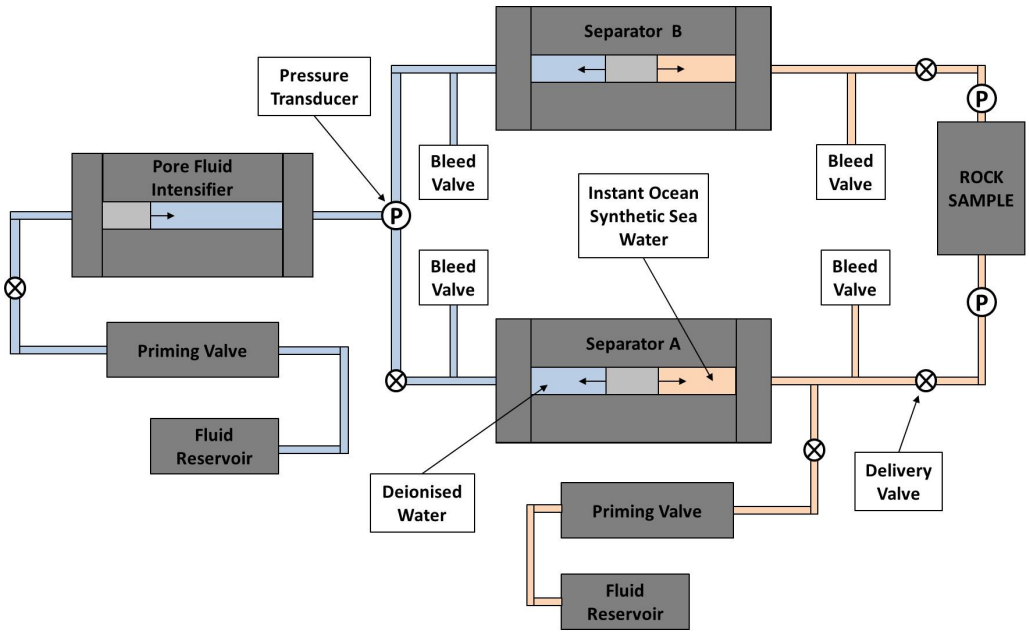


Figure 5.16: Schematic diagram showing the pore fluid plumbing system with separators incorporated (modified from Clint (1999))

## 5.3 Measurements and Data Logging

### 5.3.1 Introduction

This section describes how data was acquired during the triaxial experiments. The measurement instrumentation (i.e., the electronic recording equipment) connected to the triaxial cell is shown in Figure 5.17.

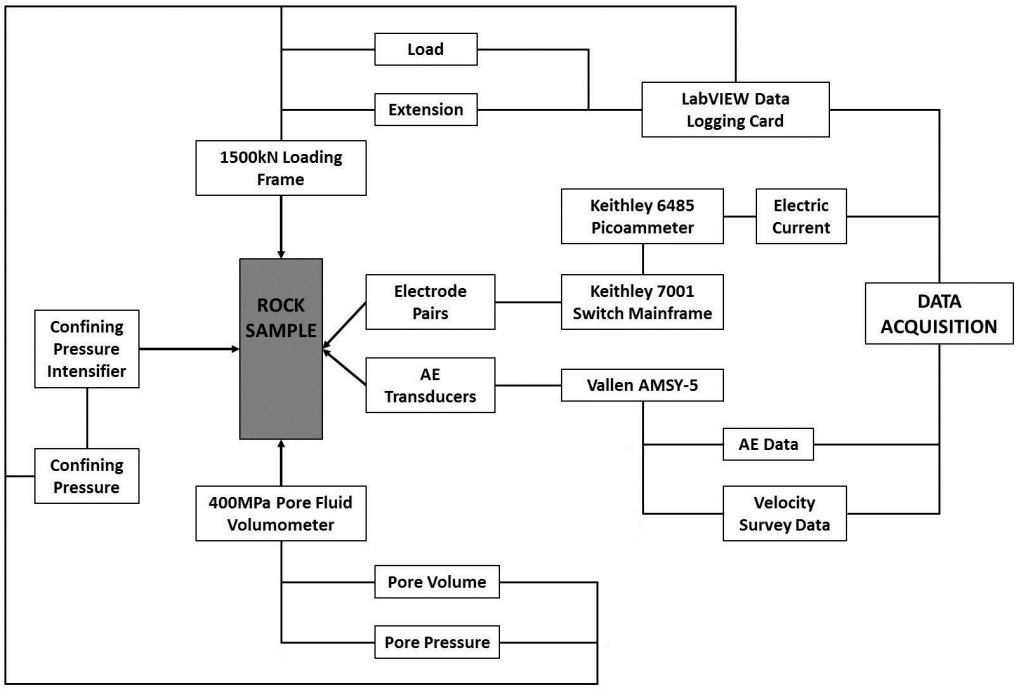


Figure 5.17: Block diagram showing the instrumentation involved in a triaxial deformation experiment and the resulting data acquired

### 5.3.2 Parametric data logging

Measurements of axial load, axial displacement, confining pressure, pore pressure and pore fluid piston displacement were acquired using a National Instruments CB-68LP multichannel data acquisition card. It was connected to a desktop computer located next to the deformation apparatus and recorded the signal voltage output from the load cell, LVDTs and pressure intensifiers. Data was recorded and saved at a sampling rate of 1Hz using a LabVIEW data acquisition program which converted the voltages into SI values of length, volume, force and pressure using conversions determined from the equipment calibrations (Section 5.4). These values were then used to control the actuator piston and pressure intensifiers via the electronic servo-controller. Real-time graphs of the incoming data, plotted in LabVIEW, allowed the experiments to be monitored throughout.

### 5.3.3 Load measurements

Load measurements were made with an external load cell which measures the compressive force applied to the end of the sample by the servo-controlled actuator. A hemispherical seat was placed between the loading actuator and the upper ram assembly to correct for distortion of angles between these surfaces, allowing for uneven loading.

The differential stress applied to the sample, $\sigma$ $(= \sigma_1 - \sigma_3)$, is calculated from the force measured by the load cell using:

$$\sigma = \frac{F}{A} \tag{5.1}$$

where F is the applied differential load (fully compensated for confining pressure) and A is the cross-sectional area of the sample (i.e., the area over which the load is applied).

### 5.3.4 Displacement measurements

During loading, changes in displacement of the loading column (top piston, top ram and sample assembly - see Figure 5.3) were recorded using the pair of LVDTs situated between the pressure vessel and the crosshead (Figure 5.2 (b)). This displacement value was first converted to linear strain, $\varepsilon$, using:

$$\varepsilon = \frac{\delta l}{l_0} \tag{5.2}$$

where $\delta l$ is the change in length of the sample from its original length, $l_0$. It was then corrected for the stiffness of the testing machine to find the sample strain, $\varepsilon_s$, using:

$$\varepsilon_s = \varepsilon - \frac{\sigma}{k_{machine}} \tag{5.3}$$

where $k_{machine}$ is the machine stiffness (see Section 5.4).

### 5.3.5 Acoustic emissions

Acoustic emissions (AE) during triaxial experiments were detected by PZT-5A (lead zirconate titanate) piezoelectric crystals housed inside the concave aluminium inserts (Figure 5.8) and recorded by a multi-channel Vallen AMSY-5. Since acoustic emissions span a range of frequencies in the 100 kHz to 1 MHz range (high frequency) (Scholz, 1968a), crystals of 1 MHz resonant frequency were chosen to reduce noise and record only signals of interest. Read et al. (1995) describe their frequency response. Ten channels were measured, enabling detection of AEs from all parts of the sample. Signals from the piezoelectric crystals were relayed from inside the pressure vessel along coaxial cable via the lead-through system in the base plate and then pre-amplified with a 40 dB relative gain before reaching the acoustic signal pre-processor in the AMSY-5 system. Since microcrack amplitudes in Carrara marble are very low, the noise threshold for each AE channel

was set as low as possible depending on the ambient noise. This was nominally 40 dB but, since each piezoelectric crystal had a slightly different susceptibility to pick up background noise, the threshold was adjusted so that no channels were triggered by noise before the experiment began. Most commonly, values between 45-55 dB were used. The Vallen AMSY-5 recorded a variety of data during the course of a test, including waveform characteristics and AE hits information (time, amplitude and energy). It is hit driven, storing information in grouping bins when an AE is detected. It is possible that high hit rates could lead to bin saturation, resulting in some data loss. Additionally, microcrack amplitudes in Carrara marble are generally small in comparison to those in more brittle rocks. The consequence of this is that data at the bottom of the amplitude range are incompletely recorded. Cox and Meredith (1993) discuss under recording of events in detail and Sammonds et al. (1994) take it into account in their *b*-value calculations and mean crack analysis. For *b*-value calculations and mean crack analysis a numerical threshold was chosen to (1) normalise the experimental data to the same amplitude level and (2) prevent errors introduced through least-significant-bit noise in the a-d converter measuring the signal amplitudes.

### 5.3.6 Ultrasonic wave velocities

Changes in ultrasonic wave velocity were measured by means of the pulse transmission technique (Birch, 1960) between pairs of AE transducers. Velocity surveys were conducted by the Vallen AMSY-5 at constant time intervals during an experiment. A pulse of acoustic energy was sent through the sample from each transducer in turn and its arrival at all the other sensors was recorded. Ten AE channels enabled velocities to be measured through the sample at five different incident angles, with the aim of obtaining enough data to solve for the full crack density tensor (Sayers and Kachanov, 1995).

During processing, wave arrival times were picked manually from these survey waveforms. Following Hornby (1998), first zero-crossing arrival times were picked rather than actual first arrivals since they were easier to pick accurately in the presence of noise. Measured travel times, $t_m$, were calculated from the difference between the picked arrival time and the emission time of the energy pulse. First zero-crossing was also used for emission time to ensure travel times were not over-estimated. Travel time through the aluminium inserts, $t_a$, was found to be 2.0 $\mu$s and 3.8 $\mu$s for P- and S-waves respectively, established by measuring the travel time through a steel dummy sample with known dimensions and wave velocity. Wave velocities, $V$, were calculated using:

$$V = \frac{D}{(t_m - t_a)} \tag{5.4}$$

where $D$ is the distance the wave travels through the sample (which varies according to the incidence angle) and $t_m - t_a$ is the travel time through the sample itself, $t_s$.

The maximum absolute error in a velocity measurement is given as (Hornby, 1998):

$$\Delta V = \frac{\Delta D}{t_m - t_a} + 2D\frac{\Delta t}{(t_m - t_a)^2} \tag{5.5}$$

where $\Delta t_m$ and $\Delta t_a$ are the errors in the travel time picks for $t_m$ and $t_a$, $\Delta t = |\Delta t_m| = |\Delta t_a|$ and $\Delta D$ is the magnitude of the error in the sample diameter or calculated off-axis length measurement (depending on the transducer pair orientation).

To estimate the measurement error, a typical sample diameter of 40 mm was used, measured to the precision of the calipers (0.01 mm). For P-wave propagation, a typical value for $t_s$ is 7.5 $\mu$s with a precision of 0.01 $\mu$s for the travel time picking (equal to the sampling rate). The absolute error of the velocity measurement is then estimated from Equation 5.5 to be $\pm 16$ ms$^{-1}$. This corresponds to a relative error in the velocity estimation of approximately 0.3% for a P-wave propagating at 5500 ms$^{-1}$. For S-wave propagation, a typical value for $t_s$ is 13 $\mu$s while the estimated absolute velocity error is $\pm 6$ ms$^{-1}$. Therefore, the relative error in the velocity estimation is approximately 0.2% for a S-wave propagating at 3000 ms$^{-1}$.

In addition to the measurement error, there is also the systematic error associated with picking the first zero-crossing arrival. However, the primary concern in this study is for velocity change during deformation, calculated as relative to an initial value, rather than absolute values of velocity. Errors associated with estimates of velocity change will be close to the measurement error since the systematic picking error applies equally to initial and instantaneous values.

### 5.3.7 Electric current

The electrodes used were concave brass inserts, 5 mm in diameter, designed to fit around the sample and seal securely in the nitrile jacket (Figure 5.7). Each channel comprises two electrodes connected together and positioned on opposite sides of the sample to measure the electric current flow between them. These channels were connected to the instrumentation by coaxial cable via the lead-through system. A Keithley 6485 Picoammeter and 7001 Switch/Control Mainframe were used to acquire the electric current data, for which I wrote a data acquisition program using LabVIEW (see Appendix A for the code).

The picoammeter has eight current measurement ranges with high speed auto-ranging capabilities and can measure currents from 20 fA to 20 mA at speeds of up to 900 readings per second externally across the IEEE-488 bus. The instrument's feedback circuitry reduces the voltage burden to <200 $\mu$V on the lower measurement ranges allowing it to function like an ideal ammeter so it can make highly accurate current measurements. Instrument noise is extremely low at 4 $\pm$1.6 fA and it has 10 fA to 1 pA resolution in the lowest ranges (<2 nA to 200 nA), making it well-suited for characterising low-current phenomena such as those in this study. Additionally, because the input impedance of the picoammeter is

much lower than the rock resistance, almost all of the electric current generated during deformation flows into the picoammeter.

In order to measure the current from more than one electrode pair channel, a switching mainframe was connected between the lead-throughs and the picoammeter to switch between multiple channels in series. This allowed the picoammeter to take readings from each channel in turn. The switching mainframe automatically adjusted the settling time before triggering a reading and the maximum sampling rate was limited to 2 Hz. Since the mainframe switched through the required channels incrementally, the sample rate for each channel depended on the number of channels used. For example, the maximum sample rate for each channel was 2 Hz but this decreased to 0.5 Hz when four channels were employed.

Background noise in the acquisition system varied between channels and from experiment to experiment with an average of 0.1 $\pm$0.25 nA. It was removed from the electric current data in post-processing:

$$I(t) = I_{raw} - I_b \tag{5.6}$$

where the background noise, $I_b$, is the average of the electric current measured between 0 and 0.0019 sample strain, $\varepsilon_s$ (see Section 5.4 for machine stiffness correction).

One of the main issues encountered during the experimental program was that of noise spikes appearing in the electrical data at intervals that coincided with the ultrasonic velocity surveys. Initially, it was thought that the spikes were due to cross-talk between the electrode lead-through connections and those of the AE transducers. So, in an attempt to remove these spikes, various combinations of lead-through connections were tried with no effect. To ensure that any effect from cross-talk was minimised, the electrical lead-throughs were connected into separate lead-through plugs of their own, away from the AE lead-through plugs, for all experiments. Since all instruments had already been grounded to minimise the background noise during acquisition and all wires and lead-through connections encased in electrically insulating polyolefin heat shrink, there was nothing more that could be done to prevent these spikes. As a result, the issue was dealt with during the data processing stage. Depending on the subsequent analysis, either the 50 s of electrical data during each velocity survey was completely discarded or the noise spikes were filtered out using a running median filter.

According to the results of Stavrakas et al. (2003; 2004) and Anastasiadis et al. (2004), spikes in electric current were observed when they abruptly altered the stress rate of their experiments. Therefore, it may be that the spikes seen in my experiments are caused directly by the passage of the elastic waves through the rock sample as they briefly change the stress field and the elastic modulus of the sample by flexing the crack edges. This could warrant further investigation in the future. It was assumed for the purposes of this study that the overall electric current generated due to inelastic deformation would be unaffected by these spikes, even if they were an immediate elastic response to the passing

seismic wave.

Streaming current is a constant current produced during fluid flow under a constant pressure gradient. The magnitude of the streaming current is the difference between the current generated due to the pressure gradient and the base value in its absence.

### 5.3.8 Angle of shear failure

The angle of shear failure in a sample is the angle between the axial compressive stress direction and the main fracture plane. It was measured using a protractor with an associated measurement error of 0.5°. Readings were taken from both sides of the fault and then averaged. Where there was a broad zone of failure, the main failure plane was considered to be the most obvious fracture plane. In the case of a conjugate main fracture, the angles of both fault planes were measured. Any samples where the main fault trace was curvilinear or went through either end of the sample (described as axial fractures) were not used for any fault angle analysis.

### 5.3.9 Experiment design

Changes and improvements to the sensor configurations and experimental procedure were made to investigate and overcome issues encountered as the experimental program progressed. The final experimental procedure for all the experiments presented in this thesis is described in Section 5.6. Sensor configurations for particular experiments are discussed with their respective results in Chapter 7.

### 5.3.10 Experimental problems

Only those experiments that produced useful data or results are described in this thesis. Out of a total of 58 experiments, four could not be used at all while others yielded useful readings for some but not all of the parameters being measured. Experimental problems leading to missing data included damage of electrodes or transducers during deformation, electrical shorting, servo-control issues leading to shock loading of a sample immediately prior to starting an experiment, confining pressure leaks, instrument failure, broken or noisy lead-through connections, loose LVDT tips and loose electrical connections between the LVDTs and the servo-control.

## 5.4 Calibration of the Experimental Equipment

### 5.4.1 Introduction

The accuracy of experimental data depends heavily on the accuracy of the equipment used to measure it. Consequently, calibration of the testing equipment prior to undertaking any experimentation is essential to eliminate systematic errors, ensure that the data are as accurate as possible and to quantify their experimental uncertainty. Uncertainty in the pore pressure, pore volume, confining pressure and strain (determined from piston displacement) readings depends on accurately calibrated pressure transducers and LVDTs, whilst that in the stress readings (calculated from applied load) relies on the accuracy of the load cell.

### 5.4.2 LVDTs

A barrel micrometer (manufactured by Mitutoyo, UK) with a resolution of 0.002 mm was used to accurately calibrate the LVDTs that measure the vertical displacement of the loading column. Each LVDT was clamped in turn into the micrometer and the barrel moved in 1 mm increments. The output voltage from the LVDT was measured at each increment and recorded. The procedure was repeated three times and the average voltage output for each 1 mm increment was calculated. The conversion factor was established by plotting the barrel displacement as a function of average output voltage (Figure 5.18 (a) and (b)) and then input into the LabVIEW configuration file.

### 5.4.3 Load cell

The load cell for the triaxial ensemble was accurately calibrated on purchase by Harry Stanger, Material Consultants (UK) using a proving ring with a maximum range of 200 kN. The servo-controlled actuator applied a load to the proving ring in increments of 25 kN as read from the proving ring and the voltage output from the load cell was recorded. The procedure was repeated three times to obtain the average voltage output for each load and the load then plotted as a function of average output voltage to find the calibration factor to input into LabVIEW (Figure 5.18 (d)).

### 5.4.4 Pressure transducers

All pressure transducers - confining pressure (Figure 5.18 (c)), pore fluid pressure (Figure 5.19 (a)) and pore fluid separator pressure (Figure 5.19 (c) and (d)) - were calibrated using a Budenberg 370 oil operated dead weight tester. Each transducer was connected to the dead weight tester and weights of known mass which corresponded to different

pressures were applied incrementally, recording the output voltage for each pressure. The procedure was repeated three times and the average voltage output for each pressure was calculated. Pressure was plotted as a function of output voltage to obtain the conversion for input into the LabVIEW configuration file. Temperature-induced pressure fluctuations were minimised by controlling the temperature in the laboratory with an air conditioning unit.

### 5.4.5 Pore volumometers

Pore volumometers were calibrated by filling the intensifier of known volume completely full of fluid and recording the voltage output of the integrated LVDT. Fluid was then expelled 10 cc at a time (measured with a measuring cylinder) and the voltage output recorded with each expulsion. Again, the procedure was repeated three times to obtain an average output voltage for each volume and then the volume plotted as a function of average output voltage to obtain the conversion (Figure 5.19 (b)).

### 5.4.6 Machine stiffness

Machine stiffness was calibrated using a 'dummy' sample of known Young's Modulus to obtain the elastic response of the apparatus. The dummy was loaded and unloaded for two consecutive cycles and the gradient of each loading and unloading curve calculated. The average of these gradient values is the measured apparent Young's modulus. Machine stiffness, $k_{mach}$, was calculated from the apparent Young's modulus, $E_{app}$, and Young's modulus of steel, $E_{steel}$, as follows:

$$k_{mach} = \frac{1}{(1/E_{app} - 1/E_{steel})} \tag{5.7}$$

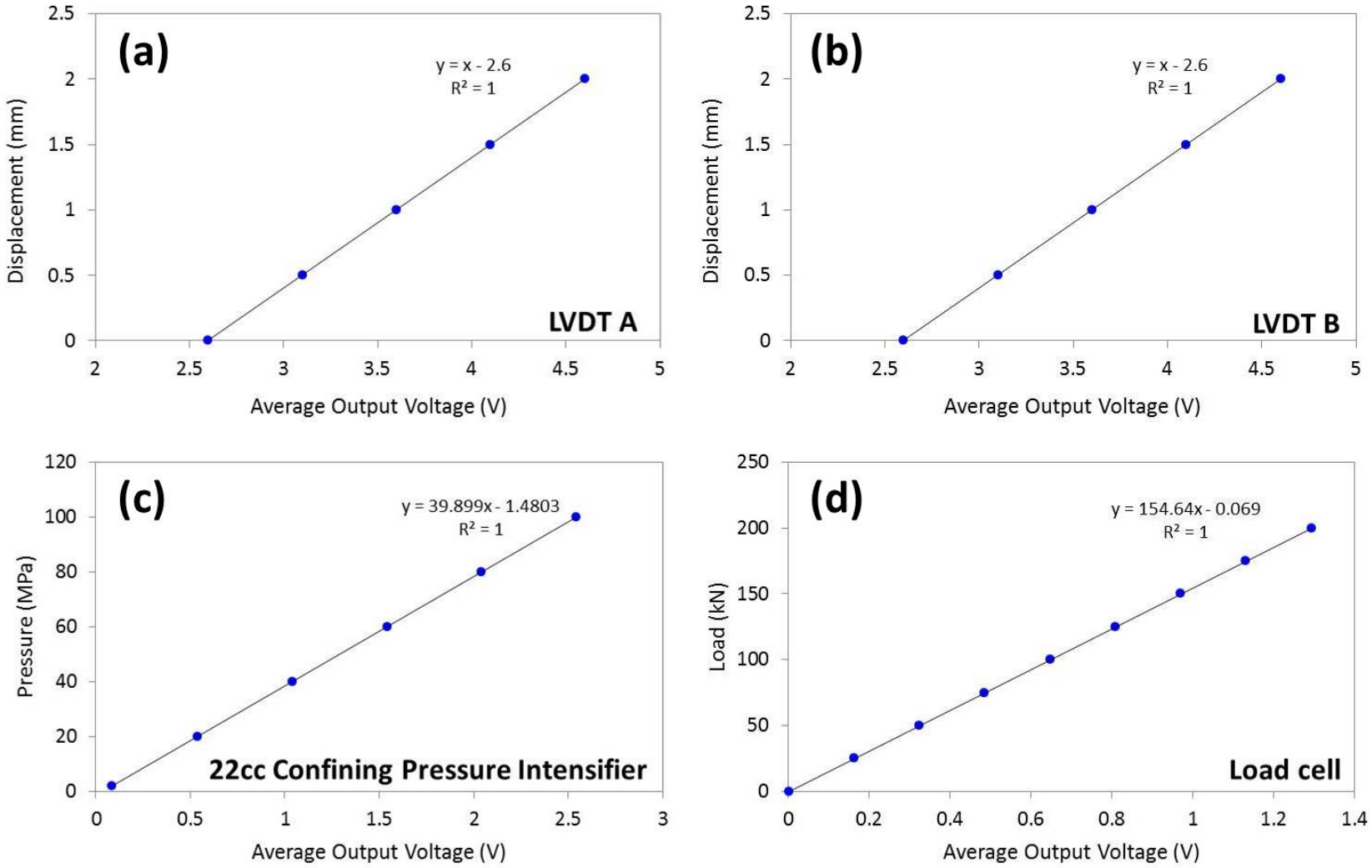


Figure 5.18: Calibrations for the triaxial apparatus: (a) LVDT A (b) LVDT B (c) Confining pressure intensifier (d) Load cell

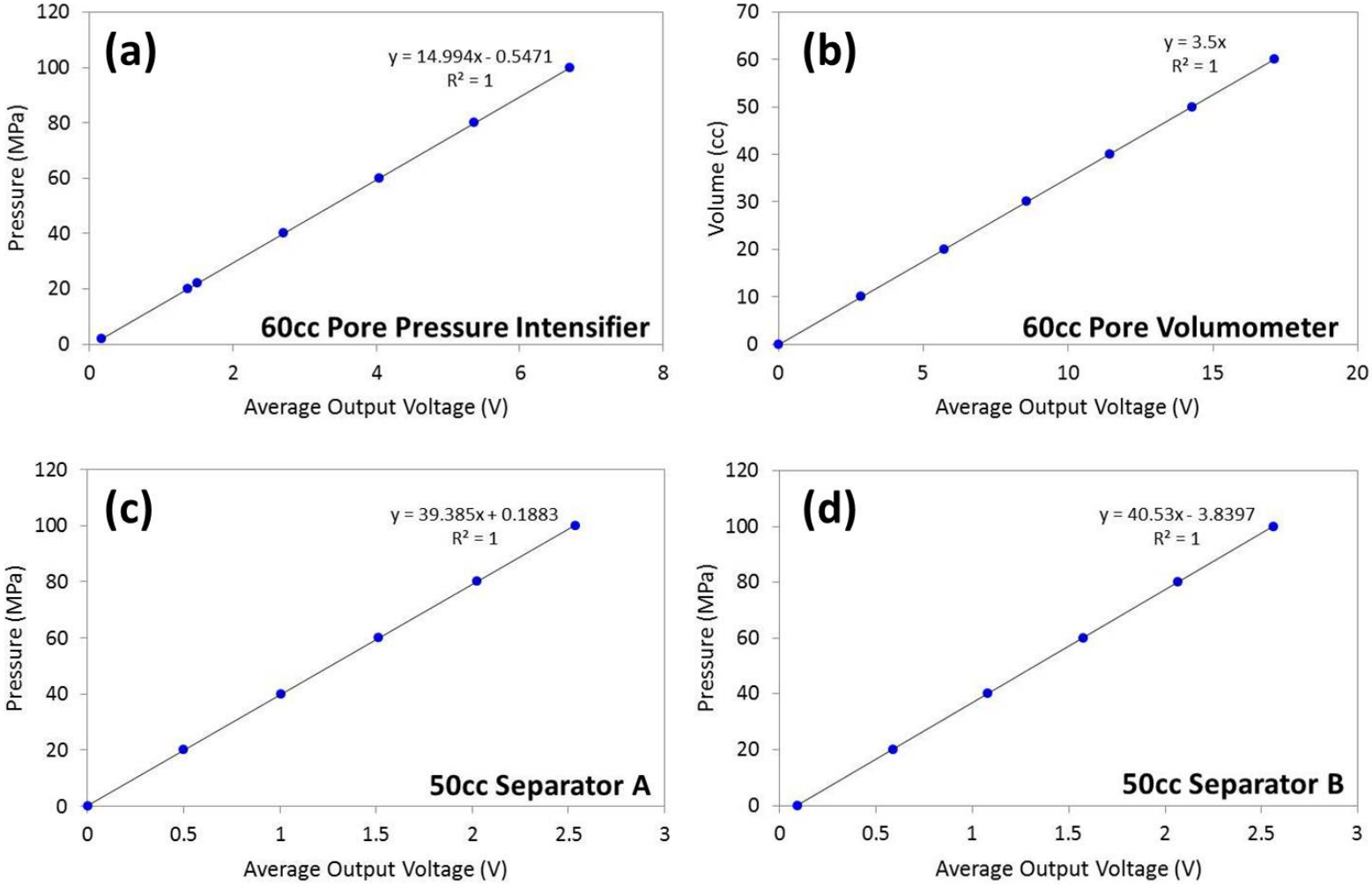


Figure 5.19: Calibrations for the pore fluid apparatus: (a) Pore pressure intensifier (b) Pore volumometer (c) Separator A (d) Separator B

## 5.5 Sample Preparation

### 5.5.1 Introduction

Systematic and careful preparation of rock samples is exceedingly important for an experimental study such as this in order to reduce experimental error. To this end, a consistent method for the preparation of samples was established in advance of any experiments being conducted. This section describes the preparation of samples for use in the triaxial ensemble. Sample preparation for specific characterisation techniques are explained in their respective sections.

### 5.5.2 Sample orientation

Preliminary benchtop ultrasonic velocity measurements on samples of Carrara marble (Section 6.4) found it to be perfectly isotropic (Figure 6.6). Thus, all samples were cored in the same direction (Z - see Figure 6.5), as determined by the size and shape of the received block.

### 5.5.3 Coring and grinding

For use in the triaxial ensemble, cylindrical samples of 40 mm diameter were cored to a length of 130 mm using a diamond-tipped coring drill. The block of material was clamped in place to prevent any movement during the coring process. Water was used to cool the drill during coring and it was lowered into the block at a slow and constant rate to avoid damage to the sample and coring apparatus.

Once cored, the sample ends were trimmed using a diamond-sintered circular saw and then ground down to a precise 100 mm. These dimensions of 40 mm diameter x 100 mm length ensured a statistically large number of grains and cracks and sufficient length to maintain a central region of homogeneous strain away from any inhomogeneous end effects. Regions of stress concentration may occur at the sample ends due to contact between the sample and steel platens (Paterson and Wong, 2005; Hawkes and Mellor, 1970). The length:diameter ratio (L/D) of 2.5:1 ensured that faults formed preferentially in the middle of the sample within the region of uniform stress distribution and that the aspect ratio had no influence on either the compressive strength or the angle of final fracture (Mogi, 2007; Paterson and Wong, 2005; Hawkes and Mellor, 1970). In addition, the application of confining pressure also acts to reduce the end effects within a sample (Mogi, 2007; Paterson and Wong, 2005), an added benefit of using the triaxial apparatus.

During grinding, the cylindrical samples were held in place using stainless steel v-clamps magnetically locked onto the grinding plate. A water-oil mixture (Ultragrind lubrication

oil) was used to lubricate the grinding wheel as it repeatedly ground off thin layers ($\leq$0.2 mm to prevent damage to the sample and apparatus) until the required length was reached. The grinding wheel ensures that the sample ends are parallel to within $\pm$0.02 mm, thus ensuring an even distribution of load across the top surface of the sample during testing (Hawkes and Mellor, 1970).

After the grinding process was completed, the samples were washed with water to remove excess oil and then placed in an oven to dry for two days, eliminating the presence of any fluids. The oven temperature was set at a laboratory standard of 50°C. At this temperature no thermal cracking is observed in the Carrara marble specimens (see Section 6.5 on thermal treatment) nor, as demonstrated by Glover et al. (1995), in various other rock types.

### 5.5.4 Preparation for electrical measurements

The effect of the confining pressure pushing against the nitrile jacket inside the vessel maintained good electrical contact between the electrodes and the rock as evidenced by the first few experiments carried out. However, since rock has a very high dielectric constant (e.g., Olhoeft (1989) and Keller (1989) report the dielectric constant of calcite to be between 6 and 9) and the currents being measured were very small, it was considered beneficial to increase the size of the electrodes. To this end, pieces of copper tape (20 mm x 19 mm) backed with conductive adhesive were attached to the sample in the required positions, measured relative to the centre of the sample and centered over the position of the brass insert (as shown in Figure 5.20). This also had the desirable additional effect of improving electrical contact. To compare between those experiments where copper tape was not used and those where it was, the measured current was divided by the contact area of the electrode to give a comparable measurement of current density in $Am^{-2}$.

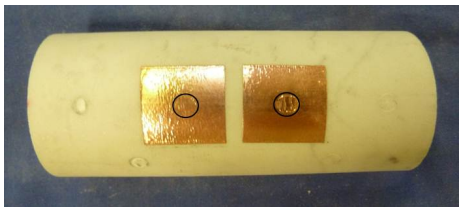

Figure 5.20: Sample of Carrara marble with adhesive Cu tape in position. Black circles highlight the indents made by the brass inserts on application of confining pressure. This indicates both their central positioning on the Cu tape and their excellent contact with the sample.

### 5.5.5 Saturating samples

Samples of Carrara marble were saturated for the porosity measurements, for use in the permeameter and for triaxial deformation experiments. Saturation to check porosity and for use in the permeameter involved fully submersing the samples in a bell jar of distilled water connected to a vacuum pump. Due to their low permeability and porosity, samples

were left under vacuum until their saturated mass remained constant for two consecutive days to ensure complete saturation.

If the sample was to be used in a wet triaxial experiment, it was saturated with the required pore fluid inside the pressure vessel after it had been mechanically fractured (see Section 6.7 for details). Saturation was performed immediately after this process to avoid crack healing. A pore fluid pressure of 20 MPa was used for the initial saturation, while the confining pressure was maintained at 30 MPa. Pore fluid entered the sample from below (via the bottom pore fluid end cap) in order to ensure that the fluid had permeated into all parts of the sample by the time it reached the top pore fluid pipe. The confining pressure was then increased to 50 MPa to achieve the relevant experimental conditions (effective pressure of 30 MPa) and the sample left overnight in the vessel under these conditions before starting the experiment. In this way, the pore pressure intensifier and the pore volumometer could guarantee complete saturation of the sample and pressure equilibration.

### 5.5.6 Heat treatment

For use in the saturated experiments, several samples of Carrara marble were heat-treated to induce thermal fracture. Specimens were clamped suspended in an insulated tube furnace and heated slowly to avoid thermal shock, ensuring that a temperature gradient did not build up within the sample and fractures were distributed homogeneously throughout. In addition, the same rate of heating and cooling was applied to all treated specimens to ensure consistency of cracking as far as possible between samples, taking into account their natural variability. The specimens were heated at 1°C/min up to a target temperature of 250°C, where samples were held for one hour to allow for thermal microcrack equilibration. Samples were then cooled back to room temperature at the same rate (1°C/min). Below a certain temperature, cooling actually occurs more slowly than this. However, it is reasonable to assume that this slower rate was the same for all samples and therefore consistency was maintained.

## 5.6 Experimental Procedure

### 5.6.1 Introduction

This section describes the procedure for performing an experiment on the triaxial deformation ensemble used during this study. First, the basic procedure to set-up and run experiments on oven-dry samples is presented, followed by the procedure I developed to pre-fracture and saturate samples with pore fluid in order to run the drained, saturated experiments.

### 5.6.2 Dry experiments

The rock sample, prepared as described in Section 5.5, was first pushed into the nitrile jacket and checked to ensure it was centrally positioned. The pore fluid distribution plates and end caps were then placed at either end with the nitrile sealing cuffs in place and the assembly placed atop the bottom ram as in Figure 5.4. Sensors within the jacket were checked to ensure they were oriented correctly and fit snugly against the curvature of the sample. Each sensor was attached to the lead-through connectors in the ceramic plugs via their coaxial cable connectors as described in Section 5.2.4.2 and the lead-through cables were connected to the individual amplifiers and logging systems. Their respective lead-through numbers and corresponding data channels were noted. All the cables were then carefully wrapped around the sample and secured with elastic bands, the pore fluid pipes were connected, assembly alignment was checked with a spirit level and the sample placed inside the vessel. A quarter turn of the vessel around the bottom breech nut sealed the vessel to the sample assembly.

At this point, the position of the ram was adjusted so that it just made contact with the top of the sample assembly. To do this, the actuator was lowered very slowly and carefully until it just touched the top piston and the load display on the servo-control changed by one unit. This ensured that contact with the sample was made gently so that the load only just overcame the seal friction and did not damage the sample at all. The external LVDTs were clamped into position and zeroed.

The confining pressure pipe was then connected via a cone and screw sealing mechanism to the appropriate port on the base plate (Figure 5.14) and confining oil pumped into the vessel from the bottom. Once the vessel was filled and the ram balanced, the relief valve was closed and the pump began to pressurise the oil. Once the desired confining pressure was reached, the vessel was isolated from the pump and the pump switched off. If additional pressure was required, it was applied manually using a hand pump attached to the confining pressure intensifier. The whole system was then left to allow the confining pressure to equilibrate, normally for about one hour.

Once the confining pressure had equilibrated, the intensifier was primed and pressurised by the control system which was set to maintain the required value and the isolation valve to the vessel was opened. All the data logging systems were set to start acquisition, with the time interval for velocity surveys set such that the first survey was carried out prior to initiating loading and the second survey occurred immediately after loading began. The strain rate was set on the servo-control and the actuator changed to a ramp-generating mode, allowing the strain rate to be maintained constant. Finally, loading was initiated and the deformation experiment begun.

### 5.6.3 Saturated experiments

All saturated experiments were conducted under drained conditions (i.e., the pore pressure was maintained constant and the pore volume change was measured). The procedure for running saturated experiments was planned very carefully due to the number of steps involved. The whole procedure took several days for each experiment due to the time required for full saturation and settling time for equilibration between each step. New data logging files were started at the beginning of each step, with each experiment consisting of five steps:

1. Dry loading and unloading to induce fractures
2. Saturation
3. Permeability and streaming current measurements
4. Saturated experiment
5. Permeability and streaming current measurements

Initially, the experiments were set up as for a dry test (described above). To induce a fracture network, loading was first initiated under dry conditions with a $P_c$ of 30 MPa and at $10^{-5}$ $s^{-1}$ strain rate until the sample had been deformed to an extension value of either 1.5 or 2 mm. By deforming the samples under cataclastic conditions, this procedure ensured as even a distribution of fractures as possible. Once the required extension value was reached, the sample was unloaded at the same rate until the load reached 8 kN, at which point the actuator was held in position. The bottom pore fluid pipe was then connected to the appropriate port on the base plate and the isolation valve between it and the intensifier opened, allowing pressurised pore fluid to flow into the sample, saturating it from below. Once fluid was seen exiting from the top pore fluid connection, complete saturation was ensured and the top pore fluid pipe was connected. Pore fluid could then enter the sample from both ends until the required pore pressure was reached, as indicated by the cessation of movement of the pore fluid volumometer piston. This saturation and equilibration process normally took around 24 hours.

Streaming current and permeability measurements were made prior to and following the saturated deformation experiments, ensuring that the system was at equilibrium prior to each stage. Since these measurements were only performed under drained conditions, the sample could be considered fully saturated. The outlet of the pore fluid pipe network at the top of the sample was opened while the pore fluid intensifier maintained pore fluid pressure at the bottom of the sample. This generated a constant pressure gradient along the sample from the applied pore fluid pressure at the bottom to atmospheric pressure at the top. At this point, the electrodes recorded streaming current while the pore volumometer recorded the volume of fluid flow through the sample, used to calculate the permeability. After the

measurement was completed, the pore fluid pipe was reconnected and the sample either re-saturated to the required pore pressure for the saturation experiment or unloaded and dismantled at the end of the experiment. Once the rock was saturated and the system equilibrated after the first set of permeability and streaming current measurements, loading was initiated for the saturated deformation experiment. At the end of the experiment, permeability and streaming current measurements were repeated.

## 5.7 Error Analysis

Two types of error must be considered when conducting experiments:

1. Systematic or instrument errors. These are minimised or corrected for through standard best practices such as averaging physical measurements and regularly calibrating all transducers and measurement equipment (see Section 5.4). Where possible, measurements were repeated on multiple samples to evaluate experimental repeatability or natural sample variability.

2. Random or experimental error. These stem from the precision to which an instrument can be read and are unavoidable errors that enter into every measurement. Table 5.4 presents the common sources of experimental error for this study and their associated uncertainty, determined from the appropriate measuring device.

Table 5.4: Sources of experimental error for this study and their associated uncertainty

| **Variable** | **Absolute Uncertainty** |
|---|---|
| Electric current | $\pm 10$ fA |
| Confining pressure | $\pm 0.05$ MPa |
| Pore pressure | $\pm 0.005$ MPa |
| LVDTs | $\pm 0.005$ mm |
| Volumometer displacement | $\pm 0.005$ cm$^3$ |
| Elastic wave travel time | $\pm 0.05$ $\mu$s |
| P-wave velocity (absolute) | $\pm 16$ ms$^{-1}$ |
| S-wave velocity (absolute) | $\pm 6$ ms$^{-1}$ |
| P-wave velocity (relative) | $\pm 0.3$ % |
| S-wave velocity (relative) | $\pm 0.2$ % |
| Sample dimensions | $\pm 0.005$ mm |
| Sample parallelism | $\pm 0.005$ mm |
| Sample mass | $\pm 0.005$ g |
| Angle of failure | $\pm 0.5^\circ$ |
| Conductivity of pore fluid | $\pm 0.1$ $\mu$Sm$^{-1}$ |
| Cu electrode dimensions | $\pm 0.5$ mm |
| Position of Cu electrode | $\pm 0.5$ mm |

Some variables in this study depend on the interpretation of acoustic or electric signals sampled continuously in time. These signals can only be measured to the precision of the instrument sampling rate. To minimise this uncertainty, the sample rate was set as low as practically possible and any readings from the signal were performed as a series with pre-defined criteria (e.g., first zero-crossing arrival times). So, while the absolute value of the measurement, being a visual interpretation of the signal, may have a larger

error associated with it, the measurement error between successive measurements (relative error) is minimised. The equations used to propagate experimental error through the data analysis are presented in Appendix B.

# Chapter 6

# Experimental Material and Sample Characterisation

## 6.1 Introduction

This chapter presents the material selected for the study, together with the techniques used for characterisation. It also discusses the methods used to introduce additional pore space in the form of fractures into the test specimens to ensure effective saturation during the experiments involving pore fluid.

The main experimental material used for this study was Carrara marble. It was selected for the reasons detailed below.

1. It is a laboratory standard material (von Karman, 1911); a pure, crystalline, monominerallic, isotropic, aggregate of low porosity (Edmond and Paterson, 1972; Ramez and Murrell, 1964) and with medium grain size (c.0.2 mm), which has been very well studied and characterised (e.g., De Bresser et al., 2005; Schubnel et al., 2005; 2006b;a; Fredrich et al., 1989; Rutter, 1972b; 1974) and for which the slip systems are well-known (Turner et al., 1954).

2. It is composed of 99% calcite ($CaCO_3$) and 1% organic impurities (Alber and Hauptfleisch, 1999). It is therefore non-piezoelectric. Also, calcite is an important rock-forming mineral and calcite tectonites play a significant role in several crustal deformation zones (De Bresser et al., 2005).

3. It can undergo the brittle-ductile transition at room temperature purely due to an increase in pressure (see Fredrich et al., 1989; Rutter, 1972b; 1974), allowing mechanisms of the brittle-ductile transition to be investigated easily in ambient temperature experiments. Behaviour is brittle below 30 MPa and semi-brittle between 30 MPa and 300 MPa, with deformation mechanisms becoming increasingly plastic as the pressure

increases (see Figure 6.1). This enables variations in electric current signals to be associated with changes in deformation mechanism over the brittle-ductile transition. In the semi-brittle regime, deformation is accommodated by brittle faulting, cataclasis, mechanical twinning and dislocation glide (Turner et al., 1954; Griggs and Handin, 1960; Fredrich et al., 1989; Lu and Jackson, 1996).

4. It is a relatively soft material, accumulating damage over a longer period of time before failure. This allows the evolution of deformation to be tracked more easily than in a harder material where the final stages of failure are more dynamic and occur much more quickly.

5. Marble was the material used in previous uniaxial experiments (Stavrakas et al., 2003; 2004; Anastasiadis et al., 2004; Vallianatos et al., 2004) showing that under dry, atmospheric conditions electric currents still accompany the process of crack formation and growth even in non-piezoelectric rocks. This study seeks to extend those observations to shallow crustal conditions.

<table>
<tr><th>Deformation regime</th><th>Deformation mechanism</th><th>Confining pressure</th><th>Initial yield stress</th><th>Differential stress at onset of dilatancy</th><th>Dilatancy coefficient</th><th>Work hardening coefficient</th><th>Dislocation glide</th><th>Twinning</th><th>Stress-induced crack densities and anisotropy</th><th>Mean dislocation density at constant differential stress</th><th>Characteristic crack length</th></tr>
<tr><td>Purely brittle</td><td rowspan="2">microcracking and twinning</td><td><30MPa</td><td rowspan="6">increases</td><td rowspan="11">increases</td><td rowspan="6">decreases rapidly</td><td rowspan="6">increases rapidly</td><td rowspan="3">doesn't occur</td><td rowspan="3">unknown (may occur locally)</td><td></td><td rowspan="6">constant and beginning to increase gently at higher pressures</td><td>constant</td></tr>
<tr><td rowspan="10">Stable, semi-brittle mode (deformation mechanisms include microcracking, twinning and dislocation glide - cracks and voids nucleate at twin boundaries, twin terminations and at intersection of twin lamellae, also observed are geometries suggestive of crack tip shielding by dislocations)</td><td>30</td><td rowspan="9">decreases with increasing pressure at constant strain (comparable to those in prefailure brittle sample up to 120MPa in samples deformed to strains of 3-5%, although energetics of deformation suggests ration of brittle energy dissipation to total energy dissipation is >60% lower here)</td><td rowspan="9">different to that in brittle field - decreases with increasing pressure at a given strain</td></tr>
<tr><td rowspan="5">microcracking, twinning and dislocation glide</td><td>50</td><td rowspan="4">occurs locally at lower pressures, with localisation decreasing as pressure increases (occurs at applied differential stress well below critically resolved shear stress for glide on easiest slip system)</td><td rowspan="5">responsible for initial yield</td></tr>
<tr><td>85</td></tr>
<tr><td>100</td><td rowspan="4">constant</td></tr>
<tr><td>120</td></tr>
<tr><td>230</td><td rowspan="4">asymptotically approaches zero</td><td rowspan="4">increases more slowly</td><td rowspan="4">increases significantly</td></tr>
<tr><td>300</td></tr>
<tr><td>Purely plastic</td><td></td><td>>300MPa</td><td></td><td></td><td></td><td></td><td></td><td></td><td></td><td></td><td></td></tr>
</table>

Figure 6.1: Deformation mechanisms and associated parameters for Carrara marble across the brittle to plastic transition (modified from Fredrich et al., 1989)

## 6.2 Description of Carrara Marble

Marble is a medium- to coarse-grained metamorphic rock consisting of roughly equigranular calcite ($CaCO_3$) crystals. It forms by the recrystallisation of limestone at high temperatures and/or pressures, mainly at convergent plate boundaries during regional metamorphism, where these conditions are associated with deep burial in an orogenic belt, and sometimes by contact metamorphism. Marble formed from pure calcite limestone is white, with a sugary texture, and will effervesce when tested with dilute (∼10%) hydrochloric acid. Carrara marble is a famous white marble from the Alpi Apuane region of the Northern Appenines in Tuscany, Italy, where it has been quarried since Roman times. Tectonically, the region is located in the internal part of the Apennines accretionary wedge, which is related to the Westward subduction of the Adriatic plate beneath the Corsica-Sardinia microplate. Carrara marble is a greenschist facies; that is, formed under the lowest temperatures (300-450°C) and pressures (200-1000 MPa) associated with regional metamorphism, and is widely known for its chemical purity, homogenous microstructure and isotropic texture (Oesterling, 2004). Marbles in the Alpi Apuane derive from stratigraphically different levels and are of Devonian, Liassic, Dogger and Cretaceous-Eocene age (Molli et al., 2000). Marble has a great many uses; as an aggregate and block stone for construction, as a whitening agent and filler, as an acid neutraliser, an abrasive and calcium additive, and most famously as an ornamental stone for sculpture. Carrara marble is arguably the finest in the world for sculpture and has been used by famous sculptors such as Donatello, Michelangelo and Canova for their masterpieces.

The marble used for this investigation was a pure, white 'Bianco Ordinario', blocks of which were obtained from a London-based stonemason who imports the stone from the quarry in Carrara, Italy. Inspection of hand specimens and thin sections demonstrated that it has a crystalline structure with no preferred grain orientation and near-equidimensional calcite grains ranging in size from 0.1-0.3 mm (in agreement with Bandini et al., 2012; De Bresser et al., 2005; Schubnel et al., 2005; Alber and Hauptfleisch, 1999). In thin section, two microstructures are visible (Figure 6.2). One is a granoblastic texture, resulting from a complete static recrystallisation of the limestone (Bandini et al., 2012; Akesson et al., 2006), where grains are regularly shaped with straight boundaries and triple points. The other is a xenoblastic texture, where grains are slightly smaller (c. 0.2 mm) than those with granoblastic texture (c. 0.25 mm) and irregular in shape with well-interlocked grain boundaries (Bandini et al., 2012). Fracture toughness experiments were carried out on the Carrara marble used in this study by Chandler (2015), who found that $K_{\mathrm{Ic}}^{\mathrm{c}} = 1.39 \pm 0.01$ MPa.m$^{\frac{1}{2}}$. This value is very close to $K_{\mathrm{Ic}} = 1.35 \pm 0.23$ MPa.m$^{\frac{1}{2}}$, previously found for Carrara marble (Migliazza et al., 2011).

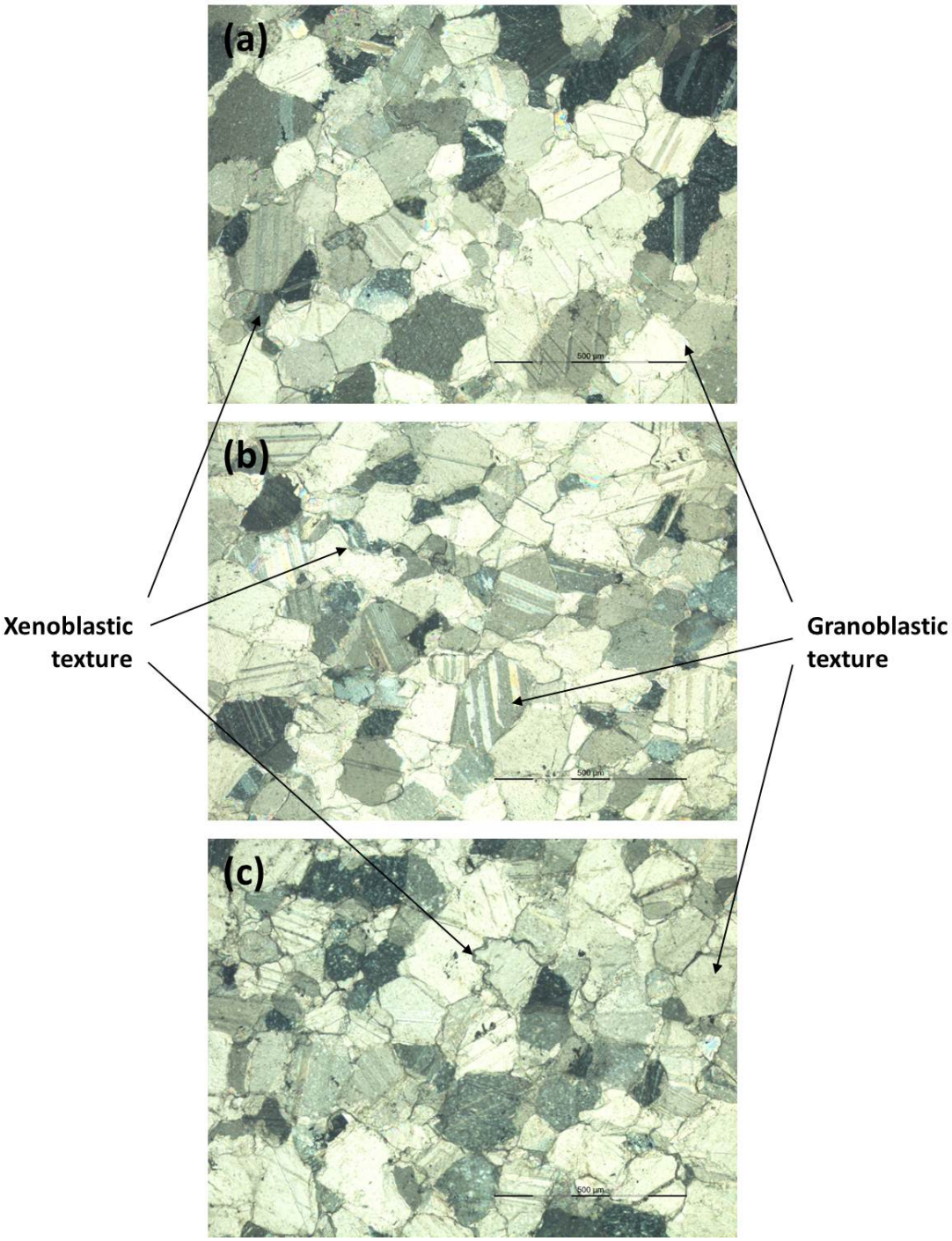


Figure 6.2: Thin section images of the Carrara marble used in this study oriented in (a) the XY plane, (b) the YZ plane and (c) the XZ plane. Orientations as per Figure 6.5

Table 6.1: Properties of Carrara marble samples for this investigation and comparison with two previous studies (carr-A from Alber and Hauptfleisch (1999) and carr-S from Schubnel et al. (2005))

| **General properties** | **This study** | **carr-A** | **carr-S** |
|---|---|---|---|
| Composition | >99% calcite | 99% calcite | >99% calcite |
| Dry density, $\rho$ (gcm$^{-3}$) | 2.7 | 2.65 | |
| Initial porosity, $\varphi$ (%) | 0.19 | 0.4 | 0.5 |
| Grain size ($\mu$m) | 100-300 | 240 | c.150 |
| **Elastic properties** | | | |
| Poisson's ratio, $\nu$ | | 0.19 | |
| Young's Modulus, $E$ (GPa) | 49 | 49 | |
| **Dynamic properties** | | | |
| Compressional wave velocity, $V_P$ (kms$^{-1}$) | 5.61 | 6.01 | 5.92 |
| Shear wave velocity, $V_S$ (kms$^{-1}$) | 3.08 | 3.27 | 3.23 |
| Young's Modulus, $E_d$ (GPa) | 65.8 | 73 | |
| Poisson's ratio, $\nu_d$ | 0.28 | 0.29 | 0.29 |
| Bulk modulus, $K_d$ (GPa) | 50.9 | | 57.5 |
| Shear modulus, $G_d$ (GPa) | 25.6 | | |
| P-wave anisotropy $A_P$ (%) | 1.16 | | <1 |
| S-wave anisotropy $A_S$ (%) | 1.33 | | |

## 6.3 Porosity Calculation

The proportion of void space within a rock is known as its porosity (Gueguen and Palciauskas, 1994). Crystalline rocks, such as marble, generally have very low porosity (<1%) due to their very tightly packed and angular mineral grains, which leave only intragranular and grain boundary fractures to provide any void space (Freeze and Cherry, 1979). Connected porosity is the volume of space accessible to fluid flow while isolated porosity is the total volume of closed off pores that are not accessible to fluids (Dullien, 1979). The total porosity of a rock comprises the combined connected and isolated porosity. Connected porosity is usually measured by determining the mass of fluid contained in a saturated sample and correcting for its buoyancy (Equation 6.1), while total porosity can be measured by crushing the rock sample and comparing the mass of the crushed rock with that of the intact sample.

For this study, effective connected porosity ($\varphi$) was calculated using the Archimedes technique and implemented on all samples immediately prior to experimentation. First, the dry mass ($M_{dry}$), the vacuum saturated wet mass ($M_{wet}$) (see Section 5.5.5 on saturating samples) and the submerged wet mass ($M_{arch}$) were determined for each of the 40 mm diameter cores. Porosity was then calculated using the following equation:

$$\varphi = \frac{M_{wet} - M_{dry}}{M_{wet} - M_{arch}} \tag{6.1}$$

The samples of Carrara marble used for this study have a connected porosity of $0.19 \pm 0.12$ %, indicating a natural variability between samples.

## 6.4 Benchtop Elastic Wave Velocity Characterisation

### 6.4.1 Introduction

Rocks contain structures and fabrics created by the alignment of voids, grains or crystals of different sizes and compositions. Such oriented structures and fabrics affect the physical, mechanical and transport properties of rock samples and the variation in these properties with orientation is known as anisotropy (Mavko et al., 2009; Nur and Simmons, 1969). Since the process of rock deformation also affects these properties, inducing a strong anisotropy due to alignment of fractures, it is particularly important for comparison purposes to establish the initial physical properties and degree of anisotropy of the material prior to experimentation.

Due to the large velocity contrast between dry air and mineral crystals (Mavko et al., 2009; Nur, 1971; Nur and Simmons, 1969), elastic wave propagation depends strongly on a rock's microstructure, in particular the void space. As a result, elastic wave velocity measurements are commonly used to evaluate anisotropy and characterise the elastic properties of rock samples (Mavko et al., 2009). The velocity anisotropy of a cylindrical sample can be established by measuring the elastic wave velocity with respect to radial azimuth around the core, thus enabling calculation of the dynamic elastic moduli and estimation of the void space anisotropy within the specimen.

### 6.4.2 Methodology

Benchtop (room temperature and pressure) measurements were made on selected dry samples prior to testing to establish initial P- and S-wave velocities and confirm velocity isotropy. The measurements were made by means of the pulse transmission technique (Birch, 1960) using an Agilent technologies 1.5 GHz Infinium digital oscilloscope, a JSR DPR300 35 MHz ultrasonic pulser/receiver and two custom-built sample assembly jigs containing either a pair of Panametrics V103 P-wave or V153 S-wave transducers with piezoelectric elements of 0.5" diameter and 1 MHz resonance frequency (Figure 6.3).

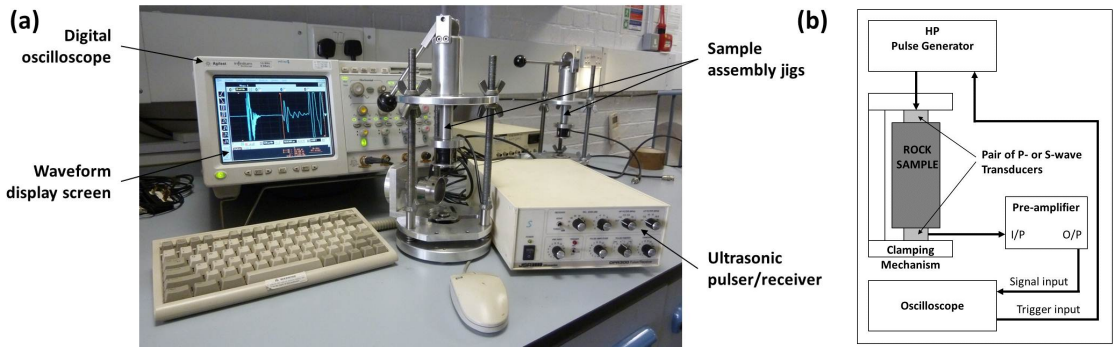


Figure 6.3: Benchtop ultrasonic velocity measurements: (a) photograph of the equipment setup and (b) schematic diagram

The pulse generator applies a square wave voltage to one transducer in the pair and at the same time triggers the oscilloscope to start recording the time base. The signal is received by the other transducer in the pair after the wave has traveled through the rock sample. The received signal is then amplified prior to being sent to the oscilloscope.

From this, the exact seismic travel time of the wave through the sample can be measured and recorded using a magnified image of the start of the received signal displayed on the oscilloscope (Figure 6.4). The start of the waveform was picked by hand by zooming into the waveform and finding the first point at which it deviated from zero (solid orange line in Figure 6.4). The measured seismic travel time was then corrected for the travel time through the transducers and electronic system. This was done by placing the two transducers in direct contact with each other and subtracting the time taken for the pulse to travel through the system from the measured travel time through the sample and system.

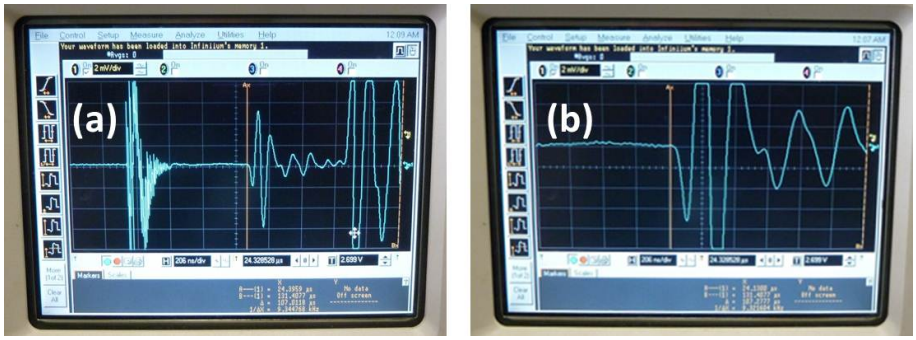


Figure 6.4: Ultrasonic wave arrival times: (a) generated and received P-wave signal through a sample of Carrara marble and (b) magnified view for accurate arrival picking. Solid orange vertical line indicates the first arrival.

Each sample assembly jig (Figure 6.3) allowed the sample to be rotated in 10° increments. A fresh reading was taken for each increment as the sample was rotated to provide a complete picture of the ultrasonic wave velocity anisotropy within the sample. This procedure was initially carried out on 40 mm diameter x 40 mm long oven-dry samples of Carrara marble cored along the orthogonal axes of the block in the XY, YZ and XZ planes (Figure 6.5) to ascertain the degree of velocity anisotropy in all orientations.

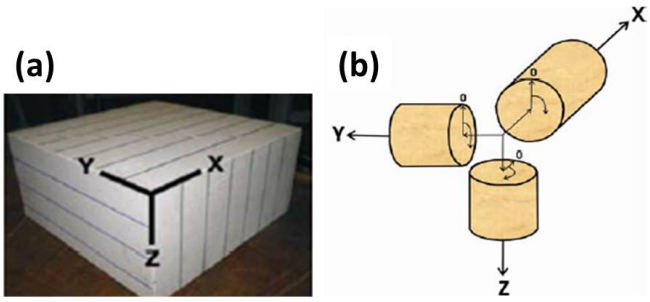


Figure 6.5: Sample orientation: (a) block of Carrara marble with orthogonal axes shown and (b) cores for each orthogonal axis. 0 is the measurement starting position from which the sample was rotated in the jig (after Heap, 2009; Benson et al., 2003)

The variation in measured ultrasonic velocity was then used to calculate the velocity anisotropy, $A_V$ (where V is the experimentally measured ultrasonic velocity) as defined by:

$$A_V = 100\left[\frac{V_{max} - V_{min}}{V_{mean}}\right] \tag{6.2}$$

Additionally, the initial dynamic elastic properties (Young's Modulus, $E_d$, Poisson's ratio, $\nu_d$, bulk modulus, $K_d$ and shear modulus, $G_d$) were calculated from elastic wave velocities using the following equations (Jaeger et al., 2007):

$$E_d = V_S^2 \rho \frac{[3(V_P/V_S)^2 - 4]}{[(V_P/V_S)^2 - 1]}, \tag{6.3}$$

$$\nu_d = \frac{[(V_P/V_S)^2 - 2]}{[2(V_P/V_S)^2 - 1]}. \tag{6.4}$$

$$K_d = \rho(V_P^2 - \frac{4}{3}V_S^2), \tag{6.5}$$

$$G_d = \rho V_S^2 \tag{6.6}$$

Average values of these properties over all three orientations are presented in Table 6.1.

### 6.4.3 Results

Figure 6.6 shows the benchtop ultrasonic velocity variation with azimuth for these specimens of Carrara marble. There is clearly very little variation in both P- and S-wave velocities over all azimuths and core orientations, indicating that the samples of Carrara marble used for this study have no pronounced anisotropy.

Table 6.2: Summary of ultrasonic wave velocity data for Carrara marble samples

| | **Velocity ($kms^{-1}$)** | | **Anisotropy parameter (%)** | | |
|---|---|---|---|---|---|
| | **Average** | **Std. dev.** | **XY plane** | **XZ plane** | **YZ plane** |
| **P-wave** | 5.61 | 0.008 | 1.04 | 1.39 | 1.03 |
| **S-wave** | 3.08 | 0.005 | 1.64 | 1.10 | 1.25 |

With values close to 1, the calculated anisotropy parameters given in Table 6.2 confirm this isotropy and Figure 6.7 shows there is also little variation in the calculated physical properties over all azimuths and core orientations. Thus, it can be deduced that there is no obvious bedding plane, that overall any existing cracks (void spaces) are isotropically distributed throughout the samples and that prior to deformation the physical properties do not vary significantly with orientation.

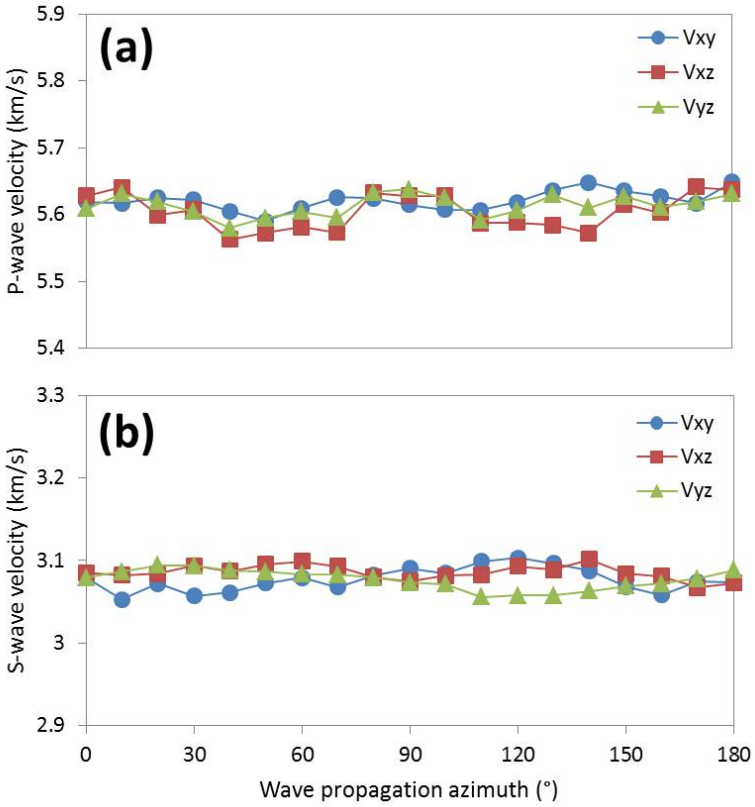


Figure 6.6: Variation of (a) P-wave and (b) S-wave velocities with wave propagation azimuth for oven-dry Carrara marble samples at atmospheric pressure and room temperature in the XY plane (circles), XZ plane (squares) and YZ plane (triangles).

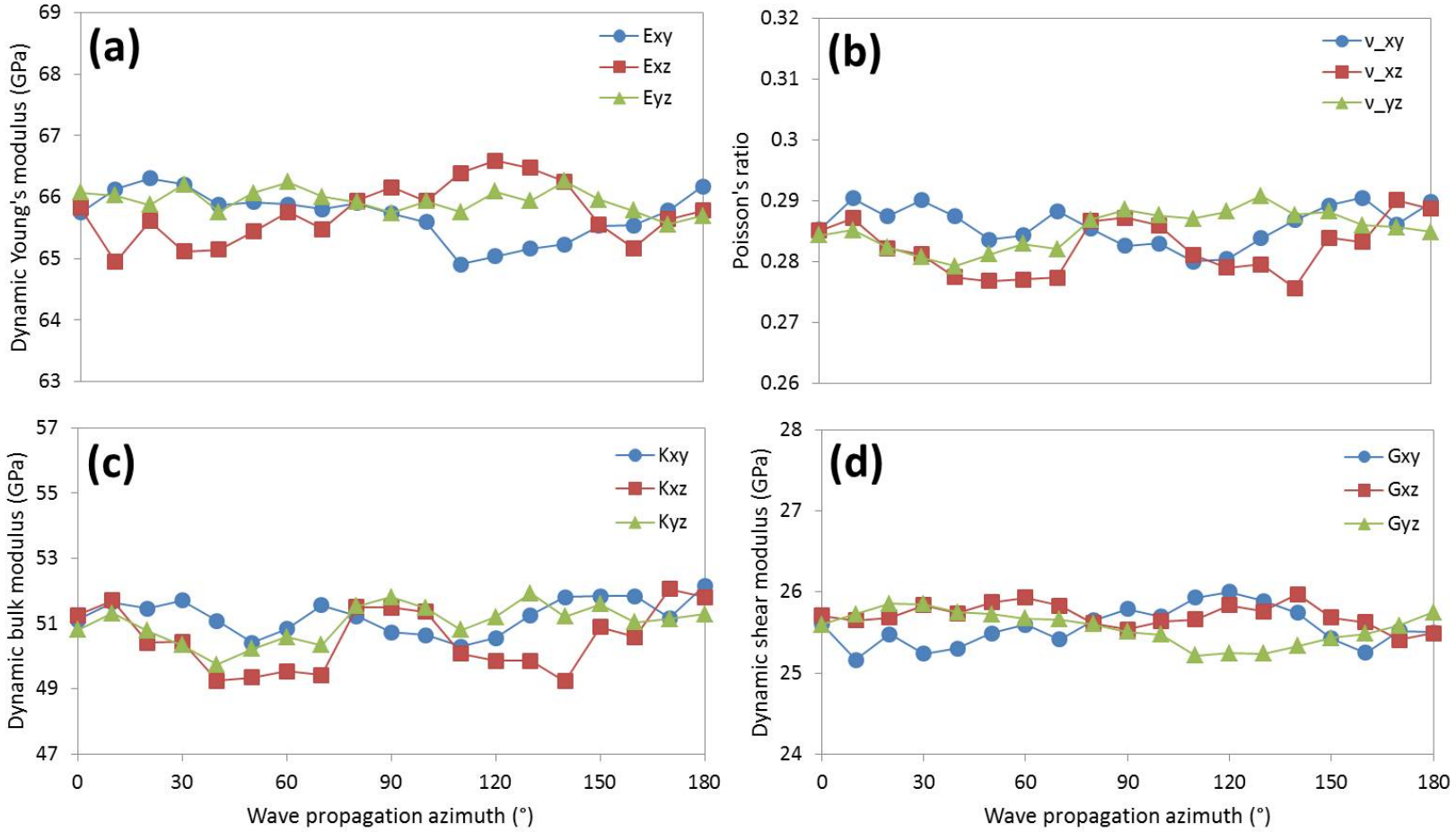


Figure 6.7: Variation of (a) dynamic Young's Modulus, (b) Poisson's ratio, (c) dynamic bulk modulus and (d) dynamic shear modulus with wave propagation azimuth for oven-dry Carrara marble samples at atmospheric pressure and room temperature in the XY plane (circles), XZ plane (squares) and YZ plane (triangles).

## 6.5 Thermal Treatment of Samples to Induce Fracture

### 6.5.1 Introduction

The very low permeability and porosity of Carrara marble means that, in order to carry out experiments using pore fluid, it was necessary to increase the void space within the samples by introducing some microfractures prior to saturation. This increases the permeability and porosity of the rock, allowing pore fluid to flow more freely though it and thus improving the accuracy of the pore volume and pore pressure measurements. A method often used to induce controlled, quasi-isotropic crack damage into rock samples is thermal stressing (e.g., Meredith et al., 2012; Lu and Jackson, 1996; Darot et al., 1992; Fredrich and Wong, 1986; Homand-Etienne and Troalen, 1984). Fracture damage reduces the P- and S-wave velocities but the level of anisotropy remains low (Meredith et al., 2000).

Since Carrara marble has a large crystalline thermal expansion anisotropy (Lu and Jackson, 1996), grain expansion upon heating and shrinkage upon cooling generates internal strains concentrated within grains and along grain boundaries, leading to the development of intragranular and grain boundary microcracks as well as crack sealing (Fredrich and Wong, 1986). Crystalline expansion would be expected to occur in all directions due to the initial isotropic nature of the rock and lack of preferred grain orientation, leading to an overall isotropic distribution of these microcracks. Homand-Etienne and Troalen (1984) studied Scanning Electron Microscopy (SEM) images and noted that thermal cycling immediately induces the opening of inter-crystalline boundaries, with inter-crystalline cracks appearing from 200°. Thermal treatment was therefore identified as a potentially effective way of introducing microcracks into samples of Carrara marble.

It should be noted here that deformation-induced microstructures in Carrara marble vary significantly with temperature (Hacker and Kirby, 1993). These range from limited dislocation glide and mechanical twinning at 400°C, through limited recrystallisation due to twin and grain boundary migration at 500°C, to widespread recrystallisation at 600-700°C and grain growth at 800-900°C. Increasing the temperature leads to ductile dislocation creep (Schmid et al., 1980; Hacker and Kirby, 1993). Thus, stress build-up in the heated samples may be accommodated by ductile processes rather than by microcracking. Dislocation creep occurs in two ways; by glide, where the dislocation steps through the crystal lattice one Burgers vector at a time, and by climb, where the dislocation climbs out of plane due to the presence of a nearby vacancy. Dislocation glide is limited by dislocations piling up and becoming entangled, increasing the resistance to dislocation motion, a process known as strain hardening. Climb prevents pile-up and entanglement, thus relaxing stresses. Dislocation climb requires the diffusion of vacancies and hence significant amounts of dislocation climb only occur at temperatures above a third of the melting temperature (Deshpande et al., 2013). Since the melting temperature of calcite is 1339°C, climb-assisted creep is active from about 450°C. Although small amounts of climb may occur at temperatures lower than this (Deshpande et al., 2013), it is very unlikely that

significant dislocation climb occurs under atmospheric pressure at temperatures below 400°C; i.e., at the temperature range used for thermal treatment during this study. However, Kennedy and White (2001) found that dynamic recrystallisation can occur at much lower temperatures (150-250°C) in fault-rock calcite veins. Their microstructural observations suggest that this occurs in response to accumulated glide-induced strain energy and twin boundary migration, rather than dislocation climb. It may therefore be expected that, in addition to microfracture, some dislocation glide and twinning will occur during thermal stressing of Carrara marble at the temperatures used during this study, leading to a strain hardening effect in the samples.

### 6.5.2 Methodology

In order to establish the most appropriate temperature for the thermal treatment of samples to be deformed in saturated experiments, one sample of Carrara marble was thermally cycled in increments of 50°C according to the procedure described in Section 5.5.6. Between each thermal stressing cycle the P- and S-wave velocities were measured along each orientation (X, Y and Z - see Figure 6.5) using the pulse transmission method discussed in Section 6.4. Measurements were made at room temperature and pressure on cooled samples. Since elastic wave velocity is sensitive to the level of void space within a rock body and the void space within crystalline rocks is almost uniquely due to fractures (Freeze and Cherry, 1979), elastic wave velocity measurements are a useful way of evaluating the variation in microfracture density with thermal treatment.

Dynamic properties were calculated from Equations (6.3) to (6.6) and crack density along each orientation was then estimated for an isotropic distribution of penny-shaped cracks using the non-interactive effective medium theory of Kachanov (1994) and Sayers and Kachanov (1995) - see Section 4.7 for equations. A simple least squares inversion procedure was used (after Benson et al., 2006; Schubnel et al., 2006a - see Appendix C for MATLAB code) with model input parameters as given in Table 6.3.

Table 6.3: Model input parameters for crack density inversion

| **Property** | **Input value** |
|---|---|
| Young's Modulus, $E_0$ (Pa) | $73\text{x}10^9$ |
| Poisson's ratio, $\nu_0$ | 0.29 |
| Fluid (air) bulk modulus, $K_f$ (Pa) | $1.01\text{x}10^5$ |
| Density, $\rho$ (kgm$^{-3}$) | $2.7\text{x}10^3$ |

### 6.5.3 Results

Elastic wave velocities as a function of heat treatment temperature are shown in Figure 6.8. P-wave velocity, $V_P$, decreased from 5.6 kms$^{-1}$ to 2.9 kms$^{-1}$ between the 50°C and 250°C thermal cycles, while S-wave velocity, $V_S$, decreased from 3.2 kms$^{-1}$ to 1.7 kms$^{-1}$. This reduction in velocity of >50% is attributed to an increasing number of thermally-induced

fractures. It can be seen from Figure 6.8 that, along all three axes, wave velocities (both $V_P$ and $V_S$) reach their minimum at 250°C. At 300°C, both $V_P$ and $V_S$ increased along all three axes, indicating healing of the damage induced during previous cycles. An apparent decrease in $V_S$ after the 350°C cycle is anomalous and may be attributed to the weakness of the received signal. Above 300-350°C, signals were too weak for reliable measurements indicating high levels of attenuation throughout the sample. Mineral grain expansion may explain the increase of $\sim$100 ms$^{-1}$ in $V_P$ along the Z-axis and $V_S$ along the Y- and X-axes after the first heating cycle (50-100°C). Little variation is seen between the three orientations up to 250°C, highlighting the isotropic nature of this material up to that temperature. The slight differences apparent between the Z-axis and other two axes are attributed to having measured along the sample length rather than across its diameter, increasing the opportunity for signal attenuation during pulse transmission.

The dynamic elastic moduli of the sample were also altered by the thermal treatment and exhibit similar trends to the elastic wave velocities (Figure 6.9 (a), (c) and (d)). In general, they decrease as temperature increases, with a significant reduction of 70-80% by the time they reach a minimum at 200-250°C. This indicates an increase in compliance due to the introduction of microcracks. Up to 250°C, variation with temperature is similar over all three orientations, indicating an isotropic distribution of fractures. Poisson's ratio (Figure 6.9 (b)) along the X- and Y-axes decreases steadily from 0.28 to 0.09 at 200°C and then fluctuates between 0.08 and 0.19 at higher temperatures, with a large increase to >0.37 at 350°C. Along the Z-axis it increases from 0.22 to 0.30 after the 100°C cycle and then remains stable at around 0.29 to 300°C apart from a drop to 0.14 at 200°C.

These results agree with the observations of Lu and Jackson (1996), who noticed a pronounced reduction in shear modulus observed during thermal cycling of Carrara marble specimens at temperatures < 300°C and those of Homand-Etienne and Troalen (1984) who found that wave velocities quickly decreased up to temperatures of 400°C. Both attributed their observations to an increase in inter-crystalline porosity due to the rapid separation of crystal boundaries during thermal fracture. The temperature range in which the reduction in velocity occurs agrees with the proposed range of Fredrich and Wong (1986) for an incremental increase in both intragranular and grain boundary cracks in a calcite rock. Thus, it can be inferred that thermal treatment of the Carrara marble samples used in this study to 250°C at atmospheric pressure causes significant thermal fracturing. Interestingly, the total reduction in shear modulus during thermal cycling observed by Lu and Jackson (1996) under a confining pressure of 50 MPa is four times smaller that that seen in this study (Figure 6.9 (d)) at atmospheric pressure. This is likely due to the increased influence of plastic deformation mechanisms and suppression of microcrack amplitudes at the raised $P_c$ (above the brittle-ductile transition pressure of $\sim$30 MPa).

At temperatures above 300°C, Lu and Jackson (1996) also found that the modulus deficit recovered, as seen here, and attributed this to crack closure by time-dependent plastic deformation processes. As the temperature increases, the large deviatoric stresses caused

by the thermal expansion anisotropy results in twinning and increased dislocation density. Cracks partially close in response to the significant plastic deformation that the combination of twin formation and migration and dislocation glide produces. In this study, recovery of the elastic moduli at temperatures >250°C is very marked in comparison to that seen by Lu and Jackson (1996) above 300°C, with the shear modulus recovering from <10 GPa to ∼20 GPa at atmospheric pressure, compared with an increase of 2 GPa at 50 MPa. Based on the arguments just given, this is indicative of significant crack closure due to plastic processes. Thus, it can be inferred that stresses due to thermal expansion anisotropy are accommodated mainly by brittle microfracture up to 250°C (at atmospheric pressure), while at temperatures > 250°C these stresses are accommodated mainly by plastic deformation in the form of twinning and dislocation glide at the temperatures reached during this study.

Furthermore, Lu and Jackson (1996) suggest that thermal cracking in Carrara marble is suppressed completely by plastic flow above 500°C and that the internal friction or attenuation of Carrara marble is low and temperature-insensitive at temperatures <400°C, increasing dramatically at 400-500°C. This supports the inference that unreliable signal detection above 350°C during this study was due to high levels of signal attenuation.

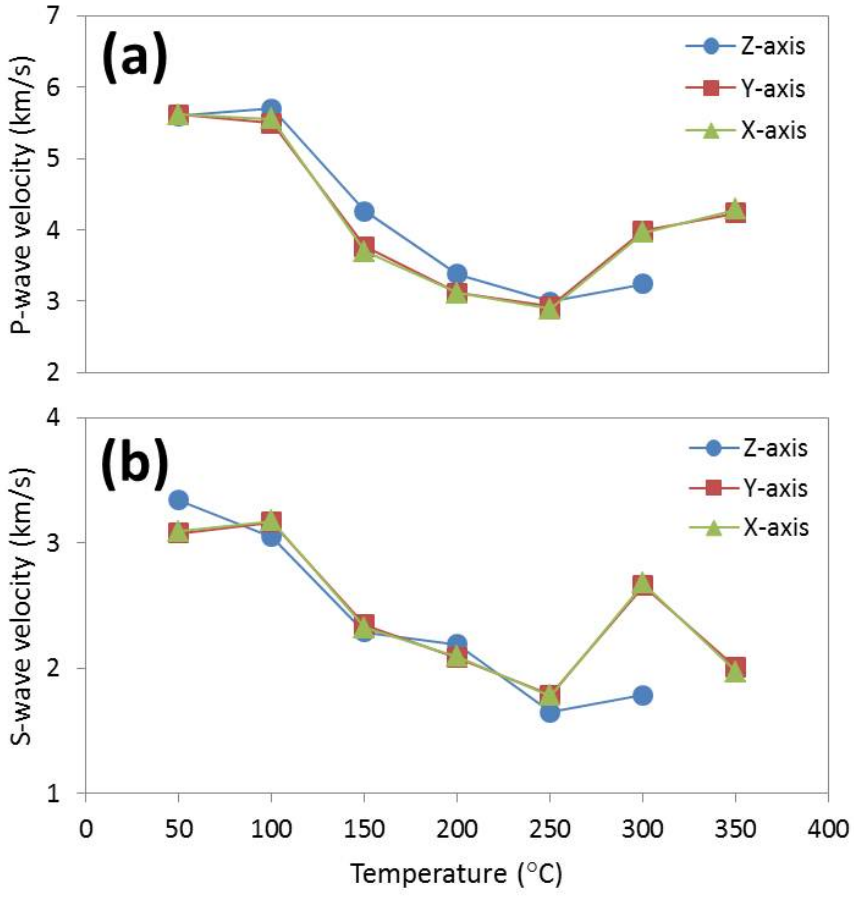


Figure 6.8: Variation of (a) P-wave and (b) S-wave velocity with thermal treatment temperature for Carrara marble samples. Velocities were measured along the Z-axis (circles), Y-axis (squares) and X-axis (triangles) at room temperature and pressure on cooled samples after each thermal cycle.

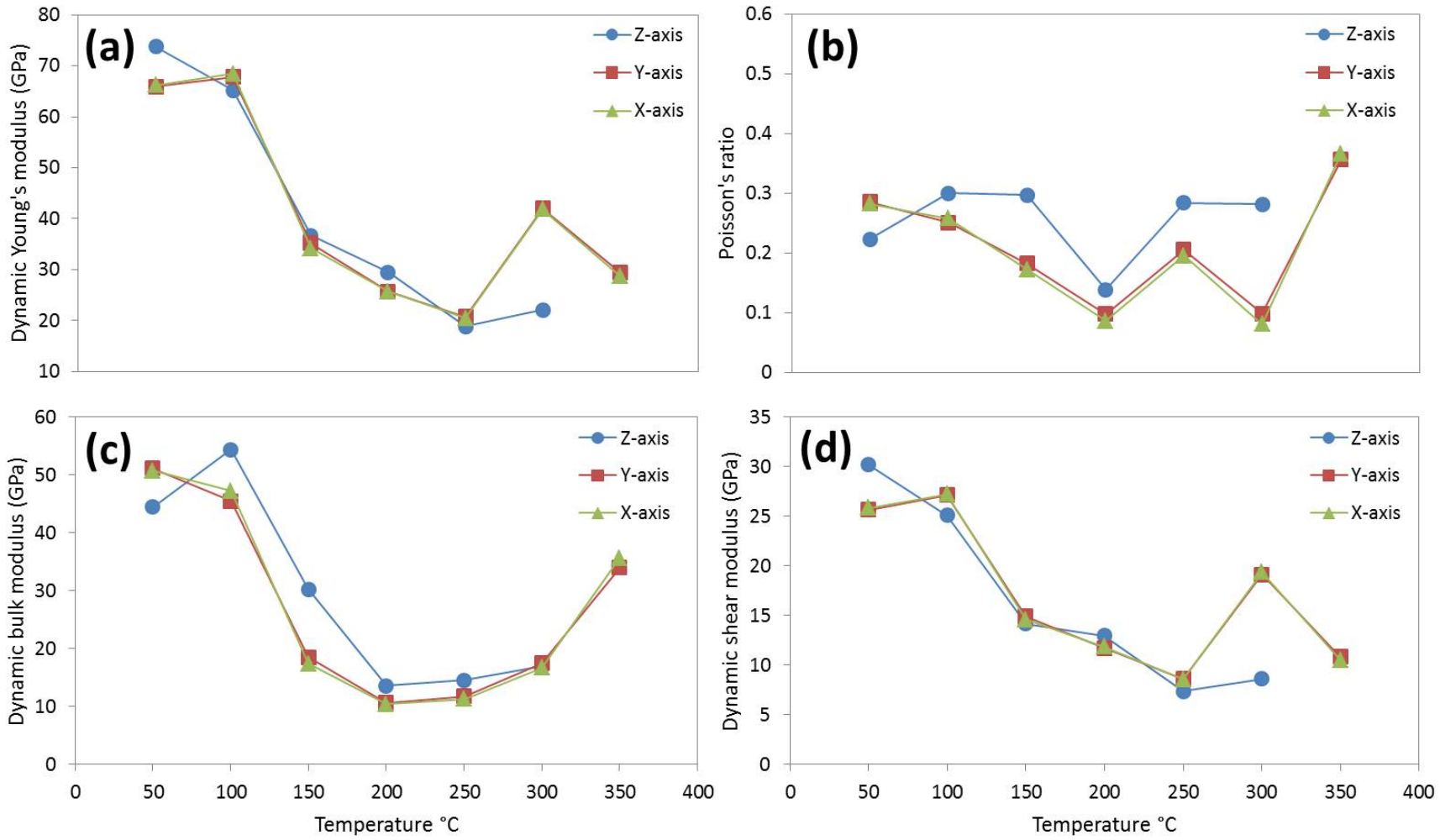


Figure 6.9: Variation of (a) dynamic Young's Modulus, (b) Poisson's ratio, (c) dynamic bulk modulus and (d) dynamic shear modulus with thermal treatment temperature for Carrara marble samples along the Z-axis (circles), Y-axis (squares) and X-axis (triangles).

Results from the crack density inversion are shown in Figure 6.10. Crack density increases steadily after 100°C, reaching a maximum around 200-300°C depending on the orientation (Figure 6.10 (a)). As expected, all three orientations show very similar trends up to 250°C, confirming an isotropic distribution of cracks. Averaging the crack density over all orientations (Figure 6.10 (b)) revealed that the highest density of cracks formed during the 250°C cycle. Consequently, a temperature of 250°C was used for all samples selected for thermal treatment.

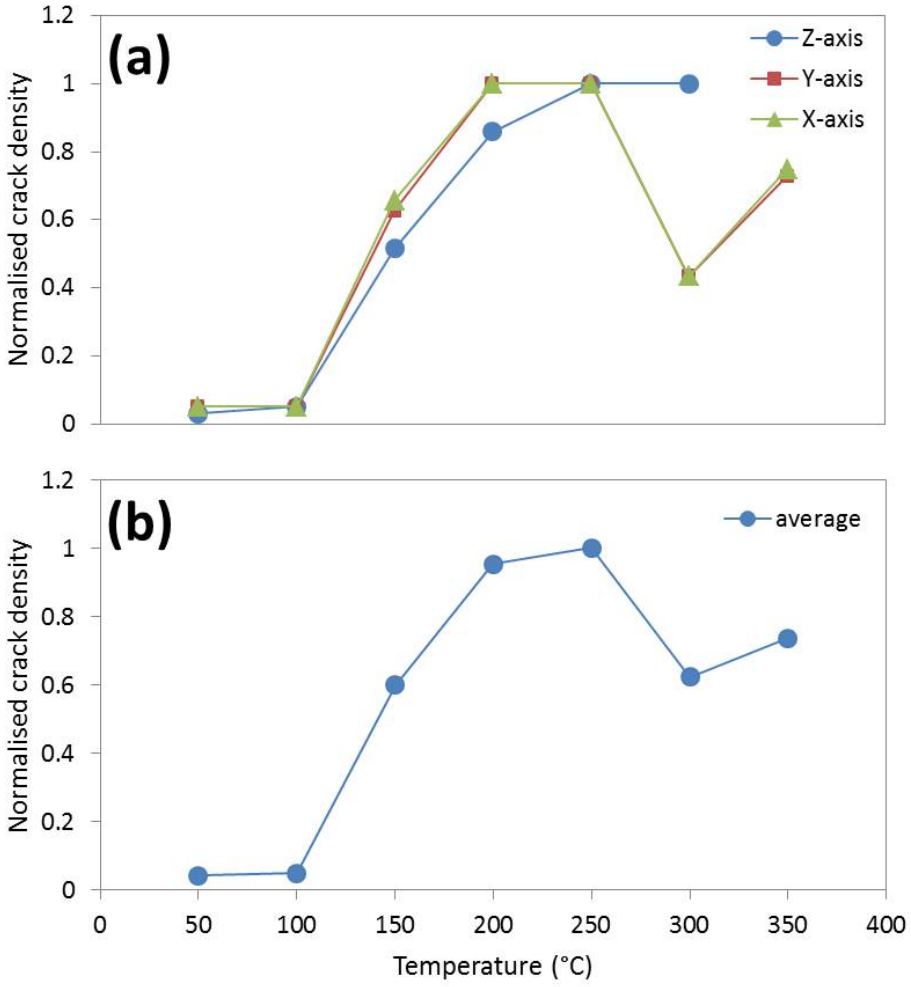


Figure 6.10: Normalised crack density variation with thermal treatment temperature estimated for (a) the Z- (circles), Y- (squares) and X- (triangles) axes and (b) averaged over all orientations. Crack densities were modelled using Equations 4.15 and 4.16 (Sayers and Kachanov, 1995) by means of a simple least squares inversion procedure (Benson et al., 2006; Schubnel et al., 2006a, - see Appendix C for MATLAB code), with model input parameters as given in Table 6.3.

The forward solution of the crack density, yielding a calculated P and S elastic wave velocity (lines) for comparison with the laboratory data used as input for the inversions (symbols), is given in Appendix D. Agreement between the laboratory data and the forward solution is very good, demonstrating the stability of the inversion due to there being no degrees of freedom (Benson et al., 2006). The overall average disagreement between measured and modelled velocities $<0.05$ kms$^{-1}$.

## 6.6 Assessing the Effectiveness of Thermal Treatment

### 6.6.1 Introduction

The planned water- and brine-saturated triaxial experiments employed deformation under drained conditions. That is, with the aim of maintaining a constant pore pressure and measuring pore volume changes during deformation directly by monitoring the variation of pore fluid volume in the volumometers. For pore pressure to be maintained, the permeability must be sufficient to allow interstitial fluid to flow into and out of the specimen as deformation continues (Handin et al., 1963). This counteracts any localised drops in pore pressure caused by an increase in porosity due to the opening of cracks, preventing dilatancy hardening and ensuring that Terzaghi's law of effective stress is obeyed (Paterson and Wong, 2005; Brace and Martin, 1968). In this way, the mechanical behaviour of dry and saturated samples is comparable. It was therefore necessary to establish the extent to which thermal treatment changed the fluid transport properties of the Carrara marble specimens. This was done by means of permeability and porosity measurements on specimens both before and after heating.

### 6.6.2 Methodology

#### 6.6.2.1 Porosity measurements

Porosity for all heat treated samples was established by the same method described in Section 6.3.

#### 6.6.2.2 Permeability measurements

Permeability measurements to assess the effect of the thermal treatment process were made using a steady-state flow-through permeameter designed by Prof. Stanley Murrell (see Jones and Meredith, 1998) to measure permeabilities as low as $10^{-21}$ m$^2$. Since the permeameter was designed to hold samples up to 38.1 mm in diameter x 70 mm in length, the 40 mm diameter x 100 mm long cores prepared for use in the triaxial apparatus could not be used. Therefore, specimens 37.5 mm diameter x 40 mm long, prepared as described in Section 5.5.3 and saturated as described in Section 5.5.5, were used instead. The following procedure was carried out on the specimens both before and after thermally stressing them to 250°C (as described in Section 5.5.6).

The permeameter consisted of a pressure vessel with confining pressure application system and pore-fluid intensifiers to provide a pore pressure. Silicone oil was the confining medium and the confining pressure was applied by means of a gas powered pump fitted with a pressure transducer which pumped the oil from a reservoir into the pressure vessel. The

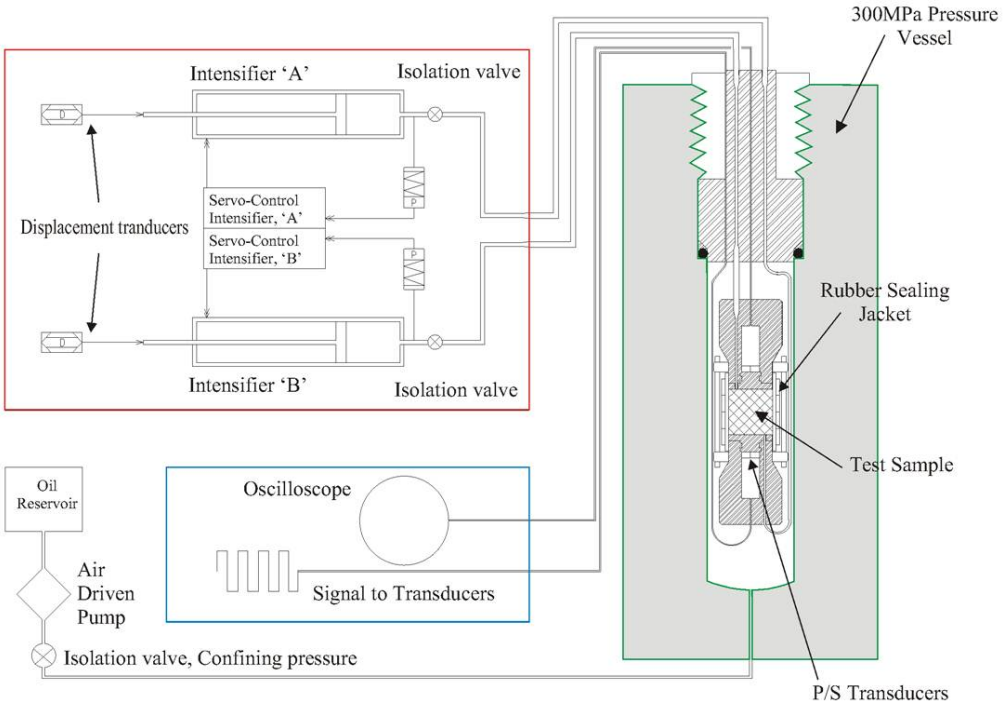


Figure 6.11: Schematic drawing of permeameter setup and sample assembly, courtesy of N. Hughes

pressure transducer enabled the confining pressure to be monitored and logged. Pore fluid (in this case water) was supplied to both ends of a saturated sample by two servo-controlled pore fluid volumometers set to slightly different constant pressures. This applied an average pore fluid pressure and pressure gradient to the sample, allowing fluid to flow through the sample from the high pressure end to the low pressure end. The pore fluid volumometers each comprise a pore fluid intensifier of known volume (46 $cm^3$) fitted with a pressure transducer connected to a controller. The position of the intensifier piston was measured by an integrated linear variable displacement transducer (LVDT) so the change in volume of fluid within the intensifier could be monitored.

A small core of Carrara marble was encased in a nitrile jacket and clamped between two stainless steel end caps through which the pore fluid piping introduces water to it. It was then placed into the pressure vessel and a 20 MPa $P_c$ applied. The two servo-controlled pore fluid volumometers were then connected to the sample assembly with the upstream intensifier full of water and the downstream intensifer almost empty to allow for maximum flow through the sample. To apply the $P_p$, in this case 10 MPa to generate $P_{eff}$ of 10 MPa, each intensifier was set to a constant pressure; the upstream one slightly higher (10.5 MPa) than the downstream one (9.5 MPa) to achieve a 1 MPa differential pressure (10% of $P_p$) along the specimen. The upstream intensifier was opened to the sample first and pore fluid allowed to flow into the sample until the desired fluid pressure was achieved and the volume in the intensifier equilibrated. Once this occurred, the downstream intensifier was opened and fluid allowed to flow through the sample. During this steady-state flow, the volume change in each intensifier was recorded as a function of time. The voltage data from all the integrated transducers were acquired by means of a LabVIEW PCI-6220 data

acqusition card and output through LabVIEW software after conversion to SI units.

All pressure transducers were calibrated using a Budenberg 370 dead weight tester as described in Section 5.4. Full details of the calibration results for the permeameter apparatus are given in Gaunt (2014). Temperature-induced pressure fluctuations were minimised by controlling the temperature in the laboratory with an air conditioning unit.

Permeability, $k$, was calculated by direct application of Darcy's Law:

$$k = \frac{Q\eta}{A}\frac{dx}{dP} \tag{6.7}$$

where $Q$ is the experimentally measured volume flow rate through sample length $dx$, $\eta$ is the dynamic viscosity of the fluid, $A$ is the surface area of the sample (cross-sectional area normal to pressure gradient) and $dP$ is the applied pressure gradient.

Other transport properties were also calculated, including the hydraulic conductivity, $K_{hyd}$, sample storage capacity, $\beta_c$, diffusivity, $D$, and characteristic diffusion time, $\tau_d$, using the following equations (Mavko et al., 2009; Zhang et al., 1994; Brace and Martin, 1968).

$$K_{hyd} = \frac{k\rho g}{\eta} \tag{6.8}$$

with sample density, $\rho$, and acceleration due to gravity, $g$

$$\beta_c = \varphi(\beta_f - \beta_m) + (\beta_b - \beta_m) \tag{6.9}$$

with sample porosity, $\varphi$, fluid compressibility, $\beta_f$, compressibility of the calcite mineral grains, $\beta_m$ and bulk compressibility of the specimen, $\beta_b$

$$D = \frac{k}{\eta\beta_c} \tag{6.10}$$

$$\tau_d = \frac{dx^2}{4D} \tag{6.11}$$

#### 6.6.2.3 Velocity measurements

Additionally, axial benchtop velocities were measured (Section 6.4) for each sample in order to compare permeability changes with elastic moduli and crack density changes using Equations (6.3) to (6.6) and the inversion procedure given in Section 6.5.

### 6.6.3 Results

Table 6.4 shows the fluid transport properties of the two 37.5 mm diameter x 40 mm length Carrara marble samples at 10 MPa $P_{eff}$ before and after thermal treatment. Also given are the dynamic elastic properties at room temperature and pressure.

#### 6.6.3.1 Porosity

Thermal treatment to 250°C increased the overall average connected porosity of all treated samples threefold from $0.18 \pm 0.04$ % to $0.56 \pm 0.12$ %. However, as can be seen from Table 6.4, porosity of the two individual samples used for the permeability measurements increased by slightly less; around twofold on average.

#### 6.6.3.2 Permeability

Table 6.4 shows that initial permeabilities were of the order of $10^{-19}$ m$^2$. The permeability of Sample 2 increased by just over one order of magnitude as a result of the thermal treatment, in agreement with the observations of Homand-Etienne and Troalen (1984). In contrast, the permeability of Sample 1 actually decreased by 1x10$^{-19}$ m$^2$ after thermal treatment. This apparent decrease is in fact extremely small and could be accounted for by a more tortuous flow path if damage accumulated in clusters of intragranular microcracks, as suggested by the simulations of Zhu and Wong (1996), or if cracks did not coalesce, as observed by Fredrich and Wong (1986). Damage accumulation in this manner would dilate the pore space, causing the observed increase in porosity and decrease in wave velocity / increase in crack density but would create a more tortuous and possibly unconnected crack network, leading to the observed decrease in the permeability. Partial crack closure due to twinning and dislocation entanglement may also contribute to this decrease by constricting the existing permeability pathways.

These results highlight a natural variability of the effect of thermal treatment between samples and suggests that, overall, it cannot always be relied upon to increase their permeability. One important issue with these results was that steady-state flow was not always sustained over the course of the experiments (three/four days). This is due to the extremely impermeable nature of the rock and the proximity of the permeability to the limit of the apparatus ($10^{-21}$ m$^2$). Although the permeability values given here were calculated from averaging the flow rates of the steady-state parts of the tests, the results are first-order estimates only.

On average over the two samples, the permeability increased by one order of magnitude, in agreement with the findings of Fischer and Paterson (1992) and Homand-Etienne and Troalen (1984). However, the variability between samples indicated that thermal treatment was not as reliably effective as initially anticipated. An additional consideration

is that initial sample permeability in this study (Table 6.4) was found to be 1-2 orders of magnitude larger than initial permeabilities reported by Zhang et al. (1994), Fischer and Paterson (1992) and Homand-Etienne and Troalen (1984). This is likely explained by the difference in effective pressure conditions during the permeability measurements (10 MPa rather than 30-50 MPa). In contrast, triaxial effective pressure for this study was 30 MPa. So, it was expected that once these conditions had been established, the sample permeability would reduce accordingly, as would the diffusion rate of fluid through it. Since the diffusion rate must be faster than the strain rate to ensure that no localised dilatancy hardening occurs, it was therefore decided that inducing fractures thermally was not sufficient for the needs of this study and an additional method was devised.

Table 6.4: Fluid transport and elastic properties of Carrara marble samples before and after thermal treatment

| | **Sample 1** | | **Sample 2** | | **Average** | |
|---|---|---|---|---|---|---|
| **Transport properties** | **Before** | **After** | **Before** | **After** | **Before** | **After** |
| Permeability, $k$ ($m^2$) | 2.23E-19 | 1.26E-19 | 4.93E-19 | 7.28E-18 | 3.58E-19 | 3.70E-18 |
| Hydraulic conductivity, $K_{hyd}$ ($ms^{-1}$) | 2.19E-12 | 1.24E-12 | 4.84E-12 | 7.14E-11 | 3.52E-12 | 3.63E-11 |
| Storage capacity, $\beta_c$ ($Pa^{-1}$) | 8.70E-11 | 2.00E-10 | 1.19E-10 | 3.40E-10 | 1.03E-10 | 2.70E-10 |
| Diffusivity, D ($m^2s^{-1}$) | 2.57E-06 | 6.32E-07 | 4.13E-06 | 2.14E-05 | 3.35E-06 | 1.10E-05 |
| Characteristic diffusion time, $\tau_d$ (s) | 243.40 | 988.59 | 151.17 | 29.15 | 186.51 | 56.63 |
| Characteristic diffusion rate, $^1/_{\tau_d}$ ($s^{-1}$) | 4.11E-03 | 1.01E-03 | 6.61E-03 | 3.43E-02 | 5.36E-03 | 1.77E-02 |
| **Elastic properties** | **Before** | **After** | **Before** | **After** | **Before** | **After** |
| Porosity, $\varphi$ (%) | 0.18 | 0.32 | 0.25 | 0.65 | 0.22 | 0.49 |
| P-wave velocity, $V_P$ ($kms^{-1}$) | 5.60 | 3.65 | 5.55 | 3.61 | 5.58 | 3.63 |
| S-wave velocity, $V_S$ ($kms^{-1}$) | 3.18 | 2.47 | 3.25 | 2.36 | 3.22 | 2.42 |
| Poisson's ratio, $\nu$ | 0.26 | 0.08 | 0.24 | 0.13 | 0.25 | 0.10 |
| Youngs' modulus, $E_d$ (GPa) | 69.02 | 35.51 | 70.80 | 33.91 | 69.91 | 34.71 |
| Bulk modulus, $K_d$ (GPa) | 48.33 | 13.94 | 45.21 | 15.19 | 46.77 | 14.57 |
| Shear modulus, $G_D$ (GPa) | 27.34 | 16.51 | 28.57 | 15.03 | 27.96 | 15.77 |
| Crack density, $\alpha$ | 0.04 | 0.60 | 0.04 | 0.66 | 0.04 | 0.63 |

## 6.7 Mechanical Loading to Induce Fracture

### 6.7.1 Introduction

As discussed in Chapter 4, mechanically loading a rock sample beyond its elastic limit also induces fracturing. Both Zhang et al. (1994) and Fischer and Paterson (1992) found that at low effective pressures (c. 30-50 MPa) the permeability of Carrara marble samples increased with deformation, with Zhang et al. (1994) reporting increases of up to two orders of magnitude with strains as low as 2%. It was therefore decided that the additional method for inducing fracture prior to conducting saturated experiments would be to mechanically load and unload dry samples under triaxial conditions, straining them by up to 2% (i.e., beyond the elastic limit but not to failure) to introduce fractures immediately prior to saturation.

### 6.7.2 Method

The procedure for inducing fracture mechanically under triaxial conditions is described in Section 5.6. The strain rate used here, $1\text{x}10^{-5}$ $s^{-1}$, was slower than that used by Fischer and Paterson (1992) and Zhang et al. (1994) in order to achieve a more evenly distributed population of fractures. The application of $P_c$ = 30 MPa (i.e., cataclastic regime) also ensured that crack localisation was minimised.

To estimate the permeability, confining pressure was then set to 50 MPa and initial pore pressure to 20 MPa. Once the pore fluid outlet at the top of the sample had been opened to atmospheric pressure, the pressure difference along the sample was 20 MPa and the average effective pressure was 40 MPa. Under the pressure gradient, pore fluid flowed out of the top of the sample and the volume flow rate out of the pore fluid volumometer over time was monitored. Permeability was calculated using Darcy's law (Equation 6.7), as for the thermally treated samples. Twelve samples were fractured in this way, five which had not been heat treated and seven which had.

### 6.7.3 Results

Summary transport properties for the mechanically fractured samples are given in Tables 6.5 and 6.6. On average over the twelve samples, permeability at 30 MPa $P_{eff}$ after mechanically fracturing the samples was found to be $1.47\text{x}10^{-19} \pm 1.7\text{x}10^{-19}$ $m^2$. Permeability remained of the order $1.5\text{x}10^{-19}$ $m^2$ regardless of whether the sample had been heat treated or not and in fact the characteristic diffusion rate ($1/\tau_d$) was slightly slower for those that had been thermally fractured. Oddly, samples deformed to 1.5% strain yielded higher permeability values on average than those deformed to 2% strain, suggesting an increase in the tortuosity of the flow path with increasing deformation, likely due

to constriction of cracks by twinning and dislocation entanglement. This indicates quite a complicated relationship between attempts to induce fracture mechanically and the resulting permeability. However, the whole procedure ensured that the characteristic diffusion rate was several orders of magnitude faster than the strain rates used for deformation under saturated conditions ($10^{-6}$ and $2x10^{-6}$ $s^{-1}$), allowing fluid to flow freely into and out of the sample in response to loading. This ensured that pore pressure was maintained constant during deformation, that no dilatancy hardening occurred and that pore fluid volume changes monitored by the pore volumometer accurately represented the change in pore volume within the sample.

Table 6.5: Summary transport properties of both intact and thermally fractured samples after mechanical fracturing

| | **Intact** | | **Thermally fractured** | | **All** | |
|---|---|---|---|---|---|---|
| **Property** | **Average** | **Std. dev.** | **Average** | **Std. dev.** | **Average** | **Std. dev.** |
| Initial porosity, $\varphi$ (%) | 0.21 | 0.07 | 0.59 | 0.03 | 0.44 | 0.20 |
| Permeability, $k$ ($m^2$) | 1.41E-19 | 1.00E-19 | 1.52E-19 | 2.16E-19 | 1.47E-19 | 1.70E-19 |
| Hydraulic conductivity, $K_{hyd}$ ($ms^{-1}$) | 1.33E-12 | 9.22E-13 | 1.42E-12 | 2.00E-12 | 1.39E-12 | 1.58E-12 |
| Storage capacity, $\beta_c$ ($Pa^{-1}$) | 1.02E-10 | 3.26E-11 | 3.15E-10 | 1.29E-11 | 2.27E-10 | 1.12E-10 |
| Diffusivity, D ($m^2s^{-1}$) | 1.22E-06 | 6.57E-07 | 4.63E-07 | 6.66E-07 | 7.79E-07 | 7.42E-07 |
| Characteristic diffusion time, $\tau_d$ (s) | 709.15 | 487.71 | 3649.70 | 2779.55 | 2424.47 | 2567.75 |
| Characteristic diffusion rate, $^1/_{\tau_d}$ ($s^{-1}$) | 1.95E-03 | 1.05E-03 | 7.41E-04 | 1.07E-03 | 1.25E-03 | 1.19E-03 |

Table 6.6: Summary transport properties of mechanically fractured samples after deforming to 1.5% or 2% strain

| | **Deformed to 1.5% strain** | | **Deformed to 2% strain** | |
|---|---|---|---|---|
| **Property** | **Average** | **Std. dev.** | **Average** | **Std. dev.** |
| Initial porosity, $\varphi$ (%) | 0.32 | 0.20 | 0.55 | 0.13 |
| Permeability, $k$ ($m^2$) | 2.10E-19 | 2.23E-19 | 8.49E-20 | 6.93E-20 |
| Hydraulic conductivity, $K_{hyd}$ ($ms^{-1}$) | 1.97E-12 | 2.06E-12 | 7.97E-13 | 6.37E-13 |
| Storage capacity, $\beta_c$ ($Pa^{-1}$) | 1.64E-10 | 1.12E-10 | 2.89E-10 | 7.51E-11 |
| Diffusivity, D ($m^2s^{-1}$) | 1.18E-06 | 7.74E-07 | 3.73E-07 | 4.67E-07 |
| Characteristic diffusion time, $\tau_d$ (s) | 860.21 | 641.64 | 3988.74 | 2867.23 |
| Characteristic diffusion rate, $^1/_{\tau_d}$ ($s^{-1}$) | 1.90E-03 | 1.24E-03 | 5.96E-04 | 7.48E-04 |

# Chapter 7

# Electric Signals in Carrara Marble During Deformation[1,2,3]

## 7.1 Introduction

This chapter, and the following three, set out the evolution of electric current during constant strain rate triaxial deformation of Carrara marble samples at room temperature (see Section 6.2 for full rock description). To establish the effect of various crustal conditions on electric current generation in a non-piezoelectric rock, dry specimens were deformed under elevated pressures ($P_c$ = 10, 20, 30, 60 and 100 MPa) at a strain rate, $\dot{\varepsilon} = 10^{-6}$ s$^{-1}$ and separately at $\dot{\varepsilon} = 10^{-4} - 10^{-6}$ s$^{-1}$ and $P_c$ = 30 MPa. The influence of pore fluid and pore fluid salinity on the electric current generated under drained (constant $P_p$) conditions was also investigated, with de-ionised water and Instant Ocean brine solution used as pore fluids. These saturated experiments were carried out at an effective pressure, $P_{eff}$ = 30 MPa ($P_p$ = 20 MPa, $P_c$ = 50 MPa) and $\dot{\varepsilon} = 10^{-6}$ s$^{-1}$. Damage evolution throughout each test was tracked by means of stress, stress rate, Young's Modulus, ultrasonic wave velocities and acoustic emissions. The relationship between electric current and these damage analogues is also presented.

This chapter is structured as follows: First, the mechanical behaviour of these Carrara marble samples is described; (a) typical dynamic stress-strain curves are presented for the various experimental conditions, together with the mechanical repeatability of the experiments under identical conditions, and (b) the specimens' deformation style is cate-

[1]Cartwright-Taylor, A., Vallianatos, F. and Sammonds, P. (2015). Deformation-induced electric current in Carrara marble across the brittle-ductile transition. *TSG Annual Meeting 2015 5-8 Jan.*

[2]Cartwright-Taylor, A., Vallianatos, F. and Sammonds, P. (2013). Fracture and electric current in the crust: a $q$-statistical (Tsallis) approach. *AGU Fall Meeting 9-13 Dec.*

[3]Cartwright-Taylor, A., Sammonds, P. and Vallianatos, F. (2012). Pressure-stimulated current emissions from triaxial compression experiments on Carrara marble. *EGU General Assembly 22-27 April.*

gorised and the mechanisms involved are discussed. Thereafter, electric current evolution is presented, with some initial observations being made regarding the electric current signals, including their variability under identical conditions and the main features consistent across experiments. This is followed by an analysis of the electric signal variation within individual specimens to establish (a) how the current recorded perpendicular to the loading axis changes along the length of the samples and (b) whether the orientation of the final failure plane affects the observed electric signal. Damage evolution and the electric current signal are then correlated for one particular experiment. Finally, features of electric current flow as failure approaches are given with respect to stress rate.

The subsequent three chapters discuss the influence of confining pressure, strain rate and pore fluid conditions on the flow of electric current and accumulated charge. In order to investigate the overall influence of deformation and environmental condition on these complicated signals and quantify their dependence, values of electric current flow, $I$, and electric charge, $Q$ (where $Q = \int I dt$), were noted for several 'strain slices' throughout the test at intervals of 0.25 % strain. Prior to calculating electric charge, a running median filter was applied to the electric current data. Values at each strain slice were then found and both the current and charge data were interpolated linearly if there was no data point at the required strain value. The variation in the *magnitude* of both the electric current flow ($I_{abs}$) and accumulated electric charge ($Q_{abs}$) at these particular values of strain are presented for each of the environmental conditions. Additionally, the dependence of the rate of current production on each of the environmental conditions was investigated. The magnitude of the approximately linear gradient of the main electric current deflection over time, $|dI/dt|$ is presented. Following this, the influence of environmental condition on the damage sustained by the sample is presented in terms of the P-wave velocity ($V_P$) and the changing Young's Modulus, together with the relationship between damage and electric current evolution. Finally, the influence of environmental condition on the relationship between electric current and differential stress is presented and discussed.

## 7.2 Mechanical Behaviour of Carrara Marble

### 7.2.1 Stress-strain behaviour

A typical stress-strain curve for the mechanical deformation of the Carrara marble samples tested is shown in Figure 7.1 (a). This test was conducted under dry conditions at the fastest strain rate ($10^{-4}$ s$^{-1}$) and intermediate confining pressure (30 MPa) and clearly illustrates all the stages of deformation. Initially, the sample compacts, deforming quasi-elastically between 0 and 0.2 % sample strain as existing cracks and pores are closed. The extremely low porosity ($\sim$ 0.2 %) of Carrara marble means that very little strain can be accommodated in this way. Decreasing pore volume (seen during the fluid-saturated, slow strain rate experiment in Figure 7.1 (b)) in this region is an indirect measure of the

compaction; in this case the reduction in pore volume is less than 0.05 $cm^3$. Beyond the elastic limit, deformation is ductile and strain hardening occurs. The stress-strain curve deviates from linearity and the degree of strain hardening gradually decreases (initial yield) until the peak stress is reached at 0.9% strain. The strain at which peak stress is reached varies with the experimental conditions. For the various strain rates tested (Figure 7.2 (a)), peak stress is reached between 0.9 and 2% strain, with the value increasing with decreasing strain rate. For the various confining pressures tested (Figure 7.2 (b)), the range is wider: from 0.4 to 2% strain at low confining pressures (10 to 30 MPa). Above 30 MPa, peak stress is not reached within the time-frame of the experiment and the overall stress supported by the sample increases significantly, as does the degree and extent of stable strain hardening beyond the initial yield.

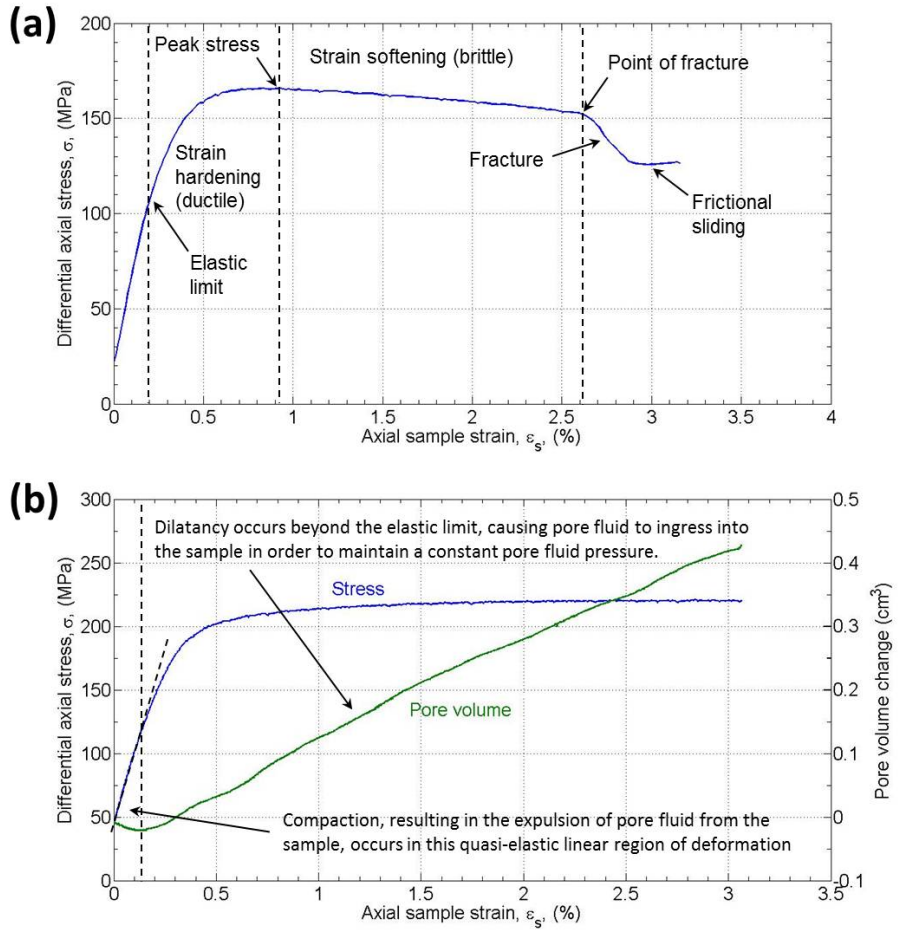


Figure 7.1: Typical stress-strain curves for triaxial deformation of Carrara marble specimens (a) illustrating the key features of deformation at 30 MPa $P_c$ and 1x10$^{-4}$ s$^{-1}$ strain rate under dry conditions [Experiment CM03] and (b) showing the correlation of the linear, quasi-elastic region with a decrease pore fluid volume, corresponding to compaction and the subsequent increase corresponding to dilatancy during permanent deformation, at 30 MPa and 1x10$^{-6}$ s$^{-1}$ strain rate under fluid-saturated conditions [Experiment CM51].

Beyond peak stress, a region of strain softening is seen as the ability of the sample to support a load diminishes. The degree of strain softening is greater at faster strain rates and low confining pressures, while the extent of the strain softening region increases at slower strain rates and with increasing confining pressure (Figure 7.2). Strain softening

is not seen at the highest confining pressures tested. At conditions of 20-30 MPa and intermediate to slow strain rates (Figure 7.1 (b) and Figure 7.2), strain hardening or strain softening occur to a very small degree and the level of stress supported by the sample remains stable; behaviour characteristic of cataclastic flow. This region, where the sample supports a constant stress over relatively large strains, indicates that the mechanisms involved in accommodating deformation (e.g., microcracks, localised faulting, fragment roll, intergranular sliding, etc.) act in small, localised areas that are distributed evenly throughout the sample, thus avoiding the concentration of damage along a local failure surface and the weakening associated with large-scale crack coalescence. Eventually, after a period of strain softening, the sample in Figure 7.1 (a) fails macroscopically at 2.6% strain, resulting in a stress-drop as it fractures. If deformation continues after fracture, stable frictional sliding occurs along the failure surfaces. Values of 3-5% strain to failure are often taken as defining the brittle-ductile transition (Heard, 1960; Evans et al., 1990; Paterson and Wong, 2005). Figure 7.2 (b) indicates that the brittle-ductile transition for the samples tested here begins at around 20-30 MPa, in good agreement with previous work on pure, coarse-grained marbles (von Karman, 1911; Paterson, 1958; Fredrich et al., 1989; 1990; Renner and Rummel, 1996), as shown in Figure 6.1.

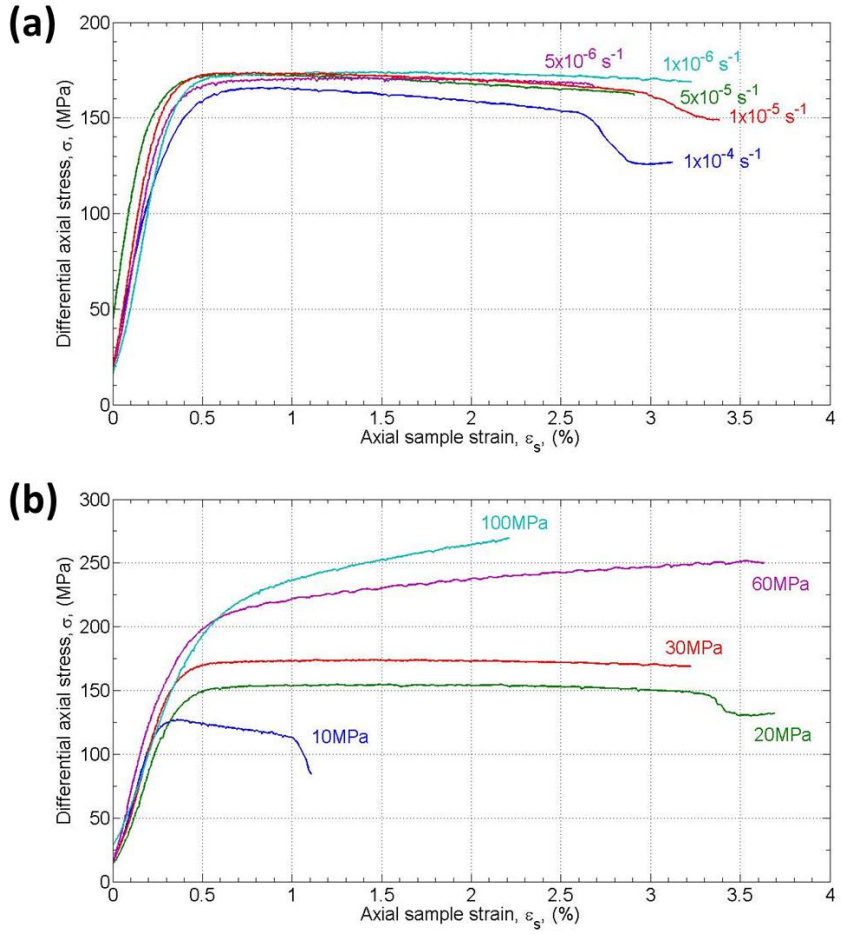


Figure 7.2: Stress-strain curves for triaxial deformation of Carrara marble specimens under (a) various strain rate conditions at 30 MPa $P_c$ [Experiments CM03, CM26, CM06, CM25 and CM07] and (b) various confining pressure conditions at $10^{-6}$ s$^{-1}$ strain rate [Experiments CM08, CM65, CM07, CM64 and CM35].

Confining pressure has greater influence on the stress-strain behaviour of the Carrara marble samples than strain rate (Figure 7.2). Strain rate has a limited effect on the overall strength of the material and the amount of strain accommodated prior to failure; a strain rate decrease of two orders of magnitude corresponds to an increase in peak strength of only around 20 MPa, while a tenfold decrease in the strain rate corresponds to an increase in the strain to failure of about 0.5%. The effect of further strain rate decrease on the strain to failure is not clear since none of these samples failed within the time-frame of the experiments. Nevertheless, it is clear that deformation becomes increasingly ductile as the strain rate slows. In comparison, a tenfold increase in confining pressure more than doubles both the overall strength of the sample and the amount of strain accommodated by deformation, with deformation becoming significantly more ductile as the confining pressure increases. This behaviour was first observed by von Karman (1911) in his pioneering triaxial experiments on Carrara marble and has been observed by many other authors since (Paterson, 1958; Rutter, 1974; Fredrich et al., 1989; 1990; Renner and Rummel, 1996; Covey-Crump, 1998). At 10MPa the sample behaves in a classic brittle manner with a constant degree of strain softening and a negative Young's Modulus beyond the point of peak stress, until the sample cannot support the load any further and it fails macroscopically. At the brittle-ductile transition (20-30 MPa), the increase in strain is almost independent of stress with the same load being supported for up to 2 mm of deformation. At 20 MPa, macroscopic fracture did occur within the time-frame of one experiment [CM65] taken to >3 % strain. In the ductile regime (>30 MPa), samples exhibited a constant degree of strain hardening after the initial yield and no macroscopic failure occurred.

The mechanical behaviour described above is observed throughout the majority of experiments performed for this study and can be considered representative of the Carrara marble specimens tested. Figure 7.3 shows the degree of repeatability obtainable in the mechanical behaviour of the Carrara marble samples used in this investigation.

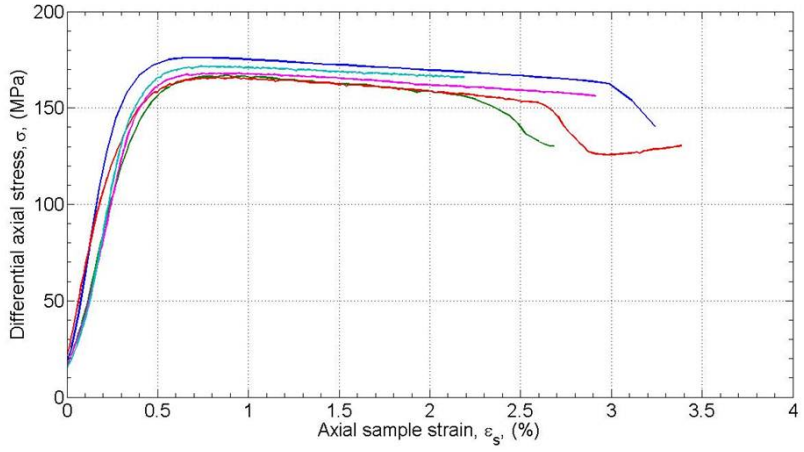


Figure 7.3: Stress-strain curves for five identical experiments showing repeatability in the mechanical response of Carrara marble samples at 30 MPa and $10^{-4}$ $s^{-1}$ strain rate [Experiments CM04, CM02, CM03, CM15, CM18]. Other conditions exhibited a similar degree of mechanical repeatability.

It should be noted here that not all samples deformed under conditions suitable for macroscopic failure were taken to failure, with experiments stopped prior to failure for several reasons. To avoid jacket rupture and sensor damage, no sample was taken to more than 3.7% axial sample strain (equivalent to 4 mm shortening). Additionally, samples were taken to varying levels of strain in order that further evidence of the damage sustained by the samples under varying degrees of deformation could be provided by microstructural analysis. This analysis is beyond the scope of this study but will be undertaken at a later date.

### 7.2.2 Deformation style and mechanisms

Five types of macroscopic deformation have been observed in previous studies of marble (Jaeger et al., 2007; Paterson and Wong, 2005; Covey-Crump, 1998; Fredrich et al., 1989; Paterson, 1958) (Figure 4.4). All Carrara marble specimens deformed during this study fell into the first four basic types of deformation. Photographs of samples from this study, with schematic overlays to highlight the main features of deformation, are displayed in Figure 7.4. To distinguish further between these deformation styles, I characterised the deformation style of the samples used in this study according to the following categories (see Table in Appendix E) from brittle to ductile behaviour:

1. Combination of sharply defined axial and shear fracture, not restricted to central region - extends to top of sample. Faint striations visible in the rock fabric indicating the presence of numerous tiny shear conjugate microcracks in the central region of the sample. No barrelling.

2. Sharply defined shear fault with numerous smaller well-defined conjugate shear fractures distributed within the central damage zone and significant barrelling.

3. Sharply defined shear fault with numerous well-defined conjugate shear fractures distributed within the central damage zone and significant barrelling. Start of main conjugate fracture visible on one side of the sample.

4. Start of main fault surface(s) visible on one or both sides of sample but no full macroscopic fault, numerous well-defined conjugate shear fractures in central damage zone and some barrelling.

5. No macroscopic shear fault, numerous small conjugate microfractures in central damage zone and little or no barrelling.

6. No barrelling or visible external damage apart from faint striations visible in the rock fabric indicating the presence of tiny shear microcracks in the central region of the sample.

7. No evidence of microfractures on the sample surface, some evidence of ductile flow of the rock fabric

8. No evidence of any deformation on the sample surface.

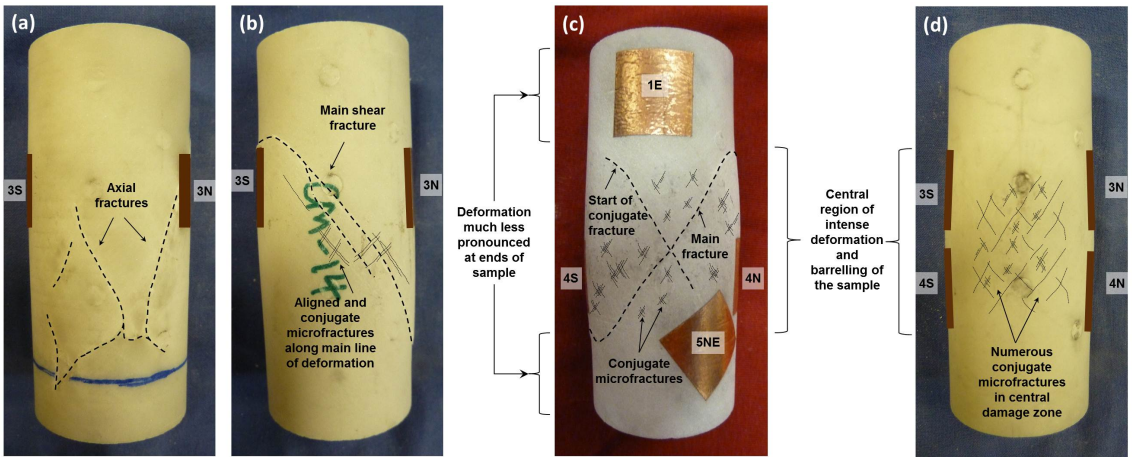


Figure 7.4: Photographs of samples from this study, highlighting the various types of deformation observed; (a) axial splitting [CM08 - category 1], (b) single shear fracture [CM14 - category 2], (c) conjugate shears [CM65 - category 3] and (d) ductile behaviour (multiple shears; cataclastic flow) [CM49 - category 5]. Electrodes are labelled with their position codes.

Deformation transitioned from localised macroscopic brittle fracture at fast strain rates ($10^{-4}$ to $10^{-5}$ $s^{-1}$) and low confining pressures (10-30 MPa) to numerous tiny conjugate shear microcracks homogeneously distributed throughout a broad region of deformation in the central part of the sample at slower strain rates ($10^{-5}$ to $10^{-6}$ $s^{-1}$) and intermediate confining pressures (c. 30 MPa) to ductile behaviour with no macroscopic evidence of any brittle deformation at higher confining pressures (60-100 MPa). The extent of deformation evident on the sample surface, such as the degree of barrelling or whether a fault was through-going or not, depended on the maximum strain reached during the experiment. Barrelling was seen in samples deformed beyond 2 % strain, with those taken to $\geq$ 3 % strain exhibiting the greatest extent. Ductile deformation in the form of cataclastic flow manifests in numerous small conjugate shear fractures which become visible on the specimen surface as the strain increases beyond about 2%. The majority of samples were deformed at $10^{-6}$ $s^{-1}$ and 30 MPa and these exhibited the whole range of deformation categories due to being subjected to varying amounts of deformation. Deformation category decreased with increasing final strain, highlighting the transition from ductile to brittle behaviour determined by the slope of the stress-strain curve (see Section 4.4). Categories 7 and 8 were seen only in samples deformed at slower strain rates ($10^{-5}$ to $10^{-6}$ $s^{-1}$) and $P_c > 50$ MPa (N.B. the fastest strain rate was not tested at these $P_c$). Category 6 spanned the same slower strain rates and all but the lowest $P_c$, while categories 3 to 5 were seen across all strain rates but only in samples deformed at intermediate confining pressures ($20 - 30$ MPa). Category 2 was seen at the faster strain rates ($10^{-4}$ to $10^{-5}$ $s^{-1}$) and intermediate $P_c$, while category 1 was seen only at the lowest $P_c$ and the slowest strain rate (N.B. fast strain rates were not tested at this $P_c$). This overall decrease in deformation category with decreasing confining pressure and increasing strain rate highlights the transition from ductile to brittle behaviour determined by the environmental conditions (see Section 4.5). The wide range of conditions at which the intermediate deformation

categories were seen is attributed to both the variation in total strain they were subjected to and the combination of deformation mechanisms (brittle fracture vs. cataclastic flow) that vie for dominance at the brittle-ductile transition.

## 7.3 Initial Observations of Electric Current

The first notable observation from the experiments carried out during this investigation is that an electric current *was* generated and sustained during the deformation of Carrara marble specimens under *all* the conditions tested. Under dry conditions, this current flow within the stressed samples was detected only in the region beyond (quasi-)linear deformation; i.e., in the region of permanent deformation beyond the yield point of the material and in the presence of microcracking and cataclastic flow. This is the first time that such an electric current has been observed under simulated crustal conditions and supports observations of similar electric current emissions generated under uniaxial conditions (Stavrakas et al., 2003; Anastasiadis et al., 2004).

Secondly, there is a natural variability in current emissions between different experiments carried out under identical conditions. Figure 7.5 (b) shows the electric current generated for three experiments conducted on dry samples under $P_c = 30$ MPa and $\dot{\varepsilon} = 10^{-6}$ s$^{-1}$. The corresponding stress-strain curves can be seen in Figure 7.5 (a). Deformation is initially quasi-elastic and then ductile as microcracks form. For all of these tests, electric current flow across the sample, perpendicular to the loading axis, was recorded on a single channel between two electrodes at positions 3S and 3N (see Figure 5.6), 12.5 mm above the centre of the sample. None of these samples reached peak stress or failed within the time limit of the experiments. In hand specimen, they exhibited some barreling and evidence of small conjugate shear striations on the surface, oblique to the loading axis and distributed throughout the central region (deformation category 6). It is clear from Figure 7.5 (b) that electric current generated under identical conditions varied by up to two orders of magnitude. This observed variability in the amount of electric current produced under identical conditions may be attributed both to the orientation of the electrode pairs to regions of damage accumulation (discussed in Section 7.4) and to natural variability in the microscopic structure of the samples. This natural variability may include: (1) impurities present in the samples in very small but varying quantities which attract extrinsic defects and form electric dipoles which then migrate under the application of stress, (2) varying quantities of peroxy bonds from which positive holes may be activated or (3) variation in defect and dislocation densities (see Section 3.5.1). However, several main features of electric current flow with respect to the evolution of deformation are consistent across experiments (Figure 7.6). No current flows during the quasi-elastic compaction phase. Once the yield point of the material is reached (0.2-0.3% strain) and the stress-strain curve enters the ductile regime, electric current begins to flow between the electrodes. It is initially observed as a small (of the order of 0.01 nA) deviation from background,

although this feature is not seen in all experiments. Significant electric current flow is observed from a point towards the end of the initial yield (~0.5% strain) with current produced at a fairly constant rate (main deflection). This continues for approximately a further 0.25% strain as the effective Young's Modulus, $E_{eff}$ decreases. Once $E_{eff}$ begins to approach zero, current production levels off and the signal exhibits fluctuations, sometimes in the form of burst-like emissions (e.g., Experiment CM05), of the order of 0.1 nA until deformation is halted.

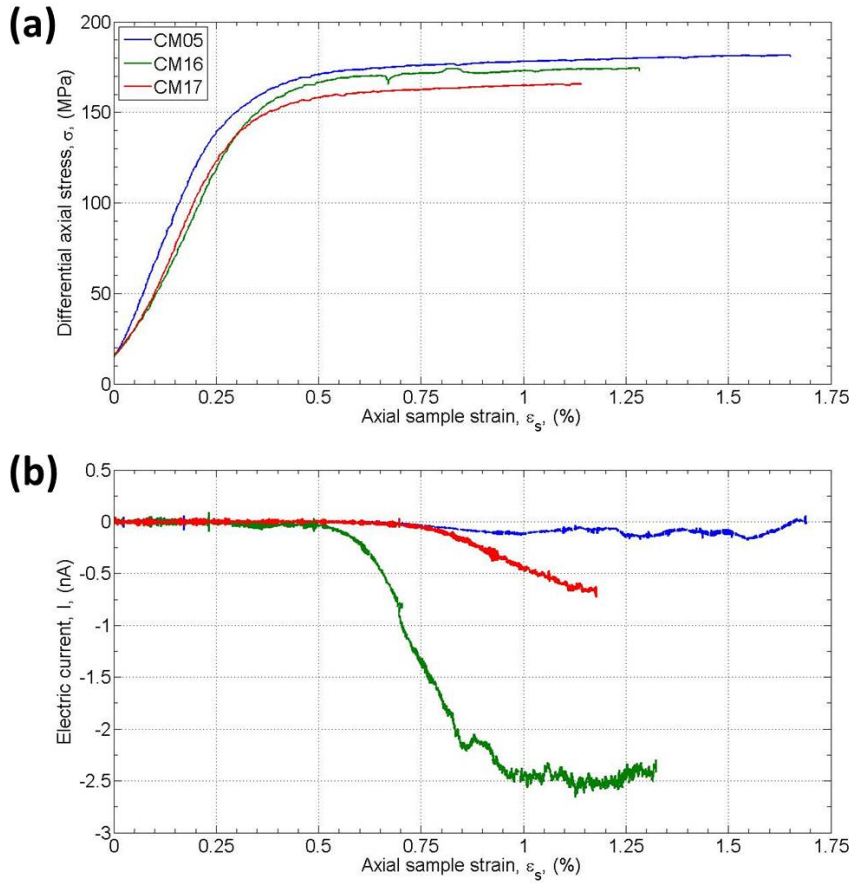


Figure 7.5: The level of repeatability obtainable, in terms of (a) differential stress and (b) electric current as a function of axial sample strain, for three identical experiments [CM05, CM16 and CM17] on specimens of Carrara marble carried out at 30 MPa $P_c$ and $10^{-6}$ $s^{-1}$ strain rate.

Finally, for the majority of experiments, the observed polarity of the main deflection was negative. Positive deflections were seen in three out of the 15 experiments conducted to investigate the influence of strain rate on dry samples at $P_c$ = 30 MPa. All three of the samples with positive main deflections were deformed at the two fastest strain rates ($10^{-4}$ and 5x$10^{-5}$ $s^{-1}$) while all samples deformed at the slower strain rates (from $10^{-5}$ to $10^{-6}$ $s^{-1}$) exhibited negatively polarised main deflections. Additionally, for four out of these 15 experiments, the main deflection exhibited a fluctuating rather than smooth rate of current production. Again, these four samples were deformed at the faster end of the strain rate range (from $10^{-4}$ to $10^{-5}$ $s^{-1}$ ) with two of them also having positive main deflections. Of the experiments carried out at $10^{-6}$ $s^{-1}$ to investigate the influence of confining pressure on dry samples, all exhibited negative polarity in the main electric

current deflection, apart from the test at 100 MPa. However, at 10 MPa there was a clear initial positive deflection of c. 0.2 nA prior to the negative main deflection.

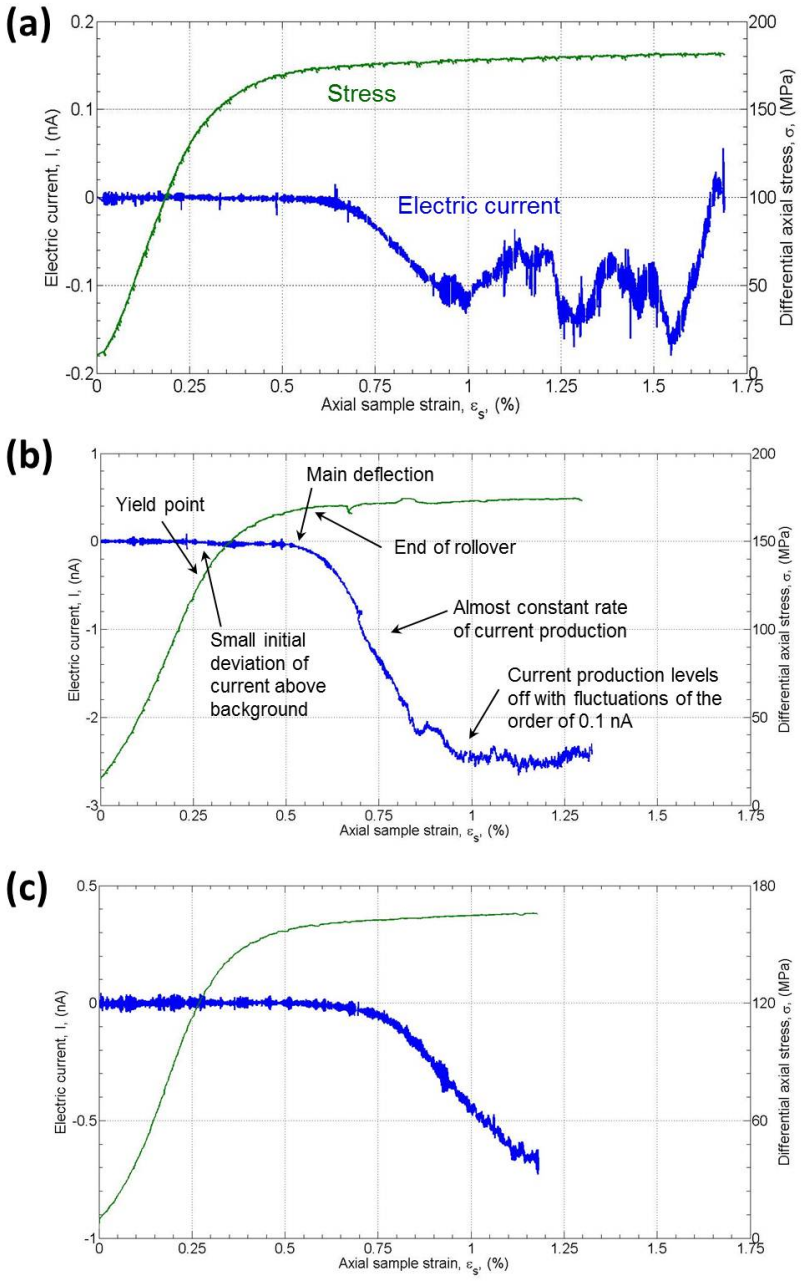


Figure 7.6: Electric current (blue) and differential stress (green) plotted as functions of axial sample strain, for three identical experiments [(a) CM05, (b) CM16 and (c) CM17] on Carrara marble specimens carried out at 30 MPa and $10^{-6}$ $s^{-1}$. All show an overall consistent shape to the current evolution, with the main features indicated in black text.

## 7.4 Electric Current Variation within Individual Specimens

### 7.4.1 Introduction

The rate of electric current production and quantity of electric current generated during deformation varied within samples, as demonstrated by six multi-channel experiments [Experiments CM03, CM04, CM06, CM07, CM12 and CM65]. This variability in electric current flow between channels indicates that charges generated within the deforming samples are not homogeneously distributed but are due rather to the presence of local electric dipoles, possibly due to localised accumulation of damage.

### 7.4.2 Relationship between electrode position and electric current

One experiment [CM12] recorded four channels perpendicular to the loading axis across a dry sample of Carrara marble at 30 MPa $P_c$ and $10^{-6}$ $s^{-1}$ strain rate. Electrode pair positions for each channel were: (a) 3S and 3N, 12.5 mm above the centre of the sample, (b) 4S and 4N, 12.5 mm below the centre of the sample, (c) 1S and 1N, 37.5 mm above the centre of the sample and (c) 6S and 6N, 37.5 mm below the centre of the sample. Figure 7.7 shows the electric current recorded during this experiment, highlighting the variation in electric current flow along the length of the sample.

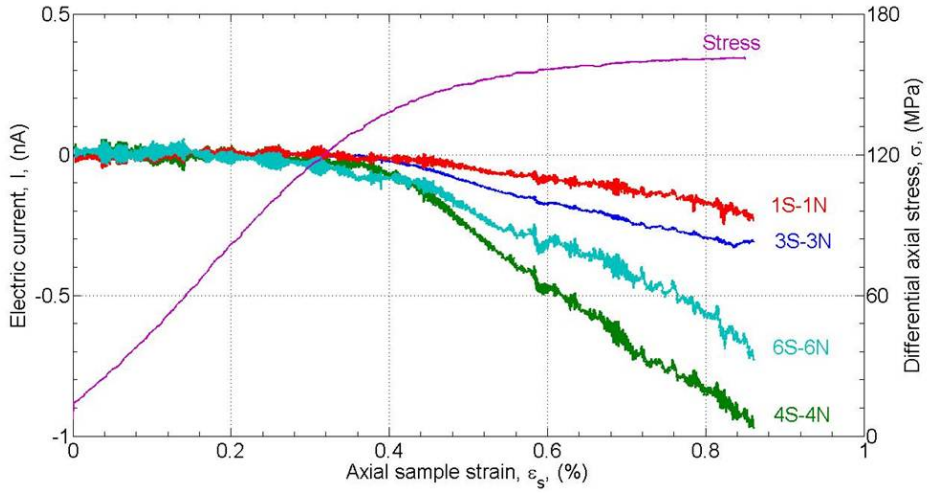


Figure 7.7: Stress and electric current as a function of axial sample strain, produced during triaxial deformation of a Carrara marble specimen at 30 MPa and $10^{-6}$ $s^{-1}$ [Experiment CM12]. Current flow between each of four electrode pairs is shown, each labelled with the electrode pair position according to the convention described in Section 5.2.4 and shown in Figure 5.6.

The sample was deformed up to 0.86 % strain and all the detected current flow was of negative polarity. Signals exhibit the same characteristic behaviour across all channels, as described in Section 7.3, of an initial small deflection from 0.3 to 0.45 % strain followed by a main deflection from 0.45 % strain to the end of the test. However, current was produced at a much greater rate in the bottom half of the sample (4S-4N and 6S-6N)

compared with the top half (3S-3N and 1S-1N). The initial rate of current production, $|dI/dt|$, was constant in the top half of the sample (1S-1N and 3S-3N) and then increased towards the bottom of the sample. Rates at the 4S-4N and 6S-6N electrode pairs were three and five times respectively that seen in the top half of the sample. The main rate of current production was greater in the centre of the sample than at the ends, with the rate at the bottom end (6S-6N) being 3 times that at the top end (1S-1N) and the rate in the lower centre (4S-4N) being 3 times that in the top centre (3S-3N). Rates in the centre of the sample were also 1.5 times their respective ends. See Table 7.1 for the values. This implies a greater number of charges accumulating in the bottom half of the sample than the top as deformation continues, and also relatively more charges developing in the centre of the sample that at the ends reflecting the localisation of damage in the sample. Additionally, the local signal fluctuations apparent from 0.6 % strain to the end of the test were larger in the bottom half of the sample (∼0.1 nA compared with ∼0.05 nA).

Table 7.1: Rates of electric current production, $|dI/dt|$, for the experiment shown in Figure 7.7

| | **Rate of current production, $\|dI/dt\|$, (pA s$^{-1}$)** | |
|---|---|---|
| **Electrode pair** | **Initial deflection** | **Main deflection** |
| 1S-1N | 4.44E-03 | 3.64E-02 |
| 3S-3N | 4.41E-03 | 5.52E-02 |
| 4S-4N | 1.35E-02 | 1.64E-01 |
| 6S-6N | 2.20E-02 | 1.07E-01 |

Another experiment [CM65] recorded two channels across the sample at 20 MPa and $10^{-6}$ s$^{-1}$. These channels were in very different places along the sample; one was at the top of the sample, oriented 1E-1W, while the other was just below the centre of the sample, oriented 4S-4N. Figure 7.8 shows the electric current results from this experiment. It is clear that both follow a very similar form, with the onset of current flow occurring at (or immediately after) the yield point and the initial deflection of electric current above background being of opposite polarity to the main flow of current, which then stabilises and fluctuates around a relatively constant value. The form of this current is something between that seen at 10 MPa and 30 MPa, with the early part of current flow emulating that seen at 10 MPa and the later part emulating that seen at 30 MPa. During the first 2% of strain, current was generated faster and more current was produced across the central part of the sample than across the top. However, beyond 2% strain, current flow in the central part decreased slightly before increasing again at about 3% strain, immediately prior to failure. This mirrored the continued increase and then decrease in current flow across the top of the sample. N.B. There is a greater fluctuation of current around the background level on both channels at the start of loading in this experiment than that seen in the original series of tests. This may be due to the sample being marginally wider than those in the original series (see Section 8.1), causing the electrodes to be closer to the vessel wall and thereby increasing the background noise in the acquisition system during this experiment.

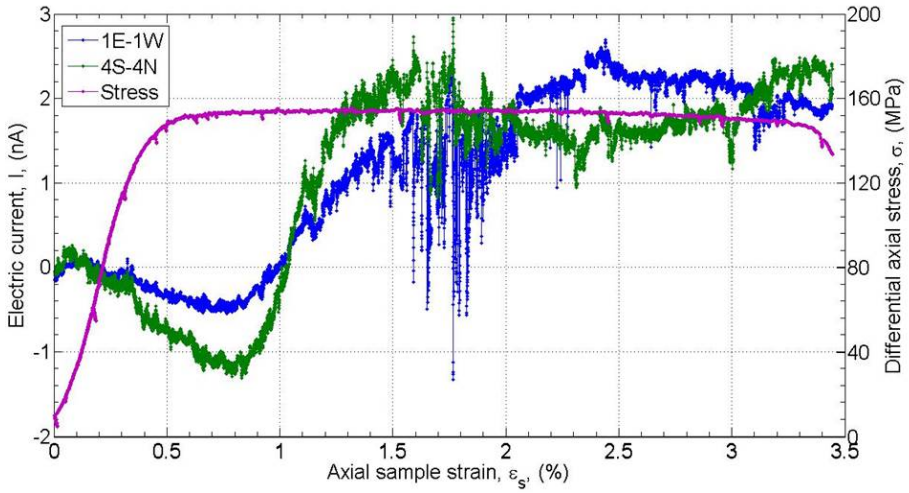


Figure 7.8: Electric current as a function of axial sample strain at 20 MPa and $10^{-6}$ $s^{-1}$ [Experiment CM65]. Current flow between each of two electrode pairs is shown, labelled according to the convention in Section 5.2.4 and Figure 5.6.

### 7.4.3 Relationship between failure zone orientation and electric current

A further three experiments [CM03, CM04 and CM06] recorded four channels at various orientations around the sample; two perpendicular to the loading axis and two oblique to it. Electrode pair positions for each channel were: (a) 4S and 4N, (b) 4E and 4W, (c) 5NW, 25 mm below the centre of the sample and 2SE, 25 mm above the centre of the sample, with current flowing through the sample at an angle of 38.66° to the loading axis and (c) 6N and 1S, with current flowing through the sample at an angle of 28.07° to the loading axis. These three samples were deformed quickly at $10^{-4}$ $s^{-1}$ [CM03 and CM04] and $10^{-5}$ $s^{-1}$ [CM06] and failed macroscopically in shear (e.g., Figure 7.4 (b)).

Figure 7.9 shows electric current flow as a function of time between the four electrode pairs for these three experiments. Velocity measurements were made every two minutes throughout these experiments so a running median filter was applied to the electric current data to remove any spikes and show the overall signal shape. The samples were deformed to 2.75-3.25% strain and the electric current signals for all channels exhibit the same characteristic behaviour of a dynamic pulse (main deflection) of current from 1 % strain at $10^{-4}$ $s^{-1}$ (Figures 7.9 (a) and (b)). Initial onset of current at the yield point (0.25 % strain) followed by a main deflection from peak stress (0.7 % strain) is seen at $10^{-5}$ $s^{-1}$ (Figure 7.9 (c)).

In order to establish the role that the ultimate orientation of the failure plane might play in the variation of electric current production within the samples, the angle, $\alpha$, between the fault plane and the direction of current flow between each electrode pair was calculated using the following standard geometrical relation: $\sin\alpha = \dfrac{\mathbf{n}.\mathbf{b}}{|\mathbf{n}||\mathbf{b}|}$, where $\mathbf{n}$ is the unit vector of the normal to the plane and $\mathbf{b}$ is the direction vector of the current flow line. This calculation and 3-dimensional visualisation of the sample geometry were made

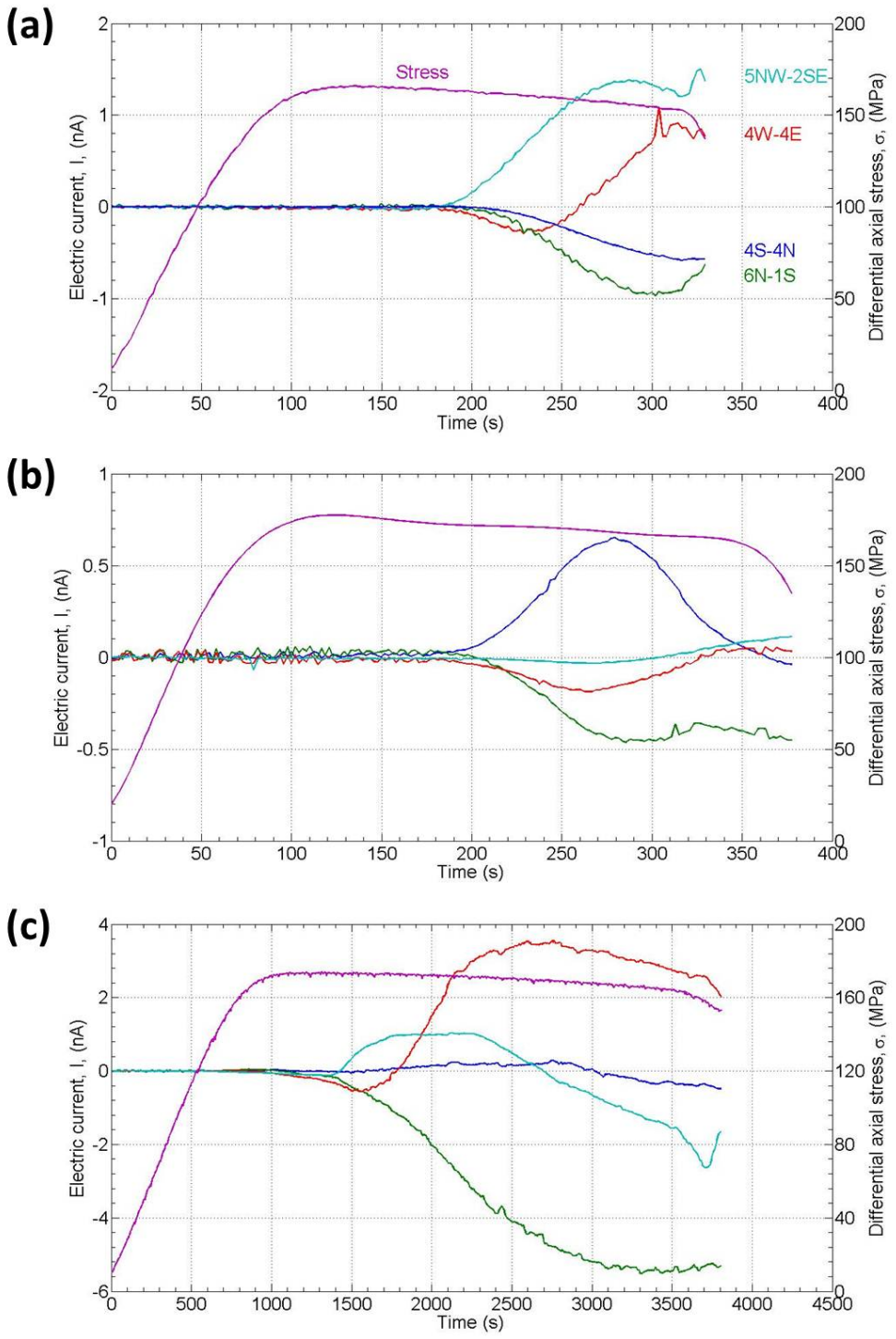


Figure 7.9: Electric current as a function of time, produced during triaxial deformation of macroscopically fractured Carrara marble specimens at 30 MPa and two different strain rates: $10^{-4}$ $s^{-1}$ [(a) Experiment CM03 and (b) Experiment CM04] and $10^{-5}$ $s^{-1}$ [(c) Experiment CM06]. Current flow between each of four electrode pairs is shown, each labelled with the electrode pair position according to the convention described in Section 5.2.4 and shown in Figure 5.6. The orientation of each channel relative to the fault plane and sample geometry is shown in Figure 7.10.

in MATLAB using the GEOM3D toolbox. Values of $\alpha$ for each electrode pair around each sample are given in Table 7.2 and Figure 7.10 presents 3-dimensional schematics of relative orientations of the fault plane and the electric current flow paths between each of the electrode pairs.

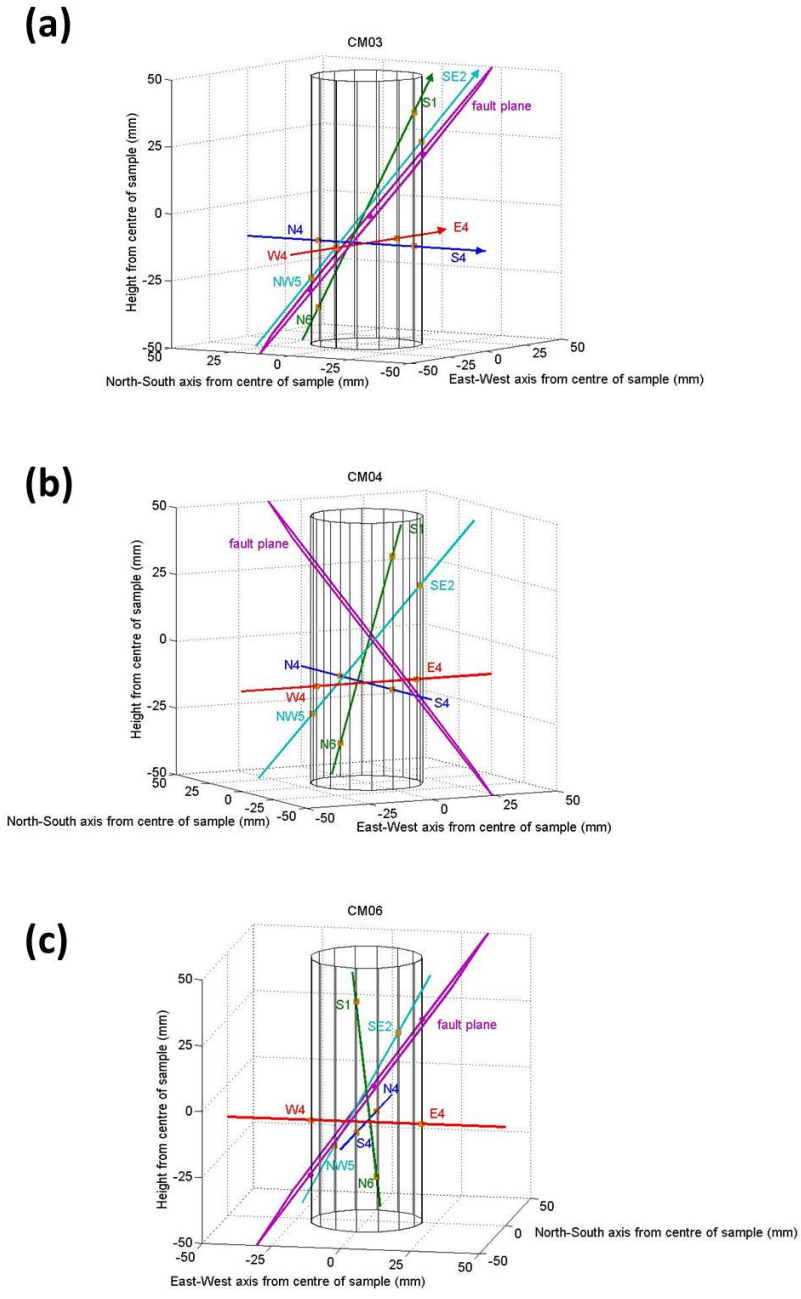


Figure 7.10: 3-dimensional schematics of the three failed samples [(a) Experiment CM03, (b) Experiment CM04 and (c) Experiment CM06] showing relative orientations of the fault plane and the electric current flow paths between each of the electrode pairs.

Both the electric current flow rate, $|dI/dt|$, during the main deflection (Figure 7.11 (a)) and the maximum amount of electric current generated, $|I_{max}|$, (Figure 7.11 (b)) show similar dependence on $\alpha$. Both $|dI/dt|$ and $|I_{max}|$ decrease with increasing $\alpha$ at $10^{-4}$ s$^{-1}$, indicating that at very fast strain rates they are larger at lower angles to the fault plane.

Table 7.2: Values of the angle, $\alpha$, between the fault plane and the electric current flow direction for each electrode pair around each of the three failed samples.

| **Electrode pair** | $\alpha$ (°) | | |
|---|---|---|---|
| | **CM03** | **CM04** | **CM06** |
| W4-E4 | 22.46 | 48.37 | 54.89 |
| N4-S4 | 43.57 | 18.03 | 2.46 |
| NW5-SE2 | 0.44 | 67.80 | 6.06 |
| N6-S1 | 12.64 | 41.63 | 31.75 |

Conversely, both $|dI/dt|$ and $|I_{max}|$ increase with increasing $\alpha$ at $10^{-5}$ $s^{-1}$. This suggests that at slower strain rates they are larger at higher angles to the fault plane. Parameters for the linear approximations shown in Figures 7.11 (a) and (b) are presented in Table 7.3.

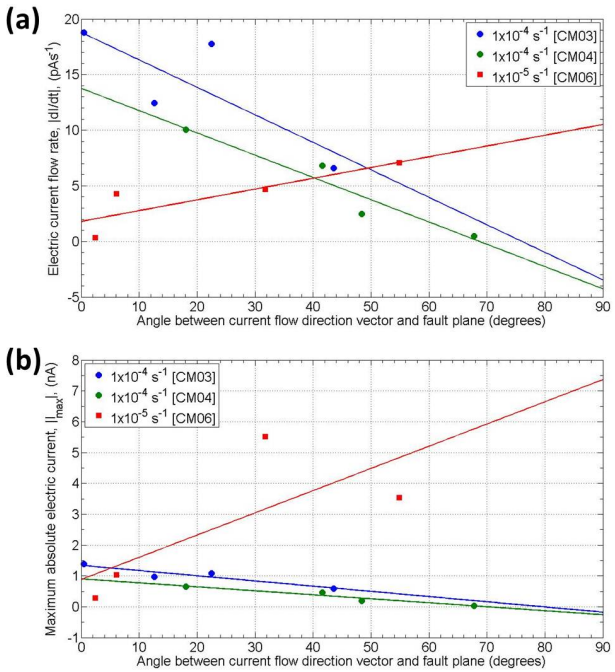


Figure 7.11: Dependence of (a) electric current flow rate, $|dI/dt|$, and (b) maximum electric current generated, $|I_{max}|$, on the angle, $\alpha$, between the electric current flow direction and the failure plane. The least squares linear trend line parameters are given in Table 7.3.

Table 7.3: Parameters for the linear scaling of electric current flow rate, $|dI/dt|$, and maximum electric current generated, $|I_{max}|$, with angle between current flow vector and fault plane, $\alpha$, (Figure 7.11).

| **Sample** | $\|dI/dt\| = A\alpha + B$ | | | $\|I_{max}\| = A\alpha + B$ | | |
|---|---|---|---|---|---|---|
| | **A** | **B** | $\mathbf{r^2}$ | **A** | **B** | $\mathbf{r^2}$ |
| CM03 | -0.247 | 18.8 | 0.474 | -1.69E-02 | 1.340 | 0.808 |
| CM04 | -0.200 | 13.8 | 0.876 | -1.29E-02 | 0.901 | 0.881 |
| CM06 | 0.0968 | 1.79 | 0.586 | 7.20E-02 | 0.883 | 0.316 |

## 7.5 Damage Evolution and Electric Current Generation

### 7.5.1 Method of analysis

Since the majority of generation models for earthquake-related electric phenomena rely on damage mechanisms as their source (Chapter 3), it is important to establish the nature of any link between damage and electric current flow during deformation. Damage evolution throughout each test was tracked by means of ultrasonic wave velocities, acoustic emissions and a damage parameter, D, related to the normalised effective Young's Modulus. Comparison between electric current and these damage analogues is presented in this chapter.

During each experiment, ultrasonic velocity data was sampled at the maximum five different incident angles available from the array of piezoelectric transducers connected to the 10-channel Vallen AMSY-5. The aim was to obtain enough data to calculate the full crack density tensor for a transversely isotropic distribution of cracks (Sayers and Kachanov, 1995). This requires five independent angles (four P-wave and one S-wave), leaving no redundancy should any problems occur. Problems with defective sensors meant that no experiment yielded sufficient data for this calculation. In particular, none of the S-wave pulses were received at their corresponding S-wave transducer for any of the experiments in spite of ensuring that they were correctly aligned prior to lowering the pressure vessel, checking the wiring and lead-through connections and replacing the sensors several times. Some P-wave transducers were also found to be defective, although problems with these were resolved with maintenance and replacement. Defective S-wave sensors also prohibited calculation of the two crack density parameters used by Ayling et al. (1995). The useable P-wave velocity results are presented. For the single channel experiments, which recorded electric current across the central part of the sample, velocity variation also recorded across the central part of the sample is shown, either along the same orientation as the measured electric current flow or at 90° if the same orientation was not available. As can be seen in Figure 7.12, the velocity variation along these two orientations are almost equivalent for all the confining pressures (10-30 MPa) which measured both orientations. This confirms the presence of a transversely isotropic crack distribution throughout deformation. Since, in crystalline rocks, anisotropy in velocity diminishes with increasing $P_c$ (Meglis et al., 1996), it was assumed that this was also the case at 100 MPa and for the water- and brine-saturated experiments, which all measured $V_P$ only at 90° to the electric current orientation. It is also apparent from Figure 7.12 that there is a smaller reduction in $V_P$ at higher confining pressures. This relationship is discussed further in Section 8.5, where the variation in average velocity across several useable orientations is compared with electric current averaged over the four electric channels.

Acoustic emissions (AE) data were filtered by hand to remove noise events that had been mistakenly recorded as real AE events. For the majority of samples, this filtering process reduced the number of useable AE events from several thousand to several hundred,

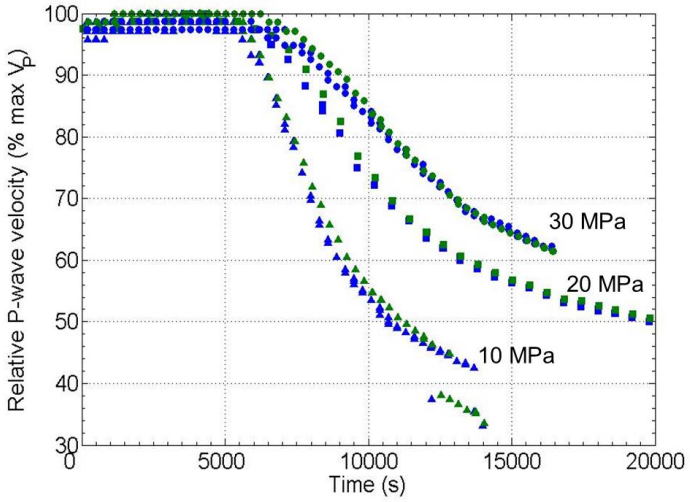


Figure 7.12: P-wave velocity variation with respect to time during deformation at several confining pressures: 10 MPa (triangles) [Experiment CM08], 20 MPa (squares) [Experiment CM65] and 30 MPa (circles) [Experiment CM05]. Blue symbols show velocity variation along the east-west orientation while green symbols show velocity variation along the north-south orientation.

while in some cases this number reduced to only several tens. This indicated significant under-recording of events, which it is reasonable to assume was the result of (a) very low microcrack amplitudes in the Carrara marble due to its softness, (b) frequent velocity surveys during some experiments, (c) saturation of the Vallen AMSY-5 detection system due to high levels of AE activity at the ten channels and (d) the prevalence of other deformation mechanisms, such as dislocation activity, frictional grain boundary sliding or twinning. Saturation of the detection equipment (as discussed in Cox and Meredith, 1993) was not found to be a problem; event arrival times did not show recording pauses, delay time distributions were not bimodal and event rates continued to increase throughout the inelastic phase with a sharply defined maximum at failure (see Figure 7.13 for an example). However, the number of useable AE events decreased with increasing $P_c$ and decreasing $\dot{\varepsilon}$ and at experimental conditions of $P_c \geq 30$ MPa and $\dot{\varepsilon} = 10^{-6}$ s$^{-1}$ not enough AE events were generated for analysis. This may be the result of amplitude suppression due to the application of confining pressure, which may be significant enough to cause the AE amplitudes to drop below the background noise threshold of the transducers. Due to the very few numbers of useable AE events, it was felt that the AE data would not give a reliable estimate of the evolution of mean crack length and strain energy release rate. For instance, Main et al. (1993) used a minimum event rate of seven events per second, whereas even the most productive brittle experiment [CM08] in this study generated less than three events per second prior to the main fracture (Figure 7.13). Accordingly, neither would the AE data yield an accurate damage parameter calculated from the mean crack density (as per Sammonds et al., 1994).

Instead, the data in this chapter is presented as a function of a damage parameter, $D$, derived from the stress-strain behaviour during deformation. This was considered reasonable for the experiments in this study since they were conducted under drained conditions, a

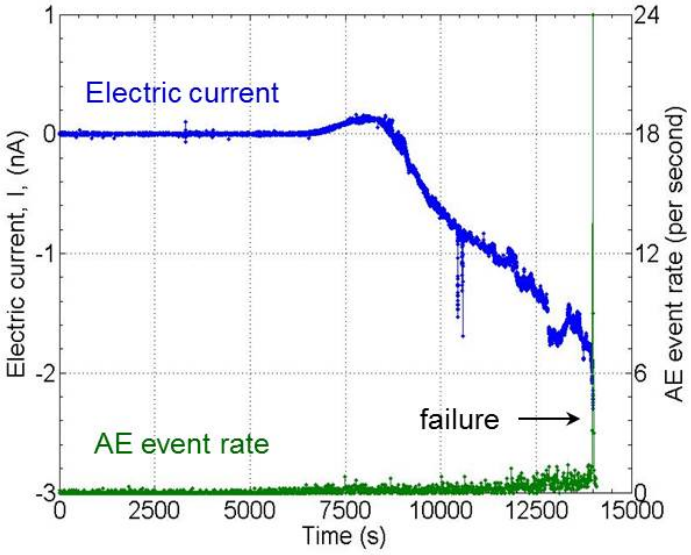


Figure 7.13: Electric current (blue) and AE event rate (green) at 10 MPa and $10^{-6}$ $s^{-1}$[Experiment CM08] showing less than three events per second before the main fracture.

condition for which Sammonds et al. (1994) showed good quantitative agreement between observed stress-strain behaviour and theoretical stress-strain behaviour predicted from AE data. $D$ is calculated in terms of the effective Young's Modulus, $E_{eff}$ (defined by Turcotte et al., 2003) normalised by the Young's Modulus of linear elasticity, $E$:

$$D = 1 - \frac{E_{eff}}{E} \tag{7.1}$$

Variation in P-wave velocity, cumulative AE event rate and cumulative AE amplitude (average amplitude of each event) are presented in terms of both time and $D$. Additionally, amplitude ($A$) distribution $b$-values were calculated using the maximum likelihood estimate shown by Aki (1965) to be related to the mean magnitude ($\bar{m}$) of the population:

$$\frac{1}{b} = \ln 10(\bar{m} - m_c) \tag{7.2}$$

where magnitude $m = \log A$ and $m_c$ is the threshold of complete recording. This threshold was set as the most frequently recorded amplitude in each data set; a value specific to each experiment. The calculation was performed in MATLAB, using the code given in Appendix C. Additionally, the instantaneous $b$-value evolution was determined for non-overlapping windows containing 50-100 events (depending on the number of useable AE events available for each experiment), following the procedure of Cox and Meredith (1993). This ensures that the errors in the $b$-value estimates are comparable throughout. Due to the relatively few events available for the calculation, the statistical errors are large (for example, for Experiment CM08, they are of the order of 25% of $< b >$) so error bars are not shown in the figures for clarity of presentation.

### 7.5.2 Observations and correlations

The relationship between electric current and accumulated damage at 10 MPa is described in this section as this experiment [CM08] recorded the largest number of AE events (2375) as well as frequent velocity surveys throughout the experiment. Figure 7.14 shows good correlation between damage evolution and electric current evolution, with changes in electric current directly coinciding with changes in $V_P$ and AE data. Figures 7.14 (a) and (b) show the evolution of stress and strain as a function of time (a) and the damage parameter, $D$ (b) for Experiment CM08. It should be noted that $D$ is really only valid from the yield point (X) onwards as prior to this it is sensitive to compaction processes that occur during the quasi-linear elastic phase of deformation.

Figure 7.14 (e) shows an increase in cumulative AE event rate with time. Overall, this increase in activity is exponential (inset plot), expected in the lead up to dynamic fracture (Sammonds et al., 1989; Ayling et al., 1995). However, the post-compaction cumulative AE event rate increases steadily in two distinct, linear phases of activity. An initial constant acceleration of 0.01 events $s^{-2}$ from about 6500 s onwards increases to 0.05 events $s^{-2}$ from about 12000 s to failure. Cumulative AE amplitude (Figure 7.14 (g)) also exhibits two phases of steady post-compaction activity over time, with an initial constant rate of 0.02 amplitude units $s^{-1}$ from about 7500 s increasing fourfold to 0.08 amplitude units $s^{-1}$ from about 12000 s to failure. The first linear phase of AE activity (both event rate and compaction) corresponds to steady, sub-critical crack growth and the onset of electric current flow occurs at the start of linear part (∼6500 s), following acceleration from the very low rate of activity during compaction. The second phase of AE activity coincides with an increase in electric current fluctuations and corresponds to the localisation of cracks along the failure surface, formation of which occurs at about 12500 s, as indicated by the sudden reduction in P-wave velocity ($V_P$) across the sample (Figure 7.14 (c)). This sudden reduction in $V_P$ is accompanied by a small and rapid fluctuation in electric current. $V_P$ variation ($V_P/V_{Pmax}$) also shows two phases of activity with time; with the rate of reduction decreasing from 0.6 to 0.2 $ms^{-1}$. This change occurs at the same time as the rate of current production decreases from 0.5 to 0.3 $pAs^{-1}$ (∼9500 s). The sample yields after a 5% reduction in $V_P$, electric current flows after a reduction of 10%, the rate of $V_P$ reduction changes at 60% of $V_{Pmax}$ and formation of the failure surface occurs at about 40% of $V_{Pmax}$.

$V_P$ variation is inversely proportional to the damage parameter, $D$ (Figure 7.14 (d)), with a ratio of 0.9 (very close to 1); i.e., the increase in $D$ corresponds almost exactly to the reduction in $V_P$. This implies that, at 10 MPa, all the mechanical damage within the sample is accommodated by microcracking. Electric current flow begins at $D = 25\%$, after a 10% reduction in $V_P$, and increases linearly by 0.2 nA between $D = 30$ and $D = 40\%$. It then rapidly reverses polarity at $D = 50\%$ with an initial flow of ∼0.7 nA in the opposite direction between 50 and 60% damage. From $60 - 70\%$, the current settles to a steady, linear (negative) increase with damage (and $V_P$ variation) of 0.5 nA over this

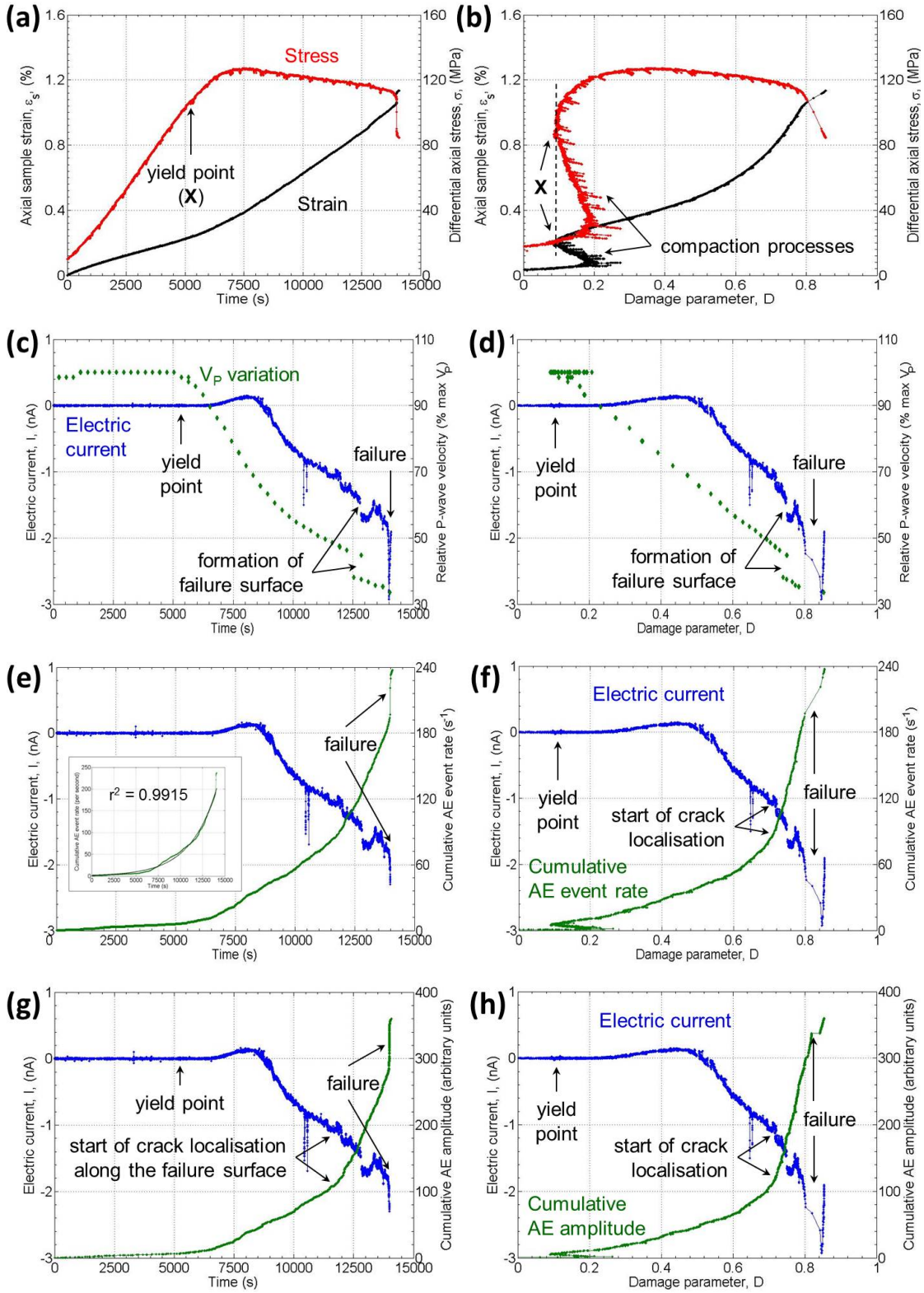


Figure 7.14: Experimental data as a function of time and $D$ [Experiment CM08]. Plots (a) and (b) show the evolution of stress (red) and strain (black), while the remaining plots show electric current (blue) with damage analogues (green): $V_P$ variation (c) and (d), cumulative AE event rate (e) and (f) and cumulative AE amplitude (g) and (h). The inset in plot (e) shows an exponential fit (black), of the form $1.84e^{3.33\text{x}10^{-4}x}$, to the cumulative AE event rate (green).

10% of damage. At 70% damage, the localised fluctuations in electric current increase and the overall increase in electric current accelerates with respect to damage, with the same amount of electric current (∼1 nA) generated in the last 10% of damage before failure as generated from the previous 20%. The sudden drop in $V_P$ and corresponding rapid increase in electric current flow occurs at 75% damage. The two-phase AE activity is also seen in terms of $D$ (Figures 7.14 (f) and (h)). Initial current flow and polarity reversal occurs during the linear increase of AE activity between 20% and 60% damage. Between 60 and 70% damage, the steady region of current production is associated with an accelerating (non-linear) increase in cumulative AE activity, while the final (non-linear) acceleration of electric current flow with respect to damage corresponds to the final linear increase in cumulative AE activity. In terms of AE event rate, ∼40 events $s^{-1}$ occur in the first 40% of damage compared with ∼100 events $s^{-1}$ in the final 10%; a tenfold increase in the ratio between the two. AE amplitudes, on the other hand increase from ∼50 amplitude units in the first 40% of damage to ∼200 in the final 10%; a twenty-fold increase in the ratio between AE amplitude and mechanical damage.

According to the moment tensor analysis by Graham et al. (2010) of AE source modes during deformation of granite samples, the transition from predominantly tensile to predominantly shear events occurs during the ductile region between the yield point and peak stress. However, during strain softening there continues to be a degree of tensile activity, with tensile events consisting of ∼ 30% of all AE, compared with nearly 50% being shear events. Analysis of the relationship between AE source mode and electric current generation in Carrara marble may help to elucidate and isolate different current-generation mechanisms. Such a study is recommended for the future.

Figure 7.15 shows the discrete frequency-magnitude distribution for the full AE data (black dots), together with the fit (red line) calculated using the maximum likelihood $b$-value. The threshold amplitude for $b$-value calculation was 75 amplitude units. It can be seen that the overall $b$-value is 1.78±0.08 and there is some scatter in the tail of the distribution.

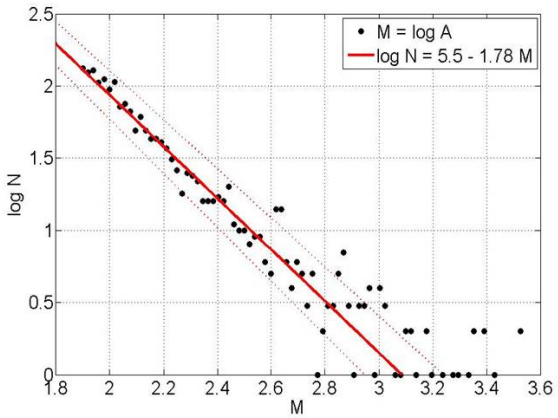


Figure 7.15: Frequency-magnitude distribution of the full AE data (black dots) from Experiment CM08 (10 MPa and $10^{-6}$), together with the fit (red line) calculated using the maximum likelihood $b$-value and its 95% confidence limits (dashed red lines).

The instantaneous $b$-value evolution throughout the experiment is shown in Figures 7.16 (a) with respect to time and (b) with respect to $D$. These $b$-values are calculated from windows containing 95 AE events. Beyond the yield point the $b$-value decreases, indicating AE activity. The initial drop from 4.25 to 2.74 corresponds to the onset of electric current flow. This decrease continues for the duration of the initial positively polarised current flow between 30 and 50% damage, to a local minimum of 2.03 at peak positive current. Polarity reversal and rapid current flow in the opposite direction between 50 and 60% damage are associated with a slight recovery to 2.38, while the region of steady flow of current with damage ($D = 60 - 70\%$) corresponds to a relatively constant $b$-value of $\sim$2, although a further reduction to 1.93 is seen, followed by another slight recovery back to 2.11. Between the start of crack localisation and the formation of the failure surface ($70 - 75\%$ damage), the $b$-value drops rapidly to the first of two minima (1.27); a consequence of the coalescence of neighbouring microcracks along the failure surface. This activity is followed by recovery to $b > 2$ at the point of failure (80% damage), followed by a rapid drop to a second minimum of 1.23 at failure due to critical coalescence of microcracks. Both minima, pre-seismic and coseismic, coincide with rapid increases in electric current flow. The pre-seismic minimum also coincides with the rapid drop in $V_P$ at 12600 s and 75% damage (Figure 7.14 (c) and (d)). These experimentally-determined $b$-values are somewhat higher than $0.5 < b < 1.5$ expected for compression experiments, possibly due to the large statistical error (mean 95% confidence interval is $\pm 0.5$ which is 25% of $< b >$). Since an increasing $b$-value is often associated with seismic quiescence (Main et al., 1989), the $b$-value evolution indicates periods of strong AE activity punctuated by calmer periods.

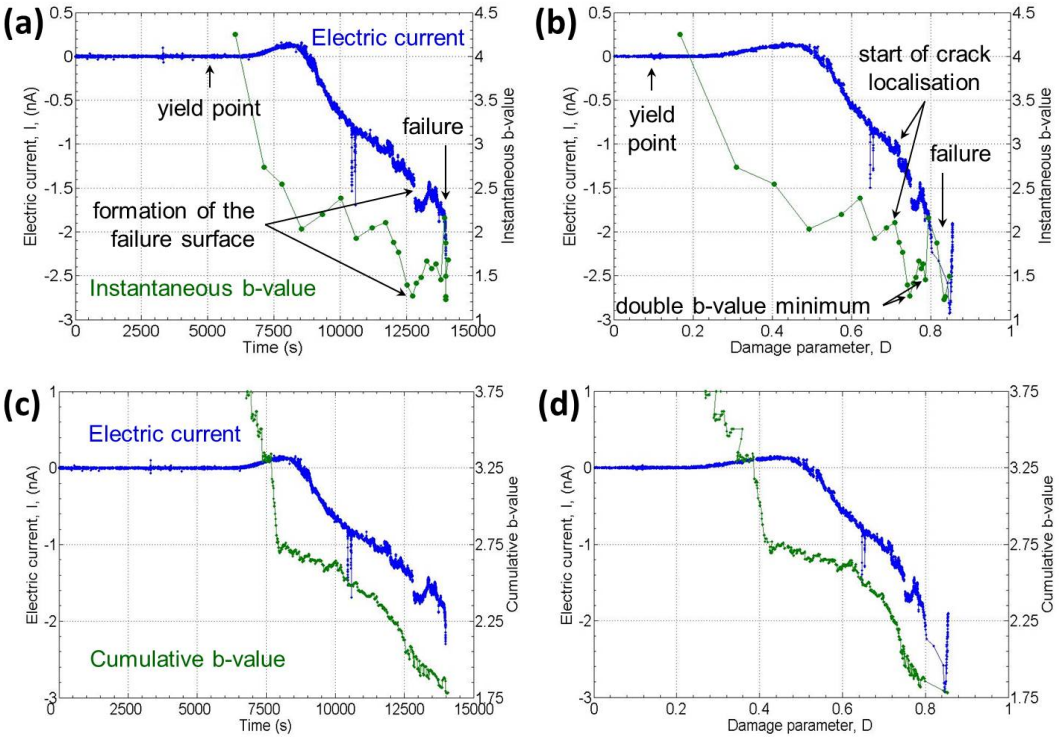


Figure 7.16: Electric current (blue) [Experiment CM08] and (a,b) instantaneous $b$-value evolution (green), with respect to time and $D$, and (c,d) cumulative $b$-value evolution (green), with respect to time and $D$.

Additionally, cumulative *b*-value evolution (Figures 7.16 (c) and (d)) was determined for expanding time windows containing $\geq$ 150 events, the width of which was increased by 10s each time. Increasing the width of each window to accommodate more events leads to a decrease in the related statistical error, which reduces steadily from $\pm$0.8 for the first few windows containing $\sim$150 events to $\pm$0.08 for the last few windows containing $>$2000 events. It can be seen that the cumulative *b*-value decreases as the experiment progresses and the number of AE events increases. The initial rapid decrease during the initial production of electric current reduces to a relatively constant level (slightly decreasing) between 40 and 60% damage as the current reverses polarity and flows rapidly in the opposite direction. From 60 to 70% damage, the steady increase in current flow is accompanied by an acceleration in the *b*-value reduction with respect to damage (although not with respect to time). From the start of crack localisation, this acceleration continues to a maximum as the failure surface is formed before slowing down immediately prior to failure, as does that of electric current flow. From 70% damage (11250 s) onwards, behaviour of the *b*-value with respect to time follows that with respect to damage, but the overall rate of current production remains constant with time, apart from the rapid fluctuation as the failure surface forms.

## 7.6 Approach to Failure and Stress Rate

Figure 7.17 shows the evolution of electric current and stress as a function of stress rate as the sample approaches failure for three different strain rates. At $10^{-4}$ (a) and $10^{-5}$ (b) $s^{-1}$, it can clearly be seen that the onset of electric current occurs at the point at which the stress drops with respect to the stress rate. In addition, the current reaches a distinct maximum, in whichever direction it is flowing between the respective electrode pair, at a time prior to failure. This is followed by a reversal in polarity (i.e, a recovery) as failure becomes imminent. Although the shape of the signal seen on each channel varies between the two experiments, this precursory behaviour is consistent. Channel 4W-4E shows two peaks of opposite polarity, the first of which is also the first seen out of all four channels and the second of which coincides with the peaks at 6N-1S and 4S-4N. The peak seen on 5NW-2SE occurs between the two peaks on 4W-4E. At $10^{-6}$ $s^{-1}$, the onset of electric current flow at both 10 MPa (c) and 20 MPa (d) occurs at $\sim$125 MPa once the stress rate has reduced by 10%, which is just before peak stress at 10 MPa (within 3%) and significantly before peak stress at 20 MPa (within 19%). At both confining pressures, the current reaches an initial peak in its respective direction of flow at the end of the initial yield and flows steadily during strain softening (10 MPa) and cataclastic flow (20 MPa). As the stress drop begins to accelerate with respect to the stress rate, current flow in both samples shows a precursory change, which reaches a maximum and then recovers as failure approaches.

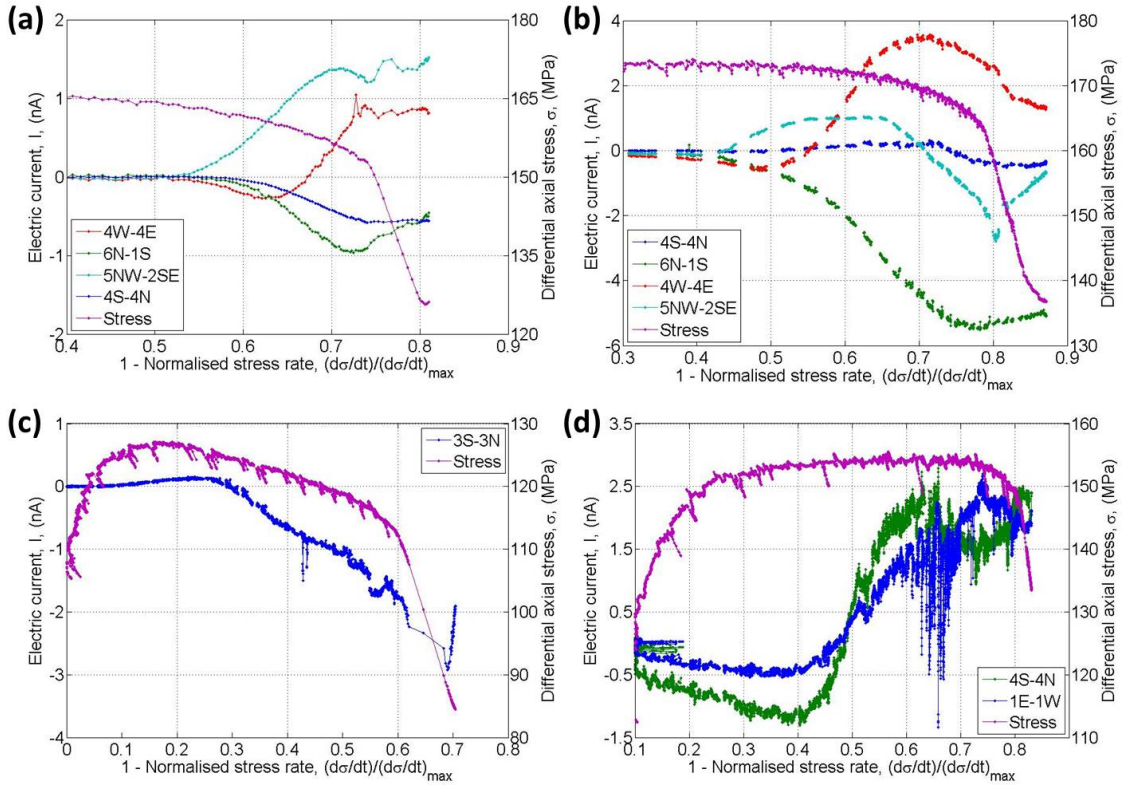


Figure 7.17: Electric current flow and stress as a function of stress rate as failure approaches, for a variety of conditions: (a) $10^{-4}$ $s^{-1}$ and 30 MPa [Experiment CM03], (b) $10^{-5}$ $s^{-1}$ and 30 MPa [Experiment CM06], $10^{-6}$ $s^{-1}$ and 10 MPa [Experiment CM08], and (d) $10^{-6}$ $s^{-1}$ and 20 MPa [Experiment CM65].

## 7.7 Summary and Deductions

In this chapter, I have presented the main observations regarding electric current signals generated during triaxial deformation of non-piezoelectric Carrara marble and correlated their evolution with the development of crack damage. To summarise, electric current *was* generated and sustained during the deformation of Carrara marble specimens under *all* the conditions tested. Under dry conditions, current flow was detected only in the region of permanent deformation beyond the yield point of the material. This production of a deformation-induced electric current in a dry, non-piezoelectric material proves that electrification *can* result solely from the mechanical processes of deformation under an applied stress for the whole range of simulated crustal conditions tested. These processes range from localised microfracture to distributed cataclastic flow, with contributions from micro-plasticity mechanisms in the form of twinning and dislocation glide.

Mechanical behaviour and deformation style observed in these Carrara marble samples (Section 7.2) corresponds to that reported in previous deformation studies on Carrara marble under similar conditions (Rutter, 1974; Edmond and Paterson, 1972; Fischer and Paterson, 1989; Fredrich et al., 1989; Zhang et al., 1994; Schubnel et al., 2005; 2006b). Visual inspection of the samples provided evidence of long and thin grain boundary and intergranular cracks at low $P_c$, compared with shorter and wider cracks at higher $P_c$. At

low pressures (<30 MPa), cracks propagate across several grains and localise around a fault plane, whereas at higher pressures (≥30 MPa) they are shorter and more evenly distributed, propagating only intragranularly or along grain boundaries. These observations, and the stress-strain behaviour (Figure 7.2 (b)), are consistent with the findings of Fredrich et al. (1989) and Zhang et al. (1994) and the notion that raising the confining pressure inhibits crack localisation by increasing the energy required to propagate cracks and enhancing the plasticity of the rock matrix.

At room temperature, calcite deforms plastically by twinning on the $e = \{0112\}$ planes and by dislocation glide on the $r = \{1011\}$ planes (Fredrich et al., 1989). The stresses required to initiate these two processes in single crystals of calcite are relatively low; ∼30 MPa and ∼330 MPa respectively (Turner et al., 1954; Griggs and Handin, 1960). Thus, extensive twinning must occur in all specimens deformed in the semi-brittle regime (≥30 MPa), while some localised twinning may occur in regions of high stress concentration in the brittle regime (<30 MPa). Dislocation glide will only occur at elevated $P_c$, when the macroscopic stresses ($\sigma$) approach those required for $r$-glide.

Fredrich et al. (1989) made the following microstructural observations of deformation in Carrara marble, which revealed the variety of ways in which brittle and plastic deformation mechanisms interact in the semi-brittle regime (see also Table 6.1):

- Microcracking is responsible both for the initial yield and the strength at $P_c < 85$ MPa, whereas twinning becomes responsible for the initial yield at higher pressures.
- Cracks nucleate at sites of high stress intensity at twin boundaries, twin terminations and at the intersection of twin lamellae and sometimes grow by dislocation emission.
- Local dislocation glide occurs within some individual grains at pressures as low as 50 MPa but continued microcracking is necessary until the sample strength reaches levels sufficient to activate dislocation glide on a large scale.
- Dislocations limit crack propagation at higher $P_c$ by shielding crack tips and arresting intragranular cracks, while twin boundaries appear to hinder dislocation glide.
- As $P_c$ and $\sigma$ increase, some grains become plastically soft and inhibit intergranular cracking because cracks impinging on such grains are more likely to induce dislocation glide rather than allow crack propagation to continue.
- For a particular strain, both stress-induced crack and dislocation densities decrease with increasing $P_c$, but are comparable between samples deformed to the pre-failure stage in the brittle field and those deformed to higher strains in the semi-brittle field.

It was clear from the visual inspection of my deformed samples that decreasing the strain rate inhibits crack localisation, with samples yielding evidence of a sharply defined shear fault and some long, thin intergranular conjugate shear fractures distributed within the

central damage zone at fast strain rates ($\geq 10^{-5}$ $s^{-1}$). At slower strain rates ($<10^{-5}$ $s^{-1}$), deformation was no longer localised along a single shear fault but accommodated entirely by intergranular conjugate shear fractures within the central damage zone. These fractures were of a similar aspect ratio as those seen at the faster strain rates. Thus, deformation transitioned from localised shear failure to distributed cataclastic flow with a reduction in strain rate. Since confining pressure was at the transition between brittle and semi-brittle regimes (30 MPa), and the stress-strain behaviour was very similar across the whole range of strain rates (Figure 7.2 (a)), it was inferred that deformation was mainly accommodated by brittle processes with a similar degree of twinning across the range of strain rate conditions and negligible dislocation glide.

Damage in sample CM08, which was deformed at 10 MPa and $10^{-6}$ $s^{-1}$, could be attributed purely to microcracking, since the 65% reduction in Young's Modulus, $D$, was accommodated entirely by the 65% reduction in P-wave velocity, $V_P$ (Figure 7.14 (d)). Electric current was produced in the sample beyond the yield point, once the stress was within 3% of the peak value and after a 10% reduction in $V_P$. That is, during dilatancy resulting purely from crack damage. The rate of current production correlates well with rates of microcracking; decreasing during strain softening as crack localisation and coalescence takes over from crack nucleation and propagation. This is evident from a corresponding reduction in the rate at which $V_P$ decreases and an increase in AE amplitudes and event rates (Figure 7.14 (c)-(h)). Acceleration of AE amplitudes and event rates towards failure also corresponds to an increase in electric current fluctuations, and formation of the failure surface is clearly marked by a sharp drop in both $V_P$ and electric current. This drop in electric current is followed by a recovery immediately prior to failure; behaviour characteristic of a precursor (see Chapter 3). Similar characteristics are also exhibited by the electric current as the stress drop accelerates towards failure in the other samples that experienced brittle failure [CM03, CM06 and CM65] (Figure 7.17). These observations of damage evolution are consistent with the previous experimental interpretations that the post peak stress region is associated with crack growth and linkage towards an ultimate macroscopic fault (Nur, 1972; Scholz et al., 1973). Therefore, the mechanisms for current generation in these samples must be related to microfracture and involve surface charging mechanisms such as those described in Section 3.5.1.4. For example, cleavage cracking of a single crystal is effective in generating high charge densities on fracture surfaces (Enomoto and Hashimoto, 1990) and therefore can produce large electric fields in which currents can flow.

The form of the electric current signal generated within sample CM08 (Figure 7.14) is consistent with that recorded at atmospheric pressure during previous constant stress rate uniaxial experiments on marble (Stavrakas et al., 2003; 2004; Anastasiadis et al., 2004; Vallianatos et al., 2004). An initial positive deflection is followed by a rapid negative deflection immediately preceding fracture and the change in sign of the Young's Modulus marks a corresponding reversal in the polarity of the emitted current (Figure 3.4). However, the constant strain rate experiment conducted for this study shows the relationship

between the variation in current and the stages of deformation more clearly, with the initial positive deflection occurring during the ductile region approaching peak stress, peak stress marking the reversal of polarity and the main negative deflection of current occurring during strain softening. The ratio of the absolute values of the negative minimum to the positive maximum is 10:1, consistent with those reported elsewhere (3:1 by Stavrakas et al., 2003 and 6:1 by Vallianatos et al., 2004). These authors attributed their signals to the motion of charged edge dislocations (MCD), but the microstructural observations of (Fredrich et al., 1989) indicate that dislocation glide is not activated during deformation at low effective pressures and the evidence presented here shows clear correlation between microcracking activity and electric current. Further comparisons between observations from this study and those from previous studies are drawn in Chapter 12.

The overall $b$-value for the whole AE population is 1.78 (Figure 7.15), slightly higher than global and regional seismic $b$-values. Additionally, instantaneous $b$-values (Figure 7.16 (a) and (b)) are high in comparison to those observed in other compression experiments (e.g., Main et al., 1989) and closer to those observed in tension experiments (e.g., Meredith and Atkinson, 1983). This may be due to the large statistical error associated with the $b$-value estimation. However, the overall shape of the $b$-value evolution with deformation is consistent with other compression experiments (e.g., Sammonds et al., 1992; Main et al., 1993). Moreover, such high $b$-values for *marble* in particular were also observed by Scholz (1968b;d). He found that cataclastic deformation, which is characteristic of marble at relatively low $P_c$, exhibits an AE frequency-magnitude relation similar to that for brittle deformation but characterised by very high $b$-values over the entire range of stress. The similarity of these $b$-values to those found during frictional sliding along a fault, as well as in the lower stress regions of deforming brittle rocks, led him to infer that cataclastic deformation is mainly due to stable intergranular sliding. Furthermore, the rapid reduction in $b$-value at the same point that there is a sudden drop in $V_P$ reflects the transition from an initial diffuse distribution of cracks during the early stages of crack nucleation and dilatancy, where there is negative feedback in stress concentration, to crack localisation and positive feedback as stresses concentrate on the failure surface (e.g., Main et al., 1993). The earthquake source model of Main et al. (1989) requires a prolonged strain softening phase before dynamic failure if a double $b$-value minimum is to be observed in nature (Sammonds et al., 1992). Such a phase is observed during experiment CM08 and thus the observed double minimum is an expected result, corresponding first to crack localisation along the final failure plane and then to imminent macroscopic failure. This may be the first time that such a double minimum has been observed without the presence of a pore fluid. The inflexion preceding the double minimum may be attributed to quasi-static crack growth during extended strain softening.

Having established a link between crack damage and electric current generation in Carrara marble, the observed variability in the amount of electric current produced during experiments carried out under identical conditions (Figure 7.5) may be explained by the relative orientation of the electrode pairs to regions of crack damage accumulation. Re-

gions where damage accumulates depends on the local stress intensity during deformation, which in turn depends on the natural variability in microstructure between samples. This natural variability may include: (a) differences in the crack and crystal defect densities and geometries between the undamaged samples, (b) the presence of impurities in the samples in very small but varying quantities which attract extrinsic defects and form electric dipoles which may then migrate or align cooperatively under the application of stress, and (c) varying quantities of peroxy bonds from which positive holes may be activated. These Carrara marble samples are >99% pure and their formation pressure was relatively low (greenschist facies), which makes it unlikely that peroxy bonds were structurally incorporated during metamorphism. Thus, it is the differences in the pre-existing network of cracks and crystal defects that will have the most effect on the deformation-induced electric current signals. Despite its almost mono-minerallic composition of calcite crystals, Carrara marble contains different types of micro-discontinuities, in the form of cleavage and grain boundary cracks (Bandini et al., 2012), which will greatly influence the mechanical properties of the calcite grains during deformation. The density of these defects is unique to each sample and so precise details of damage localisation will be unique to each experiment, leading to the variability observed in the electric signal generated between a particular pair of electrodes in several samples deformed under identical conditions.

Electric current production within individual samples was also found to vary (Figures 7.7 and 7.8), implying the presence of local electric dipoles rather than homogeneously distributed charges. For example, dipoles associated with crystal defects and those across crack surfaces, both within disordered surface layers and ionised void spaces. Cooperative reorientation of these dipoles may occur in regions of high local stress concentration, but it is more likely that localisation of accumulating electric charge reflects localised crack propagation and frictional sliding avalanches along shear crack surfaces. The observed similarities in the shape of the electric current signal recorded perpendicular to the loading axis between electrode pairs located along the length of the sample may reflect consistencies in the geometry of the developing crack network along the sample length, while variations in the magnitude of the signal may reflect differences in crack density.

In samples that failed along a single shear fault, both the maximum electric current produced and the rate of current production varied with the incidence angle between the current flow direction vector and the fault plane (Figure 7.11). At the fastest strain rate, both of these variables decreased with increasing incidence angle indicating that current production was greatest in close proximity to the fault, i.e., where the crack damage was localised. The link between earthquake lights and rift zones (Theriault et al., 2014) has been related to this type of effect, whereby electric charges generated by the stress of rocks grinding against each other during an earthquake then travel upwards along the nearly vertical geological faults common in rift zones. Interestingly, the relationship was reversed at the intermediate strain rate, probably reflecting the accumulation of crack damage in regions distributed throughout the sample, away from the final fault plane location.

# Chapter 8

# Influence of Confining Pressure on Electric Signals[1,2,3]

## 8.1 Introduction

Confining pressure increases with depth in the crust and variations in confining pressure induce volumetric strain within crustal rocks. Increases in confining pressure serve to increase the strength of a rock by reducing the volume accommodated by internal pores and cracks, i.e., the porosity. This allows the rock to achieve ductility (Paterson and Wong, 2005), as evident in Figure 7.2 (b), by acting to suppress microfracture amplitudes and encourage cataclastic behaviour because more energy is required to nucleate or grow a crack in the presence of a higher confining pressure. Additionally, due to the crack-shaped nature of their pore space, the effect of pressure on compact rocks such as marbles and granites was found to be particularly important (Birch, 1961; Brace, 1965). Cracks change shape and can even close completely under slight pressure, with closure leading to a large increase in apparent elastic modulus or P-wave velocity. Other physical properties are similarly affected, such as electrical conductivity (Brace et al., 1965; Brace and Martin, 1968; Glover et al., 1996; Glover and Adam, 2008) and permeability (Meredith et al., 2012). Both decrease rapidly with pressure and the associated reduction of electrical conduction and fluid flow pathways due to crack closure. Thus, obtaining experimental data for a range of confining pressures is essential to establish the influence of porosity reduction and deformation mechanism on the electric current signals.

---

[1]Cartwright-Taylor, A., Vallianatos, F. and Sammonds, P. (2015). Deformation-induced electric current in Carrara marble across the brittle-ductile transition. *TSG Annual Meeting 2015 5-8 Jan.*

[2]Cartwright-Taylor, A., Vallianatos, F. and Sammonds, P. (2013). Fracture and electric current in the crust: a $q$-statistical (Tsallis) approach. *AGU Fall Meeting 9-13 Dec.*

[3]Cartwright-Taylor, A., Vallianatos, F. and Sammonds, P. (2013). On the non-extensivity of electric current emissions associated with microfracture during triaxial deformation of Carrara marble. *Fractals and Dynamic Systems in Geoscience Conference 30 Sept - 2 Oct.*

To this end, the results from four experiments, carried out at confining pressures of 10, 20, 30 and 100 MPa, are presented here. The strain rate for all these experiments was $10^{-6}$ $s^{-1}$. Three of these tests recorded a single channel of electric current flow across the sample between two electrodes at positions 3S and 3N (see Figure 5.6 for sensor position map). One experiment [CM35] recorded two channels across the sample, 3S-3N and 4S-4N, but only electric current flow between the 3S-3N electrode pair was included in the confining pressure dependence analysis to ensure consistency.

The experiments carried out at 60 MPa (see Figure 7.2 (b)) are not included in the following analysis. They were part of a series of six multi-channel tests [Experiments CM63 to CM68] that included a fifth $P_c$ (60 MPa), conducted to confirm results from the series of successful single channel tests (presented here) and investigate confining pressure dependence of average current flow within the marble samples. These repeat experiments were carried out towards the end of the study using a more recently obtained block of Carrara marble and recorded three channels. Due to an electrical shorting problem inside the pressure vessel, only one of these experiments [Experiment CM65], carried out at 20 MPa, yielded useful results. After extensive investigation, the cause of this shorting problem was eventually assumed to be related to the specimen diameter being wider by 0.4 mm than the samples used for the previous successful experiments. This was due to the use of a replacement core drill after the previous drill was damaged. The replacement drill was manufactured cheaply with a poor tolerance on the required specifications. The wider samples stretched the jacket slightly and may have caused some sensors to just touch the inside of the pressure vessel wall.

## 8.2 Electric Current Signals

Figure 8.1 shows electric current flow during the four single-channel tests. In this series of experiments, only the sample deformed under 10 MPa $P_c$ [CM08] developed a main fracture. At this $P_c$, significant current production begins during the initial ductile yield, shortly before peak stress. At all other $P_c$, significant current flow is not seen until the end of the initial yield and the start of the steady strain hardening or softening region. The overall forms of the signals are similar to that described in Section 7.3, with a small initial deviation from background followed by the main deflection of significant current flow at a fairly constant rate. However, some differences in behaviour between the various confining pressures are apparent.

At 10 MPa, electric current initially begins to flow at 0.28 % strain (119 MPa; 94 % of peak stress). This flow occurs after the material yields at 0.21 % strain (99 MPa; 78 % peak stress) but before peak stress at 0.38 - 0.42 % strain (127 MPa). The polarity of this initial electric current deflection is positive and the current increases at a rate of 0.1 $pAs^{-1}$ reaching a peak of 0.15 nA at 0.44 % strain at the end of the initial yield. As the sample enters the strain softening region of deformation, the current flow decreases

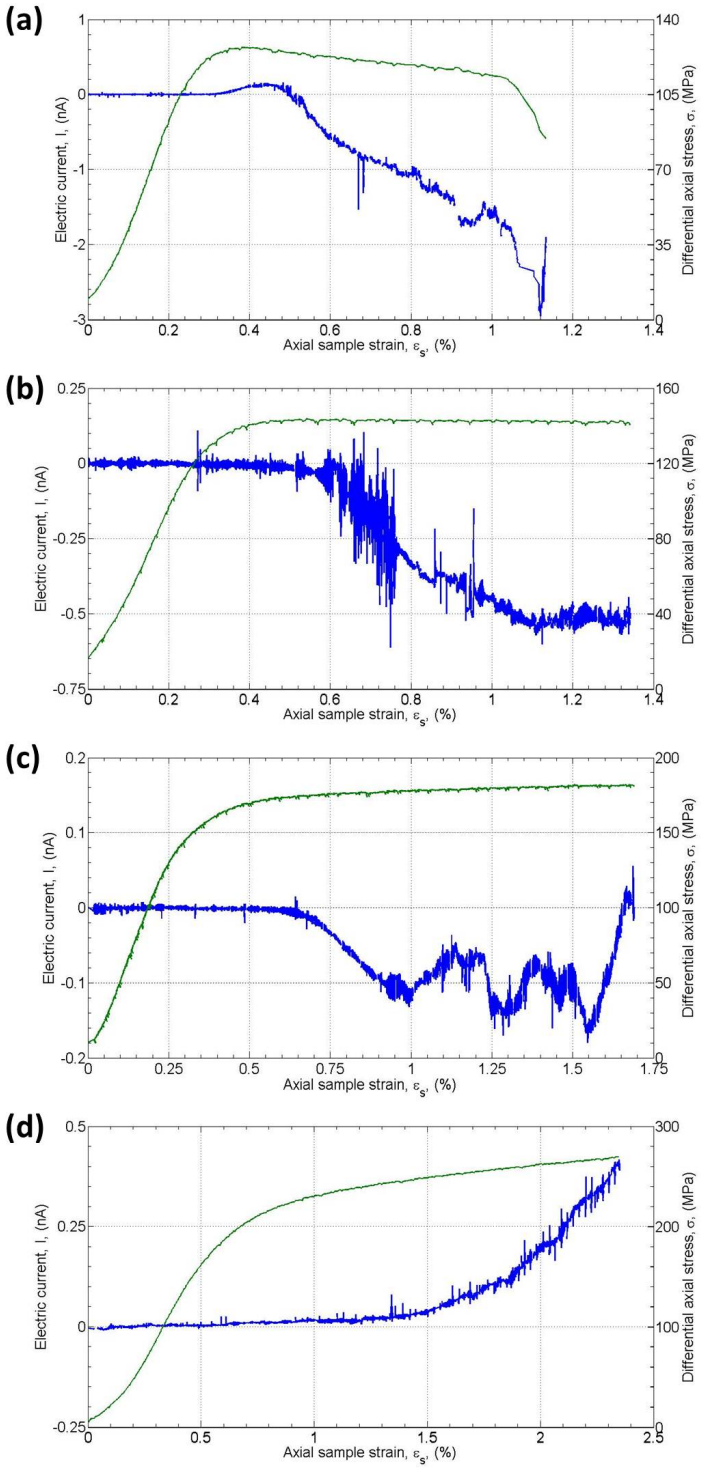


Figure 8.1: Electric current flow (blue) between a single pair of electrodes (3S-3N) and differential stress (green) as a function of axial sample strain, produced during triaxial deformation of Carrara marble specimens at $10^{-6}$ $s^{-1}$ strain rate and four different confining pressures; (a) 10 MPa [Experiment CM08], (b) 20 MPa [Experiment CM21], (c) 30 MPa [Experiment CM05] and (d) 100 MPa [Experiment CM35].

with localised fluctuations of ∼0.2 nA and then increases again in the opposite direction, flowing rapidly at first and then more slowly, both at almost constant overall rates of 0.52 and 0.28 $pAs^{-1}$. Fluctuations of the order of 0.1-0.2 nA are seen as the rate of current production slows, with two sudden drops (corresponding to an increase in current flow in the negative direction) in current of 1.7 and 1.5 nA at ∼0.68 % strain (121 MPa). Two further incidents of rapid current drop, with recovery over greater strain than the first two, occur as failure approaches; one of ∼0.4 nA at 0.84 % strain (118 MPa) and one of ∼0.6 nA occurring at 0.9 % strain (117 MPa), which recovers to the pre-drop level immediately prior to failure. A large coseismic drop of ∼1.2 nA, to a maximum negative current of -2.96 nA, is seen at the point of failure (109 MPa and 1.06 % strain) which then immediately recovers. The overall signal shape is similar to that seen in uniaxial experiments under constant stress rate (Stavrakas et al., 2003; 2004) but these authors presented no evidence for localised fluctuations or small, localised rapid drops in current.

At 20 MPa, the onset of electric current flow occurs at 0.22 % strain (104 MPa; 72 % peak stress), which coincides exactly with the yield point, in the form of a small initial deflection of -0.004 nA. The main deflection begins at 0.4 % strain shortly before peak stress (141 MPa; 98 % peak stress), with current production increasing to an overall constant rate of 0.16 $pAs^{-1}$ between 0.64 and 0.84 % strain, shortly after peak stress. At this confining pressure, peak stress (144 MPa) is maintained over 0.54 - 0.75 % strain (>0.2 %) and is characterised by significant fluctuations in the flow of current, of the order of 0.2-0.4 nA. The overall polarity of the signal remains negative throughout the test, but some of these fluctuations have positive polarity. Beyond this, stress remains fairly constant, decreasing very gradually from 144 to 142 MPa at the end of the test. A period of quiescence in the electric current fluctuations occurs between 0.76 and 0.85 % strain, although overall current production continues at about the same rate. From 0.85 to 1.1 % strain (143 MPa), the rate of current production slows to 0.07 $pAs^{-1}$ and intermittent fluctuations of the order 0.2-0.4 nA are seen, with three instances of sustained current variations; one jump at 0.85 % (corresponding to a decrease in current flow in the negative direction) and two drops at about 0.95 % (corresponding to an increase in negative current flow). At 1.1 % strain (143 MPa), current production levels off at around -0.5 nA with fluctuations of the order 0.05 nA.

At 30 MPa, the onset of electric current occurred at 0.28 % strain (144 MPa) with an initial deflection of -0.001 nA, shortly after the yield point (0.22 % strain and 126 MPa). The main deflection begins at 0.4 % strain (164 MPa), with current production at an overall constant rate of 0.03 $pAs^{-1}$ between 0.68 and 0.92 % strain (175 and 177 MPa) as the sample enters the strain hardening region. Peak stress was not reached during this test; deformation remained ductile for the duration but the degree of strain hardening was very small at 8 MPa per 1 % strain. Beyond 0.92 % strain, the current fluctuates around -0.1 nA, with localised fluctuations of the order of 0.02-0.04 nA and two larger-scale, longer duration variations of 0.08-0.1 nA. These exhibit a steady relaxation of the current and some fluctuation at a local maximum (corresponding to a local minimum in

the negative flow direction) followed by a relatively rapid current drop (rapid increase in negative current flow). A maximum negative current of -0.18 nA was reached at 1.53 % strain (181 MPa). This was followed by a rapid decrease of current at an approximately constant rate of 0.14 $pAs^{-1}$ between 1.5 and 1.65 % strain (181-182 MPa) and then a change in polarity to a maximum positive current of 0.02 nA, with a fluctuation around this value of ∼0.06 nA at the very end of the test.

At 100 MPa, the yield point occurs at 0.42 % strain (135 MPa) and electric current begins to flow shortly after, at 0.5 % strain (162 MPa). Current flow increases very slowly at an almost constant rate of 0.002 $pAs^{-1}$ during the initial yield to 0.02 nA at 1.4 % strain (245 MPa) with localised fluctuations of the order of 0.012 nA and occasional larger spikes of 0.03-0.05 nA. Peak stress was not reached during this test; deformation remained ductile for the duration but the degree of strain hardening was more than four times greater, at 63 MPa per 1 % strain, than the 30 MPa test. After the initial yield, from 1.4 % strain, the rate of current production increases significantly to a rate of 0.02 $pAs^{-1}$ between 1.5 and 1.8 % strain and then further to a rate of 0.05 $pAs^{-1}$ as ductile deformation continues, remaining at approximately this rate until the end of the test (2.3 % strain and 270 MPa) when a maximum of 0.41 nA is reached. Localised fluctuations increase two to four-fold, while the spikes increase two-fold and appear more frequently after the initial yield. The polarity of the signal remains positive for the duration of the test.

## 8.3 Electric Current and Electric Charge Magnitude

Figure 8.2 presents the absolute current, $I_{abs}$, and charge, $Q_{abs}$ at each 0.25% strain slice for the experiments shown in Figure 8.1. The measurement errors for $I_{abs}$ and $Q_{abs}$ are ±10 fA and ±10 pC respectively and therefore much smaller than the plotted data points. At a given strain, $I_{abs}$ (Figure 8.2 (a)) clearly decreases with increasing confining pressure for strains up to 1.5 %. The three smaller confining pressures exhibit a similar form in that $I_{abs}$ increases rapidly from ∼0.5 % strain and then levels off with further deformation. The variation with strain at these $P_c$ scales as a logarithmic function whereas, at 100 MPa, $I_{abs}$ increases exponentially with strain (Figure 8.2 (a) and Table 8.1). $Q_{abs}$, on the other hand, scales exponentially at the lowest and highest $P_c$, while at the two intermediate $P_c$ charge increases exponentially between 0.25 and 0.75 % strain and then increases linearly (Figure 8.2 (b) and Table 8.2).

Figure 8.3 illustrates the relationship between absolute values of electric current and charge with confining pressure. Beyond 1 % strain, the sample at 10 MPa failed so there is no data for this confining pressure and so the higher strains are not presented here. There is very little current (Figure 8.3 (a)) produced at strains less than 0.75 % and no variation with confining pressure at these smaller values of strain. At 1 % and 1.75 % strain, current flow clearly decreases with increasing confining pressure, scaling as a power law each with exponents of ∼ 2 (Table 8.3). Electric charge (Figure 8.3 (b)) also increases

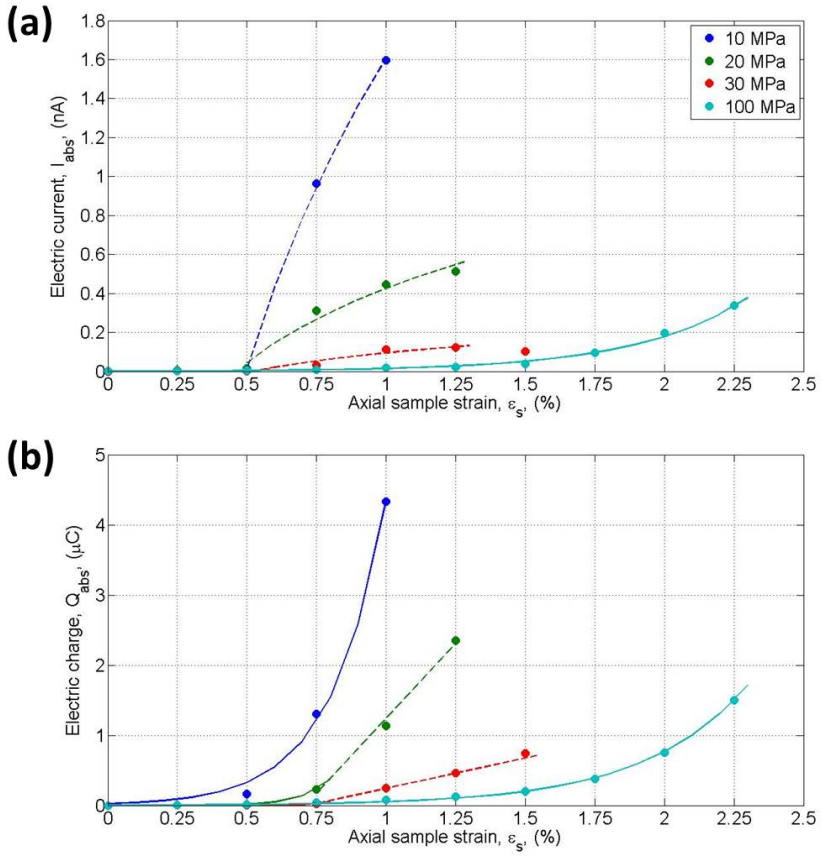


Figure 8.2: Absolute values of (a) electric current and (b) electric charge at particular values of strain as a function of axial sample strain for the experiments shown in Figure 8.1. The solid trend line in (a) is exponential and the dashed trend lines are logarithmic (see Table 8.1 for the parameters). Solid trend lines in (b) are exponential and dashed trend lines are linear (see Table 8.2 for the parameters).

Table 8.1: Parameters for scaling of absolute electric current, $I_{abs}$ (nA), with axial sample strain, $\varepsilon_s$ (%) (Figure 8.2 (a)). The fits were calculated by least squares.

| $P_c$ | $I_{abs} = A \ln \varepsilon_s + B$ | | | $I_{abs} = A \exp^{B\varepsilon_s}$ | | |
|---|---|---|---|---|---|---|
| | **A** | **B** | $\mathbf{r^2}$ | **A** | **B** | $\mathbf{r^2}$ |
| 10 | 2.30 | 1.61 | 1.000 | - | - | - |
| 20 | 0.549 | 0.426 | 0.969 | - | - | - |
| 30 | 0.144 | 0.0947 | 0.925 | - | - | - |
| 100 | - | - | - | 1.14E-03 | 2.54 | 0.995 |

Table 8.2: Parameters for scaling of absolute electric charge, $Q_{abs}$ (nA), with axial sample strain, $\varepsilon_s$ (%) (Figure 8.2 (b)). The fits were calculated by least squares.

| $P_c$ | $Q_{abs} = A \exp^{B\varepsilon_s}$ | | | $Q_{abs} = A\varepsilon_s + B$ | | |
|---|---|---|---|---|---|---|
| | **A** | **B** | $\mathbf{r^2}$ | **A** | **B** | $\mathbf{r^2}$ |
| 10 | 2.45E-02 | 5.18 | 0.994 | - | - | - |
| 20 | 1.18E-04 | 10.1 | 1.000 | 4.26 | -3.02 | 0.987 |
| 30 | 6.97E-07 | 14.1 | 0.993 | 0.86 | -0.62 | 1.000 |
| 100 | 3.59E-03 | 2.68 | 0.999 | - | - | - |

with decreasing confining pressure for strains from 0.5 % to 1.75 %, scaling as a power law with exponents that decrease as strain increases (Table 8.3).

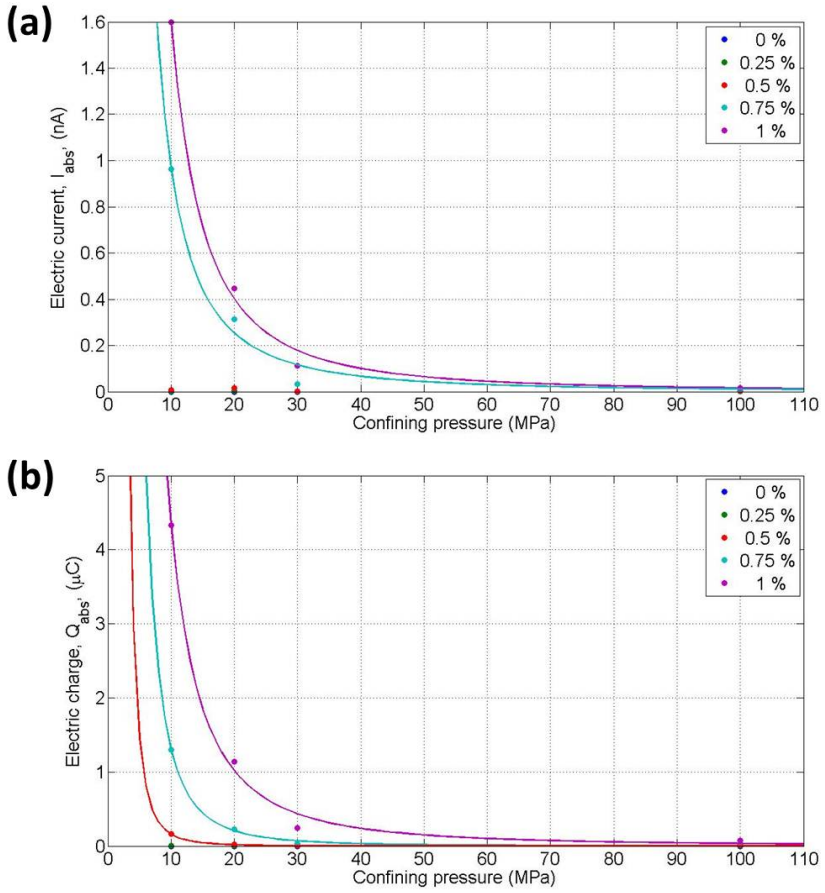


Figure 8.3: Absolute values of (a) electric current and (b) electric charge as a function of confining pressure for the experiments shown in Figure 8.1 at each strain slice. The trend lines in both (a) and (b) are power laws; see Table 8.3 for the respective parameters.

Table 8.3: Parameters for scaling of absolute electric current, $I_{abs}$ (nA) and electric charge, $Q_{abs}$ ($\mu$C) with confining pressure (MPa) (Figure 8.3). The fits were calculated by least squares.

| | $I_{abs} = AP_c^n$ | | | $Q_{abs} = AP_c^n$ | | |
|---|---|---|---|---|---|---|
| $\varepsilon_s$ (%) | **A** | **n** | $\mathbf{r^2}$ | **A** | **n** | $\mathbf{r^2}$ |
| 0.50 | - | - | - | 248 | -3.19 | 0.981 |
| 0.75 | 83 | -1.94 | 0.974 | 604 | -2.67 | 0.995 |
| 1.00 | 160 | -2.00 | 0.994 | 540 | -2.10 | 0.993 |

## 8.4 Rate of Electric Current Production

Figure 8.4 shows the absolute rate of electric current flow, $|dI/dt|$, as a function of confining pressure during the main deflection of current after the initial yield for the experiments showing in Figure 8.1. This deflection occurs between 0.5 and 1 % strain for $P_c$ = 10-30 MPa and between 1.5 and 1.8 % strain for $P_c$ = 100 MPa. Current flows at a much faster rate at the lower confining pressures, i.e., in the purely brittle regime. Once the brittle-ductile transition is reached (30 MPa), the rate of current production between these values

of strain is much smaller. The scaling can be closely approximated by a power law with exponent $n = -1.87$. The measurement error on $|dI/dt|$ is $\pm 0.01$ fA s$^{-1}$ and therefore much smaller than the plotted data points.

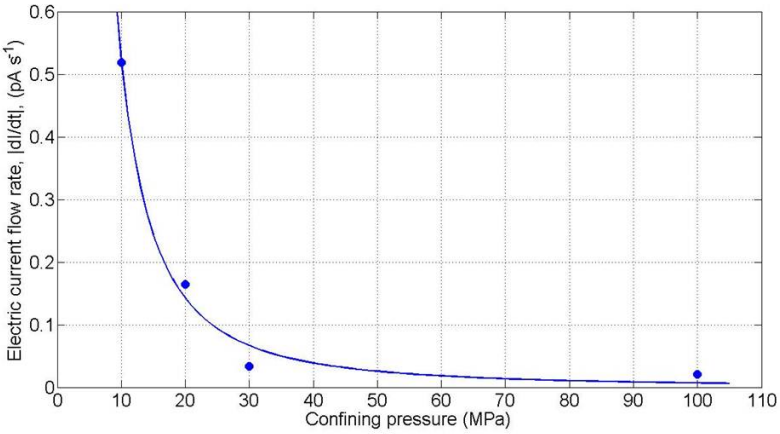


Figure 8.4: Absolute rate of electric current flow, $|dI/dt|$, as a function of confining pressure for the experiments shown in Figure 8.1. The trend line is a power law calculated by least squares: $|dI/dt| = 38.9P_c^{-1.87}$ with $r^2 = 0.983$.

A similar trend is apparent when the natural variability in $|dI/dt|$ between samples deformed under identical conditions is taken into account. Figure 8.5 plots the median value of $|dI/dt|$ for the four experiments [CM05, CM12, CM16 and CM17] carried out under identical conditions (30 MPa and $10^{-6}$ s$^{-1}$), together with error bars showing the range of $|dI/dt|$ across these four experiments. The individual values of $|dI/dt|$ for each of the experiments are also shown (open red circles). When the median value is used, the scaling of $|dI/dt|$ with $P_c$ is closer to a power law than when only Experiment CM05 is considered, with an exponent of -1.51. However, the relationship of $|dI/dt|$ with confining pressure warrants further investigation given the variability in $|dI/dt|$ across these four experiments.

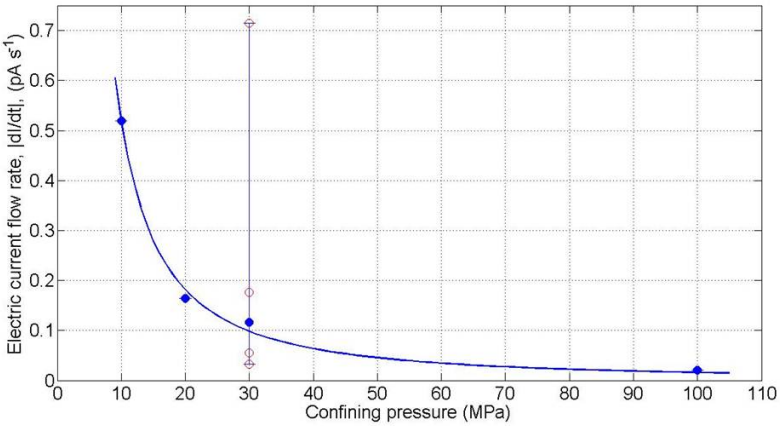


Figure 8.5: Absolute rate of electric current flow $|dI/dt|$ as a function of confining pressure for the same experiments as above, apart from at 30 MPa, where the median value of $|dI/dt|$ for the 3S-3N electrode pair over four experiments [CM05, CM12, CM16, CM17], all carried out at 30 MPa and 1x10$^{-6}$ s$^{-1}$, is shown. The trend line is a power law calculated by least squares: $|dI/dt| = 16.8P_c^{-1.51}$ with $r^2 = 0.994$.

## 8.5 Damage Evolution

It can be seen in Figure 8.6 (a) that P-wave velocity ($V_P$) decreases non-linearly with increasing strain, rapidly at first and then more slowly. Onset of crack damage, as represented by the onset of $V_P$ reduction, begins at the yield point for all $P_c$ tested. However, yield occurs after more deformation at 100 MPa (0.5% strain) than at the lower $P_c$ (0.3%). At the two intermediate $P_c$, the rate of cracking decreases from about 1% strain, which coincides with the end of the initial production of electric current. At the highest $P_c$, there is a slight levelling off in the $V_P$ reduction at 1.5% strain which corresponds to the post-yield strain hardening region and an acceleration in electric current production. The degree of reduction in $V_P$ with strain changes with increasing confining pressure. A much greater total reduction (~60%) occurs at the lowest $P_c$ compared with the highest $P_c$ (~15%) and the change occurs over an increasing degree of strain as the $P_c$ increases. Figure 8.6 (b) shows the relationship between $V_P/V_{Pmax}$ and $P_c$ for strain slices at 0.25% intervals from 0.5 to 1% strain. At each strain, $V_P/V_{Pmax}$ increases as a power law with increasing $P_c$ (see Table 8.4 for parameters). That is, the reduction in $V_P$ relative to $V_{Pmax}$ is smaller at higher confining pressures. When compared with the relationships between $P_c$ and $I_{abs}$, $Q_{abs}$ and $|dI/dt|$ described in Section 8, which all decrease with increasing $P_c$, this shows that a smaller reduction in $V_P$ is associated with a smaller amount of current flow and electric charge and a slower rate of current production. The exponents for $V_P$ variation are an order of magnitude smaller than those for electric signal variation.

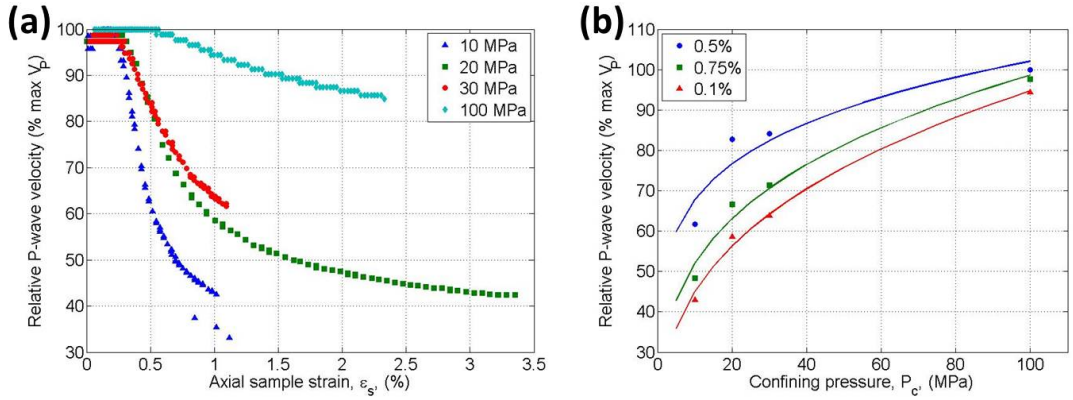


Figure 8.6: Variation in $V_P$ across the central part of the sample as a function of (a) axial sample strain and (b) confining pressure. The trend lines in (b) are power laws; see Table 8.4 for the respective parameters.

Table 8.4: Parameters for power-law scaling of $V_P$ variation ($V_P/V_{Pmax}$) with confining pressure (MPa) (Figure 8.6 (b)). The fits were calculated by least squares.

| | $\frac{V_P}{V_{Pmax}} = AP_c^n$ | | |
|---|---|---|---|
| $\varepsilon_s$ (%) | **A** | **n** | $\mathbf{r^2}$ |
| 0.50 | 44.9 | 0.178 | 0.836 |
| 0.75 | 27.4 | 0.278 | 0.966 |
| 1.00 | 21.3 | 0.324 | 0.990 |

Since $V_P$ is sensitive to void space (i.e., crack damage) in the samples, the variation in $V_P$

with confining pressure is due to the suppression of microcrack amplitudes (i.e., a reduction in crack size) and the increased contribution of plastic mechanisms to deformation as $P_c$ increases (Fredrich et al., 1989). This effect is clear from Figure 8.7 (a), which shows the variation of $V_P$ with the damage parameter, $D$. At all confining pressures, $V_P$ variation across the sample is inversely proportional to $D$. However, the degree with which $V_P$ changes with $D$ decreases with increasing $P_c$ (parameter A in Table 8.5 and Figure 8.7 (b)). At 10 MPa, 90% of the mechanical damage to the sample can be attributed to crack damage compared with only 30% at 100 MPa. This proportion of crack damage relative to the total mechanical damage is inversely proportional to confining pressure, highlighting the decreasing influence of crack damage and the increasing influence of plastic mechanisms on deformation as the confining pressure increases.

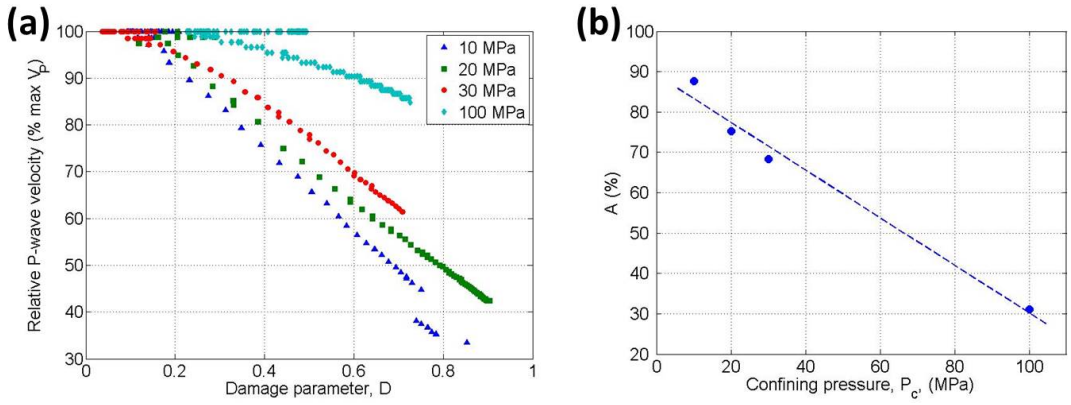


Figure 8.7: Relationship between $V_P$ variation across the sample and the damage parameter, $D$: (a) $V_P$ variation as a function of $D$ and (b) gradient, $A$, of $V_P/V_{Pmax}$ with respect to $D$ (see Table 8.5) as a function of $P_c$. The trend line in (b) is linear calculated by least squares: $y = -0.59x + 89$.

Table 8.5: Parameters for the linear scaling of $V_P/V_{Pmax}$ with $D$ for each confining pressure (Figure 8.7 (a)). The fits were calculated by least squares.

| | $\frac{V_P}{V_{Pmax}} = AD + B$ | | |
|---|---|---|---|
| $P_c$ **(MPa)** | **A** | **B** | $\mathbf{r^2}$ |
| 10 | -0.876 | 1.101 | 1.000 |
| 20 | -0.753 | 1.097 | 0.998 |
| 30 | -0.683 | 1.106 | 0.994 |
| 100 | -0.311 | 1.085 | 0.985 |

Comparing the evolution of electric current with respect to $D$ (Figure 8.8) to the evolution of $V_P$ (Figure 8.7 (a)), it's clear that in the brittle regime (<30 MPa), electric current begins to flow after ≤10% reduction in velocity and a 20% increase in $D$ (i.e., a 20% reduction in the Young's Modulus). In the semi-brittle regime (≥30 MPa), the main flow of current occurs only after a 50% increase in $D$. At this point the sample deformed at 100 MPa had experienced <10% reduction in velocity, while the sample deformed at 30 MPa had experienced twice that. Therefore, the requirement for electric current to flow is an increase in crack damage of up to 20% and the presence of a connected crack network, rather than a specific reduction in Young's Modulus. This implies that plastic deformation mechanisms play a smaller part in the current generation process than brittle mechanisms

and that the presence of a crack network provides electrical flow pathways through the rock sample.

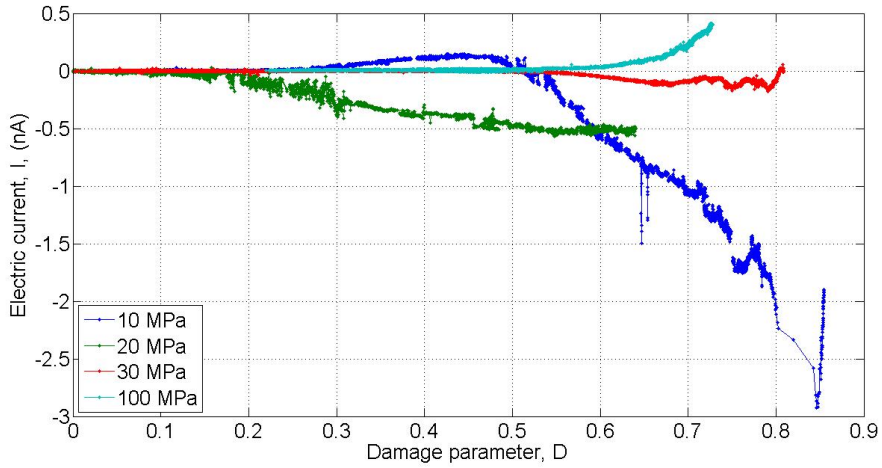


Figure 8.8: Evolution of electric current flow between electrodes 3S and 3N, at $10^{-6}$ $s^{-1}$ strain rate and four different confining pressures, as a function of the damage parameter, $D$.

## 8.6 Relationship with Stress

It is important to study the relationship between electric current and differential stress in order to establish the existence or not of a critical stress at which electric current begins to flow.

Figure 8.9 (a) shows the evolution of electric current with respect to differential stress, $\sigma$ at the four different confining pressures tested. It appears that $\sigma_{ec}$ at which electric current begins to flow (the onset stress) increases with increasing $P_c$. This is true for $P_c$ up to 30 MPa. However, although not clear from the Figure, at 100 MPa the onset of electric current occurs at 174 MPa, a very similar stress as that seen at 30 MPa (Table 8.6), and increases very gradually with stress until 240 MPa, whereupon it begins to flow much more rapidly. Thus, in the brittle regime, $\sigma_{ec}$ increases with increasing $P_c$, whereas, in the semi-brittle regime, there appears to be a particular onset stress required for electric current to flow. When the onset stress is normalised by $\sigma_{max}$, this relationship is reversed; in the brittle regime and at the semi-brittle transition ($\leq$30 MPa), electric current flows once $\sigma > 90\%$ of the maximum compressive strength of the sample (Table 8.6) but once behaviour is fully ductile, electric current flows earlier than expected. This implies that, in the brittle regime, it is the relative stress that is the critical factor rather than the stress itself, while in the ductile regime the stress itself becomes the critical factor. The rate at which electric current varies with stress is also given in Table 8.6. The negative value indicates that current varies with stress during the strain softening region beyond $\sigma_{max}$, which was only reached at 10 MPa. Overall, current varies approximately proportionally with stress, although there is some degree of scatter, with a very similar constant of

proportionality for the two $P_c$ in each deformation regime. In the brittle regime, it is an order of magnitude larger than in the semi-brittle regime.

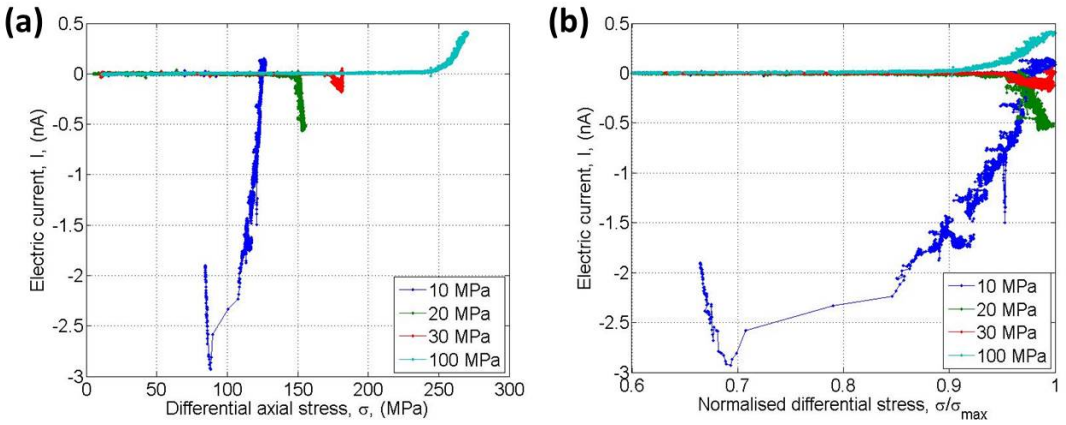


Figure 8.9: Evolution of electric current across the central part of the sample (3S-3N) as a function of (a) differential stress, $\sigma$, and (b) normalised stress, $\sigma/\sigma_{max}$ at $10^{-6}$ $s^{-1}$ and the four different confining pressure conditions.

Table 8.6: Values of electric current onset stress, $\sigma_{ec}$, normalised onset stress, $\sigma_{ec}/\sigma_{max}$, and rate of change of electric current with differential stress, $dI_{abs}/d\sigma$, for each of the four confining pressures tested.

| $P_c$ **(MPa)** | $\sigma_{ec}$ **(MPa)** | $\sigma_{ec}/\sigma_{max}$ | $dI_{abs}/d\sigma$ **(nA/MPa)** |
|---|---|---|---|
| 10 | 122 | 0.97 | -0.1287 |
| 20 | 144 | 0.92 | 0.1013 |
| 30 | 172 | 0.95 | 0.0236 |
| 100 | 174 | 0.88 | 0.0256 |

## 8.7 Summary and Deductions

In this chapter, I have presented the electric current signals generated during triaxial deformation of non-piezoelectric Carrara marble at a variety of confining pressures and $\dot{\varepsilon} = 10^{-6}$ $s^{-1}$. At the lowest three confining pressures ($P_c \leq 30$ MPa), electric current magnitude shows an overall logarithmic increase with deformation, with a more distinct 'levelling off' as $P_c$ increases (Figure 8.2 (a)). On the other hand, electric charge magnitude increases exponentially with deformation until failure at the lowest $P_c$ or until stable cataclastic flow at $20 \leq P_c \leq 30$ MPa, during which it increases linearly (Figure 8.2 (b)). The highest $P_c$ shows an exponential increase with deformation for both current and charge. Both electric current and electric charge magnitudes at a given amount of deformation decrease according to a power law as $P_c$ increases across the brittle to semi-brittle transition (Figure 8.3). A similar relationship is observed for both the main rate of current production (Figures 8.4 and 8.5) and the degree of crack damage, as represented by the reduction in $V_P$ (Figure 8.6 (b)). For $P_c \leq 30$ MPa, the initial steady rate of electric current production can be attributed to the rapid increase in stress-induced crack density, which occurs when the stress exceeds 90% of the maximum strength of the sample (Figure 8.9 (b)). At the lowest $P_c$, crack production continues until failure, although it slows down slightly as failure approaches. At $20 \leq P_c \leq 30$ MPa, crack production

slows down at peak stress and the onset of stable cataclastic flow (Figure 8.6 (a)), which coincides with slowing of the overall rate of current production (Figures 8.1 (b) and (c)). Conversely, at 100 MPa, a very slight reduction in the crack production rate coincides with an acceleration in electric current production (Figures 8.1 (d)). Post-yield, electric current is approximately proportional to differential stress (Figure 8.9 (a)), with apparently characteristic proportionality constants for the brittle and semi-brittle regimes (Table 8.6). This indicates that it could be used as an indirect measurement of stress both during dilatancy, as suggested by Eccles et al. (2005) and seen at $P_c \leq 30$ MPa, and during constant-volume strain hardening, as seen at 100 MPa.

Since dislocation glide is negligible at all but the highest $P_c$ tested (see Section 7.7), the reduction in crack damage for a given reduction in Young's Modulus with increasing $P_c$ (Figure 8.7) can be attributed to deformation being accommodated by increased twinning at $P_c \leq 30$ MPa and both increased twinning and activation of dislocation glide at 100 MPa. Thus, at $P_c \leq 30$ MPa, cracks are most likely to be nucleated as wing cracks (e.g., Ashby and Hallam, 1986) around twins, at grain boundaries and at cleavage planes, rather than from dislocation pile-ups. This implies that surface charging processes (Section 3.5.1.4) must be the dominant current-generation mechanism during deformation at $P_c$ up to 30 MPa; i.e., up to the transition between brittle and semi-brittle behaviour. Negligible contribution is expected from the movement of charged edge dislocations (MCD) within grains, although there may be an increased contribution from MCD at the tips of propagating cracks as $P_c$ increases.

The observed decrease, with increasing $P_c$, in both electric current and electric charge magnitudes (Figure 8.3) at any particular strain may, therefore, be attributed to the reduction in crack length and connectivity as the $P_c$ increases, while the observed decrease in the rate of current production with $P_c$ may be related to the ease with which cracks propagate and coalesce, since it is easier for cracks to grow longer at lower confining pressures. In terms of the capacitance model for electrification at two separating crack surfaces, this leads to charge separation across a greater area of crack surfaces over the same time-frame at lower $P_c$, while crack opening times are longer and more frequent. The higher aspect ratio of cracks at lower $P_c$ may also play a role, allowing the crack surfaces to remain closer together for longer. This would increase the charge relaxation time and maintain the high potential difference between the crack surfaces for longer, leading to a larger, longer-duration micro-current. In terms of an edge dislocation moving ahead of the crack tip, more crack propagation means that these dislocations and their charged edges are mobile for longer, maintaining the flow of charge. It is likely that these two mechanisms work in conjunction, with a greater contribution from dislocation motion at higher $P_c$. Rapid crack propagation and coalescence may be responsible for the acceleration of charge production towards failure at the lowest $P_c$, as the surface area over which charge separation occurs increases rapidly.

No crack damage was observed on the specimen deformed at 100 MPa, implying very

little dilatancy in this sample compared with the other three, an observation confirmed by the velocity results, which showed that only 30% of mechanical damage (i.e., reduction in the Young's Modulus) was accommodated by microcracking (Figure 8.7 (b)). At this pressure, twinning is responsible for the initial yield, after which production of electric current and charge accelerates with increasing deformation from the point where ductile strain hardening processes steadily increase the differential stress supported by the sample (Figures 8.1 (d) and 8.2). It is likely, therefore, that the activation of dislocation glide in an increasing number of grains is mainly responsible for the observed acceleration, with only a tiny contribution from microcracking.

The observed stability of electric current production during the constant stress region at intermediate $P_c$ ($20 - 30$ MPa), where fluctuations are superimposed on a relatively constant value (Figures 7.6 and 8.1 (b) and (c)), is likely to be due to stable cataclastic flow processes. This is evident from the velocity reduction with respect to strain (Figure 8.6), which stabilises to an almost constant level at exactly the same point as the current levels off. During cataclastic flow, hardening mechanisms such as twinning and compaction (due to frictional sliding along crack surfaces and grain boundaries and grain size reduction associated with grain rotation and fragmentation along these slip planes) act to balance the weakening effect of crack propagation, allowing the sample to support peak stress over a greater amount of deformation. In this situation, it could be argued that, during shearing, separation of positive and negative charges in an electric double layer (EDL) formed between crack surfaces creates the potential difference required for electrification, equivalent to a contact separation mechanism. Since marble is a homogeneous rock, the grains should all have the same work function with little or no contact potential between them. Therefore, only the presence of an EDL would generate a potential between the crack surfaces or grain boundaries. The EDL may be formed either by the release of high-energy electrons during fracture, which ionises atoms in the void spaces (e.g., Enomoto and Hashimoto, 1990; Enomoto, 1996), or by the release of charges from defects generated in disordered surface layers during shearing of asperities on the shear planes (crack surfaces or grain boundaries) themselves (Takeuchi and Nagahama, 2004; 2006), or, most likely, by some combination of these two mechanisms.

Systems of two fluxes in opposite directions, coupled by a physical parameter such as the electric field, often tend to go in oscillations (Freund, 2001). As such, steady current production followed by oscillatory behaviour may point to a coupled system whereby the electric field built up by charges flowing in one direction, for example by cracks opening in alignment, induces a counter-current in the other direction. For example, small, localised, stress-relieving avalanches of sliding and fragmentation may be enough to cause a burst of electric current flow in one particular direction, but since the shear planes form conjugate to each other and are distributed evenly throughout the central damage zone, the overall direction of current flow from these shear planes would balance each other, with pulses of opposing polarity oscillating around a constant level as charge accumulates between crack surfaces and the EDL separates with each avalanche of shear events. Charges accumulate

within the EDL over time because each shearing event would increase the number of defects within each sheared grain as well as releasing charges at the sheared surface. Charge separation would also occur during crack propagation at the tips of shear planes with each slip event (wing cracks), contributing to the steady rate of charge production and associated constant but fluctuating flow of electric current observed during cataclastic flow. Oscillations may also result from electrification processes occurring at regions of high local stress concentrations, such as cracks initiating in response to avalanches of twinning activity or the cooperative orientation of dipoles when local stresses reach the critical value at which alignment occurs fast enough to emit a transient electric signal (Section 3.5.1.1).

# Chapter 9

# Influence of Strain Rate on Electric Signals[1,2]

## 9.1 Introduction

Strain rate effects, such as those seen in Figure 7.2 (a), are important in deformation, playing a significant role in controlling the shear fracture of intact rock and the nucleation processes and frictional strength of faulting (Kato et al., 1992; Odedra, 1998; Odedra et al., 2001). Wing-crack models (e.g Kemeny and Cook, 1987; Kemeny, 1991; Nemat-Nasser and Deng, 1994) indicate that such effects may be a consequence of sub-critical crack growth, while the strain rate dependent friction model of Renshaw and Schulson (1998) provides an alternate interpretation that accounts for the observed unsteady growth of wing cracks. Realistic geological strain rates are of the order of $10^{-14}$ $s^{-1}$; impossible to achieve in a laboratory setting since even at a strain rate of $10^{-10}$ $s^{-1}$ it would take more than six years to reach 2% shortening. Therefore, obtaining experimental data for a range of strain rates is essential to provide a basis for extrapolation. Furthermore, when extrapolating laboratory results to geological conditions, large strains must be achieved as well as low strain rates and this is only possible in the steady-state cataclastic flow regime (Rutter, 1974). At 30 MPa, Carrara marble deforms in this regime and therefore extrapolation to crustal strain rates of electric current signals detected at this pressure is possible with some degree of confidence.

To this end, the results from a series of 15 experiments carried out to investigate the influence of strain rate on electric current signals are presented here. Confining pressure for all these experiments was 30 MPa. The majority of these tests recorded one single channel

[1]Cartwright-Taylor, A., Vallianatos, F. and Sammonds, P. (2015). Deformation-induced electric current in Carrara marble across the brittle-ductile transition. *TSG Annual Meeting 2015 5-8 Jan.*

[2]Cartwright-Taylor, A., Sammonds, P. and Vallianatos, F. (2012). Pressure-stimulated current emissions from triaxial compression experiments on Carrara marble. *EGU General Assembly 22-27 April.*

of electric current flow across the sample, perpendicular to the loading axis, between two electrodes at positions 3S and 3N, 12.5 mm above the centre of the sample (see Figure 5.6 for the sensor position map). One experiment [CM12] recorded four channels across the sample, perpendicular to the loading axis. Electric current flow between the 3S-3N electrode pair from this experiment was included in the single channel strain rate dependence analysis. A further three experiments [CM03, CM06 and CM07] recorded four channels at various orientations around the sample; two perpendicular to the loading axis and two oblique to it. Electrode pair positions for each channel were: (a) 4S and 4N and (b) 4E and 4W, all 12.5 mm below the centre of the sample, (c) 5NW, 25 mm below the centre of the sample, and 2SE, 25 mm above the centre of the sample, with current flowing through the sample at an angle of 38.66° to the loading axis and (d) 6N, 37.5 mm below the centre of the sample and 1S, 37.5 mm above the centre of the sample, with current flowing through the sample at an angle of 28.07° to the loading axis. These experiments were analysed separately for strain rate dependence to evaluate the effect of strain rate on the average current flow within the samples.

## 9.2 Single Channel Experiments

### 9.2.1 Electric current signals

The twelve single channel tests encompassed five different strain rates: $10^{-6}$, 5x$10^{-6}$, $10^{-5}$, 5x$10^{-5}$ and $10^{-4}$ $s^{-1}$. Figure 9.1 shows the electric current flow during these tests, indicating the degree of variability between experiments of identical conditions and highlighting the difficulty in interpreting the influence of strain rate from these results. However, it can be seen that, for all strain rates, there is a small initial deflection of electric current that begins immediately after the elastic limit is exceeded, at strains of 0.20 - 0.33 %, before the point of peak stress. This initial onset, which fluctuates slightly higher than the background noise level, coincides with the yield point of the material and the onset of dilatancy, i.e., the onset of microcracking. In four out of these twelve experiments, over the whole range of strain rates apart from the very fastest ($10^{-4}$ $s^{-1}$), this initial onset coincides with the main deflection. For the remaining eight experiments, the initial onset of electric current occurs before the main deflection. In these cases, at faster strain rates ($10^{-4}$ to $10^{-5}$ $s^{-1}$), the main deflection occurs at or immediately after the point of peak stress, at approximately 0.75 - 1 % strain, when the effective Young's Modulus, $E_{eff}$, has reduced to $\leq 0$ GPa. At the slowest strain rates (5x$10^{-6}$ and $10^{-6}$ $s^{-1}$), where the stress remains almost constant around the peak value until large values of strain are reached, the main deflection is seen after the initial yield, where $E_{eff}$ stabilises to an almost constant degree of strain hardening at $E_{eff} \approx 20$ GPa and smaller strains of 0.5 - 0.75 %.

Figure 9.2 shows electric current flow with differential stress for an example experiment at each strain rate. These five experiments were used for the non-extensive modelling

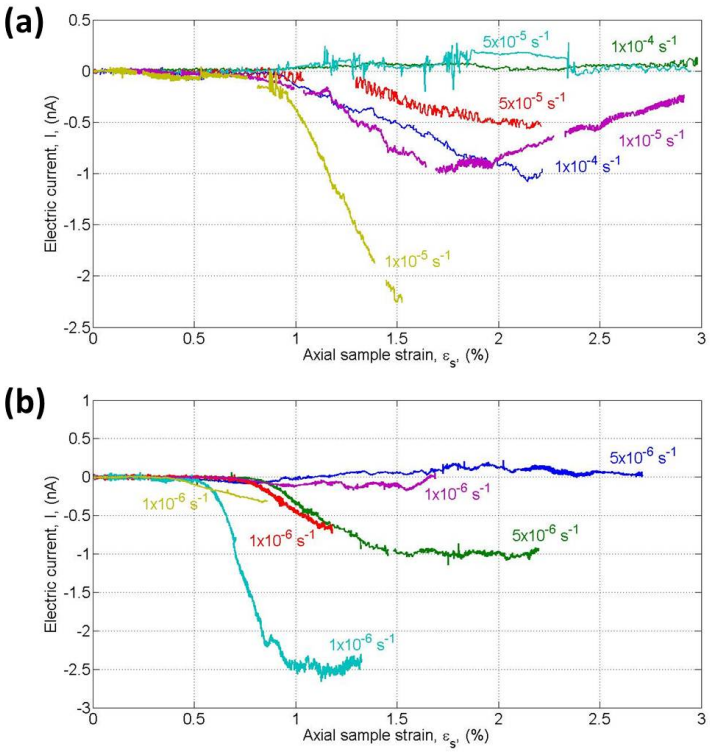


Figure 9.1: Electric current flow between a single pair of electrodes (3S-3N) as a function of axial sample strain, produced during triaxial deformation of Carrara marble samples at 30 MPa $P_c$ and five different strain rates. Faster strain rates are shown in (a) $10^{-4}$, 5x10$^{-5}$ and $10^{-5}$ s$^{-1}$, while slower strain rates are shown in (b) 5x10$^{-6}$ and $10^{-6}$ s$^{-1}$.

presented in Section 11.4. It is clear from these tests that there are three timescales of behaviour: (i) an overall background flow of electric current, (ii) high-frequency fluctuations that vary in amplitude and (iii) intermediate-frequency fluctuations that vary in amplitude and duration. This behaviour is possibly related to the competition between hardening and softening mechanisms as they balance each other during cataclastic flow. It reflects the complicated nature of the current-generating processes, their combination and interaction; more complicated than the different models suggest. The intermediate-frequency fluctuations in particular may mask the precursory change discussed in Chapter 7, with the potential for false alarms.

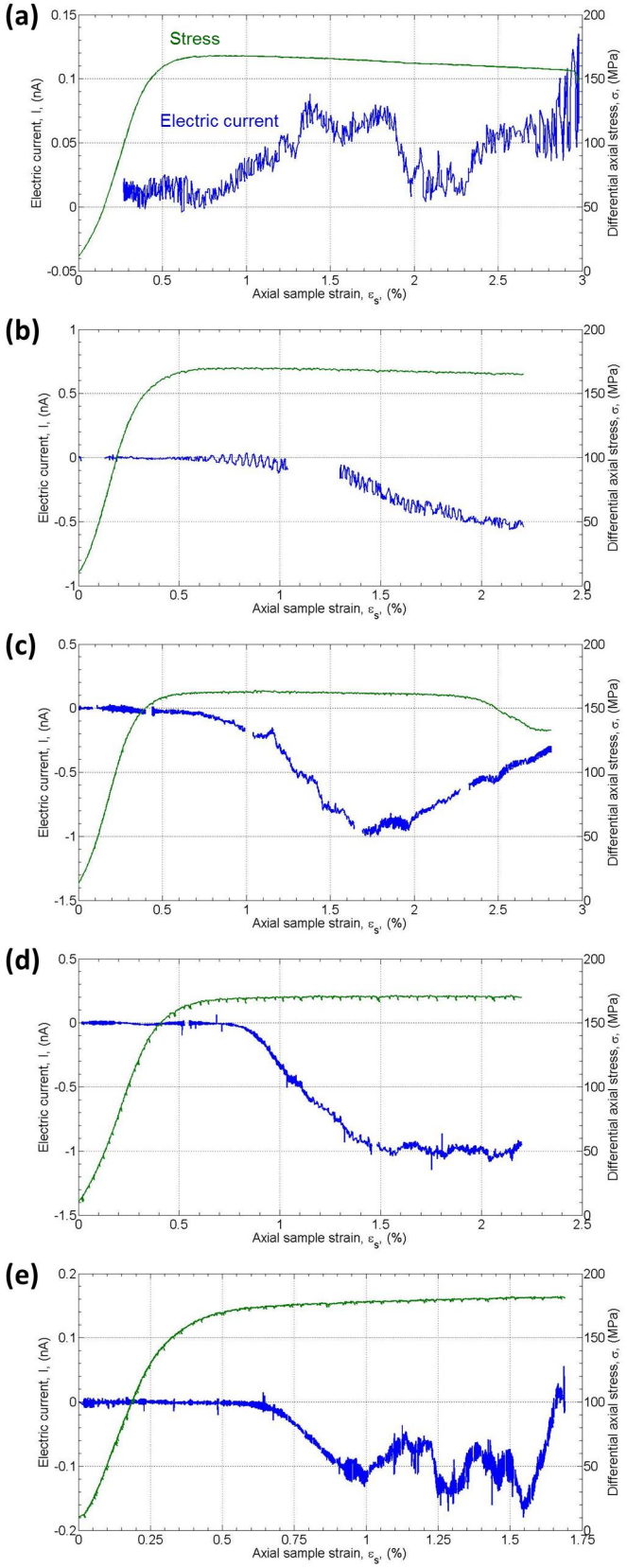


Figure 9.2: Electric current flow between electrodes 3S-3N (blue) and differential stress (green) as a function of axial sample strain. The signals were produced during triaxial deformation of Carrara marble specimens at 30 MPa confining pressure and five different strain rates; (a) $10^{-4}$ $s^{-1}$ [Experiment CM15], (b) $5x10^{-5}$ $s^{-1}$ [Experiment CM23], (c) $10^{-5}$ $s^{-1}$ [Experiment CM14], (d) $5x10^{-6}$ $s^{-1}$ [Experiment CM22] and (e) $10^{-6}$ $s^{-1}$ [Experiment CM05]. Data gaps are due to removal of data recorded during velocity surveys.

### 9.2.2 Electric current and electric charge magnitude

Figure 9.3 presents the magnitude of both electric current flow ($I_{abs}$) and accumulated electric charge ($Q_{abs}$) at each 'strain slice' for all strain rates tested. The values displayed are average readings across experiments carried out at the same strain rate. Measurement errors for $I_{abs}$ and $Q_{abs}$ are ±10 fA and ±10 pC respectively and therefore much smaller than the plotted data points. $I_{abs}$ increases with increasing deformation but little can be said about its relationship with strain rate (Figure 9.3 (a)). By contrast, not only does $Q_{abs}$ increase with increasing deformation, it also shows an overall tendency to increase as the strain rate decreases (Figure 9.3 (b)). However, this tendency is not straightforward. It splits into three stages; (1) a similar amount of electric charge accumulates for a given amount of deformation at the two fastest strain rates, (2) significantly more charge is produced for a given strain at the two intermediate strain rates, a similar amount at each, and (3) most charge for a given strain is generated at the slowest strain rate. At the two fastest strain rates, significant current flow is not seen until $\varepsilon_s \sim 0.75$ %, after which it increases approximately linearly with deformation. At the three slowest strain rates, significant current flows from 0.25-0.5 % strain, increasing exponentially until $\varepsilon_s \approx 1 \pm 0.25$ %. Beyond this, the two intermediate strain rates exhibit a linear increase in current flow with deformation up to 1.5 % strain. Parameters for both these trends are given in Table 9.1. Beyond 1.5 % strain, current flow at 5x10$^{-6}$ s$^{-1}$ appears to level off. Electric charge accumulates exponentially with deformation from 0.25-0.5 % strain. This is consistent across all strain rates. At strain rates for which the samples were taken to $\varepsilon_s > 1.5$ %, the increase becomes linear for $\varepsilon_s \geq 1.5 \pm 0.25$ %. Parameters for both these trends are given in Table 9.2.

Table 9.1: Parameters for scaling of absolute electric current, $I_{abs}$ (nA), with axial sample strain, $\varepsilon_s$ (%) shown in Figure 9.3 (a). Scaling is according to $I_{abs} = A\exp^{B\varepsilon_s}$ for $\varepsilon_s \leq 1 \pm 0.25$ % and $I_{abs} = A\varepsilon_s + B$ for $\varepsilon_s \geq 0.75$ %. The fits were calculated by least squares.

| $\dot{\varepsilon}$ (s$^{-1}$) | $I_{abs} = A\exp^{B\varepsilon_s}$ | | | $I_{abs} = A\varepsilon_s + B$ | | |
|---|---|---|---|---|---|---|
| | **A** | **B** | **r$^2$** | **A** | **B** | **r$^2$** |
| 1x10$^{-4}$ | - | - | - | 0.3856 | -0.2781 | 0.9886 |
| 5x10$^{-5}$ | - | - | - | 0.2595 | -0.2018 | 0.9756 |
| 1x10$^{-5}$ | 0.0022 | 4.8091 | 0.9978 | 2.4962 | -2.2214 | 1.0000 |
| 5x10$^{-6}$ | 0.0005 | 6.0393 | 0.9970 | 0.6564 | -0.4453 | 0.9834 |
| 1x10$^{-6}$ | 0.0005 | 9.2201 | 1.0000 | - | - | - |

Table 9.2: Parameters for scaling of absolute electric charge, $Q_{abs}$ ($\mu$C), with axial sample strain, $\varepsilon_s$ (%) shown in Figure 9.3 (b). Scaling is according to $Q_{abs} = A\exp^{B\varepsilon_s}$ for $\varepsilon_s \leq 1.5 \pm 0.25$ % and $Q_{abs} = A\varepsilon_s + B$ for $\varepsilon_s \geq 1.5 \pm 0.25$ %. The fits were calculated by least squares.

| $\dot{\varepsilon}$ (s$^{-1}$) | $Q_{abs} = A\exp^{B\varepsilon_s}$ | | | $Q_{abs} = A\varepsilon_s + B$ | | |
|---|---|---|---|---|---|---|
| | **A** | **B** | **r$^2$** | **A** | **B** | **r$^2$** |
| 1x10$^{-4}$ | 0.0001 | 3.0363 | 0.9969 | 0.0379 | -0.0451 | 0.9889 |
| 5x10$^{-5}$ | 0.0001 | 2.9358 | 0.9974 | 0.0491 | -0.0641 | 0.9769 |
| 1x10$^{-5}$ | 0.0013 | 3.9288 | 0.9989 | - | - | - |
| 5x10$^{-6}$ | 0.0011 | 4.1692 | 0.9996 | 0.9210 | -0.9631 | 0.9938 |
| 1x10$^{-6}$ | 0.0007 | 9.2164 | 0.9999 | - | - | - |

The relationship between strain rate and electric current and strain rate and electric

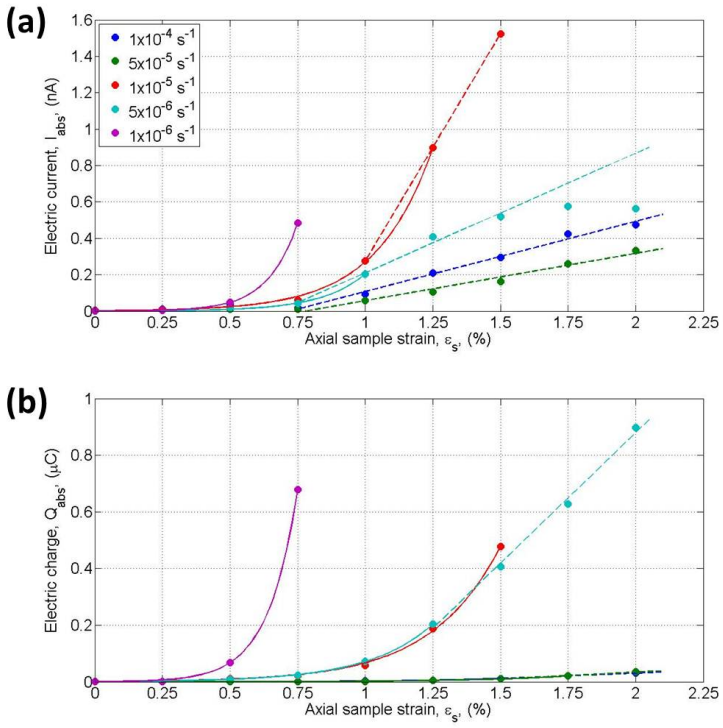


Figure 9.3: Absolute values of (a) electric current and (b) electric charge at each strain slice as a function of strain for the five different strain rates. Each data point represents an average reading from the two experiments carried out under equivalent conditions for all strain rates apart from the slowest, for which each reading is the average of four experiments (Figure 9.1) Solid trend lines are exponential and dashed trend lines are linear in both (a) and (b); see Tables 9.1 and 9.2 for the respective parameters.

charge can be seen more clearly in Figure 9.4. Electric current flow (Figure 9.4 (a)) is independent of strain rate until $\varepsilon_s = 0.75$ %, at which point it shows a power law decrease with increasing strain rate (red line). For $\varepsilon_s > 0.75$ %, data points do not exist for the slowest strain rate. At these strains, a distinct divide between the two fastest and the two intermediate strain rates is apparent with an overall decrease in current from intermediate to fast. Although not shown in (Figure 9.4 (a)), this decrease is best modelled as power-law with exponent $-0.4$ for $1\% \leq \varepsilon_s \leq 1.5\%$ but without additional data points at the slowest strain rate the fit is poor ($r^2 \sim 0.5$). Above 1.5% strain the decrease between fast and intermediate strain rates is best modelled as logarithmic but, again, there are not enough data points to confirm this. On the other hand, electric charge (Figure 9.4 (b)) shows an approximate power-law decrease with increasing strain rate at all strain slices (see Table 9.3 for the parameters). Since $Q = \int I dt$ and there is a five-fold increase in the time required to reach a particular value of strain as the strain rate decreases, this result implies that the charge accumulated between the electrode pair can be completely accounted for by the time required to achieve a certain amount of deformation at each of these strain rates; the slower the strain rate, the more charge accumulates within the sample. The average exponent, $n$, of these power-law approximations is $-1.23 \pm 0.35$. However, $n$ varies with strain, initially decreasing from $-0.7$ to $\sim -1.4$ between strains of 0.25 and 0.75 and then remaining at $\sim -1.4$ from 0.75 to 1.5 % strain before increasing

to $\sim -1.2$ at higher strains (Table 9.3).

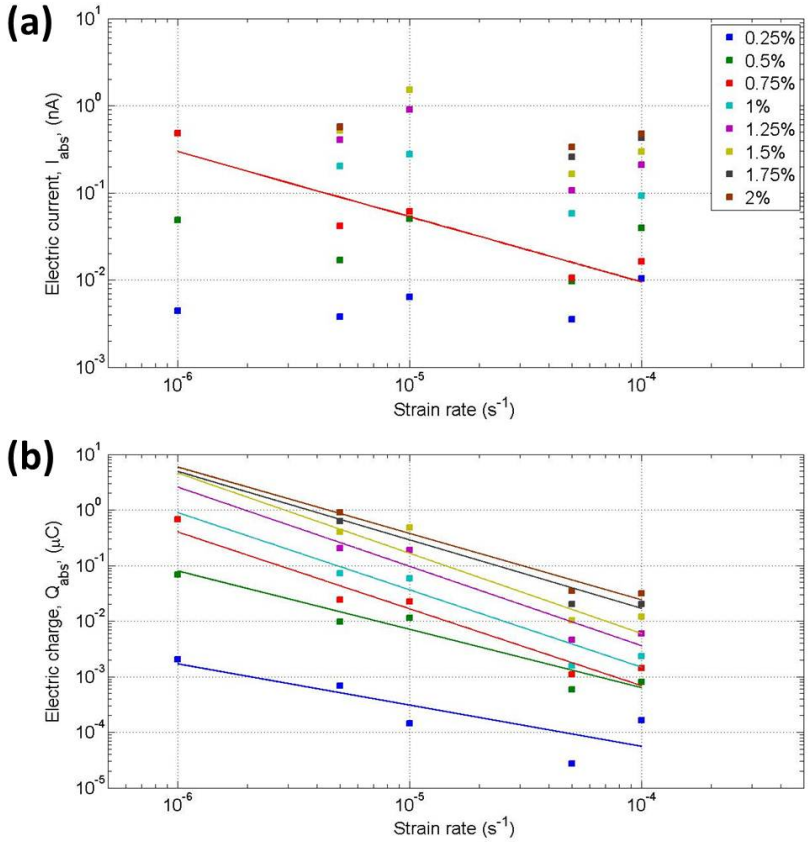


Figure 9.4: Absolute values of (a) electric current and (b) electric charge as a function of strain rate for each strain slice. The trend lines are power laws calculated by least squares. In (a) $I_{abs} = 9.64\text{x}10^{-6}\dot{\varepsilon}^{-0.748}$ with $r^2 = 0.852$ for $\varepsilon_s = 0.75$ %, while parameters for the trend lines in (b) can be found in Table 9.3.

Table 9.3: Parameters for scaling of absolute electric charge, $Q_{abs}$ ($\mu$C) with strain rate, $\dot{\varepsilon}$ ($s^{-1}$) shown in Figure 9.4 (b), according to: $Q_{abs} = A\dot{\varepsilon}^n$ for each strain slice.

| $\varepsilon_s$ (%) | A | n | $r^2$ |
|---|---|---|---|
| 0.25 | 5.51E-08 | -0.74 | 0.6905 |
| 0.50 | 3.51E-08 | -1.05 | 0.9349 |
| 0.75 | 2.19E-09 | -1.38 | 0.9482 |
| 1.00 | 3.78E-09 | -1.39 | 0.8980 |
| 1.25 | 7.32E-09 | -1.43 | 0.9013 |
| 1.50 | 1.36E-08 | -1.44 | 0.8915 |
| 1.75 | 1.66E-07 | -1.23 | 0.9510 |
| 2.00 | 3.78E-07 | -1.20 | 0.9635 |

### 9.2.3 Rate of current production

Figure 9.5 shows the absolute rate of electric current flow, $|dI/dt|$, as a function of strain rate during the *main deflection* of current after the initial yield for the experiments shown in Figure 9.1. This deflection occurs between 0.5 and 1 % strain for strain rates of $10^{-6}$ and $5\text{x}10^{-6}$ $s^{-1}$ and between 1 and 1.5 % strain for strain rates of $10^{-5}$, $5\text{x}10^{-5}$ and $10^{-4}$ $s^{-1}$. The behaviour of $|dI/dt|$ with strain rate is opposite to that of electric charge, with an overall increase in $|dI/dt|$ with strain rate and values at the two slowest strain rates

and the two intermediate strain rates clustering as pairs. Current production is fastest at the fastest strain rate, i.e., when brittle behaviour dominates. Once the strain rate is slow enough for cataclastic flow to dominate, the corresponding rate of current production is much slower. This scaling can be approximated by a power law with exponent $n = 0.45$. The measurement error on $|dI/dt|$ is $\pm 0.01$ fA s$^{-1}$ and therefore much smaller than the plotted data points. Instead, the error bars indicate the natural variability in $|dI/dt|$ between samples deformed under identical conditions and individual values of $|dI/dt|$ for each of these experiments are shown as open red circles.

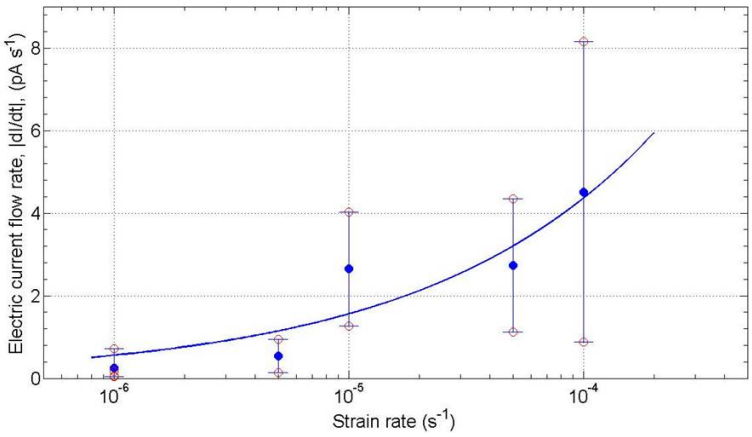


Figure 9.5: Absolute rate of electric current flow $|dI/dt|$ as a function of strain rate for the experiments shown in Figure 9.1. Solid blue circles show $< |dI/dt| >$ over tests carried out at identical conditions with error bars show the full range. Individual values are plotted as open red circles. The trend line is a power law calculated by least squares: $|dI/dt| = 267\dot{\varepsilon}^{0.447}$ with $r^2 = 0.798$.

## 9.3 Multi-Channel Experiments

### 9.3.1 Electric current signals

The multi-channel tests encompassed three different strain rates: $10^{-6}$, $10^{-5}$ and $10^{-4}$ s$^{-1}$. Figure 9.6 shows electric current flow between the four electrode pairs during these dry tests. Initial onset of electric current flow occurs at the yield point (0.25 - 0.3 % strain) for $10^{-5}$ and $10^{-6}$ s$^{-1}$, while for $10^{-4}$ s$^{-1}$ there is no current flow above background until the main deflection at 1 % strain. The strain at which the main deflection occurs increases with increasing strain rate, from 0.33 % at $10^{-6}$ s$^{-1}$ to 0.7 % at $10^{-5}$ s$^{-1}$ and 1 % at $10^{-4}$ s$^{-1}$. The corresponding Young's Modulus at the point of the main deflection therefore decreases with increasing strain rate, from 20 GPa at $10^{-6}$ s$^{-1}$ to 0.05 GPa at $10^{-5}$ s$^{-1}$ and 0 GPa (peak stress) at $10^{-4}$ s$^{-1}$. For the experiment at $10^{-6}$ s$^{-1}$, the main deflection on all channels coincided with the initial onset of electric current, earlier than for the corresponding single channel experiments where the main deflection coincided with the end of the initial yield. However, in this multi-channel test clear fluctuations occur in the current flow at the end of the initial yield (~0.5-0.6 % strain), on all channels.

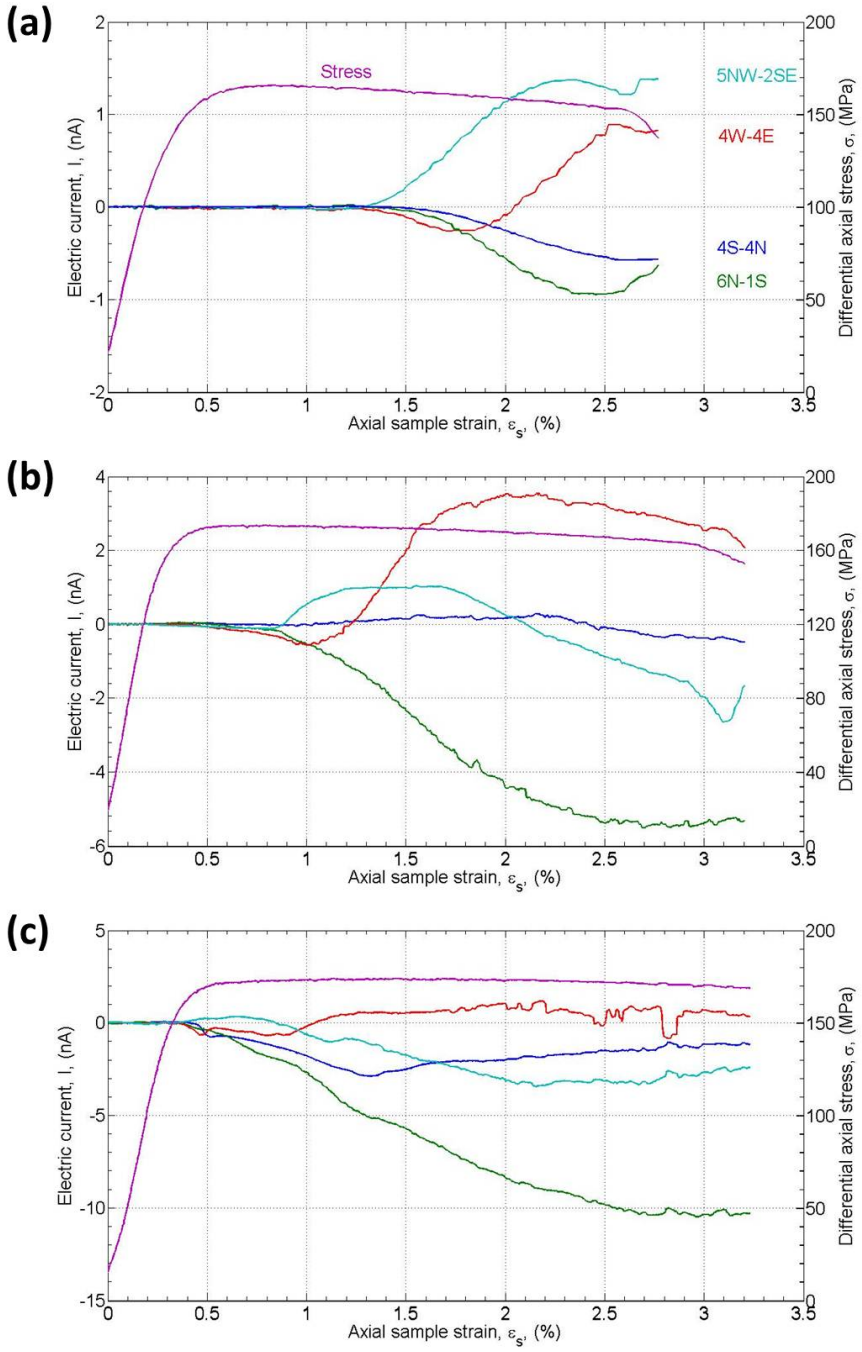


Figure 9.6: Electric current signals, as a function of axial sample strain, produced during triaxial deformation of Carrara marble samples at 30 MPa $P_c$ and three different strain rates: (a) $10^{-4}$ $s^{-1}$ [Experiment CM03], (b) $10^{-5}$ $s^{-1}$ [Experiment CM06] and (c) $10^{-6}$ $s^{-1}$ [Experiment CM07]. Current flow between each of four electrode pairs is shown, each labelled with the electrode pair position according to the convention described in Section 5.2.4 and shown in Figure 5.6. A running median filter has been applied to the electric current data to show the overall shape of the signal.

### 9.3.2 Electric current and electric charge magnitude

Analysis of average absolute electric current flow and charge within the sample during these multi-channel experiments yields similar results as current flow between a single electrode pair, with the advantage that they exhibit greater stability over the larger deformation range. Figure 9.7 shows $I_{abs}$ and $Q_{abs}$ at each strain slice as a function of strain, where each data point represents the average across the four channels recorded during each experiment. This is equivalent to stacking the data from the four channels, giving a better representation of the overall variation in current and charge within the samples during deformation. Measurement errors for $I_{abs}$ and $Q_{abs}$ are ±10 fA and ±10 pC respectively and therefore much smaller than the plotted data points.

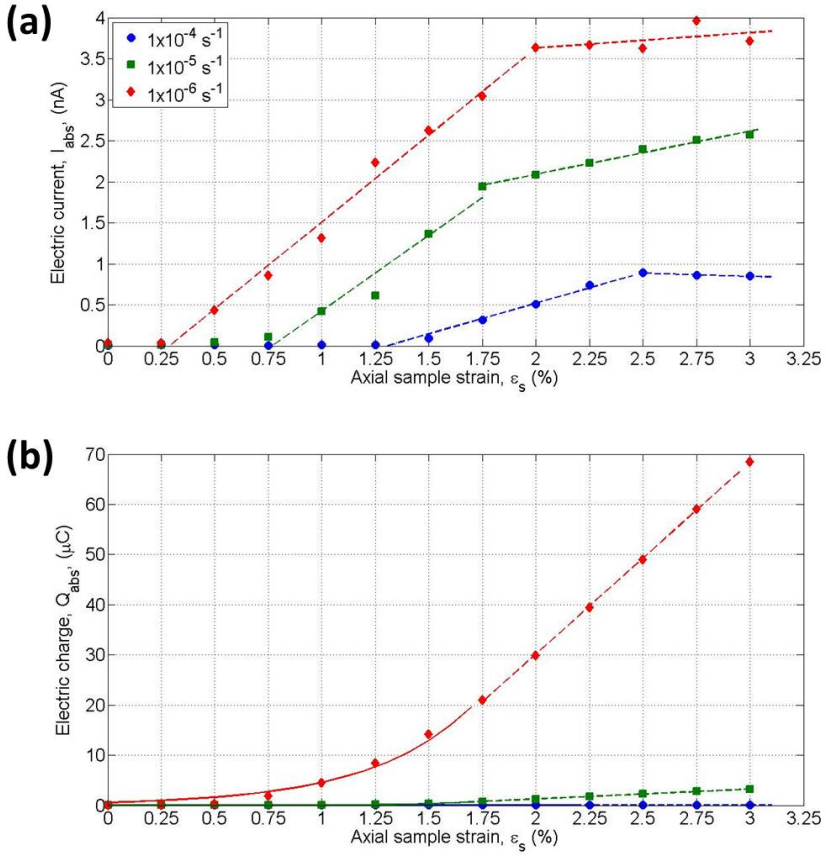


Figure 9.7: Absolute values of (a) electric current and (b) electric charge at each strain slice as a function of strain for the three different strain rates. Each data point represents an average reading from the four channels recording during each experiment shown in Figure 9.6. Solid trend lines are exponential and dashed trend lines are linear; parameters for the two linear fits in (a) are given in Table 9.4 and parameters for the exponential and linear fits in (b) are given in Table 9.5.

Average $I_{abs}$ flow within the samples increases approximately linearly with deformation (Figure 9.7 (a) and Table 9.4). At $10^{-4}$ $s^{-1}$, significant current flow is seen from 1.25 to 2.5 % strain before it stabilises to a relatively constant level at failure (2.5 to 3 % strain). At $10^{-5}$ $s^{-1}$, significant current flow is seen much earlier (from 0.5 % strain) and increases 2.5 times more steeply with deformation at first than at $10^{-4}$ $s^{-1}$, before the gradient reduces by a third between 1.75 % strain and failure at 3 %. At $10^{-6}$ $s^{-1}$, significant

current flow is seen earlier still (from 0.25 % strain), increasing with deformation with a gradient only 1.2 times steeper than at $10^{-5}$ $s^{-1}$ until around 2 % strain, after which it stabilises to a relatively constant level. There is a clear increase of $I_{abs}$ with strain rate at each strain slice.

Table 9.4: Parameters for scaling of absolute electric current, $I_{abs}$ (nA), with axial sample strain, $\varepsilon_s$ (%) shown in Figure 9.7 (a). Scaling is linear, $I_{abs} = A\varepsilon_s + B$, with two distinct gradients at each strain rate, changing at 1.75 % for $10^{-6}$, 1.5 % for $10^{-5}$ 2.25 % for $10^{-4}$ $s^{-1}$. The fits were calculated by least squares.

| $\dot{\varepsilon}$ ($s^{-1}$) | Initial trend | | | Final trend | | |
|---|---|---|---|---|---|---|
| | **A** | **B** | $r^2$ | **A** | **B** | $r^2$ |
| 1x10$^{-4}$ | 0.75 | -0.97 | 0.986 | -0.078 | 1.08 | 0.888 |
| 1x10$^{-5}$ | 1.84 | -1.41 | 0.931 | 0.527 | 1.04 | 0.978 |
| 1x10$^{-6}$ | 2.12 | -0.61 | 0.989 | 0.186 | 3.26 | 0.031 |

Average $Q_{abs}$ accumulated within the sample also increases with both strain rate and deformation, in a similar way to that for the single channel experiments. Scaling with deformation is initially exponential, up to 1.5-1.57 % strain at the two slower strain rates and 2.25 % at the fastest, and then linear. Parameters for both these trends are given in Table 9.5. The exponential exponent ($B$) is similar at $\sim 3$ for the two faster strain rates and reduces to $\sim 2$ at the slowest, whereas the scaling factor ($A$) for both exponential and linear trends increases by two orders of magnitude with each tenfold decrease in strain rate. This indicates that the accumulation of electric charge within these specimens of Carrara marble during deformation is governed by time-dependent processes.

Table 9.5: Parameters for scaling of absolute electric charge, $Q_{abs}$ ($\mu$C), with axial sample strain, $\varepsilon_s$ (%) shown in Figure 9.7 (b). Scaling is according to $Q_{abs} = A\exp^{B\varepsilon_s}$ before and $Q_{abs} = A\varepsilon_s + B$ after $\varepsilon_s$ reaches 1.75 % at $10^{-6}$, 1.5 % at $10^{-5}$ 2.25 % at $10^{-4}$ $s^{-1}$. The fits were calculated by least squares.

| $\dot{\varepsilon}$ ($s^{-1}$) | $Q_{abs} = A\exp^{B\varepsilon_s}$ | | | $Q_{abs} = A\varepsilon_s + B$ | | |
|---|---|---|---|---|---|---|
| | **A** | **B** | $r^2$ | **A** | **B** | $r^2$ |
| 1x10$^{-4}$ | 3.39E-05 | 3.04 | 0.988 | 0.069 | -0.12 | 0.993 |
| 1x10$^{-5}$ | 2.67E-03 | 3.23 | 0.997 | 1.947 | -2.60 | 0.998 |
| 1x10$^{-6}$ | 0.572 | 2.08 | 0.983 | 38.2 | -46.3 | 1 |

Figure 9.8 shows both average electric current flow (a) and average accumulated electric charge (b) within the samples as a function of strain rate for each strain slice. In contrast to electric current flow between a single electrode pair, here there is an approximately logarithmic decrease in $I_{abs}$ with increasing strain rate (Figure 9.8 (a) and Table 9.6). The scaling factor ($A$) increases steadily with deformation from 0.005 at 0.25 % to 0.6 at 1.75 % and then stabilises at $\sim 0.6-0.7$ from 2 % strain onwards. $Q_{abs}$ also decreases with increasing strain rate but follows an approximate power-law (Figure 9.8 (b) and Table 9.7). This is consistent with charge accumulated between a single electrode pair, although here the average exponent, $n$, of the power-law approximations at all values of strain is smaller at $-1.67 \pm 0.23$ (compared with$-1.23 \pm 0.23$), reflecting a steeper decrease in accumulated charge as the strain rate increases. Again, $n$ varies with strain, decreasing from -1.3 to -2 between 0.25 and 1.5 % strain before increasing again to $\sim -1.5$ at 2.5 % strain and then stabilising. It should be noted that the $r^2$ values in Tables 9.6 and 9.7 should be treated with caution since they show the goodness of fit over only three data points.

Equipment availability and time restrictions prevented the undertaking of further multi-channel experiments at intermediate strain rates to confirm these trends. Nevertheless, it is interesting that the scaling seen in Figures 9.8 (a) and (b) extends across three orders magnitude.

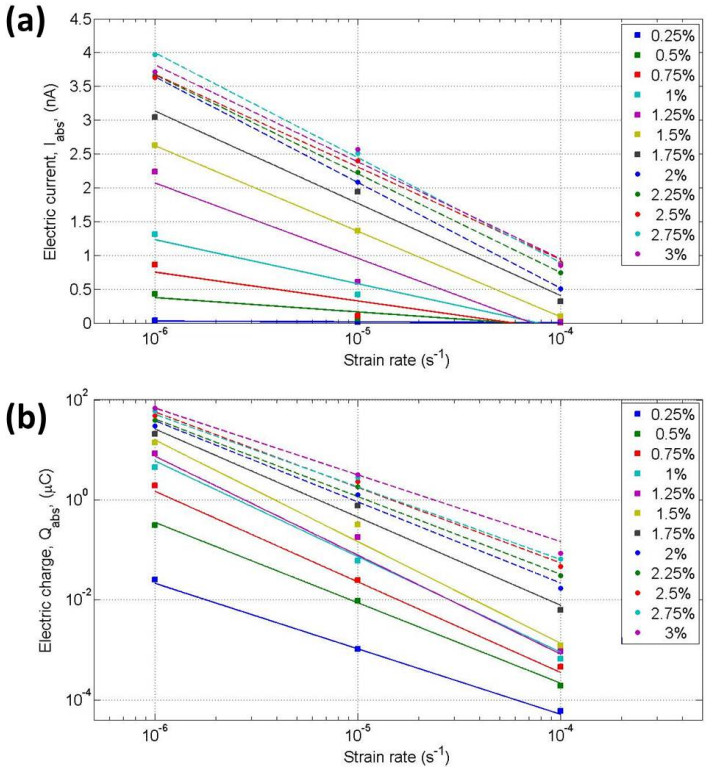


Figure 9.8: Absolute values of (a) electric current and (b) electric charge as a function of strain rate for each strain slice. The trend lines in (a) are logarithmic; see Table 9.6 for the parameters. The trend lines in (b) are power laws; see Table 9.7 for the parameters.

Table 9.6: Parameters for scaling of absolute electric current, $I_{abs}$ (nA) with strain rate, $\dot{\varepsilon}$ ($s^{-1}$) shown in Figure 9.8 (a), according to: $I_{abs} = A \ln \dot{\varepsilon} + B$. The fit was calculated by least squares.

| $\varepsilon_s$ (%) | A | B | $r^2$ |
|---|---|---|---|
| 0.25 | -0.005 | -0.04 | 0.671 |
| 0.50 | -0.092 | -0.90 | 0.813 |
| 0.75 | -0.185 | -1.80 | 0.839 |
| 1.00 | -0.283 | -2.68 | 0.955 |
| 1.25 | -0.484 | -4.62 | 0.933 |
| 1.50 | -0.550 | -4.98 | 1.000 |
| 1.75 | -0.593 | -5.06 | 0.988 |
| 2.00 | -0.679 | -5.74 | 1.000 |
| 2.25 | -0.635 | -5.10 | 1.000 |
| 2.50 | -0.595 | -4.54 | 0.997 |
| 2.75 | -0.674 | -5.31 | 0.999 |
| 3.00 | -0.623 | -4.79 | 0.987 |

Table 9.7: Parameters for scaling of absolute electric charge, $Q_{abs}$ ($\mu$C), with strain rate, $\dot{\varepsilon}$ ($s^{-1}$) shown in Figure 9.8 (b), according to: $Q_{abs} = A\dot{\varepsilon}^n$. The fit was calculated by least squares.

| $\varepsilon_s$ (%) | A | n | $r^2$ |
|---|---|---|---|
| 0.25 | 3.34E-10 | -1.31 | 0.999 |
| 0.50 | 7.57E-11 | -1.61 | 0.999 |
| 0.75 | 2.45E-11 | -1.81 | 0.999 |
| 1.00 | 1.54E-11 | -1.91 | 1.000 |
| 1.25 | 1.43E-11 | -1.98 | 0.992 |
| 1.50 | 1.21E-11 | -2.03 | 0.988 |
| 1.75 | 7.22E-10 | -1.76 | 0.989 |
| 2.00 | 6.61E-09 | -1.62 | 0.992 |
| 2.25 | 2.24E-08 | -1.55 | 0.994 |
| 2.50 | 4.94E-08 | -1.51 | 0.995 |
| 2.75 | 9.44E-08 | -1.47 | 0.997 |
| 3.00 | 1.46E-07 | -1.45 | 0.998 |

### 9.3.3 Rate of current production

Figure 9.9 shows electric current for the three multi-channel experiments as a function of time. A log time scale is used in order to show the three different strain rate experiments on the same axis. This illustrates the differences in electrical behaviour with strain rate; fast strain rates yield a dynamic pulse of electric current with very little fluctuation (Figures 9.9 (a) and (b)) in comparison to the more fluctuating electric current with intermittent pulses observed at the slowest strain rate (Figure 9.9 (c)). At the faster strain rates of $10^{-4}$ and $10^{-5}$ $s^{-1}$, current flow increases rapidly after the point of peak stress, with a maximum absolute value at or shortly before the point of failure.

Figure 9.10 shows the absolute rate of electric current flow, $|dI/dt|$, as a function of strain rate during the main deflection of current after the initial yield for the experiments shown in Figure 9.6. This deflection occurs between 0.9 and 2 % strain for $10^{-6}$ $s^{-1}$ strain rate, between 0.75 and 1.75 % strain for $10^{-5}$ $s^{-1}$ and between 1.5 and 2.5 % strain for $10^{-4}$ $s^{-1}$. As with the single-channel experiments, the average rate of current production within the sample is faster at the faster strain rates, i.e., when brittle behaviour dominates. The rate of current production slows right down once the strain rate is slow enough for cataclastic flow to dominate. This scaling can be approximated by a power law with exponent $n = 0.57$, a little larger than that for the single-channel experiments ($n = 0.45$). The measurement error on $|dI/dt|$ is $\pm 0.01$ fA $s^{-1}$ and therefore much smaller than the plotted data points. Instead, the error bars indicate the variability in $|dI/dt|$ between the four channels. Individual values of $|dI/dt|$ for each channel are also shown (open circles) but, since $|dI/dt|$ varies with the current flow path through the sample and shows some dependence on the angle between the failure plane and the current flow path (see Section 7.4), it is difficult to interpret the observed variation of $|dI/dt|$ with strain rate for the individual channels.

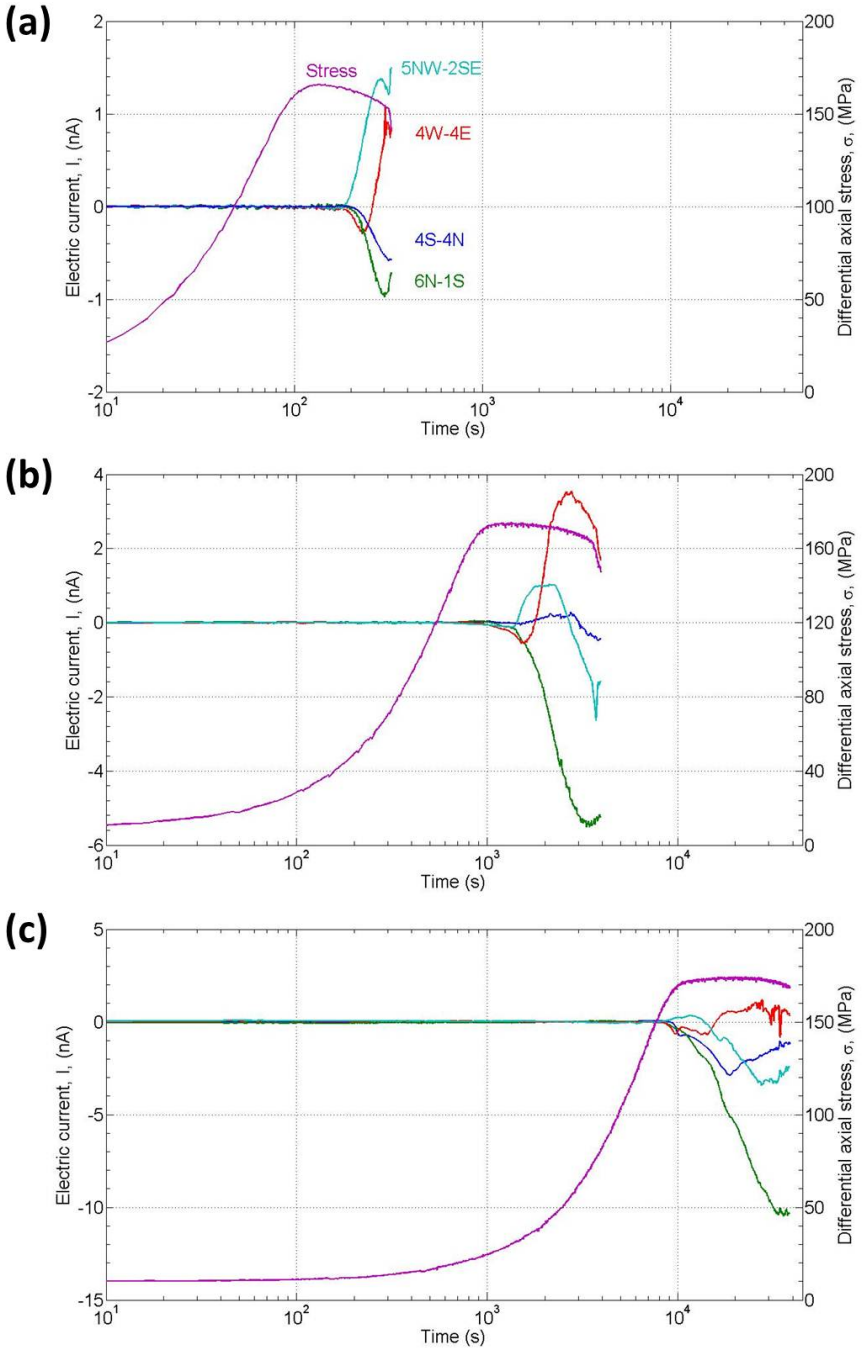


Figure 9.9: Electric current signals, as a function of time, produced during triaxial deformation of Carrara marble specimens at 30 MPa $P_c$ and three different strain rates: (a) $10^{-4}$ s$^{-1}$ [Experiment CM03], (b) $10^{-5}$ s$^{-1}$ [Experiment CM06] and (c) $10^{-6}$ s$^{-1}$ [Experiment CM07]. Time is on a logarithmic scale to show the signals from all three strain rates on the same scale. Current flow between each of the four electrode pairs is shown, each labelled with the electrode pair position according to the convention described in Section 5.2.4 and shown in Figure 5.6. A running median filter was applied to the electric current data in (b) and (c) to show the overall shape of the signal.

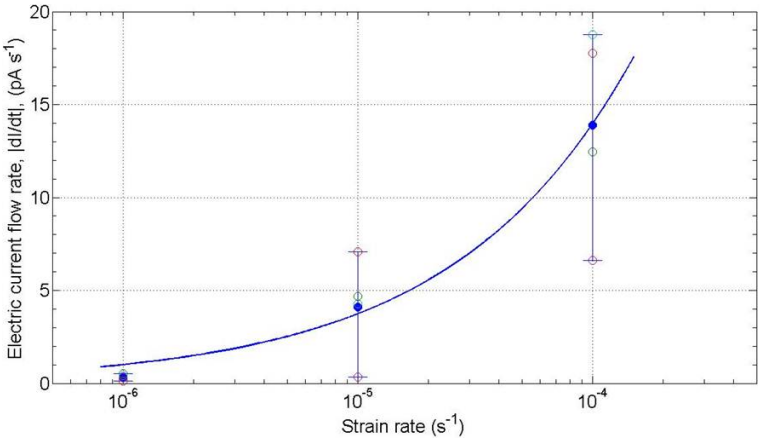


Figure 9.10: Absolute rate of electric current flow, $|dI/dt|$, as a function of strain rate for the multi-channel experiments shown in Figure 9.6. Solid blue circles show the average $|dI/dt|$ over the four recorded channels and the error bars show the full range of these values. Individual values for each channel are also plotted as open circles (green: 6N-1S, red: 4W-4E, cyan: 5NW-2SE, magenta: 4S-4N). The trend line is a power law calculated by least squares: $|dI/dt| = 2695\dot{\varepsilon}^{0.572}$ with $r^2 = 0.988$.

## 9.4 Damage Evolution

Figure 9.11 (a) shows how the $V_P$ variation, averaged over several useable orientations, evolves with time for the three multi-channel experiments discussed in Section 9.3. The evolution of velocity variation for the useable orientations, and their associated mean values, are given in Appendix F. There is very little difference ($< 5\%$) in $V_P$ reduction between the three strain rates, implying that strain rate has much less influence on the amount of crack damage the sample sustains than confining pressure, and in all three cases $V_P$ decreases rapidly at first before levelling off. There is no clear variation in $V_P$ reduction with strain rate before 1.5% strain. However, beyond this, the reduction in $V_P$ increases with increasing strain rate. Although this increase is very slight, it is pretty much constant at each point of strain and is best modelled as a logarithmic function of the form $\frac{\Delta V_P}{V_{Pmax}} = 0.01 \ln \varepsilon_s + 0.4$ with $r^2 = 0.9614$, where $\Delta V_P = V_P - V_{Pmax}$. This is similar to the logarithmic variation of electric current with strain rate presented in Chapter 9.

Average $V_P$ variation with respect to the damage parameter for the three strain rates is shown in Figure 9.11 (b). This shows a slight acceleration in $\Delta V_P$ as mechanical damage increases, with the greatest contribution from crack damage at the fastest strain rate. The very small variation in the degree of crack damage across three orders of magnitude of strain rate indicates that crack damage alone is not responsible for the differences in electric current evolution at these conditions. It is inferred, therefore, that time is the influencing factor.

Figure 9.12 presents the evolution of electric current with respect to $D$ during both the multi-channel experiments (a) and the single channel experiments (b). Comparing these to the evolution of average $V_P$ (Figure 9.11 (b)), it is apparent that, during the single channel experiments (Figure 9.12 (b)), electric current across the sample begins to flow

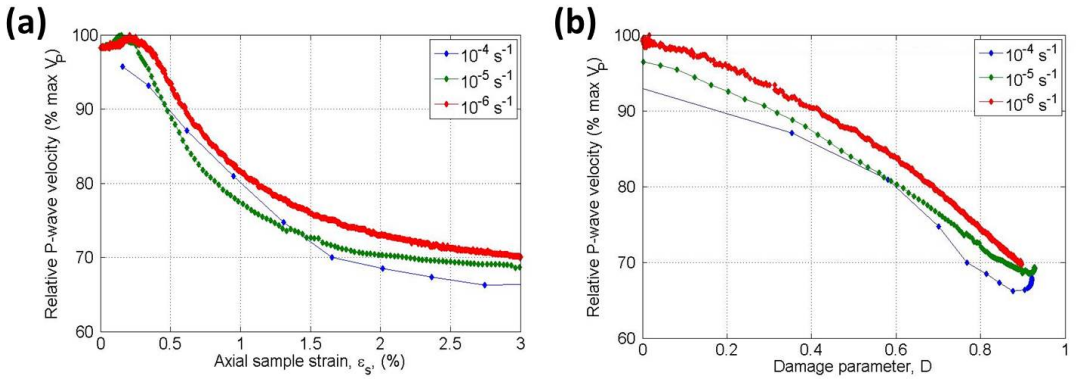


Figure 9.11: Average $V_P$ variation throughout the sample as a function of (a) axial sample strain and (b) damage parameter.

after a 50% increase in $D$ at all five strain rates. This corresponds to a 12-17% reduction in $V_P$, consistent with the findings regarding the influence of confining pressure (Section 8.5), although it is not clear whether the overall mechanical damage or purely the crack damage is the determining factor. However, during the multi-channel experiments (Figure 9.12 (a)), it can be seen that the level of mechanical damage at the onset of average electric current flow within these samples increases with strain rate. This onset, after a 20% increase in $D$ at $10^{-6}$ s$^{-1}$, a 30% increase in $D$ at $10^{-5}$ s$^{-1}$ and a 70% increase at $10^{-4}$ s$^{-1}$, corresponds to a reduction in $V_P$ of 4% at $10^{-6}$ s$^{-1}$, 12% at $10^{-5}$ s$^{-1}$ and 25% at $10^{-4}$ s$^{-1}$. This indicates that there may be a smaller contribution of brittle processes to average current flow within the samples at slower strain rates than at faster strain rates and that other deformation mechanisms play an increasing role in current generation as the strain rate decreases. The onset of current flow at $10^{-4}$ s$^{-1}$ also corresponds to a rapid acceleration in crack damage compared with the overall mechanical damage, suggesting that, in this sample [CM03], current flows in response to cracks coalescing along the final failure plane.

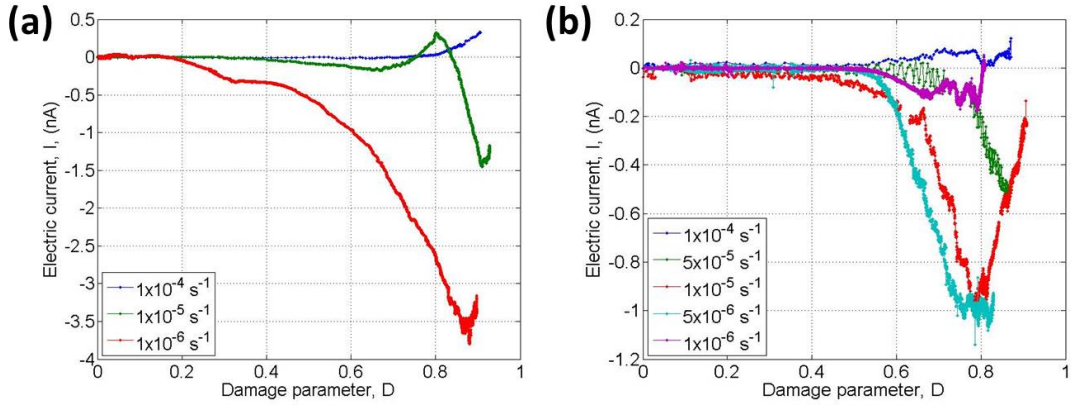


Figure 9.12: Evolution of electric current flow as a function of the damage parameter, $D$, for (a) the multi-channel experiments showing average electric current evolution within the sample at 30 MPa and three different strain rates and (b) the single channel experiments showing electric current evolution between electrodes 3S and 3N at 30 MPa and five different strain rates.

## 9.5 Relationship with Stress

### 9.5.1 Single channel experiments

Onset stress for electric current flow across the central part of the sample (3S-3N) during the single channel experiments does not vary significantly with strain rate (Figure 9.13 and Table 9.8). It varies between 160-175 MPa, which is within the natural variability for mechanical behaviour of these Carrara marble samples (Figure 7.3). The normalised onset stress appears to decrease marginally as the strain rate decreases, however it remains within 5% of $\sigma_{max}$ across all five strain rates. Conversely, the absolute rate at which electric current varies with stress increases to a maximum at 5x10$^{-6}$ s$^{-1}$ before decreasing again at the slowest strain rate. Absolute rates for the three intermediate strain rates are an order of magnitude larger than those for the fastest and slowest strain rates. Negative values for $dI_{abs}/d\sigma$ at the three fastest strain rates show that electric current flowed mainly during the strain softening (brittle deformation) region beyond $\sigma_{max}$, which was not reached at the two slowest strain rates.

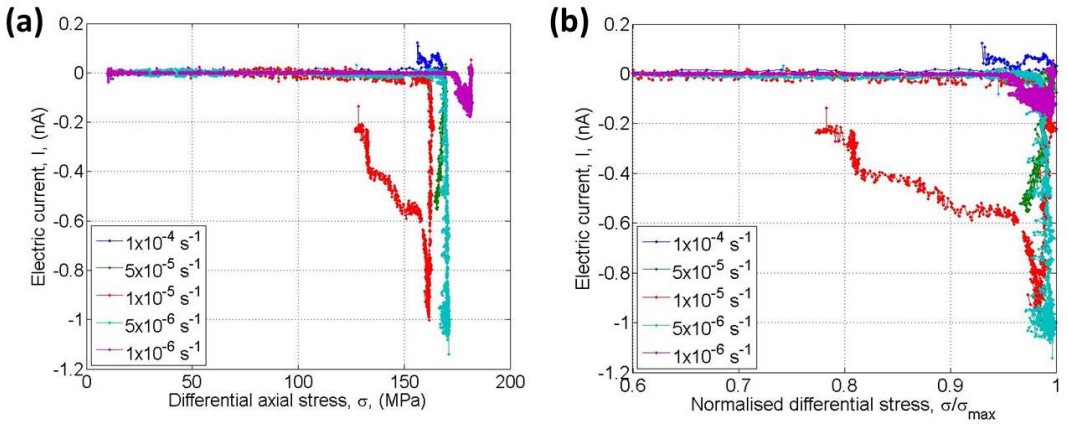


Figure 9.13: Evolution of electric current across the central part of the sample (3S-3N) as a function of (a) differential stress, $\sigma$, and (b) normalised stress, $\sigma/\sigma_{max}$ at 30 MPa and the five different strain rate conditions used for the single channel experiments.

Table 9.8: Values of electric current onset stress, $\sigma_{ec}$, normalised onset stress, $\sigma_{ec}/\sigma_{max}$, and rate of change with differential stress of electric current across the central part of the sample (3S-3N), $dI_{abs}/d\sigma$, for each of the five strain rates tested during the single channel experiments.

| $\dot{\varepsilon}$ s$^{-1}$ | $\sigma_{ec}$ (MPa) | $\sigma_{ec}/\sigma_{max}$ | $dI_{abs}/d\sigma$ (nA/MPa) |
|---|---|---|---|
| 1x10$^{-4}$ | 167 | 1.00 | -0.0313 |
| 5x10$^{-5}$ | 167 | 1.00 | -0.1032 |
| 1x10$^{-5}$ | 161 | 0.98 | -0.2503 |
| 5x10$^{-6}$ | 168 | 0.98 | 0.4931 |
| 1x10$^{-6}$ | 172 | 0.95 | 0.0236 |

### 9.5.2 Multi-channel experiments

Behaviour with stress of the average electric current generated within samples during the multi-channel experiments (Figure 9.14 and Table 9.9) is similar to that for electric

current flow across the samples (3S-3N) during the single channel experiments. Variation in the onset stress is within the natural sample variability and the normalised onset stress remains within 10% of $\sigma_{max}$, although it is smaller at the slowest strain rate than the two faster strain rates. Also, the absolute rate ($|dI_{abs}/d\sigma|$) at which the average current varies with stress increases by one order of magnitude from the fastest to the intermediate strain rate. However, $|dI_{abs}/d\sigma|$ differs from the single-channel experiments in that it increases by almost a further order of magnitude at the slowest strain rate rather than decreasing again. This may be due to the greater amount of deformation that this sample [CM07] was subjected to compared with the equivalent single-channel experiment [CM05] (3% strain compared with 1.7% strain), allowing more current to be generated per unit stress as the sample supported peak stress for twice as long. Again, negative $dI_{abs}/d\sigma$ values seen at the two faster strain rates show that the majority of electric current was generated during the strain softening stage for these two experiments.

Thus, both sets of experiments suggest that, regardless of the strain rate, these Carrara marble samples must be subjected to a critical amount of stress before electric current will flow, which, at 30 MPa $P_c$, is $166 \pm 4$ MPa and is within 10% of the maximum compressive strength of the samples. As the samples approach the semi-brittle regime (at strain rates $\geq 5\text{x}10^{-6}$ s$^{-1}$), this critical stress becomes a smaller proportion of the compressive strength of the sample but remains >90%. Across both sets of experiments, the absolute rate of change of electric current with stress ($|dI_{abs}/d\sigma|$) shows an overall increase as the strain rate decreases and ductile deformation dominates.

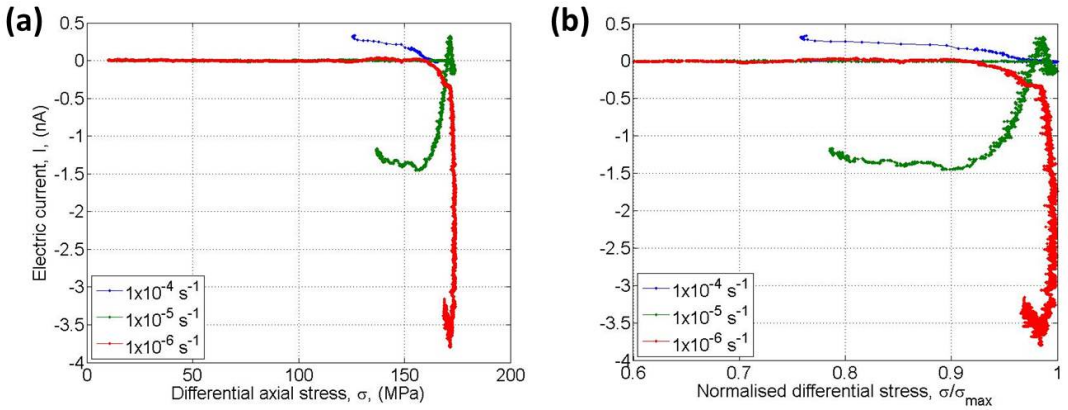


Figure 9.14: Evolution of average electric current generated within the sample as a function of (a) differential stress, $\sigma$, and (b) normalised stress, $\sigma/\sigma_{max}$ at 30 MPa and the three different strain rate conditions used for the multi-channel experiments.

Table 9.9: Values of electric current onset stress, $\sigma_{ec}$, normalised onset stress, $\sigma_{ec}/\sigma_{max}$, and rate of change with differential stress of average electric current generated within the sample, $dI_{abs}/d\sigma$, for each of the three strain rates tested during the multi-channel experiments.

| $\dot{\varepsilon}$ **s**$^{-1}$ | $\sigma_{ec}$ **(MPa)** | $\sigma_{ec}/\sigma_{max}$ | $dI_{abs}/d\sigma$ **(nA/MPa)** |
|---|---|---|---|
| 1x10$^{-4}$ | 165 | 0.99 | -0.0163 |
| 1x10$^{-5}$ | 170 | 0.99 | -0.1642 |
| 1x10$^{-6}$ | 160 | 0.92 | 0.8320 |

## 9.6 Summary and Deductions

In this chapter, I have presented the electric current signals generated during triaxial deformation of non-piezoelectric Carrara marble at a range of strain rates and 30 MPa. The overall relationship between electric current across the central part of the sample (3S-3N) and deformation changes with strain rate (Figure 9.3 (a)), with the slowest strain rate exhibiting an initial exponential increase of the current. Intermediate strain rates show an initial exponential increase followed by a linear increase, before flattening off at higher strains. The fastest two strain rates show a linear increase, with the onset of current occurring at a larger strain than for strain rates $\leq 10^{-5}$ $s^{-1}$. Averaging the signals across several recorded channels appears to have a stacking effect, changing the observed relationship to one consistent across the range of strain rates, where current increases linearly with deformation and the gradient shows a sharp reduction at higher strains (Figure 9.7 (a)). Charge accumulates exponentially with deformation at first and then linearly, regardless of whether it is measured between one pair of electrodes or averaged over several channels (Figures 9.3 (b) and 9.7 (b)). This charge accumulation shows an overall increase with decreasing strain rate as deformation transitions from brittle to semi-brittle, apparent in both the single channel and multi-channel tests for strain rates of $10^{-4}$, $10^{-5}$ and $10^{-6}$ $s^{-1}$. When intermediate strain rates (5x$10^{-5}$ and 5x$10^{-6}$ $s^{-1}$) are included, differences in charge accumulation indicate three separate regimes (Figure 9.3 (b)). Deformation style of the samples suggest that these three regimes correspond to brittle behaviour (localised fault plane), the transition between brittle and semi-brittle behaviour (some localisation but prospective fault plane incomplete and not sharply defined), and semi-brittle behaviour (distributed conjugate shear microfractures, no localisation).

Accumulated charge for a particular strain decreases as a power-law with increasing strain rate, while current flow shows a logarithmic decrease (Figure 9.8). This relationship reverses for the main rate of current production, which shows a power-law increase with increasing strain rate (Figure 9.10). These power-law relationships are reminiscent of the rate equations for power-law creep (Hunt, 2009), lending further weight to the notion that the electric signals are related to stress, as discussed in Section 8.7. With only a 5% difference in the degree of crack damage, as represented by the reduction in $V_P$ (Figure 9.11), across the whole range of strain rates, the time over which this damage occurs must be the controlling factor and these variations must be due to time-dependent differences in the deformation process. At slower strain rates, the increased time required to reach a particular strain means that (a) the sample is under a particular stress for much longer and (b) the internal stresses do not change as much or as rapidly and, as such, do not concentrate in any particular region. Thus, these smaller local variations in the internal stresses will be distributed throughout the sample and will be accommodated by local cracking and sliding events equally as distributed, with groups of cracks in closer proximity to each other leading to an enhanced degree of interactions between cracks at slower strain rates (Nemat-Nasser and Deng, 1994). Since there is more time available

between each increment of strain as the strain rate decreases, the localised avalanches of deformation, which occur in response to each stress fluctuation induced by the increasing strain, have time to subside, allowing the local stresses time to re-equilibrate before the next fluctuation. Also, since the overall work done on the sample is approximately the same across the whole range of strain rates, less energy is available for deformation over a longer time period as the strain rate decreases. This means that the same amount of deformation (and dilatancy) would manifest as smaller, more numerous microcracks and frictional sliding events in samples deformed at slower strain rates, leading to a slow build up of charge over time, compared with relatively few but larger events occurring rapidly in samples deformed faster, which would generate current abruptly but briefly until sample failure precludes the accumulation of further charge. Thus, the increased rate of electric current production at faster strain rates corresponds to the increased rate at which the sample sustains crack damage, while the reduction in current and charge magnitude corresponds to the decreased time available for charges to accumulate in the disordered layers between crack surfaces. Differences in electric current with strain rate therefore reflect the transition from localised brittle fracture to distributed cataclastic flow in terms of the change in crack network geometry, as discussed in Section 7.7, rather than an increased contribution from plastic deformation. This is illustrated by the non-linear relationship between electric current and strain rate. According to the MCD model, which relates the observed transient electric variation to the accumulation of deformation by the motion of charged edge dislocations (MCD), current-generation under MCD is expected to be proportional to strain rate (Section 3.5.1.2). Therefore, the non-linear relationship between strain rate and current flow implies that other solid-state mechanisms control current flow and charge accumulation under the conditions tested.

Post-yield, electric current flow is almost independent of differential stress but occurs at an apparently critical value (160-170 MPa and within 90% of the peak stress) at all strain rates (Figures 9.13 and 9.14), which corresponds to a $\geq$10% reduction in $V_P$ (Figure 9.11). The majority of current flow during deformation at faster strain rates occurs during the strain softening region and remains proportional to stress while the stress remains within 10% of its peak value, beyond which it varies non-linearly with a decrease in current with respect to the change in stress. At slower strain rates ($\leq 10^{-5}$ s$^{-1}$) the majority of current flows during stable cataclastic flow while the stress remains within 2% of its peak value. This suggests that cooperative re-orientation of the charge dipoles accumulating at fresh and sliding crack surfaces may provide an additional contribution as the EDL between surfaces separates.

Under dynamic deformation conditions (fast strain rates $\geq 10^{-5}$ s$^{-1}$), the current exhibits a pulse-like character as it increases rapidly within the sample beyond peak stress during strain softening, reaching a maximum absolute value shortly prior to macroscopic failure of the sample before relaxing again as failure approaches (Figures 9.6 (a) and (b)). The maximum time lag between the peak value and failure is 30 s at the fastest strain rate and 22 minutes at $10^{-5}$ s$^{-1}$. This behaviour is characteristic of a 'standard' earth-

quake precursor signature (see Chapter 3) where the precursor changes some time before the earthquake and then recovers when the earthquake is imminent (Scholz et al., 1973; Main and Meredith, 1989; Sammonds, 2008). At slower rates of deformation ($<10^{-5}$ $s^{-1}$), electric current is emitted beyond the yield point and initially increases steadily before levelling off and exhibiting intermediate-frequency fluctuations and 'burst-type' emissions as deformation continues (Figures 9.2 (e) and 9.6 (c)). The latter behaviour is typical of geoelectric time series recorded in the field, which generally exhibit a series of anomalous signals rather than a single precursory pulse. The slow strain rate experiments presented here show that this type of behaviour most likely originates from a developed network of shear cracks undergoing episodes of sliding and fragmentation during cataclastic flow (i.e., when hardening mechanisms balance softening mechanisms), which steadily release charges as deformation continues. This leads the crack network to behave as an efficient electric emitter. However, these intermediate-frequency anomalies can mask the true precursory signal, with a high potential for false alarms. Crustal deformation at crustal strain rates is similar to cataclastic flow type behaviour; episodes (or avalanches) of sliding and fragmentation events on a well-developed network of faults. Thus, anomalies in the Earth's background telluric currents may be a feature of charge accumulation in disordered surface layers and separation of the resultant EDL created during the shearing of asperities on fault surfaces.

# Chapter 10

# Influence of Pore Fluid and Pore Fluid Salinity on Electric Signals

## 10.1 Introduction

As discussed in Section 2.2, water and aqueous solutions are ubiquitous in the upper crust. Crustal evolution is strongly affected by the actions of fluids; from mechanical effects and diagenesis to mineral and fluid phase reactions (Lebedev et al., 1996). It is therefore important to include fluids during experimental deformation studies in order to fully understand the mechanics of crustal deformation. Natural crustal fluids contain varying concentrations of salts and their salinity increases with depth. The presence of these fluids within the networks of connected pores and cracks serves to increase the bulk conductivity of the fluid-filled crustal rocks. Fluid salinity affects the conductivity. This, in turn, alters the coupling strength between the fluid and electric currents because fluid conductivity is a key parameter in the coupled equations for electrokinetic behaviour.

Due to the extremely low porosity of these Carrara marble specimens, the time required to develop the experimental procedure for the saturated experiments, prepare and characterise the samples and conduct the tests (see Chapters 5 and 6) precluded a detailed investigation of streaming current changes during deformation and the influence of varying fluid conductivity on electric current signals. Also, analysis of the six experiments conducted to investigate the effect that cyclic loading of the samples might have on the electric current signals was not possible in the available time. Instead, two 'wet' experiments are presented in this section that show the influence of two different pore fluids; deionised water [Experiment CM51] and an ionic brine solution [Experiment CM42], on the electric current signals generated during deformation at an effective confining pressure of 30 MPa ($P_c$ = 50 MPa and $P_p$ = 20 MPa) and $10^{-6}$ $s^{-1}$ strain rate. The other four experiments conducted at these conditions (two with each type of pore fluid) did not yield useable results due to the electrical shorting problem discussed in Section 8.1 [Experiment CM61]

and issues regarding the LVDT connections [Experiments CM44, CM46 and CM48].

The ionic brine solution was made up using Instant Ocean synthetic sea salt mix. This was chosen because it is very close in composition to both natural sea water and typical crustal brine (Table 10.1). Electrical conductivity of the two pore fluids varies by six orders of magnitude; that of sea water at room temperature is typically 5 $Sm^{-1}$ (Kaye and Laby Online, 2005), while that of deionised water is $\sim$10 $\mu Sm^{-1}$ (Heyda, 2006).

Table 10.1: Composition of Instant Ocean synthetic sea salt mix compared with that for natural sea water and typical crustal brine as sampled from four ODP drill sites along the Juan de Fuca Ridge.

| | **Instant Ocean*** | **Sea Water*** | **Crustal Brine**** |
|---|---|---|---|
| **Salinity (ppt)** | 29.65 | 35 | 34.16 |
| **pH** | 8.35 | 8.25 | 7.51 |
| **Cations (ppm)** | | | |
| $Na^+$ | 10626 | 10810 | 10695 |
| $K^+$ | 367.54 | 398.82 | 261.97 |
| $Mg^{2+}$ | 1263.6 | 1287.9 | 36.936 |
| $Ca^{2+}$ | 376.94 | 413.03 | 2245.6 |
| $Sr^{2+}$ | 16.644 | 7.884 | 9.9864 |
| **Anions (ppm)** | | | |
| $Cl^-$ | 18495.5 | 19525 | 19702.5 |
| $SO_4^{2-}$ | 738.3 | 898.8 | 545.7 |
| **Other (ppm)** | | | |
| $CO_2$ | 22.8 | 22.8 | |
| B | 4.752 | 4.536 | 5.994 |
| **Trace (ppb)** | | | |
| Li | 372.6 | 138 | 85.56 |
| Si | 449.6 | 140.5 | |

*Atkinson and Bingman, 1996 **Wheat et al., 2000

## 10.2 Electric Current Signals

Figure 10.1 shows the electric current flow between electrodes 3S and 3N (shown in blue) for dry conditions (a) and saturated conditions with (b) deionised water and (c) Instant Ocean brine solution. Current flow was also recorded between electrodes 4S and 4N during the wet experiments (shown in red). The first points to note are that the electrical signal is an order of magnitude larger during the brine-saturated test than during the dry and water-saturated tests and that current flow between electrodes 4S and 4N exhibits small-scale fluctuations an order of magnitude larger than between electrodes 3S and 3N. Also, electric current flow takes approximately the same polarity between each electrode pair during the water-saturated test but exhibits opposite polarity between each electrode pair during the brine-saturated experiment. In addition, electric current begins to flow from the very start of the experiment during both the water- and brine-saturated experiments, but not the dry one. This current is a convection current, known as the streaming current (Section 3.5.2.2), formed due to the electrokinetic effect as pore fluid is expelled from the sample during compaction. The steady state streaming current value for each wet experiment, measured immediately prior to loading, is given in Table 10.2. As with the deformation-induced electric signal, there is an order of magnitude difference between the

two. Compaction is represented by the decrease in measured pore fluid volume (shown in black) as the deviatoric stress closes cracks perpendicular to the loading direction.

During the water-saturated experiment, a decrease of 0.025 $cm^3$ in pore fluid volume is seen as compaction continues up to 0.15% strain. At this point fluid flow out of the sample stops as dilatancy due to cracks opening parallel to the loading direction balances the compaction and the sample is ready to yield. A small electric current flows between both pairs of channels, increasing up to approximately 0.01 nA at 0.075% strain as fluid is rapidly forced out of the sample and then decreasing back to zero as the flow out slows to a halt. Electric current production between both pairs of electrodes then continues in the opposite direction as fluid flows into the sample and the current generated due to solid-state deformation mechanisms combines with convection current, contributing to the overall electric current produced. It reaches a peak of ∼0.02 nA when the Young's modulus begins to rapidly decrease at about 0.4% strain, after which it decreases back to zero at 0.8% strain (3S-3N) and at 0.7% strain (4S-4N). Current flow between electrodes 3S and 3N then increases steadily in the negative direction, before levelling off to -0.08 nA at 2.7% strain and decreasing slightly beyond that point. Conversely, electric current between electrodes 4S and 4N repeats the previous oscillation, increasing in the positive direction back to ∼0.02 nA at 1.2% strain before decreasing back to zero and increasing in the negative direction from 1.3% strain to $\sim -0.18$ nA at 2.7% strain before decreasing back to the same level as that between electrodes 3S and 3N and levelling off. This post-yield behaviour of electric current is similar in form to that seen during the dry experiments under the same effective pressure and strain rate conditions (Figures 7.6 and 10.1 (a)), with a period of steady current production which then levels off, fluctuating around a relatively constant value.

During the brine-saturated experiment, a decrease of 0.014 $cm^3$ in pore fluid volume is seen as compaction continues up to 0.1% strain. The maximum electric current associated with compactive fluid flow out of this sample is ∼0.1 nA between both pairs of electrodes, although the electric current flows in opposite directions between each electrode pair. Beyond 0.1% strain, electric current flow between electrodes 4S and 4N is nearly twice that between electrodes 3S and 3N. This difference may be due to more fluid pathways existing between electrodes 4S and 4N than electrodes 3S and 3N. Current flow between electrodes 4S and 4N exhibits a similar form to that seen in the water-saturated and dry experiments, increasing rapidly and steadily in the negative direction to $\sim -3$ nA before levelling off at about 1% strain and fluctuating between -2 and -4 nA until the end of the test. In contrast, current flow between electrodes 3S and 3N increases steadily in the positive direction throughout the experiment, rapidly at first to 0.46 nA at 0.4% strain and then more slowly to a maximum of 1.26 nA at the end of the test.

Nearly twice as much pore fluid was forced out of the water-saturated sample during compaction as out of the brine-saturated sample. Given the greater initial porosity of the brine-saturated sample, the reason for this is unclear. Axially loading the dry samples to

induce fracture mechanically would have closed most pre-existing cracks oriented perpendicular to the loading axis in both samples, accounting for the very small volume of pore fluid expelled in both cases. This closure reduced the porosity of the thermally-cracked brine-saturated sample from more than three times that of the water-saturated sample before the mechanical fracturing procedure to only 1.3 times afterwards. However, this small amount of additional crack damage may have caused dilatant fractures to nucleate at slightly lower stresses in the brine-saturated sample than in the water-saturated sample, causing less fluid to be expelled during compaction before it was balanced by fluid flow into the sample due to dilatancy. During dilatancy, the opposite was true; total pore volume increase in the brine-saturated sample was twice that seen in the water-saturated sample. The ratio of pore volume increase during dilatancy to pore volume decrease during compaction was four times greater for the brine-saturated sample than for the water-saturated sample. A small contribution of dissolution effects to the dilatant volume in the brine-saturated sample cannot be discounted since, although the solubility constants for calcite in both pure water and sea water are very low, almost to the point of insolubility, calcite is still an order of magnitude more soluble in sea water than in pure water. At standard temperature and pressure, the solubility constant for calcite in seawater is of the order of $10^{-7}$ (Morse et al., 1980) compared with $< 10^{-8}$ in pure water (Thorpe, 2008).

Beyond the yield point, the total stress supported by the saturated samples is 25-50 MPa higher than that supported by the dry sample (Figure 10.1 (a)). This hardening effect may imply that the procedures carried out in Chapter 6 did not increase the permeability of either sample sufficiently to maintain a constant pore fluid pressure during deformation, or that some healing of the mechanically-induced fractures may have occurred during the dry unloading and saturating stages of the experimental procedure (which took more than 24 hours), causing a reduction in permeability. Consequently, the pore fluid pressure inside the samples may not have reached the required 20 MPa, so the overall effective pressure during the experiment was greater than 30 MPa. However, since the monitored pore pressure remained constant at 20 MPa and the pore fluid volume increased steadily throughout both experiments, indicating that the fluid was flowing freely into the samples as the dilatant volume within them increased, this was deemed to be an unlikely scenario. More likely is the other possible explanation; that the samples were strengthened by activation of ductile hardening mechanisms (twinning and dislocation migration, pile-up and entanglement) during both the heat treatment and the dry mechanical fracturing. Also, although cataclastic flow is a fundamentally dilatant process that serves to increase the porosity and permeability in rocks by introducing cracks, it can also reduce the porosity and permeability of a rock by (a) grain-size reduction associated with microfracturing and frictional sliding (i.e., the introduction of fault gouge on a microscopic scale), (b) partial crack closure due to twinning and dislocation entanglement, and (c) crack healing (Kennedy and White, 2001; Zhang et al., 2001; Zhu, 2006). This is evident from the steady rate at which pore fluid flows into both the saturated samples (Figures 10.1 (b) and (c)), combined with the relatively constant stress seen between 1 and 3 % strain, indicating that

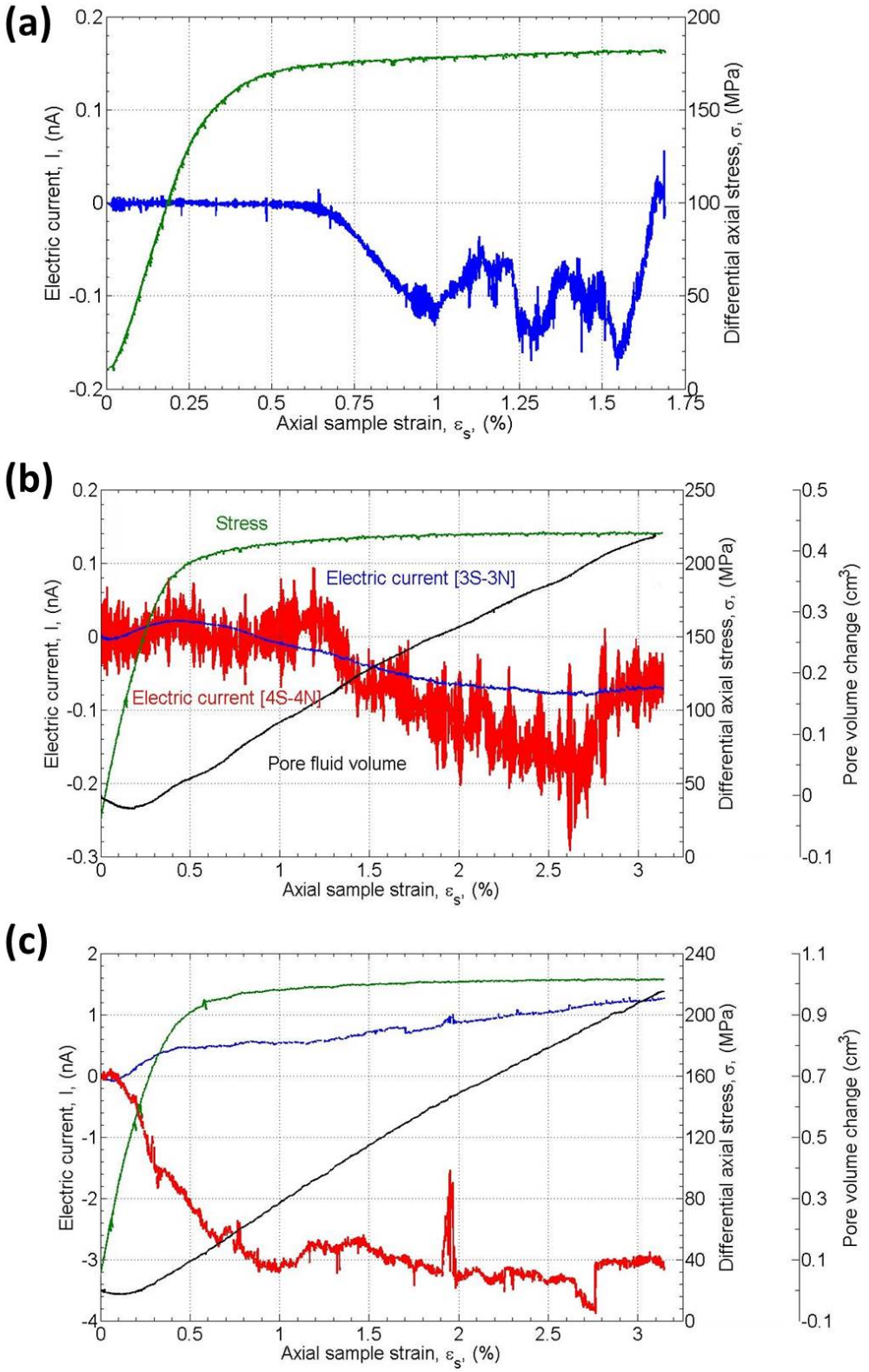


Figure 10.1: Differential stress (green), pore fluid volume (black) and electric current flow between electrodes 3S-3N (blue) and 4S-4N (red) as a function of axial sample strain, produced during triaxial deformation of Carrara marble specimens at $10^{-6}$ s$^{-1}$, 30 MPa and three different pore fluid conditions; (a) no pore fluid [Experiment CM05], (b) de-ionised water [Experiment CM51] and (c) Instant Ocean brine solution [Experiment CM42].

porosity reduction mechanisms serve to limit the acceleration of dilatancy as deformation continues, and hardening mechanisms balance softening mechanisms throughout this region of deformation. Total pore volume increase due to dilatancy in the water-saturated sample was 0.43 $cm^3$ and in the brine-saturated sample was 0.94 $cm^3$.

Initial electrokinetic properties (Table 10.2) were determined from the permeability and streaming current measurements conducted on the mechanically fractured samples after saturation and prior to loading . The hydraulic radius, $r$, (Equation 3.14), was estimated from the channel aperture, $x = 2r$, and the measured values of porosity, $\varphi$, and permeability, $k$, using the approximation of Fischer and Paterson (1992):

$$x \approx 3.5\frac{\sqrt{k}}{\varphi} \tag{10.1}$$

which assumes a theoretical tortuosity, T, where $T^2 = \varphi^{1-m}$, $m = 2$ and $b = 3$ (i.e., capillaries with a slot-shaped cross-section; microcrack geometry). The experimental tortuosity, T, for this fluid flow channel of hydraulic radius, $r$, was calculated from the measured porosity, $\varphi$, and permeability, $k$, using Equation 3.14. The zeta potential was then calculated from Equation 3.15 and the bulk conductivity, $\kappa_b$, was determined from Archie's law: $\log \kappa_b = \log \kappa_f + m \log \varphi$, where $\kappa_f$ is the fluid conductivity. This then allowed the streaming potential coefficient, $C_p$, and the formation factor, $F_1$, to be calculated and, ultimately, the initial surface conductivity, $\kappa_s$ of the fluid flow path immediately prior to deformation under drained conditions. No measurements of permeability and streaming current were made at the end of either of these tests because they were the first two 'wet' experiments carried out and the experimental procedure was still being developed.

Table 10.2: Initial electrokinetic properties of the mechanically fractured and fully saturated samples from measurements of streaming current and permeability made immediately prior to conducting the drained experiments.

| **Property** | **CM42 (IO brine)** | **CM51 (Deionised water)** |
|---|---|---|
| Fluid viscosity, $\eta$ (Pa s) | 1.00E-03 | 1.00E-03 |
| Fluid dielectric constant, $\epsilon_f$ | 85.00 | 80.00 |
| Streaming current (A) | 1.63E-09 | 2.19E-10 |
| Electrode area ($m^2$) | 3.80E-04 | 3.80E-04 |
| Current density, $\mathbf{i}$ (A $m^{-2}$) | 4.30E-06 | 5.77E-07 |
| $\nabla P_p$ (Pa $m^{-1}$) | 1.00E+08 | 1.00E+08 |
| Streaming current coefficient, $C_c$ | -4.30E-14 | -5.77E-15 |
| Permeability, $k$ ($m^2$) | 3.46E-19 | 3.54E-20 |
| Fluid volume ($m^3$) | 9.25E-07 | 6.90E-07 |
| Sample volume ($m^3$) | 1.30E-04 | 1.30E-04 |
| Porosity, $\varphi$ (%) | 0.71 | 0.53 |
| Channel aperture, $x$ (m) | 2.90E-09 | 1.24E-09 |
| Hydraulic radius, $r$ (m) | 1.45E-09 | 6.21E-10 |
| Tortuosity, $T$ | 1.43 | 1.92 |
| Zeta potential, $\zeta$ (V) | -1.46E-18 | -5.03E-19 |
| Fluid conductivity, $\kappa_f$ (S/m) | 5 | 1.00E-05 |
| Bulk conductivity, $\kappa_b$ (S/m) | 2.53 | 2.82E-06 |
| Streaming potential coefficient $C_p$ | -1.70E-14 | -2.05E-09 |
| Formation factor $F_1$ | 1.98 | 3.55 |
| Formation factor $F_2$ | 0.35 | 0.14 |
| Surface conductivity, $\kappa_s$ (S/m) | 2.32 | 9.63E-06 |

Although both samples had been mechanically fractured, one sample had been thermally

cracked [CM42] and the other had not [CM51] and their permeabilities after the mechanical fracturing differed by one order of magnitude (Table 10.2). This difference in permeability may account for the order of magnitude difference in the measured streaming current and the calculated zeta potential between the two samples, indicating that the single order of magnitude difference in permeability between the two tests may have had a greater influence on the electrokinetic signal than did the six orders of magnitude difference in electrical conductivity between the two pore fluids.

Electric current flow remains smaller than the initial streaming current value throughout the water-saturated experiment and between electrodes 3S and 3N in the brine-saturated experiment. The initial streaming current values for both experiments were measured directly before the deformation experiment and are presented in Table 10.2. However, between 4S and 4N, current flow reaches twice that of the initial streaming current. In this case, current production is very rapid up to the end of the initial yield and then levels off during stable cataclastic flow, whereas between 3S and 3N current flow slows down earlier; at the point where the effective Young's modulus decreases most rapidly, before continuing to increase at a slower rate for the rest of the experiment and not quite reaching the initial streaming current value. Variations in electric current signal between the two channels points to differences in the localisation of fluid flow between the two channels, likely related to differences in local crack propagation and permeability development.

## 10.3 Electric Current and Electric Charge Magnitude

In order to establish the influence of pore fluid condition on the electric current signals, absolute electric current, $I_{abs}$, and absolute electric charge, $Q_{abs}$, at every 0.25% strain were noted only between electrodes 3S and 3N since the dry experiment recorded this single channel. Their variation with strain are shown in Figure 10.2. The measurement errors for $I_{abs}$ and $Q_{abs}$ are $\pm$10 fA and $\pm$10 pC respectively and therefore much smaller than the plotted data points. In the presence of brine, $I_{abs}$ increases logarithmically from the start of the experiment (see Table 10.3 for parameters), levelling off at $\sim$0.5 nA between 0.75 and 1.25 % strain. It then continues to increase linearly with strain up to 1.2 nA at the end of the experiment. $Q_{abs}$, on the other hand, exhibits a linear increase with strain (see Table 10.4 for parameters), the gradient of which nearly doubles from 1.75% strain onwards. In the presence of water, $I_{abs}$ increases to 0.2 nA at 0.5% strain before decreasing back to zero at 1% strain. From 1% onwards, it increases logarithmically to the end of the test, levelling off at $\sim$0.07 nA between 2.5 and 3% strain. $Q_{abs}$ increases to 0.13 $\mu$C between 0.75 and 1% strain before decreasing back to zero at 1.5% strain. It then increases linearly from 1.5% onwards to a maximum of 1 $\mu$C at the end of the test. The dry experiment exhibits a logarithmic increase in $I_{abs}$ from 0.5 % strain onwards, levelling off to $\sim$0.12 nA between 1 and 1.5 % strain. $Q_{abs}$ increases exponentially to 0.01 $\mu$C between 0.25 and 0.75% strain and then rises linearly to a maximum of 0.75 $\mu$C at

1.5% strain. The scaling factor, $A$, for the logarithmic increase in $I_{abs}$ in the presence of deionised water is half that seen in both the dry and the brine-saturated tests (Table 10.3), while the proportionality constant for the linear increase in $Q_{abs}$ in the presence of Instant Ocean brine is an order of magnitude larger than that seen for the dry and water-saturated tests.

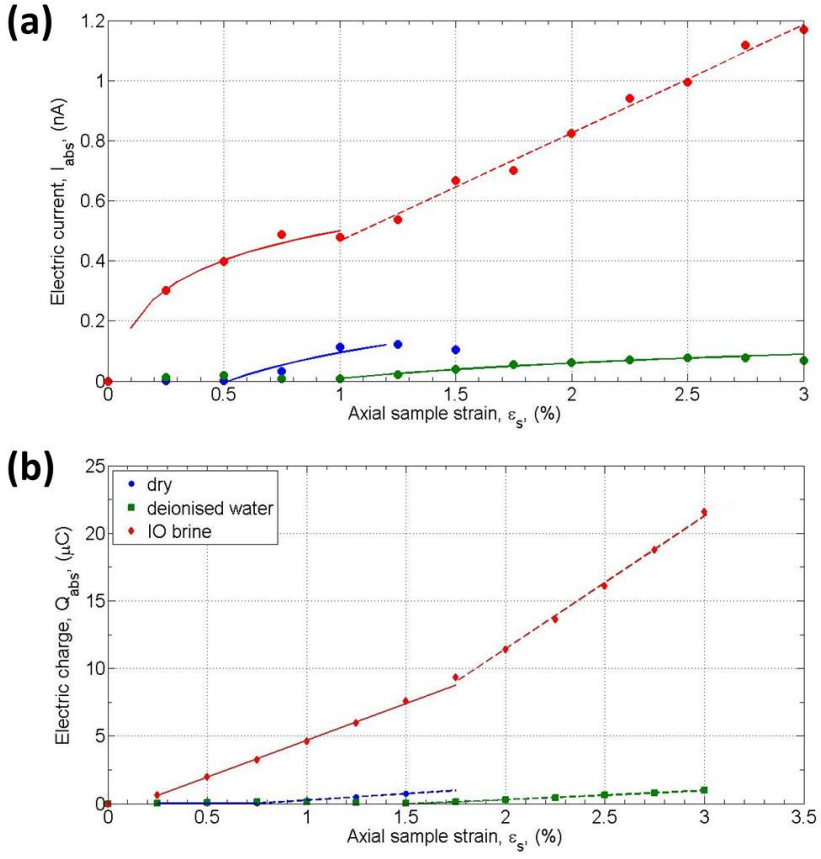


Figure 10.2: Absolute values of (a) electric current and (b) electric charge at specific strain slices as a function of axial sample strain for the experiments shown in Figure 10.1. The solid trend lines in (a) are logarithmic and the dashed trend line is linear (see Table 10.3 for the parameters). Dashed trend lines in (b) are linear, as is the solid red trend line, and the blue solid trend line is exponential (see Table 10.4 for the parameters).

Table 10.3: Parameters for scaling of absolute electric current, $I_{abs}$ (nA), with axial sample strain, $\varepsilon_s$ (%) (Figure 10.2 (a)). The fits were calculated by least squares.

| **Condition** | $I_{abs} = A \ln \varepsilon_s + B$ | | | $I_{abs} = A\varepsilon_s + B$ | | |
|---|---|---|---|---|---|---|
| | **A** | **B** | $\mathbf{r^2}$ | **A** | **B** | $\mathbf{r^2}$ |
| Dry | 0.144 | 0.0947 | 0.925 | - | - | - |
| Deionised water | 0.074 | 0.0086 | 0.978 | - | - | - |
| IO brine | 0.140 | 0.4993 | 0.9451 | 0.36 | 0.11 | 0.992 |

Figure 10.3 shows the variation of $I_{abs}$ and $Q_{abs}$ with respect to pore fluid condition. During compaction (prior to 0.5% strain), the electrokinetic current and charge observed in the presence of brine is $10 - 20$ times larger than that seen in the presence of deionised water. This ratio also holds for the combined electrokinetic and deformation-induced electric current and charge in the dilatant region (beyond 0.5% strain), during which the

Table 10.4: Parameters for scaling of absolute electric charge, $Q_{abs}$ (nA), with axial sample strain, $\varepsilon_s$ (%) (Figure 10.2 (b)). The fits were calculated by least squares.

| **Condition** | $Q_{abs} = A\exp^{B\varepsilon_s}$ | | | $Q_{abs} = A\varepsilon_s + B$ | | |
|---|---|---|---|---|---|---|
| | **A** | **B** | $\mathbf{r^2}$ | **A** | **B** | $\mathbf{r^2}$ |
| Dry | 6.97E-07 | 14.09 | 0.993 | 0.95 | -0.70 | 0.995 |
| Deionised water | - | - | - | 0.67 | -1.04 | 0.993 |
| IO brine (initial) | - | - | - | 5.47 | -0.78 | 0.999 |
| IO brine (final) | - | - | - | 9.09 | -8.15 | 0.996 |

electric current due to deformation alone (dry experiment) is approximately three to 10 times larger than the combined current seen in the presence of deionised water. Electric charge due to deformation alone increases from twice the combined charge seen in the presence of deionised water to 100 times.

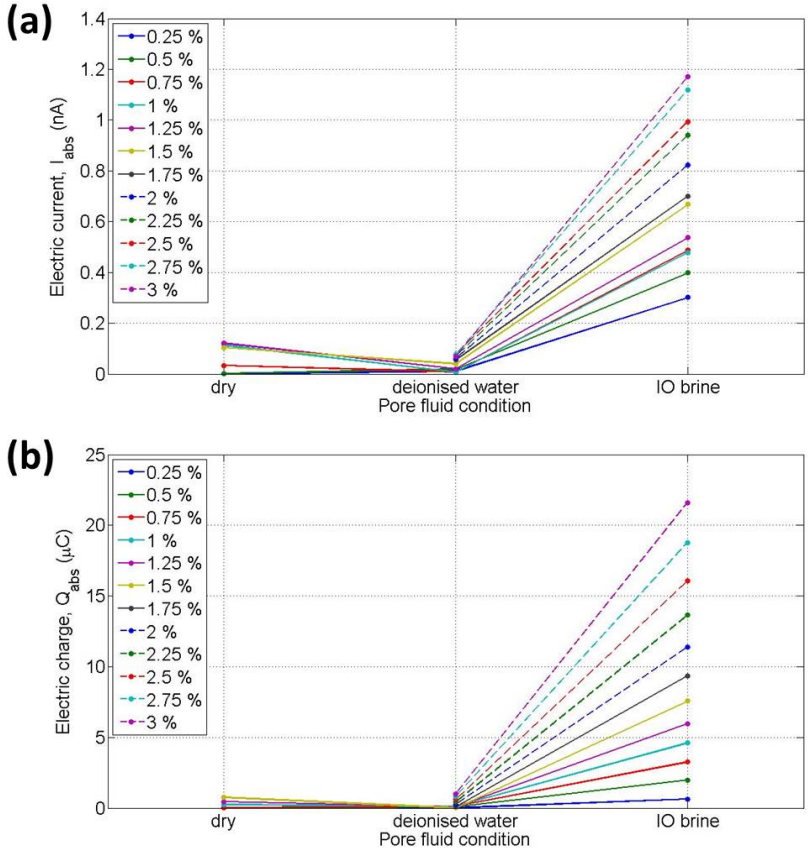


Figure 10.3: Absolute values of (a) electric current and (b) electric charge with respect to pore fluid condition for the experiments shown in Figure 10.1 at each strain slice.

## 10.4 Rate of Current Production

Figure 10.4 shows the absolute rate of electric current production, $|dI/dt|$ during three stages of deformation; (a) the initial rate during compaction (blue), (b) the rate during quasi-linear elastic phase up to the yield point (green) and (c) the main rate during dilatancy from the yield point onwards (red). In the presence of brine, the initial rate is

10 times that seen in the presence of deionised water. This ratio increases to 20 times during the quasi-linear elastic region and reduces to five times during dilatancy beyond the yield point. During dilatancy, the rate of electric current production seen in the dry experiment is equal to that seen in the brine-saturated experiment.

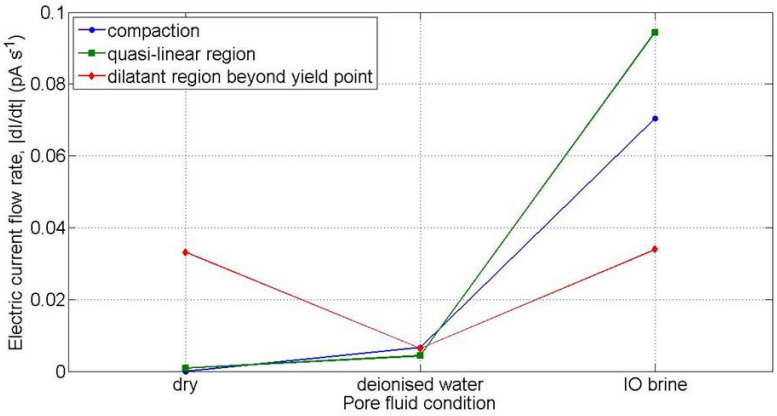


Figure 10.4: Absolute rate of electric current flow, $|dI/dt|$, with respect to pore fluid condition for the experiments shown in Figure 10.1.

## 10.5 Damage Evolution

Figures 10.5 (a) and (b) show that the initial $V_P$ is approximately 4100 ms$^{-1}$ through the water-saturated sample and approximately 4700 ms$^{-1}$ through the brine-saturated sample, compared with 5200 ms$^{-1}$ through the dry sample. The difference in $V_P$ between the dry and fluid-saturated samples is due to the introduction of microcracks in the fluid-saturated samples by the thermal and mechanical stressing procedures. However, the reason for the difference in $V_P$ between the two fluid-saturated samples is less obvious. Values for $V_P$ at 22°C and 30 MPa through deionised water with zero salinity (1538 ms$^{-1}$) and through seawater with 30 ppt salinity (1571 ms$^{-1}$) were obtained using the international standard algorithm for the speed of sound in seawater (Wong and Zhu, 1995; National Physical Laboratory, 2013). Since $V_P$ through water is only 2% less than $V_P$ through brine, the larger (13%) difference in bulk $V_P$ through the saturated rock samples implies more void space (i.e., cracks) in the water-saturated sample [CM51] than in the brine-saturated sample [CM42]. This appears to contradict observations of the connected porosity from pore volume measurements during saturation, since these show that connected porosity within CM51 is 25% less than within CM42 (Table 10.2). The difference may be due to $V_P$ being affected not only by the network of fluid-filled connected cracks but also by the presence of dry (air-filled), isolated cracks which the pore fluid would have been unable to fill. Existence of such a scenario is supported by the fact that sample CM42 has a higher permeability than CM51 (Table 10.2). Since it had been thermally cracked prior to the dry mechanical loading, it therefore already contained microcracks that would propagate and coalesce under a differential stress to form a connected network, whereas CM51 had not

and would therefore have to nucleate microcracks during the dry axial loading procedure before they could propagate and form a connected network.

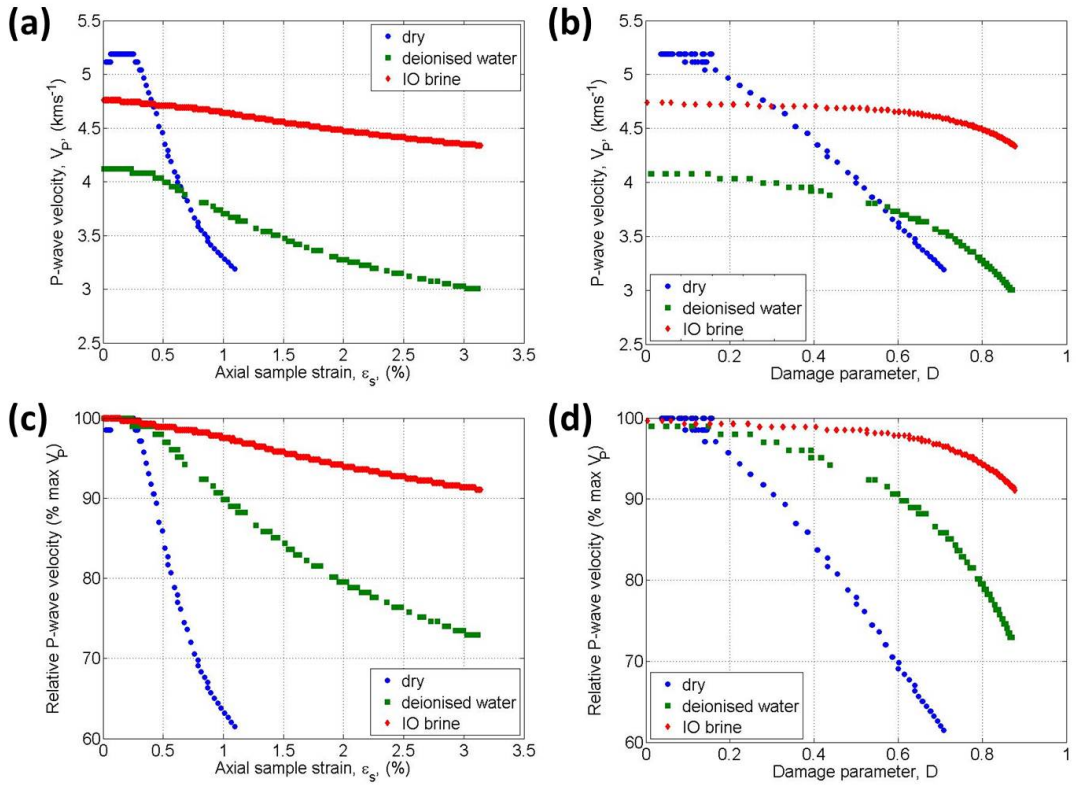


Figure 10.5: Measured $V_P$ across the central part of the sample as a function of (a) axial sample strain and (b) damage parameter, and the relative change in $V_P$ across the central part of the sample (3E-3W) as a function of (c) axial sample strain and (d) damage parameter.

Relative reduction in $V_P$ is much greater across the dry sample than across those saturated with pore fluid (Figures 10.5 (c) and (d)), indicating that deformation in the pre-cracked, fluid-saturated samples under drained conditions is accommodated in greater part by frictional sliding (cataclastic flow) along the pre-existing crack surfaces than by the creation of new cracks. Between the water and brine pore fluid conditions, the observed difference in relative $V_P$ reduction is likely to be the result of stress corrosion processes favouring crack propagation in the presence of deionised water (zero salinity) but inhibiting it in the presence of the brine solution (see Section 4.8.3). This is seen in the greater degree of macroscopic deformation sustained by sample CM51 than by sample CM42. Visual inspection of the specimens after the experiments showed that sample CM51 sustained more crack damage than CM42, forming a macroscopic fault plane (category 4, as defined in Section 7.2.2) but not completely failing, whereas CM42 showed no evidence of a fault plane (category 5). With respect to strain, the relative $V_P$ initially decreases linearly for all three conditions, before levelling off slightly towards to the end of each experiment. The rate at which $V_P$ decreases during the brine-saturated experiment is four times slower than during the water-saturated experiment, which, in turn, is five times slower than the dry experiment. A linear decrease with respect to $D$ is also seen up to 60%, with a rate of decrease six times slower under brine-saturated conditions than water-saturated condi-

tions and 3.5 times slower under water-saturated conditions than dry conditions. Beyond 60% damage, relative $V_P$ reduction for the two fluid-saturated experiments accelerates rapidly. This corresponds to an exponential increase ($r^2 = 0.9558$) in the pore volume change with respect to $D$ (Figure 10.6 (a)). Additionally, it can be seen in Figure 10.6 (b) that the pore volume change is almost directly proportional to the relative $V_P$ reduction for both types of pore fluid, although a much greater reduction in $V_P$ is associated with a much smaller increase in connected pore volume during the water-saturated experiment than during the brine-saturated experiment. This further supports the scenario described above of greater connectivity in the crack network of the brine-saturated test than the water-saturated one.

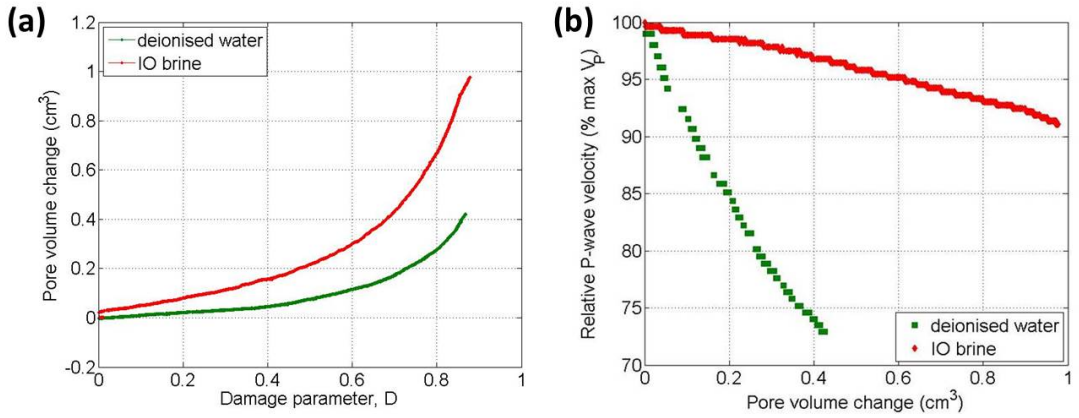


Figure 10.6: Pore volume change with (a) damage parameter, $D$, and (b) relative $V_P$ variation for the two different types of pore fluid.

Comparing the evolution of electric current with respect to $D$ (Figure 10.7) to the evolution of relative $V_P$ change (Figure 10.5 (d)), it is apparent that electric current increases rapidly beyond 60% damage during both the fluid-saturated tests, coinciding with the acceleration in dilatancy evident from both the pore volume change and the rapid reduction in $V_P$. This differs from the dry case, where electric current flows from 50% damage onwards and is associated with a continued steady reduction in $V_P$.

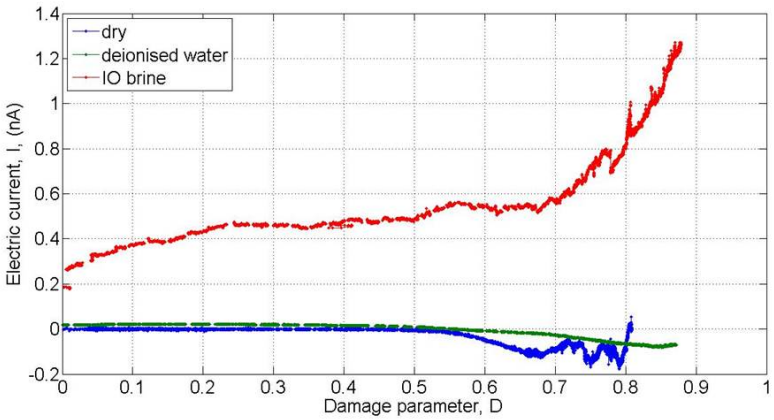


Figure 10.7: Evolution of electric current flow between electrodes 3S and 3N, at 30 MPa and $10^{-6}$ $s^{-1}$ and the three pore fluid conditions, as a function of the damage parameter, $D$.

## 10.6 Relationship with Stress

Evolution of electric current, pore fluid volume change and relative $V_P$ reduction with respect to stress for the different pore fluid conditions is presented in Figure 10.8. During the brine-saturated experiment, fluid flow (totalling 0.01 $cm^3$) out of the sample during compaction occurs between 25 and 95 MPa (10% and 42% peak stress), at which point dilatancy overtakes compaction until the original porosity is restored at 135 MPa (60% peak stress). During the water-saturated experiment, compaction also begins at 10% peak stress (22 MPa) but continues to a higher stress (125 MPa; 56% of $\sigma_{max}$), with fluid flow out of the sample totalling 0.02 $cm^3$ before dilatancy begins to overtake compaction. The original porosity is restored at 180 MPa (81% peak stress), a significantly higher stress than in the presence of brine. A gentle increase in pore volume with respect to stress is then observed up to 200 MPa ($88 - 90\%$ $\sigma_{max}$) at a similar rate for both pore fluids; 0.1 $cm^3$ increase in pore volume over 75 MPa for brine, and 0.02 $cm^3$ increase in pore volume over 20 MPa for water. Dilatancy then accelerates with respect to stress, leading to an increase in pore volume of 0.4 $cm^3$ in both samples from 200 to 220 MPa, which is the maximum stress supported by the water-saturated sample. A further 3 MPa is supported by the brine-saturated sample, which corresponds to a further 0.6 $cm^3$ increase in pore volume. This acceleration in dilatancy with stress from 90% $\sigma_{max}$ is also apparent from the $V_P$ reduction, implying that the main production of electric current seen within 90% $\sigma_{max}$ during the dry tests (including those presented in Sections 8.6 and 9.5) can be entirely accounted for by rapid dilatancy occurring at stresses close to the maximum compressive strength of the samples.

Electric current behaviour with respect to stress during the two fluid-saturated tests approximately follows the pore volume behaviour. Current onset occurs at 10% $\sigma_{max}$ and flow is initially negative to a minimum (-4 pA for water and -90 pA for brine) at 30% of the peak stress for both experiments. This point correlates with the maximum rate of fluid flow out of the samples before dilatancy in the axial direction slows it down. Electric current then reverses steadily back to zero from the point at which fluid begins to flow into the sample, before continuing at this steady rate in the positive direction up to 0.02 nA for water and rate of to 0.47 nA for brine at 88% of the peak stress. This rate is 20 times greater in the presence of brine than in the presence of water (Table 10.5). At this point, it levels off briefly before flowing rapidly, in conjunction with the rapid increase of pore fluid into the sample beyond 90% of the peak stress. This rapid flow takes opposite polarity for each type of pore fluid, reaching a maximum of 1.27 nA at the end of the brine-saturated experiment and a minimum of -0.08 nA at the end of the water-saturated test. The rate of current flow with respect to stress is again 20 times greater in the presence of brine than in the presence of water (Table 10.6). In comparison, the rate of change of current with stress under dry conditions is four times that in the presence of water and ⅙ that in the presence of brine.

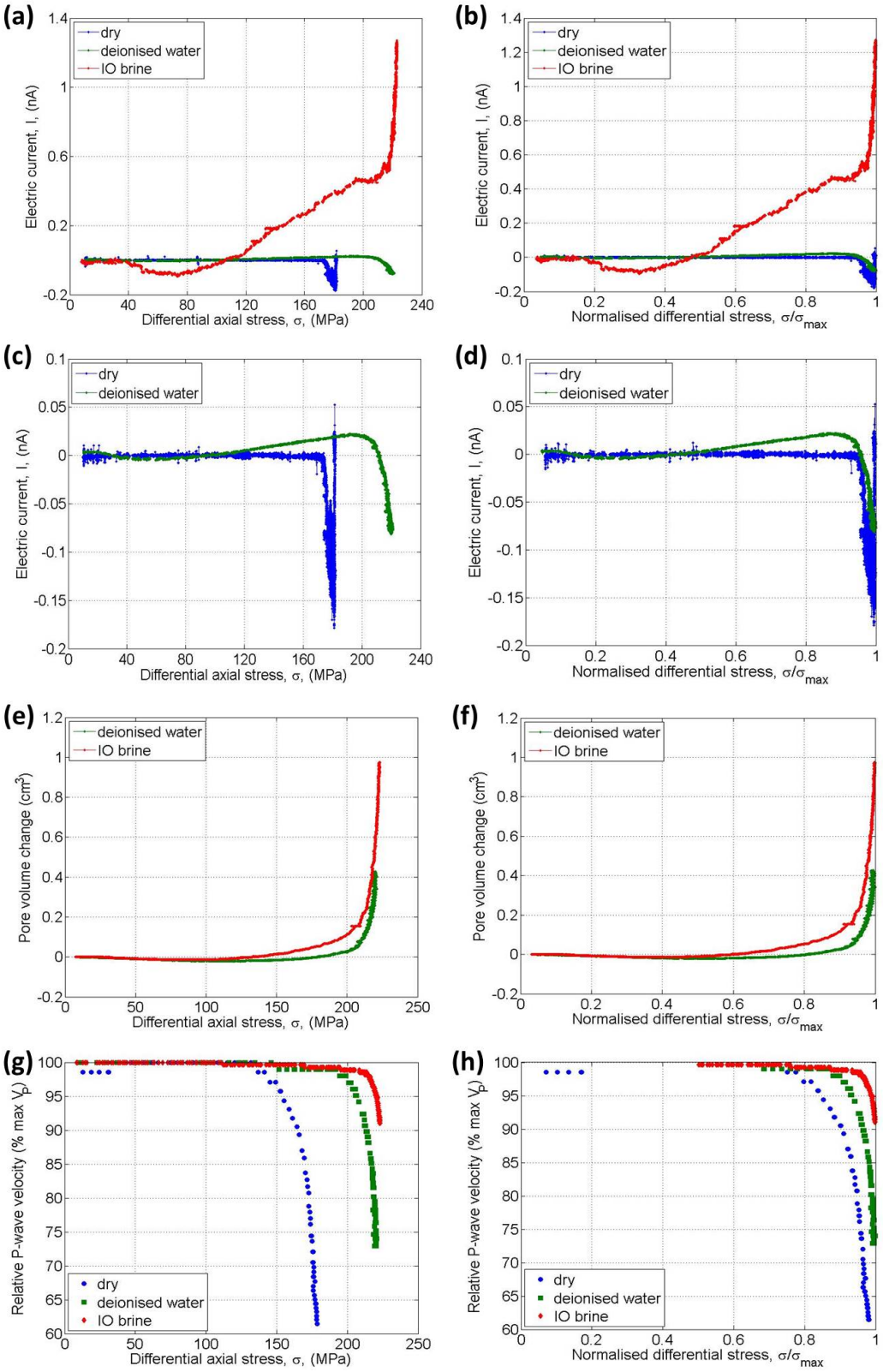


Figure 10.8: Evolution of electric current across the central part of the sample (3S-3N) as a function of (a) differential stress, $\sigma$, and (b) normalised stress, $\sigma/\sigma_{max}$ at $P_{eff} = 30$ MPa ($P_c = 50$ MPa and $P_p = 20$ MPa) and $10^{-6}$ s$^{-1}$ for the three different pore fluid conditions. graphs (c) and (d) are the same as (a) and (b) respectively but show only the dry and water-saturated experiments to illustrate more clearly the variation between the two. Pore fluid volume change under fluid-saturated conditions and relative $V_P$ change under all three conditions are also shown as a function of $\sigma$ (e and g) and $\sigma/\sigma_{max}$ (f and h).

Table 10.5: Stress and normalised stress at the post-compaction onset of the initial gradual production of electric current between electrodes 3S and 3N and $dI_{abs}/d\sigma$ for this gradual production.

| **condition** | $\sigma_{ec}$ **(MPa)** | $\sigma_{ec}/\sigma_{max}$ | $dI_{abs}/d\sigma$ **(nA/MPa)** |
|---|---|---|---|
| deionised water | 60 | 0.30 | 2.27E-04 |
| IO brine | 73 | 0.30 | 5.20E-03 |

Table 10.6: Stress and normalised stress at the onset of the final rapid production of electric current between electrodes 3S and 3N and $dI_{abs}/d\sigma$ for this rapid production.

| **condition** | $\sigma_{ec}$ **(MPa)** | $\sigma_{ec}/\sigma_{max}$ | $dI_{abs}/d\sigma$ **(nA/MPa)** |
|---|---|---|---|
| dry | 172 | 0.95 | 0.0236 |
| deionised water | 200 | 0.90 | 0.0086 |
| IO brine | 210 | 0.96 | 0.1562 |

## 10.7 Summary and Deductions

In this chapter, I have presented the electric current signals generated during triaxial deformation of non-piezoelectric Carrara marble under three different pore fluid conditions; dry, deionised water and Instant Ocean brine solution. Having established that an electric current is produced during deformation of dry Carrara marble samples and that solid-state mechanisms involved in the deformation process must be responsible for this current, deionised water and an ionic brine solution were introduced as pore fluids to establish the influence of fluid flow on the deformation-induced current. In these fluid-saturated experiments, electric current flowed from the very start of each test due to the formation of a convective streaming current induced by the flow of fluid out of the sample during compaction (Figures 10.1 (b) and (c)). The polarity of this convection current reverses as fluid flow into the sample, due to opening fractures, overtakes fluid flow out of the sample. Thus, in fluid-saturated rocks, electrokinetic effects must act in conjunction with the solid-state current-generating mechanisms active during permanent deformation.

The convection current in the presence of deionised water is very small (Figures 10.2 (a) and 10.3 (a)) due to the lack of counter-ions available in the fluid phase to compensate excess charge of the opposite polarity on the solid phase, leading to fewer charges separated in the EDL and therefore a weak zeta potential. In the presence of ionic brine, this convection current is an order of magnitude larger due to the presence of free ions in the solution. This increase in the concentration of ions in the EDL leads to a greater degree of charge separation between the solid and liquid phases and a larger zeta potential. The order of magnitude difference in current flow between the two pore fluid types corresponds to the order of magnitude difference in both the steady state streaming current and permeability measured prior to loading (Table 10.2). As the network of cracks develops, localised fluid flow in regions of accumulating damage will give rise to vari-directional convection currents, which may account for the small polarity changes in current flow observed during initial yielding of the water-saturated sample (Figure 10.1). These fluctuations are not seen in the brine-saturated sample; current flows rapidly from the onset of dilatancy in the quasi-linear region. The difference in behaviour could be attributed to

the larger initial network of cracks in the brine-saturated sample, which was both more permeable and less tortuous than that in the water-saturated sample (Table 10.2). Increases in apparent connected porosity are achieved mainly by broadening both damage zones around grain boundary regions and conjugate dilatant shear zones within specimens (Zhang et al., 1994). Since streaming current coefficient and permeability are functions of the connectivity of the flow path network (Yoshida, 2001), greater connectivity combined with a broader hydraulic radius, would allow fluid to flow more readily through the crack network, preventing fluid flow from localising in regions of damage accumulation and allowing the convection current to flow uninterrupted. During the quasi-linear and initial yield regions, new cracks are forming most rapidly and so fluid flow rates in localised regions of damage are higher at the start of dilatancy than during stable cataclastic flow. This might account for the high rate of current production seen during this region in the brine-saturated sample (Figure 10.4), with a greater contribution from electrokinetic effects to the combined electrokinetic and deformation-induced current during this stage than later on.

It can be argued that the form of electric current evolution is comparable between the three pore fluid conditions, supporting the notion of an EDL forming under dry conditions as well as drained conditions. Main current flow in both the dry and water-saturated sample begins at the onset of stable cataclastic flow after the initial yield (Figure 10.1 (a) and (b)) and after a 10% reduction in velocity (Figure 10.5 (c)); i.e., after a similar degree of crack damage. This implies a greater contribution from solid-state effects than electrokinetic effects on current generation in the water-saturated sample. However, the degree of crack damage (dilatancy) in the brine-saturated sample is much less than in the water-saturated and dry samples, while the main current begins during the quasi-linear region at the onset of dilatancy (Figure 10.1 (c)) rather than after a 10% $V_P$ reduction. This implies a greater contribution from electrokinetic effects than solid-state effects on current generation in the brine-saturated sample. This conjecture is further supported by a significant reduction in the rate of current production during stable cataclastic flow processes (shearing and frictional sliding) compared with the initial yield (crack nucleation). Since pore space may either dilate or compact in the cataclastic regime in response to an applied stress (Baud et al., 2000; Zhu, 2006), compactive processes during cataclastic flow may act to reduce the local fluid flow rate in some regions. Current flow between the two channels takes opposite polarity in the presence of the ionic brine solution but the same polarity in the presence of water. This implies the presence of a primary convective current and an opposing secondary conductive current in the brine-saturated sample, providing further evidence for the dominance of electrokinetic effects in the presence of a brine solution.

Thus, under realistic crustal pore fluid conditions, where flow of ionic crustal fluids are an integral part of deformation processes, electrokinetic effects dominate the observed signals. However, flowing of underground fluids has not been confirmed for all earthquakes associated with electric phenomena (Takeuchi and Nagahama, 2004) so some geoelectric signals may originate due to solid-state processes occurring on and around the fault itself,

and if the pore fluid in question is fresh water, then solid-state deformation processes may still dominate the observed signals. Additionally, solid-state mechanisms, working in conjunction with the electrokinetic effect, may in fact drive the variation in electrokinetic parameters by contributing charges to the EDL, thereby increasing the surface conductivity of the evolving fracture network (i.e., the fluid flow path) as charged particles accumulate at crack interfaces and increasing the zeta potential.

The results presented in this chapter, and the previous three, therefore demonstrate that electric current signals *are* generated in a non-piezoelectric rock under crustal conditions and that solid-state deformation mechanisms play a key role in their generation, in addition to electrokinetic effects.

# Chapter 11

# Non-Extensive Model for Electric Current Fluctuations[1,2,3,4]

## 11.1 Introduction

The experimental results presented in the previous four chapters have shown that (i) an electric current is generated in Carrara marble samples during the processes of microfracturing, cataclastic flow and ductile strain hardening, and (ii) the overall form of the generated signal evolves over time in conjunction with damage, as measured by AE activity and the reduction in both $V_P$ and Young's Modulus. I have argued the following:

- Steadily increasing electric current flow and the associated accelerating accumulation of charge are the result of ionic bonds breaking during accelerating crack nucleation and propagation along cleavage planes, grain boundaries and at twin junctions.
- Avalanches of shear frictional sliding events along crack surfaces during distributed cataclastic flow, together with the formation of small new wing cracks during these events, contribute to a steady accumulation of charged particles and the formation of an EDL within the crack voids by releasing charges from the disordered surface layers. The charges in the EDL separate with each shearing event, resulting in pulses of electric current flow around a steady background level.

[1]Cartwright-Taylor, A., Vallianatos, F. and Sammonds, P. (2014). Superstatistical view of stress-induced electric current fluctuations in rocks. *Physica A: Statistical Mechanics and its Applications*, 414:368-377.

[2]Cartwright-Taylor, A., Vallianatos, F. and Sammonds, P. (2015). Deformation-induced electric current in Carrara marble across the brittle-ductile transition. *TSG Annual Meeting 2015 5-8 Jan.*

[3]Cartwright-Taylor, A., Vallianatos, F. and Sammonds, P. (2013). Fracture and electric current in the crust: a $q$-statistical (Tsallis) approach. *AGU Fall Meeting 9-13 Dec.*

[4]Cartwright-Taylor, A., Vallianatos, F. and Sammonds, P. (2013). On the non-extensivity of electric current emissions associated with microfracture during triaxial deformation of Carrara marble. *Fractals and Dynamic Systems in Geoscience Conference 30 Sept - 2 Oct.*

- The accelerating increase in electric charge accumulation *and* electric current flow during ductile strain hardening at high pressure is due to the continual formation and migration of charged edge dislocations.

However, as discussed in Section 3.5.1.4, these individual processes are short-lived and therefore any long-lasting electric signal originating from them must be generated by the superposition of signals from all the simultaneous electrification events and will evolve with damage. In order to determine if this really is the case and provide further insight into the internal dynamics of such episodic deformation, this chapter presents an analysis of the electric current fluctuations using a non-extensive statistical physics (NESP) approach. Electric current fluctuations were chosen as the variable for analysis because, in the brittle regime at least, increases in the small-scale, high frequency electric current fluctuations correspond to the increased AE event rates and amplitudes associated with crack localisation around a fault. Thus, increases in these fluctuations in electric current are likely to reflect localised avalanches of deformation.

All three deformation mechanisms mentioned above have been shown to exhibit intermittent 'avalanches' of activity on a fractal network of cracks or crystal defects (Main et al., 1990; Weiss and Marsan, 2003; Sammonds, 2005; Richeton et al., 2005); behaviour characteristic of self-organised critical (SOC) systems. Such non-equilibrium systems are also characterised by correlations; long-range interactions between elements of the system. As discussed in Chapter 2, the non-extensive $q$-parameter is a measure of the interactions between the elements of a system (i.e., the strength of their correlations) and can thus provide information regarding the system's stability. It is also closely related to the seismic $b$-value (Telesca, 2012; Vallianatos, 2009) and may therefore also exhibit precursory behaviour (e.g., Main et al., 1989; 1992; Meredith et al., 1990; Sammonds et al., 1992).

If the developing fractal crack (or defect) network is indeed the source of the electric current fluctuations, then the distribution of the fluctuations should be non-Gaussian and well-described by a $q$-Gaussian distribution (i.e., of Gaussian form but with higher-probability, power-law tails), reflecting the fractal nature of the crack network. Additionally, the overall non-extensive $q$-parameter for each experiment would be expected to illustrate differences in deformation mechanism across the range of experimental conditions, while its evolution with deformation should yield useful information regarding the development of the fracture network and the potential usefulness of the $q$-parameter itself as a precursor to failure. Furthermore, if indeed the distribution of electric current fluctuations is non-Gaussian and can be modelled with a $q$-Gaussian distribution, the nature the of internal dynamics leading to this statistical behaviour may possibly be represented in terms of the super-statistical model described in Section 2.4.4.2. This model attributes the $q$-Gaussian distribution of a rapidly fluctuating variable to the superposition of local relaxations in the presence of a slowly varying driving force and is, therefore, suitable for driven, non-equilibrium systems, such as rock deformation under stress. If it can be shown that the electric current fluctuations relax to states of temporary equilibria during the course of deformation

and that a $q$-Gaussian distribution arises from such behaviour, this would provide strong evidence that the observed electric signals are indeed a response to a propagating sequence of mechanical relaxations that are effectively described by the $q$-parameter.

Thus, the main objective of this theoretical modelling stage was to apply the concepts of non-extensive statistical physics (NESP) and super-statistics discussed in Chapter 2 to the experimental electric current data, with the following aims:

- Determine the non-extensive $q$-parameter under various simulated crustal conditions.
- Assess the validity of the non-extensive statistical physics approach to the study of electric fracture and friction phenomena.
- Apply super-statistical techniques to establish a dynamic explanation for its observed statistical behaviour and highlight certain features of the system.
- Establish whether the $q$-parameter may be useful as a precursory indicator of failure, with a potential role in earthquake monitoring and forecasting.

## 11.2 Method of Analysis

An important feature of all the experiments carried out during this study, particularly those at the slowest strain rates, are the localised fluctuations of electric current, which may provide an insight into the internal dynamics of the system. This section describes the analysis procedure to investigate whether the non-extensive properties of these fluctuations can provide an insight into the processes of rock deformation and failure. Figure 11.1 is an example of one of the experimental time series showing the measured electric current, $I$, between electrodes 3S and 3N, together with stress, during deformation under 30 MPa confining pressure at a constant axial strain rate of $10^{-6}$ s$^{-1}$. The region of interest over which electric current fluctuations were analysed is between A and B; from the onset of the main deflection of electric current emissions to either the point of fracture, if the sample failed, or the end of the experiment. Fluctuations were quantified, following the approach of Caruso et al. (2007), as the incremental size difference between successive electric current measurements in the region of interest: $F_i = I(t_{i+1}) - I(t_i)$. The incremental time interval was 0.5 s for the single-channel tests, increasing by 0.5 s with each additional channel recorded to 2 s for tests recording four channels. The non-extensive parameters obtained from the analysis did not depend on the time interval adopted. This was checked on Experiment CM16 and the resulting probability distributions for each of the four time intervals are presented in Appendix G, together with their non-extensive parameters.

In order to obtain the non-extensive properties of the failure process, the variable $u_i$ was then created by subtracting the average value $\langle F \rangle$ of the incremental fluctuations, $F_i$, and dividing by their standard deviation $\sigma_F$: $u_i = \dfrac{(F_i - \langle F \rangle)}{\sigma_F}$. The subsequent analysis of

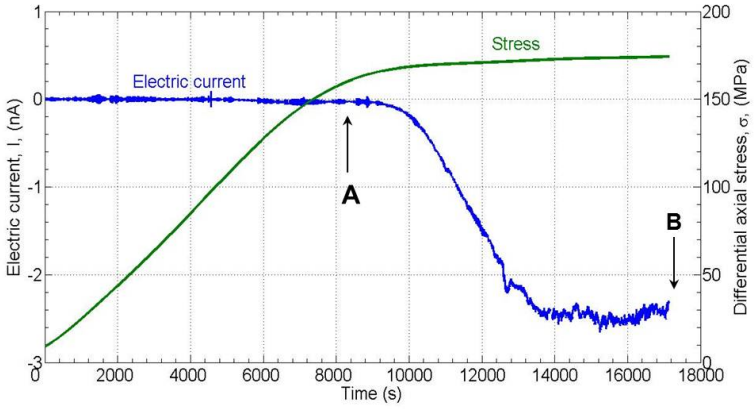


Figure 11.1: Example of a full experimental time series showing the measured electric current, $I(t)$, (blue) and the smoothed stress (green) at 30 MPa and $10^{-6}$ s$^{-1}$ [Experiment CM16] showing the region of interest between A and B.

these normalised increments, $u(t)$, proceeded by constructing the probability density function $p(u)$ and modelling $p(u)$ using the non-extensive $q$-Gaussian function (Equation 2.7). The non-extensive $q$-parameter and corresponding $B$-value were determined by means of a non-linear least squares regression algorithm written in MATLAB (see Appendix C for the code) together with a manual iteration process which minimised the mean square error between the observed data and Equation 2.7. Subsequently, the kurtosis of $u$ was calculated in moving windows of width $\Delta$, ranging from 50 to 300 data points. Since Gaussian distributions have a kurtosis close to three, this procedure established whether or not $u$ exhibits localised Gaussian behaviour, i.e., whether a super-statistical description of its dynamics would be appropriate. Once this was established, the super-statistical $\beta$-parameter was calculated as the inverse variance (Equation 2.17) from the maximum likelihood Gaussian fit for each normally distributed window; i.e., with a kurtosis close to three ($2.5 \leq \text{kurt} < 3.5$), yielding a distribution $f(\beta)$ from all these windows for each value of $\Delta$. This distribution was then modelled by a maximum likelihood gamma function with mean value $\beta_0$ (Equation 2.19) and compared with the theoretically predicted $\beta_0^{calc}$ calculated from the non-extensive $q$ and $B$ parameters according to Equation 2.21. Results from the $\Delta$-value for which $\beta_0$ was closest to $\beta_0^{calc}$ are presented here. The appropriate $\Delta$-value differed depending on the environmental condition being varied, which is why for the experiment common to all the conditions [Experiment CM05], a different value for the observed $\beta_0$ is presented for each environmental condition. The whole testing procedure was coded in MATLAB (Appendix C).

Results of the non-extensive and super-statistical modelling procedure are presented in the subsequent sections, separated by the particular environmental condition that was varied. Each section is organised as follows:

1. Electric current fluctuations, $F(t)$, together with differential stress, $\sigma(t)$, are presented as a function of time.

2. Probability densities, $p(u)$, of the normalised electric current fluctuations, $u$, fitted with

both the $q$-Gaussian and Gaussian models, illustrate the non-Gaussian nature of $p(u)$.

3. A summary table displays $q$ and $B$, together with the predicted super-statistical $\beta_0^{calc}$ and the experimental $\beta_0$ determined from the appropriate $\Delta$.

4. The variation of $q$ and $B$ with experimental condition is depicted graphically.

5. Examples of $p(u)$ in the Gaussian distributed-windows are fitted with a Gaussian model.

6. Histograms for $f(\beta)$ at the appropriate $\Delta$ are fitted with a gamma model.

7. A comparison plot of experimental $\beta_0$ values against predicted $\beta_0^{calc}$ values illustrates that the experimental data can be closely represented by super-statistical dynamics.

8. Finally, the variation of $\beta(t)$ with time is plotted with both $u(t)$ and $\sigma(t)$, highlighting the slow variation in $\beta$ compared with the rapidly fluctuating electric current, $u$.

These sections are followed by two further sections, one presenting the variability of the $q$-value across experiments of identical conditions and the other presenting the evolution of $q$-value with deformation. The latter section looks especially at the influence of approaching macroscopic failure and the influence of damage localisation within the sample.

Electric current data from the multi-channel experiments described in Chapter 9 are not included in this chapter because discarding the 50 s of cross-talk associated with each velocity survey (described in Section 5.3.7), conducted every two minutes, meant the loss of nearly half the data from each time series.

## 11.3 Influence of Confining Pressure

### 11.3.1 Results

Figure 11.2 shows the time series of electric current fluctuations, $F(t)$, between electrode positions 3S and 3N, for the experiments shown in Figure 8.1. Regions of strong activity interwoven with periods of much calmer behaviour, similar to that seen in turbulent flows, are clearly apparent at all four confining pressures. At the lowest confining pressure, the strongest activity is seen immediately after peak stress and then again about 50 s before failure with a period of slightly calmer behaviour in between. This is also seen at 20 MPa; a region of very strong activity is seen shortly after peak stress followed by relative quiescence with pulses of strong activity towards the end of the experiment (the sample did not reach failure). Although these later pulses are only one third the strength of the strongest pulses, they are around the same strength as the strong pulses at 10 MPa. At 30 MPa, strong activity begins as deformation enters the strain hardening regime, with pulses tending to increase as ductile deformation continues, although the regions of strong activity are weaker than those at the lower confining pressures. Similar behaviour

is seen at 100 MPa; initially distinct pulses are seen, of a similar strength as the strongest pulses at 30 MPa, followed by a stronger long-duration pulse after the initial yield as the strain hardening behaviour steadies to a constant rate. Behaviour then returns to shorter, smaller pulses which increase in length as deformation continues, punctuated by spikes of stronger activity.

Figure 11.3 shows the probability density function, $p(u)$, of the normalised electric current fluctuations, $u(t)$, for the same experiments. At all confining pressures, $p(u)$ exhibits a parabolic, Gaussian-like curve with extended, higher-probability, power-law tails. These distributions can be very well described by the non-extensive $q$-Gaussian function (Equation 2.7). The non-extensive parameters, $q$ and $B$, for each of the experiments shown, are presented in Table 11.1 and Figure 11.4. The $q$-values initially appear to increase with confining pressure across the transition from localised brittle fracture (<30 MPa) to the more homogeneous distribution of microcracks associated with cataclastic flow ($\geq$30 MPa), where $q$-values remain almost constant (1.78 $\pm$0.04). $B$-values vary in a similar way. This indicates an increase in long-range interactions between the current-producing microfracture events from the brittle to semi-brittle mechanisms and that the level of coupling between events stabilises once the cataclastic flow mechanism dominates and there is no macroscopic failure of the sample. The lack of sample failure at 20 MPa and the similarity of this $q$-value to those from the semi-brittle regime imply that macroscopic sample failure may have a significant influence on the $q$-parameter. This implication was investigated further with a second experiment at 20 MPa [Experiment CM65], which did fracture (Figure 11.25) and is discussed further in Section 11.7, which presents an analysis of how the $q$-parameter evolves throughout the test.

Table 11.1: Summary table showing the $q$-Gaussian $q$-value, $B$ and $\beta_0$ (theoretical $\beta_0^{calc}$ and observed $\beta_0$) with their associated errors.

| $P_c$ **(MPa)** | $q$ | $\delta q$ | $B$ | $\delta B$ | $\beta_0^{calc}$ | $\delta\beta_0^{calc}$ | $\beta_0$ | $\delta\beta_0$ | $\Delta$ |
|---|---|---|---|---|---|---|---|---|---|
| 10 | 1.53 | 0.09 | 2.74 | 0.37 | 4.02 | 0.60 | 4.11 | 0.45 | 100 |
| 20 | 1.82 | 0.09 | 9.52 | 0.40 | 11.21 | 0.74 | 11.76 | 0.09 | 100 |
| 30 | 1.78 | 0.04 | 5.27 | 0.22 | 6.41 | 0.31 | 6.35 | 0.32 | 100 |
| 100 | 1.74 | 0.13 | 4.50 | 0.63 | 5.68 | 0.90 | 4.41 | 0.74 | 100 |

At all confining pressures, kurtosis close to three was found for several thousand windows (24 $\pm$11 % of the total number of windows used) for all values of $\Delta$, indicating that $u$ in these windows is normally distributed (Figure 11.5) and that the normalised electric current fluctuations do indeed temporarily reach local equilibrium during deformation. The super-statistical $\beta$-parameter could therefore be calculated for all confining pressure conditions. Figure 11.6 presents the resulting distributions $f(\beta)$ for $\Delta = 100$, which can be modelled by a gamma distribution with mean value $\beta_0$.

The experimentally obtained $\beta_0$ values (mean value of $f(\beta)$) yielding the closest comparable fit to the model $\beta_0^{calc}$ values for all confining pressures tested were from the Gaussian windows of $u$ containing $\Delta = 100$ data points. These $\beta_0$ values are presented in Table 11.1 together with the theoretically predicted results, $\beta_0^{calc}$, from (Equation 2.21). An inspec-

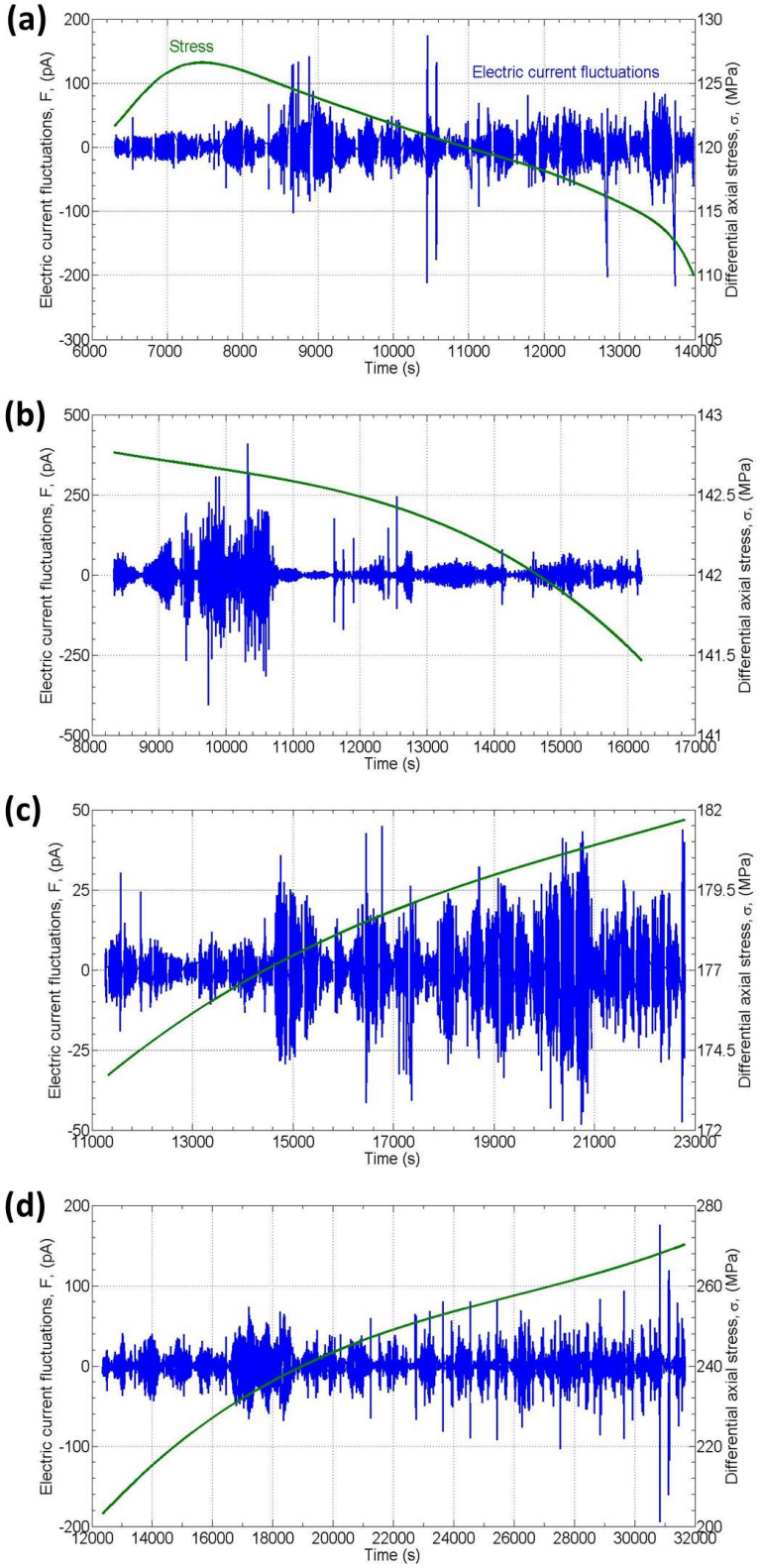


Figure 11.2: Electric current fluctuations (blue) and differential stress (green) between points A and B (see Figure 11.1) as a function of time. The signals were produced during triaxial deformation of Carrara marble samples at $10^{-6}$ $s^{-1}$ strain rate and four different confining pressures; (a) 10 MPa [Experiment CM08], (b) 20 MPa [Experiment CM21], (c) 30 MPa [Experiment CM05] and (d) 100 MPa [Experiment CM35].

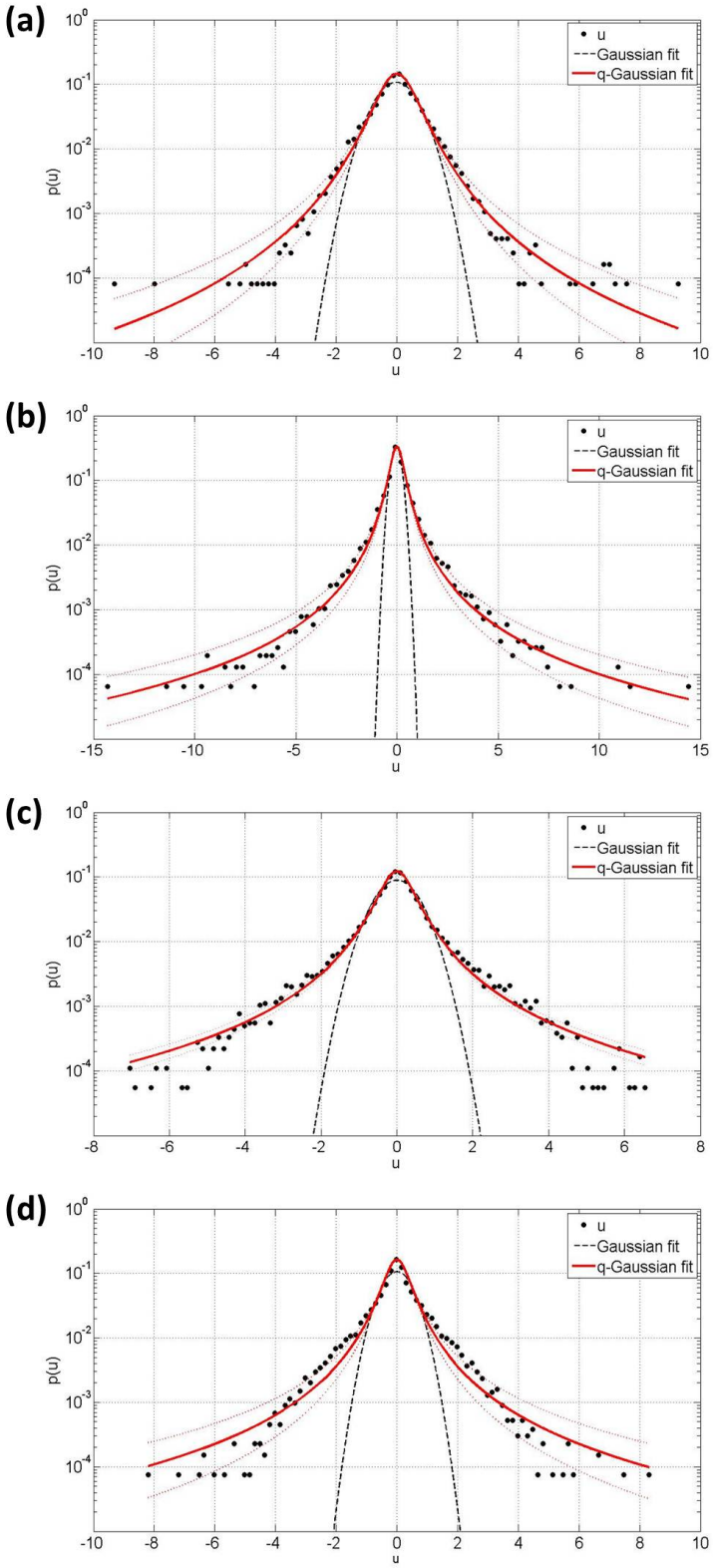


Figure 11.3: Probability density function of normalised electric current fluctuations, $u$, (black circles) and $q$-Gaussian fit (solid red line) with 95% confidence intervals (dashed red lines) and maximum likelihood Gaussian fit (dashed black line) for (a) 10 MPa with $q = 1.53$ [Experiment CM08], (b) 20 MPa with $q = 1.82$ [Experiment CM21], (c) 30 MPa with $q = 1.78$ [Experiment CM05], (d) 100 MPa with q = 1.74 [Experiment CM35].

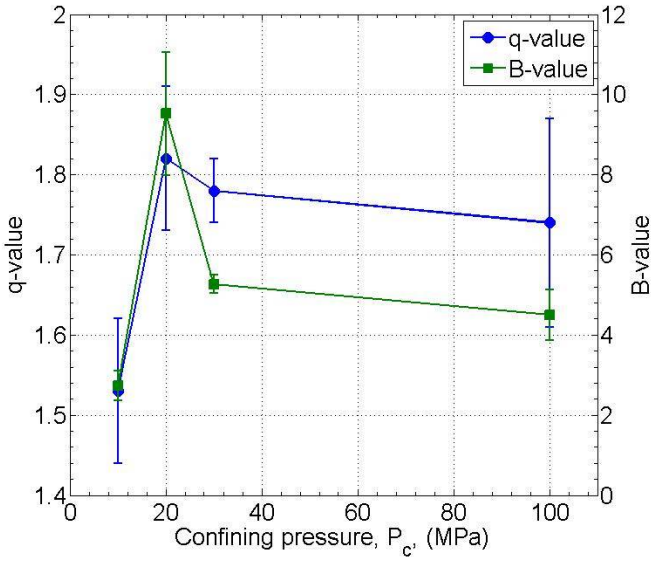


Figure 11.4: Non-extensive $q$-parameter and corresponding $B$-value with their associated statistical error as a function of confining pressure.

tion of these results shows that the observed $\beta_0$ values are consistent with the theoretically predicted $\beta_0^{calc}$, within the statistical error bounds (Figure 11.7). The result for 100 MPa is less well-predicted by the model than those for $\leq 30$ MPa and there appears to be no dependence of $\beta_0$, either observed or predicted, on confining pressure. The poorer prediction of the superstatistical model at 100 MPa is reflected in the somewhat poorer approximation of the $q$-Gaussian distribution for $p(u)$ (Figure 11.3 (d)). That is, the closer that $p(u)$ is to a $q$-Gaussian distribution, the better the predictive power of the superstatistical model.

Figure 11.8 shows the variation of $\beta(t)$ compared with that of $u(t)$. Clearly, $\beta(t)$ changes very slowly when compared with $u(t)$, a further indication that super-statistics is a good approximation for the system's dynamics at all confining pressure conditions. Peaks in $\beta(t)$ coincide with electrically calm regions, while the lowest values of $\beta$ are associated with regions of strong electrical activity. Additionally, it can be inferred that localised Gaussian processes, as indicated by the stationary $\beta$-values (black dots), occur throughout the experiments and do not exhibit any clustering in time for all but the highest confining pressure. At 100 MPa, where only 20% of the windows of $u(t)$ were normally distributed (compared with 30-35%), far fewer $\beta$-values are observed in the steady strain hardening region than are observed during the initial yield and a maximum $\beta$-value marks the transition. The maximum $\beta$-value at 30 MPa also marks the transition from initial yield to steady strain hardening, while at 20 MPa it occurs just after peak stress as the strain softening processes accelerate. At 10 MPa, the maximum $\beta$-value occurs at peak stress.

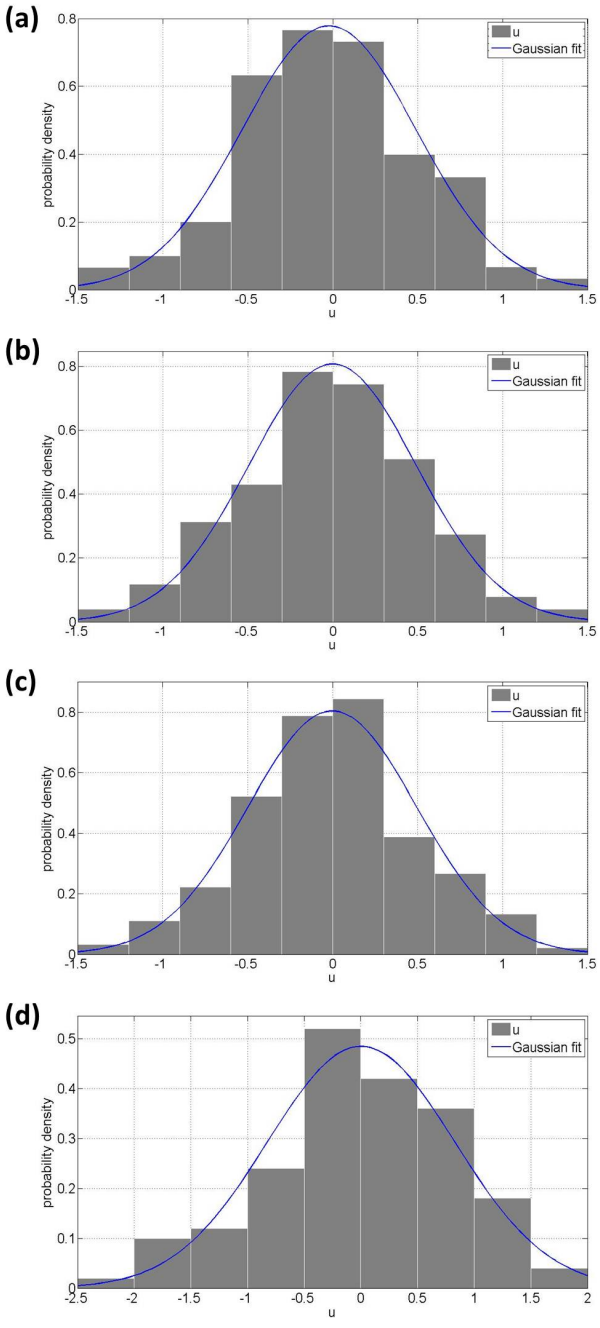


Figure 11.5: Maximum likelihood Gaussian behaviour (blue line) of the normalised electric current fluctuations, $u$, (shaded bars) for an example window at each of the four different confining pressures (a) 10 MPa, (b) 20 MPa, (c) 30 MPa, (d) 100 MPa.

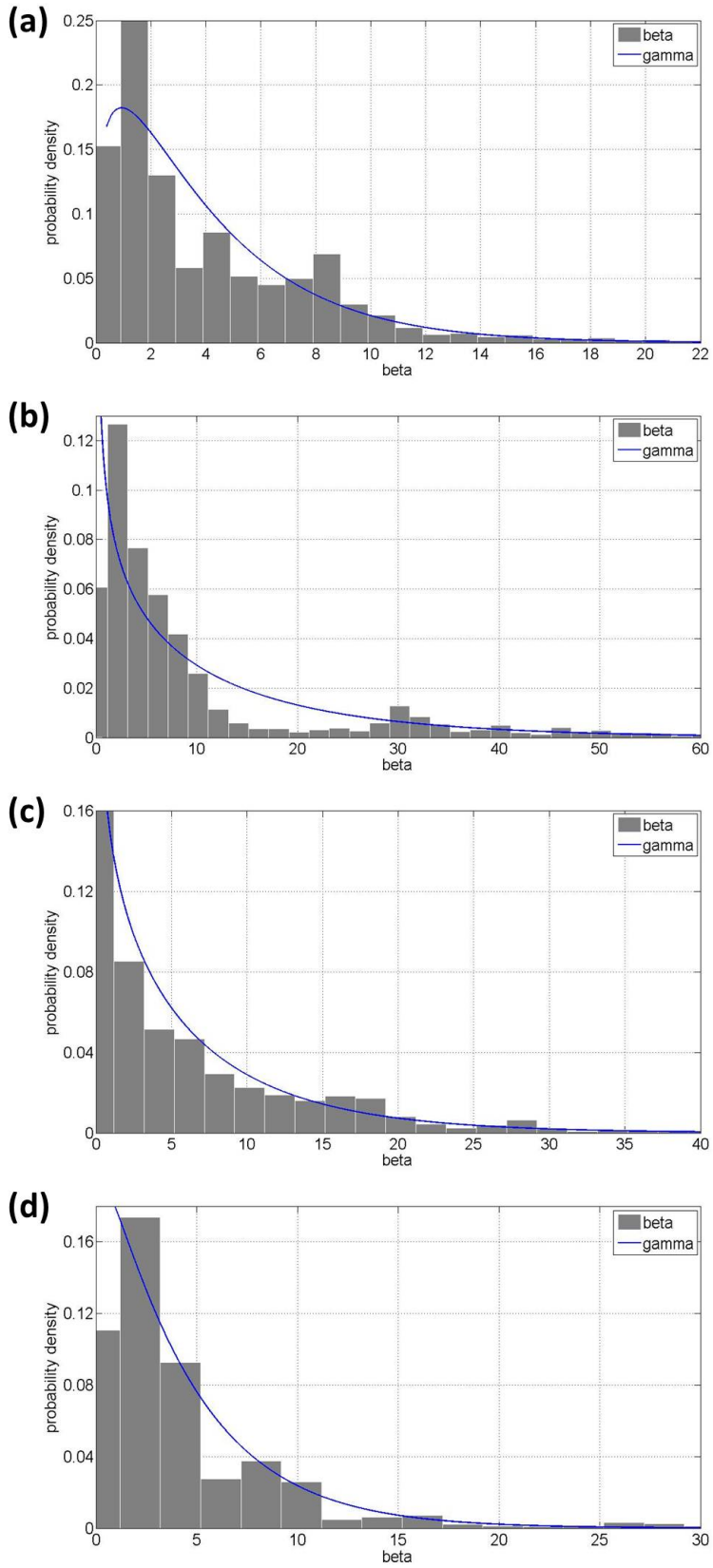


Figure 11.6: Histograms for $f(\beta)$ (shaded bars) with the maximum likelihood gamma fit (blue line) for each of the four confining pressures (a) 10 MPa, (b) 20 MPa, (c) 30 MPa, (d) 100 MPa.

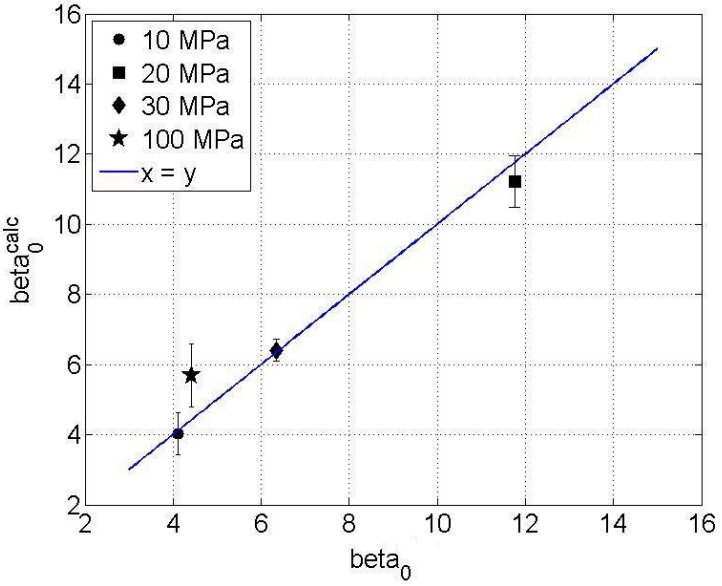


Figure 11.7: Comparison of the model $\beta_0^{calc} = (3 - q)B$ (Equation 2.21) and the observed $\beta_0$ for $\Delta = 100$ data points, together with the associated error, along the dichotomous line $x = y$ (blue line).

### 11.3.2 Discussion

At all four confining pressures, the electric current fluctuations show behaviour similar to that seen in turbulent flows; regions of strong activity punctuated with periods of much calmer behaviour. This episodic behaviour reflects the intermittent nature of the current-generating deformation events across the brittle to semi-brittle transition, at the slowest strain rate tested. At this slow strain rate, the time available between each increment of deformation allows each avalanche of stress-relieving events (microcracks, frictional sliding events, dislocation motion) to subside and the local internal stresses to relax before the next increment of deformation must be accommodated.

Normalised electric current fluctuations exhibit non-Gaussian statistical behaviour (probability densities) at all four confining pressures. The form of this behaviour; a Gaussian-like parabolic curve with extended, higher probability tails, is well-modelled by the non-extensive $q$-Gaussian distribution. The excellent agreement between the data and the model distribution reflects the fractal nature of the electric current source network, particularly at the lower confining pressures ($\leq$ 30 MPa). Thus, it can be deduced that the developing fracture network is the source of electric current. At 100 MPa, the distribution of residuals around the model is not random, perhaps indicating the existence of two separate, interacting physical processes not accounted for by the $q$-Gaussian model, possibly with different fractal dimensions. This might be due to the contribution of some tiny intragranular microcracking events to deformation in addition to the avalanches of dislocation formation and migration. Additionally, the arresting effect (hardening effect) of twin boundaries and dislocation entanglement and pile-up may influence the overall development of a fractal distribution of dislocations. An interesting question beyond the

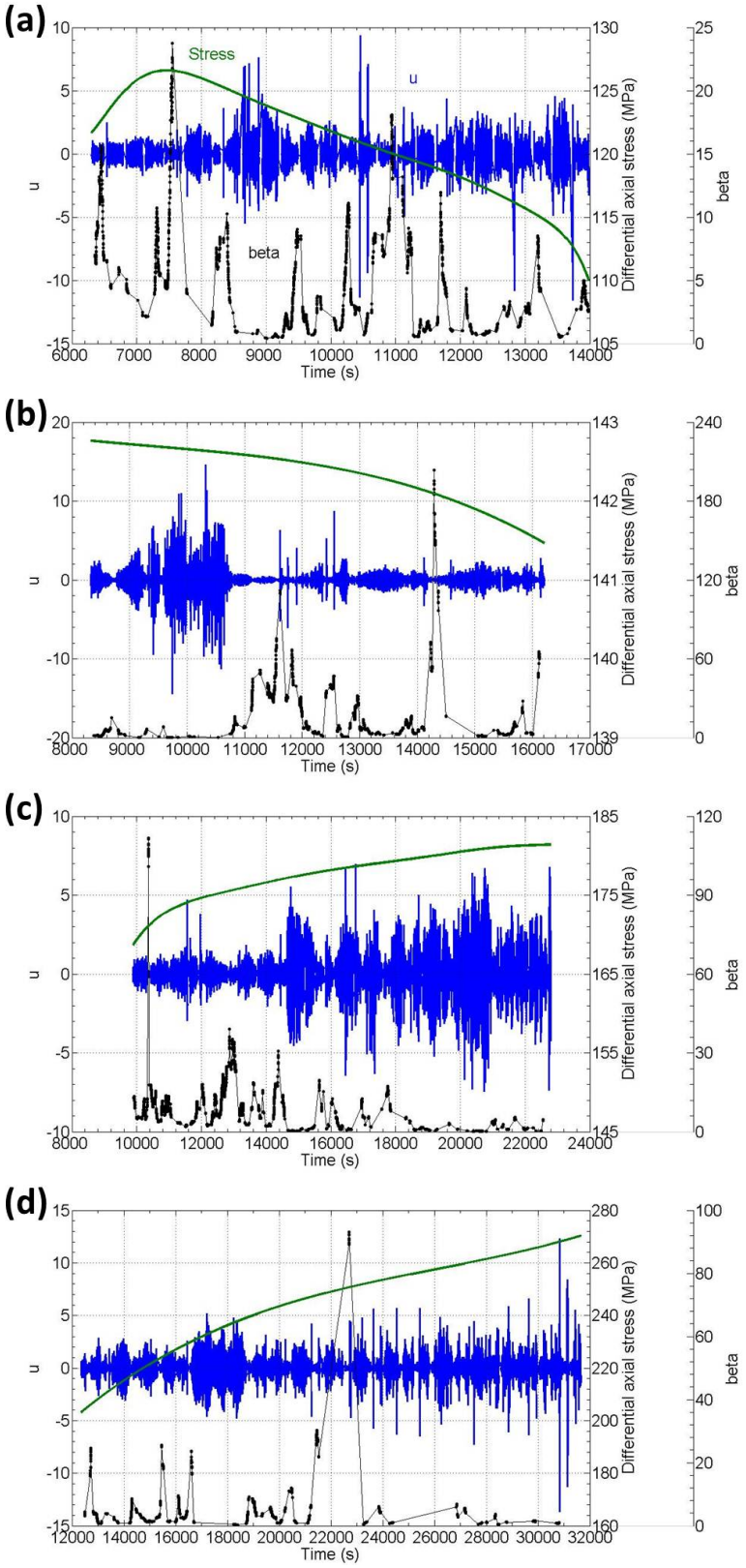


Figure 11.8: Evolution of $\beta$ (black dots), $u$ (blue line) and stress (green line) as a function of time, highlighting the slow variation in $\beta$ compared with the rapidly fluctuating electric current, $u$, for each of the four confining pressures (a) 10 MPa, (b) 20 MPa, (c) 30 MPa, (d) 100 MPa.

scope of this study would be: is it possible to separate the distributions of fluctuations due to (a) dislocation motion and (b) microcracking and, if so, how do they differ?

The variation in $q$-value with confining pressure indicates an overall increase in interactions between current-producing deformation events in the semi-brittle regime and those in the brittle regime. This could indicate that under higher confining pressures the system organises itself such that it can reach a state further from equilibrium. Physically this is possible since the strength of the rock increases with confining pressure due to compaction, manifested by the transition from localised brittle fracture (<30 MPa), where the localisation of microcracks around a main fault weakens the rock, to more homogeneous cataclastic flow (≥30 MPa), where small avalanches of microfractures, fragment roll and grain boundary sliding distributed evenly throughout the sample serve to compact it, strengthening the sample so that it accommodates higher stresses for the same amount of strain. This organisation of the internal structure of the sample to sustain a larger stress field requires additional interactions between different deformation processes, rather than purely crack-crack interactions.

The correlation between current-producing deformation events is fairly constant ($1.76 \pm 0.02$) in the semi-brittle regime when there is no macroscopic failure, even as the dominant current-producing mechanism (deformation mechanism) changes from stable cataclastic flow to dislocation migration. This relatively constant $q$-value is very close to that observed for the Earth's crust (1.75), reflected in the distribution of tectonic plate area (Vallianatos and Sammonds, 2010) and the return distribution of global earthquake sizes (Caruso et al., 2007), highlighting the similarities of deformation distributed on a well-developed, self-organising, fractal network both of faults in the crust and microcracks or crystal defects in a laboratory rock sample. The $q$-value of ∼1.8 observed during cataclastic flow may reflect a critical peak in overall $q$-value, as strengthening mechanisms (compaction) interact with weakening mechanisms (dilatancy) to maintain the peak strength of the sample over a long period of time. Telesca (2010a) attributed spatial variations in seismic $q$-values to earthquake triggering by different mechanisms, with higher values (∼1.7) related to fragment-asperity interaction. This type of interaction is characteristic of the cataclastic flow mechanism.

The elevated $q$-value at 20 MPa is seen at the transition between brittle and semi-brittle deformation, reflecting the full suppression of axial fracture, with deformation instead localising along shear planes. However, it may also reflect the fact that the sample was not taken all the way to macroscopic failure (see Section 11.7), with the higher $q$-value indicating a less-developed fracture network with deformation controlled by the nucleation of numerous small new cracks into a multifractal network rather than by coalescence into larger, more randomly distributed cracks (e.g., Vallianatos and Triantis, 2012; 2013). The development of a few large failure surfaces may also account for the lower $q$-value (∼1.5) seen at 10 MPa.

It is also apparent, from the results of the windowing procedure, that electric current

fluctuations do indeed temporarily relax back to equilibrium throughout each deformation experiment at all the $P_c$ tested. This confirms that the electric current signals reflect the cascading nature of current-generating, stress-relieving deformation processes under these conditions. The super-statistical $\beta$-parameter determined from these normally-distributed windows varies much more slowly than the electric current fluctuations; a necessary condition for superstatistics to be a good approximation. It also closely follows a gamma distribution with mean value $\beta_0$, which coincides almost exactly with the theoretical $\beta_0^{calc}$ predicted by Beck (2001), at all four $P_c$. Theoretical $\beta_0^{calc}$ values lie within the statistical error bars for the observed $\beta_0$ values at $P_c \leq 30$ MPa. At 100 MPa, the predicted value, while still very close, falls just outside the statistical error bars for the observed value, likely reflecting the slightly poorer approximation of the $q$-Gaussian function to the distribution of normalised electric current fluctuations. Thus, super-statistical dynamics can indeed account for the non-Gaussian behaviour of the normalised electric current fluctuations and are an excellent description of the dynamics governing the observed electric current signals under all the confining pressures tested, i.e., in both the brittle and semi-brittle deformation regimes. Such behaviour reflects the episodic evolution of deformation at this relatively slow strain rate ($10^{-6}$ $s^{-1}$).

## 11.4 Influence of Strain Rate

### 11.4.1 Results

Figure 11.9 shows the time series of electric current fluctuations, $F(t)$, between electrode positions 3S and 3N, for the experiments shown in Figure 9.2. Again, regions of strong activity interwoven with periods of much calmer behaviour are apparent at all five strain rates. However, the appearance of these regions throughout the experiment are more clearly apparent at the slower strain rates. In the case of the slowest strain rate ($10^{-6}$ $s^{-1}$, Figure 11.9 (e)), the overall strength of the activity increases as deformation continues in the ductile regime. Fluctuations in the regions of stronger activity become more than three times those at the onset of the electric current signal, while periods of quiescence become shorter and further apart. At 5x$10^{-6}$ $s^{-1}$ (Figure 11.9 (d)), the longest duration of stronger activity is seen as the stress rate decreases most rapidly, followed by a relatively quiet period during strain hardening. Activity then increases again in the form of shorter-duration pulses at peak stress and into the strain softening region. At faster strain rates, the variation between these two kinds of behaviour is less pronounced nearer the onset of the electric current signal, while the regions of strongest activity occur as the sample approaches macroscopic fracture. Particularly, in the case of the fastest strain rate ($10^{-4}$ $s^{-1}$, Figure 11.9 (a)), the fluctuations more than double in the last 25 s before the sample fails. The experiment at 5x$10^{-5}$ $s^{-1}$ (Figure 11.9 (b)) was stopped before the sample failed and here it can be seen that the fluctuations begin to increase, again by more than double, at around 325 s before the activity becomes slightly calmer in the last 50 s. This behaviour is repeated at $10^{-5}$ $s^{-1}$ strain rate (Figure 11.9 (c)), where the sample did fail. In this case, the fluctuations again increase by more than double from about 700 s before fracture for 300 s, before subsiding again for a further 300 s and then doubling again in the 50 s immediately prior to fracture.

Figure 11.10 shows the probability density function, $p(u)$, of the normalised electric current fluctuations, $u(t)$, for these same experiments. At all strain rates, $p(u)$ exhibits a parabolic, Gaussian-like curve with extended tails that is well described by the non-extensive $q$-Gaussian function (Equation 2.7). It should be noted that, although the distribution at the fastest strain rate (Figure 11.10 (a)) looks close to a Gaussian distribution when all but the strongest fluctuations are taken into account, the kurtosis of the overall distribution is close to seven indicating a non-Gaussian distribution. There is a much higher degree of scatter at the two fastest strain rates (Figures 11.10 (a) and (b)) than at the slower strain rates. The degree of scatter then decreases with decreasing strain rate; comparable at the two intermediate strain rates (Figures 11.10 (c) and (d)) and significantly less at the slowest strain rate (Figure 11.10 (e)). This may be due to the increasing number of data points available for constructing the distribution. The non-extensive parameters, $q$ and $B$, for each of the five experiments shown are presented in Table 11.2 and Figure 11.11. The $q$-values associated with electric current fluctuations are fairly consistent at 1.73 $\pm$0.06 for

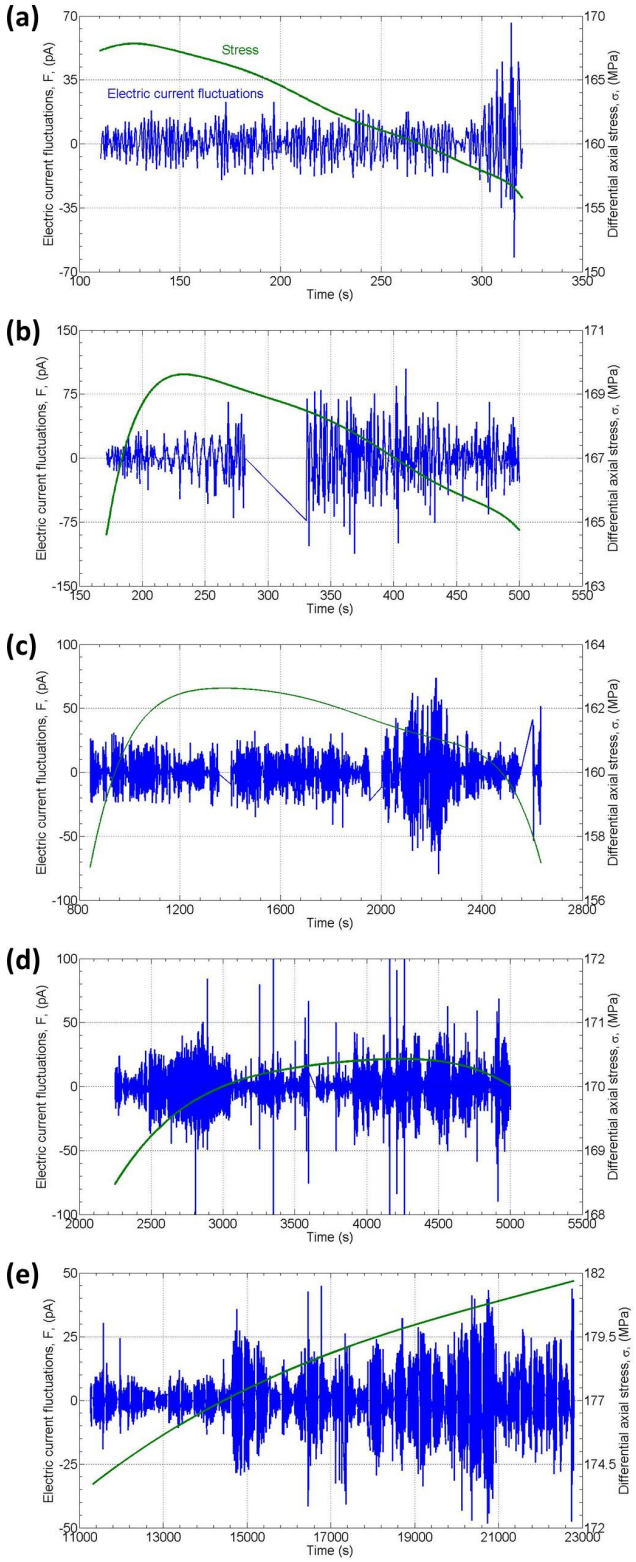


Figure 11.9: Electric current fluctuations (blue) and differential stress (green) between points A and B (see Figure 11.1) as a function of time. The signals were produced during triaxial deformation of Carrara marble specimens at 30 MPa confining pressure and five different strain rates; (a) $10^{-4}$ $s^{-1}$ [Experiment CM15], (b) $5x10^{-5}$ $s^{-1}$ [Experiment CM23], (c) $10^{-5}$ $s^{-1}$ [Experiment CM14], (d) $5x10^{-6}$ $s^{-1}$ [Experiment CM22] and (e) $10^{-6}$ $s^{-1}$ [Experiment CM05]. Data gaps are due to removal of data recorded during velocity surveys.

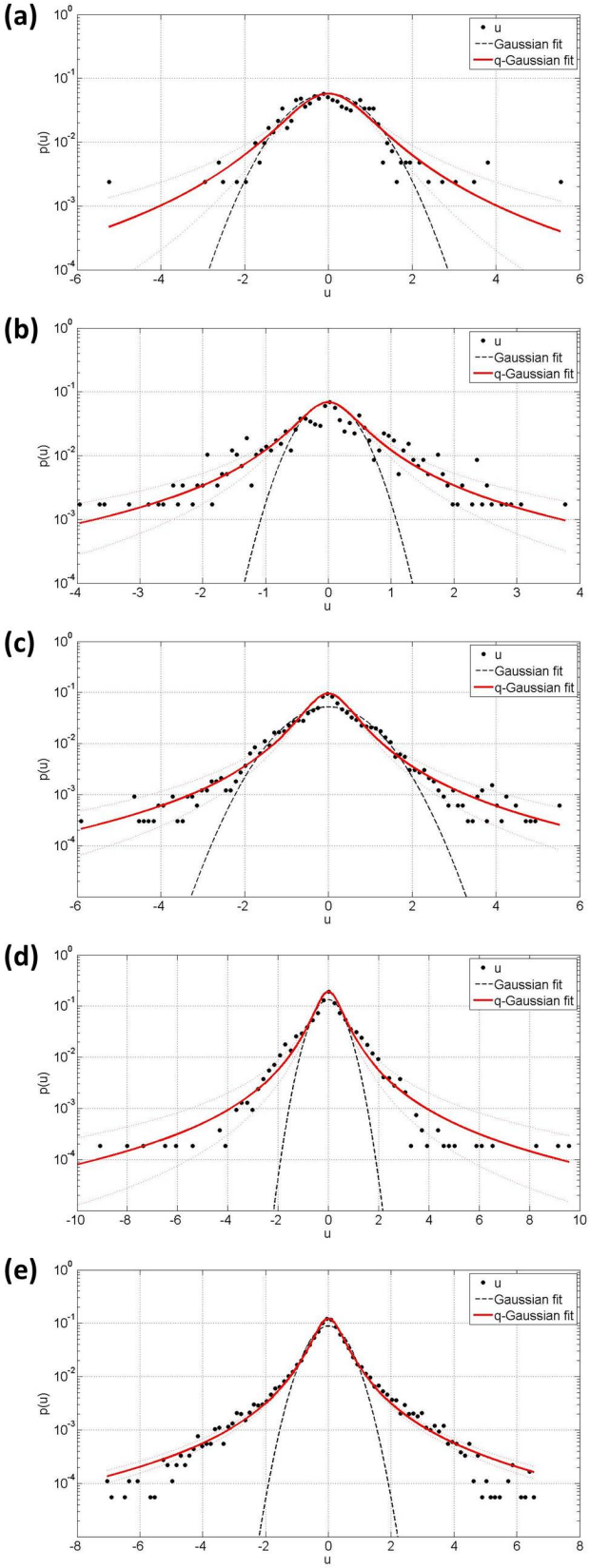


Figure 11.10: Probability density function of normalised electric current fluctuations, $u$, (black circles) and $q$-Gaussian fit (solid red line) with 95% confidence intervals (dashed red lines) and maximum likelihood Gaussian fit (dashed black line) for (a) $10^{-4}$ $s^{-1}$ with $q = 1.66$ [Experiment CM15], (b) $5x10^{-5}$ $s^{-1}$ with $q = 1.97$ [Experiment CM23], (c) $10^{-5}$ $s^{-1}$ with $q = 1.74$ [Experiment CM14], (d) $5x10^{-6}$ $s^{-1}$ with $q = 1.74$ [Experiment CM22] and (e) $10^{-6}$ $s^{-1}$ with $q = 1.78$ [Experiment CM05].

all strain rates, apart from 5x10$^{-5}$ s$^{-1}$. They initially appear to increase significantly with strain rate from 1.66 to 1.97 as the rate of strain softening beyond peak stress decreases from 60 kPa s$^{-1}$ at 1x10$^{-4}$ s$^{-1}$ to 20 kPa s$^{-1}$ at 5x10$^{-5}$ s$^{-1}$. The $q$-values then decrease to 1.74 at the slower strain rates (1x10$^{-5}$ and 5x10$^{-6}$ s$^{-1}$), where the rates of strain softening beyond peak stress are much slower (3-4 kPa s$^{-1}$), before increasing slightly to 1.78 at the slowest strain rate (1x10$^{-6}$ s$^{-1}$) where the rate of strain hardening after the initial yield has increased to 0.6 kPa s$^{-1}$ from 0.3 kPa s$^{-1}$ at 5x10$^{-6}$ s$^{-1}$. $B$-values show a similar pattern. Imminent macroscopic failure of the sample does not seem to affect the $q$-values at these three slower strain rates; the sample at 1x10$^{-5}$ s$^{-1}$ did fail (although the fault did not extend completely through the sample) and its overall $q$-value (for current fluctuations up to the point of failure) is the similar to those for the slower strain rate experiments, which did not fail. However, when the current fluctuations that occurred during failure of that sample [CM14] are included in the analysis, the overall $q$-value decreases from 1.74 to 1.67 indicating that the $q$-value decreases as a direct result of macroscopic failure.

Table 11.2: Summary table showing the $q$-Gaussian $q$-value, $B$ and $\beta_0$ (theoretical $\beta_0^{calc}$ and observed $\beta_0$) with their associated errors.

| $\dot{\varepsilon}$ (s$^{-1}$) | $q$ | $\delta q$ | $B$ | $\delta B$ | $\beta_0^{calc}$ | $\delta\beta_0^{calc}$ | $\beta_0$ | $\delta\beta_0$ | $\Delta$ |
|---|---|---|---|---|---|---|---|---|---|
| 1x10$^{-4}$ | 1.66 | 0.27 | 1.25 | 0.33 | 1.68 | 0.52 | 1.67 | 1.70 | 50 |
| 5x10$^{-5}$ | 1.97 | 0.25 | 4.53 | 0.65 | 4.64 | 0.90 | 1.79 | 0.78 | 50 |
| 1x10$^{-5}$ | 1.74 | 0.15 | 3.50 | 0.50 | 4.41 | 0.74 | 2.32 | 0.45 | 50 |
| 5x10$^{-6}$ | 1.74 | 0.17 | 4.25 | 0.58 | 5.36 | 0.89 | 4.58 | 0.75 | 50 |
| 1x10$^{-6}$ | 1.78 | 0.04 | 5.27 | 0.22 | 6.41 | 0.31 | 6.54 | 0.37 | 50 |

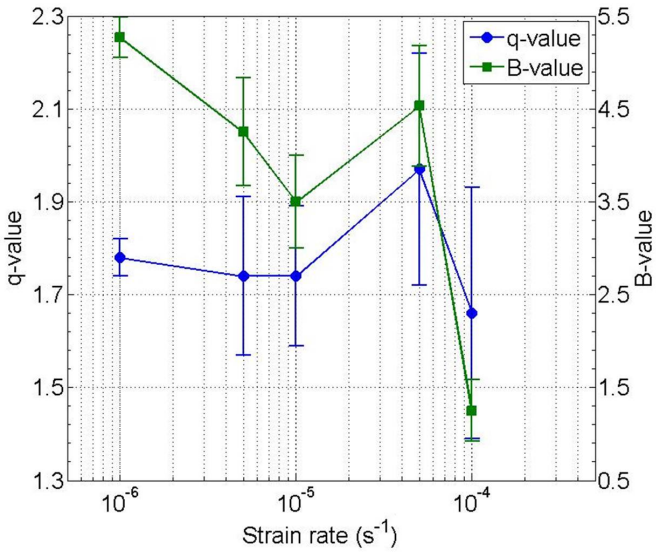


Figure 11.11: Non-extensive $q$-parameter and corresponding $B$-value with their associated statistical error as a function of strain rate.

For all strain rates, kurtosis close to three was found for 29 ±13 % of the total number of windows used for all values of $\Delta$, confirming that $u$ in these windows is normally distributed (Figure 11.12) and that the normalised electric current fluctuations do temporarily reach local equilibrium during deformation. The super-statistical $\beta$-parameter could therefore be calculated for all strain rate conditions. Figure 11.13 shows the resulting distributions

$f(\beta)$ for $\Delta = 50$, which can be modelled by a gamma distribution with mean value $\beta_0$. It should be noted that the number of Gaussian-distributed windows available for analysing $f(\beta)$ and determining $\beta_0$ increased significantly at slower strain rates (from several hundred to several thousand) due to the increasing number of data points in each experimental time series. This may be the reason for the slightly different-looking distribution in Figure 11.13 (a). At this strain rate, $f(\beta)$ is not as well-modelled by a gamma distribution as at the slower strain rates. It is, in fact, closer to a normal distribution, which may suggest that at the very fastest strain rate there is no superposition of dynamics.

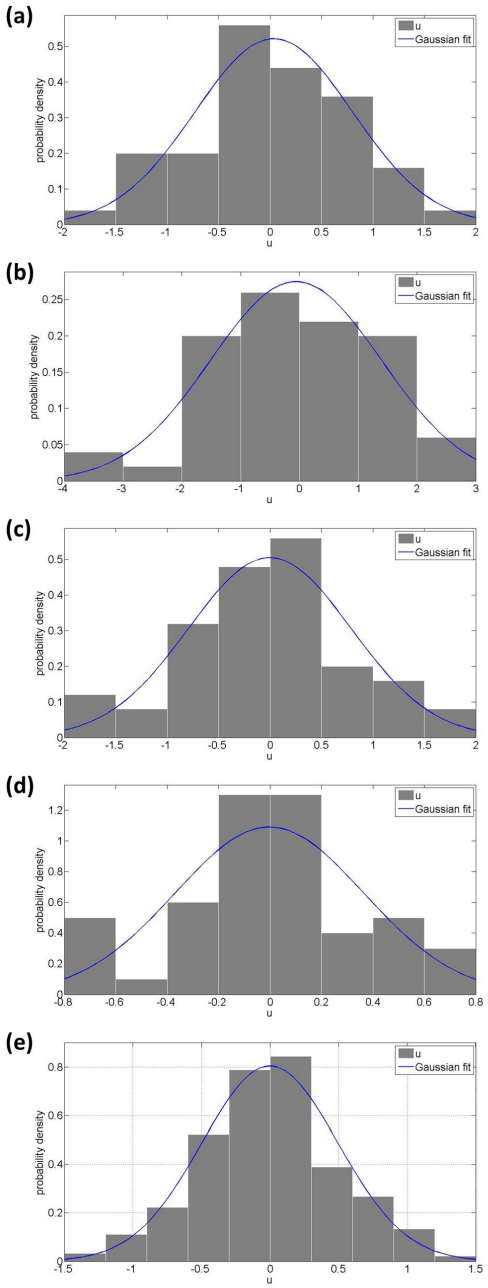


Figure 11.12: Maximum likelihood Gaussian behaviour (blue line) of the normalised electric current fluctuations, $u$, (shaded bars) for an example window at each of the five different strain rates (a) $10^{-4}$ $s^{-1}$, (b) 5x$10^{-5}$ $s^{-1}$, (c) $10^{-5}$ $s^{-1}$, (d) 5x$10^{-6}$ $s^{-1}$ and (e) $10^{-6}$ $s^{-1}$.

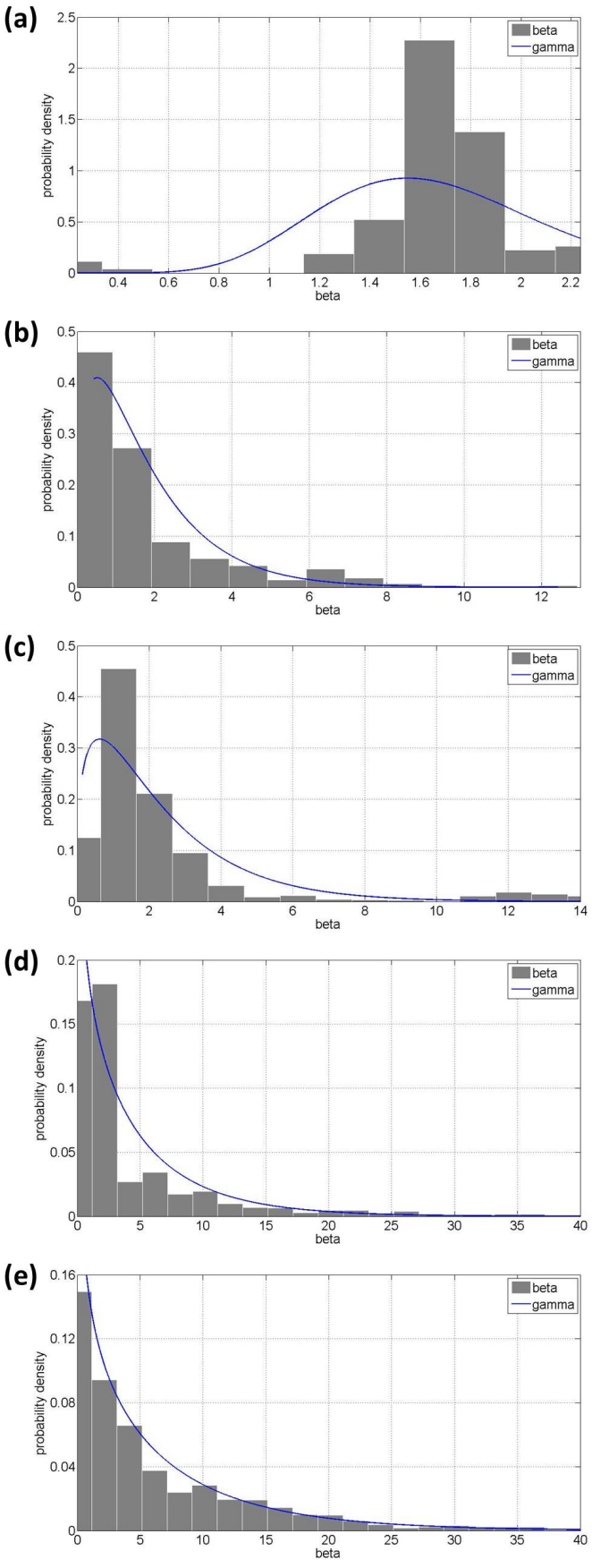


Figure 11.13: Histograms for $f(\beta)$ (shaded bars) with the maximum likelihood gamma fit (blue line) for each of the five strain rates (a) $10^{-4}$ $s^{-1}$, (b) 5x$10^{-5}$ $s^{-1}$, (c) $10^{-5}$ $s^{-1}$, (d) 5x$10^{-6}$ $s^{-1}$ and (e) $10^{-6}$ $s^{-1}$.

The experimentally obtained $\beta_0$ values (mean value of $f(\beta)$) providing the closest comparable fit for all strain rates tested are from the Gaussian windows of $\Delta = 50$ data points. These $\beta_0$ values are presented in Table 11.2 together with the theoretically predicted results, $\beta_0^{calc}$. An inspection of these results indicates that the experimentally obtained $\beta_0$ values are fairly consistent with the theoretically predicted $\beta_0^{calc}$, within the statistical error bounds (Figure 11.14). It can also be seen that the $\beta_0$ values tend to increase with decreasing strain rate, as does the extent to which they agree with the $\beta_0^{calc}$ values. The model values are much closer to the observed values at the two slowest strain rates and the fastest than at the two intermediate-fast strain rates; $\beta_0$ for the slowest strain rate agrees almost exactly with its corresponding $\beta_0^{calc}$ value. Interestingly, so does that for the fastest strain rate.

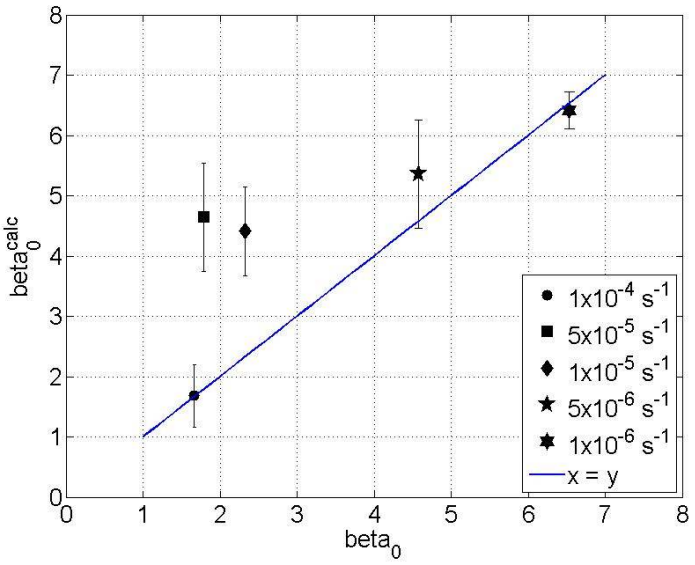


Figure 11.14: Comparison of $\beta_0^{calc} = (3-q)B$ (Equation 2.21) and the observed $\beta_0$ for $\Delta = 50$ data points (black symbols), together with the associated error, along the dichotomous line $x = y$ (blue line).

Figure 11.15 shows the variation of $\beta(t)$ compared with that of $u(t)$. For all strain rates, $\beta(t)$ changes very slowly when compared with $u(t)$, supporting the idea that superstatistics may be a good approximation for the system's dynamics. Again, peaks in $\beta(t)$ coincide with electrically calm regions, while the lowest values of $\beta$ are associated with regions of strong electrical activity. The range of $\beta$-values increases as the strain rate decreases, as does the amount of variation in $\beta$. Additionally, it can be inferred that localised Gaussian processes, as indicated by the stationary $\beta$-values (black dots), do not exhibit any significant clustering in time, occurring throughout the experiments for short periods with short intervals between. It should also be noted that $\beta$-values at the fastest strain rate fall rapidly to nearly zero at the point of failure.

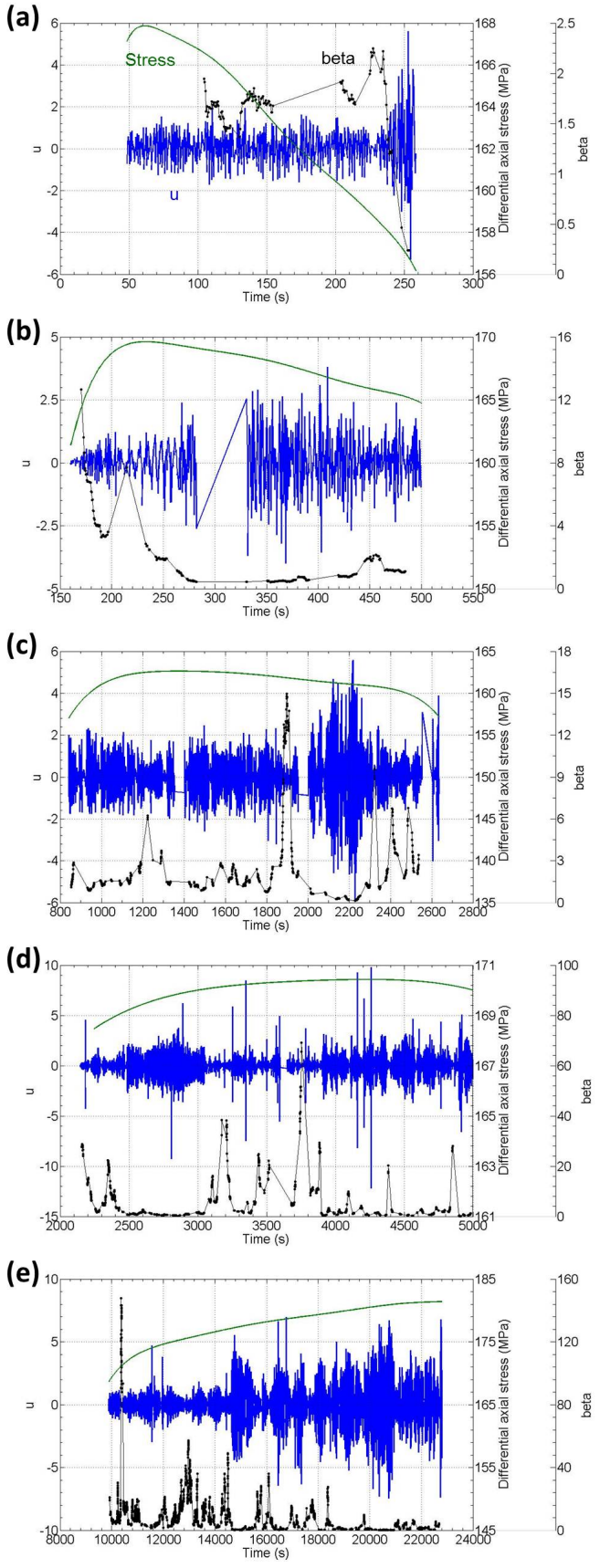


Figure 11.15: Evolution of $\beta$ (black dots), $u$ (blue line) and stress (green line) as a function of time, highlighting the slow variation in $\beta$ compared with the rapidly fluctuating electric current, $u$, for each of the five strain rates (a) $10^{-4}$ $s^{-1}$, (b) 5x$10^{-5}$ $s^{-1}$, (c) $10^{-5}$ $s^{-1}$, (d) 5x$10^{-6}$ $s^{-1}$ and (e) $10^{-6}$ $s^{-1}$.

### 11.4.2 Discussion

Electric current fluctuations show periods of strong activity among calmer periods across all five strain rates, with this behaviour becoming much more pronounced as the strain rate decreases. This illustrates the increasingly intermittent nature of deformation. As discussed in Chapter 9, the slower the incremental deformation, the more time is available for each avalanche of stress-relieving shear microcracks and frictional sliding events to subside and the internal stresses to relax.

Probability densities for the normalised electric current fluctuations exhibit non-Gaussian behaviour, well-modelled by a $q$-Gaussian distribution, at all five strain rates. Again, the excellent agreement between the non-extensive model and the data highlights the suitability of this non-equilibrium statistical mechanics approach for describing the electric current fluctuations and reflects the fractal nature of the electric current source network, i.e., the crack network. The greater degree of scatter around the $q$-Gaussian model function seen at faster strain rates may reflect the larger amount of deformation taking place between each 0.5 s fluctuation in electric current.

Variation in $q$-value with $\dot{\varepsilon}$ shows (a) an overall increase in interactions between current-producing events that occur during distributed cataclastic flow compared with those that occur during dynamic, localised shear failure, which reflects the transition from a single, large-scale event to several smaller-scale events with a greater degree of fragment-asperity interaction (e.g., Telesca, 2010a) and (b) that the difference in this degree of coupling across the range of $\dot{\varepsilon}$ is relatively small ($q = 1.74 \pm 0.04$, ignoring the elevated value at 5x10$^{-5}$ s$^{-1}$) as deformation becomes increasingly distributed throughout the sample, regardless of whether or not the sample fails macroscopically. This relatively constant degree of coupling may indicate that the same basic physical mechanism underlies both localised shear failure and distributed cataclastic flow; i.e, fracture and frictional sliding along shear faults. The lower $q$-value at $10^{-4}$ s$^{-1}$ is reflected in the probability densities, where fluctuations at the fastest strain rate exhibit behaviour that appears to be closer to a Gaussian distribution than those at slower strain rates. This is reflected in the slightly lower $q$-value obtained for this strain rate. However, the $q$-value is still relatively high; falling mid-way between that found for the combination of axial and shear macroscopic failure (at 10 MPa and $10^{-6}$ s$^{-1}$) and that found for distributed cataclastic flow (at 30 MPa and $10^{-6}$ s$^{-1}$), presented in Section 11.3. It can be deduced, therefore, that the suppression of tensile and then shear crack propagation drives the increase in $q$-value by allowing the samples to a reach a critical state far from equilibrium where deformation events self-organise and depend increasingly on each other, and that the $q$-value reflects the deformation style of the sample.

The elevated $q$-value at 5x10$^{-5}$ s$^{-1}$ may indicate imminent failure (see Section 11.7). This experiment was stopped before the sample failed but inspection of the deformed sample yielded evidence of a distinct and large (∼1 cm long) crack on one side of the sample

which would likely form the eventual fault plane. Thus, the elevated $q$-value may reflect the increased instability of the crack network and the increased probability of a large event occurring as the sample approaches failure. On the other hand, it may simply reflect an additional degree of interaction between brittle and semi-brittle deformation events at the transition.

Additionally, while the overall range of $q$-values over the full range of each environmental condition is the same (0.3 for both $P_c$ and $\dot{\varepsilon}$), the range excluding the condition at which transition from brittle to semi-brittle behaviour occurs (20 MPa; 5x10$^{-5}$ s$^{-1}$) is much smaller across the range of $\dot{\varepsilon}$ ($\pm$0.04) than across the range of $P_c$ ($\pm$0.125). Thus, the $q$-value reflects the increased influence of confining pressure on mechanical behaviour, as seen in the stress-strain curves (Section 7.2).

Results from the windowing procedure demonstrate that the electric current fluctuations do indeed relax back to equilibrium temporarily throughout each experiment at all the $\dot{\varepsilon}$ tested, indicating intermittency in deformation even under dynamic conditions. Additionally, the $\beta$-parameter does vary more slowly than the electric current fluctuations, meeting the requirement for super-statistical dynamics to be possible. However, the probability distribution $f(\beta)$ is not well-approximated by gamma distribution at the fastest strain rate; both a Gaussian and a Weibull distribution yield better approximations, implying a greater degree of randomness in the chaotic driving forces (or effective friction). Additionally, the observed $\beta_0$ is not as close to the predicted $\beta_0^{calc}$ at 5x10$^{-5}$ and 1x10$^{-5}$ s$^{-1}$ as at the other three strain rates. The predictions of $\beta_0^{calc}$ become increasingly accurate as the strain rate decreases, falling within the statistical error bars for $\beta_0$ at the two slowest strain rates. This reflects the increasing applicability of Beck-Cohen statistics to describing the dynamics of deformation as it transitions from dynamic failure to intermittent cataclastic flow. Arguably, therefore, super-statistical dynamics are representative of the dynamics of crustal deformation on a developed network of faults, and determining $\beta(t)$ from observed geoelectric time series may provide an excellent overall description of time-dependent variations in the crustal stress state.

The poor fit of the gamma distribution for $f(\beta)$ at the fastest strain rate and the poor predictions of $\beta_0^{calc}$ at 5x10$^{-5}$ and 1x10$^{-5}$ s$^{-1}$ may be explained by the timescale of the external forcing becoming increasingly closer to that of the dynamic variable as the strain rate increases; i.e., there is less time available time for the system to relax before the strength of the forcing changes. Interestingly, $\beta_0$ is exactly equal to $\beta_0^{calc}$ at the fastest strain rate, supporting the notion that the dynamic shear rupture is a large-scale equivalent to an individual shear event occurring during cataclastic flow. In other words, if deformation at the fastest strain rate is viewed as an individual event, deformation at the slowest strain rate can be viewed as the superposition of these individual events. This reflects the deduction in Chapter 9 that the electric current pulse seen at the fastest strain rate can be described as a precursor to a single shear failure event, while the series of pulses seen at the slowest strain rate reflect the series of localised cataclastic shear events.

Given the precursory nature of the signal preceding the single shear event, it is likely that individual pulses also precede individual avalanches of shear events during cataclastic flow. Experimental evidence of this was not obtained during this study as it requires a corresponding high-resolution time series of AE activity during cataclastic flow, but obtaining such evidence would be a useful avenue for future research.

## 11.5 Influence of Pore Fluid and Pore Fluid Salinity

### 11.5.1 Results

Figure 11.16 shows the time series of electric current fluctuations, $F(t)$, between electrode positions 3S and 3N for the fluid-saturated experiments shown in Figure 10.1, together with $F(t)$ between the same two electrode positions for the dry experiment at 30 MPa and $10^{-6}$ s$^{-1}$ [Experiment CM05] shown in the previous two sections. The regions of strong activity interwoven with periods of much calmer behaviour seen in the dry experiment (Figure 11.16 (a)) are also seen when water is present (Figure 11.16 (b)) but are less pronounced and of shorter duration. In addition, both the stronger fluctuations and the calm regions are an order of magnitude smaller in the presence of water than during the dry experiment. By contrast, the brine-saturated experiment (Figure 11.16 (c)) exhibited a fairly constant level of activity at around 5 pA (the same level as the calm regions in the dry experiment), punctuated by spikes of current up to five times larger than the main body of fluctuations. The frequency and magnitude of these spikes increased towards the end of the experiment, after the occurrence of a single region of stronger activity at about 24000 s. Similar spikes of current were seen in the water-saturated experiment, which again increased in frequency and magnitude towards the end of the test.

Figure 11.17 shows the probability density function, $p(u)$, of the normalised electric current fluctuations, $u(t)$, for these same experiments. For all the conditions shown, $p(u)$ exhibits a parabolic, Gaussian-like curve with extended, higher-probability, power-law tails. These distributions are well described by the non-extensive $q$-Gaussian function (Equation 2.7). The dry experiment [CM05] (Figure 11.17 (a)) and the water-saturated experiment [CM51] (Figure 11.17 (b)) are similar in shape and range. In comparison, the brine-saturated experiment [CM42] (Figure 11.17 (c)) has a much sharper distribution peak, greater scatter in the tails and a larger range of large values. Additionally, the distribution around the peak is very close to a Gaussian distribution for $-2.5 < u < 2.5$, indicating that the main body of fluctuations behaves randomly and it is the occurrence of the intermittent larger spikes during this experiment which pull the distribution towards $q$-Gaussian behaviour. The non-extensive parameters, $q$ and $B$, for each of the three experiments shown are presented in Table 11.3 and Figure 11.18. The $q$-value associated with electric current fluctuations under dry conditions is significantly higher at 1.78 than for wet conditions, which is 1.54 for both the saturated experiments. Analysis of only the dilatancy region

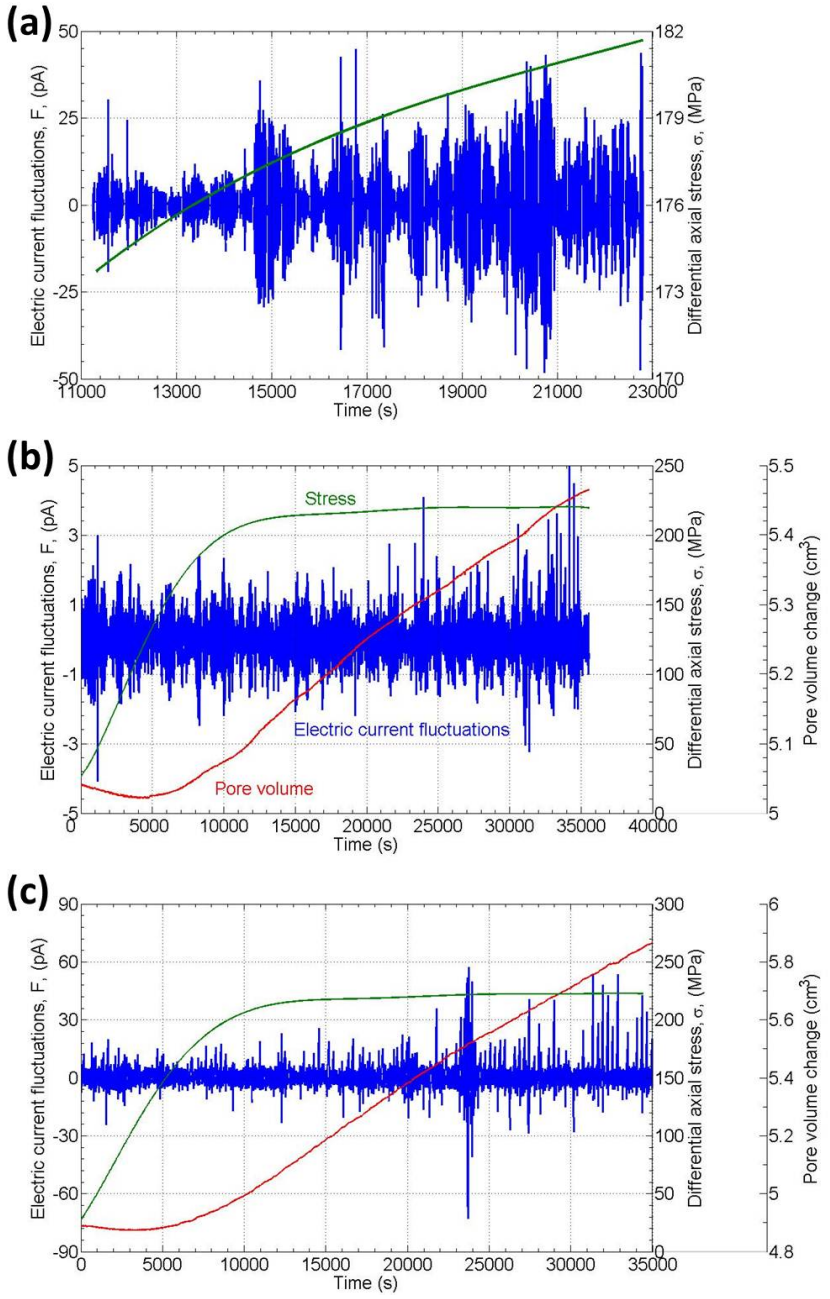


Figure 11.16: Electric current fluctuations (blue), differential stress (green) and pore fluid volume change (red) as a function of time, produced during triaxial deformation of specimens of Carrara marble at 30 MPa $P_{eff}$ and $10^{-6}$ $s^{-1}$ strain rate from the onset of current emissions above background for (a) dry conditions (between points A and B - see Figure 11.1) [Experiment CM05], (b) with de-ionised water as pore fluid [Experiment CM51] and (c) with Instant Ocean brine solution as pore fluid [Experiment CM42]. Both experiments with pore fluid were carried out at 50 MPa $P_c$ and 20 MPa $P_p$ and fluctuations for the whole time series are shown because the onset of electric current occurred at the onset of deformation.

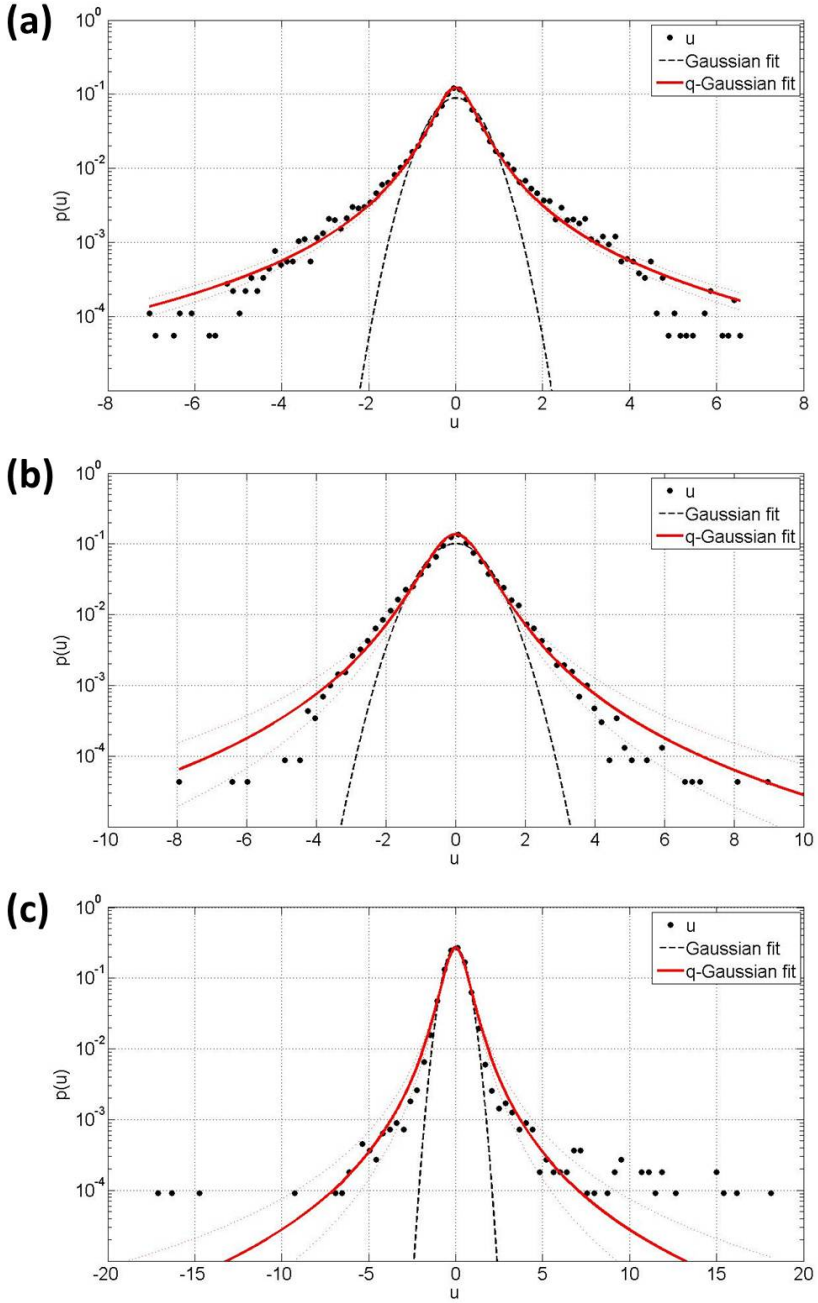


Figure 11.17: Probability density function of normalised electric current fluctuations, $u$, (black circles) and $q$-Gaussian fit (solid red line) with 95% confidence intervals (dashed red lines) and maximum likelihood Gaussian fit (dashed black line) for (a) dry conditions with $q = 1.78$ [Experiment CM05], (b) de-ionised water as pore fluid with $q = 1.54$ [Experiment CM51] and (c) Instant Ocean brine solution with $q = 1.58$ [Experiment CM42].

of the time series for the saturated tests yielded similar $q$-values to the corresponding full time series; exactly the same at 1.54 for the water-saturated experiment and a little higher at 1.60 for the brine-saturated experiment. Since the dry experiment was stopped at 1.7% strain whereas the saturated experiments were stopped at 3% strain, $q$-values for the saturated tests up to 1.7% strain were found in order to check that this did not impact the results. It was found that $q$-values at 1.7% strain are very similar to those at 3% strain; 1.53 for the water-saturated test and 1.52 for the brine-saturated test. Similarity in $q$-value between water-saturated samples and brine-saturated samples was also apparent on the other channel (4S-4N) recorded for these two experiments, where $q$-values are 1.62 and 1.59 respectively.

Table 11.3: Summary table showing the $q$-Gaussian $q$-value, $B$ and $\beta_0$ (theoretical $\beta_0^{calc}$ and observed $\beta_0$) with their associated errors.

| **Pore fluid** | $q$ | $\delta q$ | $B$ | $\delta B$ | $\beta_0^{calc}$ | $\delta\beta_0^{calc}$ | $\beta_0$ | $\delta\beta_0$ | $\Delta$ |
|---|---|---|---|---|---|---|---|---|---|
| none [3S-3N] | 1.78 | 0.04 | 5.27 | 0.22 | 6.41 | 0.31 | 6.81 | 0.39 | 75 |
| de-ionised water [3S-3N] | 1.54 | 0.09 | 1.82 | 0.15 | 2.65 | 0.27 | 2.68 | 0.57 | 75 |
| IO brine [3S-3N] | 1.54 | 0.09 | 2.65 | 0.08 | 3.87 | 0.25 | 3.53 | 0.51 | 75 |
| de-ionised water [4S-4N] | 1.62 | 0.16 | 3.33 | 0.72 | 4.62 | 1.10 | 4.37 | 0.69 | 75 |
| IO brine [4S-4N] | 1.59 | 0.20 | 4.50 | 1.84 | 6.35 | 2.72 | 3.76 | 0.41 | 75 |

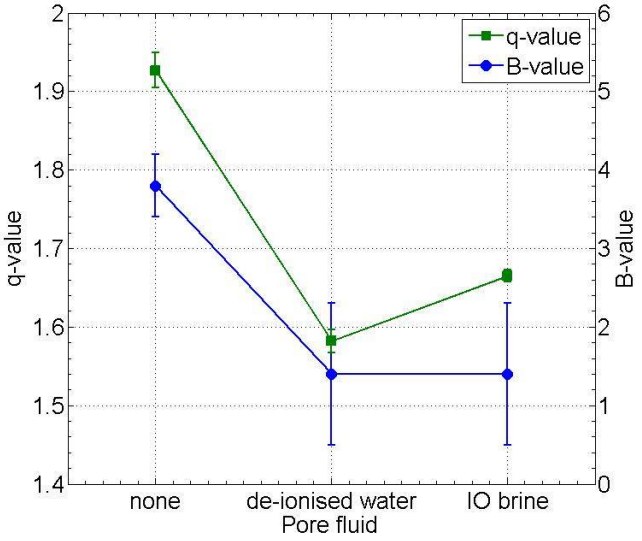


Figure 11.18: Non-extensive $q$-parameter and corresponding $B$-value with their associated statistical error for each pore fluid type, for current fluctuations between electrodes 3S and 3N.

For all three pore fluid conditions, kurtosis close to three was found for 25 ±9 % of the total number of windows used for all values of $\Delta$, confirming that $u$ in these windows is normally distributed (Figure 11.19). The normalised electric current fluctuations do therefore reach temporary local equilibrium during deformation under dry and saturated conditions, regardless of the salinity of the pore fluid. Accordingly the super-statistical $\beta$-parameter could be calculated for all the pore fluid conditions. Figure 11.20 shows the resulting distributions $f(\beta)$ for $\Delta = 75$, which can be modelled by a gamma distribution with mean value $\beta_0$.

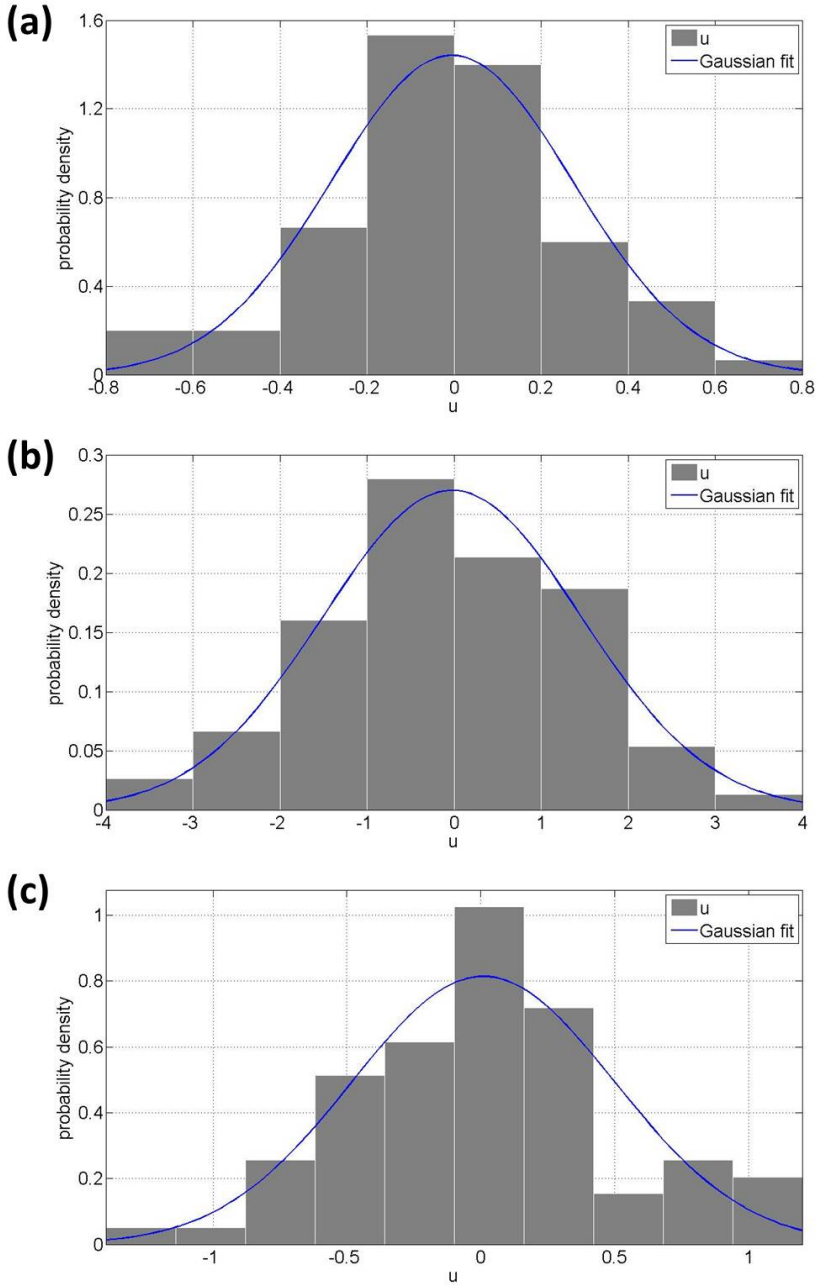


Figure 11.19: Maximum likelihood Gaussian behaviour (blue line) of the normalised electric current fluctuations, $u$, (shaded bars) for an example window at each pore fluid condition; (a) dry, (b) water-saturated and (c) saturated with Instant Ocean brine solution.

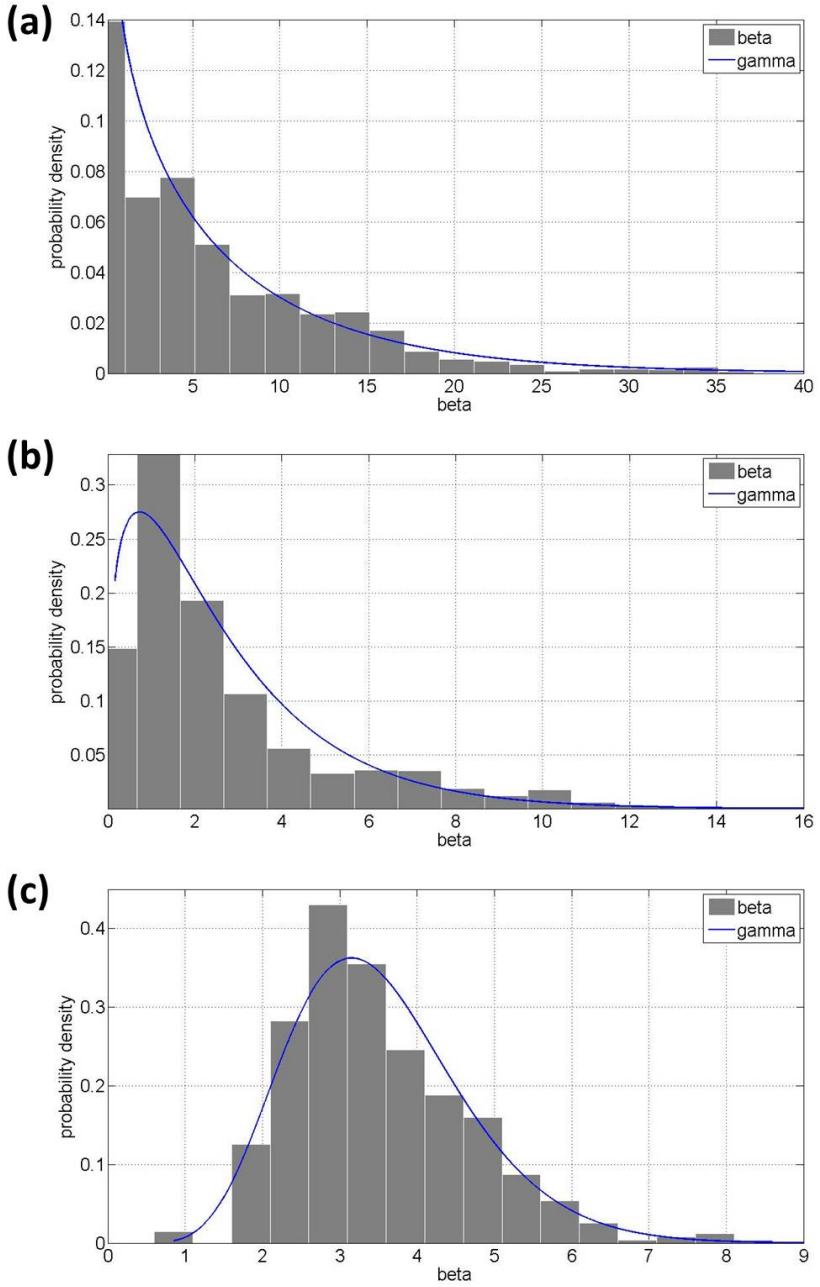


Figure 11.20: Histograms for $f(\beta)$ (shaded bars) with the maximum likelihood gamma fit (blue line) for each of the three pore fluid conditions; (a) dry, (b) water-saturated and (c) saturated with Instant Ocean brine solution.

The experimentally obtained $\beta_0$ values yielding the closest comparable fit to the model $\beta_0^{calc}$ values for all confining pressures tested (mean value of $f(\beta)$) were from the Gaussian windows of $u$ containing $\Delta = 75$ data points. These $\beta_0$ values are presented in Table 11.3 together with the theoretically predicted results, $\beta_0^{calc}$. An inspection of these results indicates that the experimentally obtained $\beta_0$ values are very close to the theoretically predicted $\beta_0^{calc}$, within the statistical error bounds, for all the pore fluid conditions (Figure 11.21). Both the theoretical and experimental $\beta_0$ values for the fluid-saturated experiments are similar to each other and around half those of the dry test. It should be noted that for all the pore fluid conditions $\beta_0$ determined from $\Delta = 100$ and $\Delta = 50$ data points yielded a similarly close fit to the model.

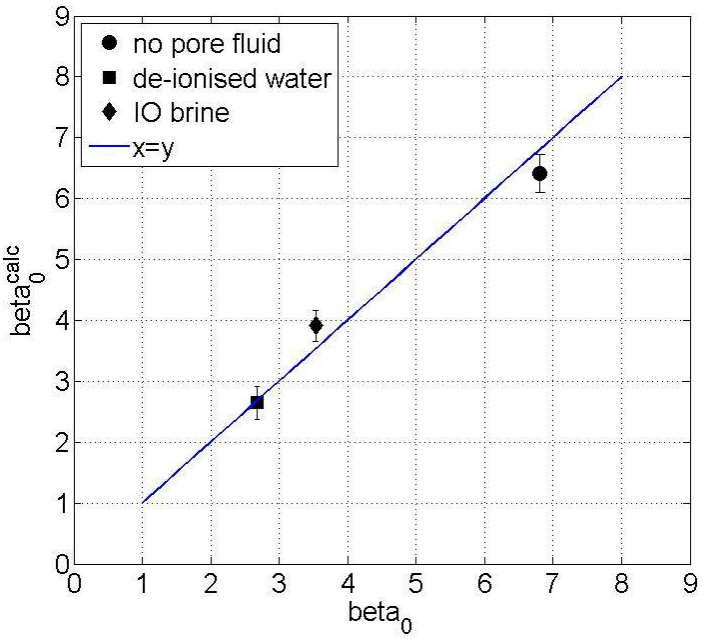


Figure 11.21: Comparison of $\beta_0^{calc} = (3-q)B$ (Equation 2.21) and the observed $\beta_0$ for $\Delta = 75$ data points, together with the associated error, along the dichotomous line $x = y$ (blue line).

Figure 11.22 shows the variation of $\beta(t)$ compared with that of $u(t)$. Clearly, $\beta(t)$ changes very slowly when compared with $u(t)$, a further indication that super-statistics is a good approximation for the system's dynamics for all the pore fluid conditions. Again, peaks in $\beta(t)$ coincide with electrically calm regions, while the lowest values of $\beta$ are associated with regions of strong electrical activity. For dry and water-saturated conditions, $\beta(t)$ peaks approximately every 1000-2000 s, whereas under brine-saturated conditions the variation is much slower with peaks approximately every 2000-5000 s. Additionally, it can be inferred that localised Gaussian processes, as indicated by the stationary $\beta$ values (black dots), occur throughout the experiments and do not exhibit any clustering in time for the dry and water-saturated conditions. By contrast, under brine-saturated conditions, $\beta$-values appear to occur more frequently at the beginning and end of the experiment, with relatively few $\beta$-values between 15000 and 32000 s. $\beta$-values for the dry experiment show an overall decrease from an early spike of ∼180 to less than eight at the end of the test, whereas they fluctuate relatively consistently below 20 for the entire water-saturated test

and below eight for the entire brine-saturated test.

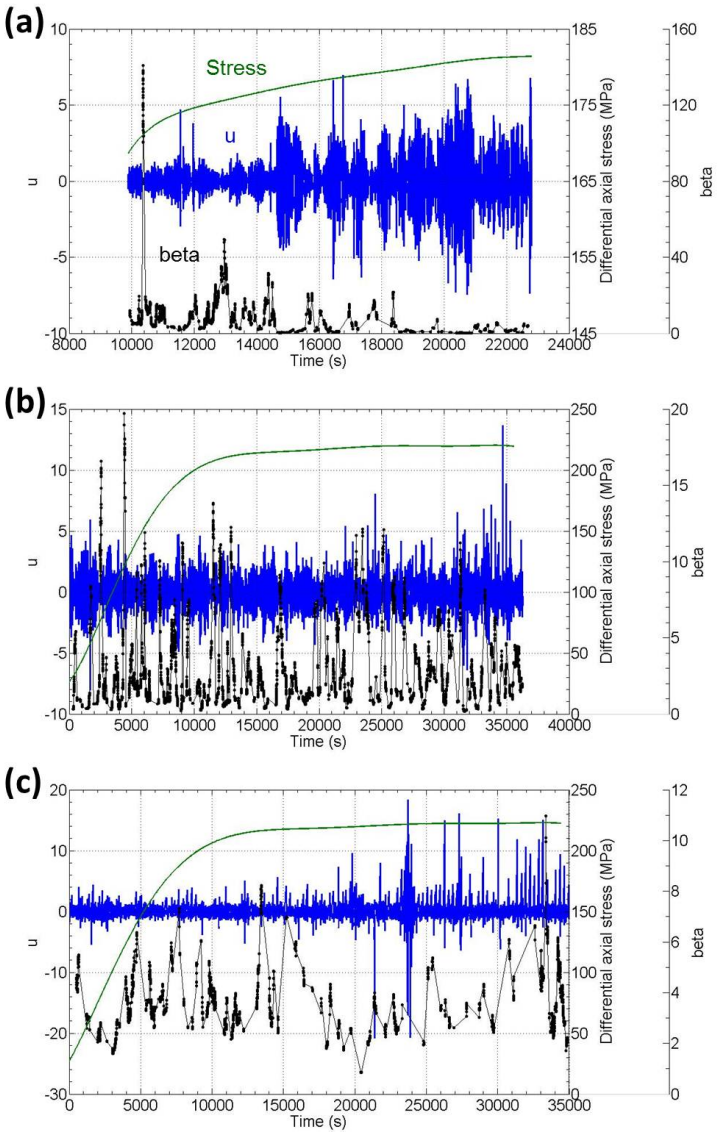


Figure 11.22: Evolution of $\beta$ (black dots), $u$ (blue line) and stress (green line) as a function of time, highlighting the slow variation in $\beta$ compared with the rapidly fluctuating electric current, $u$, for the three pore fluid conditions; (a) dry, (b) water-saturated and (c) saturated with Instant Ocean brine solution.

### 11.5.2 Discussion

In the presence of a pore fluid, regions of stronger electric current fluctuations are less distinct and of shorter duration than in the dry case, with the presence of an ionic brine solution having a greater effect on the suppression of this activity than the presence of water. This is likely due to the flow of fluid under a pressure gradient having a masking effect. As the fluid flows, the diffuse outer layer of ions in the EDL (Section 3.5.2.1) is free to move, leading to a continuous separation of charges along the EDL while the fluid flows. This masking effect is stronger in the presence of ionic brine than deionised water because the concentration of ions is very much higher (six orders of magnitude separate

their conductivities) and also because the concentration of ions in deionised water depends almost completely on the number of charged particles released into the crack network's void space. Therefore, the relative contribution of charges from solid-state mechanisms to the EDL is much lower in the brine solution than in deionised water and, as a result, the current generated due to the flow of the ionic brine solution is less affected by fluctuations in the electric field generated by solid-state effects than that due to the flow of deionised water. The observed spikes or pulses may reflect sudden changes in the local pressure gradient during episodes of microcracking, causing a sudden change in the fluid flow rate. The order of magnitude difference in the size of the fluctuations between the dry case and the water-saturated case may be accounted for by the lubricating effect of fluid flowing between crack surfaces, allowing sliding to occur with much less fragmentation along the rough surfaces and the release of fewer charges from disordered surface layers and, therefore, smaller fluctuations in current.

Under all three pore fluid conditions, the probability densities for normalised current fluctuations are of a similar non-Gaussian form, which is well-modelled by the $q$-Gaussian function. This demonstrates the suitability of the non-extensive approach for describing deformation effects in both dry and fluid-saturated rocks and reflects the fundamental connection between the fluid flow network and the electrical pathways; the development of the fractal pore structure and its connectivity. It is this that underpins the fluctuations of electric current observed during deformation in both dry and fluid-saturated rocks.

The $q$-value yielded is very similar for both types of pore fluid for both the recorded channels and significantly lower (by $\sim$0.2) than that seen in the dry case. However, this difference may simply reflect the greater degree of strain that the fluid-saturated samples were subjected to (nearly twice that of the dry sample) and indicate imminent failure (because $q$ is close to or less than 1.6; see Section 11.7), rather than showing any particular influence from the presence of pore fluid. The fact that the $q$-values were very similar for both types of pore-fluid supports this notion as, if the pore fluid were to have an effect on $q$, a difference in the $q$-value observed between the two types would be expected due to the large differences in their composition and conductivity. If this is the case, then the $q$-value determined from the distribution of normalised electric current fluctuations reflects the underlying state of damage in, and the stability of, the rock sample during deformation and this information can be extracted from the electric current time series regardless of the presence of pore fluid or pore fluid type. Experimental confirmation of this conjecture was not possible as the only test conducted under similar dry conditions and subjected to the same degree of strain as the fluid-saturated samples was Experiment CM07. During this experiment velocity surveys taken were every two minutes and so nearly half the data had to be removed from the time series, precluding the acquisition of an accurate $q$-value. If a dry experiment taken to this degree of strain were to yield similar $q$-values as that obtained for the dry case presented here, an alternative explanation for the difference between the dry and fluid-saturated cases may be the pre-existing crack network in the fluid-saturated samples. Its presence would lead pre-existing cracks to grow longer during deformation

rather than new cracks to form. Thus, the lower $q$-value may reflect the influence of larger, more randomly distributed cracks on the overall crack network, drawing the $q$-value closer to equilibrium. This explanation also implies that the $q$-value reflects the geometry of the crack network regardless of pore fluid presence or type.

This notion, that the $q$-value provides useful information regarding the dynamics of the crack network regardless of pore fluid condition, is supported by the results of the windowing procedure. These show that the $\beta$-parameter fluctuates much more slowly than the electric current fluctuations and also closely follows a gamma distribution under all three pore fluid conditions. Thus, super-statistical dynamics can account for the observed electric current fluctuations and reflect the episodic nature of cataclastic flow regardless of the presence or type of pore fluid.

## 11.6 Variability of $q$-value Across Identical Conditions

The non-extensive $q$-value showed some variation across samples deformed under identical conditions (Figure 11.23). This was attributed to the natural variability between samples in terms of their initial electronic structure, impurity content, grain assembly and fracture network, together with how these developed during deformation. In most cases, the $q$-value differed by $< 0.2$. However, at the slowest strain rate, the variation was greater at $\sim 0.45$. Average $q$-values for each strain rate are presented in Table 11.4.

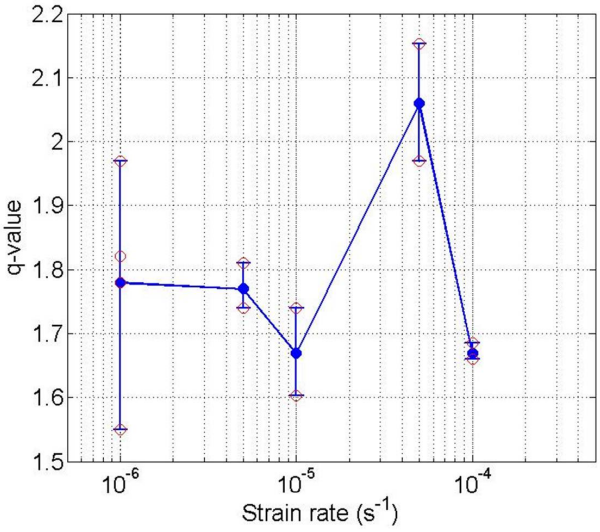


Figure 11.23: Average $q$-value for samples deformed under identical conditions as a function of strain rate. Error bars show the full range of $q$-values at each strain rate and the individual values are presented as open red circles.

Table 11.4: Average $q$-values for each strain rate

| $\dot{\varepsilon}$ ($\mathbf{s}^{-1}$) | $q$ | $dq$ |
|---|---|---|
| 1x10$^{-4}$ | 1.67 | 0.34 |
| 5x10$^{-5}$ | 2.06 | 0.21 |
| 1x10$^{-5}$ | 1.67 | 0.15 |
| 5x10$^{-6}$ | 1.77 | 0.16 |
| 1x10$^{-6}$ | 1.72 | 0.08 |

## 11.7 Evolution of $q$-value with Deformation

One important aspect of the $q$-parameter, particularly with regard to seismic hazard assessment and earthquake forecasting, is its potential as a precursor. Can the evolution of the $q$-parameter provide information about the changing state of the system during deformation and even provide an indication as to whether fracture may be imminent? In order to investigate this, each time series of normalised electric current fluctuations ($u$) was divided into 19 moving windows of length $N$ data points, with each new window incrementing by $N/2$ data points. The probability density was computed for each window and modelled with a $q$-Gaussian function, as described in Section 11.1, to obtain the corresponding $q$ and $B$ values. To ensure as much data as possible was available for fitting the $q$-Gaussian model, this analysis was done only for the experiments carried out at $10^{-6}$ $s^{-1}$ strain rate as each window in these experiments contained >1000 data points.

### 11.7.1 Influence of macroscopic failure

#### 11.7.1.1 Results

Figure 11.24 shows the $q$-value evolution for samples deformed in the brittle regime (< 30 MPa). Figures 11.24 (a) and (b) show $q$-values for two samples that failed macroscopically, deformed at $P_c$ of 10 MPa [sample CM08] and 20 MPa [sample CM65] respectively. Sample CM65 failed in shear, while sample CM08 failed axially. In both cases, it is apparent that there is a minimum $q$-value of ∼1.4-1.5 several minutes before failure (25 minutes in the case of CM08 and almost 2 hours in the case of CM65). This is followed by a rapid and significant rise in $q$-value of 0.3-0.5 to a peak of ∼1.8-1.9 at the onset of failure, i.e., the point at which the differential stress decrease accelerates to failure at the end of the strain softening region. The $q$-value then drops again slightly by 0.05-0.1 at the stress-drop itself. Overall, the $q$-value fluctuates during both experiments, rising and falling in pulses, with both exhibiting a maximum very close to the peak stress. After the peak, $q$-values at 10 MPa fluctuate consistently between 1.7 and 1.9 during the strain softening region before dropping quickly from 1.85 to 1.46 as failure approaches. This behaviour contrasts with that at 20 MPa, where $q$-values decrease steadily in small pulses which rise by 0.05 and fall by 0.15 as the applied differential stress remains constant at 145 MPa. The range of $q$-values is wider for the lower confining pressure; 0.72 at 10 MPa compared with 0.49 at 20 MPa, as is the pre-failure rise; 0.46 at 10 MPa compared with 0.29 at 20 MPa. The

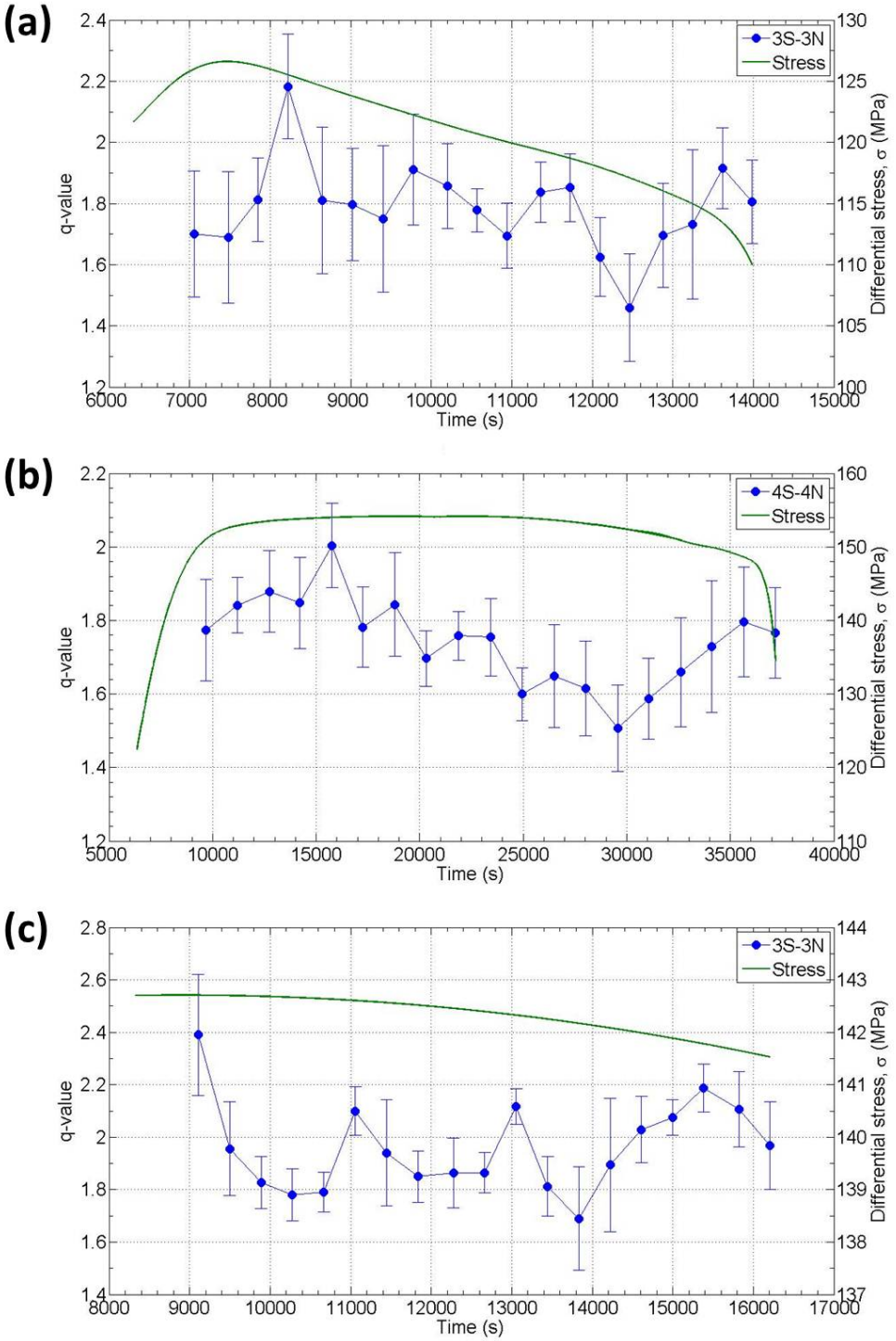


Figure 11.24: The evolution of $q$-value with its associated statistical error (blue circles) and stress (green line) over time for samples deformed in the brittle regime (< 30 MPa) at (a) 10 MPa with macroscopic failure [Experiment CM08], (b) 20 MPa with macroscopic failure [Experiment CM65], and (c) 20 MPa without macroscopic failure [Experiment CM21].

pre-failure rise at 20 MPa is very steady in comparison to both the fluctuating decrease preceding it and the slightly fluctuating pre-failure rise at 10 MPa. It should also be noted that starting $q$-values for the lower confining pressure are smaller (1.7-1.8) than those for 20 MPa (1.8-1.9), possibly indicating a less fractured system or system with smaller cracks at the higher confining pressure due to the effect of increased microcrack suppression.

Figure 11.24 (c) shows $q$-values for another sample deformed at 20 MPa $P_c$ which did not fail macroscopically [sample CM21] as it was deformed to only 1.34%, compared with 3.45% [sample CM65]. The significant increase in damage sustained by sample CM65 compared with sample CM21 can be seen in Figure 11.25. The starting $q$-value in experiment CM21 occurs at peak stress and is the maximum value (2.4 - significantly bigger than both CM65 and CM08). It appears that the $q$-values then relax to ∼1.8 before rising again to 2.1. This relax-rise then repeats itself, although relaxing and rising to slightly higher values of ∼1.85 and 2.12. The subsequent rapid decrease to a minimum of 1.69 is then followed by a significant rise of 0.5 rather than relaxing, before decreasing again at the end of the test. This final behaviour is similar to that described above of the two samples that did fail, but with one key difference: the $q$-value did not drop below 1.6. These results indicate that, in the brittle regime and at a strain rate of $10^{-6}$ $s^{-1}$, the $q$-value drops below 1.6 at the point of imminent failure (i.e., the point at which strain softening begins to accelerate) and then increases from ∼1.5 to ∼1.8 at the point of failure. It should also be noted that experiment CM21 shows greater resolution as it was nearly 1/3 shorter in comparison to experiment CM65 but the same number of windows were used for this analysis.

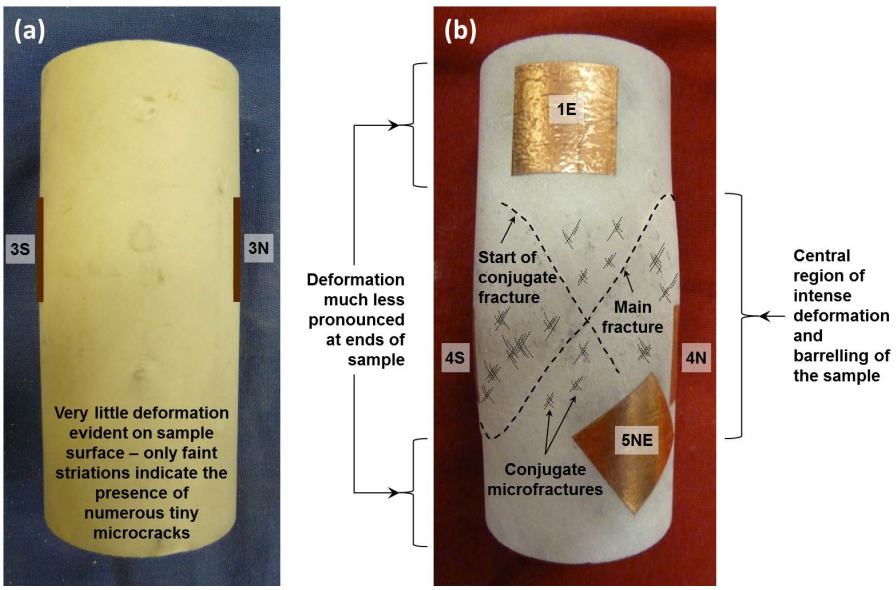


Figure 11.25: Photograph showing (a) sample CM21 after deformation to 1.34% strain, which falls into deformation category 7 and (b) sample CM65 after deformation to 3.45% strain, which falls into deformation category 3. The increased degree of damage suffered by sample CM65 is clearly apparent. Electrodes are labelled with their position codes.

#### 11.7.1.2 Discussion

The observed behaviour of the $q$-parameter as failure approaches, a minimum followed by recovery, at both 10 and 20 MPa has the appearance of a precursory change (see Chapter 3). These features coincide with similar features observed in the behaviour of the electric signals themselves. In the sample deformed at 10 MPa [CM08], the minimum in $q$-value at ∼12500 s coincides with the small but sudden drop in electric current and $V_P$ (Figure 7.14 (c)), as well as the first AE $b$-value minimum (Figure 7.16 (a)), while the recovery corresponds to the recovery of both the $b$-value and the electric current. Although there is no second minimum seen in the $q$-value evolution, the second minimum seen in the seismic $b$-value immediately prior to failure corresponds to the peak observed in the recovered $q$-value. In the sample deformed at 20 MPa [CM65], the $q$-value minimum at ∼30000 s coincides with the minimum in electric current seen during strain softening, just before 2.5% strain (Figure 7.8), and its recovery corresponds to the recovery of the electric current signal from 2.5% strain to the peak at failure. In both cases, these features are seen as the stress drop accelerates with respect to the stress rate (Figures 7.17 (a) and (b)) and are related to the localisation of cracks along the final failure surfaces. That is, the transition point at which distributed quasi-static crack growth and slip (due to negative feedback mechanisms) becomes dynamic crack coalescence and concentrated fault development (due to positive feedback mechanisms) (Main et al., 1993; Henderson and Main, 1992), as described in Section 4.5. An additional feature of $q(t)$ is the peak observed early on during deformation very close to the point of peak stress. It marks the end of the initial yield (i.e., the precursory strain release due to permanent deformation) at 20 MPa and the start of strain softening (i.e., the precursory stress drop) at 10 MPa.

Taken as a whole, these features correspond to the stages of stress intensity ($K$) evolution during deformation, as described by Main et al. (1989; 1993) and Meredith et al. (1990), and implies that the $q$-parameter obtained from the electric current fluctuations captures both the intermediate-term peak in stress intensity associated with peak stress, reflecting the transition from strain hardening to strain softening, and the short-term peak reflecting the transition from quasi-static fracture and slip to dynamic rupture (Figure 11.26). Additional experimental data at these conditions ($P_c \leq 20$ MPa and $\dot{\varepsilon} = 10^{-6}$ s$^{-1}$) would enable the proposed link between $q$ and $K$ to be tested further, since the duration of the intermediate-term peak in stress intensity (and, by extension, the $q$-value) is expected to have a duration that scales with the final stress drop (Main and Meredith, 1989). However, the repeat experiments carried out to test this were unusable for the reasons described in Section 8.1. Observation of this predicted two-stage anomaly in the $q$-value evolution for electric current fluctuations is significant as it provides additional supporting evidence that (a) the electric current fluctuations are a response to a developing fractal network of cracks and (b) the $q$-value effectively describes this development.

Physically, the $q$-value is a measure of the interactions between current-producing events, which have been associated with crack growth (Section 7.5). Its fluctuating evolution

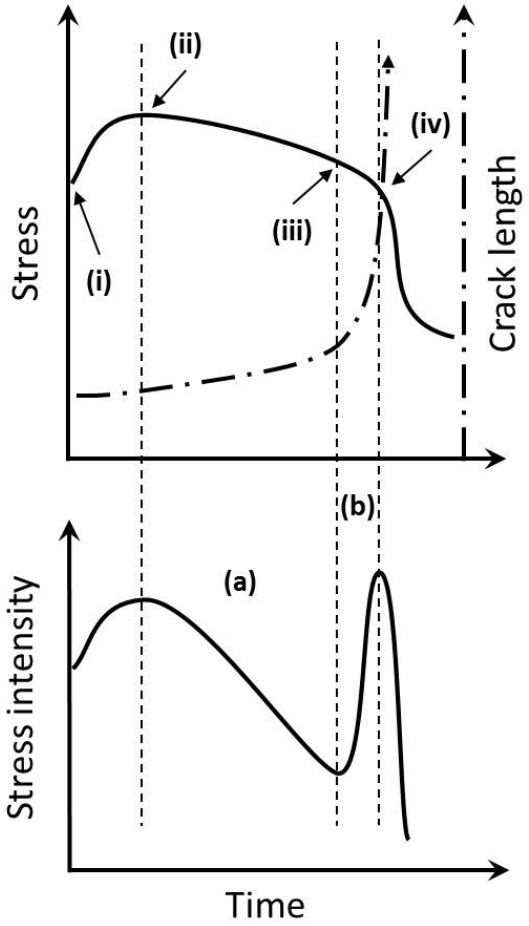


Figure 11.26: Effect of stress, $\sigma$ combined with an accelerating crack length, $x$, (top) on stress intensity factor, $K$ (bottom) during triaxial compression ($K \propto \sigma\sqrt{x}$). Redrawn from Main et al. (1993). Point (i) is the elastic limit, (ii) is peak stress, (iii) is fracture localisation along the final failure surface(s) and (iv) is the acceleration of fracture through final asperities sustaining the system, resulting in dynamic failure. In region (a) distributed fracture and slip serves to reduce the overall stress intensity in the sample, and in (b) crack localisation causes the overall stress intensity to increase along the failure surface(s) as stress concentrates increasingly on the strong asperities between cracks.

therefore highlights variations in the degree of correlation between the growing cracks throughout deformation. The higher the $q$-value, the higher the degree of correlation between the growing cracks and the higher the probability of cracks coalescing into a larger event. This is also true of the stress intensity. Quasi-static, sub-critical crack growth in compression leads to a local build-up of stress intensity as the number and length of defects on which stress can concentrate increases in any particular region. As they grow in number and length, these defects become increasing dependent on each other. At a critical crack density (peak in both interaction and stress intensity), neighbouring cracks interact and coalesce, triggering larger events, which temporarily relieve the local stress concentration and reduce the degree of correlation between future events in that region. Thus, the stress intensity and the electric current $q$-value are fundamentally linked through their relationship with the developing crack network.

Mechanically, then, the fluctuations in electric current $q$-value throughout the regions of

strain softening (10 MPa and 20 MPa) and cataclastic flow (20 MPa) reflect fluctuations in the local stress intensity between the electrode pair as localised avalanches of fracture and slip events cause local relaxations in the stress concentration. In the brittle regime (10 MPa), the increase in $q$-value (and, by association, the stress intensity) during the initial yield is likely related to the nucleation of new cracks, peaking at the critical density at which these new cracks begin to interact with each other. The subsequent fluctuation around a relatively constant value ($1.7 < q < 1.9$) throughout the steady strain softening phase reflects an overall relatively consistent degree of interaction, related to quasi-static episodes of distributed but dynamic crack growth and linkage, which build and relieve local stress intensity. The sudden decrease in interactions (from $q > 1.8$ to $q < 1.5$) relates to large-scale, but still sub-critical, crack coalescence along the final failure surface. There is then a rapid increase in interactions (from $q < 1.5$ to $q > 1.9$) as stress concentrates on the remaining asperities supporting the sample and any damage to one increases the stress intensity on others and their dependency on each other, until they become critically correlated as the stress intensity on the final few asperities exceeds the fracture toughness of the material and initiates dynamic failure. Similar behaviour is seen during the initial yield and strain softening stages at the brittle to semi-brittle transition (20 MPa), but during the cataclastic flow phase there is gradual decrease in correlations, perhaps reflecting the additional contribution of frictional sliding and local dislocation glide to the stress relaxation process.

Seismic $b$-values have been experimentally correlated with stress intensity, $K$, as $b \propto 1/K$ (Meredith and Atkinson, 1983; Main et al., 1989; 1993; Meredith et al., 1990). At 10 MPa, the fluctuating stress intensity behaviour is also reflected in the AE $b$-value evolution (Figure 7.16 (a)). The $b$-value reduces significantly following the onset of dilatancy and then exhibits an inflexion, with a first minimum that coincides with the electric current $q$-value maximum. The inflexion consists of two minima and two maxima and may represent the dominance of quasi-static crack growth and slip during steady strain softening (Main and Meredith, 1989). This is followed by the main minimum indicating crack coalescence along the failure surfaces, which is then followed by a further small maximum and the second minimum immediately prior to fracture, i.e., two short-term precursory indicators of crack coalescence occurring during region (b) in Figure 11.26. These fluctuations highlight the complicated evolution of stress intensity during triaxial deformation of Carrara marble and differences between $q(t)$ and $b(t)$ are apparent. Most noticeably, the main $b$-value minimum which reflects a stress intensity maximum coincides with the main $q$-value minimum, which should reflect a stress intensity minimum based on the arguments given above. However, these differences may be accounted for by localisation effects due to the sensor arrangement. Piezoelectric sensors were arranged in order to detect acoustic emissions occurring throughout the whole sample, whereas the electrodes were arranged to record electric current flow through a specific central region of the sample. Thus, the observed $b$-value reflects overall stress intensity variations, whereas the observed $q$-value reflects stress intensity variations occurring in a localised region.

### 11.7.2 Influence of damage sustained within the sample

#### 11.7.2.1 Results

Experiment CM65 measured three channels of current flow and illustrates how the final $q$-value can indicate the level of damage within a sample. The more damage the sample has sustained, the lower the final $q$-value of the electric current fluctuations in that region (Table 11.5). For CM65, the two channels recording current flow within the central damage zone, (1) horizontally across the main fault plane in the dip direction (4S-4N) and (2) almost exactly conjugate to the main fault plane dip angle but offset by 45° to the strike (5NE-2SW), yielded $q$-values within 0.02 of each other. By contrast, the channel recording current flow across the top of the sample (1E-1W) where deformation is much less pronounced (very little damage was evident on the sample surface and certainly no major faults) returned a $q$-value higher by 0.2.

Table 11.5: Summary table showing the $q$-Gaussian $q$-value, $B$ and $\beta_0$ (theoretical $\beta_0^{calc}$ and observed $\beta_0$ for the three channels recorded during Experiment CM65

| Electrode pair | $q$ | $dq$ | $B$ | $dB$ | $\beta_0^{calc}$ | $d\beta_0^{calc}$ | $\beta_0$ | $d\beta_0$ | $\Delta$ |
|---|---|---|---|---|---|---|---|---|---|
| 1E-1W | 1.72 | 0.12 | 7.02 | 0.56 | 9.01 | 0.97 | 8.83 | 0.21 | 175 |
| 4S-4N | 1.53 | 0.04 | 1.75 | 0.09 | 2.57 | 0.15 | 2.64 | 0.69 | 50 |
| 5NE-2SW | 1.51 | 0.04 | 1.68 | 0.06 | 2.50 | 0.11 | 2.47 | 0.58 | 100 |

Figure 11.27 shows the $q$-value evolution for the three channels of electric current flow recorded during Experiment CM65. As with the overall $q$-values, the two channels recording current flow within the central damage zone (4S-4N and 5NE-2SW) exhibit lower $q$-values than 1E-1W. Initially, channels 1E-1W and 4S-4N show a similar pattern in the evolution of $q$, rising and then falling between 10000 and 20000 s, although values for 1E-1W are higher than 4S-4N by $\sim 0.4$. Conversely, 5NE-2SW shows an opposite trend, falling and then rising over the same time period with values $\sim 0.2$ less than 4S-4N. At 20000 s, $q$-values for all three channels coincide briefly before 1E-1W rises significantly. During peak stress (20000-28000 s), all three channels show an overall decrease in $q$, with 4S-4N and 5NE-2SW following each other closely while 1E-1W is again higher by 0.4, falling to a minimum value $< 1.6$ between 28000 and 30000 s. At this point all three channels coincide again, rising together as failure approaches. At 33000 s, where the strain softening begins to accelerate, 1E-1W and 4S-4N continue to rise together to a maximum of 1.8, whereas the channel recording current flow conjugate to the forming fault plane (5NE-2SW) rises steeply in comparison, reaching a maximum $> 2$ at the point of failure.

#### 11.7.2.2 Discussion

Given the arguments in Section 11.7.1.2, differences in $q$-value evolution (i.e., the evolution of crack network correlations) for electric current flow between two electrodes at different orientations through the sample reflects localised differences in stress intensity evolution.

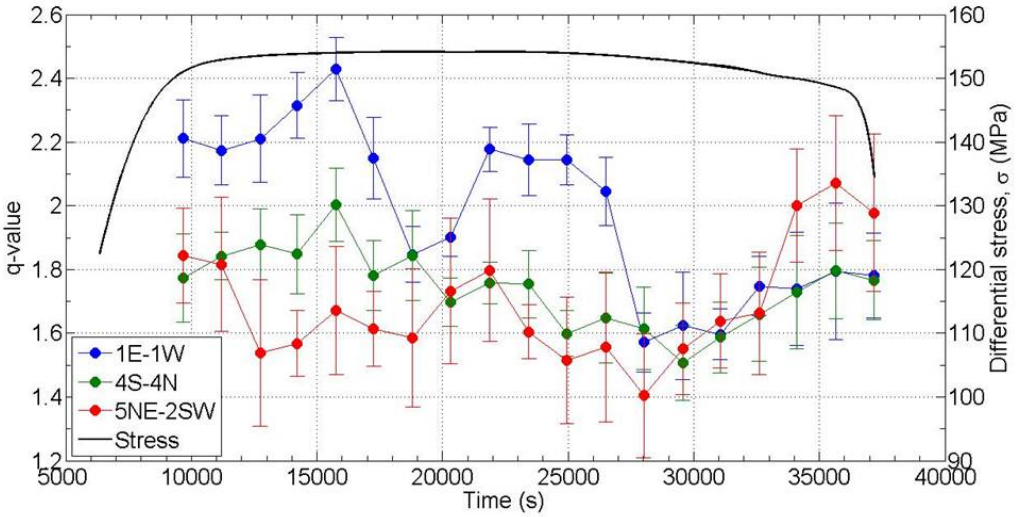


Figure 11.27: The evolution of $q$-value over time for each channel of current flow recorded during Experiment CM65: 1E-1W (blue circles), 4S-4N (green circles) and 5NE-2SW (red circles), together with stress (black line). Error bars show the 95% statistical error in $q$.

The observed differences can be explained as follows: Crack nucleation is initially evenly distributed throughout the sample. However, stress concentrates more intensely in the central part of a sample under compression (Hawkes and Mellor, 1970; Paterson and Wong, 2005), causing the nucleating cracks in this region to grow longer than those nucleating in the ends of the sample. Thus, a greater degree of correlation exists between the smaller, more numerous microcracks in the ends of the sample than between the somewhat fewer but longer microcracks in the central part of the sample, accounting for the higher initial $q$-value at the top of the sample (1E-1W) than in the centre (4S-4N and 5NE-2SW). Localised crack coalescence (drop in $q$-value) is initially observed on the channel oriented almost perpendicular to the final shear failure plane (5NE-2SW), perhaps reflecting electric polarisation across the preferential shear failure angle as microcracks coalesce locally on conjugate shear planes in the central part of the sample, while continued nucleation (increasing $q$) is seen on the other two channels. The large drop in $q$ at the top of the sample (1E-1W) may relate to an initial coalescence of cracks at the top of the final failure plane, also reflected in the smaller reductions on the other two channels. Stress intensity then builds back up in the top of the sample, while in the centre of the sample episodic avalanches of cracking and sliding during cataclastic flow build and relieve the stress intensity. The overall degree of interaction decreases, reflecting gradual crack growth and coalescence along the final failure plane as well as distributed slip. When full localisation and coalescence along the whole failure surface occurs, there is a rapid drop in $q$ at the top of the sample and the degree of correlation becomes relatively consistent between the three channels, although the $q$-value is lowest between 5NE and 2SW. As the stress intensity builds up on asperities supporting the sample, $q$-values on channels 1W-1E and 4S-4N follow each other closely, but increase much more significantly between 5NE and 2SW. Again, this probably reflects crack interaction on and electrical polarisation across the preferential shear failure angle.

## 11.8 Conclusion

Electric current fluctuations recorded during triaxial deformation of Carrara marble exhibit behaviour similar to that seen in turbulent flows; periods of strong activity interspersed with calmer regions. Although this behaviour is typical across the full range of experimental conditions tested, it is more pronounced at slower strain rates, reflecting the increasingly intermittent nature of the current-producing events as the rate of deformation slows. The non-Gaussian statistical behaviour exhibited by the normalised fluctuations is well-modelled, at all the conditions tested, by the non-extensive $q$-Gaussian function and the excellent agreement between data and model illustrates the fractal nature of the current-generating events. These events are also highly correlated, with non-extensive $q$-values greater than one for all experimental conditions, indicating the presence of long-range interactions between them. Since intermittent activity on a highly correlated, fractal crack (or defect) network is characteristic of the physical processes of deformation under triaxial compression (microcracking, frictional sliding and crystal plasticity), these findings provide strong evidence that the source of the electric current is indeed activity on the developing fractal crack (or defect) network itself.

Variation with experimental condition of the $q$-value itself reflects the different deformation regimes, with brittle behaviour observed when $1.5 < q < 1.7$, semi-brittle when $1.7 < q < 1.8$ and the transition between two when $1.8 < q < 2$. These apparently characteristic $q$-values indicate greater coupling between friction-dominated deformation events in the semi-brittle regime, which are smaller and more evenly distributed, than fracture-dominated events in the brittle regime, which are larger and more localised. Elevated $q$-values at the boundary between brittle and semi-brittle behaviour reflect not only the coupling between events of either mechanism, but also a further increase in coupling as brittle and semi-brittle mechanisms combine and compete. Microstructural observations (Schubnel et al., 2006b) indicate strong interactions between intra-crystalline plastic deformation (twinning and dislocation glide) and brittle deformation (microcracking and cataclastic flow) at the brittle-ductile transition. Reduced $q$-values in the presence of pore fluid indicate fluid flow through and deformation on a pre-existing network of cracks, where further deformation increases their length rather than nucleating new cracks and stress corrosion effects encourage crack propagation at the expense of crystal plasticity. This network evolves into one with fewer, longer, less coupled cracks than that seen in an initially uncracked sample deformed under dry conditions.

Normalised electric current fluctuations are very well described by super-statistical dynamics (Beck, 2001; Beck and Cohen, 2003) at all tested confining pressures, at the slowest strain rates ($\leq$ 5x10$^{-6}$ s$^{-1}$) and also at the most dynamic rate (10$^{-4}$ s$^{-1}$). That is, conditions found in the shallow, seismogenic crust and during fault rupture itself. Superstatistics provides a dynamic reason for the validity of Tsallis statistics to systems with a fluctuating energy dissipation rate, which is effectively modelled by the fluctuating $\beta$ (Beck, 2001). In the context of a deformation experiment, the system's external driving

force is stress. Inside the specimen, this is reflected in the localised stress intensity as stress concentrates around cracks and other microstructural defects. Thus, the energy dissipation is governed by stress intensity variations that drive the physical mechanisms of deformation and the corresponding fluctuations in electric current. Therefore, in marble samples subject to triaxial compression, the measured electric current fluctuates in response to intermittent energy dissipation and is driven to varying temporary local equilibria during deformation by the variations in stress intensity. This behaviour is similar to the avalanche-like behaviour of deformation seen in brittle fracture and plasticity in the laboratory (Sammonds, 2005), in self-organised criticality models (Caruso et al., 2007) and in real earthquakes (Caruso et al., 2007; Main and Naylor, 2010). It provides additional evidence to support the notion that the electric current signals are caused by the intermittent avalanches of mechanical relaxations, and that the observed long-lasting signal is generated by the superposition of signals from all these intermittent but simultaneously occurring local electrification events and their continuous evolution with deformation.

Thus, the analysis presented in this chapter demonstrates that the non-extensive, superstatistical approach *is* valid for studying electric fracture and friction phenomena, with the $q$-parameter yielding useful information regarding both the overall deformation mechanism and the crack network geometry. Additionally, the $q$-parameter evolves with stress intensity during deformation and has the appearance of a precursor, exhibiting the two-stage anomaly predicted by Main et al. (1989; 1993) and Meredith et al. (1990). The intermediate-term peak indicates the onset of distributed crack propagation and coalescence, the short-term minimum reflects crack localisation on the final failure plane, and the final peak indicates the onset of crack acceleration through the final asperities supporting the sample and imminent dynamic failure. Therefore, the $q$-parameter *is* a useful indicator of the stages leading up to failure and certainly has a role to play in earthquake monitoring and forecasting. In particular, for studying geoelectric anomalies in active tectonic regions, but it may also prove useful for interpreting anomalies in other non-seismic crustal transients. Furthermore, since it is linked to the seismic $b$-value, the $q$-value may also provide a unifying parameter with which to interpret multi-parameter earthquake monitoring data.

# Chapter 12

# Conclusions and Implications for Earthquake Hazard

## 12.1 Introduction

At the end of any study it is useful to review the work that was undertaken, the conclusions that can be drawn from it and the potential avenues for further research that may have arisen as a result. This final chapter provides such a review.

Pre-seismic electric signals comprise a wide range of observed anomalies whose underlying causes and relationship with deformation are still largely unknown, and whose statistical significance and potential as useful precursors to earthquakes remain controversial (Chapter 3). Rock deformation experiments (Chapter 4) are considered to be a useful tool for understanding the occurrence of earthquakes and crustal deformation (Chapter 2). In this thesis, triaxial deformation experiments have been performed on a non-piezoelectric rock with regard to investigating the generation of electric currents at the earthquake source and their statistical properties. These experiments (Chapter 5) were carried out under the following conditions: (i) at pressures consistent with those in the shallow, seismogenic crust, (ii) at a range of strain rates, to provide a basis for extrapolation to the crustal scale, and (iii) under both dry and fluid-saturated conditions, including an ionic brine solution with composition typical of that found in crustal fluids. Carrara marble was chosen (Chapter 6) because its deformation mechanisms span the brittle-ductile transition at these pressures and strain rates, and because calcite ($CaCO_3$) is an important rock-forming mineral; calcite tectonites play a significant role in numerous crustal deformation zones (De Bresser et al., 2005). The currents generated in these Carrara marble samples were very small; of the order of $10^{-9}$ A. Nevertheless, the signals were distinct and the data presented in this thesis was not filtered in any sophisticated way. Electric current was correlated with mechanical damage through the acquisition of multiparameter data: stress, strain, ultrasonic velocities, acoustic emissions and pore fluid volume.

## 12.2 Conclusions

### 12.2.1 Electric current generation in the Earth's crust

The first conclusion to be drawn from this thesis is that electric current *can* be generated and sustained solely as a result of the changing stress field and mechanical processes of deformation; i.e., brittle mechanisms (microfracture and cataclastic flow), with a contribution from other intermittent ductile mechanisms (dislocation migration), at conditions approximating those found in the Earth's crust (Chapters 7 to 10).

Secondly, electric current flow is due to the presence of localised electric dipoles rather than a homogeneous electric field. This was evident from the slight variations in the signals (magnitude, polarity and shape) within individual samples. Dipole formation was attributed to (a) breaking of ionic bonds and the release of charges (electrons, point defects and dislocations) from charge-trapping centres during localised microfracture and microscale slip (Ogawa et al., 1985; Brady and Rowell, 1986; Cress et al., 1987; Khatiashvili and Perel'man, 1989; Enomoto and Hashimoto, 1990; O'Keefe and Thiel, 1995; Molchanov and Hayakawa, 1995; 1998b; Enomoto, 1996; Scudiero et al., 1998; Takeuchi and Nagahama, 2004; 2006) at low to intermediate pressures, and (b) to the motion of charged edge dislocations (Slifkin, 1993; Ernst et al., 1993; Hadjicontis and Mavromatou, 1994; 1996; Vallianatos and Tzanis, 1998; 1999; Tzanis and Vallianatos, 2002) during ductile strain hardening observed at elevated pressure.

Applying a charge density of $10^{-2}$ $Cm^{-2}$ due to separation charging, estimated by Ogawa et al. (1985), to electrodes with area, $A = 3.8\text{x}10^{-4}$ $m^2$, used in this study, yields an estimated surface charge caused by fracturing of $10^{-6}$ C, consistent with that measured during these experiments. Additionally, according to Takeuchi and Nagahama (2001; 2002a) and Enomoto and Hashimoto (1990), fractures or stick-slip faulting lead to surface potentials of around 10 V. Assuming that the samples obey Ohm's Law and that the resistivity of marble is $\sim$0.1 G$\Omega$ (The Engineering Toolbox, 2014), the resistance of a sample is calculated to be $\sim$10 G$\Omega$, which yields a surface current of the order of nA, also in good agreement with that measured during these experiments. With respect to migrating charged edge dislocations, Equation 3.7 yields $J \approx 10^{-8}$ $Am^{-2}$. This is based on assuming the lowest excess dislocation density for rocks; $\beta = 1.5$ (Whitworth, 1975), the charge per unit length on the dislocation, $q_l \approx 10^{-11}$ $Cm^{-1}$, Burgers vector, $\mathbf{b} \approx 10^{-9}$ m, and strain rate, $\dot{\varepsilon} \approx 10^{-6}$ $s^{-1}$, equal to the experimental strain rate. The result is somewhat smaller than that seen in the experiment at the highest pressure ($J \approx 10^{-7}$ $Am^{-2}$), indicating that there is an additional contribution from brittle mechanisms.

The overall form of the recorded signals was fairly consistent across experiments carried out at the same conditions, with (a) current flow increasing rapidly and steadily with respect to strain (and time), in the presence of crack nucleation, propagation and coalescence, (b) current flow oscillating and pulsing around a sustained background level during cataclastic

flow (frictional sliding on grain boundaries and crack surfaces, grain fragmentation and crack propagation), and (c) current flow accelerating with respect to strain (and time) during post-yield ductile strain hardening (i.e., in the presence of large-scale dislocation glide and micro-scale cataclastic flow). Furthermore, in the presence of all deformation mechanisms, current flow was characterised by intermittent high-frequency fluctuations, which exhibited periods of strong activity interspersed with periods of quiescence. Amplitudes of both the high-frequency fluctuations and the lower-frequency oscillations and pulses were, in general, an order of magnitude smaller than the overall electric current, which itself decreased with an increase in both confining pressure and strain rate. Conversely, the initial rate of current production increased with strain rate but decreased with confining pressure.

Variations in electric signals with confining pressure were attributed to the suppression of microcrack nucleation, propagation and localisation at elevated pressures and the increased contribution from crystal plasticity and frictional cataclastic flow processes, evident from a decrease in the reduction of $V_P$ with respect to the overall mechanical damage. Also, current only flowed after a 10% decrease in $V_P$, indicating that a certain amount of crack damage or crack connectivity is required before current will flow. Changes with respect to strain rate were attributed to time-dependent differences in the deformation process; smaller, more intermittent deformation events occurring at slower strain rates due to smaller, less rapid variations in the internal stresses. This was evident from a similar reduction in $V_P$ (i.e., a similar increase crack void space) over a three orders of magnitude difference in deformation rate. Such time-dependent differences account for current flow associated with the initial material yield at the slowest strain rates; i.e., during dilatant inelastic strain hardening as microcracks nucleate and propagate. At dynamic strain rates, electric current was generated only during the precursory stress drop associated with strain softening; i.e., during crack propagation and linkage. It showed precursory characteristics, reaching a peak and then recovering as the stress drop accelerated towards failure. At slower strain rates, current flow was also associated with strain softening. At pressures up to the brittle to semi-brittle transition ($\leq$ 20 MPa), a similar, albeit smaller, precursory pulse was seen as the stress drop accelerated towards failure. In the field, only strain can be measured and so a precursory stress drop must be inferred (Main and Meredith, 1989). Therefore, results from this study suggest that the onset of a geoelectric anomaly or a series of anomalous pulses may reflect the onset of such a stress drop.

Steadily increasing current production in the presence of nucleating and propagating cracks is evidence of an accelerating accumulation of charge and the presence of an electric field steadily increasing in strength. The slowing of this current flow to a relatively constant level during cataclastic flow, demonstrates that the background electric field steadies but remains strong as frictional sliding and fragmentation balances crack nucleation and propagation, stabilising the accumulation of charges to an overall steady level. However, the fluctuations, oscillations and pulse-type emissions characteristic of cataclastic flow indicate that the field varies locally around this strong background level, as individual processes

influence the accumulation and flow of charged particles.

As discussed in Section 9.1, extrapolation to crustal strain rates is best done in the steady-state cataclastic flow regime, where stress levels are constant over large strains (Rutter, 1974). For the multichannel experiments described in Section 9.3, this is achieved at strains $\geq 2.5\%$ across the range of strain rates. Extrapolation is based on the respective logarithmic and power-law relationships of current and charge magnitude with strain rate, using the parameters in Tables 9.6 and 9.7 and averaging them over the three largest values of strain. Scaling these currents to a realistic crustal strain rate of $10^{-14}$ $s^{-1}$ yields an electric current of $\sim$15 nA, which equates to a current density of $\sim$12 mA $m^{-3}$ for stressed rock volumes comparable with those of the laboratory samples. Thus, for stressed rock volumes of $10^4 - 10^5$ $km^3$, such as those expected in situations that produce $6.5 < M < 7.5$ earthquakes (Freund et al., 2006), the expected current flow in a deforming region at typical crustal strain rates could be of the order of $1 - 10$ GA. Even if 99.9% of this current were dissipated, deformation-induced transient telluric current systems may still be in the $10^6$ A range, findings consistent with those of Freund et al. (2006). This corresponds to a huge accumulated net charge ($\sim 10^{22}$ C), due to the extended time over which the current flows. In reality, however, it is unlikely that accumulated charge of this quantity would ever be measured in the field as the charged particles would be gradually conducted away from the stressed rock volume, possibly by flowing fluids and/or along intergranular carbon films (e.g., Shankland et al., 1997; Chelidze and Gueguen, 1999). However, it does indicate that a significant amount of background charge produced purely from rock deformation mechanisms contributes to the Earth's background telluric currents and electric field. Therefore, any current flow and charge production concentrated in a localised region during more rapid deformation processes would certainly influence the geoelectric field; an inference supported by the apparent connection between deformation intensity and geoelectric signal generation in Taiwan, reported by Telesca et al. (2014).

Since the experiments were conducted at constant strain rates in the steady-state cataclastic flow regimes, my results should scale consistently to Earth deformation rates. Thus, given the evidence presented here that the electrical signals are caused mainly by brittle damage events, the rapid deformation processes that influence the local geoelectric field are likely to be the earthquakes themselves; i.e., the local seismicity. This is consistent with the reverse-time performance of VAN predictions (Mulargia and Gasperini, 1992). However, the observation of a precursory change in current flow prior to sample failure indicates that this change may occur in the field as regional seismicity redistributes the stress onto a particular fault and earthquake rates accelerate in that area. Although such a change may not occur as obviously in the field as in the lab, or with a significant lead-time, since the acceleration in AE rate occurs later and is sharper at slower strain rates (Ojala et al., 2004). This may also explain the lack of evidence for earthquake preparation and precursory dilatant strain at the field scale (Jordan et al., 2011), as shown by the almost total absence of strain acceleration in both InSAR and GPS data prior to the 2009 L'Aquila earthquake (Amoruso and Crescentini, 2010) and the lack of observed precursors

of any kind prior to the 2004 Parkfield earthquake (Bakun et al., 2005).

### 12.2.2 Electric current and deformation dynamics

Electric current fluctuations were analysed, using a modern, non-equilibrium statistical mechanics approach (Tsallis, 1988; 2009a), with a view to establishing whether the dynamics of rock deformation are reflected in the statistical properties of the recorded electric current (Chapter 11). The findings of this thesis, involving a super-statistical dynamic model (Beck, 2001; Beck and Cohen, 2003), confirm that this does indeed appear to be the case, at least at the sample scale.

The excellent agreement between the non-Gaussian statistical behaviour exhibited by the electric current fluctuations and the non-extensive $q$-Gaussian distribution reflects the fractal and correlated nature of electrical source network. That is, that the electric signals result from processes occurring on the fractal structures that develop within the rock matrix during deformation. This provides strong evidence that the electrical source network is the developing fractal network of cracks, and also illustrates the usefulness of the non-extensive approach for analysing deformation-induced electric signals. Although it should be noted that fat-tailed distributions may also be derived from conventional statistical mechanics by introducing a geometric degeneracy term to account for the fractal nature of the structures involved (e.g., Main and Burton, 1984), which is also consistent with the interpretation given here. Dynamically, the measured electric current, which exhibited periods of strong fluctuations punctuated with calm periods, was effectively modelled as the superposition of these short-term, deformation-induced electrical processes. This is consistent with the notion that geological deformations are the long-term cumulative trace of short-term processes such as earthquakes, with the latter being described as a high-frequency 'noise' of the former (King et al., 1988; Sornette and Sornette, 1989; Sornette and Virieux, 1992). Furthermore, it supports the proposition that each fracture plane activates an electrical process (Anastasiadis et al., 2004). The dynamic pulse and recovery of electric current seen during strain softening at the faster strain rates corresponds to an imminent single shear failure, while the oscillations and pulse-like current emissions observed at the slowest strain rates correspond to smaller, localised shear failure events, as might be expected from a self-similar, fractal, developing crack network.

According to the electric source model of Takeuchi and Nagahama (2004; 2006), where surface charges are released from charge-trapping centres on sheared asperities, the detectability of electric/magnetic field variations at a point on the ground depends strongly on the wet/dry conditions at the fault zone. During this study, the deformation of dry samples and samples saturated with either deionised water or an ionic brine solution allowed solid-state current-generating mechanisms to be isolated from electrokinetic effects and their relative contribution with respect to the pore fluid composition to be investigated. My findings indicate that the influence from electrokinetic effects depends strongly on

both the presence and ionic content of fluid in the fault zone. Indeed, electric current flow in the presence of an ionic brine solution, typical of crustal pore fluid conditions, appears to be dominated by electrokinetic effects. However, in tectonically active regions fluid flow is driven mainly by crustal movements, as compaction and dilatancy cause localised changes to the pore fluid pressure. Thus, deformation processes that contribute charges to the electric double layer also cause the pressure variations that drive the flow of fluid in an earthquake preparation zone (Scholz et al., 1973). They must also, therefore, drive the variation in electrokinetic parameters, which have been shown to evolve with deformation (Clint, 1999). It is possible, therefore, that the footprints of deformation reflected in the observed super-statistical dynamics of electric current fluctuations for all pore fluid conditions are also present in crustal geoelectric signals regardless of the presence or type of pore fluid.

Non-extensive $q$-values obtained from the Tsallis analysis demonstrate strong correlations between electric current fluctuations, which exhibit a non-extensive character similar to that observed in Earth seismicity (Telesca, 2010a;b; Vallianatos and Sammonds, 2010; Tsallis, 2009a; Abe and Suzuki, 2005; 2003) and are in agreement with field (Varotsos et al., 2002) and laboratory results (Vallianatos et al., 2011b) relating fracture with deformation-induced electrical effects. By the same token, the super-statistical behaviour exhibited by the electric current fluctuations reflects the episodic, avalanche-like behaviour of deformation observed from laboratory (Sammonds, 2005) to field (Main and Naylor, 2010; Caruso et al., 2007) and described by self-organised criticality models (Caruso et al., 2007). These non-extensive properties have been useful in understanding the mechanisms of deformation-induced current generation in laboratory samples of Carrara marble. Therefore, they may also prove to be useful in understanding earthquake mechanisms and could potentially contribute to addressing the problem of earthquake prediction.

A two-stage anomaly, similar to that predicted for the stress intensity evolution (Main et al., 1989; 1993; Meredith et al., 1990), was observed in the evolution of electric current $q$-values during deformation; behaviour that was also apparent in the seismic $b$-value evolution. The observed critical $q$-value; i.e., the value below which $q$ must fall if it is to indicate the final approach towards failure, is $\sim$1.6. This is significant as it is close to the critical $q$-value of 1.67, calculated from the theoretical relationship $q = \dfrac{2+b}{b+1}$ (Vallianatos, 2009; Telesca, 2012) using a $b$-value of 0.5; the critical $b$-value observed in the Earth, evaluated from earthquake foreshock sequences (Von Seggern, 1980; Meredith et al., 1990). This critical $q$-value is also close to the $q$-value of $\sim$1.7, obtained from the overall distributions of electric current fluctuations, that differentiates brittle behaviour from semi-brittle behaviour. Thus, deformation-induced electric signals and their corresponding $q$-values can provide information regarding the stress state, internal dynamics and stability of a deforming sample.

The stages of deformation indicated by the two-stage $q$-value anomaly are reflected in the two-stage earthquake preparation model of Kapiris et al. (2004) and (Contoyiannis

et al., 2005), which invokes the negative and positive feedback mechanisms described by Main et al. (1993) to explain the occurrence of anti-persistent MHz followed by persistent kHz pre-seismic electromagnetic anomalies in the field. Additionally, the final increase in $q$-value, from its minimum as stress concentrates on the final failure plane(s) to its final maximum at the onset of dynamic failure, is also seen at the field-scale; in the significant increase in the organisation of the persistent kHz anomalies (Papadimitriou et al., 2008; Contoyiannis and Eftaxias, 2008; Eftaxias, 2010; Potirakis et al., 2011; 2013a;b; Minadakis et al., 2012) observed shortly before the main earthquakes. This increase was attributed to the transition from breakage of fragments filling the gap between the two fault surfaces to the fracture of the strong asperities, i.e., the transition from quasi-static deformation to accelerating dynamic rupture. Furthermore, the notion that stress intensity is reflected in the electric signals lends weight to the notion that the onset of electrical anomalies in an active tectonic region marks the onset of deformation activity towards a critical point, as identified by Varotsos et al. (2011b) in the natural time domain.

My results therefore have implications for the earthquake nucleation process, where stress concentration leading to frictional failure and the shear fracture of intact rock are the controlling factors behind the nucleation of slip on a fault (Ohnaka, 2003); a process in which strong correlations between sliding fragments and locked asperities can be captured by the non-extensive fragment-asperity model (Sotolongo-Costa and Posadas, 2004; Silva et al., 2006; Telesca, 2011; 2012).

## 12.3 Implications for Earthquake Hazard

Cataclastic flow processes observed in a laboratory sample are a more accurate representation of crustal deformation than brittle fracture (crack nucleation) in a previously undamaged sample. The episodic, avalanche-like behaviour of cataclastic flow processes, characterised by intermittent slip and fragmentation on a network of microscale faults, maintain the system in a quasi-stable, but close to critical, condition. This is consistent with critical or self-organised critical models for seismicity, where the Earth's lithosphere first evolves spontaneously to a critical or near-critical state and then remains there apart from discrete fluctuations represented by individual earthquakes (Main, 1996). Similarly, the electric current fluctuations, oscillations and burst-type emissions seen during distributed cataclastic flow (e.g., Figures 8.1 (b) and (c) and 9.6 (c)) are important as they, arguably, resemble the intermittent anomalies typical of geoelectric time series recorded in the field. For example, the seismic electric signals (SES) reported to precede the 1995 $M_w$6.6 earthquake at Grevena-Kozani in Greece (Figure 12.1). Whereas, the dynamic pulse of current produced at strain rates $\geq 10^{-5}$ s$^{-1}$ (e.g., Figure 9.6 (a) and (b)) during the rapid development of a single shear fault, shares the bell-shape typical of an individual SES (electric field variation), such as those reported to precede the 1992 $M_s$5.9 Galaxidi earthquake in the Gulf of Corinth, Greece (Figure 12.2). But, these figures do

have significant potential for selection bias; the authors of these papers do not make clear what happens to the signal at the time of the earthquake, nor how often such signals are observed without a subsequent earthquake, making a true comparison difficult.

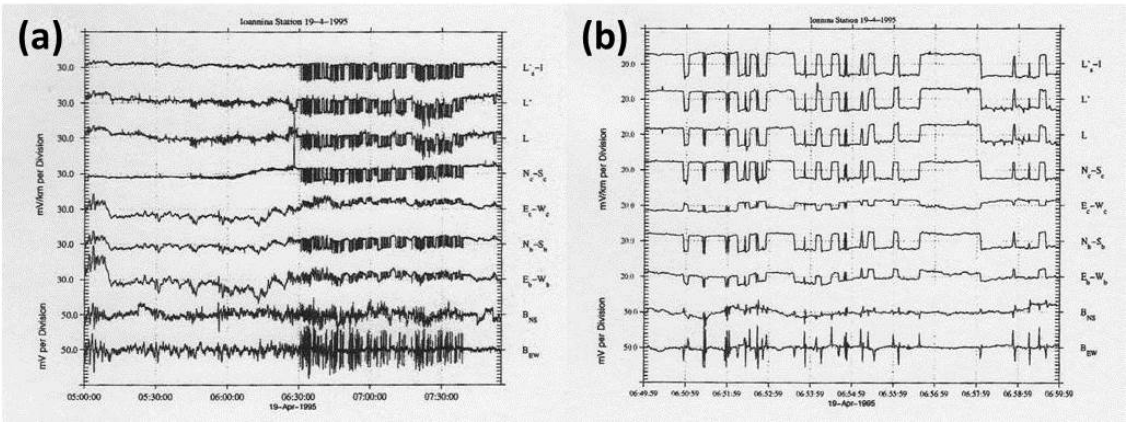


Figure 12.1: Geoelectric time series showing reported SES activity at the Ioannina station approximately one month prior to the $M_w$6.6 earthquake at Grevena-Kozani, Greece that occurred on 13 May 1995. Figure (b) is an excerpt of (a) on an expanded time scale. Taken from Varotsos et al. (2011b).

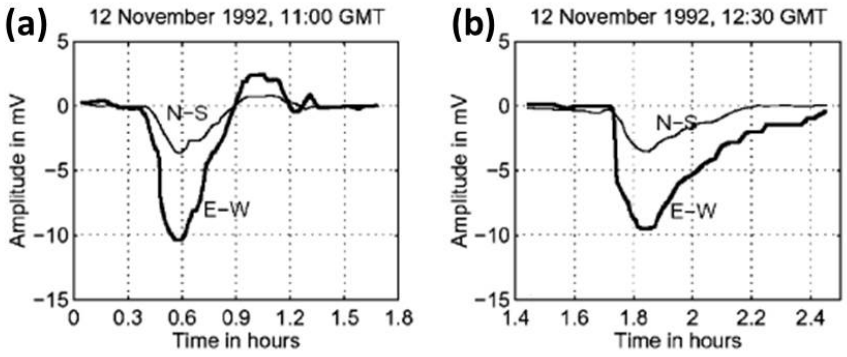


Figure 12.2: The first (a) and second (b) electric anomalies reported by Ifantis et al. (1993) as precursors to the Galaxidi earthquake on 18 November 1992 that occurred six days prior to the rupture. Taken from Vallianatos et al. (2004).

It could also be argued that the behaviour of the electric current signals, and the implied electric field variations, may provide a sample-scale explanation for the three types of precursory electrical anomalies detected in Greece (Figure 12.3), as deformation concentrates in a particular focal region. Accordingly, the increasing electric current that results from distributed, sub-critical crack nucleation and propagation in the rock sample may resemble the initial gradual variation of the Earth's electric field (GVEF), observed months to weeks prior to an eventual earthquake. This GVEF could, therefore, be the initial response to a regional increase in stress and the associated activation of a distributed fault network as stress concentrates along healed fault surfaces and at defects in the surrounding country rock, propagating existing cracks and nucleating new ones. Seismic electric signals (SES) are superimposed on the background electric field, with amplitudes an order of magnitude smaller than the overall electric field and have been observed several weeks to several hours prior to an impending shock (Varotsos and Alexopoulos, 1984a;b). These may correspond to the oscillations and pulses in electric current attributed to intermittent avalanches of

cataclastic flow processes in the rock sample, which were also an order of magnitude smaller than the overall electric current. If so, SES can be attributed to clusters of foreshock activity on the distributed fault network. Intermittent series of SES (Figure 12.1) give way to individual SES (Figure 12.2) at a lead-time of several days to hours, and finally to short duration electric pulses a few minutes preceding the earthquake. Individual SES may originate from episodic, localised slip and fragmentation on the fault itself, with the transition from intermittent series of SES to individual SES marking the localisation of foreshock activity as stress concentrates at particular points along the eventual rupture plane. Given the pulse-like nature of electric current observed in marble during the accelerating stress drop to shear failure at dynamic strain rates, the short-duration electric pulses may reflect accelerating fracture through the final few asperities supporting the fault at the point of imminent rupture. Although, given (i) the controversy and general skepticism regarding geoelectric anomalies and their potential as precursors and (ii) the difficulties of scaling the results of such experiments to the field scale, a great deal of work would be required to fully investigate this conjecture. Such a project would involve a detailed review of all previously reported electromagnetic anomalies, their characteristics and their possible link with seismicity, together with some controlled, intermediate field-scale experiments and an international, multi-parameter monitoring collaboration with agreed-on, systematic and consistent data management and processing procedures.

Regardless of whether geoelectric signals can be used to predict earthquakes, the results from this study provide evidence that (1) telluric current anomalies in the crust can be spontaneously generated solely due to brittle deformation events and (2) these currents can represent the stress state in a deforming region. However, a physical mechanism (or a combination of mechanisms) that describes all the features observed in these electric current signals is currently lacking. In addition, the problems raised two decades ago regarding geoelectric earthquake precursors (Mulargia and Gasperini, 1996a), including their sensitivity to an unknown 'selectivity effect' of the detection antenna and the difficulties discriminating deformation-induced signals from other known electrical disturbances remain unresolved.

According to Main and Meredith (1989), "the critical stage for useful earthquake warning would be to reliably detect the transition from energy release predominantly in the volume surrounding the focal region to that on the fault itself". Their fracture mechanics model (Main et al., 1989; 1993; Meredith et al., 1990; Main, 1991), based on the evolution of damage with a fractal distribution of crack lengths, indicates that two phases of earthquake warning associated with intermediate-term and short-term anomalies can be related in a simple manner to two peaks in the stress intensity (Main and Meredith, 1989). The first broad peak is further split into two halves, associated with precursory strain release (strain hardening) followed by precursory stress drop (strain softening), while the second peak responds to the transition from quasi-static fracture and slip to accelerating dynamic rupture. Their experimental results, correlating seismic $b$-values with stress intensity and observing in both the predicted two-stage anomaly, suggested that such a warning system

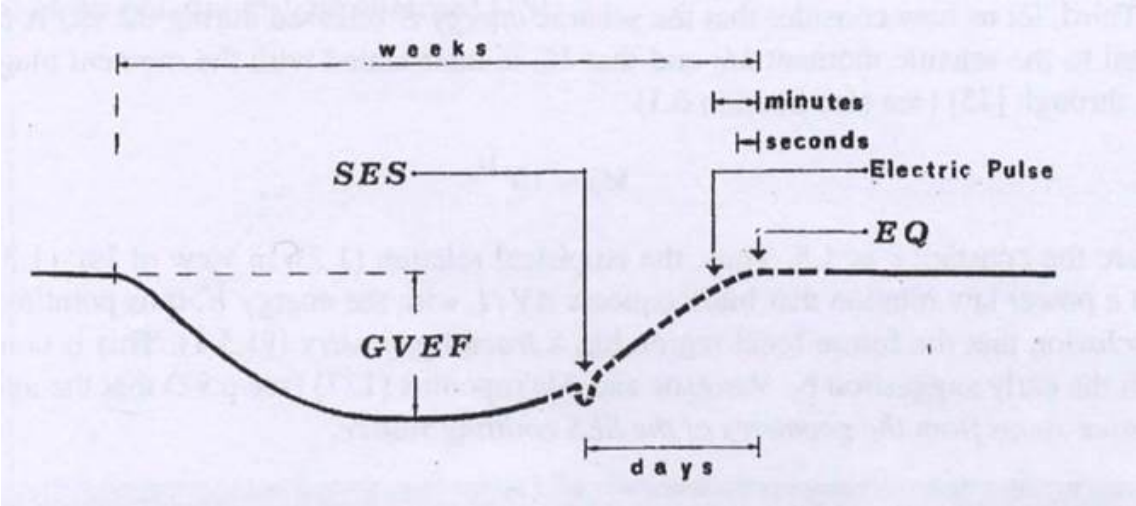


Figure 12.3: Schematic representation (not to scale) of the three types of precursory electrical anomalies observed in Greece; initial gradual variation of the electric field (GVEF), subsequent seismic electric signals (SES) and, finally, electric pulses. Modified from Varotsos et al. (1993).

may at least be a realistic goal in the medium term. My results highlight the possibility of achieving such a goal from transient electric phenomena as well as seismicity, with the stress state of the deforming region and degree of correlation between faults, fragments and asperities inferred from the $q$-parameter.

Should a generally-accepted solution for separating damage-induced anomalies from other electrical noise eventually be developed, it may be possible to compute $q$-values for the fluctuations of a geoelectric time series recorded in the field and use them to determine the stress state evolution in a region of tectonic activity, with the $q$-parameter providing useful insights into the dynamics and stability of the fault network in the deforming region. The findings from this investigation provide a solid experimental basis for comparison with such analysis. Furthermore, such an approach may also be a promising tool for analysing fluctuations in time series from a range of crustal transients that exhibit precursory changes prior to earthquakes, with the $q$-value providing a consistent variable with which to compare time series from multi-parameter studies.

Together, the experimental work and non-extensive modelling procedure undertaken during this investigation have established a link between electric current generation and the dynamics of deformation. These results provide experimental evidence that transient anomalies in the Earth's telluric currents and electric and magnetic fields may reflect the crustal stress state and the associated network of developing cracks and slip events on faults in a focal region. These observations add to the growing body of evidence that transient electric phenomena and their non-extensive properties can, in fact, reflect the development and evolution of a fracture network and have the potential to provide significant information about the stability of a tectonically active region. Thus, the non-extensive approach has a great deal of potential for earthquake monitoring and multi-precursor seismic hazard assessment, and this work may provide opportunities to develop laws suitable for testing at larger scales.

## 12.4 Avenues for Future Research

This investigation has highlighted the possibility of a correlation between stress intensity, $K$, and the non-extensive $q$-parameter. Therefore a key direction for further work in this field would be obtaining experimental corroboration of such a correlation. Such an investigation might involve an approach similar to that of Main et al. (1993), whereby the fractal dimension of the population of crack lengths would be obtained from $q$-values determined from the frequency-magnitude distribution of acoustic emissions and compared with both the mean energy release rate, $< G >$, where $G \propto K^2$ and with $q$-values determined from the distribution of electric current fluctuations. This may not be possible using Carrara marble samples due to the limited number of recordable acoustic emissions (AE), although a more sensitive AE detection system and a higher resolution electric current acquisition system in a lower noise environment might allow enough AE to be detected during experiments conducted under brittle conditions (e.g., $P_c < 30$ MPa and $\dot{\varepsilon} \leq 10^{-5}$ s$^{-1}$). Obtaining an empirical relationship between the seismic $b$-value and the non-extensive $q$-value with which to compare the proposed theoretical connections (Vallianatos, 2009; Sarlis et al., 2010a; Telesca, 2012) would be an additional benefit from such a study. As would establishing whether AE size differences also exhibit $q$-Gaussian behaviour and super-statistical dynamics, and, if so, whether their parameters coincide with those determined from the electric current fluctuations.

A maximum likelihood procedure for estimating the $q$-parameter from the $q$-Gaussian distribution would be preferred to the non-linear least squares fitting procedure used during this study as it would ensure a more consistent, accurate estimation of the $q$-parameter. It would also allow the Aikake Information Criterion (AIC) to be used to compare the likelihood that a $q$-Gaussian distribution describes the data better than a Gaussian distribution in a more statistically robust manner; important for checking the distributions from the fastest strain rate experiments. Recently, (da Silva et al., 2013) derived a maximum likelihood estimate (MLE) for the $q$-index from the $q$-Gaussian function. However, this MLE requires a numerical solution, which was beyond the scope of this project. Therefore, determining this solution to obtain maximum likelihood estimates for the $q$-values is recommended for the future.

Behaviour of the $q$-value evolution during deformation requires further testing for confirmation that the two-stage anomaly prior to failure is a consistent feature in the brittle regime. Higher resolution electric current acquisition would enable instantaneous $q$-values to be determined for faster strain rate experiments. Similar analysis of the $q$-value evolution at higher pressures would establish the influence of cataclastic flow. This analysis is possible from the data acquired during this investigation but time constraints prevented the inclusion of it in this thesis.

Microstructural studies and further experiments are needed to clarify the relationships presented here between experimental condition, deformation mechanism and electric sig-

nals. Additionally, a series of experiments conducted at pressures >100 MPa would serve to elucidate the effect of dislocation migration on the generated electric current and enable assessment of the relative contributions of brittle and plastic mechanisms. The influence of climb-assisted dislocation glide on electric current could be established with a series of experiments conducted at elevated temperatures.

Time constraints prevented detailed analysis of the cyclic loading experiments conducted during this study. However, analysis of these data may shed further light on the specific mechanisms involved; in particular, the influence of co-operative dipole alignment at a critical stress (Varotsos and Alexopoulos, 1986, and Section 3.5.1.1). This model is attractive as it also explains why some crustal electric phenomena exhibit critical dynamics (Uyeda et al., 2009b). The potential for this mechanism to play a role was illustrated by the critical stress at which current flow began in the semi-brittle regime and preliminary observations from the cyclic loading experiments, which showed that the electric current signals relax during unloading stage. Therefore, an investigation into the electric current relaxation parameters during cyclic loading in the semi-brittle regime is proposed.

Finally, it was noticed during the course of this study that the super-statistical $\beta$-parameter distributions can be equally well-modelled, better in some cases according to the AIC, with a lognormal distribution as with a gamma distribution. In such a case, instead of $\beta$ being the gamma-distributed *sum* of many random processes, it is the *product* of these processes (Beck, 2008). Such a distribution, characteristic of non-linear forcing and power-law friction forces, is relevant for cascading energy dissipation such as that seen in turbulent flows (Beck, 2008). It may therefore also be relevant for energy dissipation on a fractal crack network and warrants further investigation.

# References


Abe, S., Sarlis, N., Skordas, E., Tanaka, H., and Varotsos, P. (2005a). Origin of the usefulness of the natural-time representation of complex time series. *Physical Review Letters*, 94:170601.

Abe, S. and Suzuki, N. (2003). Law for the distance between successive earthquakes. *Journal of Geophysical Research*, 108:2113.

Abe, S. and Suzuki, N. (2004). Aging and scaling of earthquake aftershocks. *Physica A: Statistical Mechanics and its Applications*, 332:533–538.

Abe, S. and Suzuki, N. (2005). Scale-free statistics of time interval between successive earthquakes. *Physica A*, 350:588–596.

Abe, S., Tirnakli, U., and Varotsos, P. (2005b). Complexity of seismicity and nonextensive statistics. *Europhysics News*, 36:206–208.

Abercrombie, R. (1995). Earthquake source scaling relationships from -1 to 5 ml using seismograms recorded at 2.5km depth. *Journal of Geophysical Research*, 100:24015–24036.

Aceves, R., Park, S., and Strauss, D. (1996). Statistical evaluation of the van method using the historical earthquake catalog in greece. *Geophysical Research Letters*, 23(11):1425–1428.

Akesson, U., Lindqvist, J. E., Schouenbourg, B., and Grelk, B. (2006). Relationship between microstructure and bowing properties of calcite marble claddings. *Bull. Eng. Geol. Environ.*, 65:73–79.

Akhoondzadeh, M., Parrot, M., and Saradjian, M. R. (2010). Electron and ion density variations before strong earthquakes (m¿6.0) using demeter and gps data. *Natural Hazards and Earth System Sciences*, 10:7–18.

Aki, K. (1965). Maximum likelihood estimate of b in the formula logn = a - bm and its confidence limits. *Bulletin of the Earthquake Research Institute Tokyo*, 43:237–239.

Aki, K. and Richards, P. G. (1980). *Quantitative Seismology: Theory and Methods*. Freeman.

Alber, M. and Hauptfleisch, U. (1999). Generation and visualization of microfractures in carrara marble for estimating fracture toughness, fracture shear and fracture normal stiffness. *International Journal of Rock Mechanics and Mining Sciences*, 36(8):1065 – 1071.

Alexander, D. E. (2010). The l'aquila earthquake of 6 april 2009 and italian government policy on disaster response. *Journal of Natural Resources Policy Research*, 2(4):325–342.

Alexander, D. E. (2014a). Communicating earthquake risk to the public: the trial of the 'l'aquila seven". *Natural Hazards*, 72(2):1159–1173.

Alexander, D. E. (2014b). Reply to a comment by franco gabrielli and daniela di bucci: "communicating earthquake risk to the public: the trial of the 'l'aquila seven"'. *Natural Hazards*, 75:999–1003.

Ambrasey, N. (1970). Some characteristic features of the anatolean fault zone. *Tectonophysics*, 9:143–156.

Amoruso, A. and Crescentini, L. (2010). Limits on earthquake nucleation and other pre-seismic phenomena from continuous strain in the near field of the 2009 l'aquila earthquake. *Geophysical Research Letters*, 37(10):n/a–n/a. L10307.

Anagnostopoulos, G. C., Basta, M., Stefanakis, Z., Vassiliadis, V. G., Vgontzas, A. N., Rigas, A. G., Koutsomitros, S. T., Baloyannis, S. J., and Papadopoulos, G. (2013). A study of correlation between seismicity and mental health: Crete, 2008 to 2010. *Geomatics, Natural Hazards and Risk*, 0:1–31.

Anastasiadis, C., Stavrakas, I., Triantis, D., and Vallianatos, F. (2007a). Correlation of pressure stimulated currents in rocks with the damage parameter. *Annals of Geophysics*, 50(1):1–6.

Anastasiadis, C., Triantis, D., and Hogarth, C. A. (2007b). Comments on the phenomena underlying pressure stimulated currents in dielectric rock materials. *Journal of Materials Science*, 42:2538–2542.

Anastasiadis, C., Triantis, D., Stavrakas, I., and Vallianatos, F. (2004). Pressure stimulated currents (psc) in marble samples. *Annals of Geophysics*, 47(1):21–28.

Anderson, D. L., Minster, B., and Cole, D. (1974). The effect of orientated cracks on seismic velocities. *Journal of Geophysical Research*, 79:4011–4015.

Anderson, L. A. and Keller, G. V. (1966). Experimental deep resistivity probes in the central and easter united states. *Geophysics*, 31:1105–1122.

Anderson, P. W. (1972). More is different (broken symmetry and the nature of the hierarchical structure of science). *Science*, 177:393–396.

Antonopoulos, G., Michas, G., Vallianatos, F., and Bountis, T. (2014). Evidence of q-exponential statistics in greek seismicity. *Physica A*, 409:71–77.

Ashby, M. F. and Hallam, S. D. (1986). The failure of brittle solids containing small cracks under compressive stress states. *Acta Metallurgica*, 34(3):497–510.

Ashby, M. F. and Sammis, C. G. (1990). The damage mechanics of brittle solids in compression. *Pure and Applied Geophysics*, 133(3):389–521.

Athanasiou, M. A., Anagnostopoulos, G. C., Iliopoulos, A., Pavlos, G. P., and David, C. N. (2011). Enhanced ulf radiation observed by demeter two months around the strong 2010 haiti earthquake. *Natural Hazards and Earth System Sciences*, 11:1091–1098.

Atkinson, B. K. (1982). Sub-critical crack propagation in rocks: Theory, experimental results and applications. *Journal of Structural Geology*, 4:41–56.

Atkinson, B. K. (1984). Subcritical crack growth in geological materials. *Journal of Geophysical Research*, 89(B6):4077–4114.

Atkinson, M. J. and Bingman, C. (1996). Elemental composition of commercial seasalts. *Journal of Aquariculture and Aquatic Sciences*, 8(2):34–38.

Ayling, M. R., Meredith, P. G., and Murrell, S. A. F. (1995). Microcracking during triaxial deformation of porous rocks monitored by changes in rock physical properties, i. elastic-wave propagation measurements on dry rocks. *Tectonophysics*, 245:205–221.

Baddari, K., Frolov, A. D., Tourtchine, V., and Rahmoune, F. (2011). An integrated study of the dynamics of electromagnetic and acoustic regimes during failure of complex macrosystems using rock blocks. *Rock Mechanics and Rock Engineering*, 44:269–280.

Bahat, D., Rabinovitch, A., and Frid, V. (2005). *Tensile Fracturing in Rocks: Tectonofractographic and Electromagnetic Radiation Methods*. Springer, Heidelberg.

Bak, P. (1990). Self-organized criticality. *Physica A: Statistical Mechanics and its Applications*, 163(1):403–409.

Bak, P. (1996). *How Nature Works: The Science of Self-Organized Criticality*. Copernicus, New York.

Bak, P., Christensen, K., Danon, L., and Scanlon, T. (2002). Unified scaling law for earthquakes. *Physical Review Letters*, 88(17):178501.

Bak, P. and Tang, C. (1989). Earthquakes as a self-organized critical phenomenon. *Journal of Geophysical Research: Solid Earth*, 94(B11):15635–15637.

Bak, P., Tang, C., and Weisenfeld, K. (1987). Self-organized criticality: an explanation of 1/f noise. *Physical Review Letters*, 59(4):381–384.

Bakar, B. and Tirnakli, U. (2009). Analysis of self-organized criticality in ehrenfest's dog-flea model. *Physical Review E*, 79:040103.

Bakun, W. and Lindh, A. (1985). The parkfield, ca earthquake prediction experiment. *Science*, 229:619–624.

Bakun, W. H., Aagaard, B., Dost, B., Ellsworth, W. L., Hardebeck, J. L., Harris, R. A., Ji, C., Johnston, M. J. S., Langbein, J., Lienkaemper, J. J., Michael, A. J., Murray, J. R., Nadeau, R. M., Reasenberg, P. A., Reichle, M. S., Roeloffs, E. A., Shakal, A., Simpson, R. W., and Waldhauser, F. (2005). Implications for prediction and hazard assessment from the 2004 parkfield earthquake. *Nature*, 437:969–974.

Bandini, A., Berry, P., Bemporad, E., and Sebastiani, M. (2012). Effects of intra-crystalline microcracks on the mechanical behavior of a marble under indentation. *International Journal of Rock Mechanics and Mining Sciences*, 54:47–55.

Barriere, B. and Turcotte, D. L. (1991). A scale-invariant cellular-automata model for distributed seismicity. *Geophysical Research Letters*, 18:2011–2014.

Barriere, B. and Turcotte, D. L. (1994). Seismicity and self-organised criticality. *Phys. Rev. E*, 49:1151–1160.

Baud, P., Zhu, W., and Wong, T.-F. (2000). Failure mode and weakening effect of water on sandstone. *Journal of Geophysical Research*, 105:16371–16389.

Beck, C. (2001). Dynamical foundations of nonextensive statistical mechanics. *Physical Review Letters*, 87:180601.

Beck, C. (2007). Statistics of three-dimensional lagrangian turbulence. *Physical Review Letters*, 98:064502.

Beck, C. (2008). Superstatistics: Theoretical concepts and physical applications. In Klages, R., Radons, G., and Sokolov, I. M., editors, *Anomalous Transport: Foundations and Applications*, chapter 15, pages 433–457. Wiley-VCH Verlag.

Beck, C. (2013). Generalised statistical mechanics for superstatistical systems. *Philosophical Transactions of the Royal Society A*, 369:453–465.

Beck, C. and Cohen, E. (2003). Superstatistics. *Physica A: Statistical Mechanics and its Applications*, 322(0):267 – 275.

Beck, C., Cohen, E., and Rizzo, S. (2005a). Atmospheric turbulence and superstatistics. *Europhysics News*, 36:189–191.

Beck, C., Cohen, E. G. D., and Swinney, H. L. (2005b). From time series to superstatistics. *Physical Review E*, 72:056133.

Bella, F., Biagi, P., Caputo, M., Della Monica, G., Ermini, A., Plastino, W., and Sgrigna, V. (1994). Electromagnetic background and preseismic anomalies recorded in the amare cave (central italy). In Hayakawa, M. and Fujinawa, Y., editors, *Electromagnetic Phenomena Related to Earthquake Prediction*, pages 181–192. TERRAPUB, Tokyo.

Bella, F., Biagi, P., Caputo, M., Della Monica, G., Ermini, A., Plastino, W., Sgrigna, V., and Zilpimiani, D. (1995). Electromagnetic and seismoacoustic signals revealed in karst caves (central italy). *Il Nuovo Cimento C*, 18(1):19–32.

Ben-Zion, Y. and Rice, J. R. (1997). Dynamic simulations of slip on a smooth fault in an elastic solid. *Journal of Geophysical Research*, 102:17771–17784.

Benson, P., Schubnel, A., Vinciguerra, S., Trovato, C., Meredith, P., and Young, R. (2006). Modelling the permeability evolution of microcracked rocks from elastic wave velocity inversion at elevated isostatic pressure. *Journal of Geophysical Research B: Solid Earth*, 111(4):–.

Benson, P. M., Meredith, P. G., and Platzman, E. S. (2003). Relating pore fabric geometry to acoustic and permeability anisotropy in crab orchard sandstone: A laboratory study using magnetic ferrofluid. *Geophysical Research Letters*, 30(19):–.

Benson, P. M., Thompson, B. D., Meredith, P. G., Vinciguerra, S., and Young, R. P. (2007). Imaging slow failure in triaxially deformed etna basalt using 3d acoustic-emission location and x-ray computed tomography. *Geophysical Research Letters*, 34(3):n/a–n/a.

Bernabe, Y. (1986). The effective pressure law for permeability in chelmsford granite and barre granite. *International Journal of Rock Mechanics and Mining Sciences Geomechanics Abstracts*, 23(3):267–275.

Bernabe, Y. and Brace, W. (1990). Deformation and fracture of berea sandstone. In Duba, A. G., Durham, W. B., Handin, J., and Wang, H. F., editors, *The BrittleŰDuctile Transition in Rocks*, volume 56 of *Geophysical Monograph*, pages 91–101. American Geophysical Union.

Bernard, P. (1992). Plausibility of long distance electrotelluric precursors to earthquakes. *Journal of Geophysical Research*, 97(B12):17531–17546.

Bernard, P. (2001). From the search of 'precursors' to the research on 'crustal transients'. *Tectonophysics*, 338:225–232.

Bernard, P., Pinettes, P., Hatzidimitriou, P., Scordilis, E., Veis, G., and Milas, P. (1997). From precursors to prediction: a few recent cases from greece. *Geophysical Journal International*, 131:467–477.

Bernardi, A., Fraser-Smith, A., McGill, P., and Villard Jr., O. (1991). Ulf magnetic field measurements near the epicenter of the ms 7.1 loma prieta earthquake. *Physics of the Earth and Planetary Interiors*, 68:45–63.

Biagi, P. F., Maggipinto, T., Righetti, F., Loiacono, D., Schiavulli, L., Ligonzo, T., Ermini, A., Moldovan, I. A., Moldovan, A. S., Buyuksarac, A., Silva, H. G., Bezzeghoud, M., and Contadakis, M. E. (2011). The european vlf/lf radio network to search for earthquake precursors: setting up and natural/man-made disturbances. *Natural Hazards and Earth System Sciences*, 11:333–341.

Birch, F. (1960). The velocity of compressional waves in rocks to 10 kilobars, part 1. *Journal of Geophysical Research*, 65:1083–1102.

Birch, F. (1961). The velocity of compressional waves in rocks to 10 kilobars, part 2. *Journal of Geophysical Research*, 661:2199–2224.

Bleier, T., Dunson, C., Alvarez, C., Freund, F., and Dahlgren, R. (2010). Correlation of pre-earthquake electromagnetic signals with laboratory and field rock experiments. *Natural Hazards and Earth System Sciences*, 10:1965–1975.

Bleier, T., Dunson, C., Maniscalco, M., Bryant, N., Bambery, R., and Freund, F. (2009). Investigation of ulf magnetic pulsations, air conductivity changes, and infra red signatures associated with the 30 october alum rock m5.4 earthquake. *Natural Hazards and Earth System Sciences*, 9:585–603.

Bolt, B. (2003). *Earthquakes, 5th Edition*. W. H. Freeman, New York.

Boltzmann, L. (1872). Weitere studien uber das warmegleichgewicht unter gas molekulen [further studies on thermal equilibrium between gas molecules]. *Wien, Ber.*, 66:275.

Boltzmann, L. (1877). Uber die beziehung eines allgemeine mechanischen satzes zum zweiten haupsatze der warmetheorie [on the relation of a general mechanical theorem to the second law of thermodynamics]. *Sitzungsberichte, K. Akademie der Wissenschaften in Wien, Math.-Naturwissenschaften*, 75:67.

Bortnik, J., Bleier, T. E., Dunson, C., and Freund, F. (2010). Estimating the seismotelluric current required for observable electromagnetic ground signals. *Annals of Geophysics*, 28:1615–1624.

Brace, W. (1978). A note on permeability changes in geologic material due to stress. *Pure and Applied Geophysics*, 116:627–633.

Brace, W. and Bombolakis, E. (1963). A note on brittle crack growth in compression. *Journal of Geophysical Research*, 68:3709–3713.

Brace, W. and Kohlstedt, D. L. (1980). Limits on the lithospheric stress imposed by laboratory experiments. *Journal of Geophysical Research*, 85:6248–6252.

Brace, W. and Martin, R. (1968). A test of the law of effective stress for crystalline rocks of low porosity. *International Journal of Rock Mechanics and Mining Sciences*, 5:415–426.

Brace, W., Walsh, J., and Frangos, W. (1968). Permeability of granite under high pressure. *Journal of Geophysical Research*, 73(6):2225–2236.

Brace, W. F. (1964). Brittle fracture of rocks. In Judd, W. R., editor, *State of Stress in the Earth's Crust*. Elsevier, New York.

Brace, W. F. (1965). Some new measurements of linear compressibility of rocks. *Journal of Geophysical Research*, 70:391–398.

Brace, W. F. (1971). Resistivity of saturated crustal rocks to 40km based on laboratory measurements. In *Structure and Physical Properties of the Earth's Crust. Geophysical Monograph Series*, volume 14, pages 243–255.

Brace, W. F. and Orange, A. S. (1966). Electrical resistivity changes in saturated rocks under stress. *Science*, 153:1525–1526.

Brace, W. F., Orange, A. S., and Madden, T. R. (1965). The effect of pressure on the electrical resistivity of water-saturated crystalline rocks. *Journal of Geophysical Research*, 70(22):5669–5678.

Brace, W. F., Paulding Jr., B. W., and Scholz, C. (1966). Dilatancy in the fracture of crystalline rocks. *Journal of Geophysical Research*, 71(16):3939–3953.

Brady, B. T. and Rowell, G. A. (1986). Laboratory investigation of the electrodynamics of rock fracture. *Nature*, 321:488–492.

Braud, W. and Dennis, S. P. (1989). Geophysical variables and behaviour: Lviii. autonomic activity, hemolysis, and biological psychokinesis: Possible relationships with geomagnetic field activity. *Perceptual and Motor Skills*, 68:1243–1254.

Brown, S. R. and Scholz, C. H. (1985). Broad bandwidth study of the topography of natural rock surfaces. *Journal of Geophysical Research*, 90:12575–12582.

Brudy, M., Zoback, M. D., Fuchs, K., Rummel, F., and Baumgartner, J. (1997). Estimation of the complete stress tensor to 8 km depth in the ktb scientific drill holes: Implications for crustal strength. *Journal of Geophysical Research: Solid Earth*, 102(B8):18453Ű18475.

Brune, J. N. (1979). Implications for earthquake triggering and rupture propagation for earthquake prediction based on premonitory phenomena. *Journal of Geophysical Research*, 84:2195–2198.

Bruner, W. M. (1976). Comment on 'seismic velocities in dry and saturated cracked solids' by richard j. o'connell and bernard budiansky. *Journal of Geophysical Research*, 81:2573–2576.

Budiansky, B. and O'Connell, R. J. (1976). Elastic moduli of a cracked solid. *International Journal of Solids and Structures*, 12:81–97.

Burridge, R. and Knopoff, L. (1967). Model and theoretical seismicity. *Bulletin of the Seismological Society of America*, 57:341–371.

Burton, P. (1996). Dicing with earthquakes. *Geophysical Research Letters*, 23(11):1379–1382.

Burton, P. W. (1985). Electric earthquake prediction. *Nature*, 315:370–371.

Byerlee, J. D. (1967). Frictional characteristics of granite under high confining pressure. *Journal of Geophysical Research*, 72:3639–3648.

Byerlee, J. D. (1993). Model for episodic flow of high pressure water in fault zones before earthquakes. *Geology*, 21:303–306.

Cabria, I., Lopez, M. J., Alonso, J. A., and March, N. (2012). Density functional study of low-lying isomers of sio4,geo4 and co4 and their relation to tetrahedral solid phases. *European Physical Journal D*, 66:105.

Cahyadi, M. N. and Heki, K. (2013). Ionospheric disturbances of the 2007 bengkulu and the 2005 nias earthquakes, sumatra, observed with a regional gps network. *Journal of Geophysical Research: Space Physics*, 118:1777–1787.

Campbell, W. H. (2009). Natural magnetic disturbance fields, not precursors, preceding the loma prieta earthquake. *Journal of Geophysical Research*, 114:A05307.

Carlson, J. M. and Langer, J. S. (1989). Properties of earthquakes generated by fault dynamics. *Physics Review Letters*, 22:2632–2635.

Carlson, J. M., Langer, J. S., and Shaw, B. E. (1994). Dynamics of earthquake faults. *Reviews of Modern Physics*, 66:657–670.

Carter, N. L. and Tsenn, M. C. (1987). Flow properties of continental lithosphere. *Tectonophysics*, 136:27–63.

Cartwright, J. (2014). Roll over, boltzmann. *Physics World*, May:31–35.

Cartwright, J. A., Mansfield, C., and Trudgill, B. (1996). The growth of normal faults by segment linkage. In Buchanan, P. G. and Nieuwland, D. A., editors, *Modern Developments in Structural Interpretation, Validation and Modelling*, volume 99, pages 163–177. Geological Society of London Special Publication.

Caruso, F., Pluchino, A., Latora, V., Vinciguerra, S., and Rapisarda, A. (2007). Analysis of self-organized criticality in the olami-feder-christensen model and in real earthquakes. *Physical Review E*, 75:055101(R).

Caruso, F. and Tsallis, C. (2008). Nonadditive entropy reconciles the area law in quantum systems with classical thermodynamics. *Physical Review E*, 78:021102.

Celikoglu, A. and Tirnakli, U. (2012). Earthquakes, model systems and connections to q-statistics. *Acta Geophysica*, 60:535–546.

Chandler, M. (2015). *A Fracture Mechanics Study of an Anisotropic Shale*. PhD thesis, University College London.

Chelidze, T. L. and Gueguen, Y. (1999). Electrical spectroscopy of porous rocks: a review - i.theoretical models. *Geophysical Journal International*, 137:1–15.

Chen, C.-C., Telesca, L., Lee, C.-T., and Sun, T.-S. (2011). Statistical physics of landslides: new paradigm. *EPL (Europhysics Letters)*, 95:49001.

Chen, D.-Y., Zhang, D.-H., and Sun, Z.-J. (1994). Ulf electric-potential changes prior to the fracture in rock samples. In Hayakawa, M. and Fujinawa, Y., editors, *Electromagnetic Phenomena Related to Earthquake Prediction*, pages 323–329. Terra Scientific.

Chun, K.-Y., Henderson, G. A., and Liu, J. (2004). Temporal changes in p-wave attenuation in the loma prieta rupture zone. *Journal of Geophysical Research*, 109:B02317.

Cicerone, R. D., Ebel, J. E., and Britton, J. (2009). A systematic compilation of earthquake precursors. *Tectonophysics*, 476:371–396.

Clarke, J. W., McDowell, R. C., Matzko, J. R., Hearn, P. P., Milton, D. J., Percious, D. J., Vitaliano, D. B., and Ulmishek, G. (1986). The kola superdeep drill hole by y. a. kozlovskiy: A detailed summary. Technical report, US Geological Survey.

Cleri, F., Yip, S., Wolf, D., and Phillpot, S. (1997). Atomic-scale mechanism of crack-tip plasticity: Dislocation nucleation and crack-tip shielding. *Physical Review Letters*, 79(7):1309–1312.

Clint, O. C. (1999). *Electrical potential changes and acoustic emissions generated by fracture and fluid flow during experimental triaxial rock deformation*. PhD thesis, University College London.

Close, J. (2012). Are stress responses to geomagnetic storms mediated by the cryptochrome compass system? *Proceedings of the Royal B: Biological Sciences*, 279:2081–2090.

Contoyiannis, Y. F. and Eftaxias, K. (2008). Tsallis and levy statistics in the preparation of an earthquake. *Nonlinear Processes in Geophysics*, 15(3):379–388.

Contoyiannis, Y. F., Kapiris, P. G., and Eftaxias, K. A. (2005). Monitoring of a preseismic phase from its electromagnetic precursors. *Physical Review E*, 71:066123.

Contoyiannis, Y. F., Nomicos, C., Kopanas, J., Antonopoulos, G., Contoyianni, L., and Eftaxias, K. (2010). Critical features in electromagnetic anomalies detected prior to the l'aquila earthquake. *Physica A*, 389:499–508.

Cook, N. G. W. (1970). An experiment proving that dilatancy is a pervasive volumetric property of brittle rock loaded to failure. *Rock Mechanics*, 2:181–188.

Corliss, W. R. (2001). *Remarkable luminous phenomena in nature: A catalog of geophysical anomalies*. Sourcebook Project.

Correig, A., Urquizu, J., and Vila, J. (1997). Aftershock series of event february 18 1996: an interpretation in terms of self-organised criticality. *Journal of Geophysical Research*, 102:27407–27420.

Costin, L. (1985). Damage mechanics in the post failure regime. *Mechanics of Materials*, 4:149–160.

Cottrell, A. H. (1958). Theory of brittle fracture in steel and similar metals. *Transactions of the American Institute of Mining and Metallurgical Engineers*, 212:192–203.

Covey-Crump, S. J. (1998). Evolution of mechanical state in carrara marble during deformation at 400degc to 700degc. *Journal of Geophysical Research*, 103:29781–29794.

Cowie, P. A. and Scholz, C. H. (1992a). Growth of faults by accumulation of seismic slip. *Journal of Geophysical Research*, 97:11085–11095.

Cowie, P. A. and Scholz, C. H. (1992b). Physical explanation for the displacement-length relationship of faults using a post-yield fracture mechanics model. *Journal of Structural Geology*, 14:1133–1148.

Cowie, P. A., Vanneste, C., and Sornette, D. (1993). Statistical physics model for the spatio-temporal evolution of faults. *Journal of Geophysical Research*, 98:21809–21821.

Cox, S. and Meredith, P. (1993). Microcrack formation and material softening in rock measured by monitoring acoustic emissions. *International Journal of Rock Mechanics and Mining Sciences & Geomechanics Abstracts*, 30(1):11–24.

Cress, G. O., Brady, B. T., and Rowell, G. A. (1987). Sources of electromagnetic radiation from fracture of rock samples in the laboratory. *Geophysical Research Letters*, 14(4):331–334.

Cuomo, V., Lapenna, V., Macchiato, M., Serio, C., and Telesca, L. (1998). Linear and non-linear dynamics in electrical precursory time series: implications for earthquake prediction. *Tectonophysics*, 287:279–298.

da Silva, A. J., Trindade, M. A. S., Santos, D. O. C., and Lima, R. F. (2013). Maximum likelihood q-estimator reveals nonextensivity regulated by extracellular potassium in the mammalian neuromuscular junction. Online: http://arxiv.org/pdf/1311.5990v3.pdf.

Darooneh, A. and Dadashinia, C. (2008). Analysis of the spatial and temporal distributions between successive earthquakes: Nonextensive statistical mechanics viewpoint. *Physica A*, 387:3647–3654.

Darooneh, A. and Mehri, A. (2010). A nonextensive modification of the gutenberg-richter law: q-stretched exponential form. *Physica A*, 389:509–514.

Darot, M., Gueguen, Y., and Baratin, M.-L. (1992). Permeability of thermally cracked granite. *Geophysical Research Letters*, 19(9):869–872.

Davidsen, J., Stanchits, S., and Dresen, G. (2007). Scaling and universality in rock fracture. *Physical Review Letters*, 98:125502.

Davies, D. K. (1964). Trapped charges on dielectrics. *Nature*, 203:290–291.

Davies, K. and Baker, D. (1965). Ionospheric effects observed around the time of the alaska earthquake of march 1964. *Journal of Geophysical Research*, 70:2251–2253.

De Bresser, J., Urai, J., and Olgaard, D. (2005). Effect of water on the strength and microstructure of carrara marble axially compressed at high temperature. *Journal of Structural Geology*, 27(2):265–281.

de Groot, S. R., , and Mazur, P. (1962). *Non-equilibrium Thermodynamics*. North Holland, New York.

Dennis, S. M. and Atkinson, B. K. (1982). The influence of water on the stress supported by experimentally faulted westerly granite. *Geophysical Journal International*, 71:285–294.

Derr, J. S. (1973). Earthquake lights: a review of observations and present theories. *Bulletin of the Seismological Society of America*, 63(6):2177–2187.

Derr, J. S. (1986). Luminous phenomena and their relationship to rock fracture. *Nature*, 321:470–471.

Deshpande, V., Ayas, C., and van Dommelen, H. (2013). A coupled framework for climb-assisted glide in discrete dislocation plasticity. In *50th Annual Technical Meeting*. Society of Engineering Science.

Dewey, J. and Bird, J. (1970). Mountain belts and the new global tectonics. *Journal of Geophysical Research*, 75:2625–2647.

Dienes, J. K. (1982). Permeability, percolation and statistical crack mechanics. In Goodman, H. E. and Heuze, F. E., editors, *Issues in Rock Mechanics*, pages 86–94. American Institute of Mining, Metallurgical and Petroleum Engineering, New York.

Diniz, P., Murta-Junior, L., Brum, D., de Araujo, D., and Santos, A. (2010). Brain tissue segmentation using q-entropy in multiple sclerosis magnetic resonance images. *Brazilian Journal of Medical and Biological Research*, 43:77–84.

Dodge, D., Beroza, G., and Ellsworth, W. (1995). Foreshock sequences of the 1992 landers, california, earthquake and its implication for earthquake nucleation. *Journal of Geophysical Research*, 100:9865–9880.

Dologlou, E. (1993). A three year continuous sample of officially documented predictions issued in greece using the van method: 1987-1989. *Tectonophysics*, 224(1):189 – 202.

Dologlou, E. (2008). Power law relationship between parameters of earthquakes and precursory electrical phenomena. *Natural Hazards and Earth System Sciences*, 8:977–983.

Donath, F. A. and Fruth, L. S. J. (1971). Dependence of strain rate effects on deformation mechanism and rock type. *Journal of Geology*, 79:347–371.

Douglas, P., Bergamini, S., and Renzoni, F. (2006). Tunable tsallis distributions in dissipative optical lattices. *Physical Review Letters*, 96(11):110601.

Drakopoulos, J. and Stavrakakis, G. (1996). A false alarm based on electrical activity recorded at a van-station in northern greece in december 1990. *Geophysical Research Letters*, 23(11):1355–1358.

Duba, A., Heikamp, S., Meurer, W., Nover, G., and Will, G. (1994). Evidence from borehole samples for the role of accessory minerals in lower-crustal conductivity. *Nature*, 367:59–61.

Dullien, F. A. L. (1979). *Porous Media: Fluid Transport and Pore Structure*. Academic Press, Inc.

Eccles, D., Sammonds, P. R., and Clint, O. C. (2005). Laboratory studies of electrical potential during rock failure. *International Journal of Rock Mechanics and Mining Sciences*, 42:900–910.

Edmond, J. and Paterson, M. (1972). Volume changes during the deformation of rocks at high pressures. *International Journal of Rock Mechanics and Mining Sciences & Geomechanics Abstracts*, 9(2):161–182.

Eftaxias, K. (2010). Footprints of nonextensive tsallis statistics, selfaffinity and universality in the preparation of the l'aquila earthquake hidden in a pre-seismic em emission. *Physica A: Statistical Mechanics and its Applications*, 389(1):133–140. cited By (since 1996)14.

Eftaxias, K., Kapiris, P., Dologlou, E., Kopanas, J., Bogris, N., Antonopoulos, G., Peratzakis, A., and Hadjicontis, V. (2002). Em anomalies before the kozaniŰgrevena earthquake: A study of their behavior through laboratory experiments. *Geophysical Research Letters*, 29(8):69/1–4.

Eftaxias, K., Kapiris, P., Polygiannakis, J., Bogris, N., Kopanas, J., Antonopoulos, G., Peratzakis, A., and Hadjicontis, V. (2001). Signature of pending earthquake from electromagnetic anomalies. *Geophysical Research Letters*, 28(17):3321–3324.

England, P. and Jackson, J. (2011). Uncharted seismic risk. *Nature Geoscience*, 4:348–349.

Englmant, R., Rivier, N., and Jaeger, Z. (1987). Fragment-size distribution in disintegration by maximum-entropy formalism. *Philosophical Magazine Part B*, 56(6):751–769.

Enomoto, Y. (1996). Notes on generation and propagation of seismic transient electric signals. In Lighthill, J., editor, *A Critical Review of VAN*, pages 324–331. World Scientific, Singapore.

Enomoto, Y. (2012). Coupled interation of earthquake nucleation with deep earth gases: a possible mechanism for seismo-electromagnetic phenomena. *Geophysical Journal International*, 191:1210–1214.

Enomoto, Y. and Hashimoto, H. (1990). Emission of charged particles from indentation fracture of rocks. *Nature*, 346:641–643.

Enomoto, Y. and Hashimoto, H. (1992). Transient electrical activity accompanying rock under indentation loading. *Tectonophysics*, 211:337–344.

Enomoto, Y., Hashimoto, H., Shirai, N., Murakami, Y., Mogi, T., Takada, M., and Kasahara, M. (2006). Anomalous geoelectric signals possibly related to the 2000 mt. usu eruption and 2003 tokachi-oki earthquakes. *Physics and Chemistry of the Earth*, 31:319–324.

Enomoto, Y., Shimamoto, T., Tsutsumi, A., and Hashimoto, H. (1994). Transient electric signals prior to rock fracturing: potential use as an immediate earthquake precursor. In Hayakawa, M. and Fujinawa, Y., editors, *Electromagnetic Phenomena Related to Earthquake Prediction*, pages 253–259. Terra Scientific, Tokyo.

Enomoto, Y. and Zheng, Z. (1998). Possible evidences of earthquake lightning accompanying the 1995 kobe earthquake inferred from the nojima fault gouge. *Geophysical Research Letters*, 25:2721–2724.

Ernst, T., Jankowski, J., Rozluski, C., and Teisseyre, R. (1993). Analysis of the electromagnetic field recorded in the friuli seismic zone, ne italy. *Tectonophysics*, 224(1):141–148.

Evans, B., Frederich, J., and Wong, T.-f. (1990). The brittle-ductile transition in rocks: recent experimental and theoretical progress. In Duba, A., Durham, W., Handin, J., and Wang, H., editors, *The Brittle-Ductile Transition in Rocks: The Heard Volume*, volume 56 of *Geophysical Monograph Series*, page 1Ű20. American Geophysical Union, Washington, D.C.

Fan, Y. Y., Du, X. B., Zlotnicki, J., Tan, D. C., An, Z. H., Chen, J. Y., Zheng, G. L., Liu, J., and Xie, T. (2010). The electromagnetic phenomena before the ms8.0 wenchuan earthquake. *Chinese Journal of Geophysics*, 53(6):997–1010.

Faulkner, D. R., Mitchell, T. M., Healy, D., and Heap, M. J. (2006). Slip on 'weak' faults by the rotation of regional stress in the fracture damage zone. *Nature*, 444:922–925.

Fenoglio, M., Johnston, M., and Byerlee, J. (1995). Magnetic and electric fields associated with changes in high pore pressure in fault zones: Application to the loma prieta ulf emissions. *Journal of Geophysical Research*, 100:12951–12958.

Fidani, C. (2010). The earthquake lights (eql) of the 6 april 2009 aquila earthquake, in central italy. *Natural Hazards and Earth System Sciences*, 10:967–978.

Fiffolt, D., Petrenko, V., and Schulson, E. (1993). Preliminary study of electromagnetic emissions from cracks in ice. *Philosophical Magazine Part B*, 67:289–299.

Fischbach, D. and Nowick, A. (1958). Some transient electrical effects of plastic deformation in nacl crystals. *Physics and Chemistry of Solids*, 5:302–315.

Fischer, G. and Paterson, M. S. (1992). Measurement of permeability and storage capacity in rocks during deformation at high temperature and pressure. *International Geophysics*, 51:213–252.

Fischer, G. J. and Paterson, M. S. (1989). Dilatancy during rock deformation at high temperatures and pressures. *Journal of Geophysical Research: Solid Earth*, 94(B12):17607–17617.

Ford, I. (2011). Statistical thermodynamics. Oral presentation and lecture notes.

Fortin, J., Stanchits, S., Dresen, G., and Gueguen, Y. (2005). Elastic wave velocities and permeability evolution during compaction of bleurswiller sandstone. *International Journal of Rock Mechanics and Mining Sciences*, 42:873–889.

Fortin, J., Stanchits, S., Dresen, G., and Gueguen, Y. (2006). Acoustic emission and velocities associated with formation of compaction bands in sandstone. *Journal of Geophysical Research*, 111:B10203.

Fowler, C. M. R. (2005). *Theorem Solid Earth: An Introduction to Global Geophysics*. Cambridge University Press.

Francois, D. and Wilshaw, T. (1968). The effect of hydrostatic pressure on the cleavage fracture of polycrystalline materials. *Journal of Applied Physics*, 39(9):4170–4177.

Fraser-Smith, A., Bernardi, A., McGill, P., Ladd, E., Helliwell, R., and Villard Jr, O. (1990). Low-frequency magnetic field measurements near the epicenter of the ms 7.1 loma prieta earthquake. *Geophysical Research Letters*, 17:1465–1468.

Fraser-Smith, A. C., Bernadi, A., McGill, P. R., and Villard Jr., O. (1991). Ulf magnetic field measurements near the epicenter of the ms 7.1 loma prieta earthquake. *Physics of the Earth and Planetary Interiors*, 68:45–63.

Fredrich, J., Evans, B., and Wong, T.-f. (1990). Effect of grain size on brittle and semibrittle strength: implications for micromechanical modelling of failure in compression. *Journal of Geophysical Research*, 95:10907Ű10920.

Fredrich, J. T., Evans, B., and Wong, T.-F. (1989). Micromechanics of the brittle to plastic transition in carrara marble. *Journal of Geophysical Research: Solid Earth*, 94(B4):4129–4145.

Fredrich, J. T. and Wong, T.-f. (1986). Micromechanics of thermally induced cracking in three crustal rocks. *Journal of Geophysical Research: Solid Earth*, 91(B12):12743–12764.

Freeze, A. R. and Cherry, J. A. (1979). *Groundwater*. Prentice Hall.

Frenkel, J. (1926). Uber die warmebewegung in festen und flussigen korpern. *Zeitschrift fur Physik*, 35:652–659.

Freund, F. (1999). Earthquake prediction is worthy of study. *EOS*, 80(20):–.

Freund, F. (2000). Time-resolved study of charge generation and propagation in igneous rocks. *Journal of Geophysical Research*, 105(B5):11001–11019.

Freund, F. (2001). Electronic charge carriers in igneous rocks and their activation through tectonic processes. Southern California Earthquake Centre website: http://www.scec.org/news/01news/es_abstracts/Freund.pdf.

Freund, F. (2002). Charge generation and propagation in igneous rocks. *Journal of Geodynamics*, 33(4):543–570.

Freund, F. (2003a). On the electrical conductivity structure of the stable continental crust. *Journal of Geodynamics*, 35:353–388.

Freund, F. (2003b). Rocks that crackle and sparkle and glow: strange pre-earthquake phenomena. *Journal of Scientific Exploration*, 17(1):37–71.

Freund, F. (2010). Toward a unified solid state theory for pre-earthquake signals. *Acta Geophysica*, 58(5):719–766.

Freund, F. (2011a). The future of forecasting earthquakes. SETI Institute Science Blog: http://www.seti.org/seti-institute/project/details/friedemann-freund- Accessed: 9 May 2014.

Freund, F. (2011b). Pre-earthquake signals: Underlying physical processes. *Journal of Asian Earth Sciences*, 41(4-5):383–400.

Freund, F. and Borucki, J. (1999). Charge carrier generation and charge cloud propagation following 100 m/sec impacts on igneous rocks. In Hayakawa, M., editor, *Atmospheric and Ionospheric Electromagnetic Phenomena Associated with Earthquakes*, pages 839–857. Terra Scientific, Tokyo.

Freund, F., Dickinson, J. T., and Cash, M. (2002). Hydrogen in rocks: An energy source for deep microbial communities. *Astrobiology*, 2:83–92.

Freund, F. and Stolc, V. (2013). Nature of pre-earthquake phenomena and their effects on living organisms. *Animals*, 3(2):513–531.

Freund, F., Whang, E.-J., and Lee, J. (1994). Highly mobile charge carriers in minerals: Key to the enigmatic electrical earthquake phenomena. In Hayakawa, M. and Fujinawa, Y., editors, *Electromagnetic Phenomena related to Earthquake Prediction*, pages 271–292. Terra Scientific, Tokyo.

Freund, F. T. (2007a). Pre-earthquake signals? part i: Deviatoric stresses turn rocks into a source of electric currents. *Natural Hazards and Earth System Sciences*, 7(5):535–541.

Freund, F. T. (2007b). Pre-earthquake signals? part ii: Flow of battery currents in the crust. *Natural Hazards and Earth System Sciences*, 7(5):543–548.

Freund, F. T., Takeuchi, A., and Lau, B. W. (2006). Electric currents streaming out of stressed igneous rocks - a step towards understanding pre-earthquake low frequency em emissions. *Physics and Chemistry of the Earth, Parts A/B/C*, 31(4-9):389–396.

Freund, F. T., Takeuchi, A., Lau, B. W. S., Post, R., Keefner, J., Mellon, J., and Al-Manaseer, A. (2004). Stress-induced changes in the electrical conductivity of igneous rocks and the generation of ground currents. *TAO*, 15(3):437–467.

Frid, V., Bahat, D., Goldbaum, J., and Rabinovitch, A. (2000). Experimental and theoretical investigations of electromagnetic radiation induced by rock fracture. *Israel Journal of Earth Sciences*, 49:9–19.

Frid, V., Goldbaum, J., Rabinovitch, A., and Bahat, D. (2011). Time-dependent benioff strain release diagrams. *Philosophical Magazine*, 91(12):1693–1704.

Frid, V., Rabinovitch, A., and Bahat, D. (2003). Fracture induced electromagnetic radiation. *Journal of Physics D: Applied Physics*, 36:1620–1628.

Frid, V., Rabinovitch, A., and D., B. (1999). Electromagnetic radiation associated with induced triaxial fracture in granite. *Philosophical Magazine Letters*, 79(2):79–86.

Frid, V. and Vozoff, K. (2005). Electromagnetic radiation induced by mining rock failure. *International Journal of Coal Geology*, 64(1-2):57–65.

Frost, H. and Ashby, M. F. (1982). *Deformation Mechanism Maps: The Plasticity and Creep of Metals and Ceramics*. Pergamon Press.

Fujinawa, Y. and Takahashi, K. (1990). Emission of electromagnetic radiation preceding the ito seismic swarm of 1989. *Nature*, 347:376–378.

Fung, Y. C. (1965). *Foundations of Solid Mechanics*. Prentice-Hall.

Gabrielli, F. and Di Bucci, D. (2014). Comment on "communicating earthquake risk to the public: the trial of the 'l'aquila seven"' by david e. alexander. *Natural Hazards*, 75:991–998.

Gao, Y. and Crampin, S. (2004). Observations of stress relaxation before earthquakes. *Geophysical Journal International*, 157:578–582.

Gaunt, H. E. (2014). *Experimental study of permeability under simulated volcanic conditions on lava dome rocks from Mt. St. Helens: constraints on degassing and eruption style*. PhD thesis, University College London.

Geilikman, M. B., Golubeva, T. V., and Pisarenko, V. F. (1990). Multifractal patterns of seismicity. *Earth and Planetary Science Letters*, 99:127–132.

Gelfand, I., Guberman, S., Keilis-Borok, V., Knopoff., L., Press, F., Ranzman, E., Rotwain, I., and Sadovsky, A. (1976). Pattern recognition applied to earthquake epicenters in california. *Physics of the Earth and Planetary Interiors*, 11:227–283.

Geller, R. J. (1997). Earthquake prediction: a critical review. *Geophysical Journal International*, 131(3):425–450.

Geller, R. J., Jackson, D., Kagan, Y., and Mulargia, F. (1997). Earthquakes cannot be predicted. *Science*, 275:1616–1617.

Gensane, O., Konyukov, B., Le Mouel, J.-L., and Morat, P. (1999). Sp coseismic signals observed on an electrodes array in an underground qarry. *Geophysical Research Letters*, 26(23):3529–3532.

Gervino, G., Cigolini, C., Lavagno, A., Marino, C., Prati, P., Pruiti, L., and Zangari, G. (2004). Modelling temperature distributions and radon emission at stromboli volcano using a non-extensive statistical approach. *Physica A: Statistical Mechanics and its Applications*, 340(1-3):402–409.

Gibbs, J. W. (1902). *Elementary Principles in Statistical Mechanics Ű Developed with Especial Reference to the Rational Foundation of Thermodynamics*. C. ScribnerŠs Sons, New York.

Gilman, J. J. (2003). *Electronic Basis of the Strength of Materials*. Cambridge University Press, Cambridge, UK.

Glover, P. and Adam, A. (2008). Correlation between crustal high conductivity zones and seismic activity and the role of carbon during shear deformation. *Journal of Geophysical Research*, 113:B12210.

Glover, P., Baud, P., Darot, M., Meredith, P., Boon, S., LeRevelec, M., Zoussi, S., and Reuschle, T. (1995). a/b phase transition in quartz monitored using acoustic emissions. *Geophysical Journal International*, 120(3):775–782. cited By (since 1996)32.

Glover, P. W. J., Gomez, J. B., Meredith, P. G., Boon, S. A., Sammonds, P., and Murrell, S. A. F. (1996). Modelling the stress-strain behaviour of saturated rocks undergoing triaxial deformation using complex electrical conductivity measurements. *Surveys in Geophysics*, 17:307–330.

Glover, P. W. J. and Vine, F. J. (1992). Electrical conductivity of carbon-bearing granulite at raised temperatures and pressures. *Nature*, 360:723–726.

Gokhberg, M., Morgounov, V. A., Yoshino, T., and Tomizawa, I. (1982). Experimental measurement of electromagnetic emissions possibly related to earthquakes in japan. *Journal of Geophysical Research*, 87(B9):7824–7828.

Gokhberg, M. B., Morgounov, V. A., and Pokhotelov, O. A. (1995). *Earthquake Prediction - Seismo-Electromagnetic Phenomena*. Gordon and Breach Publishers.

Gomberg, J. and Davis (1996). Stress-strain changes and triggered seismicity at the geysers in california. *Journal of Geophysical Research*, 101:733–749.

Goncharov, A., Korjakov, V. P., and Kuznetzov, V. M. (1980). Acoustic emission and electromagnetic radiation during uniaxial compression. *Doklady Akademii Nauk SSSR*, 255(4):821–824.

Graham, C. C., Stanchits, S., Main, I. G., and Dresen, G. (2010). Comparison of polarity and moment tensor inversion methods for source analysis of acoustic emission data. *International Journal of Rock Mechanics and Mining Sciences*, 47(1):161–169.

Grant, R. A., Halliday, T., Balderer, W. P., Leuenberger, F., Newcomer, M., Cyr, G., and Freund, F. T. (2011). Ground water chemistry changes before major earthquakes and possible effects on animals. *International Journal of Environmental Research and Public Health*, 8:1936–1956.

Grasso, J. R. and Sornette, D. (1998). Testing self-organised criticality by induced seismicity. *Journal of Geophysical Research*, 103:29965–29987.

Griffith, A. A. (1921). The phenomena of rupture and flow in solids. *Philosophical Transactions of the Royal Society of London Series A*, 221:163–198.

Griffith, A. A. (1924). The theory of rupture. In *Proceedings of the First International Congress of Applied Mechanics, Delft*, pages 55–63.

Griggs, D. T. and Handin, J. (1960). Observations on fracture and a hypothesis of earthquakes. *Geological Society of America Memoirs*, 79:347–364.

Gruszow, S., Rossingnol, J., Tzanis, A., and Le Mouel, J.-L. (1996). Identification and analysis of electromagnetic signals in greece: the case of the kozani earthquake van prediction. *Geophysical Research Letters*, 23:2025–2028.

Gueguen, Y. and Palciauskas, V. (1994). *Introduction to the Physics of Rocks*. Princeton University Press.

Gueguen, Y. and Schubnel, A. (2003). Elastic wave velocities and permeability of cracked rocks. *Tectonophysics*, 370(1-4):163–176.

Gufeld, I. L., Gusev, G., and Pokhotelov, O. (1994). Is the prediction of earthquake date possibe by vlf radio wave monitoring method? In Hayakawa, M. and Fujinawa, Y., editors, *Electromagnetic Phenomena Related to Earthquake Prediction*. Terra Scientific, Tokyo.

Gutenberg, B. and Richter, C. F. (1944). Frequency of earthquakes in california. *Bulletin of the Seismological Society of America*, 57:341–371.

Gutenberg, B. and Richter, C. F. (1954). *Seismicity of the Earth and Associated Phenomena*. Princeton University Press.

Hacker, B. R. and Kirby, S. H. (1993). High-pressure deformation of calcite marble and its transformation to aragonite under non-hydrostatic conditions. *Journal of Structural Geology*, 15(9-10):1207–1222.

Hadjicontis, V. and Mavromatou, C. (1994). Transient electric signals prior to rock failure under uniaxial compression. *Geophysical Research Letters*, 21:1687–1690.

Hadjicontis, V. and Mavromatou, C. (1996). Laboratory investigation of electric signals preceding earthquakes. In Lighthill, J., editor, *Critical Review of VAN*, pages 105–117. World Scientific, Singapore.

Hadley, K. (1975). Azimuthal variation of dilatancy. *Journal of Geophysical Research*, 80:4845–4850.

Hadley, K. (1976). Comparison of calculated and observed crack densities and seismic velocities in westerly granite. *Journal of Geophysical Research*, 81:3484–3494.

Hallbauer, D. K., Wagner, H., and Cook, N. G. W. (1973). Some observations concerning the microcscopic and mechanical behaviour of quartzite specimens in stiff triaxial compression tests. *International Journal of Rock Mechanics and Mining Sciences Geomechanics Abstracts*, 10:713–726.

Handin, J., Hager, R., Friedman, M., and Feather, J. (1963). Experimental deformation of sedimentary rocks under confining pressure: pore pressure effects. *Bulletin of the American Association of Petroleum Geologists*, 47:717–755.

Hanel, R., Thurner, S., and Gell-Mann, M. (2011). Generalized entropies and the transformation group of superstatistics. *Proceedings of the National Academy of Sciences*, 108(16):6390–6394.

Harada, M., Hattori, K., and Isezaki, N. (2004). Transfer function approach to signal discrimination of ulf geomagnetic data. *Physics and Chemistry of the Earth*, 29(4-9):409–417.

Harper, W. R. (1951). The volta effect as a cause of static electrification. *Proceedings of the Royal Society*, A205:83–103.

Hasumi, T. (2007). Interoccurrence time statistics in the two-dimensional burridgeŰknopoff model. *Physical Review E*, 76(2):026117.

Hasumi, T. (2009). Hypocenter interval statistics between successive earthquakes in the two-dimensional burridgeŰknopoff model. *Physica A*, 388:477–482.

Hatton, C. G., Main, I. G., and Meredith, P. G. (1994). Non-universal scaling of fracture length and opening displacement. *Nature*, 367:160–162.

Hattori, K. (2004). Ulf geomagnetic changes associated with large earthquakes. *TAO*, 15:329–360.

Hattori, K., Akinaga, Y., Hayakawa, M., Yumoto, K., Nagao, T., and Uyeda, S. (2002). Ulf magnetic anomaly preceding the 1997 kagoshima earthquakes. In Hayakawa, M. and Molchanov, O., editors, *Seismo-Electromagnetics: Lithosphere-Atmosphere-Ionosphere Coupling*, pages 19–28. Terra Scientific.

Hattori, K., Serita, K., Gotoh, K., Yoshino, C., Harada, M., Isezaki, N., and Hayakawa, M. (2004). Ulf geomagnetic anomaly associated with 2000 izu islands earthquake swarm, japan. *Physics and Chemistry of the Earth*, 29:425–436.

Hawkes, I. and Mellor, M. (1970). Uniaxial testing in rock mechanics laboratories. *Engineering Geology*, 4(3):179–285.

Hayakawa, M., editor (1999). *Atmospheric and Ionospheric Electromagnetic Phenomena Associated with Earthquakes*. Terra Scientific, Tokyo.

Hayakawa, M. and Fujinawa, Y., editors (1994). *Electromagnetic Phenomena Related to Earthquake Prediction*. Terra Scientific, Tokyo.

Hayakawa, M. and Hobara, Y. (2010). Current status of seismo-electromagnetics for short-term earthquake prediction. *Geomatics, Natural Hazards and Risk*, 1(2):115–155.

Hayakawa, M., Hobara, Y., Ohta, K., and Hattori, K. (2011). The ultra-low-frequency magnetic disturbances associated with earthquakes. *Earthquake Science*, 24:523–534.

Hayakawa, M., Itoh, T., Hattori, K., and Yumoto, K. (2000). Ulf electromagnetic precursors for an earthquake at biak, indonesia on february 17, 1996. *Geophysical Research Letters*, 27(10):1531–1534.

Hayakawa, M., Kawate, R., Molchanov, O. A., and Yumoto, K. (1996a). Results of ultra-low-frequency magnetic field measurements during the guam earthquake of 8 august 1993. *Geophysical Research Letters*, 23(3):241–244.

Hayakawa, M. and Molchanov, O., editors (2002). *Seismo Electromagnetics: Lithosphere Ű Atmosphere Ű Ionosphere Coupling*. TERRAPUB.

Hayakawa, M., Molchanov, O., Ondoh, T., and Kawai, E. (1996b). Anomalies in the subionospheric vlf signals for the 1995 hyogo-ken nanbu earthquake. *Journal of Physics of the Earth*, 44:413–418.

Hayakawa, M., Molchanov, O. A., and team, N. . U. (2004). Achievements of nasdaŠs earthquake remote sensing frontier project. *TAO*, 15(3):311–327.

Healy, D., Jones, R. R., and Holdsworth, R. E. (2006). Three-dimensional brittle shear fracturing by tensile crack interaction. *Nature*, 439(7072):64–67.

Heap, M. (2009). *Creep: Time-dependent brittle deformation in rocks*. PhD thesis, University College London.

Heap, M. J. and Faulkner, D. R. (2008). Quantifying the evolution of static elastic properties as crystalline rock approaches failure. *International Journal of Rock Mechanics and Mining Sciences*, 45:564–573.

Heard, H. (1960). Transition from brittle fracture to ductile flow in solenhofen limestone as a function of temperature, confining pressure, and interstitial fluid pressure. In Griggs, D. and Handin, J., editors, *Rock Deformation*, volume 79, page 193Ű226. Geol Soc Am Mem.

Heard, H. (1963). Effect of large changes in strain rate in the experimental deformation of yule marble. *Journal of Geology*, 71(2):162–195.

Heki, K. (2011). Ionospheric electron enhancement preceding the 2011 tohoku-oki earthquake. *Geophysical Research Letters*, 38:L17312.

Hellmann, R., Renders, P. J. N., Gratier, J.-P., and Guiguet, R. (2002). Experimental pressure solution compaction of chalk in aqueous solutions part 1. deformation behavior and chemistry. In *Water-Rock Interactions, Ore Deposits, and Environmental Geochemistry: A Tribute to David A. Crerar*, Special Publication No. 7. The Geochemical Society, St. Louis, MO, USA.

Helmstetter, A., Kagan, Y., and Jackson, D. (2006). Comparison of short-term and long-term earthquake forecast models for southern california. *Bulletin of the Seismological Society of America*, 96:90–106.

Helmut, F. and Kolbesen, B., editors (1976). *Agglomerate von Zwischengitteratomen (Swirl-Defekte) in Silizium - ihre Bedeutung fur Grundlagenforschung und Technologie*. Jahrbuch der Akademie der Wissenschaften in Gottingen.

Henderson, J. R. and Main, I. G. (1992). A simple-fracturemechanical model for the evolution of seismicity. *Geophysical Research Letters*, 19:365–368.

Henderson, T., Sonwalkar, V., Helliwell, R., Inan, U., and Fraser-Smith, A. (1993). A search for elf/vlf emissions induced by earthquakes as observed in the ionosphere by the de-2 satellite. *Journal of Geophysical Research*, 98:9503–9509.

Heyda, M. (2006). A practical guide to conductivity measurement. Online: http://www.mbhes.com/conductivity_measurement.htm. Accessed: 12 February 2013.

Hickman, S., Zoback, M., and Ellsworth, W. (2004). Introduction to the special section: preparing for the san andreas fault observatory at depth. *Geophysical Research Letters*, 31:L12S01.

Hill, D. P. and other authors, . (1993). Seismicity remotely triggered by the magnitude 7.3 landers, california earthquake. *Science*, 260:1617–1623.

Hirata, T. and Imoto, M. (1991). Multfractal analysis of spatial distribution of earthquakes in the kanto region. *Geophysical Journal International*, 107:155–162.

Hoek, E. and Bieniawski, Z. (1965). Brittle fracture propagation in rock under compression. *International Journal of Fracture Mechanics*, 1:137–155.

Holcomb, D. J. (1993). General theory of the kaiser effect. *International Journal of Rock Mechanics and Mining Sciences*, 30:929–935.

Holliday, J. R., Nanjo, K. Z., Tiampo, K. F., Rundle, J. B., and Turcotte, D. L. (2005). Earthquake forecasting and its verification. *Nonlinear Processes in Geophysics*, 12:965–977.

Homand-Etienne, F. and Troalen, J.-P. (1984). Behaviour of granites and limestones subjected to slow and homogeneous temperature changes. *Engineering Geology*, 20:219–233.

Honkura, Y. and Tanaka, H. (1996). Probability of earthquake occurrence in greece with special reference to the v an predictions. *Geophysical Research Letters*, 23(11):1417–1420.

Horii, D. and Nemat-Nasser, S. (1985). Compression induced microcrack growth in brittle solids: axial splitting and shear failure. *Journal of Geophysical Research*, 87(B4):3105–3125.

Hornby, B. E. (1998). Experimental laboratory determination of the dynamic elastic properties of wet, drained shales. *Journal of Geophysical Research*, 103(B12):29945–29964.

Huang, J., Narkounskaia, G., and Turcotte, D. L. (1992). A cellular-automata, slider-block model for earthquakes ii. demonstration of self-organised criticality for a 2-d system. *Geophysical Journal International*, 111(2):259–269.

Huang, J. and Turcotte, D. L. (1990). Are earthquakes an example of deterministic chaos? *Geophysical Research Letters*, 17:223–226.

Huang, Y., Saleur, H., Sammis, C. G., and Sornette, D. (1998). Precursors, aftershocks, criticality and self-organized criticality. *Europhysics Letters*, 41:43–48.

Hubbert, M. K. and Rubey, W. W. (1959). Role of fluid pressure in mechanics of overthrust faulting. i. mechanics of fluid filled porous solids and its application to overthrust faulting. *Bulletin of the Geological Society of America*, 70:115–166.

Hull, D. and Bacon, D. (2001). *Introduction to Dislocations*. Butterworth Heineman, 4th edition.

Hunt, S. (2009). *Deforming the Earth: An experimental study of subduction-zone rheology*. PhD thesis, University College London.

Hunt, S., Dobson, D., Wood, I., J., B., Mecklenburgh, J., and Oliver, E. (2009). Deformation of olivine at 5 gpa and 350-900 degrees c. *Physics of the Earth and Planetary Interiors*, 172:84–90.

Ifantis, A., Tselentis, G.-A., Varotsos, P., and Thanasoulas, C. (1993). Long term variations of the earthŠs electric field preceding two earthquakes in greece. *Acta Geophysica Polonica*, XLI 4:337–350.

Igarashi, G., Saeki, S., Takahata, N., Sumikawa, K., Tasaka, S., Sasaki, Y., Takashasi, M., and Sano, Y. (1995). Ground-water radon anomaly before the kobe earthquake in japan. *Science*, 269:60–61.

Iida, I., Mori, Y., Obata, Y., and Mogi, K. (2000). Measurement of ae and electric potential changes in fracture of brittle materials. *Progress in Acoustic Emission*, 10:325–330.

III (2014). Earthquakes and tsunamis. Website: http://www.iii.org/fact-statistic/earthquakes-and-tsunamis. Accessed: 8 July 2014.

Ikeya, M., Furuta, H., Kajiwara, N., and Anzai, H. (1996). Ground electric field effects on rats and sparrows: seismic anomalous animal behaviors (saabs). *Japanese Journal of Applied Physics*, 35:4587–4594.

Inan, S., Balderer, W. P., Leuenberger-West, F., Yakan, H., Zvan, A., and Freund, F. T. (2012). Springwater chemical anomalies prior to the mw 7.2 van earthquake (turkey). *Geochemical Journal*, 46:e11–e16.

Isacks, B., Oliver, J., and Sykes, L. R. (1968). Seismology and the new global tectonics. *Journal of Geophysical Research*, 73:5855–5899.

Ishido, T. and Mizutani, H. (1981). Experimental work and theoretical basis of electrokinetic phenomena in rock-water systems and its application to geophysics. *Journal of Geophysical Research*, 86:1763–1775.

Ismail, I. and Murrell, S. (1976). Dilatancy and the strength of rocks containing pore water under undrained conditions. *Geophysical Journal of the Royal Astronomical Society*, 44:107–134.

Ito, K. and Matsuzaki, M. (1990). Earthquakes as self-organised critical phenomena. *Journal of Geophysical Research*, 95:6853–6860.

Jackson, D. (1996). Earthquake prediction evaluation standards applied to the van method. *Geophysical Research Letters*, 23(11):1363–1366.

Jaeger, J. C. and Cook, N. G. W. (1979). *Fundamentals of Rock Mechanics*. Chapman and Hall, 3rd edition.

Jaeger, J. C., Cook, N. G. W., and Zimmerman, R. W. (2007). *Fundamentals of Rock Mechanics*. Blackwell, 4th edition.

Jaume, S. C. (2000). Changes in earthquake size-frequency distributions underlying seismic moment / energy release. In Rundle, J. B., Turcotte, D. L., and Klein, W., editors, *GeoComplexity and the Physics of Earthquakes*, Geophysical Monograph Series. American Geophysical Union.

Johnston, M. (1990). Near-field high resolution strain measurements prior to the october 18 1989 loma prieta ms 7.1 earthquake. *Geophysical Research Letters*, 17:1777–1780.

Johnston, M. (1997). Review of electrical and magnetic fields accompanying seismic and volcanic activity. *Surveys in Geophysics*, 18:441–475.

Johnston, M. and Mueller, R. (1987). Seismomagnetic observation during the 8 july 1986 magnitude 5.9 north palm springs earthquake. *Science*, 237:1201–1203.

Johnston, M., Mueller, R., and Sasai, Y. (1994). Magnetic field observations in the near-field the 28 june 1992 mw 7.3 landers, california, earthquake. *Bulletin of the Seismological Society of America*, 84:792–798.

Johnston, M. J. S. (2002). Electromagnetic fields generated by earthquakes. In Lee, W. H. K., Kanamori, H., Jennings, P. C., and Kisslinger, C., editors, *IASPEI International Handbook of Earthquake and Engineering Seismology: Part A*, chapter 38, pages 621–635. Academic Press.

Jones, C. and Meredith, P. G. (1998). Experimental study of elastic wave propagation anisotropy and permeability anisotropy in an illitic shale. *Proceedings of the SPE/ISRM Rock Mechanics in Petroleum Engineering Conference*, 2:307–313.

Jones, L. and Molnar, P. (1976). Frequency of foreshocks. *Nature*, 262:677–679.

Jordan, T., Chen, Y.-T., Gasperini, P., Madariaga, R., Main, I., Marzocchi, W., Papadopoulos, G., Sobolev, G., Yamaoka, K., and Zschau, J. (2011). Operational earthquake forecasting. state of knowledge and guidelines for utilization. *Annals of Geophysics*, 54(4).

Jordan, T. H. (2006). Earthquake predictability, brick by brick. *Seismological Research Letters*, 77(1):3–6.

Jouniaux, L., Masuda, K., Lei, X., Nishizawa, O., Kusunose, K., Liu, L., and Ma, W. (2001). Comparison of microfracture localisation in granite between fracturation and slip of a preexisting macroscopic healed joint by acoustic emission measurements. *Journal of Geophysical Research*, 106:8687–8698.

Jouniaux, L. and Pozzi, J.-P. (1995a). Permeability dependence of streaming potential in rocks for various fluid conductivities. *Geophysical Research Letters*, 22(4):485–488.

Jouniaux, L. and Pozzi, J.-P. (1995b). Streaming potential and permeability of saturated sandstones under triaxial stress: Consequences for electrotelluric anomalies prior to earthquakes. *Journal of Geophysical Research*, 100(B6):10197–10209.

Jouniaux, L. and Pozzi, J.-P. (1997). Laboratory measurements of anomalous 0.1Ű0.5 hzstreaming potential under geochemical changes: Implications for electrotelluric precursors to earthquakes. *Journal of Geophysical Research*, 102(B7):15335–15343.

Kachanov, M. (1994). Elastic solids with many cracks and related problems. In Hutchinson, J. and Wu, T., editors, *Advances in Applied Mechanics*, volume 30, pages 259–445. Academic Press.

Kagan, Y. (1992). Seismicity: the turbulence of solids. *Nonlinear Science Today*, 2:123–134.

Kagan, Y. (1996). Van earthquake predictions - an attempt at statistical evaluation. *Geophysical Research Letters*, 23(11):1315–1318.

Kagan, Y. (2006). Why does theoretical physics fail to explain and predict earthquake occurrence? In Bhattacharyya, P. and Chakrabarti, B., editors, *Modelling Critical and Catastrophic Phenomena in Geoscience: A Statistical Physics Approach*, Lecture Notes in Physics, pages 303–362. Springer.

Kagan, Y. and Jackson, D. (1996). Statistical tests of van earthquake predictions: Comments and reflections. *Geophysical Research Letters*, 23:1433–1436.

Kagan, Y. Y. (1997). Are earthquakes predictable? *Geophysical Journal International*, 131(3):505–525.

Kaiser, L. (1953). Erkenntnisse und folgerungen aus der messung von geräuschen bei zugbeanspruchung von metallischen werkstoffen. *Archiv. für das Eisenhüttenwesen*, 24:43–45.

Kalimeri, M., Papadimitriou, C., Balasis, G., and Eftaxias, K. (2008). Dynamical complexity detection in pre-seismic emissions using nonadditive tsallis entropy. *Physica A*, 387:1161–1172.

Kamogawa, M., Ofuruton, H., and Ohtsuki, Y.-H. (2005). Earthquake light: 1995 kobe earthquake in japan. *Atmospheric Research*, 76:438–444.

Kanamori, H. and Anderson, D. L. (1975). Theoretical bases of some empirical relations in seismology. *Bulletin of the Seismological Society of America*, 65:1073–1095.

Kapiris, P. G., Eftaxias, K. A., and Chelidze, T. L. (2004). Electromagnetic signature of prefracture criticality in heterogeneous media. *Physical Review L*, 92(6):065702.

Kapiris, P. G., Eftaxias, K. A., Nomikos, K. D., Polygiannakis, J., Dologlou, E., Balasis, G. T., Bogris, N. G., Peratzakis, A. S., and Hadjicontis, V. E. (2003). Evolving towards a critical point: A possible electromagnetic way in which the critical regime is reached as the rupture approaches. *Nonlinear Processes in Geophysics*, 10:511–524.

Karakelian, D., Klemperer, S., Fraser-Smith, A., and Thompson, G. (2002). Ultra-low frequency electromagnetic measurements associated with the 1988 mw 5.1 san juan bautista, california earthquake and implications for mechanisms of electromagnetic earthquake precursors. *Tectonophysics*, 359:65–79.

Karasev, V., Krotova, N., and Deryagin, B. (1953). Studies in electron emission when a polymer film is pulled from glass in a vacuum. *Doklady Akademii Nauk SSSR*, 88(5):715.

Kato, N., Yamamoto, K., Yamamoto, H., and Hirasawa, T. (1992). Strain-rate effect on frictional strength and the slip nucleation process. *Tectonophysics*, 211(1âĂŞ4):269–282.

Kay, R. W. (1994). Geomagnetic storms: association with incidence of depression as measured by hospital admission. *British Journal of Psychiatry*, 164:403–409.

Kaye and Laby Online (2005). Tables of physical and chemical constants (16th edition 1995). 2.7.9 physical propertiesof seawater. Version 1.0. www.kayelaby.npl.co.uk.

Kearey, P. and Vine, F. (1990). *Global Tectonics*. Blackwell, Oxford.

Keilis-Borok, V. and Soloviev, A. (2003). *Nonlinear Dynamics of the Lithosphere and Earthquake Prediction*. Springer, Heidelberg.

Keller, G. V. (1989). Electrical properties. In Carmichael, R. S., editor, *Practical Handbook of Physical Properties of Rocks and Minerals*, pages 359–428. CRC Press, Boca Raton, FL.

Keller, G. V., Anderson, L. A., and Pritchard, J. I. (1966). Geological survey investigations of the electrical properties of the crust and upper mantle. *Geophysics*, 31:1078–1087.

Kemeny, J. (1991). A model for non-linear rock deformation under compression due to sub-critical crack growth. *International Journal of Rock Mechanics and Mining Sciences & Geomechanics Abstracts*, 28(6):459 – 467.

Kemeny, J. and Cook, N. (1987). Crack models for the failure of rock under compression. In *Proc. 2nd Int. Conf. Constitutive Laws for Engineering Materials*, volume 2, pages 879–887.

Kennedy, L. A. and White, J. C. (2001). Low-temperature recrystallization in calcite: Mechanisms and consequences. *Geology*, 29(11):1027–1030.

Khatiashvili, N. and Perel'man, M. (1989). On the mechanism of seismo-electromagnetic phenomena and their possible role in the electromagnetic radiation during periods of earthquakes, foreshocks and aftershocks. *Physics of the Earth and Planetary Interiors*, 57:169–177.

King, G. C. P., Stein, R. S., and Rundle, J. B. (1988). The growth of geological structures by repeated earthquakes 1. conceptual framework. *Journal of Geophysical Research*, 93(B11):13307–13318.

Klimenko, M., Klimenko, V., Zakharenkova, I., Pulinets, S., Zhao, B., and Tsidilina, M. (2011). Formation mechanism of great positive tec disturbances prior to wenchuan earthquake on may 12, 2008. *Advances in Space Research*, 48:488–499.

Kopytenko, Y., Matiashvili, T., Voronov, P., Kopytenko, E., and Molchanov, O. (1993). Detection of ultra-low-frequency emissions connected with the spitak earthquake and its aftershock activity, based on geomagnetic pulsations data at dusheti and vardzia observatories. *Physics of the Earth and Planetary Interiors*, 77:85–95.

Kuhn, T. (1962). *The Structure of Scientific Revolutions*. University of Chicago Press.

Kyriazopoulos, A., Anastasiadis, C., Triantis, D., and Brown, C. (2011a). Non-destructive evaluation of cement-based materials from pressure-stimulated electrical emission - preliminary results. *Construction and Building Materials*, 25(4):1980–1990.

Kyriazopoulos, A., Stavrakas, I., Anastasiadis, C., and Triantis, D. (2011b). Study of weak electric current emissions on cement mortar under uniaxial compressional mechanical stress up to the vicinity of fracture. *Journal of Mechanical Engineering*, 57(3):237–244.

Lajtai, E. Z., Schmidtke, R. H., and Bielus, L. P. (1987). The effect of water on the deformation and fracture time-dependent of a granite. *International Journal of Rock Mechanics and Mining Sciences Geomechanics Abstracts*, 24:247–255.

Larkina, V., Migulin, V., Molchanov, O., Kharkov, I., Inchin, A., and Schvetcova, V. (1989). Some statistical results on very low frequency radiowave emissions in the upper ionosphere over earthquake zones. *Physics of the Earth and Planetary Interiors*, 57:100–109.

Larkina, V., Nalivayko, A., Gershenzon, N., Gokhberg, M., Liperovskiy, V., and Shalimov, S. (1983). Observations of vlf emissions related with seismic activity, on the interkosmos-19 satellite. *Geomagnetism and Aeronomy*, 23:684–687.

Lavrov, A. (2003). The kaiser effect in rocks: principals and stress estimation techniques. *International Journal of Rock Mechanics and Mining Sciences*, 40:151–171.

Lay, T. and Wallace, T. (1995). *Modern Global Seismology*. Academic Press, New York.

Lazarus, D. (1996). Physical mechanisms for generation and propagation of seismic electrical signals. In Lighthill, J., editor, *A Critical Review of VAN: Earthquake Prediction from Seismic Electric Signals*, pages 91–96. World Scientific, Singapore.

Leary, P. C. (1997). Rock as a critical-point system and the inherent implausibility of reliable earthquake prediction. *Geophysical Journal International*, 131(3):451–466.

Lebedev, E. B., Ryzhenko, B. N., Dorfman, A. M., Zebrin, A. M., Sokolova, N. T., Burkhardt, H., Morig, R., and Wulff, A. (1996). Influence of fluids on the elastic properties of sandstone at high pressure and temperature. *Geophysical Research Letters*, 23(22):3115–3118.

Lee, W. H. K., Kanamori, H., Jennings, P. C., and Kisslinger, C., editors (2002). *IASPEI International Handbook of Earthquake and Engineering Seismology: Part A*. Academic Press.

Lee, W. H. K., Kanamori, H., Jennings, P. C., and Kisslinger, C., editors (2003). *IASPEI International Handbook of Earthquake and Engineering Seismology: Part B*. Academic Press.

Lei, X., Kusunose, K., Rao, M. V. M. S., Nishizawa, O., and Satoh, T. (2000a). Quasi-static fault growth and cracking in homogeneous brittle rock under triaxial compression using acoustic emission monitoring. *Journal of Geophysical Research*, 105:6127–6139.

Lei, X., Masuda, K., Nishizawa, O., Jouniaux, L., Liu, L., Ma, W., Satoh, T., and Kusunose, K. (2004). Detailed analysis of acoustic emission activity during catastrophic failure of faults in rock. *Journal of Structural Geology*, 26:247–258.

Lei, X. and Satoh, T. (2007). Indicators of critical point behavior prior to rock failure inferred from pre-failure damage. *Tectonophysics*, 431(1-4):97–111.

Lei, X. L., Kusunose, K., Nishizawa, O., Cho, A., and Satoh, T. (2000b). On the spatiotemporal distribution of acoustic emissions in two granitic rocks under triaxial compression: the role of pre-existing cracks. *Geophysical Research Letters*, 27:1997–2000.

Lerchl, A., Nonaka, K. O., and Reiter, R. J. (1991). Pineal gland 'magnetosensitivity' to static magnetic fields is a consequence of induced electric currents (eddy currents). *Journal of Pineal Research*, 10(3):109–116.

Li, C. and Nordlund, E. (1993). Experimental verification of the kaiser effect in rocks. *Rock Mechanics and Rock Engineering*, 26:333–351.

Li, N., Du, X. B., and Tan, D. C. (2007). Imminent electro-magnetic phenomenon related to earthquake recorded at the songshan station. *Earthquake (in Chinese)*, 27:103–111.

Lighthill, J. (1996). *A Critical Review of Van: Earthquake Prediction from Seismic Electrical Signals*. World Scientific, Singapore.

Liu, J., Chen, Y., Pulinets, S., Tsai, Y., and Chuo, Y. (2000). Seismo-ionospheric signatures prior to m6.0 taiwan earthquakes. *Geophysical Research Letters*, 27:3113–3116.

Liu, J., Chuo, Y., Pulinets, S., Tsai, H., and Zeng, X. (2002). A study on the tec perturbations prior to the rei-li, chi-chi and chia-yi earthquakes. In Hayakawa, M. and Molchanov, O., editors, *Seismo-Electromagnetics: LithosphereŰAtmosphereŰIonosphere Coupling*, pages 297–301. TERRAPUB.

Liu, J., Chuo, Y., Shan, S., Tsai, Y., Pulinets, S., and Yu, S. (2004). Pre-earthquake ionospheric anomalies monitored by gps tec. *Annals of Geophysics*, 22:1585–1593.

Liu, J., Du, X. B., Zlotnicki, J., Fan, Y. Y., An, Z. H., Xie, T., Zheng, G. L., Tan, D. C., and Chen, J. Y. (2011). The changes of the ground and ionosphere electric/magnetic fields before several great earthquakes. *Chinese Journal of Geophysics*, 54(11):2885–2897.

Lockner, D. (1993). The role of acoustic emission in the study of rock fracture. *International Journal of Rock Mechanics and Mining Sciences & Geomechanics Abstracts*, 30(7):883–899.

Lockner, D. A. and Beeler, N. M. (2002). Rock failure and earthquakes. In Lee, W. H. K., Kanamori, H., Jennings, P. C., and Kisslinger, C., editors, *IASPEI International Handbook of Earthquake and Engineering Seismology: Part A*, chapter 32, pages 505–537. Academic Press.

Lockner, D. A. and Byerlee, J. D. (1992). Fault growth and acoustic emissions in confined granite. *Applied Mechanics Reviews*, 45:165–173.

Lockner, D. A., Byerlee, J. D., Kuksenko, V., Ponomarev, V., and Sidorin, A. (1992). Observations of quasi-static fault growth from acoustic emissions. In Rice, J. R., Evans, B., and Wong, T.-F., editors, *Fault Mechanics and Transport Properties of Rocks*, pages 3–31. Academic Press, London.

Lockner, D. A., Byerlee, J. D., Ponomarev, V., and Sidorin, A. (1991). Quasi-static fault growth and shear fracture energy in granite. *Nature*, 350:39–42.

Lu, C. and Jackson, I. (1996). Seismic-frequency laboratory measurements of shear mode viscoelasticity in crustal rocks i: competition between cracking and plastic flow in thermally cycled carrara marble. *Physics of the Earth and Planetary Interiors*, 94:105–119.

Lutz, E. (2003). Anomalous diffusion and tsallis statistics in an optical lattice. *Physical Review A*, 67(5):051402.

Lutz, E. (2004). Power-law tail distributions and nonergodicity. *Physical Review Letters*, 93(19):190602.

Ma, W. and Cross, L. (2005). Flexoelectric effect in ceramic lead zirconate titanate. *Applied Physics Letters*, 86:072905.

Madariaga, R. and Olsen, K. (2002). Earthquake dynamics. In Lee, W. H. K., Kanamori, H., Jennings, P. C., and Kisslinger, C., editors, *IASPEI International Handbook of Earthquake and Engineering Seismology: Part A*, chapter 12, pages 175–194. Academic Press.

Madden, T. (1983). Microcrack connectivity in rocks: a renormalization group approach to the critical phenomena of conduction and failure in crystalline rocks. *Journal of Geophysical Research*, 88:585–592.

Main, I. (1991). A modified griffith criterion for the evolution of damage with a fractal distribution of crack lengths: application to seismic event rates and b-values. *Geophysical Journal International*, 107:353–362.

Main, I. (1996). Statistical physics, seismogenesis and seismic hazard. *Reviews of Geophysics*, 34(4):433–462.

Main, I. (1997). Long odds on prediction. *Nature*, 385:19–20.

Main, I. (1999). Is the reliable prediction of individual earthquakes a realistic scientific goal? http://www.nature.com.libproxy.ucl.ac.uk/nature/debates/earthquake/.

Main, I. and Burton, P. (1984). Information theory and the earthquake frequency-magnitude distribution. *Bulletin of the Seismological Society of America*, 74:1409–1426.

Main, I. and Meredith, P. (1989). Classification of earthquake precursors from a fracture mechanics model. *Tectonophysics*, 167:273–283.

Main, I., Meredith, P., and Jones, C. (1989). A reinterpretation of the precursory seismic b-value anomaly from fracture mechanics. *Geophysical Journal*, 96:131–138.

Main, I., Meredith, P., and Sammonds, P. (1992). Temporal variations in seismic event rate and b-values from stress corrosion constitutive laws. *Tectonophysics*, 211:233–246.

Main, I. G. and Al-Kindy, F. H. (2002). Entropy, energy, and proximity to criticality in global earthquake populations. *Geophysical Research Letters*, 29(7):1121.

Main, I. G., Henderson, J. R., Meredith, P. G., and Sammonds, P. R. (1994). Self-organised criticality and fluid-rock interactions in the brittle field. *Pure and Applied Geophysics*, 142(3-4):529–543.

Main, I. G., Meredith, P. G., Sammonds, P. R., and Jones, C. (1990). Influence of fractal flaw distributions on rock deformation in the brittle field. *Deformation mechanisms, rheology and tectonics*, pages 81–96.

Main, I. G. and Naylor, M. (2010). Entropy production and self-organized (sub)criticality in earthquake dynamics. *Philosophical Transactions of the Royal Society A: Mathematical, Physical and Engineering Sciences*, 368(1910):131–144.

Main, I. G., Sammonds, P. R., and Meredith, P. G. (1993). Application of a modified griffith criterion to the evolution of fractal damage during compressional rock failure. *Geophysical Journal International*, 115(2):367–380.

Makhmudov, K. and Kuksenko, V. (2005). Electromagnetic phenomena entailed by deformation and fracture of dielectric solids. *Physics of the Solid State*, 47(5):856–859.

Mandelbrot, B. (1967). How long is the coastline of britain? statistical self-similarity and fractional dimension. *Science*, 156(3775):636–638.

Mandelbrot, B. (1982). *The Fractal Geometry of Nature*. Freeman, New York.

Martyshev, J. (1965). Studies in phosphorescence and electrification of crystals under deformation. *Kristallografiya*, 10(2):224.

Masuda, K. (2001). Effects of water on rock strength in a brittle regime. *Journal of Structural Geology*, 23(11):1653–1657.

Masuda, K., Mizutani, H., and Yamada, I. (1987). Experimental study of strain-rate dependence and pressure dependence of failure properties of granite. *Journal of Physics of the Earth*, 35(1):37–66.

Matcharashvili, T., Chelidze, T., Javakhishvili, Z., Jorjiashvili, N., and Fra Paleo, U. (2011). Non-extensive statistical analysis of seismicity in the area of javakheti, georgia. *Computers and Geosciences*, 37:1627–1632.

Matthews, J. and Lebreton, J. (1985). A search for seismic related wave activity in the micropulsation and ulf frequency ranges using geos-2 data. *Annals of Geophysics*, 3:749–754.

Mavko, G., Mukerji, T., and Dvorkin, J. (2009). *The Rock Physics Handbook: Tool for Seismic Analysis of Porous Media*. Cambridge University Press, 2nd edition.

Mavromatou, C. and Hadjicontis, V. (1994). Highly mobile charge carriers in minerals: Key to the enigmatic electrical earthquake phenomena. In Hayakawa, M. and Fujinawa, Y., editors, *Electromagnetic Phenomena related to Earthquake Prediction*, pages 293–305. Terra Scientific, Tokyo.

McClintock, F. and Walsh, J. (1962). Friction of griffith cracks in rock under pressure. In *Proceeding of the Fourth US Congress of Applied Mechanics, Berkeley*, pages 1015–1021.

McCloskey, J. (2011). Focus on known active faults. *Nature Geoscience*, 4:494.

Meglis, I. L., Greenfield, R. J., Engelder, T., and Graham, E. K. (1996). Pressure dependence of velocity and attenuation and its relationship to crack closure in crystalline rocks. *Journal of Geophysical Research*, 101(B8):17523–17533.

Meredith, P., Main, I., and Jones, C. (1990). Temporal variations in seismicity during quasi-static and dynamic rock failure. *Tectonophysics*, 175:249–268.

Meredith, P., Main, I. G., Clint, O. C., and Li, L. (2012). On the threshold of flow in tight rock. *Geophysical Research Letters*, 39:L04307.

Meredith, P. G. and Atkinson, B. K. (1983). Stress corrosion and acoustic emission during tensile crack propagation in whin sill dolerite and other basic rocks. *Geophysical Journal of the Royal Astronomical Society*, 75:1–21.

Meredith, P. G., Main, I. G., Clint, O. C., Odling, N. W., Elphick, S. C., and Ngewenya, B. (2000). Crack damage and permeability evolution near the percolation threshold in a near-perfect crystalline rock. Oral presentation.

Merzer, M. and Klemperer, S. (1997). Modeling low-frequency magnetic-field precursors to the loma prieta earthquake with a precursory increase in fault-zone conductivity. *Pure and Applied Geophysics*, 150:217–248.

Michael, A. J. (1997). Testing prediction methods: Earthquake clustering versus the poisson model. *Geophysical Research Letters*, 24(15):1891–1894.

Michas, G., Vallianatos, F., and Sammonds, P. (2013). Non-extensivity and long-range correlations in the earthquake activity at the west corinth rift (greece). *Nonlinear Processes in Geophysics*, 20(5):713–724.

Migliazza, M., Ferrero, A., and Spagnoli, A. (2011). Experimental investigation on crack propagation in carrara marble subjected to cyclic loads. *International Journal of Rock Mechanics and Mining Sciences*, 48:1038–1044.

Milne, J. (1890). Earthquakes in connection with electric and magnetic phenomena. *Transactions of the Seismological Society of Japan*, 15:135–140.

Miltenberger, P., Sornette, D., and Vanneste, C. (1993). Fault self-organization as optimal random paths selected by critical spatiotemporal dynamics of earthquakes. *Physical Review Letters*, 71:3604–3607.

Minadakis, G., Potirakis, S. M., Nomicos, C., and Eftaxias, K. (2012). Linking electromagnetic precursors with earthquake dynamics: An approach based on nonextensive fragment and self-affine asperity models. *Physica A: Statistical Mechanics and its Applications*, 391(6):2232–2244.

Mitchell, T. M. and Faulkner, D. R. (2008). Experimental measurements of permeability evolution during triaxial compression of initially intact crystalline rocks and implications for fluid flow in fault zones. *Journal of Geophysical Research: Solid Earth*, 113:B11412.

Mizutani, H., Ishido, T., Yokokura, T., and Ohnishi, S. (1976). Electrokinetic phenomena associated with earthquakes. *Geophysical Research Letters*, 3:365–368.

Mogi, K. (1959). Experimental study of deformation and fracture of marble. i. on the fluctuation of compressive strength of marble and and the relation to the rate of stress application. *Bulletin of the Earthquake Research Institute Tokyo*, 37:155–170.

Mogi, K. (1962a). The fracture of a semi-infinite body caused by an inner stress origin and its relation to earthquake phenomena, 1st. paper. *Bulletin of the Earthquake Research Institute*, 40:815–829.

Mogi, K. (1962b). Magnitude frequency relation for elastic shocks accompanying fractures of various materials and some related problems in earthquakes. *Bulletin of the Earthquake Research Institute*, 40:831–853.

Mogi, K. (1962c). Study of elastic shocks caused by the fracture of heterogeneous materials and its relations to earthquake phenomena. *Bulletin of the Earthquake Research Institute Tokyo*, 40:125–173.

Mogi, K. (1963a). The fracture of a semi-infinite body caused by an inner stress origin and its relation to earthquake phenomena, 2nd paper. *Bulletin of the Earthquake Research Institute*, 41:595–614.

Mogi, K. (1963b). Some discussion of aftershocks, foreshocks, and earthquake swarms - the fracture of a semi-infinite body caused by an inner stress origin and its relation to earthquake phenomena, 3rd paper. *Bulletin of the Earthquake Research Institute*, 41:615–618.

Mogi, K. (1968). Source locations of elastic shocks in the fracturing process in rocks. *Bulletin of the Earthquake Research Institute Tokyo*, 46:1103–1125.

Mogi, K. (1985). *Earthquake Prediction*. Academic, London.

Mogi, K. (2007). *Experimental Rock Mechanics*. Taylor & Francis, London, UK.

Mohanalin, Beenamol, Kalra, P. K., and Kumar, N. (2010). A novel automatic microcalcification detection technique using tsallis entropy and a type ii fuzzy index. *Computers & Mathematics with Applications*, 60(8):2426 – 2432.

Molchanov, O., Fedorov, E., Schekotov, A., Gordeev, E., Chebrov, V., Surkov, V., Rozhnoi, A., Andreevsky, S., Iudin, D., Yunga, S., Lutikov, A., Hayakawa, M., and Biagi, P. F. (2004). Lithosphere-atmosphere-ionosphere coupling as governing mechanism for preseismic short-term events in atmosphere and ionosphere. *Natural Hazards and Earth System Sciences*, 4:757–767.

Molchanov, O. and Hayakawa, M. (1995). Generation of ulf electromagnetic emissions by microfracturing. *Geophysical Research Letters*, 22(22):3091–3094.

Molchanov, O. and Hayakawa, M. (1998a). On the generation mechanism of ulf seismogenic electromagnetic emissions. *Physics of the Earth and Planetary Interiors*, 105:201–210.

Molchanov, O. and Hayakawa, M. (1998b). Subionospheric vlf signal perturbations possibly related to earthquakes. *Journal of Geophysical Research: Space Physics*, 103(A8):17489–17504.

Molchanov, O., Kopytenko, Y., Voronov, P., Kopytenko, E., Matiashvili, T., Fraser-Smith, A., and Bernardi, A. (1992). Results of ulf magnetic field measurements near the epicenters of the spitak (ms = 6.9) and loma prieta (ms = 7.1) earthquakes: comparative analysis. *Geophysical Research Letters*, 19:1495–1498.

Molchanov, O., Mazhaeva, O., Goliavin, A., and Hayakawa, M. (1993). Observation by the intercosmos-24 satellite of elf-vlf electromagnetic emissions associated with earthquakes. *Annals of Geophysics*, 11:431–440.

Molchanov, O., Schekotov, A., Fedorov, E., Belyaev, G., and Gordeev, E. (2003). Preseismic ulf electromagnetic effect from observation at kamchatka. *Natural Hazards and Earth System Sciences*, 3:203–209.

Molli, G., Conti, P., Giorgetti, G., Meccheri, M., and Oesterling, N. (2000). Microfabric study on the deformational and thermal history of the alpi apuane marbles (carrara marbles), italy. *Journal of Structural Geology*, 22:1809–1825.

Moreland, N. C. and Roberts, G. P. (1999). Lateral propagation of the surface of the south alkyonides normal fault segment, central greece: its impact of models of fault growth and displacement-length relationships. *Journal of Structural Geology*, 21:635–652.

Morgan, F., Williams, E., and Madden, T. (1989). Streaming potential properties of westerly granite with applications. *Journal of Geophysical Research*, 94:12449–12461.

Mori, Y. and Obata, Y. (2008). Electromagnetic emission and ae kaiser effect for estimating rock in-situ stress. *Report of the Research Institute of Industrial Technology, Nihon University*, 93:–.

Mori, Y., Sato, K., Obata, Y., and Mogi, K. (1998). Acoustic emission and electric potential changes of rock samples under cyclic loading. *Progress in Acoustic Emission*, 9(2):1–8.

Mori, Y., Sedlak, P., and Sikula, J. (2006). Estimation of rock in-situ stress by acoustic and electromagnetic emission. *Advanced Materials Research*, 13-14:357–362.

Morse, J. W., Mucci, A., and Millero, F. J. (1980). The solubility of calcite and aragonite in seawater of 35at 25řc and atmospheric pressure. *Geochimica et Cosmochimica Acta*, 44(1):85–94.

Mueller, R. and Johnston, D. H. (1998). Review of magnetic field monitoring near active faults and volcanic calderas in california: 1974Ű1995. *Physics of the Earth and Planetary Interiors*, 105(3-4):131–144.

Mueller, R. and Johnston, M. (1990). Seismomagnetic effect generated by the october 1989, ml 7.1 loma prieta, california, earthquake. *Geophysical Research Letters*, 23:241–244.

Mulargia, F. and Gasperini, P. (1992). Evaluating the statistical validity beyond chance of 'van' earthquake precursors. *Geophysical Journal International*, 111(1):32–44.

Mulargia, F. and Gasperini, P. (1996a). Precursor candidacy and validation: The van case so far. *Geophysical Research Letters*, 23(11):1323–1326.

Mulargia, F. and Gasperini, P. (1996b). Van: Candidacy and validation with the latest laws of the game. *Geophysical Research Letters*, 23(11):1327–1330.

Murrell, S. (1965). The effect of triaxial stress systems on the strength of rocks at atmospheric temperatures. *Geophysical Journal International*, 10:231–281.

Nagahama, H. and Teisseyre, R. (1998). Thermodynamics of line defects and transient electric current: electromagnetic field generation in earthquake preparation zone. *Acta Geophysica Polonica*, 46:35–54.

Nagamoto, H., Fukushima, T., Ida, Y., Matsudo, Y., and Hayakawa, M. (2008). Disturbances in vhf/uhf telemetry links as a possible effect of the 2003 hokkaido tokachi-oki earthquake. *Natural Hazards and Earth System Sciences*, 8:813–817.

Nagao, T., Uyeshima, M., and Uyeda, S. (1996). An independent check of van's criteria for signal recognition. *Geophysical Research Letters*, 23(11):1441–1444.

Nardi, A. and Caputo, M. (2009). Monitoring the mechanical stress of rocks through the electromagnetic emission produced by fracturing. *International Journal of Rock Mechanics and Mining Sciences*, 46(5):940–945.

National Physical Laboratory (2013). Technical guides - speed of sound in sea-water. http://resource.npl.co.uk/acoustics/techguides/soundseawater/content.html#UNESCO. Accessed 04 February 2013.

Nemat-Nasser, S. and Deng, H. (1994). Strain-rate effect on brittle failure in compression. *Acta Metallurgica et Materialia*, 42(3):1013–1024.

Nitsan, U. (1977). Electromagnetic emission accompanying fracture of quartz-bearing rocks. *Geophysical Research Letters*, 4:333–336.

Nur, A. (1971). Effects of stress on velocity anisotropy in rocks with cracks. *Journal of Geophysical Research*, 76(8):2022–2034.

Nur, A. (1972). Dilatancy, pore fluids, and premonitory variations of ts/tp travel times. *Bulletin of the Seismological Society of America*, 62:1217–1222.

Nur, A. and Simmons, G. (1969). Stress-induced velocity anisotropy in rock: An experimental study. *Journal of Geophysical Research*, 74(27):6667–6674.

Nur, A. and Walder, J. (1990). Time-dependent hydraulics of the earth's crust. In *The Role of Fluids in Crustal Processes*, pages 113–127. National Academy Press.

Nye, J. F. (1985). *Physical Properties of Crystals: their representation by tensors and matrices.* Oxford University Press, Oxford, UK, 2nd edition.

O'Connell, R. and Budiansky, B. (1974). Seismic velocities in dry and saturated rocks. *Journal of Geophysical Research*, 79:5412–5426.

Odedra, A. (1998). *Laboratory studies on shear fracture of granite under simulated crustal conditions*. PhD thesis, University of London.

Odedra, A., Ohnaka, M., Mochizuki, H., and Sammonds, P. (2001). Temperature and pore pressure effects on the shear strength of granite in the brittle-plastic transition regime. *Geophysical Research Letters*, 28(15):3011–3014.

Oesterling, N. (2004). *Dynamic recrystallization and deformation mechanisms of naturally deformed Carrara Marble: a study on one- and two-phase carbonate rocks*. PhD thesis, University of Basel.

Ogawa, T., Oike, K., and Miura, T. (1985). Electromagnetic radiations from rocks. *Journal of Geophysical Research*, 90(D4):6245–6249.

Ohnaka, M. (1973). The quantitative effect of hydrostatic confining pressure on the compressive strength of crystalline rocks. *Journal of Physics of the Earth*, 21:125–140.

Ohnaka, M. (2003). A constitutive scaling law and a unified comprehension for frictional slip failure, shear fracture of intact rock, and earthquake rupture. *Journal of Geophysical Research: Solid Earth*, 108(B2):–.

Ohnaka, M. (2013). *Rock Failure and Earthquakes*. Cambridge University Press.

Ohnaka, M. and Mogi, K. (1982). Frequency characteristics of acoustic emission in rocks under uniaxial compression and its relation to the fracturing process to failure. *Journal of Geophysical Research*, 87(B5):3873–3884.

Ojala, I., Main, I., and Ngwenya, B. T. (2004). Strain rate and temperature dependence of omori law scaling constants of ae data: implications for earthquake foreshock-aftershock sequences. *Geophysical Research Letters*, 31:L24617.

O'Keefe, S. G. and Thiel, D. V. (1995). A mechanism for the production of electromagnetic radiation during fracture of brittle materials. *Physics of the Earth and Planetary Interiors*, 89:127–135.

Olami, Z., Feder, H. J., and Christensen, K. (1992). Self-organised criticality in a continuous, nonconservative cellular automaton modelling earthquakes. *Physical Review Letters*, 68(8):1244–1247.

Olhoeft, G. R. (1989). Electrical properties of rocks. In Touloukian, Y. S., Judd, W. R., and Roy, R. F., editors, *Physical Properties of Rocks and Minerals*, pages 257–329. Hemisphere Publishing Corporation, New York.

Omori, F. (1894). On the aftershocks of earthquakes. *Journal of the College of Science, Imperial University of Tokyo*, 7:111–200.

Orihara, T., Kamogawa, M., Nagao, T., and Uyeda, S. (2012). Pre-seismic anomalous telluric current signals observed in kozu-shima island, japan. *Proceedings of the National Academy of Sciences USA*, 109(47):19125–19128.

Orowan, E. (1949). Fracture and strength of solids. *Reports on Progress in Physics*, 12:185–232.

Otsuka, M. (1972). A simulation of earthquake occurrence. *Physics of the Earth and Planetary Interiors*, 6:311–315.

Ouellet, M. (1990). Earthquake light and seismicity. *Nature*, 348:492.

Ouillon, G. and Sornette, D. (1996). Hierarchical scaling of faulting. *Journal of Geophysical Research*, 101:5477–5487.

Ouzounov, D., Liu, D., Chunli, K., Cervone, G., Kafatos, M., and Taylor, P. (2007). Outgoing long wave radiation variability from ir satellite data prior to major earthquakes. *Tectonophysics*, 431(1-4):211–220.

Overbeek, J. T. G. (1952). Electrochemistry of the double layer. In Kruyt, H. R., editor, *Colloid Science: Irreversible Systems v.1*. Elsevier, New York.

Papadakis, G., Vallianatos, F., and Sammonds, P. (2013). Evidence of nonextensive statistical physics behavior of the hellenic subduction zone seismicity. *Tectonophysics*, 608:1037–1048.

Papadakis, G., Vallianatos, F., and Sammonds, P. (2014). A non-extensive statistical physics analysis of the 1995 kobe, japan earthquake. *Pure and Applied Geophysics*, Published online 4th July:–.

Papadimitriou, C., Kalimeri, M., and Eftaxias, K. (2008). Nonextensivity and universality in the earthquake preparation process. *Physical Review E - Statistical, Nonlinear, and Soft Matter Physics*, 77(3):036101. cited By (since 1996)32.

Park, S., Johnston, M., Madden, T., Morgan, F., and Morisson, H. (1993). Electromagnetic precursors to earthquakes in the ulf band: A review of observations and mechanisms. *Reviews of Geophysics*, 31(2):117–132.

Parkhomenko, E. and Martyshev, J. (1975). Electrification and phosphorescence of minerals during deformation and failure. In *Physics of the Earthquake Focus*, page 151. Nauka, Moscow.

Parrot, M. (1994). Statistical study of elf/vlf emissions recorded by a low-altitude satellite during seismic events. *Journal of Geophysical Research*, 99:23339–23347.

Parrot, M. (2002). The micro-satellite demeter. *Journal of Geodynamics*, 33:535–541.

Parrot, M., Benoist, D., Berthelier, J., Blecki, J., Chapuis, Y., Colin, F., Elie, F., Fergeau, P., Lagoutte, D., Lefeuvre, F., Legendre, C., Leveque, M., Pincon, J., Poirier, B., Seran, H.-C., and Zamora, P. (2006a). The magnetic field experiment imsc and its data processing onboard demeter: Scientific objectives, description and first results. *Planetary and Space Science*, 54:441–455.

Parrot, M., Berthelier, J., Lebreton, J., Sauvaud, J., Santolik, O., and Blecki, J. (2006b). Examples of unusual ionospheric observations made by the demeter satellite over seismic regions. *Physics and Chemistry of the Earth*, 31:486–495.

Parrot, M. and Lefeuvre, F. (1985). Correlation between geos vlf emissions and earthquakes. *Annals of Geophysics*, 3(6):737–748.

Patella, D., Tramacere, A., and Di Maio, R. (1997). Modelling earth current precursors in earthquake prediction. *Annals of Geophysics*, 40(2):495–517.

Paterson, M. S. (1958). Experimental deformation and faulting in wombeyan marble. *Geological Society of America Bulletin*, 69(4):465–476.

Paterson, M. S. and Wong, T.-f. (2005). *Experimental Rock Deformation: The Brittle Field*. Springer.

Pavlenkova, N. I. (1991). The kola superdeep drill hole and the nature of seismic boundaries. *Terra Nova*, 4:117–123.

Pavlenkova, N. I. (2004). Low velocity and low electrical resistivity layers in the middle crust. *Annals of Geophysics*, 47(1):157–169.

Peach, C. and Spiers, C. (1996). Influence of plastic deformation on dilatancy and permeability development in synthetic salt rock. *Tectonophysics*, 256:101–128.

Penrose, O. (1970). *Foundations of Statistical Mechanics: A Deductive Treatment*. Pergamon, Oxford.

Pham, V., Boyer, D., Le Mouel, J.-L., Chouliaras, G., and Stavrakakis, G. (1999). Electromagnetic signals generated in the solid earth by digital transmission of radio-waves as plausible source for some so-called 'seismo-electric' signals. *Physics of the Earth and Planetary Interiors*, 114:141–163.

Picoli Jr., S., Mendes, R., Malacarne, L., and Santos, R. (2009). q-distributions in complex systems. *Brazilian Journal of Physics*, 39(2A):468–474.

Pinettes, P., Bernard, P., Artru, J., Blum, P.-A., and Verhille, R. (1998). Strain constant on the source of the alleged varostos-alexopoulos-nomicos (van) precursor of the 1995 aigon earthquake (greece). *Journal of Geophysical Research*, 103:15145–15155.

Poirier, J. (1985). *Creep of Crystals: High Temperature Deformation Processes in Metals, Ceramics and Minerals*. Cambridge University Press.

Pollitz, F. F., Stein, R. S., Sevilgen, V., and Burgmann, R. (2012). The 11 april 2012 east indian ocean earthquake triggered large aftershocks worldwide. *Nature*, 490(7419):250–253.

Potirakis, S., Karadimitrakis, A., and Eftaxias, K. (2013a). Natural time analysis of critical phenomena: The case of pre-fracture electromagnetic emissions. *Chaos*, 23(2). cited By (since 1996)0.

Potirakis, S., Minadakis, G., Nomicos, C., and Eftaxias, K. (2011). A multidisciplinary analysis for traces of the last state of earthquake generation in preseismic electromagnetic emissions. *Natural Hazards and Earth System Sciences*, 11(10):2859–2879. cited By (since 1996)3.

Potirakis, S. M., Minadakis, G., and Eftaxias, K. (2012). Analysis of electromagnetic pre-seismic emissions using fisher information and tsallis entropy. *Physica A*, 391:300–306.

Potirakis, S. M., Zitis, P. I., and Eftaxias, K. (2013b). Dynamical analogy between economical crisis and earthquake dynamics within the nonextensive statistical mechanics framework. *Physica A: Statistical Mechanics and its Applications*, 392(13):2940–2954.

Power, W. L. and Tullis, T. E. (1991). Euclidean and fractal models for the description of rock surface roughness. *Journal of Geophysical Research*, 96:415–424.

Price, N. J. and Cosgrove, J. W. (1990). *Analysis of Geological Structures*. Cambridge University Press.

Pride, S. R. (1994). Governing equations for the coupled electromagnetics and acoustics of porous media. *Physical Review B*, 50:15678–15696.

Pulinets, S. (1998a). Seismic activity as a source of the ionospheric variability. *Advances in Space Research*, 22(6):903–906.

Pulinets, S. (1998b). Strong earthquakes prediction possibility with the help of topside sounding from satellites. *Advances in Space Research*, 21(3):455–458.

Pulinets, S. (2004). Ionospheric precursors of earthquakes; recent advances in theory and practical applications. *TAO*, 15(3):445–467.

Pulinets, S. and Boyarchuk, K. (2004). *Ionospheric Precursors of Earthquakes*. Springer, Hedelberg, New York.

Pulinets, S. and Ouzounov, D. (2011). LithosphereŰatmosphereŰionosphere coupling (laic) model Ű an unified concept for earthquake precursors validation. *Journal of Asian Earth Sciences*, 41:371–382.

Pulinets, S., Ouzounov, D., Karelin, A., Boyarchuk, K., and Pokhmelnykh, L. (2006). The physical nature of thermal anomalies observed before strong earthquakes. *Physics and Chemistry of the Earth*, 31:143–153.

Rabinovitch, A., Frid, V., and Bahat, D. (1998). Parametrization of electromagnetic radiation pulses obtained by triaxial fracture in granite samples. *Philosophical Magazine Letters*, 77(5):289–293.

Rabinovitch, A., Frid, V., and Bahat, D. (2001). Gutenberg-richter-type relation for laboratory fracture-induced electromagnetic radiation. *Physical Review E*, 65:011401.

Rabinovitch, A., Frid, V., and Bahat, D. (2007). Surface oscillations - a possible source of fracture induced electromagnetic radiation. *Tectonophysics*, 431(1-4):15–21. Mechanical and electromagnetic phenomena accompanying preseismic deformation: from laboratory to geophysical scale.

Rabinovitch, A., Frid, V., Bahat, D., and Goldbaum, J. (2000). Fracture area calculation from electromagnetic radiation and its use in chalk failure analysis. *International Journal of Rock Mechanics and Mining Sciences*, 37:1149–1154.

Rabinovitch, A., Frid, V., and D., B. (1999). A note on the amplitude-frequency relation of electromagnetic radiation pulses induced by material failure. *Philosophical Magazine Letters*, 79:195–200.

Ramez, M. R. H. and Murrell, S. A. F. (1964). A petrofabric analysis of carrara marble. *International Journal of Rock Mechanics and Mining Sciences & Geomechanics Abstracts*, 1:217–229.

Ranalli, G. (1995). *Rheology of the Earth*. Chapman and Hall, UK.

Read, M., Ayling, M., Meredith, P., and Murrell, S. (1995). Microcracking during triaxial deformation of porous rocks monitored by changes in rock physical properties, ii. pore volumetry and acoustic emission measurements on water-saturated rocks. *Tectonophysics*, 245:223–235.

Reasenberg, P. (1999). Foreshock occurrence before large earthquakes. *Journal of Geophysical Research*, 104:4755–4768.

Reches, Z. and Lockner, D. A. (1994). Nucleation and growth of faults in brittle rocks. *Journal of Geophysical Research: Solid Earth*, 99(B9):18159–18173.

Renner, J. and Rummel, F. (1996). The effect of experimental and microstructural parameters on the transition from brittle failure to cataclastic flow of carbonate rocks. *Tectonophysics*, 258:151Ű170.

Renshaw, C. E. and Schulson, E. M. (1998). Non-linear rate dependent deformation under compression due to state variable friction. *Geophysical Research Letters*, 25(12):2205–2208.

Reuschle, T. (2003). Microstructural control on the elastic properties of thermally cracked granite. *Tectonophysics*, 370:95–104.

Rhoades, D. and Evison, F. (1996). The van earthquake predicitons. *Geophysical Research Letters*, 23(11):1371–1373.

Richeton, T., Weiss, J., and Louchet, F. (2005). Dislocation avalanches: Role of temperature, grain size and strain hardening. *Acta Materialia*, 53(16):4463–4471.

Richter, C. F. (1958). *Elementary Seismology*. W. H. Freeman, San Francisco.

Riedel, K. (1996). Statistical tests for evaluating earthquake prediction methods. *Geophysical Research Letters*, 23(11):1407–1409.

Rikitake, T. (1975). Dilatancy model and empirical formulas for an earthquake area. *Pure and Applied Geophysics*, 113:141–147.

Rikitake, T. (1976). *Earthquake Prediction*. Elsevier, Amsterdam.

Rikitake, T. (1987). Earthquake precursors in japan: precursor time and detectability. *Tectonophysics*, 136:265–282.

Rist, M. A., Sammonds, P. R., and Murrell, S. A. F. (1991). Strain rate control during deformation of ice: An assessment of the performance of a new servo-controlled triaxial testing system. *Cold Regions Science and Technology*, 19:189–200.

Rivier, N., Guyon, E., and Charlaix, E. (1985). A geometrical approach to percolation through random fractured rocks. *Geological Magazine*, 122:157–162.

Rocchi, V., Sammonds, P., and Kilburn, C. (2003). Flow and fracture maps for basaltic rock deformation at high temperatures. *Journal of Volcanology and Geothermal Research*, 120(1-2):25–42.

Rodger, C., Thomson, N., and Dowden, R. (1996). A search for elf/vlf activity associated with earthquakes using isis satellite data. *Journal of Geophysical Research*, 101(13):13369–13378.

Roeloffs, E. and Langbein, J. (1994). The earthquake prediction experiment at parkfield, california. *Reviews of Geophysics*, 32:315–356.

Rokityanski, I. I. and Varotsos, P. (2006). Magnetotelluric data collection and analysis in the ses sensitive site of ioannina area (greece). *Physics and Chemistry of the Earth*, 31:198–203.

Rostom, F., Royne, A., Dysthe, D. K., and Renard, F. (2012). Effect of fluid salinity on subcritical crack propagation in calcite. *Tectonophysics*, 583:68–75.

Ruff, L. J. (2002). State of stress within the earth. In Lee, W. H. K., Kanamori, H., Jennings, P. C., and Kisslinger, C., editors, *IASPEI International Handbook of Earthquake and Engineering Seismology: Part A*, chapter 33, pages 539–557. Academic Press.

Rummel, F. and Fairhurst, C. (1970). Determination of the post-failure behavior of brittle rock using a servo-controlled testing machine. *Rock mechanics*, 2(4):189–204.

Rundle, J. B. and Klein, W. (1995). New ideas about the physics of earthquakes. *Reviews of Geophysics*, 33:283–286.

Rundle, J. B., Turcotte, D. L., and Klein, W., editors (2000). *GeoComplexity and the Physics of Earthquakes*. Geophysical Monograph Series. American Geophysical Union.

Rundle, J. B., Turcotte, D. L., Shcherbakov, R., Klein, W., and Sammis, C. (2003). Statistical physics approach to understanding the multiscale dynamics of earthquake fault systems. *Reviews of Geophysics*, 41(4):1019.

Rutter, E. H. (1972a). The effects of strain-rate changes on the strength and ductility of solenhofen limestone at low temperatures and confining pressures. *International Journal of Rock Mechanics and Mining Sciences*, 9:183–189.

Rutter, E. H. (1972b). The influence of interstitial water on the rheological behaviour of calcite rocks. *Tectonophysics*, 14(1):13–33.

Rutter, E. H. (1974). The influence of temperature, strain rate and interstitial water in the experimental deformation of calcite rocks. *Tectonophysics*, 22(3âĂŞ4):311–334.

Rutter, E. H. (1995). Experimental study of the influence of stress, temperature and strain on the dynamic recrystallisation of carrara marble. *Journal of Geophysical Research*, 100:24651–24663.

Sammis, C. G. and Ashby, M. F. (1988). The damage mechanics of brittle solids in compression. Technical report, University of Southern California.

Sammis, C. G., Osborne, R. H., Anderson, J. L., Banerdt, M., and White, P. (1986). Self-similar cataclasis in the formation of fault gouge. *Pure and Applied Geophysics*, 124(1-2):53–78.

Sammonds, P. (2005). Deformation dynamics: Plasticity goes supercriticial. *Nature Materials*, 4(6):425–426.

Sammonds, P. (2008). Forecasting earthquakes. Oral presentation and lecture notes.

Sammonds, P. and Ohnaka, M. (1998). Evolution of microseismicity during frictional sliding. *Geophysical Research Letters*, 25:699–702.

Sammonds, P. R. (1999). Understanding the fundamental physics governing the evolution and dynamics of the earth's crust and ice sheets. *Philosophical Transactions of the Royal Society of London. Series A: Mathematical, Physical and Engineering Sciences*, 357(1763):3377–3401.

Sammonds, P. R., Ayling, M. R., Meredith, P. G., Murrell, S. A. F., and Jones, C. (1989). A laboratory investigation of acoustic-emission and elastic wave velocity changes during rock failure under triaxial stresses. In Maury, V. and Fourmaintraux, D., editors, *Rock at Great Depth: Rock Mechanics and Rock Physics at Great Depth*, volume 1, pages 233–240. A A Balkema.

Sammonds, P. R., Meredith, P. G., and Main, I. G. (1992). Role of pore fluids in the generation of seismic precursors to shear fracture. *Nature*, 359(6392):228–230.

Sammonds, P. R., Meredith, P. G., Murrell, S. A. F., and Main, I. G. (1994). Modelling the damage evolution in rock containing pore fluid by acoustic emission. In Balkema, A. A., editor, *Rock Mechanics In Petroleum Engineering*, pages 897–904.

Sarkar, S., Gwal, A., and Parrot, M. (2007). Ionospheric variations observed by the demeter satellite in the mid-latitude region during strong earthquakes. *Journal of Atmospheric and Solar-Terrestrial Physics*, 69:1524–1540.

Sarlis, N., Skordas, E., Lazaridou, M., and Varotsos, P. (2008). Investigation of seismicity after the initiation of a seismic electric signal activity until the main shock. *Proceedings of the Japanese Academy Series B*, 84(8):331–343.

Sarlis, N., Skordas, E., Varotsos, P., Nagao, T., Kamogawa, M., Tanaka, H., and Uyeda, S. (2013). Minimum of the order parameter fluctuations of seismicity before major earthquakes in japan. *Proceedings of the National Academy of Sciences USA*, 110:13734–13738.

Sarlis, N. V., Skordas, E. S., and Varotsos, P. A. (2010a). Nonextensivity and natural time: The case of seismicity. *Physical Review E*, 82:021110.

Sarlis, N. V., Skordas, E. S., and Varotsos, P. A. (2010b). Order parameter fluctuations of seismicity in natural time before and after mainshocks. *EPL (Europhysics Letters)*, 91:59001.

Sasaoka, H., Yamanaka, C., and Ikeya, M. (1998). Measurements of electric potential variation by piezoelectricity in granite. *Geophysical Research Letters*, 25(12):2225–2228.

Sayers, C. M. and Kachanov, M. (1995). Microcrack-induced elastic wave anisotropy of brittle rocks. *Journal of Geophysical Research: Solid Earth*, 100(B3):4149–4156.

Schlische, R. W., Young, S. S., Ackermann, R. V., and Gupta, A. (1996). Geometry and scaling relations of a population of very small rift-related normal faults. *Geology*, 24(8):683–686.

Schmid, S., Paterson, M., and Boland, J. (1980). High temperature flow and dynamic recrystallisation in carrara marble. *Tectonophysics*, 65:245–280.

Schmittbuhl, J., Schmitt, F., and Scholz, C. (1995). Scaling invariance of crack surfaces. *Journal of Geophysical Research*, 100:5953–5973.

Scholz, C. (1968a). Experimental study of the fracturing process in brittle rock. *Journal of Geophysical Research*, 73(4):1447–1454.

Scholz, C. (1968b). The frequency-magnitude relation of microfracturing in rock and its relation to earthquakes. *Bulletin of the Seismological Society of America*, 58(1):399–415.

Scholz, C. (1968c). Microfractures, aftershocks and seismicity. *Bulletin of the Seismological Society of America*, 58(3):1117–1130.

Scholz, C. (1991). Earthquakes and faulting. self-organised critical phenomena with a characteristic dimension. In Riste, T. and Sherington, D., editors, *Spontaneous Formation of Space-Time Structures and Criticality*. Klawer Academic Publishers, Netherlands.

Scholz, C., Boitnott, G., and Nemat-Nasser, S. (1986). The bridgeman ring paradox revisited. *Pure and Applied Geophysics*, 124:587–599.

Scholz, C., Dawers, N. H., Anders, M. H., and Cowie, P. (1993). Fault growth and fault scaling laws: preliminary results. *Journal of Geophysical Research*, 98:21951–21961.

Scholz, C., Molnar, P., and Johnson, T. (1972). Detailed studies of frictional sliding of granite and implications for the earthquake mechanism. *Journal of Geophysical Research*, 77(32):6392–6406.

Scholz, C., Sykes, L. R., and Aggarwal, Y. P. (1973). Earthquake prediction: a physical basis. *Science*, 181(4102):803–810.

Scholz, C. H. (1968d). Microfracturing and the inelastic deformation of rock in compression. *Journal of Geophysical Research*, 73(4):1417–1432.

Scholz, C. H. (1998). Earthquakes and friction laws. *Nature*, 391:37–42.

Scholz, C. H. (2002). *The Mechanics of Earthquakes and Faulting*. Cambridge University Press.

Schottky, W. (1935). The mechanism of ionic motion in solid electrolytes. *Zeitschrift fur Physikalische Cemie B*, 29:335–355.

Schubnel, A., Benson, P. M., Thompson, B. D., Hazzard, J. F., and Young, R. P. (2006a). Quantifying damage, saturation and anisotropy in cracked rocks by inverting elastic wave velocities. *Pure and Applied Geophysics*, 163(5-6):947–973.

Schubnel, A., Fortin, J., Burlini, L., and Gueguen, Y. (2005). Damage and recovery of calcite rocks deformed in the cataclastic regime. *Geological Society, London, Special Publications*, 245(1):203–221.

Schubnel, A., Nishizawa, O., Masuda, K., Lei, X. J., Xue, Z., and Gueguen, Y. (2003). Velocity measurements and crack density determination during wet triaxial experiments on oshima and toki granites. *Pure and Applied Geophysics*, 160:869–887.

Schubnel, A., Walker, E., Thompson, B., Fortin, J., Gueguen, Y., and Young, R. (2006b). Transient creep, aseismic damage and slow failure in carrara marble deformed across the brittle-ductile transition. *Geophysical Research Letters*, 33(17):–.

Schulson, E. M., Iliescu, D., and Renshaw, C. E. (1999). On the initiation of shear faults during brittle compressive failure: A new mechanism. *Journal of Geophysical Research: Solid Earth*, 104(B1):695–705.

Schultz, R., Hauber, E., Kattenhorn, S., Okubo, C., and Watters, T. (2010). Interpretation and analysis of planetary structures. *Journal of Structural Geology*, 32:855–875.

Schwarz, G. (1990). Electrical conductivity of the earth's crust and upper mantle. *Surveys in Geophysics*, 11:133–161.

Scudiero, L., Dickinson, J., and Enomoto, Y. (1998). The electrification of flowing gases by mechanical abrasion of mineral surface. *Physics and Chemistry of Minerals*, 24(8):566–573.

Segall, P. (1989). Earthquakes triggered by fluid extraction. *Geology*, 17:942–946.

Serebryakova, O., Bilichenko, S., Chmyrev, V., Parrot, M., Rauch, J., Lefeuvre, F., and Pokhotelov, O. (1992). Electromagnetic elf radiation from earthquake regions as observed from low-altitude satellites. *Geophysical Research Letters*, 19:91–94.

Shalimov, S. and Gokhberg, M. (1998). LithosphereŰionosphere coupling mechanism and its application to the earthquake in iran on june 20, 1990: a review of ionospheric measurements and basic assumptions. *Physics of the Earth and Planetary Interiors*, 105:211–218.

Shankland, T. J. and Ander, M. E. (1983). Electrical conductivity, temperatures and fluids in the lower crust. *Journal of Geophysical Research*, 88(B11):9475–9484.

Shankland, T. J., Duba, A. G., Mathez, E. A., and Peach, C. L. (1997). Increase of electrical conductivity with pressure as an indicator of conduction through a solid phase in midcrustal rocks. *Journal of Geophysical Research: Solid Earth*, 107(B7):14741–14750.

Shaw, B. E. (1993). Generalised omori law for aftershocks and foreshocks from a simple dynamics. *Geophysical Research Letters*, 20:907–910.

Shaw, B. E. (1994). Complexity in a spatially uniform continuum model. *Geophysical Research Letters*, 21:1983–1986.

Shaw, B. E. (1995). Frictional weakening and slip complexity in earthquake faults. *Journal of Geophysical Research*, 102:18239–18251.

Shaw, B. E., Carlson, J. M., and Langer, J. S. (1992). Patterns of activity preceding large earthquakes. *Journal of Geophysical Research*, 97:479–488.

Shcherbakov, R. and Turcotte, D. (2003). Damage and self-similarity in fracture. *Theoretical and Applied Fracture Mechanics*, 39(3):245–258.

Shearer, P. (1999). *Introduction to Seismology*. Cambridge University Press.

Shinbrot, T., Daniels, K., Marone, C., and Tsiu, T. (2014). Unexplained voltage signals from granular materials. *Bulletin of the American Physical Society: APS March Meeting 2014*, 59(1):–.

Shinbrot, T., Kim, N. H., and Thyagu, N. N. (2012). Electrostatic precursors to granular slip events. *PNAS*, 109(27):10806–10810.

Shitov, A. V. (2010). Health of people living in a seismically active region. In Florinsky, I. V., editor, *Man and the geosphere*, pages 185–213. Nova Science Publishers.

Sikula, J., Lokajicek, T., and Mori, Y. (2002). Cracks characterisation by electromagnetic and acoustic emission. In *Proceedings of 8th ECNDT, AEND, Barcelona, CDR No. 62*.

Sill, W. R. (1983). Self-potential modelling from primary flows. *Geophysics*, 48:76–86.

Silva, R., Franca, G., Vilar, C., and Alcaniz, J. (2006). Nonextensive models for earthquakes. *Physical Review E*, 73(2):026102.

Simmons, G. and Brace, W. (1965). Comparison of static and dynamic measurements of compressibility of rocks. *Journal of Geophysical Research*, 70:5649–5656.

Slifkin, L. (1993). Seismic electric signals from displacement of charged dislocations. *Tectonophysics*, 224(1):149–152.

Smith, B. E. and Johnston, M. J. S. (1976). A tectonomagnetic effect observed before a magnitude 5.2 earthquake near hollister, california. *Journal of Geophysical Research*, 81(20):3556–3560.

Soga, N., Mizutani, H., Spetzlet, H., and Martin, R. (1978). The effect of dilatancy on velocity anisotropy in westerly granite. *Journal of Geophysical Research*, 83:4451–4458.

Sornette, A., Davy, P., and Sornette, D. (1990a). Growth of fractal fault patterns. *Physics Review Letters*, 65:2266–2269.

Sornette, A. and Sornette, D. (1989). Self-organised criticality and earthquakes. *Europhysics Letters*, 9:197–202.

Sornette, D. (1991). Self-organised criticality in plate tectonics. In Riste, T. and Sherrington, D., editors, *Spontaneous Formation of Space-Time Structures and Criticality*, Proc. NATO ASI, Geilo, Norway, pages 57–106, Dordrecht. Kluwer.

Sornette, D. (1999). Earthquakes: From chemical alteration to mechanical rupture. *Physics Reports*, 313:237–291.

Sornette, D. (2006). *Critical Phenomena in Natural Sciences*. Springer.

Sornette, D., Davy, P., and Sornette, A. (1990b). Structuration of the lithosphere in plate tectonics as a self-organised critical phenomenon. *Journal of Geophysical Research*, 95:17353–17361.

Sornette, D., Miltenberger, P., and Vanneste, C. (1994). Statistical physics of fault patterns self-organized by repeated earthquakes. *Pure and Applied Geophysics*, 142:491–527.

Sornette, D., Miltenberger, P., and Vanneste, C. (1995). Statistical physics of fault patterns self-organized by repeated earthquakes: synchronization versus self-organized criticality. In Bouwknegt, P., Fendley, P., Minahan, J., Nemeschansky, D., Pilch, K., Saleur, H., and Warner, N., editors, *Recent Progresses in Statistical Mechanics and Quantum Field Theory: Proceedings of the conference 'Statistical Mechanics and Quantum Field Theory', USC, Los Angeles, May 16-21, 1994*, pages 313–332, Singapore. World Scientific.

Sornette, D. and Virieux, J. (1992). Linking short-timescale deformation to long-timescale tectonics. *Nature*, 357:401–404.

Sornette, D. and Werner, M. J. (2009). Statistical physics approaches to seismicity. In Meyers, R. A., editor, *Encyclopedia of Complexity and Systems Science*, pages 7872–7891. Springer, New York.

Sotolongo-Costa, O. (2012). Non-extensive framework for earthquakes: the role of fragments. *Acta Geophysica*, 60(3):526–534.

Sotolongo-Costa, O., Antoranz, J. C., Posadas, A., Vidal, F., and Vazquez, A. (2000). Levy flights and earthquakes. *Geophysical Research Letters*, 27(13):1965–1968.

Sotolongo-Costa, O. and Posadas, A. (2002). Tsallis entropy: A non-extensive frequency-magnitude distribution of earthquakes. Online: http://arxiv.org/ftp/cond-mat/papers/0211/0211160.pdf.

Sotolongo-Costa, O. and Posadas, A. (2004). Fragment-asperity interaction model for earthquakes. *Physical Review Letters*, 92(4):–.

Sotolongo-Grau, O., Rodriguez-Perez, D., Antoranz, J. C., and Sotolongo-Costa, O. (2010). Tissue radiation response with maximum tsallis entropy. *Physical Review Letters*, 105:158105.

Sotolongo-Grau, O., Rodriguez-Perez, D., Sotolongo-Costa, O., and Antoranz, J. (2013). Tsallis entropy approach to radiotherapy treatments. *Physica A: Statistical Mechanics and its Applications*, 392(9):2007 – 2015.

Spetzler, H. and Martin, R. J. (1974). Correlation of strain and velocity during dilatancy. *Nature*, 252:30–31.

Spyropoulos, C., Griffith, W. J., Scholz, C. H., and Shaw, B. E. (1999). Experimental evidence for different strain regimes of crack populations in a clay model. *Geophysical Research Letters*, 26(8):1081–1084.

St-Laurent, F. (2000). The saguenay, quebec, earthquake lights of november 1988Űjanuary 1989. *Seismological Research Letters*, 71:160–174.

St-Laurent, F., Derr, J. S., and Freund, F. T. (2006). Earthquake lights and the stress-activation of positive hole charge carriers in rocks. *Physics and Chemistry of the Earth*, 31:305–312.

Stanchits, S., Vinciguerra, S., and Dresen, G. (2006). Ultrasonic velocities, acoustic emission characteristics and crack damage of basalt and granite. *Pure and Applied Geophysics*, 163:974–993.

Stark, M. A. and Davis, S. D. (1996). Remotely triggered microearthquakes at the geysers geothermal field, california. *Geophysical Research Letters*, 23:945–948.

Stavrakakis, G. and Drakopoulos, J. (1996). The van method: Contradictory and misleading results since 1981. *Geophysical Research Letters*, 23(11):1347–1350.

Stavrakas, I., Anastasiadis, C., Triantis, D., and Vallianatos, F. (2003). Piezo stimulated currents in marble samples: precursory and concurrent-with-failure signals. *Natural Hazards and Earth System Sciences*, 3(3/4):243–247.

Stavrakas, I., Triantis, D., Agioutantis, Z., Maurigiannakis, S., Saltas, V., Vallianatos, F., and Clarke, M. (2004). Pressure stimulated currents in rocks and their correlation with mechanical properties. *Natural Hazards and Earth System Sciences*, 4(4):563–567.

Stein, R. S., King, G. C. P., and Lin, J. (1994). Stress triggering of the 1994 m=6.4 northridge, california earthquake by its predecessors. *Science*, 265:1432–1435.

Stein, S. and Klosko, E. (2002). Earthquake mechanisms and plate tectonics. In Lee, W. H. K., Kanamori, H., Jennings, P. C., and Kisslinger, C., editors, *IASPEI International Handbook of Earthquake and Engineering Seismology: Part A*, chapter 7, pages 69–78. Academic Press.

Stein, S. and Wysession, M. (2003). *An Introduction to Seismology, Earthquakes and Earth Structure*. Wiley Blackwell.

Stergiopoulos, C., Stavrakas, I., Hloupis, G., Triantis, D., and Vallianatos, F. (2013). Electrical and acoustic emissions in cement mortar beams subjected to mechanical loading up to fracture. *Engineering Failure Analysis*, 35:454–461.

Stern, O. (1924). Zur theori der elekrolischen doppelschicht. *Zeit Elekrochem*, 30:508.

Stoll, A. and Wilkinson, A. J. (2010). Dislocation modeling of quasi-static crack propagation in an elasto-plastic medium. *International Journal of Fracture*, 164:103–115.

Strassman, R. J. (1990). The pineal gland: current evidence for its role in consciousness. In *Psychedelic Monographs and Essays*, volume 5, pages 167–205. PM&E Publications, Boynton Beach, FL.

Streit, J. E. and Cox, S. F. (2001). Fluid pressures at hypocentres of moderate to large earthquakes. *Journal of Geophysical Research: Solid Earth*, 106(B2):2235–2243.

Sykes, L., Shaw, B., and Scholz, C. (1999). Rethinking earthquake prediction. *Pure and Applied Geophysics*, 155:207–232.

Takahashi, I., Hattori, K., Harada, M., Yoshino, C., and Isezaki, N. (2007). Anomalous geoelectrical and geomagnetic signals observed at southern boso peninsula, japan. *Annals of Geophysics*, 50(1):123–135.

Takemura, T. and Oda, M. (2005). Changes in crack density and wave velocity in association with crack growth in triaxial tests of inada granite. *Journal of Geophysical Research*, 110(B5):B05401.

Takeuchi, A., Lau, B. W., and Freund, F. T. (2006). Current and surface potential induced by stress-activated positive holes in igneous rocks. *Physics and Chemistry of the Earth*, 31(4-9):240–247.

Takeuchi, A. and Nagahama, H. (2001). Voltage changes induced by stick-slip of granites. *Geophysical Research Letters*, 28(17):3365–3368.

Takeuchi, A. and Nagahama, H. (2002a). Interpretation of charging on fracture or frictional slip surface of rocks. *Physics of the Earth and Planetary Interiors*, 130:285–291.

Takeuchi, A. and Nagahama, H. (2002b). Surface charging mechanism and scaling law related to earthquakes. *Journal of Atmospheric Electricity*, 22:183–190.

Takeuchi, A. and Nagahama, H. (2004). Scaling laws between seismo-electric/magnetic fields and earthquake magnitude. *Terra Nova*, 16(3):152–156.

Takeuchi, A. and Nagahama, H. (2006). Electric dipoles perpendicular to a stick-slip plane. *Physics and Chemistry of the Earth and Planetary Interiors*, 155:208–218.

Takeuchi, A., Nagahama, H., and Hashimoto, T. (2004). Surface electrification of rocks and charge trapping centers. *Physics and Chemistry of the Earth*, 29:359–366.

Takeuchi, A. and Nagao, T. (2013). Activation of hole charge carriers and generation of electromotive force in gabbro blocks subjected to nonuniform loading. *Journal of Geophysical Research: Solid Earth*, 118:915–925.

Tang, C. and Bak, P. (1988). Mean field theory of self-organised critical phenomena. *Journal of Statistical Physics*, 51(5-6):797–802.

Teisseyre, R. (1992). Earthquake premonitory processes: Evolution of stresses and current generation. *Terra Nova*, 4:509–513.

Teisseyre, R. (1996). Motion and flow equation of stresses. *Acta Geophysica Polonica*, 44:19–29.

Teisseyre, R. (1997). Dislocation-stress relations and evolution of dislocation fields. *Acta Geophysica Polonica*, 45:205–214.

Teisseyre, R. (2001). Dislocation dynamics and related electromagnetic excitation. *Acta Geophysica Polonica*, 49:55–73.

Teisseyre, R. and Nagahama, H. (1998). Dislocation field evolution and dislocation source/sink function. *Acta Geophysica Polonica*, 46:13–33.

Telesca, L. (2010a). Analysis of italian seismicity by using a nonextensive approach. *Tectonophysics*, 494(1âĂŞ2):155 – 162.

Telesca, L. (2010b). A non-extensive approach in investigating the seismicity of l'aquila area (central italy), struck by the 6 april 2009 earthquake (ml=5.8). *Terra Nova*, 22(2):87–93.

Telesca, L. (2010c). Nonextensive analysis of seismic sequences. *Physica A: Statistical Mechanics and its Applications*, 389(9):1911–1914.

Telesca, L. (2011). Tsallis-based nonextensive analysis of the southern california seismicity. *Entropy*, 13(7):1267–1280.

Telesca, L. (2012). Maximum likelihood estimation of the nonextensive parameters of the earthquake cumulative magnitude distribution. *Bulletin of the Seismological Society of America*, 102:886–891.

Telesca, L. and Chen, C.-C. (2010). Nonextensive analysis of crustal seismicity in taiwan. *Natural Hazards and Earth System Sciences*, 10(6):1293–1297.

Telesca, L., Lovallo, M., Romano, G., Konstantinou, K. I., Hsu, H.-L., and chih Chen, C. (2014). Using the informational fisherŰshannon method to investigate the influence of long-term deformation processes on geoelectrical signals: An example from the taiwan orogeny. *Physica A*, 414:340–351.

Terzaghi, K. (1943). *Theoretical Soil Mechanics*. John Wiley and Sons, New York.

The Engineering Toolbox (2014). Resistance and resistivity. http://www.engineeringtoolbox.com.

Theriault, R., St-Laurent, F., Freund, F. T., and Derr, J. S. (2014). Prevalence of earthquake lights associated with rift enviornments. *Seismological Research Letters*, 85(1):159–178.

Thomas, J. N., Love, J. J., and Johnston, M. J. (2009). On the reported magnetic precursor of the 1989 loma prieta earthquake. *Physics of the Earth and Planetary Interiors*, 173:207–215.

Thorpe, G. S. (2008). *CliffsAP Chemistry, 4th Edition*. Wiley Publishing, Canada.

Townend, J. and Zoback, M. D. (2000). How faulting keeps the crust strong. *Geology*, 28:594–604.

Triantis, D., Anastasiadis, C., and Stavrakas, I. (2008). The correlation of electrical charge with strain on stressed rock samples. *Natural Hazards and Earth System Sciences*, 8(6):1243–1248.

Triantis, D., Anastasiadis, C., Vallianatos, F., Kyriazis, P., and Nover, G. (2007). Electric signal emissions during repeated abrupt uniaxial compressional stress steps in amphibolite from ktb drilling. *Natural Hazards and Earth System Sciences*, 7:149–154.

Triantis, D., Stavrakas, I., Anastasiadis, C., Kyriazopoulos, A., and Vallianatos, F. (2006). An analysis of pressure stimulated currents (psc) in marble samples under mechanical stress. *Physics and Chemistry of the Earth, Parts A/B/C*, 31(4-9):234–239.

Tributsch, H. (1983). *When Snakes Awake: Animals and Earthquake Prediction*. MIT Press, Cambridge, Mass.

Trigunait, A., Parrot, M., Pulinets, S., and Li, F. (2004). Variations of the ionospheric electron density during the bhuj seismic event. *Annals of Geophysics*, 22:4123–4131.

Tsallis, C. (1988). Possible generalization of boltzmann-gibbs statistics. *Journal of Statistical Physics*, 52(1-2):479–487.

Tsallis, C. (1999). Non-extensive statistics: theoretical, experimental and computational evidences and connections. *Brazilian Journal of Physics*, 29:1–35.

Tsallis, C. (2001). Non-extensive statistical mechanics and thermodynamics: historical background and present status. In Abe, S. and Okamoto, Y., editors, *Nonextensive Statistical Mechanics and Its Applications*, Lecture Notes in Physics. Springer.

Tsallis, C. (2009a). *Introduction to Nonextensive Statistical Mechanics*. Springer.

Tsallis, C. (2009b). Nonadditive entropy and nonextensive statistical mechanics - an overview after 20 years. *Brazilian Journal of Physics*, 39(2A):337–356.

Tsallis, C. (2013). Nonadditive entropies and nonextensive statistical mechanics. Oral presentation. Heraklion, Crete, Greece.

Tsallis, C. and Leonardo, C. J. (2013). Black hole thermodynamical entropy. *The European Physical Journal C*, 73(7):2487 (1–7).

Tselentis, G.-A. and Melis, N. (1996). A note on evaluating van earthquake predicitons. *Geophysical Research Letters*, 23(11):1411–1414.

Tsubokawa, I. (1969). On relation between duration of crustal movement and earthquake magnitude. *Journal of the Geodetic Society of Japan*, 15:75–88 (in Japanese).

Tsubokawa, I. (1973). On relation between duration of precursory geophysical phenomena and duration of crustal movement before earthquake. *Journal of the Geodetic Society of Japan*, 19:116–119 (in Japanese).

Tsukuda, T. (1997). Size and some features of luminous sources associated with the 1995 hyogo-ken nanbu earthquake. *Journal of Physics of the Earth*, 45:73–82.

Tsunogai, U. and Wakita, H. (1995). Precursory chemical changes in groundwater: Kobe earthquake, japan. *Science*, 269:61–63.

Tsutsumi, A. and Shirai, N. (2008). Electromagnetic signals associated with stickŰslip of quartz-free rocks. *Tectonophysics*, 450:79–84.

Tuck, B., Stacey, F., and Starkey, J. (1977). A search for the piezoelectric effect in quartz-bearing rock. *Tectonophysics*, 39:7–11.

Tuffen, H., Smith, R., and Sammonds, P. R. (2008). Evidence for seismogenic fracture of silicic magma. *Nature*, 453(7194):511–514.

Turcotte, D. (1991). Earthquake prediction. *Annual Review of Earth and Planetary Sciences*, 19:263–281.

Turcotte, D., Newman, W., and Shcherbakov, R. (2003). Micro and macroscopic models of rock fracture. *Geophysical Journal International*, 152:718–728.

Turcotte, D. L. (1992). *Fractals and Chaos in Geology and Geophysics*. Cambridge University Press, New York.

Turcotte, D. L., Newman, W. I., and Gabrielov, A. (2000). A statistical physics approach to earthquakes. In Rundle, J. B., Turcotte, D. L., and Klein, W., editors, *GeoComplexity and the Physics of Earthquakes*, Geophysical Monograph Series. American Geophysical Union.

Turner, F. J., Griggs, D. T., and Heard, H. (1954). Experimental deformation of calcite crystals. *Geological Society of America Bulletin*, 65(9):–.

Twiss, R. J. and Moores, E. M. (1992). *Structural Geology*. W. H. Freeman.

Tzanis, A. and Vallianatos, F. (2001). A critical review of electric earthquake precursors. *Annals of Geophysics*, 44(2):429–460.

Tzanis, A. and Vallianatos, F. (2002). A physical model of electrical earthquake precursors due to crack propagation and the motion of charged edge dislocations. In Hayakawa, M. and Molchanov, O. A., editors, *Seismo Electromagnetics: LithosphereŰAtmosphereŰIonosphere Coupling*, pages 117–130. TERRAPUB, Tokyo.

Tzanis, A., Vallianatos, F., and Gruszow, S. (2000). Identification and discrimination of transient electrical earthquake precursors: fact, fiction and some possibilities. *Physics of the Earth and Planetary Interiors*, 121:223–248.

Umarov, S., Tsallis, C., and Steinberg, S. (2008). On a q-central limit theorem consistent with nonextensive statistical mechanics. *Milan Journal of Mathematics*, 76(1):307–328.

USGS (2012). Largest and deadliest earthquakes by year 1990 - 2011. Website: http://earthquake.usgs.gov/earthquakes/eqarchives/year/byyear.php. Accessed: 8 July 2014.

Utada, H. (1996). Difficulty of statistical evaluation of an earthquake prediction method. *Geophysical Research Letters*, 23(11):1391–1394.

Utsu, T. (1961). A statistical study on the occurrence of aftershocks. *Geophysical Magazine*, 30:521–605.

Uyeda, S. (2002). Continental drift, seafloor spreading and plate/plume tectonics. In Lee, W. H. K., Kanamori, H., Jennings, P. C., and Kisslinger, C., editors, *IASPEI International Handbook of Earthquake and Engineering Seismology: Part A*, chapter 6, pages 51–67. Academic Press.

Uyeda, S., Hayakawa, M., Nagao, T., Molchanov, O., , Hattori, K., Orihara, Y., Gotoh, K., Akinaga, Y., and Tanaka, H. (2002). Electric and magnetic phenomena observed before the volcano-seismic activity in 2000 in the izu island region, japan. *PNAS*, 99(11):7352–7355.

Uyeda, S., Kamogawa, M., and Tanaka, H. (2009a). Analysis of electrical activity and seismicity in the natural time domain for the volcanic-seismic swarm activity in 2000 in the izu island region, japan. *Journal of Geophysical Research*, 114(B2):–.

Uyeda, S., Nagao, T., and Kamogawa, M. (2009b). Short-term earthquake prediction: Current status of seismo-electromagnetics. *Tectonophysics*, 470(3-4):205–213.

Uyeda, S., Nagao, T., Orihara, T., Yamaguci, T., and Takahashi, I. (2000). Geoelectric potential changes: Possible precursors to earthquakes in japan. *PNAS*, 97(9):4561–4566.

Vallianatos, F. (2009). A non-extensive approach to risk assessment. *Natural Hazards and Earth System Sciences*, 9(1):211–216.

Vallianatos, F. (2011). A non-extensive statistical physics approach to the polarity reversals of the geomagnetic field. *Physica A: Statistical Mechanics and its Applications*, 390(10):1773–1778.

Vallianatos, F. (2013a). On the non-extensivity in mars geological faults. *EPL (Europhysics Letters)*, 102(2):28006.

Vallianatos, F. (2013b). On the statistical physics of rockfalls: A non-extensive view. *EPL (Europhysics Letters)*, 101(1):10007.

Vallianatos, F., Benson, P., Meredith, P., and Sammonds, P. (2012a). Experimental evidence of a non-extensive statistical physics behaviour of fracture in triaxially deformed etna basalt using acoustic emissions. *EPL (Europhysics Letters)*, 97(5):58002.

Vallianatos, F., Kokinou, E., and Sammonds, P. (2011a). Non-extensive statistical physics approach to fault population distribution. a case study from the southern hellenic arc (central crete). *Acta Geophysica*, 59(4):770–784.

Vallianatos, F. and Kouli, M. (2013). Evidence of non extensive statistical physics behavior in the watershed distribution in active tectonic areas. examples from greece. In *Proceedings of SPIE - The International Society for Optical Engineering*, volume 8795.

Vallianatos, F., Michas, G., Benson, P., and Sammonds, P. (2013a). Natural time analysis of critical phenomena: The case of acoustic emissions in triaxially deformed etna basalt. *Physica A*, 392:5172–5178.

Vallianatos, F., Michas, G., and Papadakis, G. (2014). Non-extensive and natural time analysis of seismicity before the mw6.4, october 12, 2013 earthquake in the south west segment of the hellenic arc. *Physica A*, 414:163–173.

Vallianatos, F., Michas, G., Papadakis, G., and Sammonds, P. (2012b). A non-extensive statistical physics view to the spatiotemporal properties of the june 1995, aigion earthquake (m6.2) aftershock sequence (west corinth rift, greece). *Acta Geophysica*, 60(3):758–768.

Vallianatos, F., Michas, G., Papadakis, G., and Tzanis, A. (2013b). Evidence of non-extensivity in the seismicity observed during the 2011-2012 unrest at the santorini volcanic complex, greece. *Natural Hazards and Earth System Sciences*, 13(1):177–185.

Vallianatos, F., Nardi, A., Carluccio, R., and Chiappini, M. (2012c). Experimental evidence of a non-extensive statistical physics behavior of electromagnetic signals emitted from rocks under stress up to fracture. preliminary results. *Acta Geophysica*, 60(3):894–909.

Vallianatos, F. and Nomikos, K. (1998). Seismogenic radio emissions as earthquake precursors in greece. *Physics and Chemistry of the Earth*, 23(9-10):953–957.

Vallianatos, F. and Sammonds, P. (2010). Is plate tectonics a case of non-extensive thermodynamics? *Physica A: Statistical Mechanics and its Applications*, 389(21):4989–4993.

Vallianatos, F. and Sammonds, P. (2011). A non-extensive statistics of the fault-population at the valles marineris extensional province, mars. *Tectonophysics*, 509(1-2):50–54.

Vallianatos, F. and Sammonds, P. (2013). Evidence of non-extensive statistical physics of the lithospheric instability approaching the 2004 sumatran-andaman and 2011 honshu mega-earthquakes. *Tectonophysics*, 590:52–58.

Vallianatos, F. and Triantis, D. (2008). Scaling in pressure stimulated currents related with rock fracture. *Physica A*, 387:4940–4946.

Vallianatos, F. and Triantis, D. (2012). Is pressure stimulated current relaxation in amphibolite a case of non-extensivity? *EPL (Europhysics Letters)*, 99(1):18006.

Vallianatos, F. and Triantis, D. (2013). A non-extensive view of the pressure stimulated current relaxation during repeated abrupt uniaxial load-unload in rock samples. *EPL (Europhysics Letters)*, 104(6):68002.

Vallianatos, F., Triantis, D., and Sammonds, P. (2011b). Non-extensivity of the isothermal depolarization relaxation currents in uniaxial compressed rocks. *EPL (Europhysics Letters)*, 94(6):68008.

Vallianatos, F., Triantis, D., Tzanis, A., Anastasiadis, C., and Stavrakas, I. (2004). Electric earthquake precursors: From laboratory results to field observations. *Physics and Chemistry of the Earth*, 29(4-9):339–351.

Vallianatos, F. and Tzanis, A. (1998). Electric current generation associated with the deformation rate of a solid: preseismic and coseismic signals. *Physics and Chemistry of the Earth*, 23:933–938.

Vallianatos, F. and Tzanis, A. (1999). A model for the generation of precursory electric and magnetic fields associated with the deformation rate of the earthquake focus. In Hayakawa, M., editor, *Atmospheric and Ionospheric Electromagnetic Phenomena Associated with Earthquakes*, pages 287–305. Terra Scientific, Tokyo.

Vallianatos, F. and Tzanis, A. (2003). On the nature, scaling and spectral properties of pre-seismic ulf signals. *Natural Hazards and Earth System Sciences*, 3:237–242.

Valverde-Esparza, S. M., Ramirez-Rojas, A., Flores-Marquez, E. L., and Telesca, L. (2012). Non-extensivity analysis of seismicity within four subduction regions in mexico. *Acta Geophysica*, 60(3):833–845.

Van der Straeten, E. and Beck, C. (2009). Superstatistical fluctuations in time series: Applications to share-price dynamics and turbulence. *Physical Review E*, 80:036108.

Vanyan, L. and Shilovski, A. (1989). Fluids in the lower crust inferred from electromagnetic data. In *Properties and Processes of the Earth's Lower Crust. Geophysical Monograph Series*, volume 51, pages 243–246.

Varotsos, P. and Alexopoulos, K. (1984a). Physical properties of the variations of the electric field of the earth preceding earthquakes, i. *Tectonophysics*, 110:73–98.

Varotsos, P. and Alexopoulos, K. (1984b). Physical properties of the variations of the electric field of the earth preceding earthquakes, ii. *Tectonophysics*, 110:99–125.

Varotsos, P. and Alexopoulos, K. (1986). *Thermodynamics of Point Defects and their Relation with Bulk Properties*. North Holland, Amsterdam.

Varotsos, P., Alexopoulos, K., and Lazaridou, M. (1993). Latest aspects of earthquake prediction in greece based on seismic electric signals, ii. *Tectonophysics*, 224(1):1–37.

Varotsos, P., Alexopoulos, K., and Nomicos, K. (1982). Electrotelluric precursors to earthquakes. *Proceedings of the Academy of Athens*, 57:341–363.

Varotsos, P., Eftaxias, K., Lazaridou, M., Nomicos, K., Sarlis, N., Bogris, N., Makris, J., Antonopoulos, G., and Kopanas, J. (1996). Recent earthquake prediction results in greece based on the observations of seismic electric signals. *Acta Geophysica Polonica*, 44(4):301–327.

Varotsos, P., Hadjicontis, V., and Nowick, A. (2001). The physical mechanism of seismic electric signals. *Acta Geophysica Polonica*, 49:415–421.

Varotsos, P. and Lazaridou, M. (1991). Latest aspects of earthquake prediction in greece based on seismic electric signals. *Tectonophysics*, 188:321–347.

Varotsos, P., Sarlis, N., and Lazaridou, M. (1999). Interconnection of defect parameters and stress-induced electric signals in ionic crystals. *Physical Review B*, 59:24–27.

Varotsos, P., Sarlis, N., Lazaridou, M., and Kapiris, P. (1998). Transmission of stress induced electric signals in dielectric media. *Journal of Applied Physics*, 83:60–70.

Varotsos, P., Sarlis, N., Skordas, E., and Lazaridou, M. (2013). Seismic electric signals: An additional fact showing their physical interconnection with seismicity. *Tectonophysics*, 589:116–125.

Varotsos, P., Sarlis, N., Skordas, E., Uyeda, S., and Kamogawa, M. (2011a). Natural time analysis of critical phenomena. *Proceedings of the National Academy of Sciences USA*, 108:11361–11364.

Varotsos, P. A. (2005). *The Physics of Seismic Electric Signals*. TerraPub.

Varotsos, P. A., Sarlis, N. V., and Skordas, E. S. (2002). Long-range correlations in the electric signals that precede rupture. *Physical Review E*, 66:011902.

Varotsos, P. A., Sarlis, N. V., and Skordas, E. S. (2011b). *Natural Time Analysis: The New View of Time*. Springer.

Varotsos, P. A., Sarlis, N. V., Skordas, E. S., and Lazaridou, M. S. (2007). Electric pulses some minutes before earthquake occurrences. *Applied Physics Letters*, 90(6):064104.

Varotsos, P. A., Sarlis, N. V., Skordas, E. S., Tanaka, H. K., and Lazaridou, M. S. (2006). Entropy of seismic electric signals: Analysis in natural time under time reversal. *Physical Review E*, 73:031114.

Varotsos, P. A., Sarlis, N. V., Tanaka, H. K., and Skordas, E. S. (2005). Similarity of fluctuations in correlated systems: The case of seismicity. *Physical Review E*, 72:041103.

Vermilye, J. M. and Scholz, C. H. (1998). The process zone: a microstructural view of fault growth. *Journal of Geophysical Research*, 103:12223–12237.

Vilar, C. S., Franca, G. S., Silva, R., and Alcaniz, J. S. (2007). Nonextensivity in geological faults? *Physica A*, 377:285–290.

Vita-Finzi, C. (2003). *Monitoring the Earth: Physical Geology in Action*. Oxford University Press.

Volti, T. and Crampin, S. (2003). A four-year study of shear-wave splitting in iceland: 2. temporal changes before earthquakes and volcanic eruptions. *Geological Society of London Special Publications*, 212:135–149.

von Karman, T. (1911). Festigkeitsversuche unter allseitigem druck. *Z. Verhandl. Deut. Ing.*, 55:1749–1757 (in German).

Von Seggern, D. (1980). A random stress model for seismicity statistics and earthquake prediction. *Geophysical Research Letters*, 7:637–640.

Walsh, J. B. (1965). The effect of cracks on the uniaxial elastic compression of rocks. *Journal of Geophysical Research*, 70:399–411.

Warwick, J. W., Stoker, C., and Meyer, T. R. (1982). Radio emission associated with rock fracture: Possible application to the great chilean earthquake of may 22 1960. *Journal of Geophysical Research*, 87:2851–2859.

Wawersik, W. and Brace, W. (1971). Post-failure behavior of a granite and diabase. *Rock mechanics*, 3(2):61–85.

Weiss, J. and Marsan, D. (2003). Three-dimensional mapping of dislocation avalanches: clustering and space/time coupling. *Science*, 299:89–92.

Wheat, C. G., Elderfield, H., Mottl, M. J., and Monnin, C. (2000). Chemical composition of basement fluids within an oceanic ridge flank: Implications for along-strike and across-strike hydrothermal circulation. *Journal of Geophysical Research*, 105(B6):13437–13447.

Whitcomb, J. H., Garmany, J. D., and Andersonn, D. L. (1973). Earthquake prediction: variation of seismic velocities before the san fernando earthquake. *Science*, 180:632–635.

Whitten, C. A. (1956). Crustal movements in california and nevada. *Transactions of the American Geophysical Union*, 37:393–398.

Whitworth, R. W. (1975). Charged dislocations in ionic crystals. *Advances in Physics*, 24:203–304.

Wilk, G. and Wlodarczyk, Z. (2000). Interpretation of the nonextensivity parameter q in some applications of tsallis statistics and levy distributions. *Physical Review Letters*, 84:2770–2773.

Wilson, B. W., Wright, C. W., Morris, J. E., Buschbom, R., Brown, D. P., Miller, D. L., Sommers-Flannigan, R., and Anderson, L. E. (1990). Evidence for an effect of elf electromagnetic fields on human pineal gland function. *Journal of Pineal Research*, 9(4):259–269.

Wilson, J. (1968). Static or mobile earth: The current scientific revolution. *American Philosophical Society Proceedings*, 112:309–320.

Wong, G. and Zhu, S. (1995). Speed of sound in seawater as a function of salinity, temperature and pressure. *Journal of the Acoustical Society of America*, 97(3):1732–1736.

Wong, T.-F. (1990). A note on the propagation behaviour of a crack nucleated by a dislocation pileup. *Journal of Geophysical Research*, 95(B6):8939–8646.

Wood, D. S. (1973). Patterns and magnitudes of natural strain in rocks. *Philosophical Transactions of the Royal Society of London*, 274:373–382.

Wyss, M. and Allman, A. (1996). Probability of chance correlations of earthquakes with predictions in areas of heterogeneouss eismicityr ate: the van case. *Geophysical Research Letters*, 23(11):1307–1310.

Wyss, M. and Booth, D. C. (1997). The iaspei procedure for the evaluation of earthquake precursors. *Geophysical Journal International*, 131(3):423–424.

Yalcin, G. C. and Beck, C. (2013). Environmental superstatistics. *Physica A: Statistical Mechanics and its Applications*, 392(21):5431 – 5452.

Yamada, I., Masuda, K., and Mizutani, H. (1989). Electromagnetic and acoustic emission associated with rock fracture. *Physics of the Earth and Planetary Interiors*, 57:157–168.

Yamasaki, K. and Nanjo, K. (2009). A new mathematical tool for analyzing the fracturing process in rock: Partial symmetropy of microfracturing. *Physics of the Earth and Planetary Interiors*, 173:297–305.

Yasui, Y. (1968). A study on the luminous phenomena accompanied with earthquakes (part 1). *Mem. Kakioka Mag. Obs.*, 13:25–61.

Yen, H. Y., Chen, C. H., and Liu, J. Y. (2004). Geomagnetic fluctuations during the 1999 chi-chi earthquake in taiwan. *Earth, Planets and Space*, 56:39–45.

Yoshida, S. (2001). Convection current generated prior to rupture in saturated rocks. *Journal of Geophysical Research*, 106(B2):2103–2120.

Yoshida, S., Clint, O. C., and Sammonds, P. R. (1998). Electric potential changes prior to shear fracture in dry and saturated rocks. *Geophysical Research Letters*, 25(10):1577–1580.

Yoshida, S., Manjgaladze, P., Zilpimani, D., Ohnaka, M., and Nakatani, M. (1994). Electromagnetic emissions associated with frictional sliding of rock. In Hayakawa, M. and Fujinawa, Y., editors, *Electromagnetic Phenomena Related to Earthquake Prediction*, pages 307–322. Terra Scientific Publishing Company, Tokyo.

Yoshida, S. and Ogawa, T. (2004). Electromagnetic emissions from dry and wet granite associated with acoustic emissions. *Journal of Geophysical Research*, 109:B09204.

Yoshida, S., Uyeshima, M., and Nakatani, M. (1997). Electric potential changes associated with slip failure of granite: Preseismic and coseismic signals. *Journal of Geophysical Research*, 102(B7):14883–14897.

Young, T. (1807). *A Course of Lectures in Natural Philosophy and Mechanical Arts*. Taylor and Walton, London.

Zang, A., Wagner, F. C., and Dresen, G. (1996). Acoustic emission, microstructure and damage model of dry and wet sandstone stressed to failure. *Journal of Geophysical Research*, 101:17507–17521.

Zhang, G. Q., Tirnakli, U., Wang, L., and Chen, T. L. (2011). Self organized criticality in a modified olami-feder-christensen model. *European Physical Journal B*, 82(1):83–89.

Zhang, S., Cox, S. F., and Paterson, M. S. (1994). The influence of room temperature deformation on porosity and permeability in calcite aggregates. *Journal of Geophysical Research: Solid Earth*, 99(B8):15761–15775.

Zhang, S., Paterson, M. S., and Cox, S. F. (2001). Microcrack growth and healing in deformed calcite aggregates. *Tectonophysics*, 335(1âĂŞ2):17–36.

Zhao, H. Y., Ruan, A. G., Yang, R., Liang, Z. B., and Han, D. S. (2002). The geoelectric field anomaly of tianzhu and relationship with yongding earthquake (ms 5.8) in 1995 and tianzhu earthquake (ms 5.4) in 1996. *Northwestern Seismological Journal (in Chinese)*, 24(1):56–64.

Zhao, Y. and Qian, F. (1994). Geoelectric precursors to strong earthquakes in china. *Tectonophysics*, 233:99–113.

Zhao, Y. and Qian, F. (2009). Impending hrt wave precursors to the wenchuan ms 8.0 earthquake and methods of earthquake impending prediction by using hrt wave. *Science in China, Series D: Earth Sciences*, 39(1):11–23.

Zhu, W. (2006). Quantitative characterization of permeability reduction associated with compactive cataclastic flow. In *Earthquakes: Radiated Energy and the Physics of Faulting*, volume 170. American Geophysical Union Geophysical Monograph Series.

Zhu, W. and Wong, T.-F. (1996). Permeability reduction in a dilating rock: Network modelling of damage and tortuosity. *Geophysical Research Letters*, 23(22):3099–3102.

Zhu, W. and Wong, T.-F. (1997). The transition from brittle faulting to cataclastic flow: Permeability evolution. *Journal of Geophysical Research*, 102(B2):3027–3041.

Zhu, W. L. (2007). The brittle field: localisation and flow. Online powerpoint presentation: http://www.whoi.edu/science/GG/people/lmontesi/myres/documents/lectures/Zhu.pdf.

Zoback, M. D. (1992). First and second order patterns of tectonic stress: The world stress map project. *Journal of Geophysical Research*, 97:11703–11728.

Zoback, M. D. and Byerlee, J. D. (1975). The effect of microcrack dilatancy on the permeability of westerly granite. *Journal of Geophysical Research*, 80(5):752–755.

Zoback, M. D. and Zoback, M. J. (1989). Tectonic stress field of the conterminous united states. *Geological Society of America Memoirs*, 172:523–539.

Zoback, M. D. and Zoback, M. L. (2002). State of stress in the earth's lithosphere. In Lee, W. H. K., Kanamori, H., Jennings, P. C., and Kisslinger, C., editors, *IASPEI International Handbook of Earthquake and Engineering Seismology: Part A*, chapter 34, pages 559–568. Academic Press.

Zoback, M. L. and Magee, M. (1991). Stress magnitudes in the crust: constraints from stress orientation and relative magnitude data. *Philosophical Transactions of the Royal Society of London A*, 337:181–194.

Zolotov, O. V., Namgaladze, A. A., Zakharenkova, I. E., Martynenko, O. V., and Shagimuratov, I. I. (2012). Physical interpretation and mathematical simulation of ionospheric precursors of earthquakes at midlatitudes. *Geomagnetism and Aeronomy*, 52(3):390–397.

Zubko, P., Catalan, G., Buckley, A., Welche, P., and Scott, J. (2007). Strain-gradient-induced polarization in srtio3 single crystals. *Physical Review Letters*, 99(16):167601.

# Appendices

# A LabVIEW Programs for Acquisition of Electrical Data

Single-channel DAQ software: front panel

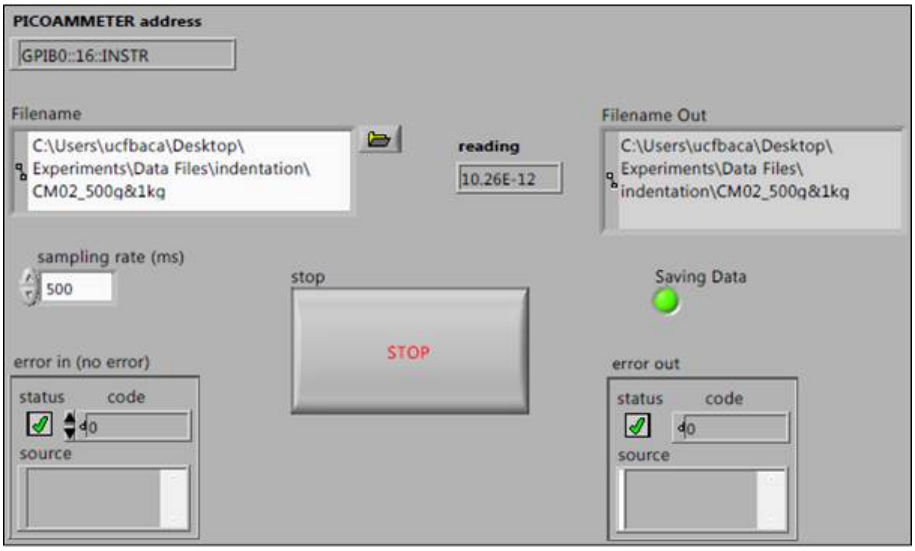

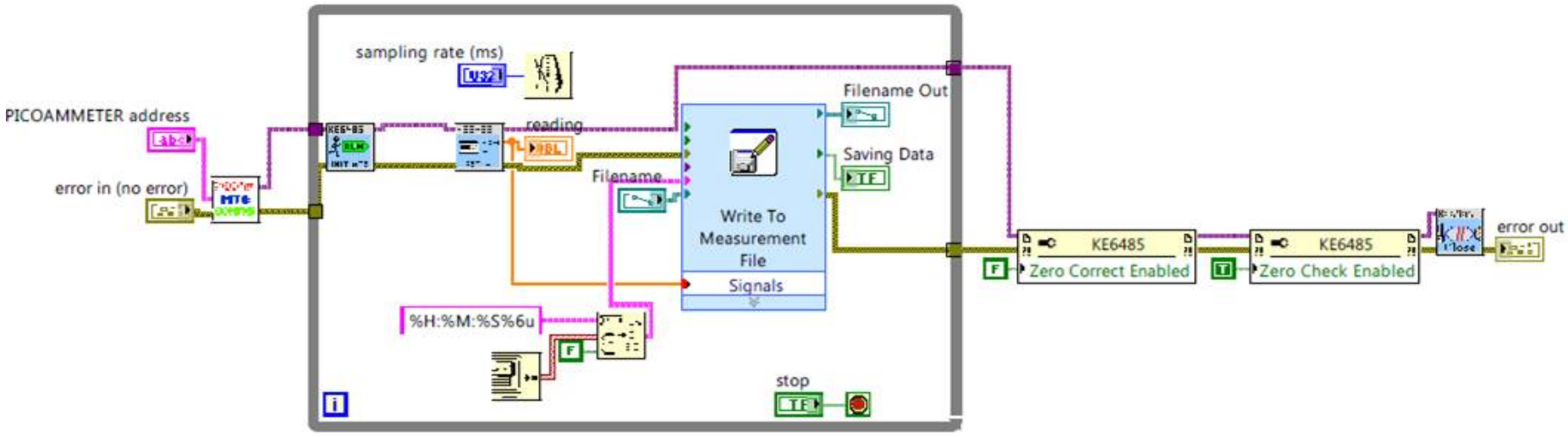
sampling rate (ms)
PICOAMMETER address
error in (no error)
reading
Filename
Filename Out
Saving Data
Write To Measurement File
Signals
%H:%M:%S%6u
stop
KE6485
Zero Correct Enabled
KE6485
Zero Check Enabled
error out

# Multi-channel DAQ software: front panel

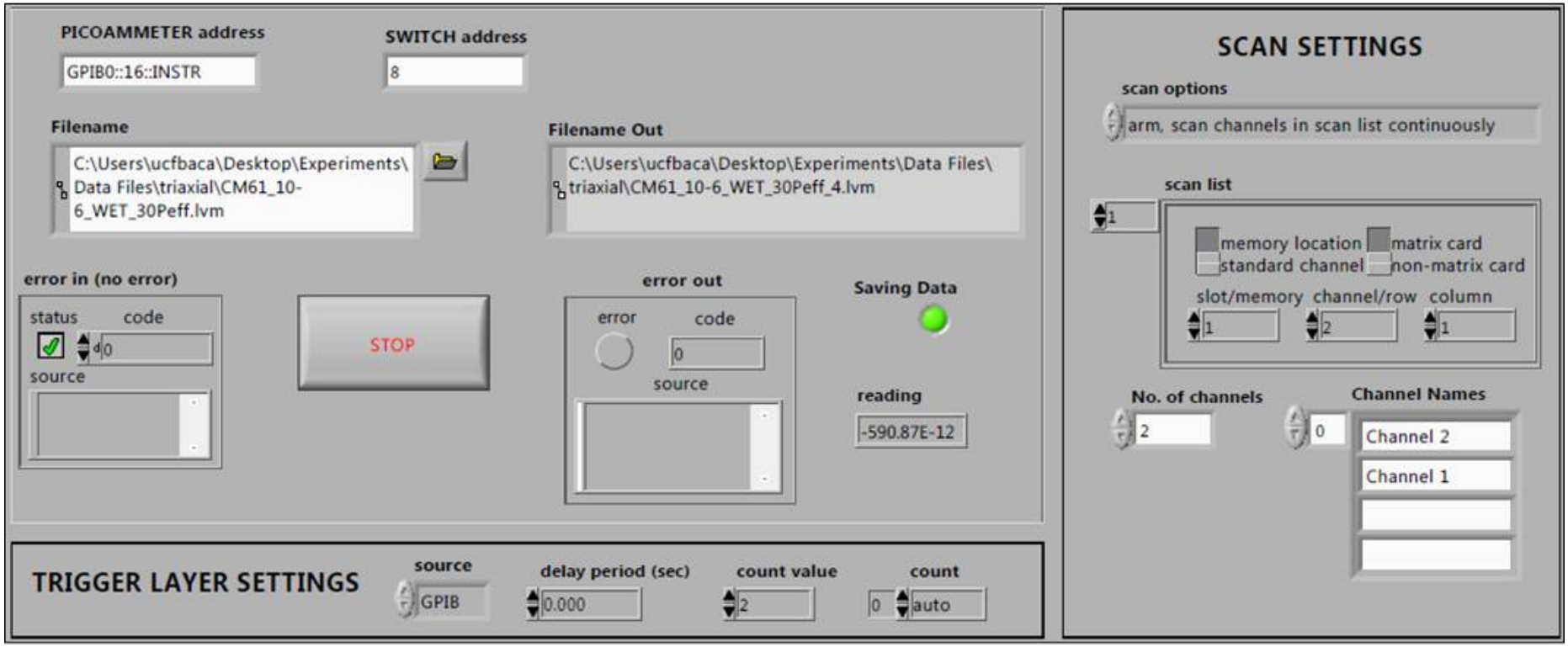

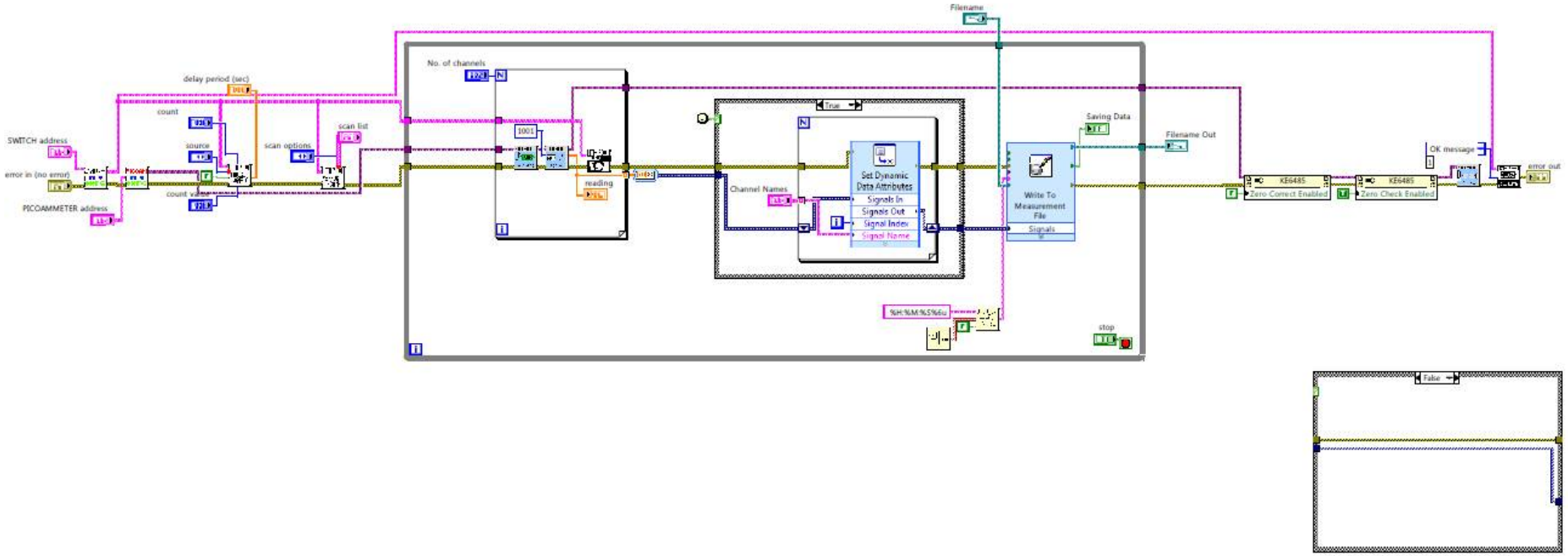
Filename
No. of channels
delay period (sec)
count
source
count value
SWITCH address
error in (no error)
PICOAMMETER address
scan options
scan list
1001
reading
True
Channel Names
Set Dynamic Data Attributes
Signals In
Signals Out
Signal Index
Signal Name
Write To Measurement File
Signals
Saving Data
Filename Out
KE6485
Zero Correct Enabled
KE6485
Zero Check Enabled
OK message
error out
%H:%M:%S%u
stop
False

# B Error Analysis Equations

Uncertainty functions used for error propagation calculations:

$Z = A \ \pm \ B$.....$(\Delta Z)^2 = (\Delta A)^2 + (\Delta B)^2$

$Z = A \ \times \div \ B$.....$(\frac{\Delta Z}{Z})^2 = (\frac{\Delta A}{A})^2 + (\frac{\Delta B}{B})^2$

$Z = A^n$.....$\frac{\Delta Z}{Z} = n\frac{\Delta A}{A}$

# C MATLAB Code

## Code for Crack Density Inversion

Modified from code kindly given to me by Phil Benson (Benson et al., 2006).

```
% clear memory
clear;

% Initial elastic matrix and parameters
E_o = 73e+9;
nu_o = 0.29;
K_f = 1.01e+5;
d = 2.7e+3;

lambda_o = E_o*nu_o/[(1+nu_o)*(1-2*nu_o)];
K_o = E_o/[3*(1-2*nu_o)];
mu_o = E_o/(2+2*nu_o);

% Initial elastic wavespeeds
Vp_o = sqrt((lambda_o+2*mu_o)/d);
Vs_o = sqrt(mu_o/d);

% Initial Crack parameters
rho = 0.; % zero crack density
zeta = 0.0001; % intial average aspect ratio
phi_o=0.0; % zero prosity

% read data file
[DATA,TEXT] = xlsread('permeability.xlsx');
[n,p]=size(DATA);

TEXT = ['Temp (degC)','Vp_d,','Vp_m','Vs_d','Vs_m','cd''ar'];
```

```
% least square fit

for m=1:n

  lsq_o=1e+3;

  for i=1:100

    for j=1:2500

    rho = (i-1)*0.01;
    zeta = (j)*1e-4;

    h = 16*(1-nu_o^2)/[9*(1-nu_o/2)];
    delta = (1-nu_o/2)*h*E_o*zeta/K_f;
    sat = delta/(1+delta);

    % Effective compliances
    E = E_o/ [1+(1+3/5*[(1-nu_o/2)*sat-1])*h*rho];
    mu = mu_o/[1+(1+2/5*[(1-nu_o/2)*sat-1])*h*rho/(1+nu_o)];
    nu = E/(2*mu)-1;
    lambda = E *nu /[(1+nu)*(1-2*nu)];

    % wavespeeds
    Vp(i,j) = sqrt((lambda+2*mu)/d)/1000;
    Vs(i,j) = sqrt(mu/d)/1000;

% fit
lsq=((DATA(m,2)-Vp(i,j))/DATA(m,2))^2+((DATA(m,3)-Vs(i,j))/DATA(m,3))^2;
        if lsq < lsq_o lsq_o=lsq;
        Vp_m=Vp(i,j);
        Vs_m=Vs(i,j);
        rho_m=rho;
        zeta_m=zeta;end
end
  end
  lsq_o;
  OUT(m,1)=DATA(m,1);
  OUT(m,2)=DATA(m,2);
  OUT(m,3)=Vp_m;
  OUT(m,4)=DATA(m,3);
```

```
  OUT(m,5)=Vs_m;
  OUT(m,6)=rho_m;
  OUT(m,7)=zeta_m;
end

% File write
csvwrite('permeability.txt', OUT);
```

# Code for $b$-value Calculation

```
% Calculates b-value from AE amplitude using Aki-Utsu maximum likelihood
% estimator together with 95% confidence limits.

function [b,ci] = bvalue(av_ampl)

m = log10(av_ampl);
[freq,mag] = hist(m,100);
m_min = mag(freq==max(freq));
m=m(m>=m_min(1));

beta = 1./(mean(m) - m_min(1));
b = beta./log(10);

ciL_beta = (1-(1.96./sqrt(length(m)))./(mean(m)-m_min(1));
ciL_b = ciL_beta./log(10);
ciU_beta = (1+(1.96./sqrt(length(m)))./(mean(m)-m_min(1));
ciU_b = ciU_beta./log(10);

ci(:,1) = ciL_b;
ci(:,2) = ciU_b;

end

% Finds instantaneous b-value for N=25 non-overlapping windows containing
% T=95 AE events.

function [av_ampl_win,eq_t_win,bout,ciout,dbout,qout,dqout]...
= bvalue_inst(av_ampl,eq_t,T)

n=length(av_ampl);
```

```
N = fix(n/T);
av_ampl_win=zeros(T,N);
eq_t_win=zeros(T,N);
bout=zeros(1,N);
ciout=zeros(N,2);
dbout=zeros(1,N);

for l=1:N
av_ampl_win(:,l)=av_ampl(1,((l-1)*T)+1:l*T);
eq_t_win(:,l)=eq_t(1,((l-1)*T)+1:l*T);
[b,ci] = bvalue(av_ampl_win(:,l));
bout(1,l)=b;
ciout(l,1:2)=ci(1,1:2);
dbout(1,l)=bout(1,l)-ciout(l,1);
end

qout=(2+bout)./(bout+1);
dqout=2.*qout.*dbout./bout;

end
```

## Code for Fitting $q$-Gaussian Model

Modified from code kindly given to me by George Michas (Vallianatos et al., 2013b).

```
function [val,A1,xrange,mse,ci] = qGaussian_actedit(data)

[n,x]=hist(data,100);
y=(n./sum(n))';
ind = find(y);
y=y(ind,:);
x=x';
x=x(ind,:);
A1=max(y);

%q-Gaussian fit
modelfun=@(b,x) A1.*((1+((b(1)-1).*(b(2))).*(x.^2))).^(-1/(b(1)-1));

beta0=[1.5 1.5];
```

```
[val,r,J,cov,mse]=nlinfit(x,y,modelfun,beta0);
ci=nlparci(val,r,'Jacobian',J);

%Gaussian fit
[sigma,mu,A]=mygaussfit(x,y,A1);

% Plot
xrange=min(x):0.001:max(x);
figure,semilogy(x,y,'o','MarkerEdgeColor','k','MarkerFaceColor','k');
ylim([0.00001 1]);
hold on
yg=A .* exp( -(xrange-mu).^2 ./ (2*sigma^2) );
plot(xrange,yg,'k--','LineWidth',2);
plot(xrange,modelfun(val,xrange),'r','LineWidth',3);
plot(xrange,modelfun(ci(:,1),xrange),'r:');
plot(xrange,modelfun(ci(:,2),xrange),'r:');
xlabel('u','FontSize',20);
ylabel('p(u)','FontSize',20);
set(gca,'XGrid','on','YGrid','on');
set(gca,'XMinorGrid','off','YMinorGrid','off');
set(gca,'FontSize',20);
legend('u','Gaussian fit','q-Gaussian fit');
hold off

end


% Function mygaussfit
function [sigma,mu,A]=mygaussfit(x,y,h)

% threshold
if nargin==2, h=0.2; end

% cutting
ymax=max(y);
xnew=[];
ynew=[];
for n=1:length(x)
    if y(n)>ymax*h;
        xnew=[xnew,x(n)];
        ynew=[ynew,y(n)];
    end
```

```
end

% fitting
ylog=log(ynew);
xlog=xnew;
p=polyfit(xlog,ylog,2);
A2=p(1);
A1=p(2);
A0=p(3);
sigma=sqrt(-1/(2*A2));
mu=A1*sigma^2;
A=exp(A0+mu^2/(2*sigma^2));
```

# Code for Testing Beck-Cohen Model

```
function T_tests(T,binwidth)

m=matfile('I_diff_qGauss');
u=m.I_diff_norm3;
time=m.time;
n=length(u);
k=kurtosis(u,0);

for l=1:n-T
    w(:,l)=u(l:T+(l-1),1); % u split into a moving window of length T
 % incrementing by 1 data point each time
end

kl=kurtosis(w,0);

i_kg=find(kl>=2.5 & kl<3.5)'; % find the gaussian windows of w
kg=kl(i_kg)';
wg=w(:,i_kg);

for n=1:length(i_kg)
[muhat(1,n),sigmahat(1,n),muci(1:2,n),sigmaci(1:2,n)] = normfit(wg(:,n));
wg_pdf(:,n) = normpdf(wg(:,n),muhat(1,n),sigmahat(1,n));
wg_pdf0(1,n) = normpdf(muhat(1,n),muhat(1,n),sigmahat(1,n));
beta = (1./(sigmahat.^2))';
d_sigmahat=sigmaci(2,n)-sigmaci(1,n)./2;
```

```
end

beta0 = mean(beta);
dbeta = mean(d_sigmahat);

mom2=moment(w,2);
mom4=moment(w,4);
theta=mom4-3.*((mom2).^2);
epsilon=sum(theta)/(3*sum((mom2).^2));

prop_g = n/l;

[xout,pdhist,phat,pci,xrange,gpdf,gnlogL] = mygamfit(beta,binwidth);

hgsave(['beta_hist_gamma','_chan3','_binwidth',num2str(binwidth),...
'_T_movwind',num2str(T)])

a=phat(1);
da=(pci(2,1)-pci(1,1))/2;
b=phat(2);
db=(pci(2,2)-pci(1,2))/2;

b_calc=beta0/phat(1);

ans(1)=beta0;
ans(2)=dbeta;
ans(3)=abs(epsilon);
ans(4)=prop_g;
ans(5)=a;
ans(6)=da;
ans(7)=b;
ans(8)=db;
ans(9)=b_calc;

[lnxout,lnpdhist,parmhat,parmci,lnxrange,lnpdf,nlogL]...
= mylognfit(beta,binwidth);

hgsave(['beta_hist_lognormal','_chan3','_binwidth',num2str(binwidth),...
'_T_movwind',num2str(T)])

mu=parmhat(1);
dmu=(parmci(2,1)-parmci(1,1))/2;
```

```
sigma=parmhat(2);
dsigma=(parmci(2,2)-parmci(1,2))/2;

lnb_calc=beta0/parmhat(1);

ansln(1)=beta0;
ansln(2)=dbeta;
ansln(3)=abs(epsilon);
ansln(4)=prop_g;
ansln(5)=mu;
ansln(6)=dmu;
ansln(7)=sigma;
ansln(8)=dsigma;
ansln(9)=lnb_calc;

AICln = 2*nlogL+2*2;
AICg = 2*gnlogL+2*2;

AIC(1) = AICln;
AIC(2) = AICg;

tf = AICln < AICg;  %if 1 then lognormal better model than gamma

save(['find_T_movwind',num2str(T),'_3'])

end

% Function mygamfit
function [xout,pdhist,phat,pci,xrange,gpdf,gnlogL]...
= mygamfit(data,binwidth)

[freq,xout]=hist(data,min(data):binwidth:max(data));
prob=(freq./sum(freq))';
pdhist=prob./binwidth;

[phat,pci] = gamfit(data);
gnlogL = gamlike(gamfit(data),data);
xrange=min(xout):0.001:max(xout);
gpdf=gampdf(xrange,phat(1,1),phat(1,2));

figure,bar(xout,pdhist)
hold on
```

```
plot(xrange,gpdf,'b','LineWidth',2);
xlabel('beta');
ylabel('probability density');
ylim([min(pdhist) max(pdhist)])
xlim([min(xout) max(xout)])
legend('beta','gamma')
hold off
hgsave(['beta_hist_gamma_',num2str(binwidth)])

end

% Function mylognfit
function [lnxout,lnpdhist,parmhat,parmci,lnxrange,lnpdf,nlogL]...
= mylognfit(data,binwidth)

[freq,lnxout]=hist(data,min(data):binwidth:max(data));
prob=(freq./sum(freq))';
lnpdhist=prob./binwidth;

[parmhat,parmci] = lognfit(data);
nlogL = lognlike(lognfit(data),data);
lnxrange=min(lnxout):0.001:max(lnxout);
lnpdf=lognpdf(lnxrange,parmhat(1,1),parmhat(1,2));

figure,bar(lnxout,lnpdhist)
hold on
plot(lnxrange,lnpdf,'b','LineWidth',2);
xlabel('beta');
ylabel('probability density');
ylim([min(lnpdhist) max(lnpdhist)])
xlim([min(lnxout) max(lnxout)])
legend('beta','lognormal')
hold off
hgsave(['beta_hist_lognormal_',num2str(binwidth)])

end
```

# D Forward Solution for Thermal Treatment Crack Density Model

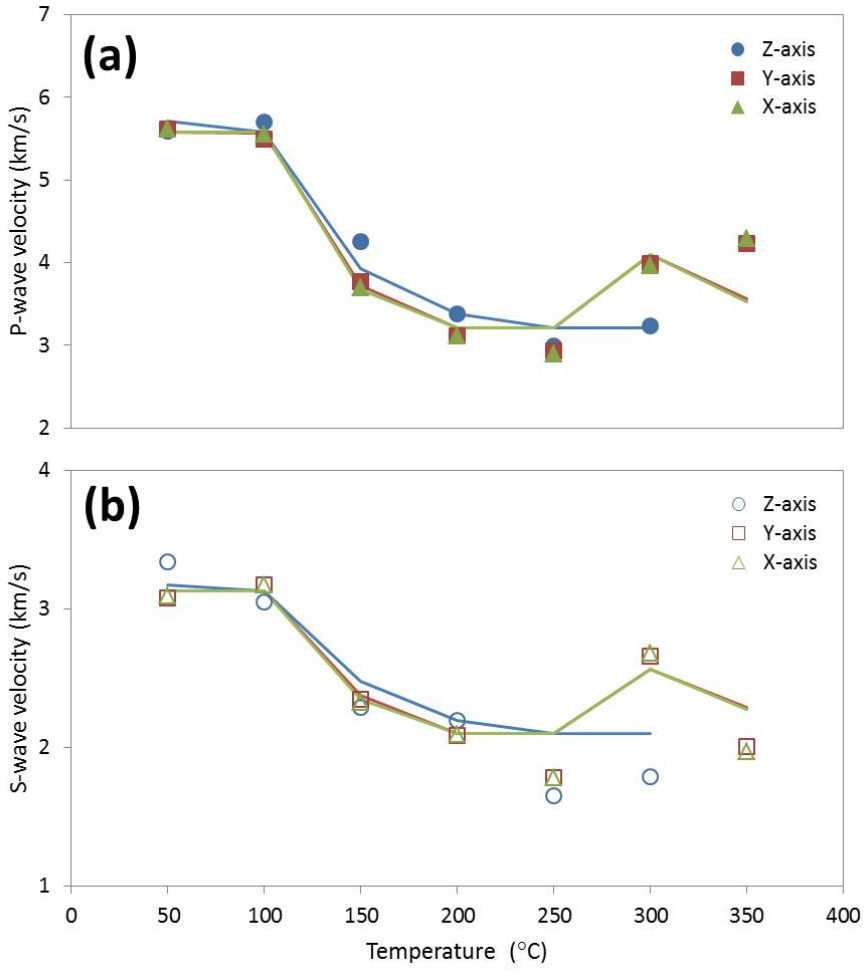


Forward solution (i.e., velocity) of Carrara marble samples from the model crack density and aspect ratio (lines) with experimental data shown as symbols (solid symbols denote $V_P$ data; open symbols denote $V_S$). Variation with thermal treatment temperature of (a) P-wave velocity and (b) S-wave velocity is shown for the Z-axis (circles), Y-axis (squares) and X-axis (triangles).

# E Deformation Categories

Deformation categories and barrelling degree for all samples tested.

| Sample | Deformation category | Barrelling degree | Sample | Deformation category | Barrelling degree |
|---|---|---|---|---|---|
| CM01 | 3 | 2 | CM30 | 0 | 1 |
| CM02 | 2 | 1 | CM32 | 8 | 0 |
| CM03 | 2 | 2 | CM34 | 8 | 0 |
| CM04 | 2 | 1 | CM35 | 8 | 0 |
| CM05 | 6 | 0 | CM42 | 5 | 1 |
| CM06 | 2 | 2 | CM43 | 6 | 1 |
| CM07 | 4 | 1 | CM44 | 4 | 3 |
| CM08 | 1 | 0 | CM45 | 6 | 0 |
| CM09 | 6 | 0 | CM46 | 6 | 0 |
| CM10 | 6 | 0 | CM47 | 6 | 0 |
| CM11 | 6 | 0 | CM48 | 5 | 1 |
| CM12 | 0 | 0 | CM49 | 5 | 2 |
| CM13 | 6 | 0 | CM50 | 6 | 1 |
| CM14 | 2 | 1 | CM51 | 4 | 1 |
| CM15 | 4 | 1 | CM52 | 5 | 1 |
| CM16 | 6 | 0 | CM53 | 5 | 1 |
| CM17 | 6 | 0 | CM57 | 6 | 0 |
| CM18 | 5 | 1 | CM58 | 6 | 0 |
| CM19 | 5 | 1 | CM59 | 6 | 0 |
| CM20 | 5 | 0 | CM60 | 4 | 1 |
| CM21 | 6 | 0 | CM61 | 5 | 1 |
| CM22 | 5 | 0 | CM62 | 5 | 1 |
| CM23 | 5 | 1 | CM63 | 7 | 0 |
| CM25 | 5 | 1 | CM64 | 7 | 1 |
| CM26 | 4 | 1 | CM65 | 3 | 2 |
| CM27 | 4 | 0 | CM66 | 1 | 0 |
| CM28 | 0 | 0 | CM67 | 8 | 0 |
| CM29 | 2 | 1 | CM68 | 5 | 2 |

# F Velocity Evolution for Strain Rate Experiments

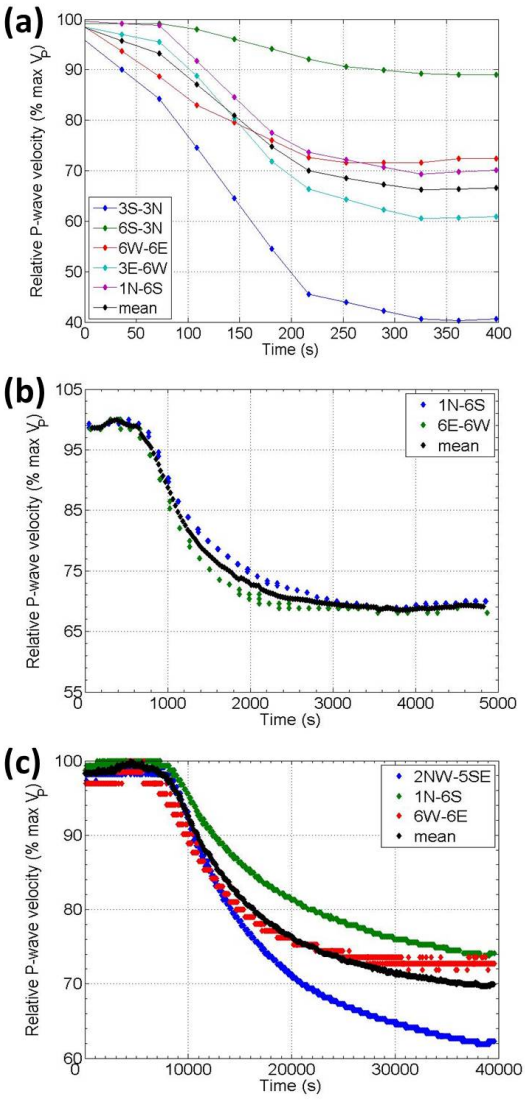


Velocity evolution for the useable orientations, together with mean values, during deformation of Carrara marble at 30 MPa and strain rates of (a) $10^{-4}$ $s^{-1}$ [CM03], (b) $10^{-5}$ $s^{-1}$ [CM06] and (c) $10^{-6}$ $s^{-1}$ [CM07].

# G $q$-Gaussian Time Interval Test

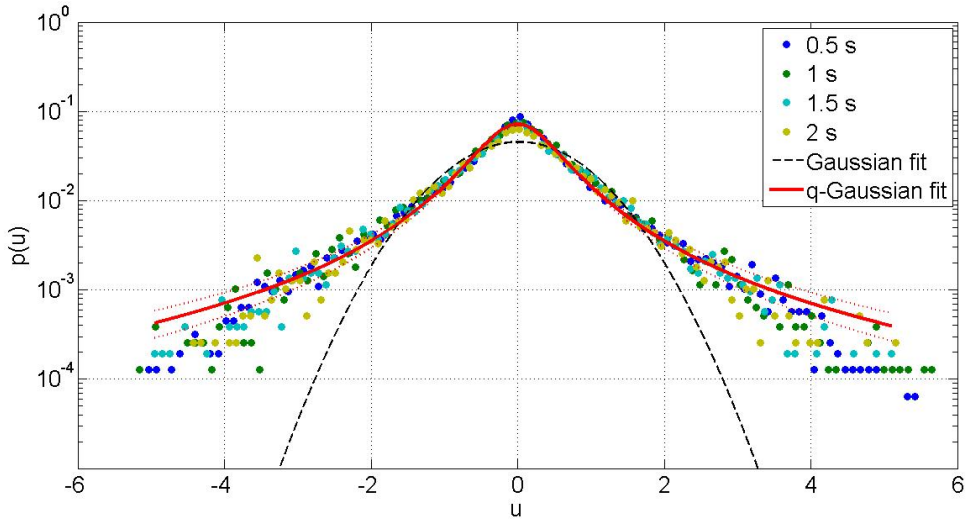


Probability distributions for electric current fluctuations calculated at four different time intervals. The Gaussian fit (dashed black line) and $q$-Gaussian fits (solid red line) shown are those for the average of these four distributions. Non-extensive parameters for the average $q$-Gaussian fit are given in the table below.

Non-extensive parameters for each of the four distributions shown in the figure above and their average.

| $\Delta t$ **(s)** | $q$ | $\delta q$ | $B$ | $\delta B$ | **mse** |
|---|---|---|---|---|---|
| 0.5 | 1.8214 | 0.0706 | 4.3440 | 0.3724 | 7.31E-06 |
| 1 | 1.8239 | 0.0501 | 3.1282 | 0.1497 | 3.13E-06 |
| 1.5 | 1.8199 | 0.0728 | 3.0726 | 0.2200 | 6.34E-06 |
| 2 | 1.8137 | 0.0561 | 2.6405 | 0.1396 | 3.19E-06 |
| average | 1.8197 | 0.0624 | 3.2963 | 0.2204 | 4.99E-06 |